Broadband emitting materials doped with thulium and holmium ions for solid-state lasers at 2 μm and beyond

Kirill Eremeev

Normandie Université

UNIVERSITÉ CAEN NORMANDIE

THÈSE

Pour obtenir le diplôme de doctorat

Spécialité **PHYSIQUE**

Préparée au sein de l'**Université de Caen Normandie**

Broadband emitting materials doped with thulium and holmium ions for solid-state lasers at 2 µm and beyond

Présentée et soutenue par

KIRILL EREMEEV

Thèse soutenue le 13/11/2024

devant le jury composé de :

M. ALAIN BRAUD	Professeur des universités - Université de Caen Normandie (UCN)	Directeur de thèse
M. DAVID LE COQ	Professeur des universités - Université de Rennes	Président du jury
M. PAVEL LOIKO	Chargé de recherche - Université de Caen Normandie (UCN)	Co-encadrant
MME ANNE DHOLLANDE	Directeur de recherche - Institut franco-allemand de recherches de Saint-Louis (ISL)	Membre du jury
M. JULIEN LE GOUËT	Ingénieur de recherche - Office National d'Etudes&recherches Aéro	Membre du jury
M. XAVIER PORTIER	Professeur des universités - ENSICAEN	Membre du jury
M. YANNICK PETIT	Maître de conférences HDR - Universite de Bordeaux	Rapporteur du jury
MME AUDREY POTDEVIN	Maître de conférences HDR - UNIVERSITE CLERMONT FERRAND 1 AUVERGNE	Rapporteur du jury

Thèse dirigée par **ALAIN BRAUD** (Centre de recherche sur les ions, les matériaux et la photonique (Caen))

ED 591 PSIME

CiMap

Université de Caen Normandie
UFR de Sciences

Centre de Recherche sur les Ions, les Matériaux et la Photonique
UMR 6252 CNRS-CEA-ENSICAEN

DOCTORAL THESIS

submitted in fulfilment of the requirements for the
degree of Doctor of Philosophy in Physics

Broadband emitting materials doped with thulium and holmium ions for solid-state lasers at 2 µm and beyond

Author
Kirill EREMEEV

Director
Alain BRAUD, Professeur des universités,
Université de Caen Normandie

Co-director
Pavel LOIKO, Chargé de Recherche HDR,
CIMAP UMR 6252 CNRS

13 November 2024

Acknowledgments

This PhD thesis was carried out at the Centre de recherche sur les Ions, les Matériaux et la Photonique in Caen. Over these 3 years, I have not only developed as a researcher but have also gained invaluable insights, friendships, and experiences that will stay with me throughout my academic journey. This thesis would not have been possible without the guidance, support, and collaboration of many individuals, to whom I am grateful.

First and foremost, I would like to express my deepest thank to my PhD supervisors, Alain Braud and Pavel Loiko. Their unwavering support, direct assistant in lab experiments, insightful guidance, and deep expertise in their respective fields have been crucial to the success of my research. I am sincerely grateful for their encouragement, mentorship, and the countless hours they invested in helping me shape this work. I would also like to thank them for their help in overcoming the difficulties I faced in France as a non-French speaker in the first months after my arrival.

I would also like to thank the researchers and engineers of OML team in particularly Gurvan Brasse for assisting some measurements, Abdel Benayad for grow of fluoride crystals and Vivien Menard for teaching me about laser crystal polishing. I want to thank other the members of the OML team with whom I have interacted over these years: Esrom Kifle and Simone Normani, the administration staff represented by Sarah Colineaux and Delphine Hasley and the other members of the CIMAP lab.

I would like to thank our collaborators who provided key materials and carried some measurements: Stanislav Balabanov (Institute of Chemistry of High-Purity Substances, Russia), Roman Maksimov (Institute of Electrophysics, Russia), Clara Saraceno (Ruhr University Bochum, Germany), Ying Hang (Shanghai Institute of Optics and Fine Mechanics), Zhongben Pan (Shandong University, China), Jiang Li (Shanghai Institute of Ceramics, China), Alexey Kornienko (Vitebsk State Technological University, Belarus). Their contributions have been crucial in achieving the results presented in this work.

Beyond the academic environment, I am fortunate to have met many wonderful friends who have made these years more enjoyable. I want to thank Anya, Amandine, Ahmed, Arnaud, Ghassen, Karel, Kirill, Kou, Min, Ji Eun, Jonathan, Lucas, and Liza for their companionship and the memorable experiences we have shared. Their friendship has been a source of strength, laughter, and encouragement, and I will always cherish the moments we spent together, both in and out of the lab.

Finally, I would like to express my deepest gratitude to my parents for their unwavering belief in me and constant support.

Table of Contents

Abstract

Novel laser-active inorganic materials doped with thulium and holmium ions have been investigated for their potential in broadly tunable and ultrafast lasers operating in the short-wave infrared spectral range of 2 to 3 μm. Lasers emitting within this spectral range find numerous applications, including light detection and ranging systems, gas sensing, medicine. They are used as amplifying systems for high harmonic generation and terahertz generation, and further frequency conversion into the mid-infrared region.

The present PhD thesis establishes relationships between the structural properties of oxide and fluoride crystalline materials, in the form of single crystals and transparent ceramics, and the spectroscopic properties of thulium and holmium dopant ions, along with their laser characteristics, which are essential for laser development. Moreover, the physical processes underlying unexpected laser behaviour are revealed. This systematic study of laser materials allows for the identification of the most promising compositions for the development of broadly tunable and ultrashort pulse lasers.

This study mainly focuses on materials that exhibit significant inhomogeneous spectral line broadening, resulting in broad and structureless absorption and emission spectra of the dopant ions. In order to promote this effect, several strategies have been considered, including rare-earth ion clustering, local structure disorder, compositional disorder in solid-solution compounds, and phonon-sidebands arising from electron-phonon interactions.

The formation of thulium and holmium clusters in calcium fluoride crystals enables efficient and broadly tunable laser operation around 2.1 μm. A polarized spectroscopic study of the emission properties of holmium ions in disordered calcium rare-earth aluminate crystals sheds light on its broadband spectral properties and on the role of multiphonon assisted emission, which occurs beyond electronic transitions, in unexpected laser emissions observed in mode-locked lasers. In solid-solution sesquioxide ceramics of the yttria-lutetia-scandia ternary system doped with thulium ions, there is a strong and nearly linear variation of the crystal-field strength with the mean size of the host-forming cation. This relationship allows for the customization of both the position and width of the emission band above 2 μm by appropriately adjusting the host composition. Highly efficient laser operations of thulium- and holmium-doped sesquioxides around 2.1 μm and 2.3 μm have been demonstrated.

General Introduction

LASER is an acronym for Light Amplification by Stimulated Emission of Radiation. Since the 1960s, laser technology has been transforming and enhancing our daily lives. Current trends in laser development include integrated optics, quantum technology, ultrafast and extreme light physics. Particularly, ultrafast optics, as a part of laser physics, focuses on ultrafast phenomena occurring on a time scale of picoseconds or less. To achieve ultrafast pulses, mode-locked lasers are typically used. They have found unique applications where lasers working in the continuous-wave regime cannot be used. These applications include pump-probe time-resolved spectroscopy on the pico- and femtosecond time scale, terahertz science and technology, nonlinear frequency conversion, generation of frequency combs, and high harmonic generation. The latter plays an important role in achieving attosecond pulses to monitor electron dynamics using pump-probe spectroscopy while frequency combs are important for high precision optical metrology.

Since the first development of ultrafast lasers based on mode-locked titanium-sapphire lasers in 1986, they have dominated the field of ultrashort pulses generation. Subsequently, the advancement of ytterbium-based mode-locked lasers emitting around 1 μm has expanded the range of applications for ultrafast lasers.

Presently, there is a growing trend in the development of pump sources for mid-infrared (3-15 μm) ultrafast optical parametric oscillators based on non-oxide nonlinear crystals. This wavelength range can be seen as a connection to the mid-infrared region, also referred to as the molecular fingerprint region, due to its inclusion of characteristic absorption lines of various important bio- and atmospheric molecular species. Atmospheric transparency windows at 3-5 μm and around 10 μm also lie in this spectral region, which can be used for mid-infrared optical communication. To effectively pump these laser sources, ultrafast lasers operating between 2 and 3 μm, within the short-wavelength infrared spectral range are required.

The main challenge in developing ultrafast lasers emitting in the short-wavelength infrared spectral range currently lies in the field of materials science. As core of any laser, the active laser medium doped with optically active rare-earth ions is the source of optical gain within a laser. Consequently, laser engineering progresses in tandem with advancements in the materials science of laser-active media. For solid-state lasers, these materials include amorphous materials (glasses in shape of fibers), single-crystals or polycrystalline materials (transparent ceramics). To develop solid-state lasers capable of generating ultrashort pulses, the gain medium must possess a significant inhomogeneous spectral line broadening (broad and structureless fluorescence spectra) caused by the disorder in the structure. A well-known and representative example of such a material is glass doped with thulium and holmium ions, which exhibits smooth and broad emission gain profiles. However, glasses exhibit poor thermal and mechanical properties compared to single crystals. Therefore, it is essential to shape these glasses into fibers to compensate for their low thermal conductivity, although this also complicates the laser setup.

On the other hand, certain crystals exhibit high thermal conductivity and are available in various shapes. For instance, they can be fabricated in the form of thin disks with a thickness on the order of µm. Transparent ceramic technology has become competitive with single-crystal growth methods and is even superior in some cases. Fabrication techniques for waveguide structures are widely available, including liquid phase epitaxy and femtosecond direct laser writing. All of these fabrication methods allow for precise control over the size of laser elements and, consequently, all laser setups. However, in general, thulium and holmium ions in these materials possess structural profiles that hinder the generation of femtosecond pulses from these lasers in a mode-locked regime.

This PhD thesis is part of the ANR project Short Pulse solid state LasErs aND amplIfiers beyonD 2 µm (SPLENDID2), which aims to develop novel laser-active inorganic materials for ultrafast lasers and amplifiers operating in the short-wave-infrared spectral range between 2 and 3 µm. Specifically, this thesis focuses on creating materials doped with thulium and holmium ions to achieve broadly tunable and ultrafast laser performance within this spectral range.

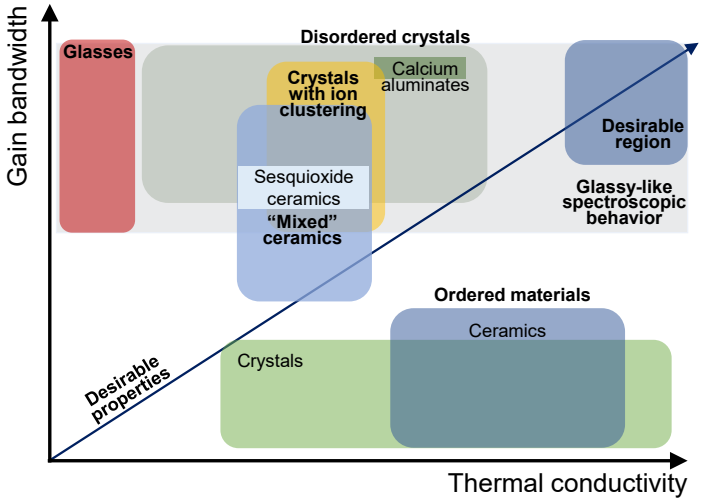

Figure 1. Connection .between thermal conductivity and gain bandwidth of rare-earth ions in glasses, disordered and ordered crystals.

To achieve desirable properties in the gain media for ultrafast lasers, a dedicated approach based on material engineering should be employed. Figure 1 shows a schematic diagram illustrating the dependence of the gain bandwidth of dopant ions with the thermal conductivity in glasses, disordered, and ordered crystals. We propose in this work strategies that induce strong inhomogeneous spectral line broadening, resulting in structureless and broad gain profiles of the dopant ions. This material engineering approach could enable the generation of few-optical-cycle pulses from mode-locked lasers. The strategies are: i) formation of rare-earth ion clusters in fluorite-type crystals; ii) utilization of naturally structurally disordered crystals with random site distribution for cations (such as aluminates); iii) formation of compositional disorder in solid-solution compounds using transparent ceramic technology, *e.g.*, for "mixed" cubic sesquioxides. Moreover, homogeneous broadening caused by the interaction of dopant

ion electrons with phonons in host matrices of ordered crystals plays an important role in generating ultrashort pulses.

Another challenge for a laser material designed to support femtosecond pulse generation and broadband wavelength tuning is the strong structured water vapor absorption in the atmosphere at 2 μm. This issue can be addressed through two strategies: using materials with strong crystal-fields, where dopant thulium ions naturally emit above 2 μm, holmium-doped or materials codoped with both thulium and holmium ions.

This thesis begins with Chapter I, which provides an overview of lasers operating at 2 μm and beyond, along with their potential applications. It discusses the general aspects of rare-earth ion spectroscopy, focusing on intra-ionic and inter-ionic processes in lanthanide ions within solid-state materials. Additionally, various strategies for inducing spectral line broadening in dopant ions in crystals and ceramics are explored.

Chapter II presents the results of efficient and broadly tunable thulium- and holmium-doped calcium fluoride lasers operating at 2.1 μm, featuring rare-earth ion clustering. It also introduces the first thulium-doped calcium fluoride waveguide laser at 1.9 μm, produced by femtosecond direct laser writing.

Chapter III examines structurally disordered calcium aluminate, scandate, and garnet crystals. It describes the unexpected laser behavior of a holmium-doped calcium gadolinium aluminate laser in the mode-locked regime. The chapter further explains the broad spectral properties of thulium and holmium ions in gadolinium scandate crystals and demonstrates efficient laser operation at 2.1 μm. Additionally, it discusses the influence of codoping with ytterbium and europium ions on the spectroscopic properties and luminescence lifetimes of holmium ions in calcium niobium gallium garnet crystals.

Chapter IV provides results of a comprehensive investigation on compositionally "mixed" transparent cubic sesquioxide ceramics doped with thulium and holmium ions, with a particular focus on their emission properties at 2 μm and the inhomogeneous spectral line broadening resulting from compositional disorder. The first 2.3 μm laser operation of thulium-doped sesquioxide is also presented.

The final Chapter V presents the results on polarized spectroscopic properties of thulium doped rare-earth orthovanadate crystals with a strong electron-phonon interaction at 2.3 μm.

Chapter I

State-of-the-art: Materials doped with Thulium and Holmium Ions for Lasers at 2 μm and Beyond

Thulium (Tm^{3+}) and holmium (Ho^{3+}) ions are trivalent lanthanide cations that were discovered by the Swedish chemist Per Theodore Cleve in 1878 as their sesquioxides Tm_2O_3 and Ho_2O_3. The introduction of stimulated emission by Albert Einstein in 1917 and the first LASER (Light Amplification by Stimulated Emission of Radiation) from Tm^{3+} and Ho^{3+} doped materials at 2 μm was achieved in 1963, which sparked interest in the development of 2 μm lasers. They have found applications in medicine, LIDAR (Light Detection And Ranging), direct optical communication, material processing, and as a pump source for Cr^{2+}-based lasers, emitting further in the mid-infrared spectral region. The current trends in laser development include the generation of femtosecond pulses and the miniaturization of laser cavities, expanding the application field of 2 μm lasers. The applications extend across various fields such as quantum technology, integrated photonics, high-intensity physics, frequency metrology, laser spectroscopy, nonlinear frequency conversion, and terahertz science.

This chapter is organized as follows: in Section I.1, an overview of lasers emitting at 2 – 3 μm, the current trends in ultrafast laser development, and the potential of waveguide lasers at 2 μm are provided. In Section I.2, general aspects of rare-earth ion spectroscopy are summarized. In Section I.3, the laser operation schemes of thulium and holmium ions, processes affecting the laser efficiency, and approaches to quantify the energy-transfer between thulium and holmium ions are discussed. In Section I.4, the current trends in material engineering for 2 μm solid-state lasers and methods to induce inhomogeneous spectral line broadening of dopant ions in laser materials to achieve ultrashort pulses are discussed.

I.1. Lasers emitting at 2 – 3 μm: operation schemes and applications

This section provides an overview of various types of laser sources emitting in the 2 – 3 μm spectral range. The principles of their work, applications, and various geometries are discussed. The detailed consideration of thulium and holmium ions as viable solutions for the 2.3 and 3 μm spectral range is presented. The current trends in developing ultrashort pulse lasers and the potential of waveguide lasers at 2 μm are discussed.

I.1.A. Laser sources emitting at 2 – 3 μm: an overview

Since Laser requires amplification of the desired radiation to achieve laser operation, amplification is only possible if a population inversion is achieved. If an inverted medium is placed between two resonator mirrors, spontaneously emitted photons can travel back and forth between the mirrors and initiate stimulated emission inside the inverted medium. This

results in an amplified light field inside the resonator. Through a partially reflective mirror, a portion of this light field can be extracted, forming the laser beam.

Since the first laser operations of crystals doped with rare-earth ions (RE^{3+}) around 2 and 3 μm was achieved [Joh63, Rob67], it has gained significant interest in laser sources emitting at wavelengths between 2 and 3 μm, within the short-wavelength infrared (SWIR, IR-B,) spectral range. This range bridges the gap between the near- and mid-infrared regions. The mid-infrared (MIR) region is known as the molecular fingerprint region due to the multiple characteristic absorption lines of biological and atmospheric molecular species. This region is also relatively eye-safe, as such light is absorbed by the eye before it can reach the retina.

Figure I.1 shows the laser sources covering the spectral range of 2 – 3 μm. The generation of coherent radiation at these wavelengths can be achieved through a number of different approaches. Table I.1 summarizes rare-earth and transition metal laser channels within the SWIR and MIR spectral regions.

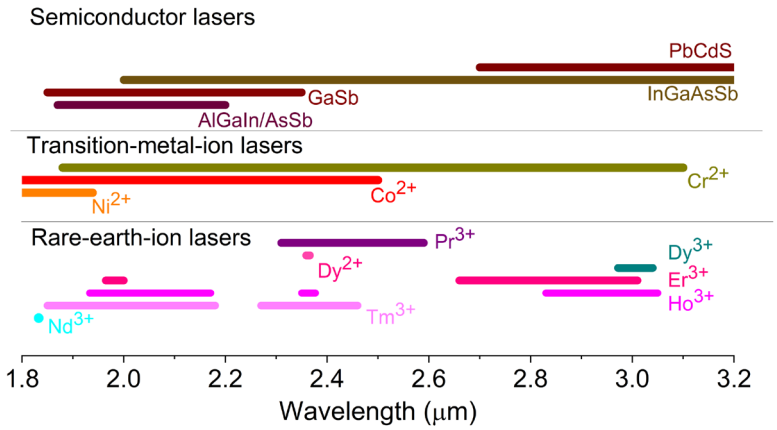

Figure I.1. Laser sources covering the 2 – 3 μm spectral range (after [Kam13]).

Table I.1. Rare-earth and transition metal laser channels in SWIR and MIR spectral ranges [Kam13].

Spectral range, (μm)	Lasing ion	SE channel	*T*, (K)	Pumping
1.833	Nd^{3+}	$^4F_{3/2} \rightarrow {}^4I_{15/2}$	300	Xe
1.85 to 2.18	**Tm^{3+}**	**$^3F_4 \rightarrow {}^3H_6$**	77 to 300	Xe, Hg, W, laser, LD
1.88 to 3.10	Cr^{2+}	$^5E \rightarrow {}^5T_2$	300	Laser, OPO
1.965 to 2.003	Er^{3+}	$^4F_{9/2} \rightarrow {}^4I_{11/2}$	300	Xe
1.933 to 2.171	**Ho^{3+}**	**$^5I_7 \rightarrow {}^5I_8$**	77 to 300	Xe, Kr, W, PCh, solar, laser, LD
2.234 to 2.827	U^{3+}	$^4I_{11/2} \rightarrow {}^4I_{9/2}$	77 to 300	Xe, Hg, laser
2.274 to 2.46	**Tm^{3+}**	**$^3H_4 \rightarrow {}^3H_5$**	300	Xe, laser, LD
2.31 to 2.59	Pr^{3+}	$^3F_3 \rightarrow {}^3H_5$	300	laser
2.35 to 2.377	Ho^{3+}	$^5F_5 \rightarrow {}^5I_5$	100	Xe
2.359 to 2.366	Dy^{2+}	$^5I_7 \rightarrow {}^5I_8$	4.2 to 120	Xe, solar, PCh, LED, laser
2.432	Dy^{3+}	$^6H_{9/2}+{}^6F_{11/2} \rightarrow {}^6H_{13/2}$	300	laser
2.660 to 3.01	Er^{3+}	$^4I_{11/2} \rightarrow {}^4I_{13/2}$	77 to 400	Xe, laser, LD
2.83 to 3.05	Ho^{3+}	$^5I_6 \rightarrow {}^5I_7$	77 to 350	Xe
2.972 to 3.040	Dy^{3+}	$^6H_{13/2} \rightarrow {}^6H_{15/2}$	77 to 300	Xe, laser

[a]LED – light-emitting diode; PCh – pyrochemical pumping; FL – fiber laser; OPO – optical parametric oscillator; Xe – xenon, W – tungsten-iodine, Hg – mercury, and Kr – krypton lamps, respectively. **This work**.

Lasers based on RE^{3+} ions. Thulium – Tm^{3+}, holmium – Ho^{3+}, erbium – Er^{3+} in transparent dielectric host matrices are among the most studied lasers based on RE^{3+} ions. Typical host matrices are oxide and fluoride single-crystals / ceramics, glasses in the form of fibers, crystalline layers / microstructured crystals. Such lasers benefit from optical pumping by commercial semiconductor laser diodes, which enables power scalability, high laser efficiencies and well-developed technology of single-crystal growth/glass melt casting. However, the main drawback is related to the relatively narrow and typically structured emission bands of rare-earth ions, which limits the range of accessible wavelengths and constrains the generation of ultrashort pulses. From the perspective of material properties, oxide matrices are not optimal for the development of SWIR lasers. They exhibit limited transparency in the infrared (a state-of-the-art example is fused silica) and high phonon energies, which result in strong non-radiative relaxation. Consequently, the use of non-oxide matrices, such as fluoride ones, is preferable. However, the fabrication of fluoride materials is considerably more challenging due to the necessity of a controlled atmosphere during synthesis.

Lasers based on transition metal ions (TM^{2+}). Another class of SWIR laser sources is found with TM^{2+} such as Cr^{2+} or Fe^{2+} doped binary (*e.g.*, ZnSe, ZnS, CdSe, etc.) and ternary chalcogenide semiconductor crystals. They represent solid-state gain media with strong and ultra-broad absorption and emission bands in the SWIR spectral range, see Figure I.2 [Sor04, Mir18, Eva23]. As wide bandgap II–VI semiconductor crystals, they have a tendency to crystallize as tetrahedral-coordinated structures and the heavy anions in the crystals provide a very low energy optical phonon cutoff, which makes them transparent in a wide spectral region and decreases the efficiency of nonradiative decay, thus increasing the yield of fluorescence at room temperature.

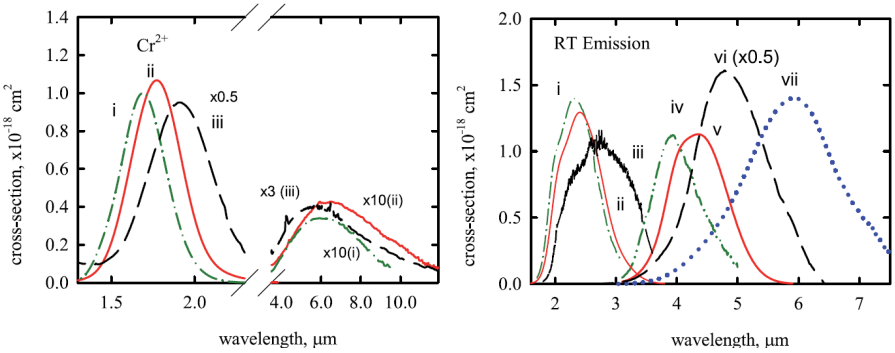

Figure I.2. Absorption (*left*) and stimulated-emission (*right*) cross-sections of Cr^{2+} ions in (i) ZnS, (ii) ZnSe, (iii) CdSe crystals and Fe^{2+} ions in (iv) ZnS, (v) ZnSe, (vi) CdSe and (vii) CdTe crystals at room-temperature (After [Mir18]).

Cr^{2+}-doped II–VI lasers provide access to the 2-3 µm wavelength region. Their main advantages are broad absorption and emission bands and high transition cross-sections (T_d sites), leading to a broadband and smooth tunability, 100-sub-femtosecond pulse generation at the high efficiency, as well as Watt-level output powers and narrow spectral linewidth. One of the crystals of this family, Cr^{2+}:ZnSe, exhibited efficient room-temperature diode-pumped continuous-wave and mode-locked operation also in the ceramic form [Sor14].

The main drawbacks of these lasers limiting their widespread use are: i) complicated synthesis procedure, limited optical quality of II–VI compounds, complicated doping by Cr^{2+} ions; ii) low to moderate laser induced damage threshold (LIDT); iii) strong thermal lensing; iv) expensive and complex pump sources are needed.

Semiconductor lasers. Semiconductor lasers emitting in different spectral ranges are shown in Figure I.3 [Ele99, Tou12]. There exist two distinct approaches for the fabrication of semiconductor laser diodes operating near 2 μm and beyond. The first employs the formation of a laser heterostructure comprising layers of AlGaInAsSb. This approach offers the advantage of enabling the emission wavelength range to extend well beyond the 2 μm range, as well as providing a solution that avoids some of the challenges associated with previous approaches. The second approach involves the utilisation of strained-layer InGaAs quantum wells (QWs) embedded within an InGaAsP heterostructure laser diode. It is possible to operate high-power InGaAs/InGaAsP broad-area and single-stripe index-guided laser diodes. These laser sources, which are commonly used for in-band pumping of Ho lasers, are particularly suited to applications requiring the generation of high power at specific wavelengths. It has been demonstrated that the GaInAsSb/AlGaAsSb quaternary/quaternary system, which is grown in close lattice match to GaSb substrates, is a promising candidate for developing laser diodes operating at wavelengths above 2 μm. Al-rich AlGaAsSb compounds, exhibiting wide bandgaps and low refractive indices, are employed as cladding and barrier layers. The narrow gap GaInAsSb alloy is dedicated to emitting layers. The main limitations of these types of laser sources relate to their low brightness, namely, the low output beam quality.

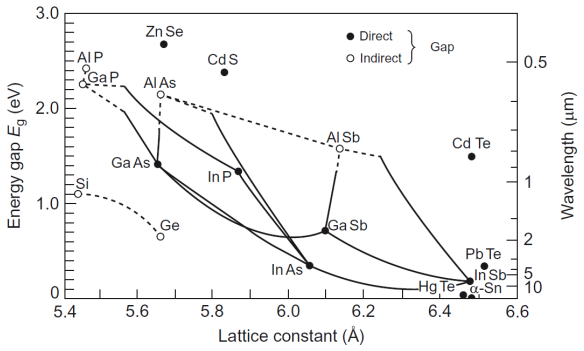

Figure I.3. Bandgap and lattice parameters of various semiconductors [Tou18].

Raman-shifted lasers. The generation of laser emission in the 2 μm and beyond wavelength range can be achieved via stimulated Raman scattering (SRS) using Raman-active crystals [Vod20]. The wavelengths in the 2 μm range can be achieved either by multiple (cascade) conversion stages or by a single-stage conversion process using a long-wavelength pumping method, which employs nanosecond erbium or thulium lasers. The primary challenge is that the SRS threshold in crystals rapidly increases with an increase in the pumping wavelength due to a reduction in gain. The currently employed Raman-active crystals are typically mono- and double-tungstates, such as $BaWO_4$ and $KGd(WO_4)_2$. For example, Raman shifted Nd^{3+}-doped $Y_3Al_5O_{12}$ laser at 2.92 μm (2^{nd} Stokes) can be used as pump source for Fe^{2+}:ZnSe laser system

[Fed06]. However, bulk Raman lasers exhibit low beam quality and limited conversion efficiency.

Optical parametric sources. Examples of such devices include optical parametric oscillators (OPOs), optical parametric generators (OPGs), and difference frequency generators (DFGs) which offer a universal solution for generating laser emission at wavelengths where other lasers are not available or have limitations [Pet15]. For example, OPOs convert an input laser wave (referred to as the "pump") with a frequency ω_P into two output waves of lower frequency (idler, ω_i, and signal, ω_S) through second-order nonlinear optical interaction. The OPO is essentially composed of an optical resonator and a nonlinear optical crystal. The sum of the output waves' frequencies is equal to the input wave frequency: $\omega_i + \omega_S = \omega_P$. For historical reasons, the two output waves are designated as "signal" and "idler", with the output wave with a higher frequency designated as the "signal". However, it should be noted that any OPO requires a pump source with high optical intensity and relatively high spatial coherence. Although these systems offer broadband wavelength tuning over the desired spectral range, they are complex and costly. They require nonlinear optical crystals to be cut along special (phase-matching) directions, and they suffer from compromised beam quality and sensitivity to the instabilities of the pump laser.

I.1.B. Applications of 2 µm lasers

Laser sensing and spectroscopy. Since the 2 µm radiation is considered "eye-safe," it makes 2 µm lasers particularly relevant for free-space optical communications or light detection and ranging systems [Sch10, Li23]. They have almost similar operating principles to radar systems, except that aerosol particles suspended in the air provide the return signal, (see in Figure I.4) making 2 µm lasers well-suited for measuring greenhouse gases [Sin15]. These lasers can be used for the direct measurement of wind velocity and the detection of both water vapor and carbon dioxide concentration [Tac98, Sch10, Pal12, Miz18, Lah21].

• *Atmospheric sensing*: measuring water vapor concentration, cloud properties, gas and aerosol concentrations, surface irradiance, top of atmosphere irradiance, and detecting pollutants in the atmosphere [Sch10].

• *Detection of atmospheric gases and molecules*: the wavelength range at 2 µm consists of absorption lines of several atmospheric gases, such as H_2O, CO_2, N_2O, which can be detected and analyzed in this spectral region. Techniques for chemical sensing based on short, medium, and long detection paths can be employed. These systems are based on the backscattered light measurement. In the chemical and petroleum sectors, these lasers enhance safety, quality control, and regulatory compliance by enabling the accurate detection of hazardous substances [Sch10].

• *Wind velocity measurements*: the wind velocity can be measured using a Doppler-LIDAR system operating with heterodyne detection. In this system, aerosol particles, which move at the same speed as the surrounding air, scatter the incident laser radiation [Ebe80]. This scattering imparts a slight Doppler shift to the returning radiation, see Figure I.4. By employing heterodyne detection, the Doppler shift can be accurately measured, allowing the

determination of wind velocity at the scattering location. This method provides precise and reliable measurements of wind speed and direction, aiding in weather forecasting and climate studies.

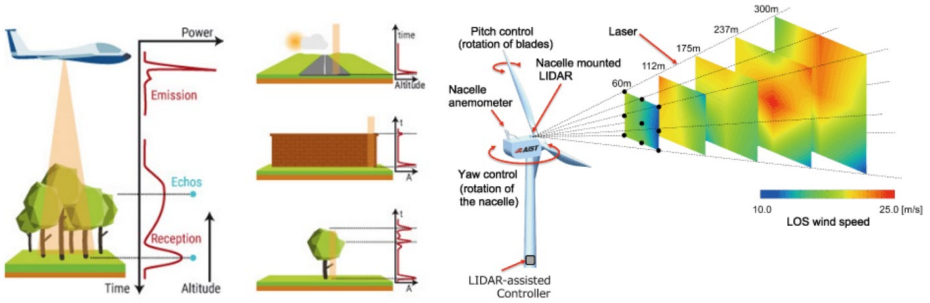

Figure I.4. Illustration of working principle of a LIDAR to produce a digital elevation model or a digital terrain model for 3D mapping (*left*) and a Dopler-LIDAR to measure velocity of wind (*right*). Taken from [https://www.yellowscan.com/knowledge/how-does-lidar-work/] [https://www.aist.go.jp/fukushima/en/unit/WPT_e.html].

• Also, ground-based 2 µm *Doppler-LIDAR systems* can be used at airports to identify the formation of wake vortices during take-off and landing of aircraft. The goal of this system is to detect wake-vortex formation during approach and landing to wind shear and clear-air turbulences during the flight to increase the capacities of airports and the flight safety.

• *Infrared countermeasures*: due to the atmospheric window around 2 µm, lasers are used in infrared countermeasure systems to protect aircraft and other vehicles from heat-seeking missiles. The lasers can confuse or blind the missile's infrared guidance system, enhancing the survivability of platforms.

Free-space optical communication. 2 µm lasers can be used for free-space optical communications if a laser emits at emission wavelengths in the first water absorption window at 2 µm. The long ranges can be reached if a laser operates slightly above 2 µm and high-power can be achieved due to the "eye-safe" wavelength [Wil96, Sch10].

Medical applications. The favorable water absorption also makes such lasers highly useful in medical applications. As illustrated in Figure I.5, the wavelength of 2 µm exhibits a pronounced water absorption peak, which results in a reduction of the penetration depth of this wavelength in tissues to a few hundred micrometers. Due to the strong absorption of water, a substantial amount of heat is generated in small areas, which is beneficial for the precise cutting of tissues [The07]. Additionally, the bleeding that occurs during laser cutting is suppressed by coagulation, which renders 2 µm lasers optimal for numerous surgical procedures [Szl09, Sch10, Yin17].

Furthermore, the laser radiation can be delivered by common silica-based fibers, allowing minimally invasive surgery. This is not possible at other wavelengths that exhibit high absorption in water, such as 3 µm, or wavelengths that are even further in the infrared. For instance, breath analysis using these lasers can detect chemical markers like ammonia (NH_3), facilitating the early diagnosis of chronic medical conditions. Their precise and non-invasive sensing capabilities make 2 µm lasers valuable tools for improving safety and health.

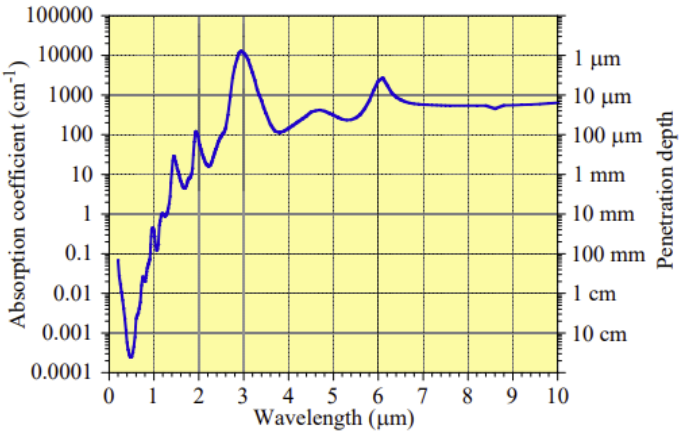

Figure I.5. Optical absorption in water (*y*-axis scale is logarithmic) [Wal09].

Scientific applications. 2 µm-lasers are also relevant for scientific applications and laser development, for example, the pumping of mid-infrared OPOs based on non-oxide non-linear crystals [Bud00, Pet15] or Cr^{2+}-based lasers, see Figure I.2. Efficient pumping of Cr^{2+} lasers has already been demonstrated with diode lasers and thulium lasers [Mir10]. OPOs can be ideally pumped by Ho lasers around 2.1 µm.

Material processing. The 2 µm lasers are highly attractive for material processing, especially for plastics, because it can process plastic materials that are transparent in the visible wavelength range. Figure I.6 illustrates the welding process for two transparent plastics and provides examples of plastic welds made using a thulium 2 µm YAG laser. Plastic materials absorb sufficiently at around 2.0 µm, which enhances direct processing with lasers at this wavelength. This absorption enables efficient cutting, welding, and marking. In contrast, "standard" 1 µm lasers require additives to increase plastic absorption, complicating the fabrication process and potentially introducing issues, especially in medical applications where such additives may be prohibited [Sch10].

Laser systems designed for these applications must provide high continuous-wave output powers with excellent beam quality are suitable for industrial use. Additional applications include the processing and fabrication of transparent bio-fluidic chips, where precise welding or the generation of micro-channels is essential for biological or medical mass-screening experiments.

Many applications of lasers with wavelengths in the 2 µm region demand high output powers. Depending on the considered application, further requirements need to be fulfilled, such as high beam quality or the option to select particular wavelengths.

I.1.C. 2.3 µm laser sources: thulium ions offer a viable solution.

As mentioned earlier, there exist several possibilities to achieve laser emission around 2.3 µm.

• The first option is to use transition-metal-ion doped II-VI materials, i.e., Cr^{2+}:ZnS or Cr^{2+}:ZnSe [Sor04, Mir14]. Sorokina et al. reported on a continuous-wave Cr^{2+}:ZnS laser delivering 100 mW at 2.35 µm with a slope efficiency of 16%, tunable between 2.19 and 2.47 µm [Sor02]. Further power scaling reaching multi-watt regime with improved slope efficiency

was demonstrated later on [Sor04, Mir10]. Mode-locked Cr^{2+}:ZnS and Cr^{2+}:ZnSe lasers that generate femtosecond pulses are reported [Car00, Tol14, Sor15]. Examples of broadly tunable and high-power CW Cr^{2+}:ZnSe laser are shown in Figure I.7.

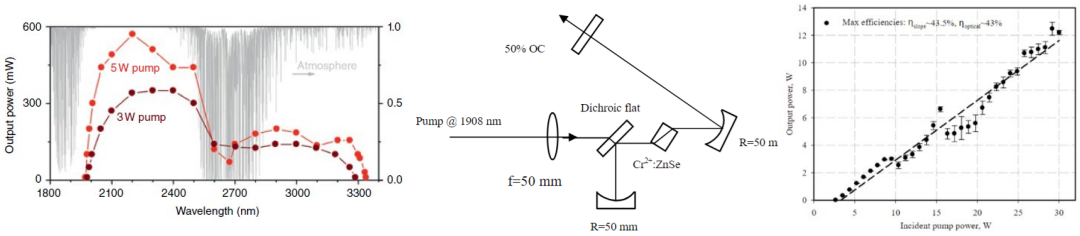

Figure I.7. Tunability range of a CW Cr^{2+}:ZnSe laser. Transmission of the atmosphere is shown in the background (*left*), taken from [Vod20]; schematic diagram of the Cr^{2+}:ZnSe laser and output power vs incident pump power (*middle*). Input-output dependencies (*right*). (after [Mos09]).

• The second option involves the use of semiconductor materials (GaInAs / InP or GaInAsSb / GaSb) in Vertical-Cavity Surface-Emitting Lasers [Boe11] or diode lasers [Gee06]. Despite the relatively complex design and fabrication methods, the power scaling capabilities of such lasers (single-emitters) are limited. Geerlings et al. presented a GaSb-based diode laser that generates 16.5 mW at 2.23 µm with a wavelength tunability between 2.21 and 2.39 µm [Gee06]. The output power can be scaled to reach watt-level in an array configuration; however, this comes with a trade-off in spatial quality [Sht04]. Furthermore, the ultrafast operation of such lasers has been poorly studied.

• After the first demonstration of 2.3 µm laser emission from Tm^{3+} ions in a $YAlO_4$ crystal through the $^3H_4 \rightarrow {}^3H_5$ transition [Hob72], this laser emission gained significant attention [Cai75, Pin94]. However, it was considered inefficient, and the $^3F_4 \rightarrow {}^3H_6$ transition at 2 µm received much more attention [Sto90]. Due to the development of high-power and low-cost pump sources (*e.g.*, AlGaAs laser diodes [Yor18] whose emission at 0.8 µm well overlaps with an intense and broad $^3H_6 \rightarrow {}^3H_4$ Tm^{3+} absorption band, see Figure I.8), the advantage of 2.3 µm lasers based on Tm^{3+} ions, compared to other sources emitting in this spectral range and different pumping schemes (i.e., upconversion pumping scheme) have allowed Tm-based lasers to be considered a viable alternative for the 2.3 µm region.

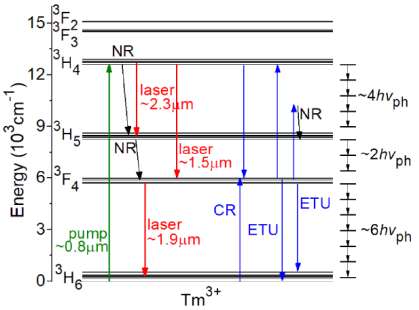

Figure I.8. Energy-level scheme of Tm^{3+} ions demonstrating the achieving 2.3 laser emission [Loi21].

In Figure I.9 shows the Ti:Sapphire pumped Tm:$LiYF_4$ laser emitting at 2.3 µm. The laser generated a maximum output power of 0.73 W at 2306 nm with a slope efficiency of 34% [Loi19a]. Under diode pumping a maximum output power of 2.4 W with a slope efficiency of 11% and a laser threshold of 2 W was achieved [Loi19a]. Canbaz et al. achieved the shortest reported pulses with a duration of 514 fs from a Kerr-lens mode-locked Tm:$LiYF_4$ laser at 2.3 µm [Can17]. More details on the processes responsible for 2.3 µm laser emission of Tm^{3+} ions are given in Section I.3.

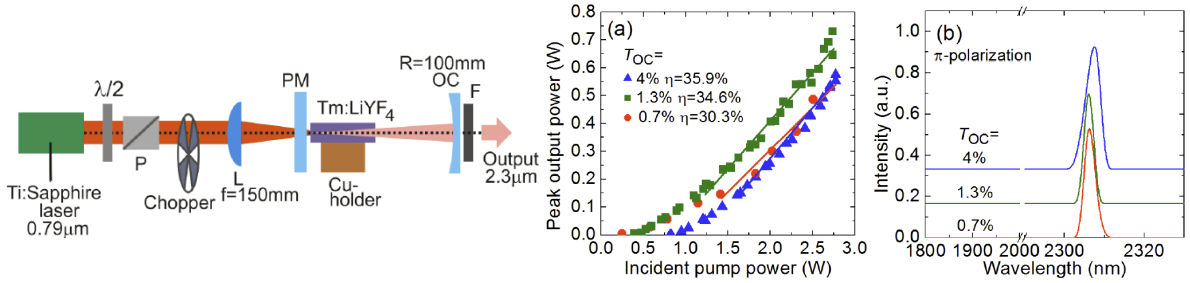

Figure I.9. Layout of the Ti:Sapphire pumped Tm:$LiYF_4$ laser operating on the $^3H_4 \rightarrow {}^3H_5$ transition: P, Glan-Taylor polarizer; PM, pump mirror; OC, output coupler; F, long-pass filter (*left*); (a) laser performance input–output dependences, η, slope efficiency, T_{OC}, transmission output coupler; (b) typical spectra of laser emission measured well above the laser threshold (π-polarized emission) [Loi19a].

Applications of 2.3-µm lasers. The 2.3 – 2.4 µm spectral range is the seat of strong absorption lines of atmospheric species such as hydrogen fluoride (HF), carbon monoxide (CO), nitrous oxide (N_2O), methane (CH_4), and formaldehyde (H_2CO), as shown in Figure I.10. Thus, wavelength-tunable 2.3 µm lasers are used for gas sensing in the atmosphere and optical metrology of combustion processes [Mca97, Web00]. Figure I.10 (*left*) shows a scheme of an experimental set-up for combustion measurements [Web00].

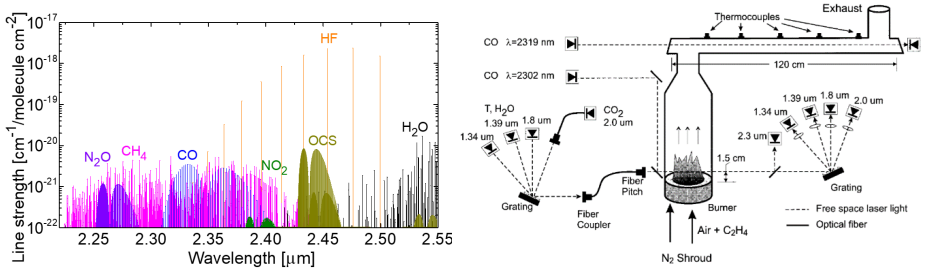

Figure I.10. Simulation of absorption of molecular species in the 2.3 µm spectral range (*left*) [Tya23]; Experimental schematic of the diode-laser absorption sensor for multiparameter measurements in the combustion region and stack above a premixed C_2H_4 -air burner (*right*) [Web00].

There are articles in the literature about the detection of carbon monoxide, methane, and formaldehyde using lasers emitting around 2.3 µm [Wan00, Vic02, Cih09]. The applications mainly involve in situ gas leak detection in installations such as waste incinerators or coal mines (Figure I.10). The development of more powerful, energetic, and high-quality spatial sources at 2.3 µm, particularly in terms of range, allows to extend their use to other molecules such as nitrous oxide, hydrofluoric acid, and organosulfur compounds (OCS).

Additionally, the absorption of the C-H bond around 2.3 µm indicates that other compounds, such as humus and petroleum derivatives, exhibit absorption bands in this region, suggesting various potential applications for these lasers. Specifically, absorption at 2.3 µm has been successfully used to map oil residues from oil spills and to measure the humus content in soil [Ben02, Kok13]. Experiments have also reported the detection of glucose using 2.3 µm laser diodes. As such, there is considerable interest in developing non-invasive methods for measuring blood glucose levels, particularly for diabetic patients (Figure I.11) [Far08, Kay23]. Additionally, such NIR emission also falls into an atmospheric transparency window, the K band that makes 2.3 µm lasers attractive for the free-space optical communication and countermeasures.

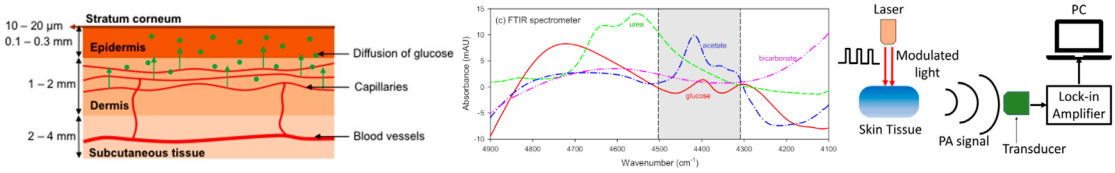

Figure I.11. Schematic representation of the components of human skin (*left*) [Kot16]; absorption spectrum of glucose and some other biomolecules in the region between 2.0 and 2.5 µm (*middle*), after [Ole05]; the basic principle of generation and detection of acoustic signal for photoacoustic spectroscopy (*right*), after .

I.1.D. Mid-infrared lasers around 3 µm: a challenge for Holmium ions

The 2.7-3 µm spectral range is usually well-addressed by Er, Ho and Dy lasers as shown in Figure I.12. Lasers emitting at these wavelengths have been thus applied in "minimally invasive" dentistry, dermatology and urology. However, achieving an efficient laser emission in this spectral range remains a challenge especially for Ho-lasers.

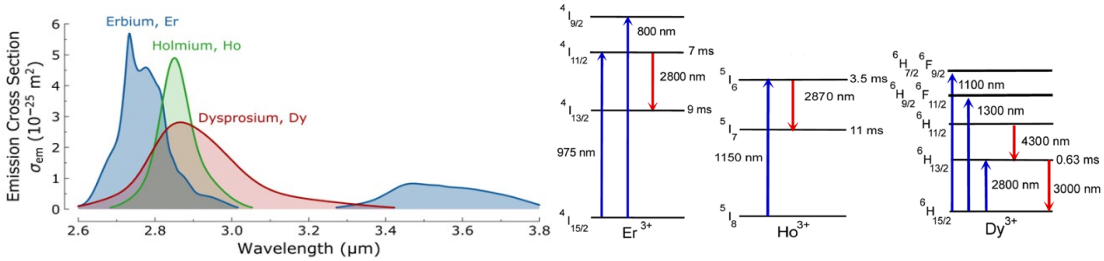

Figure I.12. Stimulated-emission cross-section of rare-earth ions in ZBLAN fiber laser (*right*) (after [Woo18]) and simplified energy-level diagram of Er^{3+}, Ho^{3+} and Dy^{3+} ions showing possible pump wavelength (*blue arrows*) and primary wavelength of laser emission in mid-infrared (*red arrows*) (after [Joc20]).

The main problem which is common for Er and Ho lasers operating around 3 µm is that the luminescence lifetime of the upper laser levels ($^4I_{11/2}$ Er^{3+} and $^5I_6$ Ho^{3+}) is shorter than the lower laser levels ($^4I_{13/2}$ Er^{3+} and $^5I_7$ Ho^{3+}). This difference in lifetimes leads to the so-called "bottleneck effect" causing the self-termination of the $^4I_{11} \rightarrow {}^4I_{13}$ Er^{3+} and $^5I_6 \rightarrow {}^5I_7$ Ho^{3+} laser transitions. It prevents the steady-state inversion population (excited ions are accumulated into the lower laser level) and, at a glance, the continuous-wave laser operation appears impossible. Figure I.13 (left) demonstrates this effect. In the case of Er^{3+} ions, the continuous-wave 2.8 µm

laser emission is reached thanks to two different energy-transfer upconversion (ETU) processes. To induce efficient ETU processes, high Er^{3+}-doping is required at about 10 at.%.

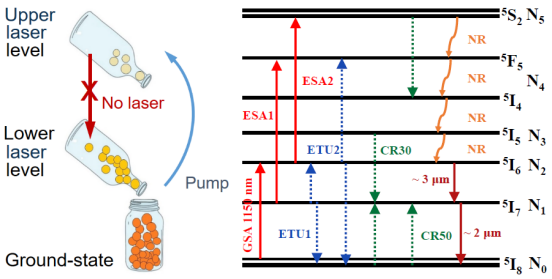

Figure I.13. Schematic illustration of the "bottleneck effect" (*left*) and energy level scheme of Ho^{3+} ions demonstrating mechanisms operate spontaneously in the erbium ion system, which corresponds to the 3 µm laser behavior (*right*), where GSA – ground-state absorption, ESA – excited-state absorption, ETU – energy-transfer upconversion, CR – cross-relaxation, NR – nonradiative multiphonon relaxation. Taken from [Ye22].

Besides the self-terminated nature of the $^5I_6 \rightarrow {}^5I_7$ Ho^{3+} transition, the lack of pump sources is an additional problem in realizing 3 µm Ho-lasers. A flashlamp can be used to achieve Ho^{3+} laser emission at 3 µm. Like Er^{3+} ions, Ho^{3+} ions exhibit a weak concentration quenching of the upper laser level, therefore, the 3 µm laser operation can be expected at high Ho^{3+} doping concentrations. However, the laser operation of a $Ho:Y_3Al_5O_{12}$ crystal pumped by a flashlamp was achieved with a Ho^{3+} concentration of 10 at.% [Kam13]. The drawback of a flashlamp pumped laser system with a long lower laser level lifetime is that cross-relaxation processes from higher excited states can bypass the upper laser level and directly populate the lower laser level. This prevents the formation of a population inversion [Ant90]. Alternatively, 3 µm Ho laser emission can be achieved using Nd-lasers [Ant90, Bow90, Rab91].

Recently, Raman fiber lasers have become more available, allowing a direct pumping into the $^5I_6$ upper level and power scaling. Reports show the CW laser operation of $Ho:YAlO_4$ crystal pumped by a Raman fiber laser [Nie17, Nie18, Qia23a, Qia23b] . In case of direct pumping of the $^5I_6$ upper laser level, the doping with a high concentration of Ho^{3+} facilitates the recycling of ions from $^5I_7$ back to $^5I_6$ via the energy transfer upconversion process (ETU1 in Figure I.13), thereby creating a "quenching effect" that reduces the luminescence lifetime of the $^5I_7$ terminal level. However, this quenching effect also shortens the lifetime of the $^5I_6$ upper level via ETU2 and induces severe thermal effects due to high doping concentrations, limiting power scaling. Additionally, cross-relaxation processes (CR30 and CR50) at high doping levels can transfer ions from higher levels directly to $^5I_7$ [Ye22].

Another way to circumvent the long luminescence lifetime of the $^5I_7$ level is codoping. [Kam07] showed that codoping with Nd^{3+} and Pr^{3+} ions can quench the long luminescence lifetime of the $^5I_7$ lower laser level through energy-transfer (ET) towards the codopant. The example of Pr^{3+} codoping is shown in Figure I.14 (left). A significant improvement in laser efficiency was achieved using this codoping scheme [Ant90, Qia23b]. High power and efficient laser operation of $Ho,Pr:LiLuF_4$ and $Ho,Pr:LiYF_4$ crystals was also achieved [Nie17, Nie18]. Ho-

lasers can be doped with Yb^{3+} ions as well to sensitize the 3 µm laser emission [Umy96, Die98, Die00] as shown in Figure I.14 (right).

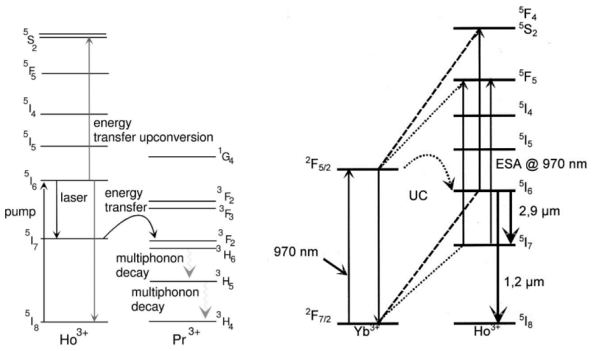

Figure I.14. Schematic energy-level diagram for: (*left*) Ho^{3+} and Pr^{3+} and (*right*) Yb^{3+} and Ho^{3+} corresponding to the 2.9 µm laser behavior. After [Jac09, Die00].

From the material point of view, to develop mid-infrared lasers, the host matrices possessing low phonon energies is essential. This leads to longer luminescence lifetime of the $^5I_6$ upper level due to decreasing the multiphonon nonradiative probability (more details on this process are given in Section I.2). Therefore, it leads to an improvement in laser efficiency as shown in Figure I.15.

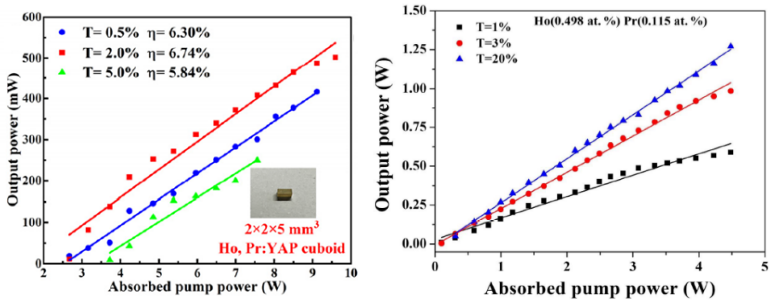

Figure I.15. Comparison laser performance of Ho,Pr:YAP and Ho,Pr:$LiYF_4$ 3-µm bulk lasers pumped by a Raman fiber laser at 1.15 µm. Taken from [Qia23, Nei18].

Applications of 3-µm lasers. *Medical applications*. The 2.7 – 3 µm spectral region contains much stronger water absorption than around 2 µm that makes lasers emitting at these wavelengths of primary importance for medicine. Such radiation is strongly absorbed by high moisture content materials such as biological tissues resulting in a small penetration depth and surgical precision of incisions [Kim03], as shown in Figure I.16. These lasers can be used for laser surgery, which is more beneficial to human tissue cutting and blood coagulation than conventional surgery. High-energy single-pulse 3 µm lasers are used for soft tissue and bone cutting, excision surgery [Ami10], dental ablation surgery [Vag23], and cosmetic laser rhytidectomy. Moreover, mass spectrometry instruments combined with a 3 µm laser radiation have also been developed for tumor biopsy [Woo17, Sau18].

• *Industrial material processing* (cutting and welding).

• Due to the atmosphere transparency window between 3 and 5 µm with low propagation losses, these lasers can be used for atmospheric monitoring, sensitive detection of atmospheric

gases and molecules, space science research, LIDAR systems [Amb00, Pra05, Lam15, Ehr17] and countermeasures [Eld10].

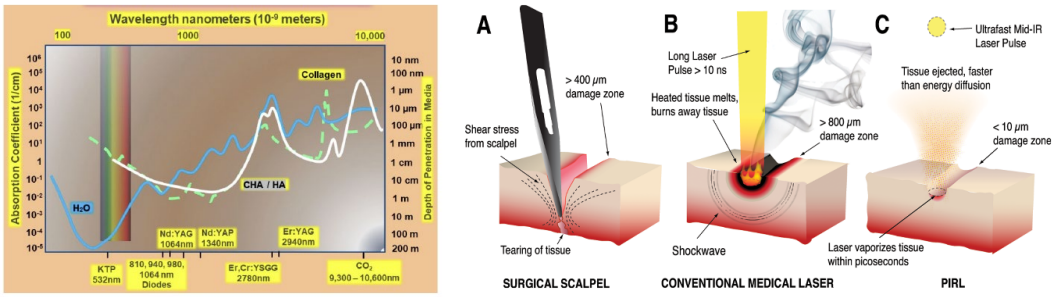

Figure I.16. Absorption spectra and depth of penetration of biological tissues at different spectral ranges. *Blue* and *white solid lines* – water and hydroxyapatite (HA) respectively, *green solid line* – collagen (*left*) [Par20] and schematic of cutting modalities (*right*) [Ami10].

• *Pumping source* for lasers emitting further in mid-infrared region. Such as Fe^{2+}-based lasers, see Figure I.17, [Jel15, Li21], OPOs [Vod00], and supercontinuum lasers [Mic16, Gau18, Rob20]. Also, Er and Ho lasers can serve as pump sources for lasers based on Dy^{3+} ions, since they have absorption bands around 2.8 μm (the $^6H_{15/2} \rightarrow {}^6H_{13/2}$ transition) [Woo18], see Figure I.12.

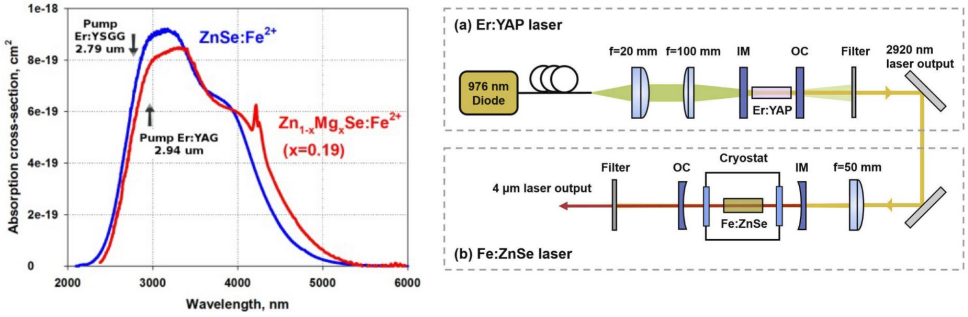

Figure I.17. Absorption cross-section spectra of the Fe^{2+}:ZnSe and Fe^{2+}:$Zn_{0.71}Mg_{0.19}Se$ lasers (*right*) and an example of scheme of a laser set-up for pumping these lasers (*left*). Taken from [Jui15, Li21].

I.1.E. Various 2-μm laser geometries: bulk, thin-disk, waveguide and fiber lasers

Thulium and holmium solid-state lasers emitting around 2 μm can be operated in different laser geometries to provide power scalability.

• *Bulk (rod) lasers* are typical solid-state lasers in which the lasing medium is a solid crystalline material (single crystals or transparent ceramics) doped with rare-earth or transition metal ions. They employ "bulk" pieces of solid materials. The fist laser was a pulsed ruby laser, demonstrated by Maiman in 1960 [Mai60]. The laser cavity (resonator) is built by two types of mirrors: (i) a pump mirror with high reflection at the laser wavelength and transparent at the pump wavelength and (ii) an output mirror partially transparent at the laser wavelength. The typical laser set-up scheme for Ho-laser at 2 μm and input-output dependences are shown in Figure I.18.

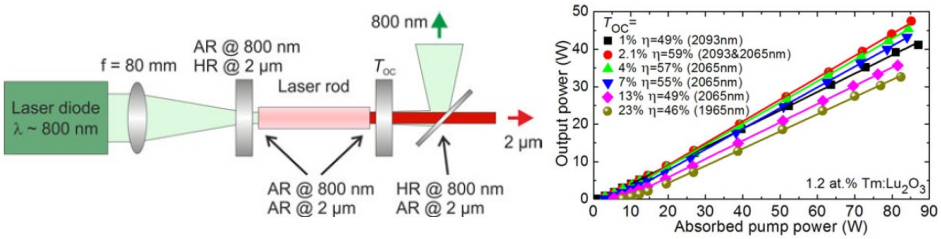

Figure I.18. Schematic of the laser set-up of bulk solid-state laser (*left*) and input-output dependences with insert laser emission spectrum (*right*). Taken from [Loi18].

One of the common pumping configurations used in solid-state lasers is end-pumping, also known as the longitudinal pump scheme. In end-pumped lasers, the pumping beam is coaxial with the resonator beam, resulting in highly efficient lasers with good beam quality. In this configuration, the pumping beam is delivered to the end of the active medium using focusing lenses or optical fibers. End-pumping yields better results for low power operations (less than a few watts).

• *The thin-disk* (also called active mirror) laser architecture consists of a disk-shaped active element. Its rear face is in thermal contact with a bulk heat-sink. The heat flow in the disk is predominantly unidirectional. The rear face of the disk has a dielectric coating that serves as a cavity mirror. The laser radiation is propagating almost perpendicular to the disk surface. The thin-disk laser design is promising for power-scalable laser sources operating in the continuous-wave and mode-locked regimes. A typical laser set-up of thin-disk laser and input-output dependences are shown in Figure I.19.

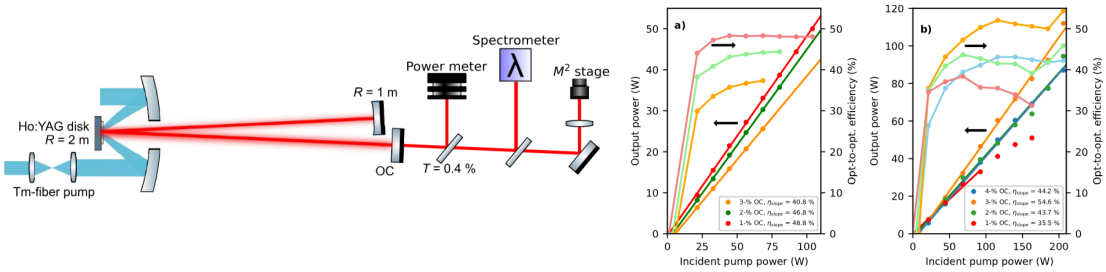

Figure I.19. Laser cavity of thin-disk laser and Laser slope and optical to optical efficiencies with (a) 1 at.% doping concentration, (b) 2 at.% doping concentration. Taken from [Tom21].

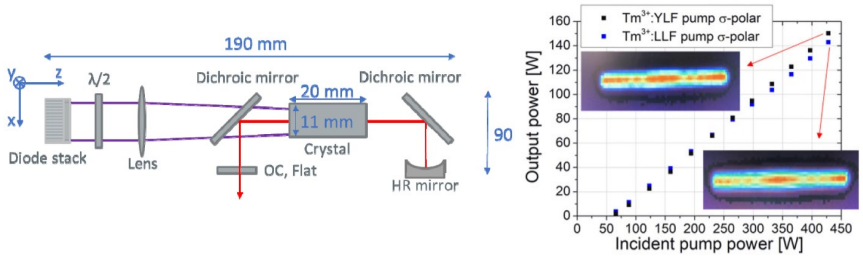

Figure I.20. Laser performance of $Tm:LiYF_4$ and $Tm:LiLuF_4$ slab lases: top view of the laser setup (*right*) and input-output dependences (*left*), the insert pictures are the laser beam profiles at maximum output power. Taken from [Ber18].

• *Slab lasers* represent a prominent class of high-power solid-state bulk lasers characterized by a slab-shaped gain medium. This geometry, thin in one dimension and extended in the other

two, facilitates superior thermal management and efficient heat dissipation. This is crucial for maintaining beam quality and stability at high power levels. The slab design allows for uniform gain distribution and minimizes thermal lensing effects, resulting in excellent spatial mode control and high beam quality. The scalability and versatility in pumping configurations further enhance their applicability and performance in various high-power laser systems, see Figure I.20.

• *Fiber lasers* are a special form of solid-state lasers where the gain medium is an optical fiber (oxide or fluoride glasses) doped with rare-earth ions. The optical fiber serves as both the gain medium and the waveguide, confining and guiding the light along its length. The pump is typically coupled into the fiber core which is surrounded by a cladding. Fiber lasers possess high optical-to-optical efficiency, high scalability, excellent beam quality. However, the developing cost of fiber lasers is high and they are less robust than bulk solid-state lasers. Figure I.21 shows one example of high power Tm^{3+}-doped silica fiber laser [Mou09].

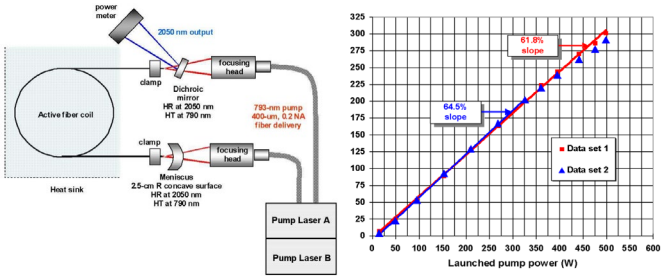

Figure I.21. Laser performance of Tm-doped silica fiber laser operating at 1.9 µm: schematic of fiber laser design for high power laser operation (*right*), fiber laser output power *vs* launched pump power (*left*). Taken from [Mou09].

• *Microchip lasers* are alignment-free monolithic solid-state lasers in which the laser element is in direct contact with the end mirrors of the laser resonator. They typically emit an average power of a few hundred milliwatts, although sometimes exceeding 1 watt. In some cases, there may be another optical device between the laser medium and an end mirror, such as a nonlinear crystal used as an electro-optic modulator for Q-switching or intracavity frequency doubling, or an undoped transparent plate for improving the power handling capability and increasing the effective mode area. Figure I.22 shows one example of microchips lasers based on Tm^{3+}-doped cubic sesquioxides.

Most microchip lasers do not have intentionally curved resonator mirrors. The resonator modes are usually determined by thermal lensing in the laser crystal, which may include possible bulging of the crystal's end faces. In some cases, there is also a significant influence from gain guiding. The stability zone of the simple resonator extends from zero dioptric power to a maximum value, which is determined by the resonator length. This also determines the minimum beam radius of the fundamental mode, which is relatively small due to the short resonator. One usually achieves stable diffraction-limited beam quality by pumping within the fundamental resonator mode. The utilization of thermal lensing for the generation of resonator modes imposes significant limitations, such as constraints on the achievable range of pump powers or the use of gain media with negative dn/dT [Pas08].

Without special measures, microchip lasers often exhibit single-frequency operation. This is because the short resonator length results in a large free spectral range. When the temperature of the laser crystal changes, the emission frequency may drift over a wide range (up to many gigahertz) until a mode hop occurs.

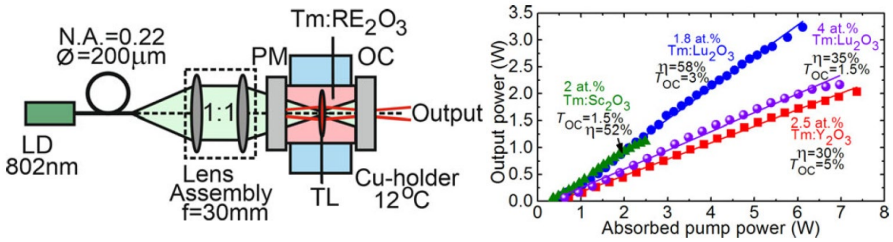

Figure I.22. Laser performance of $Tm:RE_2O_3$ (where RE stands for Y, Lu, Sc) microchip lasers operating around 2 µm: scheme of the laser set-up (*right*); the comparison of the output performance of microchip lasers (*left*). *TL* – thermal lens, η – slope efficiency [Loi18].

• *Waveguide lasers* employing active optical waveguides, which are spatially inhomogeneous structures designed to guide light by i.e. restricting the spatial region in which light can propagate. More details are given in Section I.1.G.

To increase output power and manage thermal issues, the active thermal cooling or/and different geometries of solid-state lasers can be employed such as rod, thin-disk, slab, and fiber geometers. Most commercial end-pump systems involve rod lasers.

I.1.F. Current trends in the development of ultrafast lasers at 2 µm and beyond

Mode-locking is a group of methods to obtain periodic ultrashort pulses (picosecond or femtosecond) from continuous-wave laser by inducing a fixed phase relationship between the longitudinal modes. The constructive interference between these modes can create a set of periodic light pulses. Lasers in which the mode-locking is observed are called mode-locked lasers. The pulse repetition rate is determined by the resonator's round-trip time. For example, a 10-ns round-trip time for a single pulse result in a 100 MHz repetition rate. Typical values range between 50 MHz and 500 MHz, but miniature lasers can achieve repetition rates around 100 GHz. In contrast, lasers with extended resonators may have repetition rates below 10 MHz. The pulse energy cannot be very high because of the high pulse repetition rate [Pas08].

There are mainly two types of mode-locking.

• *Active mode-locking* is achieved through the use of a modulator, *e.g.*, electro-optic type, which modulates the resonator losses in precise synchronization with the resonator round-trips. The modulator is often placed close to one end of the resonator, as shown in Figure I.23. The saturated gain then only supports a net gain around the minimum of the loss modulation, thus only accommodating pulses that are significantly shorter than the cavity round-trip time.

• *Passive mode-locking* is achieved with saturable absorbers (SA) such as GaSb-based SEmiconductor Saturable Absorber Mirrors (SESAMs) and carbon nanostructures, see Table I.1. When the light intensity increases, the absorption of the SAs decreases and they become more transparent at high intensities, allowing strong pulses to pass while reducing

lower-intensity light. This difference in the absorption enables the formation of ultrashort and intense pulses.

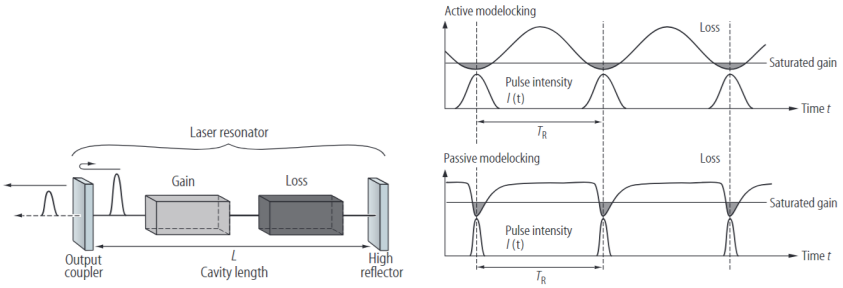

Figure I.23. Schematic laser cavity for active and passive mode-locking. T_R is the resonator round-trip time; loss can be an electro-optical modulator or a saturable absorber [Kel07].

Kerr lens mode locking (KLM) is a technique for passively mode-locking a laser by employing transient Kerr lensing in the gain medium. This method utilizes the nonlinear optical effect known as the Kerr effect, where the refractive index of the gain medium changes with the intensity of the light passing through it, $n(I) = n_0 + n_2 I$. This effect acts as a lens that varies with the laser intensity. This selective focusing mechanism supports the formation of ultrashort pulses by preferentially amplifying high-intensity light pulses. This enables stable and efficient mode-locking without the need for additional saturable absorber materials. The change in the refractive index affects the spatial profile of the incident beam and its temporal profile. If the incident beam has a Gaussian shape, n changes according to the spatial beam profile. It will result in a lensing effect and self-focusing of the beam (Kerr-lensing), causing more intense light to undergo tighter focusing [Pas08]. The scheme of this effect is shown in Figure I.24.

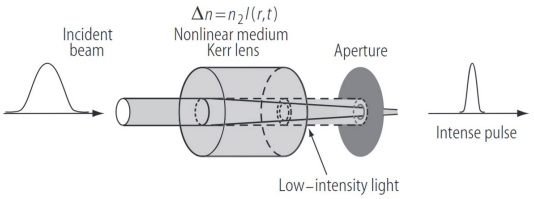

Figure I.24. Scheme of the Kerr lens effect in gain medium. Taken from [Kel07].

Passive mode-locked lasers operating at 2 μm have been demonstrated using various geometries, including fiber lasers, bulk lasers [Rud14, Ma19, Suz23, Gra24], and thin-disk lasers [Zha18, Tom22].

Mode-locked lasers emitting ultrashort pulses in the 2 μm spectral range at high (~100-MHz) repetition rates are important for time-resolved molecular spectroscopy in this molecular fingerprint region. They are also of particular interest as pump sources for synchronously-pumped optical parametric oscillators operating in the mid-IR above 5 μm, including frequency comb generators. Additionally, they serve as seeders of near-degenerate chirped-pulse optical parametric amplifiers pumped at ~1 μm for high-order harmonic and soft-X-ray generation, for seeding regenerative laser amplifiers to increase pulse energy at lower repetition rates, and for IR supercontinuum and THz generation [Pet19, Ma19].

Figure I.25 shows a typical set-up of a passively mode-locked bulk laser at 2 μm. It consists in an X-shaped linear cavity with the active element (AE) placed between two concave folding mirrors M_1 and M_2 (one of which, M_1, serves as a pump mirror). One cavity arm contains a concave highly reflective mirror M_3 which creates a secondary beam waist on the saturable absorber. Another arm is terminated by a plane-wedge output coupler (OC). The intracavity dispersion management is provided by chirped mirrors (CM). Optionally, additional external compression of laser pulses is realized using a polycrystalline ZnS plate.

• *Dispersion management*: For the majority of laser gain materials, the material group velocity dispersion (GVD) around 2 μm is negative and needs to be compensated. This is typically provided by dispersive mirrors with engineered reflection and dispersion spectral profiles. The total group delay dispersion (GDD) introduced by the mirrors can be managed by the number of bounces on them.

• *Saturable absorber*: Currently, commercial SAs operating around 2 μm are not available. The existing viable solutions include custom-made reflection-type GaSb-based SESAMs and transmission-type saturable absorbers based on carbon nanostructures, such as graphene (a single layer of carbon atoms in a honeycomb lattice) and single-walled carbon nanotubes (SWCNTs, rolled sheets of graphene) embedded in a polymer film.

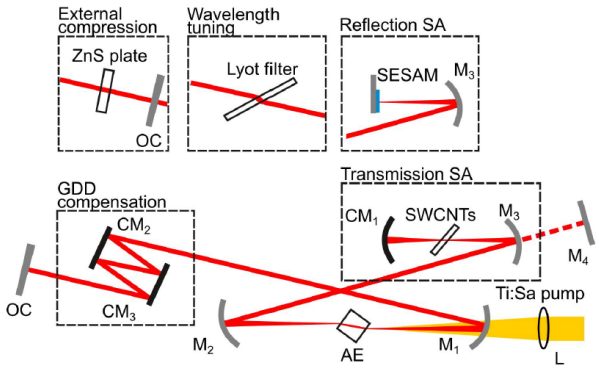

Figure I.25. A typical scheme of passively mode-locked laser operating at 2 μm: L – focusing lens, M_1 and M_2 – dichroic curved folding mirrors, M_3 – curved highly-reflective mirror, CM – chirped mirrors, OC – output coupler, SESAM – SEmiconductor Saturable Absorber Mirrors, SWCNTs – single-walled carbon nanotube-based saturable absorber. After [Pet19]

Table I.2 summarizes the properties of SAs which are mostly used for passively mode-locking [Cho10, Cho11, Paa14]. The SAs have to have broad operation wavelength range, short relaxation time, optimal modulation depth, and small non-saturable losses.

Table I.2. Relevant properties of SAs for 2 μm.

	GaSb-based, SESAMs	SWCNT-SA	Mono/bilayer, graphene
Operation wavelength [μm]	1.9 – 3	0.8 – 2.1	Full range
Modulation depth ΔR_{ns} [%]	3 – 6	< 0.5	0.5 / 1.3
Non-saturable losses ΔR_{ns} [%]	3 – 6	0.7 – 1.2	1.8 / 3.4
Relaxation time [ps]	2 – 10	1.2	1.3
Fabrication	Complex/expensive	Simple	Simple

One should identify laser gain materials that combine the following properties in order to optimize ultrafast lasers operating around 2 µm:

• *Gain medium*: The gain medium should provide broad and smooth spectral gain profiles, naturally extending > 2 µm to avoid the structured water vapor absorption in the atmosphere. It is also desirable for the material to have a high n_2 to enhance nonlinear effects. It is important to note that the value of n_2 at 2 µm is generally much lower than that at ~1 µm);

• Smooth and structureless emission / gain profiles (ideally exhibiting "glassy-like" spectroscopic behavior). Such spectral properties are expected for materials with a strong inhomogeneous spectral broadening induced, *e.g.*, in (i) crystals with a structure disorder, (ii) solid-solution ("mixed") materials or (iii) crystals with a heterovalent doping mechanism.

• Emission spectra naturally extend well beyond 2 µm. First, for singly Tm^{3+}-doped materials, host matrices with strong crystal fields (such as garnets or sesquioxides) can provide a large total Stark splitting of the ground-state ($^3H_6$), leading to the electronic transitions $^3F_4 \rightarrow {}^3H_6$ naturally occurring at 2 µm. Second, Tm^{3+}, Ho^{3+} codoping can shift the emission wavelength beyond that for singly Tm^{3+}-doped materials due to the $^5I_7 \rightarrow {}^5I_8$ electronic transitions of Ho^{3+} ions. It is also useful for combining the gain bandwidths of both ions. Emission at even longer wavelengths can exploit the electron-phonon interaction, known as phonon sidebands.

• Good thermal, thermo-mechanical, and thermo-optical properties are desired to support power scalability, especially considering the negative effect of the crystal / compositional disorder on the thermal conductivity of laser crystals.

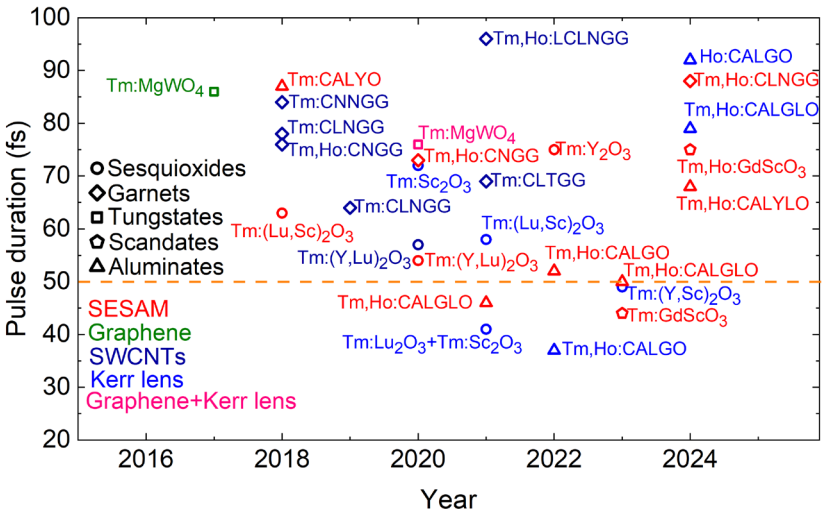

Figure I.26. Ever reported sub-100 femtosecond pulse duration of mode-locked Tm^{3+} and/or Ho^{3+} doped solid-state lasers; *aluminates* – Tm,Ho:CALYO [Zha18b], Tm,Ho:CALGO [Che22, Wan22], Tm,Ho:CALYGO [Din23]; Tm,Ho:CALGLO [Wan21a, Zen24], Tm,Ho:CALYLO [Liu24a] Ho:CALGO [Yao24]; *garnets* – Tm:CLNGG [Wan18, Suz24], Tm,Ho:CLNGG [Zha19], Tm,Ho:CNGG [Pan18, Wan20a], Tm:CNNGG [Pan18a],Tm:CLTGG [Wan21], Tm,Ho:LCLNGG [Pan21]; *tungstates* – $Tm:MgWO_4$ [Wan17, Wan20]; *sesquioxides* – $Tm:Sc_2O_3$ [Suz20], $Tm:Y_2O_3$ [Zha22], $Tm:(Y,Sc)_2O_3$ [Suz23], $Tm:(Y,Lu)_2O_3$ [Zha20], $Tm:(Lu,Sc)_2O_3$ [Wan18a, Zha21a]; *scandates* – $Tm:GdScO_3$ [Zha23], $Tm,Ho:GdScO_3$ [Liu24].

Figure I.26 shows the sub-100 femtosecond pulses reported from passively mode-locked Tm- and/or Ho-doped lasers using different SAs and optical Kerr-effect. To achieve sub-100

femtosecond pulses, garnets with a structural disorder such as $CaGdAlO_4$, $Ca_3Nd_{1.5}Ga_{3.5}O_{12}$, and cubic sesquioxides R_2O_3 (where R stands for Y, Lu and Sc) and their solid-solutions showed a great potential. Recently, orthorhombic perovskite crystals such as $GdScO_3$ have been established as potential materials for generating sub-100 fs pulses beyond 2 µm [Zha23, Liu24].

Figure I.27 summarizes some of the applications of femtosecond and picosecond 2-µm mode-locked lasers as building blocks of complex laser or parametric frequency conversion systems, with the goal of enhancing single pulse energy and extend the wavelength coverage. Note that these applications are rather different from those pursued with nanosecond (Q-switched) 2-µm laser systems (as mentioned earlier).

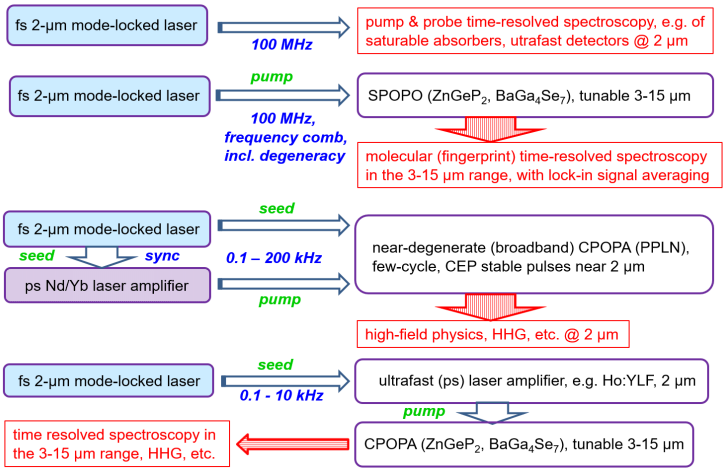

Figure I.27. Applications of femtosecond (fs) and picosecond (ps) 2-µm mode-locked lasers operating at high repetition rates: SPOPO – synchronously pumped optical parametric oscillator, CPOPA – chirped-pulse optical parametric amplifier, PPLN – periodically poled lithium niobate, CEP – carrier-envelope phase, HHG – high-harmonic generation, YLF – $LiYF_4$ (after [Pet19]).

I.1.G. The potential of waveguide lasers at 2 µm

Waveguide lasers are crucial elements in integrated photonic circuits. Their compatibility with optical fibers and various on-chip devices enables their use in optical sensing, on-chip spectroscopy, microfluidics, telecommunications, medicine, and soft material processing [Mar09, Che14]. When we speak about waveguide lasers we have to consider the basics of optical waveguides.

An optical waveguide is a confined spatial region in which light can propagate, as shown in Figure I.28. The critical condition for the guiding by total internal reflection determines the maximum light acceptance angle of the waveguide known as the numerical aperture (N.A.). It is related to the relative refractive index difference between the core and the cladding Δ,

$$N.A. \approx \left(2n_1\Delta\right)^{1/2}. \qquad \text{(I.1)}$$

The number of guided modes of a waveguide depends on the light wavelength: the shorter the wavelength, the more modes can be guided. For long wavelengths there may be only a single guided mode in waveguide with dielectric boundary conditions whereas multimode behavior is still obtained at shorter wavelengths. When a particular mode ceases to exist beyond a certain

wavelength, that wavelength is called its cut-off wavelength. For an optical waveguide, the cut-off wavelength for the fundamental mode sets a limit to the single-mode regime. Single-mode waveguides are optical waveguides which are designed such that they support only one propagation mode per polarization direction for a given wavelength.

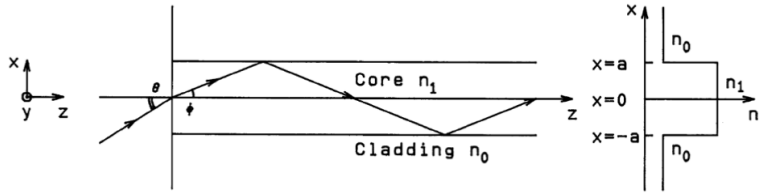

Figure I.28. Basic structure and refractive index profile of the optical waveguide [Oka21].

Optical waveguides can be classified according to their geometry (buried / surface, planar / channel), mode structure (single-mode, multi-mode), refractive index distribution (step or gradient index), ability to amplify / generate light (passive / laser-active), and material (crystal, glass, polymer, semiconductor). There are two main types of laser waveguides: planar and channel, see Figure I.29. We will mainly focus on the latter.

A planar waveguide consists of a thin layer of active material deposited on top of a bulk (optically passive) substrate. The waveguiding is ensured by a refractive index difference at the layer/substrate and layer/air interfaces. The active layer can be optionally covered by cladding, which reduces propagation losses and protects the upper surface of the active layer. In planar waveguides, mode confinement through index-guiding is only in one direction (orthogonal to the layer's plane). The laser mode of a planar waveguide laser in the near field exhibits a characteristic stripe profile. It typically features a nearly Gaussian intensity distribution in the vertical direction and demonstrates strongly multimode behavior in the horizontal direction.

In channel waveguides, the mode confinement is provided in two directions, resulting in a well-defined index profile and typically enabling single-transverse-mode operation. Channel waveguides offer several advantages, including a small mode area that results in high intracavity light intensity, low laser threshold, good spatial beam quality, and high efficiency due to the effective overlap of pump and laser modes. Practical advantages also include their compact and robust design and compatibility with fiber technology.

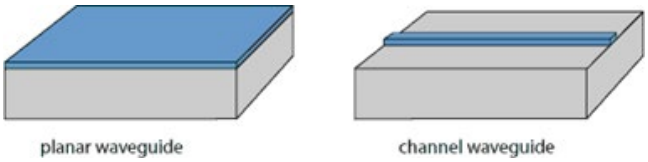

Figure I.29. Two main types of laser waveguides [Pas08].

Channel waveguides can be fabricated by the Liquid Phase Epitaxy (LPE) [Fer99] or the fs-Direct-Laser-Writing (fs-DLW) technique. We will consider only the latter. The fs-DLW allows to fabricate passive and active waveguides in transparent dielectric materials. Waveguide structures are fabricated in these materials by absorbing the energy of fs pulses leading to modifications at the μm-scale and a change in the refractive index compared to unirradiated regions [Mar09, Che14, She23]. It is a powerful technique for fabricating 3D photonic

microstructures in transparent dielectric materials doped with rare-earth ions for WG laser applications. It benefits from: i) fast inscription time; ii) high precision of damage tracks positioning inside the material; iii) variety of photonic microstructures; iv) suitable for different transparent dielectric materials (crystals, ceramics, glasses); v) low to moderate propagation losses.

The fs-DLW allows to fabricate a variety of WG geometries. There are four types of WG geometries [Che14]: i) type I directly written WG; ii) type II stress-induced WG; iii) type III depressed cladding WG; iv) type IV ablated ridge WG. This technique relies on forming a strongly localized, permanent, and thermally stable variation of the refractive index within the material volume using tightly focused fs laser radiation. The light-guiding is ensured by a difference in the refractive index (Δn) between the laser damage tracks and the unmodified (bulk) material. The Δn can be positive (guiding within the damage tracks, type I structures, typically observed in glasses [Dav96]) or negative (guiding between the damage tracks, type II or type III structures) depending on the material. A type III waveguide consists of a core surrounded by a number of low-index tracks forming the cladding. Those tracks are close to each other (a few µm), constructing a quasi-continuous low-index barrier wall, which allows the confinement of the light field inside, see Figure I.30.

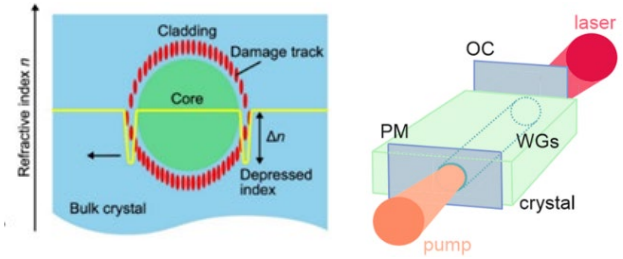

Figure I.30. An illustration of the geometry of a depressed-index WG with a circular cladding (type III structure, end-facet view) (*left*) and an example of a cavity of a channel waveguide laser, PM – pump mirror, OC – output coupler (*right*).

The femtosecond direct-laser-written channel waveguide lasers in Tm^{3+} and Ho^{3+}-doped materials demonstrate high-power and efficient laser operation around 2 µm [Dal14, Mcd17, Kif20, Kif21, Bei24]. Figure I.30 illustrates the layout of a continuous-wave waveguide laser with external mirrors. Two plane mirrors (the pump mirror and the output coupler) are positioned very close to the waveguide end-facets (butt-coupled). To reduce losses at the waveguide or mirror interfaces, an index-matching liquid can be applied. The cavity length is determined by the length of the waveguide, with the pump radiation being coupled into the waveguide through the pump mirror. This laser geometry is conducive to power-scalable operation and is similar to microchip lasers with plano-plano cavities, though the mode guiding mechanism differs: index-guiding in waveguide lasers and thermal guiding in microchip lasers

Figure I.31 shows the laser results obtained with Thulium channel WGs which are produced by microstructuring Tm^{3+}:$LiYF_4$/$LiYF_4$ epitaxy layers via diamond-saw dicing pumped by a Raman fiber laser [Loi19b].

In this work, to develop lasers, the gain media in bulk geometry and linear hemispherical cavity were used.

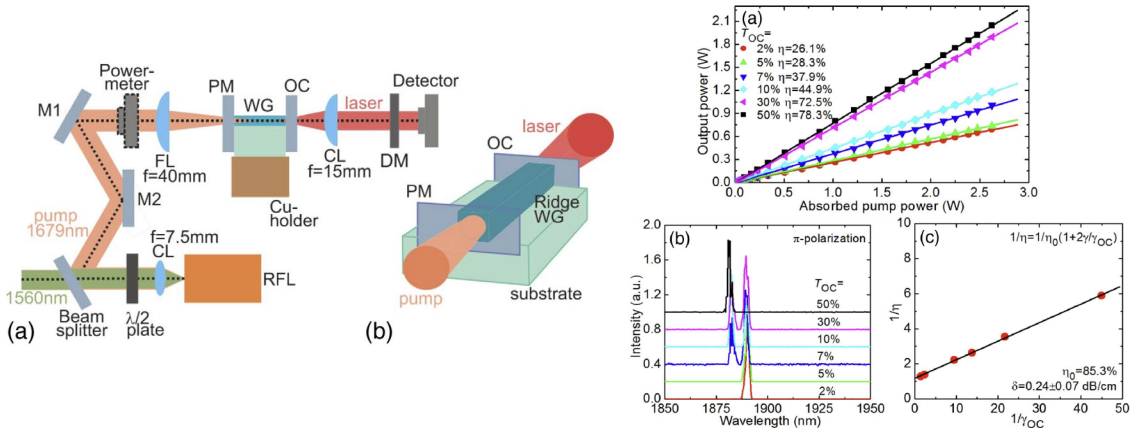

Figure I.31. *Left part of the figure*: (a) scheme of the WG laser setup: RFL, Raman fiber laser; CL and FL, collimating and focusing lens respectively;M1and M2,HR folding mirrors; PM, pump mirror; OC, output coupler; DM, dichroic mirror, WG, waveguide. (b) Scheme of the ridge WG geometry. *Right part of the figure*: output characteristics of the in-band-pumped Tm:$LiYF_4$ channel WG laser: (a) input–output dependences; η, slope efficiency; (b) typical laser emission spectra measured; (c) Caird analysis [a plot of inverse of the slope efficiency, $1/\eta$, versus inverse of the output-coupling loss. Taken from [Loi19b].

I.2. General aspects of the rare-earth ion spectroscopy

In this section, the fundamental aspects of rare-earth ions spectroscopy within solid-state materials are given. The description of the intra- and inter-ionic radiative and nonradiative processes and their quantification are provided.

I.2.A. General information about trivalent rare-earth ions

The term "*rare-earths*" (RE) refers to a group of 17 metallic elements, including scandium (Sc), yttrium (Y), and the lanthanides, which have similar chemical properties. *The lanthanides* are a series of elements with atomic numbers 57 (lanthanum, La) to 71 (lutecium, Lu), all of which, except promethium (Pm), occur naturally. The rare earth elements, being chemically similar to one another, invariably occur together in minerals and behave as a single chemical compound. The discovery of the RE themselves occurred over nearly 160 years, from 1788 to 1947 [Gup04].

Atomic number	Element	Electron configuration		Ground term RE^{3+}
		RE	RE^{3+}	
21	Scandium (Sc)	$[Ar]3d^14s^2$	[Ar]	
34	Yttrium (Y)	$[Kr]4d^15s^2$	[Kr]	
57	Lanthanum (La)	$[Xe]4f^05d^16s^2$	$[Xe]4f^0$	$^1S_0$
58	Cerium (Ce)	$[Xe]4f^15d^16s^2$	$[Xe]4f^1$	$^2F_{5/2}$
59	Praseodymium (Pr)	$[Xe]4f^36s^2$	$[Xe]4f^2$	$^3H_4$
60	Neodymium (Nd)	$[Xe]4f^46s^2$	$[Xe]4f^3$	$^4I_{9/2}$
61	Promethium (Pm)	$[Xe]4f^56s^2$	$[Xe]4f^4$	$^5I_4$
62	Samarium (Sm)	$[Xe]4f^66s^2$	$[Xe]4f^5$	$^6H_{5/2}$
63	Europium (Eu)	$[Xe]4f^76s^2$	$[Xe]4f^6$	$^7F_0$
64	Gadolinium (Gd)	$[Xe]4f^75d^16s^2$	$[Xe]4f^7$	$^8S_{7/2}$
65	Terbium (Tb)	$[Xe]4f^96s^2$	$[Xe]4f^8$	$^7F_6$
66	Dysprosium (Dy)	$[Xe]4f^{10}6s^2$	$[Xe]4f^9$	$^6H_{15/2}$
67	Holmium (Ho)	$[Xe]4f^{11}6s^2$	$[Xe]4f^{10}$	$^5I_8$
68	Erbium (Er)	$[Xe]4f^{12}6s^2$	$[Xe]4f^{11}$	$^4I_{15/2}$
69	Thulium (Tm)	$[Xe]4f^{13}6s^2$	$[Xe]4f^{12}$	$^3H_6$
70	Ytterbium (Yb)	$[Xe]4f^{14}6s^2$	$[Xe]4f^{13}$	$^2F_{7/2}$
71	Lutecium (Lu)	$[Xe]4f^{14}5d^16s^2$	$[Xe]4f^{14}$	$^1S_0$

Figure I.32. Electronic configuration of the RE elements and RE^{3+} ions. [Ar] = $1s^22s^22p^63s^23p^6$, [Kr] = $1s^22s^22p^63s^23p^63d^{10}4s^24p^6$.

The ground state electronic configuration of the lanthanides represents $[Xe]4f^n5d^x6s^2$, where [Xe] = $1s^22s^22p^63s^23p^63d^{10}4s^24p^64d^{10}5s^25p^6$ is the ground state electronic configuration of the xenon nucleus, $4f^n5d^x6s^2$ represent the valence shell configuration, and n and x are numbers of electrons filling the 4f and 5d orbitals (n = 0 – 14, x = 0 – 1), respectively. Figure I.32 shows the electronic configurations and typical oxygen states of RE elements. Following the Aufbau principle, after the 4f orbitals are fully occupied, the filling of the 5d orbitals is expected to start since the 4f subshell is at lower energy than the 5d subshell . However, the 5d orbital of Gd possesses one electron because a half-filled f orbital is more stable than a partially filled f orbital. Since the energy difference between the 4f orbital and the 5d orbital is not significant, one

electron from the 4*f* orbital (which is expected to have 8 electrons) jumps to the 5*d* orbital, making it $5d^1$.

Each of the *n* electrons in the $4f^n$ configuration is associated with one of the seven 4*f* orbitals and can have a spin of ±1/2. There exists a number of ways to associate the *n* electrons within the 4*f* orbitals, taking the spin into account; this number corresponds to the multiplicity (or degeneracy) of the configuration and is given by the following combinatorial formula:

$$d(4f^n) = C_{14}^n = \frac{14!}{n!(14-n)!}. \quad \text{(I.2)}$$

The outer electron orbitals 5*d* and 6*s* are most important for chemical bonding. Their filling and spatial extent remain practically unchanged throughout the entire lanthanide series. The 4*f* electrons are more spatially localized, being held closer to the nucleus and shielded from the coordination environment by the outer 5*s* and 5*p* electrons. Figure I.33(*left*) shows the radial charge densities for the 4*f*, 5*s*, 5*p*, and 6s electrons for Gd^+ in order to display visually the fact that the 4*f* shell really is deeply imbedded inside the 5*s* and 5*p* shells. These shells are almost totally unaffected by the presence of the 6s electrons, as shown in Figure I.33 (left) [Fre62].

Because of this shielding effect the interaction between the 4*f* electrons and the environment is very weak. As the atomic number increases, the effective attraction between the nucleus and the outer electrons also increases. This increased attraction leads to a contraction of the 4*f* wavefunction and thus a reduction of the atomic, and ionic radii. The lanthanum ion, La^{3+}, has an ionic radius of 1.061 Å, whereas the heavier lutetium ion, Lu^{3+}, has a radius of 0.850 Å. This phenomenon is known as the "*lanthanide contraction*", see Figure I.33 (right).

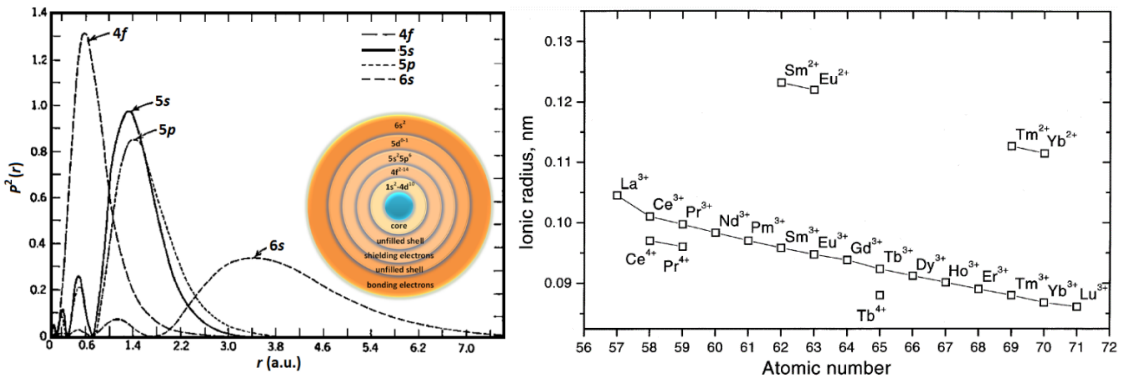

Figure I.33. Square of the radial wavefunctions for the 4*f*, 5*s*, 5*p* and 6*s* energy levels from Hartree-Fock for Gd^+ [Fre62]. Picture inset schematically shows that the 4*f* orbital is within the 6*s*, 5*p* and 5*s* levels (*left*) [Riv12]; lanthanide contraction (*right*) [Gup04].

Rare-earth are acting as dopants within laser materials. Before discussing the RE Hamiltonian, we discuss the definition such a dopant.

Dopant ions. *A dopant* is a trace of a controlled impurity element that is introduced into a chemical material to change its original electrical or optical properties. The amount of dopant necessary to cause changes is typically very low. When doped into crystalline substances, the dopant's atoms get incorporated into its crystal lattice. The procedure of doping tiny amounts of rare-earth or transition-metal ions into transparent crystals, ceramics, or glasses is used to produce media for solid-state lasers.

The concentration of RE^{3+} dopant ions is typically between a few tens and a few at.% with respect to the substituted host-forming cations. The concentration is determined from several considerations. i) The doping level should ensure sufficient pump absorption, which depends on the absorption cross-section, ion density and sample thickness. ii) It should balance the desirable and detrimental energy-transfer processes among the rare-earth ions of the same type or different types, such as energy-transfer, cross-relaxation or energy-transfer upconversion, which may enhance the laser slope efficiency or act as loss mechanisms. iii) It should not lead to excessive concentration quenching of the upper laser level lifetime.

Crystalline materials with high doping levels, typically about a few 10 at.%, as well as stoichiometric crystals are also sometimes used in laser development to enhance the weak absorption properties. However, increasing the doping concentration to such high levels will inevitably lead to a strong cross-interaction between the ions.

More than one type of dopant ion can be introduced into a host matrix to create a laser gain medium, a process known as *codoping*. It is important to distinguish between optically active dopants, called activator ions, which participate in the absorption and emission processes critical to laser operation, and optically passive dopants, which are introduced to modify material properties. Unlike activator ions, passive dopants do not participate in optical transitions, as they lack absorption or emission bands in the relevant spectral range.

Three different *codoping mechanisms* can be distinguished: i) codoping with optically passive cations serving for local charge compensation or for the goal of changing the optical properties of the laser material, such as its refractive index or (indirectly) the spectroscopic properties of the active ions; ii) codoping with two or more optically active ions with the goal of promoting the energy-transfer processes between them.

The terms impurity ions and dopant ions for laser crystals should be distinguished. The former term relates to uncontrolled impurities (such as transition-metal or rare-earth) present as traces in the starting reagents. Although such impurities typically have low concentrations (from a few ppm up to a few tens of ppm), they may significantly deteriorate the spectroscopic properties of laser-active ions.

During the crystal growth, a segregation of the dopant ions can take place because of the difference of solubility of the impurity components in the liquid phase and the solid phase.

The segregation is quantitatively described by *the segregation coefficient* (*K*) which is the ratio of the solubility in the solid phase to that in the liquid phase. Hence, if the value of *K* is 1, it implies there is no depletion or accumulation of dopants in the melt when the crystal grows, which is indicative of a homogenous solid solution in the crystal. The segregation coefficient is also related to the relative size difference between the dopant ion and the host ion it replaces.

RE Hamiltonian: the free ion. To determine the energy levels of the lanthanide free ion, the eigenvalues with the wavefunction Ψ have to be found by solving the Schrödinger equation :

$$H\Psi = E\Psi. \quad \text{(I.3)}$$

The Hamiltonian operator of an atom with *N* electrons when neglecting the spin orbit coupling is determined as following:

$$H = \sum_i \left(-\frac{\hbar^2}{2m_e}\nabla_{r_i}^2 - \frac{Zq_e^2}{4\pi\varepsilon_0 r_i} \right) + \sum_{i<j} \frac{q_e^2}{4\pi\varepsilon_0 r_{ij}}, \quad \text{(I.4)}$$

where from the left to the right appear the kinetic energy of the 4*f* electrons, the potential energy of the 4*f* electrons in the field of the nucleus, and the electrostatic repulsion between them. $\hbar$ is the reduced Planck constant $\hbar = h/(2\pi)$, (h, the Planck constant), m_e is the mass of the electron, $q_e = -e$ is the electrical charge, Z is the atomic number of the atom and ε_0 is the vacuum permittivity. r_i is the distance between the electron i and the nucleus, and $r_{ij} = \boldsymbol{r}_i - \boldsymbol{r}_j$ is the distance between the electrons i and j.

In order to facilitate the calculation of the 4*f* wavefunctions, the central field approximation is used, in which an effective radial field $V(r_i)$ is introduced for each electron, containing the potential of the nucleus and the shielding of the remaining (N – 1) electrons. The central field Hamiltonian can be obtained using the Hartree-Fock method. With this approximation, the Hamiltonian operator can be described as:

$$H_0 = \sum_i \left(-\frac{\hbar^2}{2m_e}\nabla_{r_i}^2 - V(r_i) \right). \quad \text{(I.5)}$$

The Coulomb interaction between individual electrons (H_C) and the spin-orbit coupling (H_{SO}), are incorporated into the full Hamiltonian as perturbations, which are written as:

$$H_C = \sum_{i<j} \frac{e^2}{4\pi\varepsilon_0 r_{ij}} - \sum_i \left(-\frac{Ze^2}{4\pi\varepsilon_0 r_i} + V(r_i) \right), \quad \text{(I.6)}$$

$$H_{SO} = -\sum_i \frac{1}{2m_e^2 c^2} \frac{dV(r_i)}{dr_i} \vec{l}_i \vec{s}_i, \quad \text{(I.7)}$$

where c – the speed of light.

Therefore, the full Hamiltonian is described as:

$$H = H_0 + H_C + H_{SO}. \quad \text{(I.8)}$$

For atoms with small atomic numbers, the Coulomb interaction H_C is greater than the spin-coupling, and the wavefunctions are obtained by first diagonalizing the Hamiltonian $H_C + H_0$. The spin orbit coupling is then added as a perturbation. The introduction of spin-orbit coupling places us in the Russell-Saunders approximation (*LS* coupling) with wave functions characterized by the quantum numbers L, S, J and M_J. In this approximation, the spin-orbit coupling causes each *LS* term to split into multiplets, each with different values of J (see Figure I.34).

In the case of high atomic numbers, the spin-orbit interaction is dominant over the coulomb interaction H_C leading to the coupling of the orbital and the spins angular momenta of individual electrons to form an individual total angular momentum:

$$\vec{j}_i = \vec{l}_i + \vec{s}_i. \quad \text{(I.9)}$$

The total angular momentum is then the sum of the individual angular momenta:

$$\vec{J} = \sum_i \vec{j}_i. \quad \text{(I.10)}$$

This interaction is called *jj*-coupling.

Due to their intermediate atomic number, the lanthanides experience perturbations H_C and H_{SO} of comparable magnitude, leading to what is known as intermediate coupling. In this scheme, the eigenstates are linear combinations of *LS*-states with the same total angular momentum *J*. These states are labelled $^{2S+1}L_J$ (*term symbol* or *spectroscopic term*) according to the Russell-Saunders notation. Their typical energetic splitting is about 10^3 cm^{-1}. Each state exhibits a (2*J*+1) degeneracy.

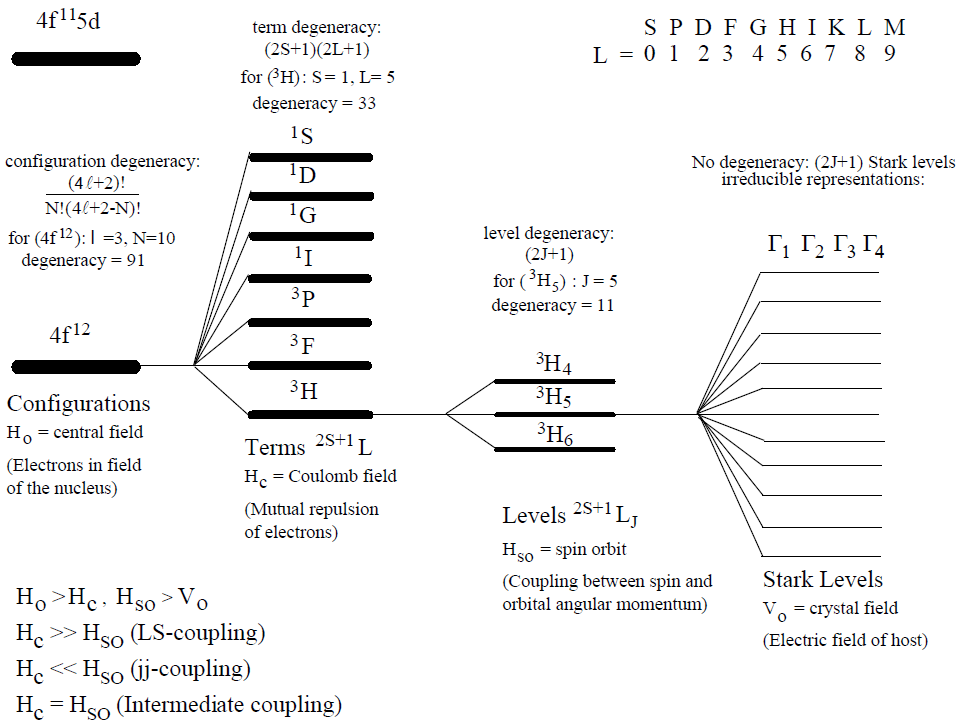

Figure I.34. Energy-level scheme of Tm^{3+} indicating the splitting of the $4f^{12}$ configuration by Coulomb interaction, spin-orbit coupling, and Stark splitting by the crystal-field of the host matrix. Taken from [Wal08].

I.2.B. Absorption, emission processes and transition cross-sections

Intra-ionic processes take place when one ion or a coupled ion-pair interacts with photons or phonons. The latter leads to nonradiative transitions and the former to radiative transitions.

An ideal two-level system comprises two distinct energy levels such as the ground state E_1 and an excited state E_2, with $E_2 > E_1$, see Figure I.35. The ground state has a corresponding population density N_1 and the excited a population density N_2. Their initial population is determined by the Boltzmann statistics in thermal equilibrium:

$$N_1 = N_2 e^{\frac{E_2 - E_1}{kT}}, \tag{I.11}$$

with *T* the temperature and *k* the Boltzmann constant.

Absorption. A photon with an energy $E_{ph} = h\nu_{ph} = E_2 - E_1$, can be absorbed by an ion in ground state E_1 (Ground-State Absorption (GSA)). As a consequence, the population densities N_1 and N_2 change with time and can be written as:

$$\left(\frac{dN_1}{dt}\right)_{abs} = -\sigma_{12} F N_1 = -W_{12} N_1, \tag{I.12}$$

with σ_{12} the absorption cross-section F – the incident photon flux, and W_{12} – the absorption rate from the E_1 level to the E_2 level.

Spontaneous emission. When an ion is excited into E_2, it can relax back to the ground state by emitting spontaneously a corresponding photon with the energy difference $E_2 - E_1$, as shown in Figure I.35 (*center*). The relaxation rate A_{21}, of the E_2 state is inversely proportional to the E_2 radiative lifetime as given by:

$$A_{21} = \frac{1}{\tau_{rad}} \tag{I.13}$$

A is known as the spontaneous emission rate.

The change of population of the E_2 excited state is expressed as:

$$\left(\frac{dN_2}{dt}\right)_{sp} = -AN_2, \tag{I.14}$$

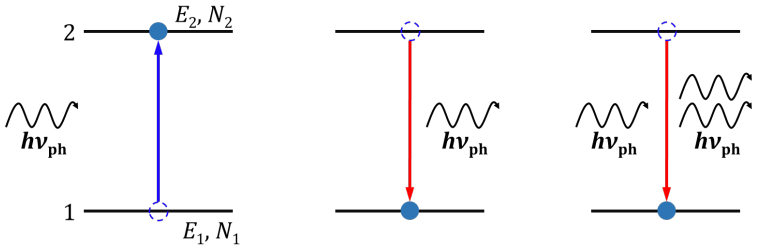

Figure I.35. Schematic illustration of the three fundamental processes: absorption (*left*), spontaneous emission (*center*) and stimulated emission (*right*).

Stimulated-emission. In the case of an already excited ion in the E_2 level the excited ion can be forced to undergo the transition from level 2 to level 1 by an incident photon with an energy $E_2 - E_1$. In this case, a second photon is emitted that adds to the incident one.

The difference between stimulated and spontaneous emissions is that in the case of spontaneous emission, the ion emits a photon that has no definite phase relation with that emitted by another ion and is emitted in any direction. In the case of stimulated emission, because the process is induced by the incident photon, the photon emission adds in phase to that of the incoming wave and in the same direction.

The rate equation of stimulated emission is defined as:

$$\left(\frac{dN_1}{dt}\right)_{SE} = -\sigma_{21} F N_2 = -W_{21} N_2. \tag{I.15}$$

In the case of identical degeneracy, W_{12} equals W_{21} and therefore $\sigma_{12} = \sigma_{21}$.

As a consequence, for a two-level system, the rate of photon flux change through a crystal is:

$$\frac{dF}{dz} = \sigma_{21} F N_2 - \sigma_{12} F N_1 = \sigma F \left(N_2 - N_1\right), \tag{I.16}$$

Therefore, amplification is only possible if $N_2 > N_1$, which is known as *population inversion*. In a two-level system, this condition cannot be achieved. The m4aximum occupation of the upper

level is $N_2 = N_1$, since absorption and emission are compensating each other. Thus, to achieve population inversion, systems with at least three levels are needed to satisfy the condition.

Selection rules for radiative transitions. The radiative transitions in the trivalent lanthanides occur mainly between levels inside the electronic 4*f* shell and sharp spectral lines are expected. Such transitions are known to be forbidden by the Laporte selection rule, which says that states with even parity can undergo electric dipole transitions only with states of odd parity, and odd states only with even ones. Another way of saying this is that the algebraic sum of the angular momenta of the electrons in the initial and final state must change by an odd integer. For transitions within the 4*f* shell, ED transitions are forbidden, but allowed for magnetic dipole or electric quadrupole transitions. The operators for electric dipole, magnetic dipole and quadrupole transitions are shown in Figure I.36 along with their selection rules.

$\vec{P} = -e\sum_i \vec{r}_i$ Electric dipole operator (odd operator)

$\vec{M} = -\frac{e\hbar}{2mc}\sum_i \vec{l}_i + 2\vec{s}_i$ Magnetic dipole operator (even operator)

$\vec{Q} = \frac{1}{2}\sum_i \left(\vec{k}\cdot\vec{r}_i\right)\vec{r}_i$ Quadrupole operator (even operator)

Selection rules

Transition	S	L	J (No 0↔0)	Parity
Electric dipole	ΔS=0	ΔL=0, ±1	ΔJ=0, ±1	opposite
Magnetic dipole	ΔS=0	ΔL=0	ΔJ=0, ±1	same
Electric quadrupole	ΔS=0	ΔL=0, ±1, ±2	ΔJ=0, ±1, ±2	same

Figure I.36. Multipole operators and selection rules [Wal06].

4*f* to 5*d* transitions which are allowed interconfigurational transitions exhibit broad spectral lines in contrast to the 4*f* interconfigurational sharp lines. Magnetic dipole transitions could explain some of the observed 4*f* transitions, but not all, and represents a special case. Electric quadrupole transitions could explain all the transitions, but are too weak to justify the observed intensities. However, the odd-order terms of a noncentral crystalline field can force a coupling between odd and even states, resulting in mixed parity states that mitigates Laporte's rule and enables electric dipole transitions.

Calculation of transition cross-sections. In laser physics, transition cross-sections are defined as material parameters to quantify the probability of optically induced transition events such as absorption, stimulated emission or excited-state absorption. For a laser ion in a certain electronic state, the rate of transitions (in events per second) is given as the corresponding cross-section times the photon flux density (in photons per square meter and second):

$$R = \sigma \frac{I}{h\nu}, \tag{I.17}$$

where R is the transition rate (in s^{-1}), I is the optical intensity. Such transition rates are used in rate equation modelling.

Transition cross-sections depend on the optical frequency (or wavelength). Depending on the spectral shape, one can encounter strongly peaked cross-section spectra or rather smooth spectra.

Absorption cross-section. The absorption cross-section is related to the probability that a photon passing through a specific material will be absorbed by optically active ions with an ion density N:

$$\sigma_{abs} = \frac{\alpha_{abs}}{N}, \tag{I.18}$$

with α_{abs} the absorption coefficient. Absorption cross-sections for transitions starting from the ground-state are often obtained from absorption spectra, measured using the transmission of a white light source for instance.

Stimulated-emission cross-section. The stimulated-emission cross-section quantifies the probability that an incident photon will stimulate the emission of another photon from an excited ion, leading to amplification of light.

The spectral profile of the emission cross-sections (usually without absolute scaling) can be obtained from fluorescence spectra, provided that no reabsorption modifies the spectral shape and there is no spectral overlap of different fluorescent transitions. Absolute values of emission cross-sections can be calculated using two methods. The first one is the *reciprocity method* (RM) [Pay92]:

$$\sigma_{\mathrm{SE}}^{i}(\lambda) = \sigma_{\mathrm{abs}}^{i}(\lambda)\frac{Z_l}{Z_u}\exp\left(-\frac{(hc/\lambda) - E_{\mathrm{ZPL}}}{kT}\right), \tag{I.19}$$

$$Z_{l(u)} = \sum_k g_k^{l(u)} \exp(-E_k^{l(u)}/kT). \tag{I.20}$$

where i indicates the light polarization, E_{ZPL} is the zero-phonon-line (ZPL) i.e. the energy corresponding to transitions between the lowest Stark sub-levels of the involved multiplets, $Z_{l(u)}$ are the partition functions of the lower (l, $^3H_6$) and upper (u, $^3F_4$) manifolds, $g^{l(u)}{}_k$ is the degeneracy of each Stark sub-levels for the given point group symmetry of dopant ions in a host matrix, and $E^{l(u)}{}_k$ is the energy of Stark sub-levels measured from the lower-lying sub-level of each multiplet (k is numbering the sub-levels).

The second method is based on the *Füchtbauer–Ladenburg equation*, that links the stimulated emission cross sections to the spontaneous emission intensity [Aul82]:

$$\sigma_{\mathrm{SE}}^{i}(\lambda) = \frac{\lambda^5}{8\pi\langle n\rangle^2 \tau_{\mathrm{rad}} c}\frac{B(JJ')3W_i(\lambda)}{\sum_{i=a,b,c}\int \lambda W_i(\lambda)\mathrm{d}\lambda}, \tag{I.21}$$

where λ is the emission wavelength, $\langle n\rangle$ is the refractive index at the average emission wavelength, B(JJ') is the luminescence branching ratio, c is the speed of light, τ_{rad} is the radiative lifetime of the emitting level, i = ***a***, ***b***, ***c*** denotes light polarization, $W_i(\lambda)$ is the luminescence spectrum calibrated with the apparatus function of the set-up.

I.2.C. Transition intensities (Judd-Ofelt theory)

The Judd-Ofelt theory [Jud62, Ofe62] is a model describing the transition intensities of lanthanide ions in solids and solutions. As mentioned earlier, in a free ion, electric dipole transitions ($f-f$ transitions) are prohibited by the Laporte rule; however, this restriction is removed when a noncentrosymmetric field (*e.g.*, a crystal field) is present. The crystal field mixes the states of excited configurations with opposite parity (*e.g.*, $4f^{n-1}5d^1$) into the ground configuration $4f^n$, enabling electric dipole transitions. The Judd-Ofelt approach can be used to predict oscillator strengths, branching ratios, energy level radiative lifetimes and emission probabilities by using only three spectroscopic intensity parameters (so-called Judd-Ofelt

parameters) Ω_t (t = 2, 4, 6) which are assumed to be identical for all transitions. The Judd-Ofelt computation requires the reduced matrix element of the single electron $U^{(k)}$, (k = 2, 4, 6) for ED transitions and $L + 2S$ tensor operations for MD transitions. The tensor $U^{(k)}$, (k = 2, 4, 6) characterizes the electric-dipole induced $4f \leftrightarrow 4f$ transition intensities. Four assumptions introduced in the J-O formalism allow the expansion of oscillator strengths as the sum of three even-ranked tensors: i) the ground $4f^n$ and excited $4f^{n-1}5d^1$ configurations are degenerate with the excited one being higher in energy; ii) the Stark sub-levels of the ground configuration are equally populated; iii) the energy gap between the ground configuration $4f^n$ and any excited configuration is much higher than the energies of the multiplets involved in $4f^n$ transition; iv) The material is optically isotropic (the absorption data must be averaged over all polarizations).

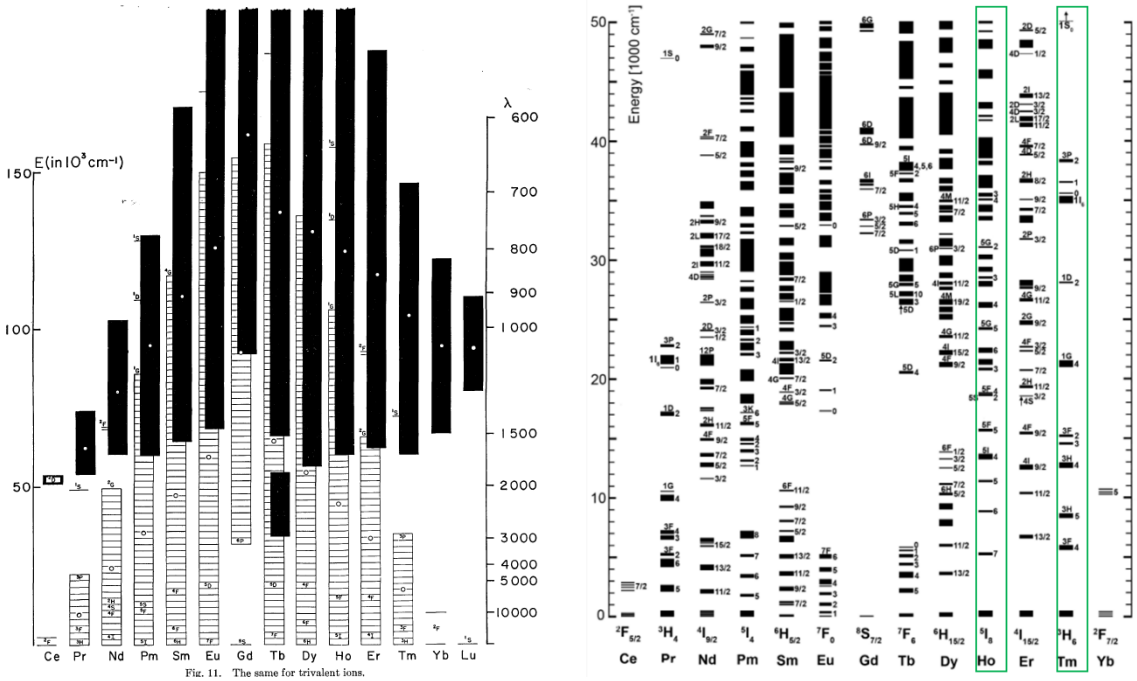

Figure I.37. Schematic diagram of the $4f^n$ (*white*) and $4f^{n-1}5d$ (*black*) configurations of the Ln^{3+} (*left*) and a close look at the energy levels of the $4f^n$ shell in LaF_3 (*right*) [Die63, Car89].

To calculate, the Judd-Ofelt intensity parameters Ω_t, we use the experimentally measured GSA spectra of the studied lanthanide ions in the considered host matrix.

The absorption line strengths can be determined from the experimental GSA spectra using the following equation [Wal06]:

$$S_{\exp}(JJ') = \frac{3ch(2J+1)}{8\pi^3 e^2 \langle\lambda\rangle} n\left(\frac{3}{n^2+2}\right)^2 \int_{manifold} \sigma_{abs}(\lambda)d\lambda, \qquad \text{(I.22)}$$

with q_e is the electron charge, c is the speed of light, J is the total angular momentum of the initial ground state, n is the refractive index, $\langle\lambda\rangle$ is the mean wavelength of the considered absorption band, and σ_{abs} is the absorption cross-section.

The three J-O intensity parameters can then be adjusted by fitting the measured absorption line strengths values using Eq. I.23:

$$S_{\exp}^{ED} = \sum_{k=2,4,6} U^{(k)}\Omega_k \qquad \text{(I.23)}$$

$$U^{(k)} = \left\langle (4f^n)SLJ \left\| U^k \right\| (4f^n)S'L'J' \right\rangle^2, \quad \text{(I.24)}$$

with $U^{(k)}$ is the reduced squared matrix elements of the $J \rightarrow J'$ electric-dipole transition. The intensity parameters (Ω_k) contain the odd-order parameters of the crystal-field, radial integrals of the wavefunctions of the ground $4f^n$ and perturbing configurations, etc. In principle, it is possible to calculate the (Ω_k) parameters ab initio. The simplification proposed by Judd and Ofelt consists in considering the three parameters as a set of phenomenological parameters fitting the experimental absorption data.

The accuracy of the J-O refinement can be calculated by a root mean square deviation Δrms as:

$$\Delta rms = \left[\frac{\sum \left(\left\langle S_{\exp}(JJ') \right\rangle - S^{\Sigma}_{calc}(JJ') \right)^2}{p_a - q_j} \right]^{\frac{1}{2}}, \quad \text{(I.25)}$$

where p_a – the number of absorption bands taken into account during the fitting experimental data and q_j – the number of intensity parameters.

This approach represents the so-called weak configuration interaction (WCI) or standard Judd-Ofelt theory.

Modified Judd-Ofelt Theory. If only the lower-energy excited configuration of the opposite parity $4f^{n-1}\ 5d^1$ contributes to the configuration interaction, the ED line strengths are determined as [Kor90]:

$$S^{ED}_{calc} = \sum_{k=2,4,6} U^{(k)} \tilde{\Omega}_k, \quad \text{(I.26a)}$$

$$\tilde{\Omega}_k = \Omega_k [1 + 2\alpha (E_J + E_{J'} - 2E^0_f)], \quad \text{(I.26b)}$$

with $\tilde{\Omega}_k$ – the modified intensity parameters , E_f^0 – the average energy of the $4f^n$ configuration and $\alpha \sim 1/(2\Delta)$, here Δ is the average energy difference between the $4f^n$ and $4f^{n-1}\ 5d^1$ configurations. This approximation leads to a modified version of the Judd-Ofelt (mJ-O) theory [Kor90, Loi18]. One can notice that the $\tilde{\Omega}_k$ parameters for the mJ-O theory are transformed into Ω_k ones for the standard theory assuming a high-lying $4f^{n-1}\,5d^1$ excited electronic configuration (i.e., the energy difference $\Delta \rightarrow \infty$ or, equivalently, $\alpha \rightarrow 0$).

In the modified J-O theory, three $\tilde{\Omega}_k$ parameters and α are adjusted. The mJ-O theory is accounting for the fact that different multiplets of the ground configuration have different energies and, consequently, different energy gaps with respect to the excited configuration of opposite parity $4f^{n-1}5d^1$ (which is considered to be completely degenerated). In this case, the intensity parameters should depend on the energy of the two multiplets involved in the transition, as well as the average energy gap between the $4f^n$ and $4f^{n-1}5d^1$ configurations, as represented by Eq. I.26b.

It should be noted that one of the main assumptions of the standard Judd-Ofelt theory (the energy gap between the ground configuration $4f^n$ and any excited configuration is much higher than the energies of the multiplets involved in the considered transition) is violated for almost all the trivalent rare-earth ions except for Yb^{3+} and Ce^{3+}. It is especially clear for higher lying $4f^n$ multiplets. Thus, strictly speaking, the configuration interaction should be considered for all

these ions. The effect of excited configurations is especially evident for Pr^{3+} ions for which the standard J-O theory fails to explain the experimental transition intensities. The explanation of the particular case of Pr^{3+} can be found elsewhere [Heh13].

The J-O parameters are first used to calculate the ED line strengths and then one can derive the probabilities of radiative transitions for emission channels $J \rightarrow J'$ as according to:

$$A_{calc}^{\Sigma}(JJ') = \frac{64\pi^4 e^2}{3h(2J+1)\langle\lambda\rangle^3} n \frac{(n^2+2)^2}{3} S_{calc}^{ED}(JJ') + A_{calc}^{MD}(JJ'). \quad \text{(I.27)}$$

The total probabilities of radiative transitions from the different emitting level A_{tot}, the corresponding radiative lifetimes τ_{rad} and the luminescence branching ratios for the particular emission channels $B(JJ')$ can be calculated using the A_{calc} values:

$$A_{tot} = \sum_{J'} A_{calc}^{\Sigma}(JJ'), \quad \text{(I.28)}$$

$$\tau_{rad} = \frac{1}{A_{tot}}, \quad \text{(I.29)}$$

$$B(JJ') = \frac{A_{calc}^{\Sigma}(JJ')}{A_{tot}}. \quad \text{(I.30)}$$

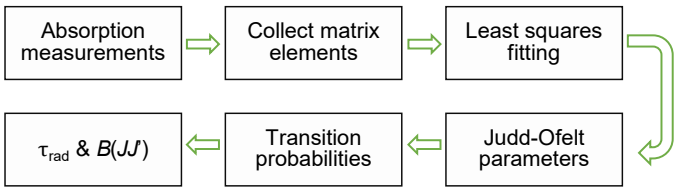

Figure I.38. Procedure of Judd-Ofelt analysis. Taken from [Wal06].

Also, J-O theory can be applied for non-transparent materials for which absorption spectra are unavailable. Other approaches can be used based on the analysis of i) excitation or diffuse-reflection spectra [Luo10, Zha18a]; ii) luminescence spectra for certain lanthanides ions with purely MD transitions [Tia11, Vol18]; iii) luminescence decay curves [Luo20].

I.2.D Crystal-field splitting and barycenter plot

The lanthanide ions in crystal field. When the lanthanides are incorporated into host matrices, they usually exhibit a stable oxidation state +3 due to losing the two 6*s* electrons and one 4*f* or one 5*d* electron, in the case of Ce and Gd, to bond with the surrounding ligands and their electronic configuration changes to [Xe]$4f^n$, see Figure I.32. Divalent REs can appear in crystals with divalent lattice sites if a local charge compensation is provided by crystal defects, such as F-centers, or by the presence of quadrivalent co-dopants in the host matrix [Kap62].

The outer shells screen the 4*f* orbital from outside perturbing influences and protect the optically active 4*f* electrons to some extent from the influence of the crystal field, as shown in Figure I.39. It determines the typical spectroscopic characteristic of lanthanides cations, *e.g.*, a low variation of the 4*f*-states in different local environments and narrow transition line-widths compared to those observed in transition metals, divalent rare-earths, and RE^{3+} 5*d*-states. It makes RE^{3+} ions spectra almost similar to the corresponding free ion spectra.

The crystal field significantly influences the characteristics of the optical spectra and plays a crucial role in the Stark effect, which leads to the splitting of $^{2S+1}L_J$ energy levels of ions in solids. The ligand or crystalline field, which is external to the optically active dopant ion, has a symmetry determined by the chemical composition of the host.

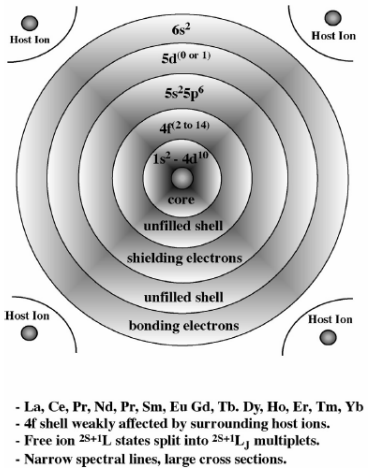

Figure I.39. Atomic structure of Ln^{3+} ions. After [Wal06].

In a free atom, each $^{2S+1}L_J$ multiplet exhibits a $2J + 1$ degeneracy. However, when the ion is placed in a crystal environment, the degeneracy is lifted partially or totally under the influence of the crystal field treated as a perturbation. The extent to which the $2J+1$ degeneracy is removed depends on the point symmetry surrounding the ion. The perturbed free ion Hamiltonian for an ion in a crystal is written as:

$$H = H_0 + H_C + H_{SO} + V_O,$$
$$V_O = \sum_{kq} A_{kq} \sum_i r_i^k Y_{kq}(\vartheta_i, \varphi_i), \quad \text{(I.31)}$$

where the summation over i involves all electrons, with position r_i^k, of the ion. $Y_{kq}(\vartheta_i, \varphi_i)$ are spherical harmonics with ϑ_i and φ_i angular coordinates of the ion. The A_{kq} are structural parameters in the static crystal field expansion. They depend only on the host and can be calculated in a point charge lattice sum using crystallographic data and charges of the host lattice. The point charge model assumes that the ligand charges are all point charges. The A_{kq} are then given by [Wal06]:

$$A_{kq} = -q_e \sum_i \frac{Z_i Y_{kq}(\vartheta_i, \varphi_i)}{R_i^{k+1}}, \quad \text{(I.32)}$$

where Z_i is the charge value at the position R_i corresponding to the surrounding atoms composing the crystal. The interaction between the dopant ion and the ligand crystal field is about one order of magnitude smaller than the previously described effects. As mentioned earlier, it breaks the M_J degeneracy of the $^{2S+1}L_J$ manifolds and leads to splitting on an energy range of some $\sim 10^2$ cm^{-1}. For ions with an even number of electrons the manifold can be splitted into $(2J+1)$ sublevels when the symmetry is low, see Figure I.34, while for ions with an odd number of electrons a 2-fold degeneracy remains, following the Kramers theorem, and the manifolds split into $(2J + 1)/2$ sublevels. The extent to which the Stark split sublevels spread

depends on the strength of the crystal field. The larger the crystal field, the larger the spread of the *J* sublevels will be.

A dopant ion replaces a host cation and forms an optically active center with a specific point group symmetry. The symmetry at the ion site can be used to predict the number of Stark sub-levels for a particular *J* state [Run56], as illustrated in Figure I.40. Alternatively, rare-earth ions can be used to probe the crystal symmetry, provided that the exact number of Stark levels can be experimentally determined.

J =	0	1	2	3	4	5	6	7	8
Cubic	1	1	2	3	4	4	6	6	7
Hexagonal	1	2	3	5	6	7	9	10	11
Tetragonal	1	2	4	5	7	8	10	11	13
Lower symmetry	1	3	5	7	9	11	13	15	17

Cubic	O	O_h	T_d	T_h	T							
Hexagonal	C_3	C_{3v}	C_{3h}	C_6	C_{6v}	C_{6h}	D_3	D_{3d}	D_{3h}	D_6	D_{6h}	S_6
Tetragonal	C_4	C_{4v}	C_{4h}	D_4	D_{2d}	D_{4h}	S_4					
Lower symmetry	C_1	C_2	C_s	C_{2v}	C_{2h}	D_2	D_{2h}	S_2				

Figure I.40. Number of levels that a given *J* state will split into for a given point symmetry (*left*) and general symmetry classes include the 32 crystallographic point groups (*right*) [Wal08].

Barycenter plot. Antic-Fidancev reported on a new approach called *the barycenter plot* [Ant00]. This approach is based on the fact that the barycenter energy of any $^{2S+1}L_J$ level belonging to the $4f^n$ shell shows a linear variation with the barycenter energy of any other $^{2S+1}L'_{J'}$ level.

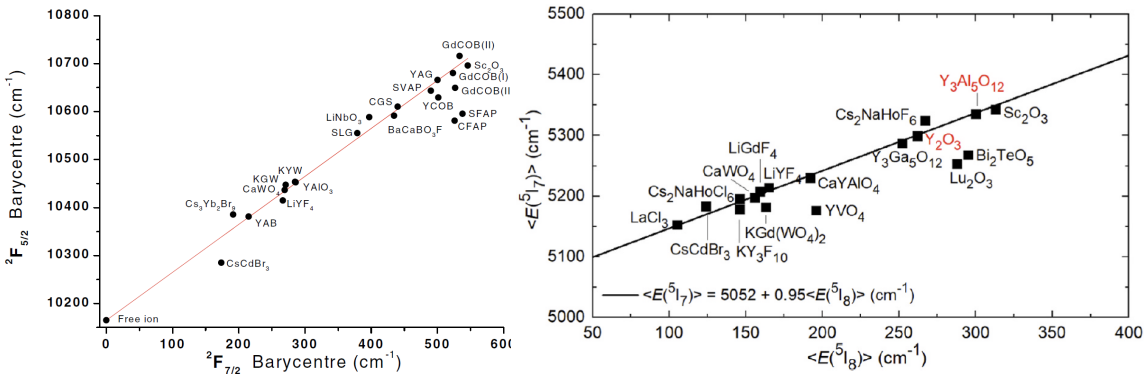

Figure I.41. Barycenter plot: for the $^2F_{7/2}$ and $^2F_{5/2}$ Yb^{3+} manifolds (*left*) and for $^5I_8$ and $^5I_7$ Ho^{3+} manifolds (*right*) in different materials. Taken from [Hau01, Loi21a].

Figure I.41 shows examples of the barycenter plots for the $^2F_{7/2}$ and $^2F_{5/2}$ manifolds of Yb^{3+} ions, and the $^5I_8$ and $^5I_7$ manifolds of Ho^{3+} ions in different host matrices [Hau01, Loi21a]. The linear dependence between the two manifolds with a slope equal to one indicates that the energy difference between the two barycenters remains constant regardless of the host and is equal for instance to 5052 cm^{-1} in the case of the Ho^{3+} $^5I_8$ and $^5I_7$ manifolds. The deviation from this linear dependence shows towards a wrong identification of the Stark sub-levels energies.

I.2.E. Multiphonon non-radiative relaxation

This section and further ones discuss processes involving *phonons* which can be defined as the quantum mechanical description of an elementary vibrational motion in which a lattice of atoms or molecules uniformly oscillates at a single frequency.

The multiphonon relaxation is the consequence of the electron-phonon interaction and is also a non-radiative intra-ionic process occurring between two levels (an excited state and a lower-lying manifold), as shown in Figure I.42. It is a decay from the excited state into the lower-lying one by interaction with one or several lattice phonons. During this process, the energy is transformed into heat which is released in the host matrix. The weak coupling of 4*f* electrons with lattice vibrations leads to multiphonon relaxation.

This process is host dependent and its probability varies with the energy gap ΔE between an excited state and the next lower-lying state as well as the maximum phonon energy of the host matrix. The spectrum of phonon energies of a material (a Raman spectrum) is characteristic for each host and could be represented by an effective phonon energy $\hbar\omega_{\text{eff}}$. This spectrum depends on oscillation factors related to the host including the masses of the lattice ions, the binding strengths, and the lattice structure.

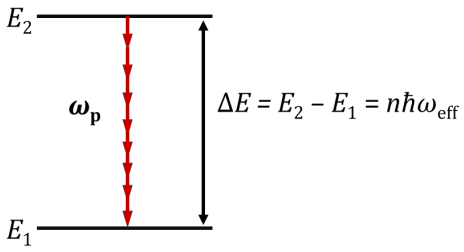

Figure I.42. Two level system showing the multiphonon nonradiative relaxation process.

The number of phonons needed to bridge the energy gap depends on the value of the energy gap and the energy of the involved phonon (so-called "energy gap law") [Sch04]:

$$p = \frac{\Delta E}{\hbar\omega_{eff}}. \tag{I.33}$$

Decreasing the number of the involved phonons in multiphonon relaxation increases the probability of non-radiative transitions. For instance, when p = 4, the probability of radiative and non-radiative transitions is of the same order of magnitude. If more than 5 phonons are needed to bridge the energy gap, radiative transitions become dominant [Ris67].

The temperature dependent multiphonon non-radiative relaxation rate W_{NR} can be expressed as [Moo70]:

$$W_{NR}(T) = Ce^{-\alpha\Delta E}\left[1 - e^{\frac{\hbar\omega_{eff}}{kT}}\right]^{-p}. \tag{I.34}$$

For the fixed temperature (RT), W_{NR} can be described as the dependence on ΔE [Web67]:

$$W_{NR} = Ce^{-\alpha\Delta E}, \tag{I.35}$$

where C and α are constants, which are determined by the host matrix: C has the meaning of the multiphonon rate at the limit of zero energy gap and α is given by the formula:

$$\alpha = \frac{\ln(\varepsilon)}{h\nu_p}, \tag{I.36}$$

where ε is the ratio between the probabilities of m-phonon and (m – 1)-phonon relaxation, and $h\nu_p$ is the maximum phonon energy of the host matrix mainly contributing to the NR relaxation. Thus, for materials with smaller phonon energies, weaker multiphonon rates are expected.

Figure I.43 (*left*) shows the theoretical temperature dependences of W_{NR} calculated by [Ris68] and involving 4, 5 and 6 phonons with equal energies. The temperature dependence is stronger for processes involving higher number of phonons, as seen at elevated temperatures. Figure I.43 (*right*) shows W_{NR} as a function of the energy-gap to the lower-lying level for different RE^{3+} ions in $YAlO_4$ at 77 K. The exponential dependence is expressed by Eq. I.35 [Ris77].

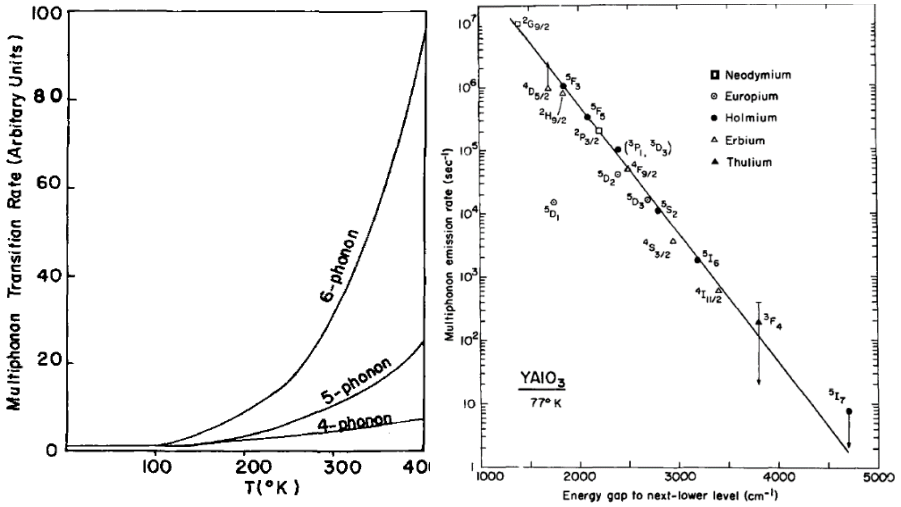

Figure I.43. Theoretical temperature dependences of multiphonon relaxation for the single frequency model; $\Delta E = 1500$ K and $p_i = 4$, 5 and 6 (*left*); Dependence of the rate of multiphonon relaxation on energy gap to the next lower-lying level for excited states of rare-earth ions in $YAlO_4$ at 77 K (*right*) [Ris77].

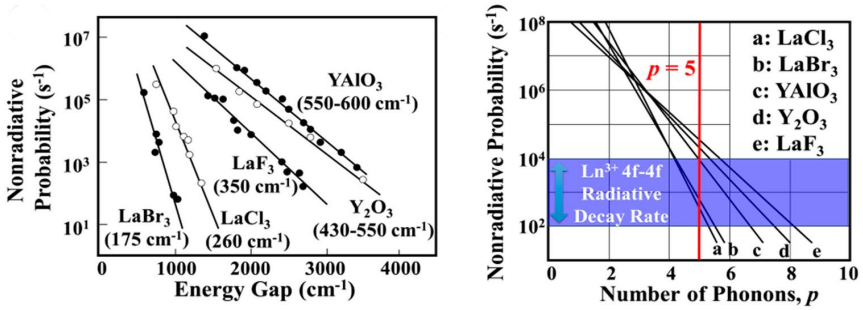

Figure I.44. (*left*) Probabilities of nonradiative relaxation of Ln^{3+} 4*f* states in different host lattices, plotted against the energy gap to the next lower-lying state. The lines represent the exponential fits of these data, *numbers* are the effective phonon frequencies. (*right*) Plots of these exponential fitting lines against the number of phonons involved in the relaxation process. The violet-blue-shaded area denotes the range of typical radiative decay rates of Ln^{3+} 4*f* → 4*f* transitions in the crystalline lattices [Shi22].

When the energy gap decreases, there is a significant increase in the multiphoton non-radiative relaxation (MNR) rate, which is exponential in nature, as shown in Figure I.44(b). This indicates that the MNR is prevalent when the energy gap between the Ln^{3+} 4*f* states is small. In such systems, a new relationship between MNR rate and the number of phonons (p) was

established, Figure I.44(c). The value of p is determined by dividing the energy gap by the highest phonon frequency ($h\omega_{max}$) of the host lattice. The results indicate that this process becomes dominant for electron de-excitation when the energy gap is less than five phonons. This "five phonons" criterion has now become a standard way to evaluate the relaxation probability of Ln^{3+} 4*f* state. [Shi22].

The non-radiative lifetime of the excited state can be defined as:

$$\tau_{NR} = \frac{1}{W_{NR}}. \quad \text{(I.37)}$$

The luminescence lifetime can be derived from radiative and non-radiative one as:

$$\frac{1}{\tau_{lum}} = \frac{1}{\tau_{rad}} + \frac{1}{\tau_{NR}}. \quad \text{(I.38)}$$

From this question, it can be seen that the luminescence lifetime is affected by non-radiative processes by reducing its lifetime. The multiphonon non-radiative relaxation reduces fluorescence quantum efficiency further impacting the laser performance, i.e., via heat generation, and increasing the laser threshold.

I.2.F. Energy-transfer processes among rare-earth ions

We already considered the intra-ionic processes in Section I.2.B. Inter-ionic processes play an important role to achieve laser emission. Let us discuss these processes which occur between the same group of RE^{3+} ions, when they are introduced in solid-state hosts. Two types of ions can be distinguished in these processes, namely donors (D) and acceptors (A). The former ones absorb photons and the latter ones receive the energy from the donors. In this process, multiphonon relaxation can be involved, as shown in Figure I.45.

The main inter-ionic processes including radiative (reabsorption) and nonradiative processes (energy migration, EM, energy-transfer upconversion, ETU, and cross-relaxation, CR) are shown in Figure I.46. These processes have a great impact on laser efficiency as will be shown later in this chapter.

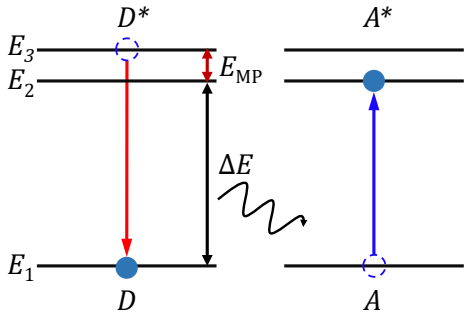

Figure I.45. An example inter-ionic process between two ions with the presence of multiphonon relaxation. D and D*, A and A* are donor and acceptor ions in ground and excited states, respectively. E_{MP} – multiphonon energy of upper manifold.

Energy-transfer upconversion. ETU process occurs when donor and acceptor ions are in an excited state, and the donor transfers its energy to the acceptor as it relaxes to its ground

state. Then, the acceptor ion absorbs energy and goes to a higher energy state, as illustrated in Figure I.46(a).

Cross-relaxation. CR occurs when a donor ion is in a higher-lying excited state, while an acceptor ion is in the ground state. This process is similar to ETU, with the difference being that the final state of both ions is an excited one. If the CR process results in both ions being in the same final excited state, it leads to the "two-for-one" process. During this process, the absorbed energy of a pump photon is divided between the donor and acceptor ions, resulting in the emission of two photons with equal energy.

Energy migration. An excited ion can transfer its energy nonradiatively to a neighbouring ion, which is initially in the ground state, during relaxation to its ground state. The second ion becomes excited, see Figure I.46(c). This phenomenon is known as donor-donor transfer because the newly excited ion can subsequently act as a donor for other energy transfer events, such as ETU and CR. This sequential process of energy transfer can continue, with each excited ion acting as a donor for the next ion, forming a chain of energy transfer. However, this process can result in losses if the excitation energy transfers to an impurity.

Reabsorption. When a donor ion emits a photon, it can be absorbed by an acceptor ion within a host matrix. This process can occur several times before the photon emits and leaves the material, see Figure I.46(d). This process is resonant and has an influence on several spectroscopic measurements, such as the luminescence lifetime of the emitted ion and luminescence spectra of the material. This process is crucial for quasi-three-level laser systems due to their absorption and emission bands are spectrally overlapping.

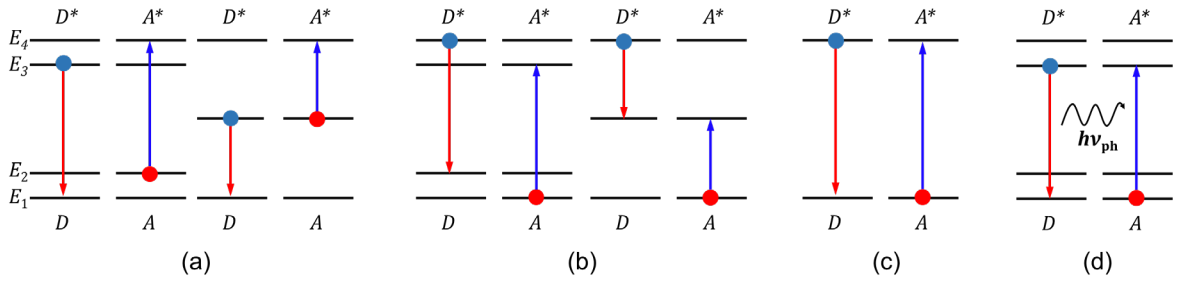

Figure I.46. Inter-ionic processes: (a) energy transfer upconversion; (b) cross-relaxation; (c) energy migration; (d) reabsorption.

I.2.G. Excited-state absorption

Excited-state absorption (ESA) is an intra-ionic process, where a single atom, ion, or molecule in a lower-lying excited-state, |1>, is excited to a higher-lying one |2> with the absorption of a photon [Koe95]. ESA can occur only if the system has been already excited to the |1> state from the ground-state |0> by GSA, as shown in Figure I.47(a) Hence, to excite an ion to the |2> state though ESA, at least two pump photons are needed. The energy differences between the (|0> and |1>) and (|1> and |2>) states can be resonant or different. Two pump photons with different wavelengths are needed to observe ESA in the latter case [Gui22].

ESA is commonly observed in molecules and materials doped with transition metal ions [Yum02]. It is less common for RE^{3+} doped materials due to their narrow bandwidth transitions.

Among RE^{3+} ions, a larger variety of ESA processes occur in those with rich (ladder-like) energy-level schemes [Gar96]. Figure I.47(b) shows the summary of ESA transitions of Tm^{3+} ions exploited so far.

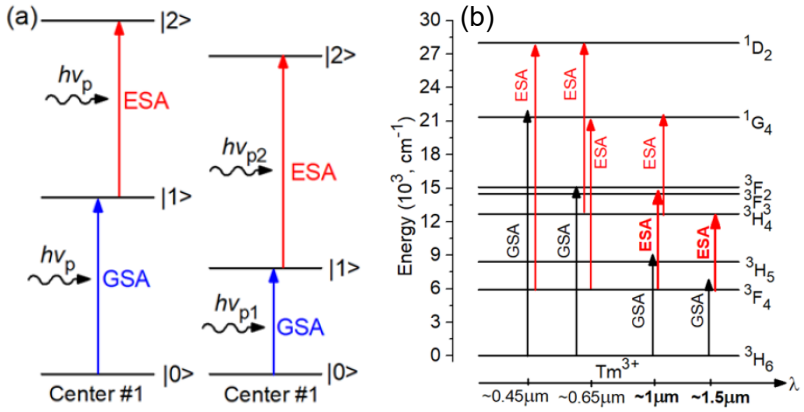

Figure I.47. (a) Schematic illustration of the ESA process and (b) possible ESA transitions of Tm^{3+} ions. Taken from [Gui22].

For laser materials, the ESA process can be both:

• *a drawback* – especially when ESA cross-sections are higher than the GSA cross-sections leading to a depopulation of the excited state and, hence, lower laser efficiency;

• *an advantage* – it can populate energy levels of higher energy to achieve laser operation from those levels or it can be involved in pumping schemes, *e.g.*, upconversion pumping scheme of Tm lasers emitting at 2.3 µm [Gui19].

I.2.H. Electron-phonon interaction

When optically active ions are incorporated into a crystal lattice, they interact with it though lattice vibrations (phonons). This process is called *electron-phonon interaction*. It is described as an additional term supplementary to the free ion Hamiltonian:

$$H_{EP} = \sum_k \left[\frac{p_k^2}{2M_k} + V_c(r_{k,0}, Q_k) \right], \qquad \text{(I.39)}$$

where p_k is the momentum of the k^{th} oscillating ion with a mass M_k, $r_{k,0}$ is its equilibrium position, and Q_k is the distance of this ion to the first coordination sphere (ligand) defined as *configurational coordinate*. The second term $V_c(r_{i,0}, Q_k)$ couples the electronic and dynamic lattice systems and is termed as the electron-phonon coupling [Hen89].

The lattice vibrations can be shown as periodic displacement of ions, as illustrated in Figure I.48. It shows irreducible representations of an optically active center in a crystal lattice surrounded by six equidistant neighboring ligands.

Electron-phonon interaction causes several spectroscopic effects of RE^{3+} ions in materials: i) multiphonon nonradiative relaxation; ii) phonon-assisted energy transfer between two different optically active ions, *e.g.*, CR and ETU; iii) temperature broadening (homogeneous) of spectral lines (see Section I.4); iv) multiphonon-assisted Stokes and anti-Stokes excitation; v)

cooperative processes; and iv) Stokes and anti-Stokes phonon sidebands due to vibronic transitions.

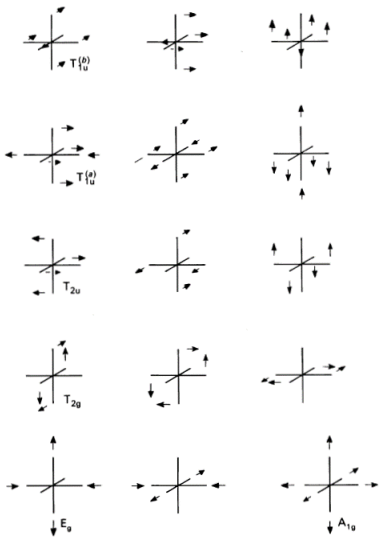

Figure I.48. Normal modes of distortion of a complex consisting of an electronic center with six equidistant neighboring ions along the ± *x*, ± *y*, ± *z*-directions [Hen89].

The electron-phonon interaction is well-known for transition-metal ions and is classified as strong interaction since 3*d* shell is the outer shell and is not shielded leading to strong coupling of electronic states with lattice vibrations. It leads to broad absorption and emission spectra of these ions. Thus, there can be optical transitions where not only a photon is absorbed or emitted, but also one or several phonons. This vibrational–electronic (vibronic) interaction leads to a strong homogeneous spectral line broadening and, consequently, to a large gain bandwidth. Vibronic lasers are sometimes referred to as phonon-terminated lasers. In transition-metal ion lasers, laser oscillations are frequently observed in the phonon wing of the emission spectrum rather than in the sharp electronic lines.

To describe optical properties caused by the electron-phonon interaction, *the configuration coordinate model* is employed [Wil51, Hen89, Bla94]. The configurational coordinate diagram is a plot of the system energy as a function of the displacements of the nuclei (atoms or ions) which make up the system [Mar69].

In the case of lanthanide ions, the coupling of 4*f* electrons with their surrounding is weak due to the shielding effect. It gives luminescence spectra dominated by sharp *zero-phonon lines*. The zero-phonon line is the wavelength at which an excitation / relaxation is not phonon assisted, see Figure I.49. Still, many important phenomena (see above) are only possible due to the electron-phonon interaction.

The coupling of intra-configurational $4f^n$ transitions of rare-earth ions with the lattice vibrations can vary by three orders of magnitude depending on the ion and the chemical nature of the ligand.

Vibronic sidebands. Vibronic sidebands are caused by vibronic transitions (vibrationally induced electric-dipole transitions), where electronic and vibrational transitions occur simultaneously. These sidebands appear because the energy differences between sequential

vibrational levels within a given electronic state amount to $\hbar\omega$. Therefore, the vibronic transitions are found at a distance of $\hbar\omega$ from the zero-phonon line. One type of vibration gives rise to one vibronic transition, but since there are many types of vibrations, a number of vibronic transitions can be observed. Therefore, a number of vibronic sidebands can be found near the ZPL.

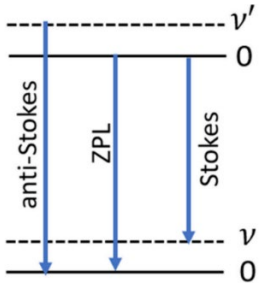

Figure I.49. Schematic representation of the zero-phonon (ZPL), the Stokes and anti-Stokes vibronic emission transitions, 0 - electronic states, v and v' - vibrational levels [Bee23].

Figure I.50 shows one example of assignment of vibronic sidebands in the low-temperature emission and absorption spectra of Tm^{3+} ions in the $LiYF_4$ crystal. The numbers indicate the position of vibronic transitions and their energy correlated with the energy of Raman or infrared modes. The vibronic coupling strength appears to be similar for Raman and IR-active vibrations [Don92, Ell96].

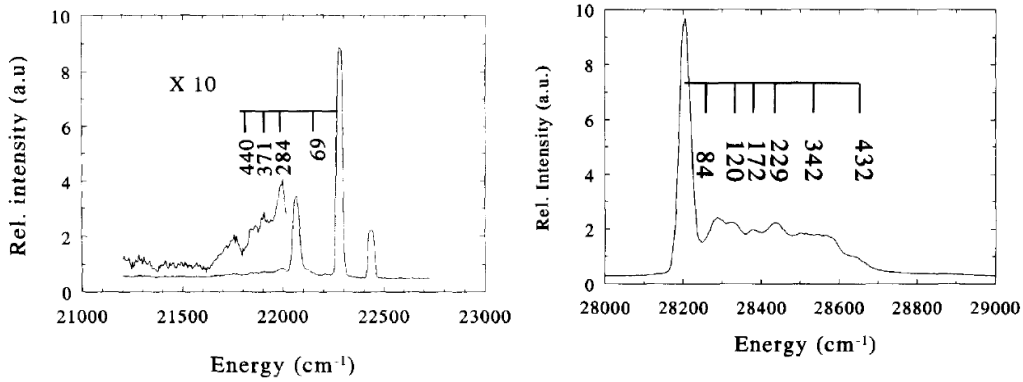

Figure I.50. Low-temperate (4.2 K) luminescence spectrum for the $^1D_2 \rightarrow {}^3F_4$ transition (*left*) and absorption spectrum for the $^3H_6 \rightarrow {}^1D_2$ transition of Tm^{3+} ions in the $LiYF_4$ crystal (*right*). *Numbers* assign vibronic transitions [Ell96].

It should be noted that vibronic transitions can be coupled with electronic ones leading to a deformation of splitting of transitions [Bla92]. Since the intensity of the vibronic transitions is determined by the *strength of the electron-phonon coupling*, the relative intensities of vibronic lines are considered as probes for the interaction of RE^{3+} ions with the lattice.

Figure I.51 shows two contributions to the vibronic transition probability. The coupling of an IR-active vibrational mode leads to mixing of opposite-parity wave functions into the wave functions of the 4*f* term levels. This coupling gives rise to Stokes and anti-Stokes vibronic structure in the emission spectra. This process is called *the M process* and also known as vibrationally induced forced electric-dipole transitions. A shift in the equilibrium position of the

states involved also induces vibronic structure in emission. This process is called *the Δ process*. It stands for classical phonon replicas (the Franck-Condon principle), *i.e.*, transitions induced by a shift in the equilibrium position of the lattice configurational coordinates. The Franck–Condon principle states that during an electronic transition, a change from one vibrational energy level to another one will be more likely to happen if the two vibrational wave functions overlap more significantly.

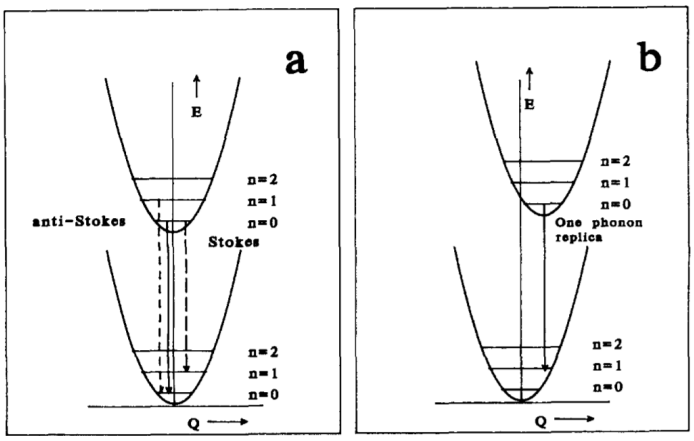

Figure I.51. (a) Vibronically-induced forced electric-dipole transitions: the M process. The *solid arrow* indicates the ZPL transition. (b) Vibronic transitions due to a shift of the equilibrium position of the lattice coordinate: the Δ process or Franck-Condon principle [Syt91].

Temperature-dependent linewidth. According to the Heisenberg principle, the uncertainty in the energetic position ΔE of the initial and final states is determined by the lifetimes of these states:

$$\tau_{rad}\Delta E = \hbar. \tag{I.40}$$

Therefore, the ZPL linewidth depends on the radiative lifetime. However, for lanthanide ions, it ranges between μs and ms so that the radiative lifetime is not the main contribution to the spectral linewidth. The main contribution originates from one-phonon and two-phonon processes, as shown in Figure I.52 [Hen89].

The linewidth of RE^{3+} transitions is caused by several mechanisms and the temperature-dependent total linewidth $\Delta E(T)$ of energy levels can be expressed as [Ell97]:

$$\Delta E(T) = E^{inh} + E^{D}(T) + E^{R}(T) + E^{orb}(T) + E^{MR}(T) + E^{rad}, \tag{I.41}$$

• E^{inh} is the *inhomogeneous spectral line broadening*. The inhomogeneous contribution to the linewidth is due to a disorder in the crystal lattice. This temperature-independent contribution results in a Gaussian line shape and depends on the disorder in the host lattice. Typically, around 4 K, the inhomogeneous linewidth for transitions of lanthanide ions varies from 0.1 cm^{-1} in an ordered single crystal to about 100 cm^{-1} in a glass [Yen64, Rie92].

• E^{D} is the direct process (one-phonon process). This contribution is due to the direct or one-phonon process: one phonon is emitted or absorbed. This contribution is described by:

$$E^{D}(T) = E^{D}_{em}(T) + E^{D}_{abs}(T) = \sum_{a<b}\beta_{ba}(n+1) + \sum_{a>b}\beta_{ba}(n), \tag{I.42}$$

where n is the phonon occupation number, $n = 1/(\exp(\Delta E_{ba}/kT - 1))$, i and j are two levels, *e.g.*, Stark sub-levels of one manifold at a distance ΔE_{ba} from each other. The energy difference ΔE_{ba} is within the range of phonon energies of the system. β_{ba} is the electron-phonon coupling coefficient for the direct process. The direct process gives a Lorentzian line shape. From the formula, it can be derived that at low temperatures, the contribution of one-phonon absorption vanishes, whereas the contribution of one-phonon emission does not.

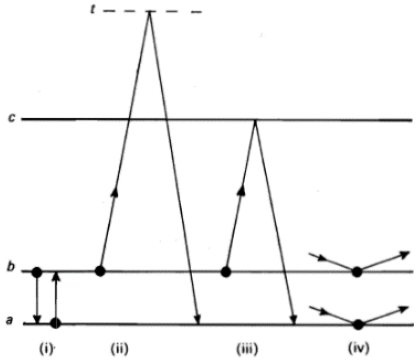

Figure I.52. Phonon-induced relaxation processes between states *a* and *b*: (i) the one-phonon direct process; (ii) the two-phonon Raman relaxation process from *b* to *a* proceeding through a virtual intermediate state *t*; (iii) the two-phonon Orbach process from *b* to *a* proceeding though a real electronic state *c*; (iv) intrinsic Raman broadening mechanisms in *a* and *b*. After [Hen89].

• E^{R} is the Raman (two-phonon) process. In this process, a certain level *b* absorbs a phonon that bridges the gap to the virtual level *t*; the system relaxes with a higher energetic phonon to level *a*. The Raman two-phonon process is a non-resonant process, and the energy differences ΔE_{ba} and ΔE_{ta} are assumed to be much larger than the range of phonon energies in the system. There is also an intrinsic Raman two-phonon process: the phonons that are absorbed and emitted are of the same energy [Hen89].

Using *the Debye approximation* (where the density of phonon states $\rho(\omega)$ scales with ω^2, the square of the phonon frequency) of phonon energies, it can be derived that the temperature-dependent contribution to the linewidth by the Raman process is described by [Ell97]:

$$E^{R}(T) = \bar{\alpha}\left(\frac{T}{T_D}\right)^{7}\int_{0}^{\frac{T}{T_D}}\frac{x^{6}e^{x}}{\left(e^{x}-1\right)^{2}}dx, \qquad \text{(I.43)}$$

where $\bar{\alpha}$ is the electron-phonon coupling parameter for the Raman process, T_D is the effective Debay temperate, and $x = \hbar\omega/kT$. The Debye temperature can be derived from the phonon cutoff energy or calculated from specific-heat data [Dan81].

• E^{orb} is the Orbach two-phonon process. This process arises from a resonant two-phonon process: the energy differences between levels *b*, *a*, and *c* are within the range of phonon energies of the system. In most linewidth studies, the contribution of the Orbach process is neglected.

• E^{MR} is multiphonon relaxation, the simultaneous emission of more than one phonon to bridge the energy difference to a lower lying level. The contribution of this process is also assumed to be negligible in most cases [Yen64].

• E^{rad} is the contribution due to the radiative relaxation of a state. Since the radiative relaxation times of intra $4f^n$ transitions of trivalent lanthanide ions are of the order of μs to ms, this contribution can be neglected.

Neglecting the contribution of E^D, E^{orb}, E^{MR}, and E^{rad}, Eq. I.41 is written as [Ell97]:

$$\Delta E(T) = E^{inh} + \bar{\alpha}\left(\frac{T}{T_D}\right)^7 \int_0^{\frac{T}{T_D}} \frac{x^6 e^x}{\left(e^x - 1\right)^2} dx. \qquad \text{(I.44)}$$

where T_D and $\bar{\alpha}$ are fit values.

Figure I.53 shows the fits and simulations to the temperature-dependent linewidths of the electronic transitions of Pr^{3+} ions in $LiYF_4$.

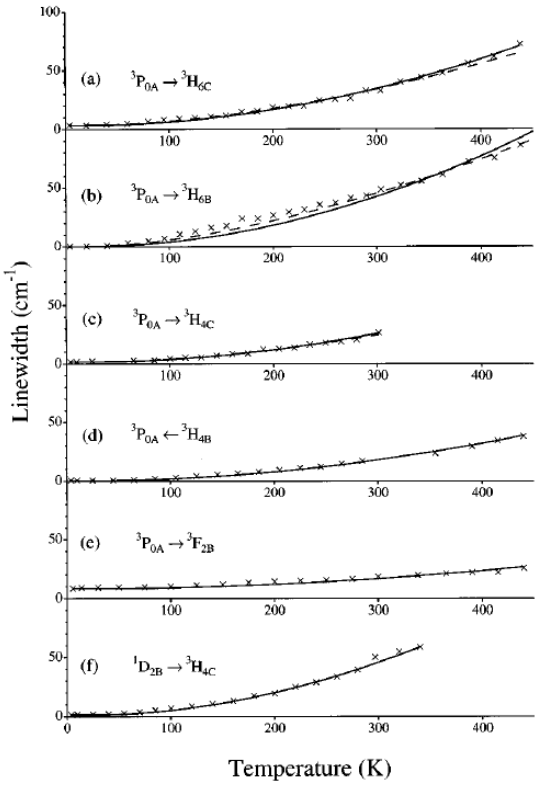

Figure I.53. Fits and simulations to the temperature-dependent linewidths of Pr:$LiYF_4$ for different transitions. *The solid lines* are the fits according to the Raman process only; *the dashed lines* are the fits/simulations including both Raman and direct processes [Ell97].

The electron-phonon coupling strength. *The strength of electron-phonon interaction* of Ln^{3+} ions in solids can be quantified using (i) intensity of vibronic transitions, and (ii) dependence of linewidth of absorption and emission spectra on temperature (Eq. I.44). The latter equation presents a satisfying approximation of the temperature dependence of the linewidth, and it is used to estimate the electron-phonon coupling strength of intraconfigurational $4f^n$ transitions of lanthanide ions. Although it is known that the electron-phonon coupling strength of the

trivalent lanthanide ions is weak, the data show clearly that within this range of small electron-phonon coupling strength values, there is a significant variation.

Figure I.54 shows the $\bar{\alpha}$ values of the intraconfigurational 4*f* transitions of Ln^{3+} ions in $LiYF_4$ crystal [Ell97a]. To explain this trend for the electron-phonon coupling strength, qualitatively, two parameters can be considered:

• *Lanthanide contraction*. Due to the lanthanide contraction, the average electron nucleus distance decreases through the series. Since this will cause a decrease of the overlap of the 4*f* orbitals with the orbitals of the ligands, it is supposed that the lanthanide contraction induces a decrease of the electron-phonon coupling strength through the lanthanide-ion series.

• *Shielding of the 4f electrons*. The shielding parameter gradually decreases from Ce^{3+} to Yb^{3+}. This means that 4*f* electrons in the beginning of the lanthanide-ion series are better screened from the crystal-field than the 4*f* electrons at the end of the series: this implies an increase of the electron-phonon coupling strength through the series.

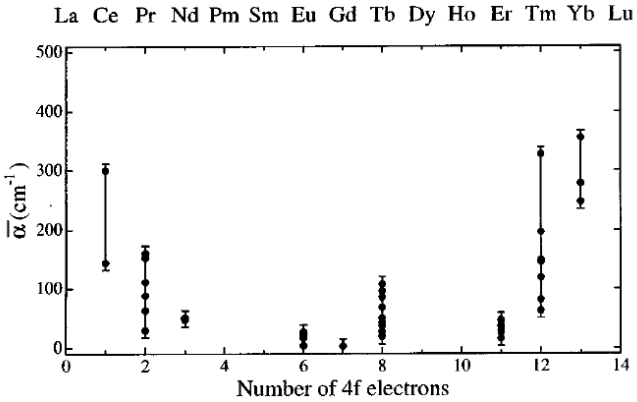

Figure I.54. $\bar{\alpha}$ values of the intraconfigurational 4*f* transitions of trivalent lanthanide ions in $LiYF_4$ [Ell97a].

I.3. Tm^{3+} and Ho^{3+}: spectroscopic properties

I.3.A. Energy levels and laser transitions of Tm^{3+} and Ho^{3+} ions

As mentioned before in this chapter, Tm^{3+} and Ho^{3+} ions have the following configurations [Xe] $4f^{12}$ and [Xe] $4f^{10}$, respectively, when they are incorporated in a solid. The energy diagram of Tm^{3+} and Ho^{3+} ions in Figure I.55 indicates the possible laser transitions. The positions of the multiplets are taken from [Car68] and the laser transitions are taken from [Kam07].

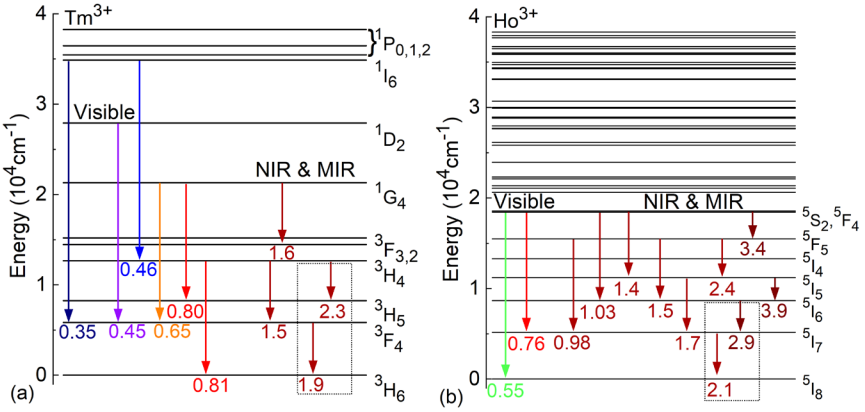

Figure I.55. Energy diagram of Tm^{3+} and Ho^{3+} ions [after Car68]. *Narrows* – possible laser transitions in visible and near- and mid-infrared spectral region, *numbers* is in µm taken from [Kam07]. *Dashed rectangle* – the studied laser transitions.

Thulium ions. Figure I.55(a) shows the energy level scheme of a free Tm^{3+} ion with the ground state being $^3H_6$ and $^3F_4$ the first excited state. In the visible spectral region, there are six possible laser transitions: the $^1I_6 \rightarrow {}^3F_4$, $^1D_2 \rightarrow {}^3F_4$, $^1I_6 \rightarrow {}^3H_4$, $^1G_4 \rightarrow {}^3F_4$, $^1G_4 \rightarrow {}^3H_5$, and $^3H_4 \rightarrow {}^3H_6$.

In the near-infrared spectral region, there are three possible laser transitions: $^1G_4 \rightarrow {}^3F_3$, $^3H_4 \rightarrow {}^3F_4$, and $^3F_4 \rightarrow {}^3H_6$ transitions. The latter one is the most famous since it has a long luminescence lifetime, which makes the $^3F_4$ manifold a metastable state in a variety of host matrices.

It should be noted that in some publications the labels of the $^3F_4$ and $^3H_4$ manifolds of Tm^{3+} ions are inverted with the $^3H_4$ manifold being at lower energy. This is due to the strong spin-orbit coupling present in Tm^{3+} ions, resulting in a significant mixing of *LS*-states for a given *J* value. Usually, the lowest manifold in energy with $J = 4$, exhibits a larger contribution from the $^3F_4$ *LS* state than the $^3H_4$ itself [Kru65] and is therefore labelled as $^3F_4$.

As noted above in this chapter, Tm^{3+} ions offer an interesting laser emission in the mid-infrared region around 2.3 µm originating from the $^3H_4 \rightarrow {}^3H_5$ Tm^{3+} transition.

In many hosts, Tm^{3+} ions exhibit broadband emission properties owing to a large total Stark splitting of the $^3H_6$ ground-state for the emission around 2 µm, and the $^3H_5$ level for the emission around 2.3 µm. These broadband transitions are thus attractive for ultrashort pulse laser sources around 2 and 2.3 µm.

Holmium ions. Figure I.55(b) shows the energy level scheme of a free Ho^{3+} ion with $^5I_8$ being the ground state and $^5I_7$ the first excited state. In the visible spectral region, there are two possible laser transitions: $^5S_2 \rightarrow {}^5I_8$, and $^5S_2 \rightarrow {}^5I_7$.

Ho^{3+} ions have plenty of laser transitions in the near- and mid-infrared spectral range. The $^5I_7 \rightarrow {}^5I_8$ transition at ~2.1 μm is the most famous one in different host matrices due to a long luminescence lifetime of the $^5I_7$ level. In the mid-infrared, the most famous transition is the $^5I_6 \rightarrow {}^5I_7$. However, to achieve this laser emission at ~2.9 μm is difficult due to the fast non-radiative multiphonon relaxation from the $^5I_6$ upper laser level. Mostly, this laser emission can be achieved in materials with low phonon energies.

In this work, the following laser transitions will be studied:

- $^3F_4 \rightarrow {}^3H_6$ Tm^{3+} (~1.9 μm) and $^3H_4 \rightarrow {}^3H_5$ Tm^{3+} (~2.3 μm
- $^5I_7 \rightarrow {}^5I_8$ Ho^{3+} (~2.1 μm) and $^5I_6 \rightarrow {}^5I_7$ Ho^{3+} (~2.9 μm).

I.3.B. Operation schemes of Tm and Ho lasers

Continuous-wave operation occurs when a laser is continuously pumped and continuously emits coherent light. The main condition to achieve this operation is to reach steady-state population inversion, when the population of the lower laser level is smaller than the upper laser level.

Tm and Ho lasers are generally classified as quasi-three or quasi-four level laser systems. Before considering the different possible pumping schemes to achieve the laser operation of Tm and Ho lasers in the near- and mid-infrared spectral range, it is necessary to define quasi-three laser and four-level laser systems working in continuous-wave regime. Figure I.56 shows a schematic of the quasi-three and four-level laser systems. In this figure, there is an upper manifold and a lower manifold that are each split into Stark sub-levels by the crystal field. The fraction of the population within the sub-levels of the lower manifold is given by [Fan93]:

$$f_1 = \frac{g_1 \exp(-\frac{E_1}{kT})}{Z_l}, \tag{I.45}$$

with f_1 the fractional population in the lower manifold, E_1 the energy of the lower manifold, k the Boltzmann constant, Z_l is the partition function of the lower manifold (see Eq. I.20), and E_i is the energy of the i^{th}-sub-level in the lower manifold which contains m sub-levels. The fractional population of the upper manifold f_2 can be found using the same equation I.45.

To achieve laser emission, the condition for laser gain, i.e. population inversion should be satisfied. The population density in the upper level should be greater than for the lower one. Therefore, the laser transition between the levels 2 and 1 can be described as follows:

$$\Delta N = f_2 N_2 - f_1 N_1 > 0, \quad f_2 N_2 > f_1 N_1, \quad N = N_1 + N_2, \tag{I.46}$$

with N_1 and N_2 – ion density in the lower and upper manifolds, N – total density of dopant ions. Then, the minimum fraction of the population $\beta = \frac{N_2}{N}$, that needs to be in the upper manifold to attain the population inversion is:

$$\beta_{\min} = \frac{f}{1+f}, \quad f = \frac{f_1}{f_2}. \tag{I.47}$$

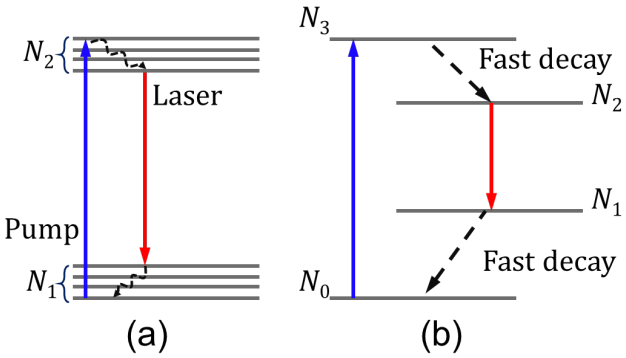

Figure I.56. Schematics of (a) a quasi-three-level laser, (b) a four-level laser. The sinusoidal lines denote fast nonradiative relaxations while the straight lines denote radiative transitions.

Quasi-three level laser system. Ions in the upper manifold are distributed within the Stark sub-levels according to the Boltzmann distribution. Consequently, the excited ions are relaxed to the lower manifold through radiative or nonradiative processes. The rate equation for the excited state is described as follows:

$$\frac{dN_2}{dt} = W_p N_1 - \frac{qc}{A_{eff} l_c}(\sigma_{SE} N_2 - \sigma_{abs} N_1) - \frac{N_2}{\tau_{lum}}, \tag{I.48}$$

with W_p is the pumping rate, q is the photon number in the laser mode, A_{eff} is the effective laser mode area inside the crystal, l_c is the optical path length of the cavity. The parameter $l_c = l_m + (n-1)t$, describes the effective length of the resonator, taking into account the refractive index n of the crystal and the distance between the mirrors l_m, and the length of the crystal t. σ_{SE} and σ_{abs} are the stimulated emission and absorption cross-sections, respectively, and τ_{lum} the luminescence lifetime of the upper manifold. In the steady state regime Eq. I.48 equals to 0.

The threshold pump power of a quasi-three level laser system with intracavity loss L and an output coupling transmission T_{OC} can be described as follows [Tak97]:

$$P_{th} = \frac{h\nu_p (\frac{V_{eff}}{l_c})}{2\eta_q \eta_a (f_1 + f_2)\sigma_{gain}\tau_{lum}}(L + T_{OC} + 2N_1^0 \sigma_{gain} t), \tag{I.49}$$

with $h\nu_p$ is the pump photon energy, η_q is the quantum efficiency indicating the number of ions in the upper laser level created by one absorbed photon, η_a is the pump power absorption efficiency, f_1 and f_2 are the fractional populations in the lower laser level and upper one, respectively, σ_{gain} is the gain cross-section, $\Delta N^0 = N_2^0 - N_1^0 \approx -N_1^0$ – the unpumped population-inversion density (doped ion density), V_{eff} is the effective mode volume defined as:

$$V_{eff} = \frac{1}{\iiint r_p(x,y,z)\phi_0(x,y,z)} dV, \tag{I.50}$$

with $r_p(x,y,z)$ is the spatial distribution of the pump energy and $\phi_0(x,y,z)$ is the spatial distribution of the laser photons. The laser output power linearly increases with the pump power as

$$P_{out} = \eta(P_{pump} - P_{th}), \tag{I.51}$$

where η is the slope efficiency including the efficiencies which affect the laser performance and can be described as:

$$\eta = \eta_{St,L}\eta_q\eta_{\text{mode}}\eta_{OC}, \tag{I.52}$$

where η_q is the quantum efficiency discussed in the laser threshold equation (Eq. I.49), $\eta_{St,L}$ is the Stokes efficiency determined by the ratio between the pump λ_p and laser wavelengths λ_L :

$$\eta_{St,L} = \frac{\lambda_p}{\lambda_L}, \tag{I.53}$$

η_{mode} is the mode overlap efficiency can be determined as [Loi18a]:

$$\eta_{\text{mode}} = \frac{4w_L^2\left\langle w_p\right\rangle^2}{\left(w_L^2+\left\langle w_p^2\right\rangle\right)^2}, \tag{I.54}$$

with $\langle w_p \rangle$ and $\langle w_L \rangle$ are the mean pump and laser spot size, respectively.

η_{OC} is the output-coupling efficiency and it equals to

$$\eta_{OC} = \frac{-\ln[1-T_{OC}]}{-\ln[(1-T_{OC})(1-L)]}, \tag{I.55}$$

where $-\ln[1 - T_{OC}]$ and $-\ln[(1 - T_{OC})(1 - L)]$ describe useful losses (output-coupling) and total losses, respectively. If the round-trip passive losses $L \sim 0$, therefore, $\eta_{OC} = 1$. The slope efficiency can be derived from the pump power and the laser output power and it should be:

$$\eta \leq \eta_{St,L}\eta_q\eta_{\text{mode}}\eta_{OC}, \tag{I.57}$$

The above description of a quasi-three laser level system can be applied to the case of the Tm^{3+} $^3F_4 \rightarrow {}^3H_6$ and the Ho^{3+} $^5I_7 \rightarrow {}^5I_8$ transitions.

Four-level laser system. The main difference between a four-level laser system (Figure I.56(b)) and a quasi-three level is that the lower laser level is essentially empty in a four-level laser due to a fast nonradiative relaxation from the level 1 to the ground state. In this scheme, the population inversion can be reached with less efforts due to the unpopulated lower level 1 compared to the quasi-three-level laser. Therefore, the threshold power P_{th} is lower, see Eq. I.49. Due to the lack of reabsorption in a four-level laser system, σ_{abs} equals to 0 and Eq. I.48 becomes:

$$\frac{dN_2}{dt} = W_p N_0 - \frac{qc}{A_{eff} l_c}(\sigma_{SE} N_2) - \frac{N_2}{\tau_{lum}}, \tag{I.58}$$

Operation schemes of Tm lasers. The main Tm laser operation schemes to achieve laser emission at ~1.9 μm ($^3F_4 \rightarrow {}^3H_6$) and ~2.3 μm ($^3H_4 \rightarrow {}^3H_5$) are shown in Figure I.57

• Two pumping schemes exist to achieve laser emission around 1.9 μm. The first one is well-known as a "two-for-one" pumping scheme due to the strong cross-relaxation $^3H_4 + {}^3H_6 \rightarrow {}^3F_4 + {}^3F_4$ where one excited ion in the $^3H_4$ level leads to two excited ions in the $^3F_4$ level, see Figure I.57(a). More details about cross-relaxation will be provided in the next subsection. The absorption band of the $^3H_4$ manifold peaks at around 0.79 μm and exhibits a high absorption cross-section, which aligns with the emission wavelength of commercially available high-power AlGaAs laser diodes. Several hundred of watts can be obtained with cheap and compact multimode fiber-coupled laser diodes.

Another famous pumping source is found with Ti:Sapphire lasers. They deliver up to 4 W with a nearly diffraction-limited beam ($M^2 \sim 1$). The main disadvantages of this pumping

scheme whether with laser diodes or Ti:Sa lasers are relatively large quantum defect around 60%. This quantum defect is partially compensated by the cross-relaxation which however does not reach 100% in most cases. If an ion is not involved into cross-relaxation it will lead to some extent to multi-phonon relaxation resulting in thermal load. It is mostly the case of high-power laser operation under laser diode pumping at 0.79 µm. In this case, an active cooling is required.

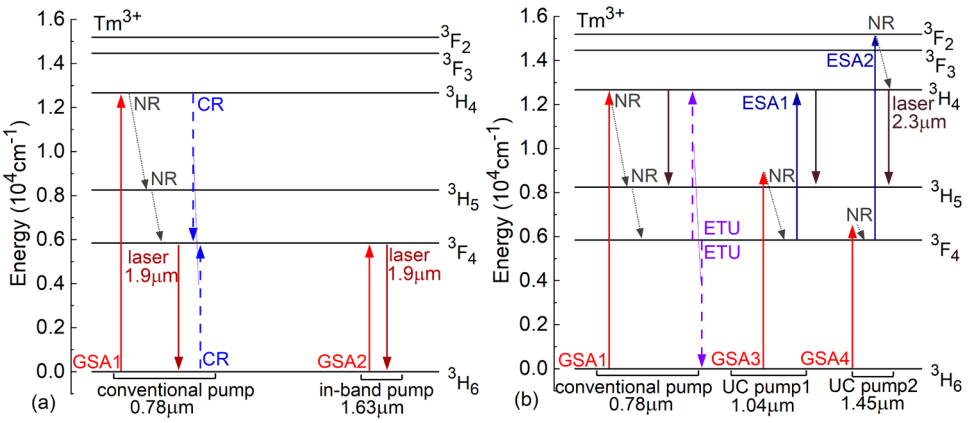

Figure I.57. Energy diagram of Tm^{3+} ions showing different pumping schemes to achieve laser emissions at (a) 1.9 µm and (b) at 2.3 µm; GSA – ground state absorption, NR – nonradiative relaxation, CR – cross-relaxation, ETU – energy-transfer upconversion, ESA – excited-state absorption.

• The second pumping scheme corresponds to a direct pumping of the $^3F_4$ level with a wavelength around 1.63 µm ($^3H_6 \rightarrow {}^3F_4$ transition). This wavelength can be delivered by Er-fiber lasers or InP-based laser diodes [Fuj16, Phe19]. Compared to the "two-for-one" pumping scheme, this scheme has a smaller quantum defect of around 18%. High doping levels are not needed to achieve highly efficient laser operation and this reduces the concentration quenching affecting the emitting $^3F_4$ level at high doping level.

• To achieve 2.3 µm laser emission on the $^3H_4 \rightarrow {}^3H_5$ transition, there are three possible pumping schemes which are depicted in Figure I.57(b). The first one is the same conventional pumping at 0.79 µm. In this case, the 2.3 µm laser emission is in strong competition with the high-gain 1.9 µm laser emission from the $^3F_4 \rightarrow {}^3H_6$ transition. The 2.3 µm laser emission is quenched by the CR process at high doping levels and suffers from fast non-radiative relaxation from the $^3H_4$ level. Despite those obstacles, efficient and high-power continues-wave laser operation of crystals with low and high phonon energies at 2.3 µm were achieved [Loi19a, Gui19a, Gui20, Gui20a, Loi21, Yu22].

The other two pumping schemes are referred to as upconversion pumping [Kom95]. The main principle is based on the photon avalanche effect [Jou94]. It consists in a resonant ESA from an intermediate metastable state to the higher-lying emitting state followed by a CR process, see Figure I.57(b). First, ions are excited by non-resonant (phonon-assisted) weak GSA, the $^3H_6 \rightarrow {}^3H_5$ or $^3H_6 \rightarrow {}^3F_4$ transitions, then by multiphonon non-radiative relaxation energy, ions end up in the $^3F_4$ level. From the $^3F_4$ level a resonant ESA process takes place, the $^3F_4 \rightarrow {}^3F_{2,3}$ or $^3F_4 \rightarrow {}^3H_4$ transitions promoting the ions in the $^3H_4$ level. It should be noted that due to the

small energy gaps between the ($^3H_5$ and $^3F_4$) and the ($^3F_{2,3}$ and $^3H_4$) levels, the excitation of the higher-lying levels quickly relaxes down to the lower ones through non-radiative multiphonon relaxation. From the $^3H_4$ level an efficient CR process facilitates the population of the intermediate metastable state ($^3F_4$), which is again followed by ESA and then again by the CR process and so on. This loop creates a photon avalanche effect leading to an efficient population of the upper laser level ($^3H_4$). Continues-wave laser operation around 2.3 μm was achieved by employing these pumping schemes [Gui19, Gui20, Tya23, Dup23, Dup24,Tya24].

Operation schemes of Ho lasers. The main Ho laser operation schemes to achieve laser emission at ~2.1 μm ($^5I_7 \rightarrow {}^5I_8$) and ~2.9 μm ($^5I_6 \rightarrow {}^5I_7$) are shown in Figure I.58.

The laser emission due to the $^5I_7 \rightarrow {}^5I_8$ Ho^{3+} transition results in a maximum gain slightly above 2 μm, thus avoiding the structured water vapor absorption in the atmosphere. Due to a strong energy-transfer upconversion (ETU1) from the $^5I_7$ laser level, the choice of Ho doping level is the result of a compromise between pump absorption and laser efficiencies. As consequence, 1 at.% Ho^{3+}-doped crystals are usually used. The laser emission from this quasi-3-level laser system can be achieved by in-band pumping, *e.g.*, by means of bulk or fiber Tm lasers or GaSb laser diodes [She12, Lam12], directly exciting the ions into the upper $^5I_7$ laser level. In-band pumping leads to high laser slope efficiencies approaching the Stokes limit and very weak heat loading, although the required pump sources are expensive and complex.

In contrast, this laser emission of Ho^{3+} ions at 2.1 μm can also be achieved through energy transfer from Yb^{3+} or Tm^{3+} ions. In the case of codoping with Tm^{3+} ions, the excitation of Tm^{3+} ions (donors, D) around 0.79 μm leads to the population of the $^3F_4$ metastable state via the above mentioned cross-relaxation process. Then, the energy can be non-radiatively transferred to Ho^{3+} ions (acceptors, A), leading to laser emission ($^5I_7 \rightarrow {}^5I_8$ transition) [Eld98, Wal09]. Combined gain bandwidths of both Tm^{3+} and Ho^{3+} ions are advantageous for extending the laser tunability range and generating ultrashort pulses. The predominantly unidirectional energy transfer from D (Tm^{3+}) to acceptor A (Ho^{3+}) is obtained by an appropriate Ho^{3+}/Tm^{3+} codoping ratio, typically ranging from 1:5 to 1:10. Meanwhile, the reduced energy-transfer upconversion from the $^5I_7$ Ho^{3+} metastable state is ensured by selecting relatively low Ho^{3+} doping levels (<0.5 at.%). For non-optimized codoping levels and high intracavity losses, Tm^{3+} and Ho^{3+} co-lasing is possible, which is generally considered a detrimental effect that reduces the Ho laser efficiency. Increased heat loading can result in weaker power scaling capabilities at room temperature or the need of cryogenic cooling for solid-state lasers [Eld98]. This drawback is partially removed for fiber lasers with a distributed heat loading. However, watt-level and efficient laser operation of Tm,Ho-codoped lasers were achieved in this work.

The 2.9 μm laser emission of Ho^{3+} ions from the $^5I_6 \rightarrow {}^5I_7$ transition is quite challenging to achieve due to a "bottleneck effect" where the population accumulates in the lower laser level. It prevents continuous-wave laser operation. Secondly, the direct pumping into the $^5I_6$ level at 1.15 μm lacks the proper pump source technology. Only recently, 1.15 μm Raman fiber lasers have gradually become suitable pump sources to achieve 2.9 μm laser emission of Ho^{3+} ions. They deliver high power with temporal stability and possess high beam quality. Despite the drawbacks of the $^5I_6 \rightarrow {}^5I_7$ laser transition, the CW laser operation of single Ho^{3+}-doped $YAlO_4$

crystal was reported recently [Qia23a]. Previous reports showed that laser operation at 2.9 µm in pulse regime of single Ho^{3+}-doped oxides crystals was achieved pumped by Nd-lasers [Bow90, Ant90].

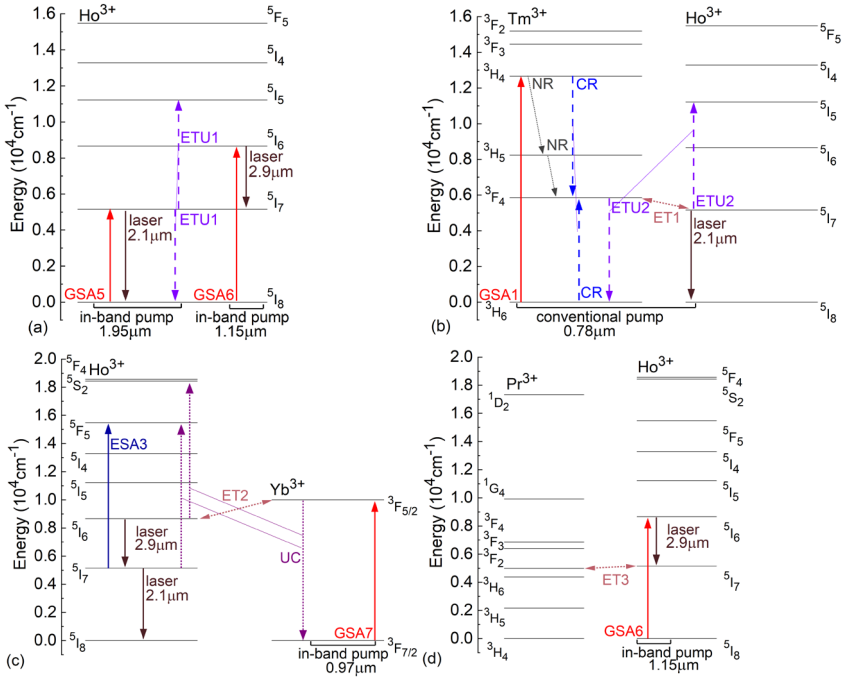

Figure I.58. Energy diagram of Ho^{3+} ions showing different pumping schemes to achieve laser emissions at (a) 2.1 µm and at 2.9 µm by in-band pumping, and (b-d) by an energy-transfer; GSA – ground state absorption, NR – nonradiative relaxation, ET – nonradiative energy-transfer, ETU – energy-transfer upconversion, ESA – excited-state absorption.

Another way to achieve laser operation at 2.9 µm is to use codoping with Yb^{3+} ions. The process starts with the pumping of ytterbium ions at 970 nm. This excitation is then transferred to the upper $^5I_6$ laser level of Ho^{3+}. A second excited Yb^{3+} ion can then transfer its energy to a Ho^{3+} ion in the $^5I_6$ or $^5I_7$ multiplet, resulting in the excitation to higher energy levels. These higher energy levels mainly decay non-radiatively to the upper laser level. The energy transfer with an ion in the $^5I_7$ multiplet facilitates the depopulation of the $^5I_7$ multiplet alongside with an ESA process at the pump wavelength, see Figure I.58(c). Both processes enable a significant population inversion between the $^5I_6$ and the $^5I_7$ multiplets explaining why this laser operating scheme has been demonstrated [Umy96, Die98, Die00].

Another possibility for this 2.9 µm Ho-laser is the codoping with Pr^{3+} ions. Pr^{3+} ions significantly quench the luminescence lifetime of the lower laser $^5I_7$ level via an efficient energy-transfer $^5I_7(D) \rightarrow {}^3H_6(A)$, as shown in Figure I.58(d). This laser operation scheme was demonstrated in Ho and Pr-codoped $LiLuF_4$ [Nie17], $LiYF_4$ [Nie18], CaF_2 [Wan23], and $YAlO_4$ [Qia23b] crystals.

Finally, the bottlenecking effect of the $^5I_6 \rightarrow {}^5I_7$ transition can be suppressed by cascade generation. Cascade lasing involves the simultaneous oscillation on both transitions of Ho^{3+} ions ($^5I_6 \rightarrow {}^5I_7$ and $^5I_7 \rightarrow {}^5I_8$ transitions) in the same resonator. This cascade oscillation scheme has

been successfully demonstrated in Cr^{2+},Yb^{3+},Ho^{3+}:YSGG [Zav93] and in single Ho^{3+} doped $LiYF_4$ crystals [Ye22].

I.3.C. Cross-relaxation and energy-transfer upconversion

We have already discussed the possible pumping schemes for Tm^{3+} and Ho^{3+} ions, where the nonradiative interionic processes have a strong impact on quasi-three-level and four-level laser systems. In this section we investigate in more details the impact of the CR and ETU processes on 1.9 μm and 2.3 μm Tm-lasers, as well as 2.1 μm and 2.9 μm Ho-lasers.

Impact of CR on Tm-lasers. The cross-relaxation process among Tm^{3+} ions can enable an efficient pumping at 0.79 μm of the 1.9 μm laser ($^3F_4 \rightarrow {}^3H_6$), leading to reduced heat loading and laser slope efficiency well exceeding the Stokes limit due to a positive effect of the CR process, Tm1($^3H_4$) + Tm2($^3H_6$) → Tm1($^3F_4$) + Tm2($^3F_4$).

There are several methods to determine the relevant parameters to describe the CR process. The first method is based on measuring the luminescence lifetimes of the $^3H_4$ state as a function of the Tm^{3+} concentration which follows the dependence :

$$\frac{1}{\tau_{3lum}} = \frac{1}{\tau_{lum,0}} + W_{CR}, \tag{I.59}$$

$$W_{CR} = K_{CR} N_{Tm} = C_{CR} N_{Tm}^2, \tag{I.60}$$

with $\tau_{lum,0}$ the intrinsic $^3H_4$ luminescence lifetime, i.e. without energy transfer, W_{CR} is the CR rate in s^{-1} and C_{CR} the concentration-independent energy transfer parameter in cm^6s^{-1}.

Experimental data are fitted using Eq. I.59-60 to determine the intrinsic luminescence lifetime, τ_{30}, as shown in Figure I.59(a) and W_{CR} the CR rate.

C_{CR} is then determined from the fit of the cross-relaxation rate as a function of the Tm^{3+} doping concentration as shown in Figure I.59(b).

The second method to estimate the rate constant of the CR is [Loi19a]:

$$W_{CR} = \frac{1}{\tau_{30}} \left(\frac{C_{Tm}}{C_0} \right)^2, \tag{I.61}$$

where C_{Tm} is the doping level (in at.%) and C_0 is the critical doping level for which the cross-relaxation rate W_{CR} becomes equal to the intrinsic relaxation rate $1/\tau_{30}$. For Tm:$LiYF_4$, we calculated C_0 as 0.96 at.% which corresponds to the ion density of 1.325×10^{20} at/cm^3.

The pump quantum efficiency for the $^3F_4$ level of Tm^{3+}-doped materials, η_{q1}, defined as the ratio between the number of excited ions in the $^3F_4$ level and the number of absorbed pump photons, can exceed unity and approach 2 due to the CR effect, as illustrated in Figure I.59(c). Assuming no ground-state bleaching and no other processes such as ETU, and ESA, Honea et al. determined η_{q1} as [Hon97]:

$$\eta_{q1} = \frac{1/\tau_{30} + 2W_{CR} - (1/\tau_{3rad})(1-\beta_{32})}{1/\tau_{30} + W_{CR}}. \tag{I.62}$$

Here, β_{32} represents the total luminescence branching ratio for the $^3H_4 \rightarrow {}^3F_4 + {}^3H_5$ transitions. Due to the strong NR relaxation from the $^3H_5$ state, all ions in the $^3H_5$ state quickly accumulate in the $^3F_4$ level. Since $LiYF_4$ features a relatively low maximum phonon frequency $h\nu_{ph}$,

(~450 cm^{-1}) W_{NR} from the $^3H_4$ state is almost zero [Hon97]. Thus, $\tau_{lum,0}$ can be considered equal to τ_{rad} for the $^3H_4$ level. Note that this condition is typically not satisfied in oxide materials. Figure I.59(c) shows that for small Tm^{3+} doping concentrations (less than 1 at.%), η_{q1} does not exceed unity. For higher concentrations of Tm^{3+} ions, W_{CR} increases and the quantum efficiency η_{q1} can reach 2 The experimental results based on the luminescence lifetime are in good agreement with the estimation of So et al. based on the analysis of the laser performance [So06].

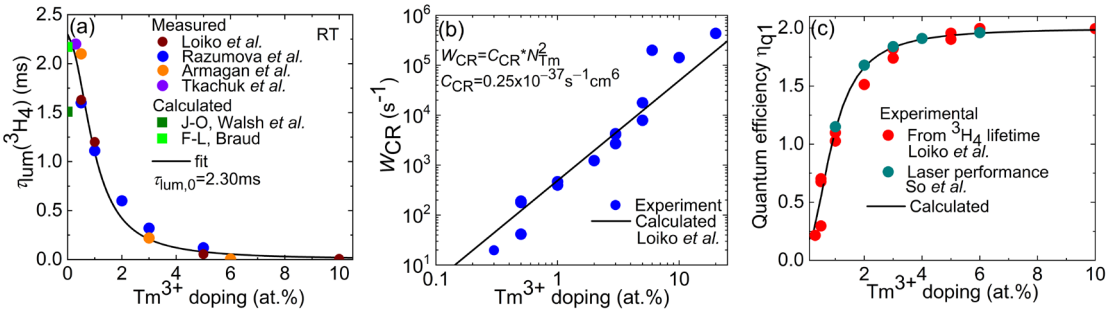

Figure I.59. (a) luminescence lifetime of the $^3H_4$ state τ_{lum} vs. the Tm^{3+} doping concentration: *symbols* – experimental data, *curve* – their fit with Eqs. I.59-60. All results correspond to room temperature. Quantification of cross-relaxation parameters: (b) cross-relaxation rate W_{CR}: symbols – determined from the experimental data on τ_{lum} ($^3H_4$), *line* – theoretical calculation using Eq. I.61; (c) pump quantum efficiency for the $^3F_4$ state η_{q1}: *symbols* –determined from the experimental W_{CR} rates [Loi19a] and from the laser performance [So06], *curve* – theoretical calculation using Eq. I.62 [Loi19a].

Impact of ETU on Tm-lasers. This section deals with the influence of the energy-transfer upconversion on the laser performance of Tm-lasers. The ETU process, $Tm1(^3F_4) + Tm2(^3F_4) \rightarrow Tm1(^3H_4) + Tm2(^3H_6)$, is a phonon-assisted process which is detrimental for the 1.9 µm laser transition, and can however, be useful for the 2.3 µm laser transition.

There are several methods to quantify concentration-independent (C_{ETU}) and concentration dependent (K_{ETU}) ETU parameters, and ETU rate (W_{ETU}). So far, these parameters have been obtained from: (i) luminescence decay measurements [Fal98, Wal04]; (ii) stationary luminescence-intensity measurements [Loi19a]; (iii) theoretical calculations [Per01]; (iv) modelling of Tm laser performance [Loi18]; (v) absorption and stimulated-emission cross-section spectral overlap using the hopping model [Gui22].

Figure I.60(a) illustrates an example of K_{ETU} evaluation using steady state luminescence intensity measurements. In this example, Tm^{3+} ions in $LiYF_4$ crystals were excited to the $^3F_4$ level, and the power dependence of luminescence from the $^3H_4 \rightarrow {}^3F_4$ and $^3F_4 \rightarrow {}^3H_6$ transitions was monitored. The occurrence of the $^3H_4 \rightarrow {}^3F_4$ emission is a clear evidence of ETU. The ratio of populations $N(^3H_4)/N(^3F_4)$ was determined by comparing the measured ratio of integrated intensities of those emissions and a rate-equation modeling. The concentration dependence of the ETU parameters can be expressed in a similar way as for the CR parameters:

$$W_{ETU} = K_{ETU} N_{Tm} = C_{ETU} N_{Tm}^2. \quad \text{(I.63)}$$

$$K_{ETU} = C_{ETU} N_{Tm}. \quad \text{(I.64)}$$

In the case of Tm:YLF crystals, $C_{ETU} = 3.9 \times 10^{-40}$ cm^{6}s^{-1} and one can see that this value is by two orders of magnitude smaller than $C_{CR} = 0.2 \times 10^{-37}$ cm^{6}s^{-1}.

The concentration dependence of K_{ETU} values for Tm:YLF crystals reported so far is shown in Figure I.60(b), where the dependence can be modeled by a linear function with a slope equal to C_{ETU}.

The presence of ETU plays a positive role on the performance of 2.3 µm lasers recycling the energy towards the $^3H_4$ level and thus enabling the laser slope efficiency to exceed the Stokes limit, with a pump quantum efficiency η_{q2} above one, as shown in Figure I.60(c).

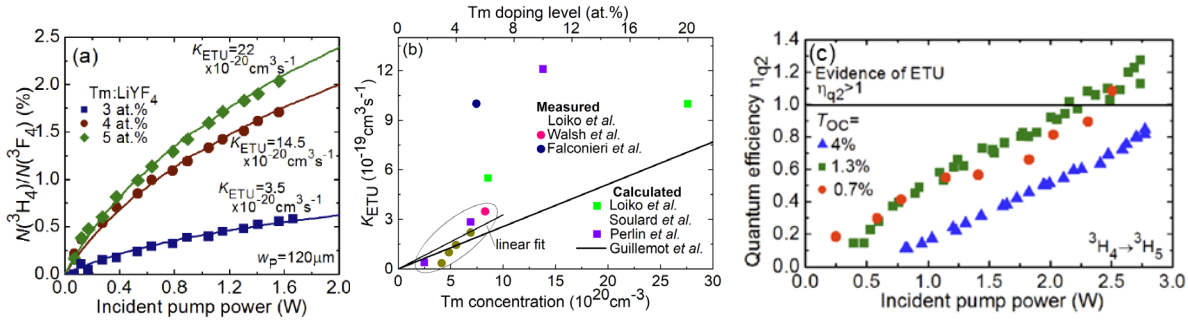

Figure I.60. Evaluation of the ETU parameter for Tm:LiYF$_4$: (a) the $^3H_4$ and $^3F_4$ Tm^{3+} multiplets for the 1.68 µm excitation vs. the incident pump power for various Tm^{3+} concentrations [Loi19a]; (b) summary of the ETU parameters K_{ETU} reported so far [Gui22]; (c) Pump quantum efficiency for the $^3H_4 \rightarrow {}^3H_5$ laser channel, [Loi19a].

The effect of CR and ETU on the pump quantum efficiency η_{q2} for the $^3H_4 \rightarrow {}^3H_5$ laser transition can be written as [Loi19a]:

$$\eta_{q2} = 1 - \frac{K_{CR} N_1 N_3}{\sigma_{abs}^P I_P N_1} + \frac{K_{ETU} N_2^2}{\sigma_{abs}^P I_P N_1}, \quad \text{(I.65)}$$

In this equation, N_1, N_2, and N_3 stands for the population of the $^3H_6$, $^3F_4$, and $^3H_4$ levels, σ^P_{abs} is the absorption cross-section at the pump wavelength, I_P is the pump intensity expressed in photons/(s·cm^2).

The equation (I.65) shows that the CR and ETU are two competitive energy transfer processes which are the determining factors for the quantum efficiency η_{q2}. In the ideal case of a negligible doping concentration, both processes are minimal, resulting in $\eta_{q2} \approx 1$, and the laser slope efficiency is limited solely by the Stokes efficiency. In the absence of ETU, the quantum efficiency will remain below unity due to the influence of the CR. However, when both processes are presented and the effect of ETU exceeds the detrimental effect of CR, η_{q2} can exceed unity. The upper limit can be reached for a material exhibiting a strong ETU and long lifetimes of the $^3H_4$ and $^3F_4$ multiplets when the laser operates solely at the $^3H_4 \rightarrow {}^3H_5$ transition. This occurs when the laser is pumped well above the laser threshold, resulting in the $^3H_4$ level being depopulated by ~2.3 µm laser emission and the $^3F_4$ level being depopulated by ETU. [Loi19a].

Impact of CR and ETU on Ho-lasers. The CR and ETU processes can also affect the 2.1 and 2.9 µm Ho^{3+} laser emissions. In fact, there are various ETU processes occurring between Ho^{3+} ions [Lya15]. We have already shown and discussed in section I.1.D some ETU processes occurring in Pr^{3+} or Yb^{3+} codoped Ho-lasers (see Figure I.58). The ETU processes increase the

thermal load on Ho-doped lasers by promoting ions to higher energy level which then relax non-radiatively.

It is well known that Ho^{3+} ETU imposes a limit on the energy storage of Ho-lasers, limiting both the Q-switched energy and the laser efficiency. ETU1 (see Figure I.58(a)) occurs when two Ho^{3+} ions in the $^5I_7$ manifold interact, promoting one of the ions to the $^5I_5$ manifold while demoting the other Ho^{3+} ions to the $^5I_8$ manifold. Because the $^5I_5$ manifold quickly decays to the $^5I_6$ manifold, typically through nonradiative processes, the reversal of this process has a low probability. As a result, the Ho ETU is a deleterious process. Because the upconversion process involves two closely spaced Ho^{3+} ions in the $^5I_7$ manifold, the effect is most likely to be observed when the population density of the $^5I_7$ manifold is high. Thus, upconversion is most important when the energy storage is high, a situation common for Q-switching [Bar03]. If the ETU between Ho^{3+} ions is small, the energy in long pump pulses can be stored efficiently. Longer diode pump pulses translate into fewer laser diodes, resulting in lower costs. Another ETU process can depopulate the $^5I_6$ manifold towards the $^5F_5$ level , $^5I_6 + {}^5I_6 \rightarrow {}^5I_8 + {}^5F_5$ while the CR from the $^5F_5$ level can populate the $^5I_7$ lower laser level and $^5I_6$ upper laser level, $^5F_5 + {}^5I_8 \rightarrow {}^5I_6 + {}^5I_7$.

I.3.D. Tm ↔ Ho energy-transfer: different approaches to quantify its parameters

As shown before, the Tm,Ho-codoping scheme is an efficient way to achieve the 2.1 µm Ho^{3+} laser emission using low-cost and high-power laser diodes at 0.79 µm. There exist three main methods to interpret and quantify the $Tm^{3+} \leftrightarrow Ho^3$ energy-transfer: (i) using the crystal-field splitting of the $^3F_4$ Tm^{3+} and $^5I_7$ Ho^{3+} manifolds involved in the ET [Wal97] (ii) using the dynamic model developed by Walsh *et al.* [Wal00], (iii) using the Förster-Dexter theory [For48, Dex53].

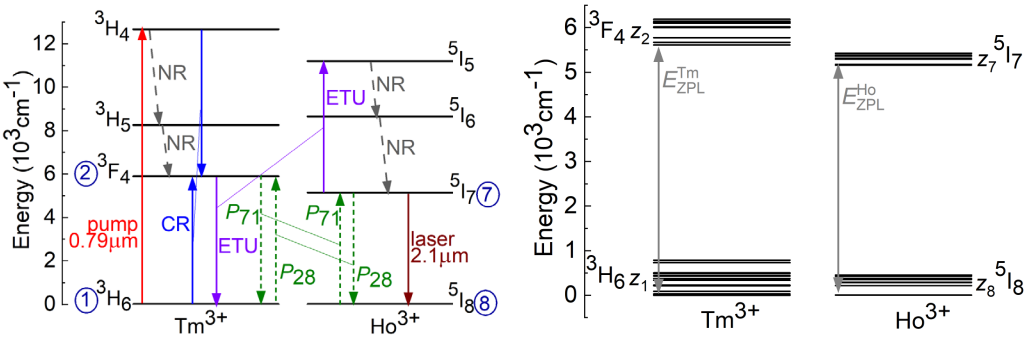

Figure I.61. A simplified scheme of energy levels of Tm^{3+} and Ho^{3+} ions showing processes relevant for laser operation around 2.1 µm, P_{28} is back ET and P_{71} is direct ET processes. E^{Tm}_{ZPL} and E^{Ho}_{ZPL} are zero-phonon line energies between the $^3H_6$ and $^3F_4$ Tm^{3+} manifolds, and the $^5I_8$ and $^5I_7$ Ho^{3+} manifolds, respectively; z_1, z_2 and z_8, z_7 are partition functions of the $^3H_6$, $^3F_4$ Tm^{3+} and $^5I_8$, $^5I_7$ Ho^{3+}manifolds, respectively.

Energy-transfer between Tm^{3+} and Ho^{3+} ions occurs due to the interaction of excited ions in the Tm^{3+} $^3F_4$ manifold with ions in the Ho^{3+} $^5I_8$ ground-state. The excited Tm^{3+} $^3F_4$ ions transition to the Tm^{3+} $^3H_6$ ground manifold, transferring their energy to Ho^{3+} ions and promoting them from the $^5I_8$ ground state to the $^5I_7$ excited one. It is referred to as direct energy-transfer, with P_{28}, the energy transfer parameter in cm^3s^{-1}, see Figure I.61(a). It can be written schematically

as Tm^{3+} ($^3F_4 \rightarrow {}^3H_6$) → Ho^{3+} ($^5I_8 \rightarrow {}^5I_7$). This process can occur in the opposite direction. The back energy transfer can be written as Ho^{3+} ($^5I_7 \rightarrow {}^5I_8$) → Tm^{3+} ($^3H_6 \rightarrow {}^3F_4$) and is labelled as P_{71} in Figure I.61(a). The back energy-transfer results in a distribution of shared energy between Tm^{3+} and Ho^{3+} ions. As a result, the $Tm^{3+} \leftrightarrow Ho^{3+}$ energy-transfer is considered as a coupled system in quasi-thermal equilibrium. A significant back energy transfer can depopulate the $^5I_7$ Ho^{3+} manifold, which can increase the laser threshold and consequently reduce the laser efficiency [Wal97]. The $Tm^{3+} \leftrightarrow Ho^{3+}$ energy-transfer is described by the equilibrium constant, Θ which is defined as follows:

$$\Theta(T) = \frac{P_{71}}{P_{28}}. \tag{I.65}$$

This constant is temperature-dependent because the distribution of excitations in the Stark sub-levels of the $^3F_4$ Tm^{3+} and $^5I_7$ Ho^{3+} changes with temperature, while the constant is independent on the concentration of dopant ions [Wal97].

Using crystal-field splitting of the $^3F_4$ Tm^{3+} and $^5I_7$ Ho^{3+} manifolds involved in the ET. The (i) first method for the quantitative evaluation of the $Tm^{3+} \leftrightarrow Ho^3$ energy-transfer is based on the crystal-field splitting of the $^3H_6$, $^3F_4$ Tm^{3+} and $^5I_8$, $^5I_7$ Ho^{3+} manifolds. The equilibrium constant Θ can be expressed as [Wal97]:

$$\Theta = \frac{z_2 z_8}{z_1 z_7} \exp\left[\frac{-(E_{ZPL}^{Tm} - E_{ZPL}^{Ho})}{kT}\right] \tag{I.66}$$

where z_1, z_2, z_7 and z_8 are the partition functions of the $^3H_6$, $^3F_4$ Tm^{3+} and $^5I_7$, $^5I_8$ Ho^{3+} states, respectively, E_{ZPL} are the energies of the zero-phonon-line (ZPL) transitions for Tm^{3+} and Ho^{3+} occurring between the lowest Stark sub-levels of their ground and excited manifolds, k is the Boltzmann constant and T is the crystal temperature. It will be shown below that the value obtained using Eq. I.66 is usually underestimated as compared to the value determined from the luminescence decay studies or Förster-Dexter theory. The reason for that comes from the fact that Eq. I.66 considers only energy-transfers between Stark sub-level with nearly resonant differences in energy, while the Θ value obtained from the measured luminescence decay curves also encompasses phonon-assisted processes.

Using luminescence decay curves involved in the ET. The (ii) second method is based on luminescence decay dynamics. The $Tm^{3+} \leftrightarrow Ho^{3+}$ energy-transfer leads to non-exponential luminescence decay curves from the $^3F_4$ Tm^{3+} and $^5I_7$ Ho^{3+} manifolds under resonant excitation into the $^3F_4$ Tm^{3+} manifold. A fast rise of Ho^{3+} luminescence (within a few hundred microseconds) is accompanied by a corresponding fast reduction of luminescence intensity for Tm^{3+} ions. This corroborates a direct $Tm^{3+} \rightarrow Ho^{3+}$ energy transfer before a thermal equilibrium is established. At longer times, the luminescence from the $^3F_4$ Tm^{3+} and $^5I_7$ Ho^{3+} manifolds decays with nearly the same rate. During this decay stage, bidirectional energy transfers take place, creating an apparent thermal quasi-equilibrium between the involved multiplets, see Figure I.62.

The experimental kinetics can be fitted by the dynamic model developed by Walsh *et al*. [Wal00]. The model for Tm^{3+} excitation is described as:

$$\frac{n_2(t)}{n_2(0)} = \frac{\beta}{\alpha+\beta}\exp(-\frac{t}{\tau_0}) + \frac{\alpha}{\alpha+\beta}\exp[-(\alpha+\beta)t], \quad \text{(I.67)}$$

$$\frac{n_7(t)}{n_2(0)} = \frac{\alpha}{\alpha+\beta}\exp(-\frac{t}{\tau_0}) - \frac{\alpha}{\alpha+\beta}\exp[-(\alpha+\beta)t]. \quad \text{(I.68)}$$

In the case of the Ho^{3+} excitation, the model has the following solutions:

$$\frac{n_7(t)}{n_7(0)} = \frac{\alpha}{\alpha+\beta}\exp(-\frac{t}{\tau_0}) + \frac{\beta}{\alpha+\beta}\exp[-(\alpha+\beta)t], \quad \text{(I.69)}$$

$$\frac{n_2(t)}{n_7(0)} = \frac{\beta}{\alpha+\beta}\exp(-\frac{t}{\tau_0}) - \frac{\beta}{\alpha+\beta}\exp[-(\alpha+\beta]t), \quad \text{(I.70)}$$

where t is time after a short-pulse excitation, τ_0 is the equilibrium decay time, n_2 and n_7 are the populations of the $^3F_4$ Tm^{3+} and $^5I_7$ Ho^{3+} manifolds, respectively, α and β are the energy-transfer rates (in μs^{-1}) of direct and back energy-transfer, respectively.

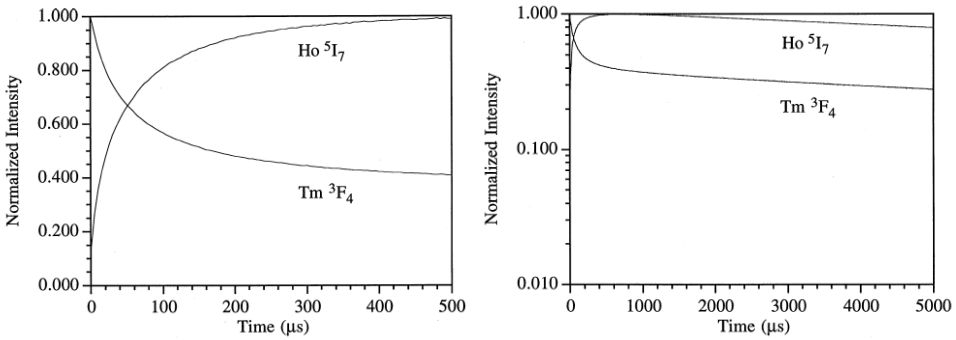

Figure I.62. Experimental decay curves from the $^3F_4$ Tm^{3+} and $^5I_7$ Ho^{3+} manifolds under excitation of the $^3F_4$ Tm^{3+} in Tm,Ho:$LiYF_4$. The right plot is the decay at early time and the left one at later time. Taken from [Wal00].

From equations I.67 and I.68, one can derive α and β and then the concentration-independent rate parameters, P_{28} and P_{71}, in $cm^3/\mu s^{-1}$ using:

$$\alpha = P_{28}N_{Ho}, \quad \text{(I.71)}$$

$$\beta = P_{71}N_{Tm}. \quad \text{(I.72)}$$

Knowing P_{28} and P_{71}, it is then possible to determine the equilibrium constant Θ using Eq. I.65.

Förster-Dexter theory. According to the Förster-Dexter theory, the energy transfer parameters are proportional to the overlap integral between the emission band corresponding to the donor transition and the absorption band of the acceptor [För48, Dex53]. It allows to find the probability of resonant energy-transfer between D and A, by treating energy transfer as a dipole-dipole interaction. To quantify the $Tm^{3+} \rightarrow Ho^{3+}$ energy-transfer, the transfer microparameters [cm^6s^{-1}] can be found as [Cai91, Pay92a, Bre93, Bra98]:

$$C_{D\rightarrow A} = \frac{3c}{8\pi^4 n^2}\int \sigma_D^{SE}(\lambda)\sigma_A^{abs}(\lambda)d\lambda, \quad \text{(I.73)}$$

From this C_{DA} energy transfer microparameter one can derive the energy transfer rate [Pay94]:

$$W_{D\rightarrow A} = \frac{32}{9}\pi^3 C_{D\rightarrow A}^6 \frac{N_A}{\tau_{rad}}. \quad \text{(I.74)}$$

I.4. Material engineering for lasers emitting at 2 µm

In this section, the current trend in the material engineering for solid-state lasers emitting at 2 µm and beyond and mechanisms of spectral line broadening in crystals are discussed. Different types of disorder in crystal structures are presented. Finally, the transparent ceramic technology is discussed as a suitable method to fabricate laser-graine quality ceramics.

I.4.A. Current trends in material engineering for solid-state lasers

Material engineering plays a crucial role to reach the optimal properties in the development of solid-state lasers. For instance, to develop mode-locked lasers with broadly tunable range, glasses in shape of fiber are ideal candidates since their disordered structure enhances flat and broad spectra as shown in Figure I.63. One of the most famous glass fibers is the silica fiber, from which many fiber laser sources are well-developed and commercially available. However, silica fibers are transparent only up to 2.2 µm that makes them unsuitable to develop lasers sources beyond this wavelength. Whereas fluoride glasses (ZBLAN fibers) exhibit a broader transparency range up to 8 µm and possess lower phonon energies (580 cm^{-1}). That makes them suitable for in the development of mid-infrared lasers.

Well-known single crystals such as Tm and Ho doped YAG lasers, well-address multi-Watt output power and exhibit high efficiency. However, their quite narrow gain profiles do not support the generation of femtosecond pulses. Figure I.63 shows the comparison between the stimulated-emission cross-section spectra of Ho^{3+} ions in an ordered Ho:YAG crystal and a disordered Ho:CALGO crystal around 2 µm. One can see that the emission spectrum of Ho^{3+} ions in CALGO exhibits a strong inhomogeneous spectral line broadening, resulting in a broad and smooth spectrum. This behavior is comparable to the emission spectrum of a Ho^{3+}-doped glass and is called "glassy-like" spectroscopic behavior, as shown in Figure I.64(*right*). In contrast, the spectrum of Ho:YAG is more structured with narrow peaks. Due to a narrow gain bandwidth of Ho^{3+} ions in YAG, only picosecond pulses were achieved in mode-locked laser configurations [Glu15, Wan18].

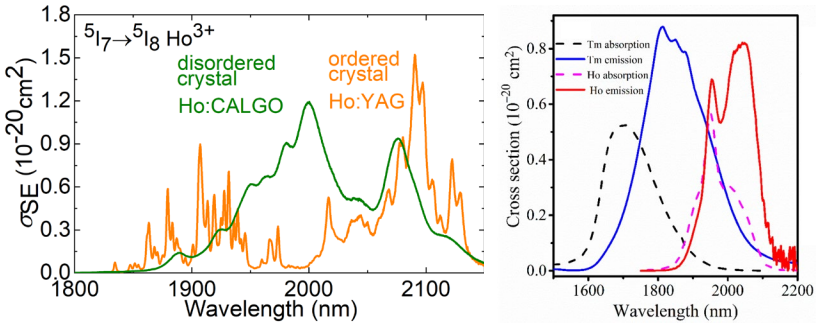

Figure I.63. The stimulated-emission cross-section spectra for the $^5I_7 \rightarrow {}^5I_8$ transition Ho^{3+} ions in YAG and CALGO ($CaGdAlO_4$) crystals demonstrate difference in spectral properties of the ordered and disordered crystals (*left*) and for the $^5I_8 \rightarrow {}^5I_7$ and $^5I_7 \rightarrow {}^5I_8$ transitions of Ho^{3+} ions in gallium tellurite glasses (*right*) [Yua21].

While glasses possess broad and smooth gain profiles due to their disordered structure, they have poor thermal conductivity. The former allows to reach sub-300-fs pulses or even lower [Jia12, Nom14, Tan15] while the latter limits the available output power from a single fiber.

Relatively compact bulk lasers in form of single crystals or ceramics can overcome these issues. However, materials with disordered structure are needed to obtain broad emission bands and thus achieve ultra-short pules. Such crystals doped with Tm^{3+} and Ho^{3+} ions have demonstrated sub-100-fs pulses in mode-locked regime, as shown in Figure I.26. Figure I.64 shows four strategies to induce a significant spectral broadening in single crystals or transparent ceramics. Within these four strategies one can find various crystals such as tetragonal calcium aluminates ($CaGdAlO_4$), cubic multicomponent garnets, cubic sesquioxides (Lu_2O_3) and their solid-solutions ($(Y,Sc)_2O_3$), monoclinic tungsten oxides ($MgWO_4$), and orthorhombic scandates ($GdScO_3$). These materials exhibit good thermal properties and broad and smooth gain profiles.

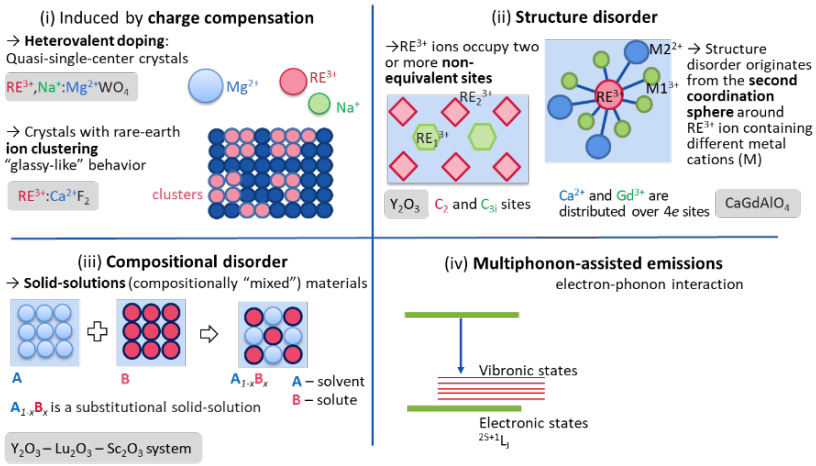

Figure I.64. Diagram showing material engineering for inducing spectral broadening of Tm^{3+} and Ho^{3+} doped materials for applications in broadly tunable and mode-locked lasers emitting at 2 μm and beyond.

I.4.B. Mechanisms of spectral line broadening in crystals

As mentioned before, crystal field exhibit a static and a dynamic (electron-phonon interaction) component, which affects the electronic spectra of RE^{3+} ions. The latter leads to a broadening and shifts of spectral lines in the energy scale up to few cm^{-1}.

Spectral broadening is a physical phenomenon that affects the spectroscopic line shape for transitions associated with absorption or emission of a photon. Broadening mechanisms can be grouped under two main categories:

• *Homogeneous broadening*. In homogeneous broadening, the mechanism has the same effect on each ion, so that the spectral response of each activator ion is broadened in an identical manner. Each ion of the ensemble thus has the same resonant frequency (peak wavelength) and atomic line shape.

We already considered the reasons of the homogeneous line broadening in Section I.2 of this chapter, Eq. I.41.

• *Inhomogeneous line broadening.* The resonance frequency of each active ion is different and spread out, resulting in a band of frequencies for the entire ensemble even though the lines of individual ions are not necessarily broadened. Thus, each ion has a different resonance frequency for the same optical transition. In solid, inhomogeneous line broadening is caused by crystalline defects in the host lattice. For inhomogeneous broadening, the overall line-shape function is the convolution of the functions of individual atoms.

This broadening is due to the strains and defects in the solid host. Such strains and defects result in sites occupied by individual ions being slightly different, and since the energies of the electronic states of the ions depend on their environment, the ions in a given state exhibit various resonance energies. One can say that the electronic levels of the solid as a whole are strain/defect broadened. For a random strain/defect distribution, the observed spectral lines have a Gaussian shape. This temperature-independent contribution depends on the disorder in the host lattice. The final line shape when both homogeneous and inhomogeneous mechanisms are taking place is a convolution of Gaussian and Lorentzian line shapes, known as a Voigt profile, as shown in Figure I.65 Experimental results on the temperature dependence of the spectral line shape of activator ions used in ordered single crystals have revealed that at about 150 K and higher temperatures, the inhomogeneous broadening is negligible and the line shape may be considered Lorentzian. These considerations show that the inhomogeneous linewidth may be used at very low (helium) temperatures to estimate internal crystal homogeneity / disorder.

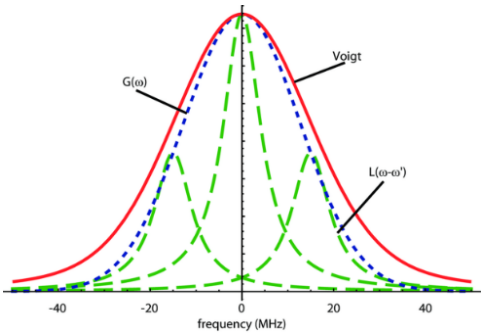

Figure I.65. Examples of Gaussian (G), Lorentzian, and Voigt line profiles. After [Dor09].

Figure I.66 shows different types of the inhomogeneous spectral line broadening for RE^{3+} ions in solid materials. The opposite to those cases is the structurally ordered single-site crystals with isomorphic and homovalent impurity distribution, such as cubic $Y_3Al_5O_{12}$, tetragonal YVO_4 and $LiYF_4$ and orthorhombic $YAlO_3$.

The crystals with different types of disorder in their structure are considered in the next sections of this chapter.

The concepts of *order* and *disorder* are fundamental to condensed matter physics and materials science. An integrated understanding of materials across the entire spectrum of disorder necessitates a grasp of both extreme cases (perfect crystals and amorphous solids) and the intermediate states. A solid is crystalline if it has long-range order, meaning the arrangement of atoms in its crystal lattice repeats itself periodically throughout the material. A

perfect crystal, the epitome of order, is an ideal infinite crystalline solid with no defects. Conversely, glasses are highly disordered, lacking long-range structural periodicity and exhibiting only short-range order, where the arrangement of atoms is regular only over a limited distance. Naturally, a crystal can lose its perfect crystalline order and eventually become amorphous when disorder is introduced.

Crystalline materials can exhibit disorder in a multitude of ways, including variations in composition, atom displacements, bonding arrangements, molecular orientations, conformations, charge states, orbital occupancies, or magnetic structure. This disorder can sometimes be random, but more often it is correlated. Current research into disordered crystals seeks to control and exploit the unusual properties of these correlated disordered solids in order to access functional responses that are inaccessible to conventional crystals [Sim20].

It should be noted that all real solid materials are disordered at finite temperature. In crystals, where this disorder is usually dominated by thermal motion (dynamic disorder), the equilibrium atomic positions themselves are periodic and hence ordered. Nevertheless, even crystals can exhibit disorder in ways other than thermal motion. This occurs whenever there is an internal degree of freedom in a component. In general, this can be referred to as static disorder, as the disordered parts will remain in their positions even if the ambient conditions are changed.

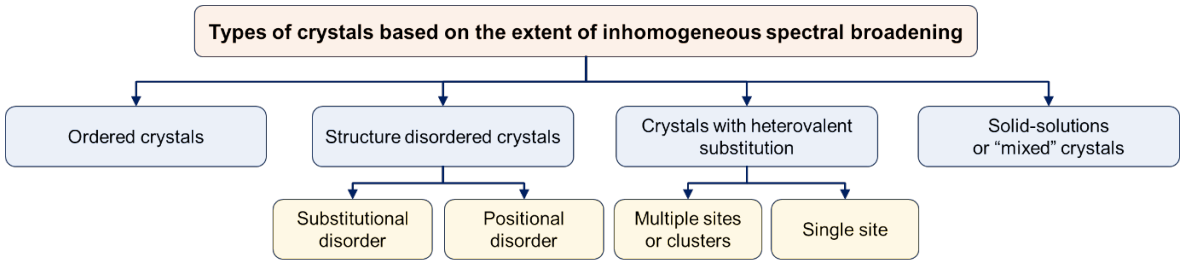

Figure I.66. Classification of laser crystals according to the mechanisms of inhomogeneous spectral broadening.

1. *Crystals with structural disorder* can be categorized into two cases [Mul06].

• *Substitutional disorder*. Structural disorder can arise from the random distribution of two or more host-forming cations over one or more crystallographic sites. This may involve some host-forming cations not being replaced by the activator ions. In this scenario, inhomogeneous spectral broadening results from variations in the composition of the second coordination sphere around the activator ions, due to differences in weights, ionic radii, and possibly charges of host-forming cations at different crystallographic positions.

• *Positional disorder*. Activator ions may occupy multiple (two or more) non-equivalent crystallographic positions, resulting in multi-site behavior. Each site has specific spectroscopic properties. The spectra of such crystals depend on the properties of ions in each site as well as their site occupancies.

2. *Crystals with heterovalent substitution*. Where the substituting and substituted ions are close in size but differ in charge, the center formation is dictated by how charge compensation

is achieved to maintain local electrical neutrality. This can result in both single-center crystals and multi-center crystals.

3. *Solid-solution (compositionally "mixed") materials*. These structures are compositionally disordered, leading to numerous kinds of centers. Unlike simple multi-center crystals, which have clearly resolved lines in their optical spectra, "mixed" systems generally do not exhibit good line resolution even at very low temperatures, and their spectra are characterized by broad bands formed by superposition of a great many lines. In other words, spectral lines for activator impurities in mixed crystals are always inhomogeneously broadened.

I.4.C. Crystals with a substitutional disorder

Notable examples of crystals with a substitutional disorder are cubic multicomponent garnets and tetragonal calcium rare-earth aluminates These crystals doped with trivalent lanthanide cations represent a great potential for material engineering for laser applications in broadly tunable and mode-locked lasers.

Cubic multicomponent garnets. They have a general formula $\{A\}_3[B]_2(C)_3O_{12}$, where {A}, [B], and (C) are dodecahedral (Wyckoff symbol: 24c), octahedral (16a), and tetrahedral (24d) sites with a coordination number (C.N.) VIII, VI and IV, for these sites respectively. These compounds belong to the cubic class (space group $Ia\bar{3}d$)

An example, which will be discussed in more details in Chapter III.3, is the disordered calcium niobium gallium garnet crystal (CNGG). Stoichiometric CNGG has a chemical formula $\{Ca_3\}[Nb_{1.5}Ga_{0.5}](Ga_3)O_{12}$ [Shi93, Vor02] but the actual crystal composition deviates from the stoichiometry resulting in a distribution of both Ga^{3+} and Nb^{5+} cations over the [B] and (C) sites and a presence of cationic vacancies [Cas16, Ser17, Pan18b]. The cationic vacancies □ are present to compensate for the charge. This can be represented as $Ca_3Nb_{2-x}Ga_{3+x}\square_yO_{12} = \{Ca_3\}[Nb_{2-x}Ga_x](Ga_3\square_y)O_{12}$ (x = 0.5 and y = 0 for stoichiometry).

In these crystals, the disorder in the structure is introduced by the random distribution of Nb^{5+} and Ga^{3+} cations over the same octahedral lattice sites. The dopant RE^{3+} ions substitute for the Ca^{2+} ones in {A} sites and their absorption and emission spectra exhibit significant inhomogeneous broadening owing to the possible different environments of local ligands [Pan18b].

CNGG-type crystals melt congruently around 1430-1470 °C and they can be easily grown by the conventional Czochralski method. CNGG crystals exhibit moderate thermal conductivity (~4.3 Wm^{-1} K^{-1}), weak thermal expansion ($\alpha = 7.8\times10^{-6}$ K^{-1}) and a positive thermo-optic coefficient ($dn/dT = 7.8\times10^{-6}$ K^{-1} at ~1 mm). CNGG shows a broad transparency range of 0.28 – 8 μm (among oxide crystals) and, thus, it is suitable for short-wave infrared emission.

Since the dopant ions exhibit a strong inhomogeneous spectral line broadening, RE:CNGG-type crystals, where RE stands for Nd^{3+}[Xie08, Xie10], Yb^{3+} [Sch10a, Lou14, Zha15, Lin23], Tm^{3+} and Ho^{3+} [Pan18a, Pan18, Zha19, Wan21, Pan21, Pan21a Suz24] ions, have shown fs pulse generation in mode-locking in the near-infrared and short-wave-infrared regions.

Pan *et al.*, achieved ultrashort pulses as short as 63 fs from a Tm,Ho:LCLNGG (lanthanum calcium lithium niobium gallium garnet) mode-locked laser at 2072 nm with an average output

power of 63 mW at a pulse repetition rate of ~102.5 MHz. La^{3+} and Li^{+} ions were added for a pair charge compensation for additional broadening [Pan21]. The pump source was a Ti:Sapphire.

Suzuki *et al.*, demonstrated LD-pumped mode-locked sub-100-fs Tm,Ho:CLNGG laser at 2.1 μm wavelength for the first time. The laser generated an average output power of 120 mW at a pulse repetition rate of 70.3 MHz with a pulse duration as short as 88 fs at 2090 nm [Suz24].

Calcium rare-earth aluminates. Calcium rare-earth aluminates $CaREAlO_4$ crystals, where RE stands for Gd or Y (denoted as CALGO / CGA and CALYO / CYA, respectively) belong to a class of oxide materials with a general chemical formula of $ABCO_4$, where A^{2+} = Ca^{2+} or Sr^{2+}, B^{3+} is a rare-earth cation, and C^{3+} = Al^{3+} or Ga^{3+} [Paj98].

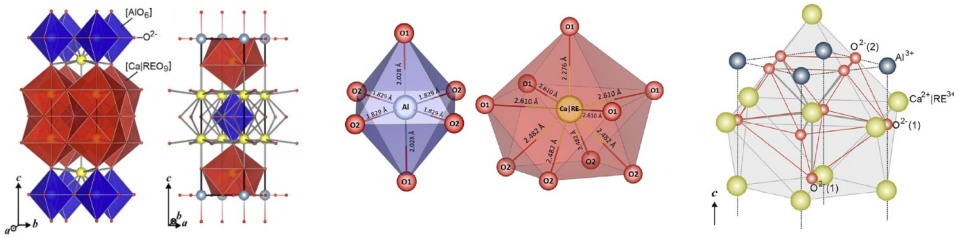

Figure I.67. Fragment of the structure of a Tm,Ho:Ca(Gd,Lu)AlO4 crystal, *black lines* mark the unit-cell, *blue* and *red polyhedra* – $[AlO_6]$ and $[Ca|REO_9]$, RE = Gd, Tm or Ho (*left*); schematic of the $[AlO_6]$ and $[Ca|REO_9]$ polyhedra (*middle*); second coordination sphere of $Tm^{3+}|Ho^{3+}$ ions by $Ca^{2+}|RE^{3+}$ cations in this crystal (*right*) [Pan22].

$CaREAlO_4$ crystallizes in the tetragonal system with space group D^{17}_{4h} – *I4/mmm*. It belongs to the K_2NiF_4 type structure. The structure of $CaREAlO_4$ crystals is formed by octahedrally coordinated by oxygen $[AlO_6]$ polyhedra, which form a framework structure, as shown in Figure I.67. The Ca^{2+} and RE^{3+} cations occupy the C_{4v} sites symmetry and form $[Ca|REO_9]$ polyhedral locating between layers of the $[AlO_6]$ [Sha92, Woe97, Pan22]. As a result, $CaREAlO_4$ doped with laser-active trivalent rare-earth ions such as Yb^{3+}, Tm^{3+}, Ho^{3+}, etc. exhibit a significant inhomogeneous broadening of the spectral bands. [Lag97, Pet08, Di14].

CALGO and CALYO crystals melt congruently at 1750 °C and ~1810 °C, respectively. They possess high and moderate thermal conductivity (κ_a = 6.9 Wm^{-1} K^{-1}, κ_c = 6.3 Wm^{-1} K^{-1}) for 1.1 at.% Yb:$CaGdAlO_4$ and κ_a = 3.6 Wm^{-1} K^{-1}, κ_c = 3:2 Wm^{-1} K^{-1} for a pure 1 at.% Yb:$CaYAlO_4$, while for pure $CaYAlO_4$ κ_c = 3:3 Wm^{-1} K^{-1}, κ_a = 3.7 Wm^{-1} K^{-1} with a moderate dependence on the RE^{3+} doping concentration [Li11, Jaf13]. They also exhibit a weak anisotropy of the thermal expansion and negative thermo-optic coefficients leading to an almost "athermal" behavior [Loi14].

Due to good thermal properties and disordered nature, these host matrices are attractive for broadly tunable and mode-locked lasers [Pet05, Die13, Zha18b, Wan22].

For instance, sub-100 fs pulses were achieved form $CaGdAlO_4$ lasers doped with Yb^{3+}, Tm^{3+} and Ho^{3+} ions.

Wang *et al.* demonstrated pulses as short as 17.8 fs with a spectral bandwidth of 145 nm and a central wavelength of 1118 nm from a Kerr-lens mode-locked Yb:CALGO oscillator. The oscillator operates at an average power of 26 mW and a repetition rate of 95.9 MHz [Wan21].

Wang *et al*. reported on a Tm,Ho:CALGO laser passively mode-locked by a GaSb-based SESAM generating pulses as short as 52 fs at a central wavelength of 2015 nm with a broad spectral bandwidth of 82 nm (full width at half maximum) owing to the combined gain profiles of both dopants for σ-polarized light. The average output power reached 376 mW at a repetition rate of 85.65 MHz [Wan22].

Yao et al. report on a GHz fundamental repetition rate Kerr-lens mode-locked Ho:CALGO laser emitting at 2.1 μm. The laser employs a ring cavity to increase the fundamental repetition rate to 1.179 GHz and can be made to oscillate in both directions stably with nearly identical performance: for the counterclockwise oscillation, it generates 93-fs pulses at 1.68 W of average power [Yao24].

I.4.D. Materials with a multisite behavior: the case of cubic sesquioxides

Host matrices with multisite behavior are positional disorder (multicenter disordered crystals), where an ion occupies more than a single site. In certain crystals, the dopant ions replacing for the host-forming cations can be statistically distributed over two or more non-equivalent crystallographic positions with different local symmetries and geometries of the first coordination sphere.

A sesquioxide is any oxide containing three oxygen atoms for every two atoms of another element. Sesquioxides of rare-earth elements with a chemical formula R_2O_3 (R = Sc – Lu) can crystallize in three different crystal structures: trigonal (type A, sp. gr. $P3m1$), monoclinic (type B, sp. gr. $C2/m$), and body-centered cubic (type C, sp. gr. $Ia\bar{3}$). The cubic phase in particular is of increasing interest for optical applications

Cubic sesquioxides R_2O_3 with optically passive host-forming cations, where R stands for Y, Lu and Sc (called respectively yttria, lutecia and scandia), are attractive host crystals for doping with laser-active rare-earth ions [Kra15]. As host matrices, they offer:

(i) good thermal properties, i.e., high thermal conductivity (12.8 Wm^{-1} K^{-1} for undoped Lu_2O_3) with a weak dependence on the rare-earth doping level in the case of similar ionic radii as shown in Figure I.68, *e.g.*, Yb^{3+} [Pet11]; (ii) weak isotropic thermal expansion and positive thermo-optic coefficients [Loi15] leading to positive thermal lensing; (iii) low phonon energies among oxide crystals (*e.g.*, 612 cm^{-1} for Lu_2O_3), [Abr14]; (iv) a broad transparency range; (v) possible high rare-earth doping levels.

In addition, the dopant ions in R_2O_3 crystals experience strong crystal-fields leading to large total Stark splitting of their multiplets and, consequently, broadband emission properties. A particular feature of cubic sesquioxides is the sensitivity of their crystal-field strengths to the host-forming cations leading to a significant variation of the spectroscopic properties in the R = Y → Lu → Sc series [Loi18a]. The relatively low phonon energy of R_2O_3 crystals leads to weak rates of multiphonon non-radiative relaxation from the excited states of the dopant ions [Web68].

At low temperatures, the absorption and emission spectra of the dopant ions in such crystals still contain narrow lines assigned to transitions of ions in both sites. The shape of these spectral lines weakly depends on the concentration of activator ions. The different spectral behavior can

be revealed by site-selective spectroscopy. At room temperature, the thermal line broadening (homogeneous linewidth) still dominates. The overall spectral response of such crystals is determined by the relative fractions of activator ions occupying the available sites, as well as by the individual properties of the ion species in these sites.

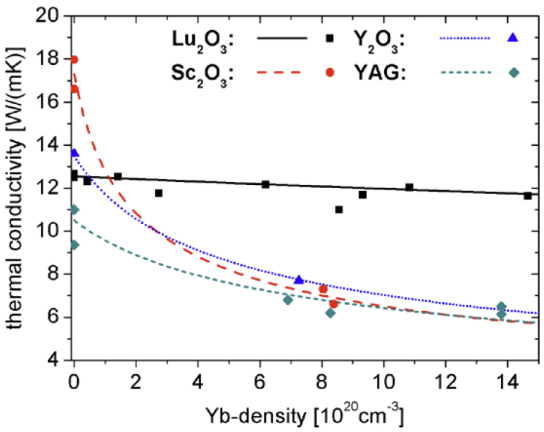

Figure I.68. Measured (*symbols*) and fitted (*lines*) thermal conductivity of the different Yb:R_2O_3 and Yb:YAG for Yb-concentrations between 0 and 15×10^{20} cm^{-3} (corresponding to Yb (10.9 at.%):YAG, Yb (5.3 at.%):Lu_2O_3, Yb (4.5 at.%):Sc_2O_3, and Yb (5.6 at.%):Y_2O_3) [Pet11].

Due to their broadband emission properties and excellent thermo-optical and thermo-mechanical properties, they have found applications in wildly tunable and mode-locked lasers, as well as for high power laser applications [Pet11, Kra15, Loi18a].

Suzuki *et al*. presented a combined gain media Kerr-lens mode-locked laser based on a Tm:Lu_2O_3 ceramic and a Tm:Sc_2O_3 single crystal. Pulses as short as 41 fs, corresponding to less than 6 optical cycles, were obtained with an average output power of 42 mW at a wavelength of 2.1 µm and a repetition rate of 93.3 MHz [Suz21]. Also, Suzuki *et al*. reported on a high quality-factor Kerr-lens mode-locked Tm:Sc_2O_3 laser operating around 2.1 µm. Using a simple four mirror Z-shaped cavity, pulses as short as 72 fs with an average power of 130 mW were obtained at a center wavelength of 2108 nm [Suz20].

Another example of a multi-site crystal is the monoclinic R_2SiO_5, where R stands for Y, Lu and Sc, [Li93]. The spectra of such crystals depend on the properties of ions in each site as well as their site occupancies.

I.4.E. Crystals with rare-earth ion clustering: the case of CaF_2

CaF_2 was discovered by Stockbarger in 1927 [Sto49]. The unit cell is described as a face-centered cubic structure of Ca^{2+} ions, with fluoride ions (F^-) occupying all tetrahedral sites. A simple structure of F^- ions can also be defined, where the fluoride ions form a cubic lattice with an edge of $a/2$, and the Ca^{2+} ions occupy every other cube center. Each Ca^{2+} ion is subjected to a cubic symmetry field (O_h). The fluoride ion site exhibits a tetrahedral symmetry as it is surrounded by four Ca^{2+} ions as its nearest neighbors.

The fact that every other cube of the fluoride ion lattice is occupied by a Ca^{2+} ion indicates that there are unoccupied cubic symmetry interstitial sites. This feature allows the matrix to

accommodate a wide range of impurities, including both divalent and trivalent ions. When trivalent rare earth ions are introduced into the lattice, they substitute for the Ca^{2+} ions ($M_{1-x}^{2+}RE_x^{3+})F_{2+x}$. In this case, charge compensation is necessary to maintain the electrical neutrality of the lattice. This compensation can be provided either by an interstitial F_i^- ion or by a parasitic impurity such as oxygen (O^{2-}) or sodium (Na^+, K^+). It gives rise to the formation of different optical centers, depending on the position of doping RE^{3+} ions and the corresponding local symmetries created by the additional F_i^- ions.

Depending on the concentration of RE^{3+} doping, ionic radius, and the thermal history of the samples, they can form clusters with different local site geometries within clusters [Cor82]. In CaF_2 doped with 0.1-0.2 at.% Ho^{3+} ions, the dominant cluster centers are dimers resulting from the preferential aggregation of pairs of monomers [Muj01]. The higher-order clustering of clusters increases with the doping concentrations of RE^{3+} ions. RE^{3+} ions with small radii, such as Yb^{3+} or Tm^{3+}, tend to form large clusters consisting of six ions, known as hexamers, rather than dimers or tetramers. Within these clusters, the RE^{3+} ions are arranged in cubo-octahedral environments [Cat84, Nes88]. More recent studies, including EPR measurements and computer simulations, have revealed that Er^{3+}, Tm^{3+}, and Yb^{3+} ions are organized in hexameric clusters of the RE_6-F_{37} type, which are embedded in the fluorite lattice [Nik05, Kaz05]. The different types of clusters in Tm^{3+}-doped and Yb^{3+}-doped CaF_2 crystals were directly observed by employing scanning transmission electron microscopy [Dra08, Loc14]. [Dra08] reported that Tm^{3+} ions were distributed inhomogeneously at the host sites and form sub-nm agglomerations of 3-5 atoms, rather than individual ions. The spatial extent of the inhomogeneous Tm^{3+} concentration was 2.6-6 nm and originates from ionic density fluctuations in the liquid phase. [Lac14] reported that Yb:CaF_2 crystal should be considered as a multisite system whose luminescent and lasing property are dominated by a series of Yb^{3+} clusters from dimers to tetramers. Hexameric clusters may be dominant at high dopant concentrations (above 20 at.% but not at the intermediate dopant concentrations between about 0.5 and 10 at.%.

These clusters result in broadened emission and absorption bands of RE^{3+} ions, similar to what can be found in glasses. These broad bands are well suited for diode laser pumping and can be exploited for tunable or short-pulse lasers.

Figure I.69 shows the results on the fraction of Tm^{3+} ions with neighbors *f* as a function of Tm doping level, taken from [Loi20]. When Tm doping level increases, the fraction of isolated ions (1 – *f*) gradually decreases. The critical Tm doping level for which at least half of the active ions are clustered is only 0.7±0.1 at.%. The dependence shown in Figure I.69 (*top*) was fitted using a statistical approach [Vor74, Loi16]:

$$P_{m,n} = \frac{n!}{m!(n-m)!} p^m (1-p)^{n-m}, \tag{I.75}$$

where $P_{m,n}$ is the probability for occurrence of neighbor Tm^{3+} ions in the first coordination sphere of the considered Tm^{3+} ion, *n* is the coordination number (C.N.) for the nearest-neighbor rare-earth sites, *m* is the actual number of Tm^{3+} ions in the first coordination sphere (*m* = 0 corresponds to a single ion and $m \geq 1$ – to an ion pair or cluster), and $p = N_{Tm}/N_{max}$ represents the relative doping concentration (N_{max} is the maximum possible concentration). The

expression for the fraction of ions with neighbors ($m \geq 1$, not specifying the exact m number) is:

$$f = 1 - [1 - (N_{Tm} / N_{\max})]^{C.N.}. \quad \text{(I.76)}$$

Figure I.69 (*bottom*) shows a modeling of the thermodynamic stable rare-earth clusters in CaF_2 [Liu23].

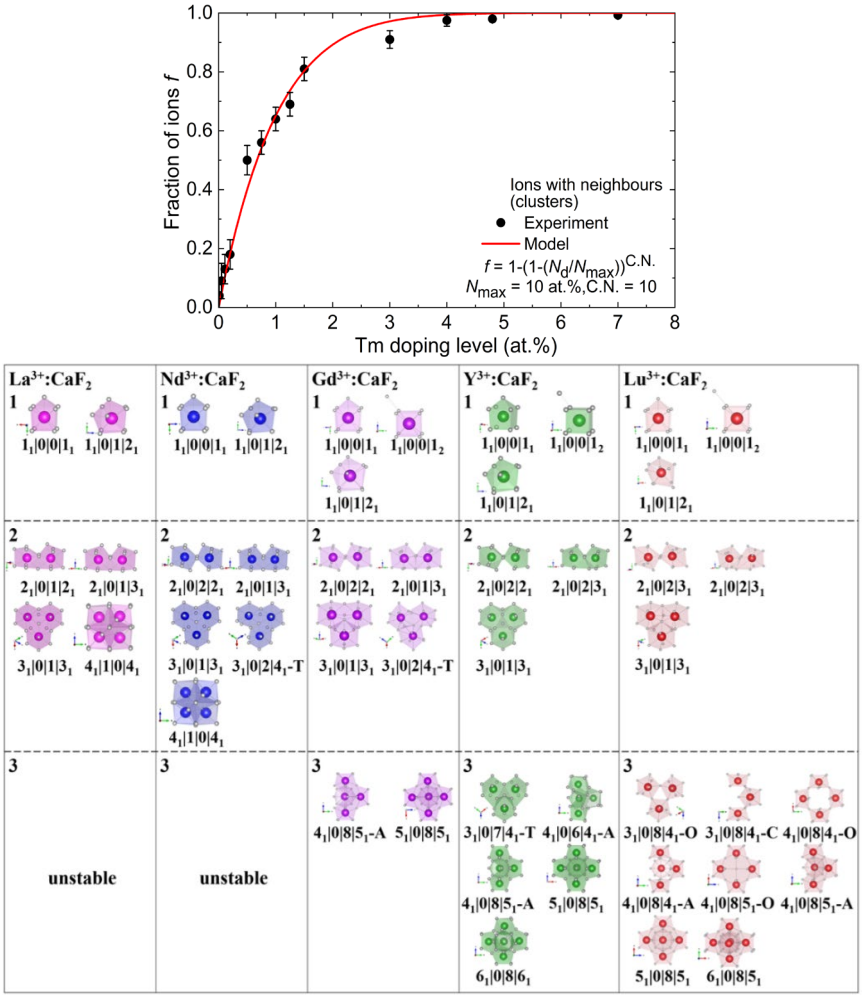

Figure I.69. Ion clustering in RE^{3+}:CaF_2: fraction of Tm^{3+} ions with neighbors *f*, symbols – data extracted from the modeling of the experimental luminescence decay curves using the rate-equation model of distinct ion classes, *curve* – their fit using Eq. I.75 (*top*) [Loi20]; the simulation of the potentially thermodynamic stable RE^{3+} clusters, where The symbol $i_1|v|d|s_r$-O/A/T/C describes the clusters. i_1 is the number of RE^{3+} ions; *v* is the number of lattice fluorine vacancies; *d* is the number of lattice fluorines that deviated from the normal site; and *s* means the number of interstitial fluorines (F_i^-); *r* = 1 and 2 point to that the interstitial fluorines located at the nearest and next nearest site of rare earth ion, respectively. O, A, T, C refer to the shape of the cluster resembling a circle (O), an armchair (A), a crescent moon (C) and a tack nail (T), respectively (*bottom*) [Liu23].

I.4.F. Solid-solution (compositionally "mixed" materials)

The term solid-solution was introduced by J. H. van't Hoff in 1890 [Wal96, Kor05]. Solid-solutions are homogenous mixtures of several kinds of atoms in solid state having a single-crystal structure. These are homogeneous solid materials containing several components whose concentrations can be varied within certain limits under a given temperature and

pressure without losing the homogeneity. The word "solution" is used to describe the intimate mixing of components at the atomic level and distinguishes such homogeneous materials from physical mixtures of components. Two terms are mainly associated with solid solutions – *solvents* and *solutes*, depending on the relative abundance of the atomic species.

The formation of a solid solution preserves the structure of the crystalline lattice of the solvent accompanied by a variation of its unit-cell parameters.

Almost all minerals are able to tolerate variations in their chemical composition leading to a change of their properties.

There exist different types of solid-solutions, as shown in Figure I.70.

• *Interstitial solid solutions* are formed when the atoms of the solute (component B) go into the spaces between the atoms of the solvent (component A) in its crystalline lattice. The spaces between the atoms of a crystal lattice are known as interstitial sites. Interstitial solid solutions always have limited solubility of the solute. When the atomic radius of the element B is sufficiently small, this element can occupy interstitial sites in the structure of A.

• *Substitutional solid solutions* are formed when the atoms of the solute B partially occupy a fraction of the lattice sites in place of the solvent A. Such solutions are formed by components with identical types of crystalline lattices with a small difference of their unit-cell parameters. Substitutional solid solutions can be of complete or limited solubility. In the former ones, any concentration of the dissolved component (between 0 and 100 at.%) is possible.

A substitutional solid solution with complete solubility represents a family of materials with a chemical formula $A_{1-x}B_x$ ($0 < x < 1$) having a single-crystal structure. Solid-solutions are frequently called "mixed" materials indicating the mixing of components at the atomic level. The origin materials (A and B) are also called parent materials.

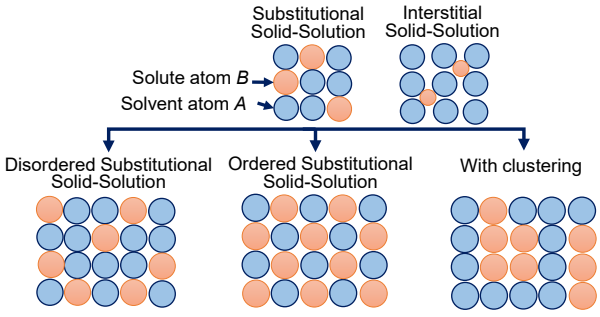

Figure I.70. Schematic representation of two types of solid solutions: substitutional and interstitial. The former is classified as disordered, ordered and with clustering.

Substitutional solid solutions can be additionally classified by the character of distribution of the atoms of the solute through the crystalline lattice of the solvent.

(i) *Disordered substitutional* – the atoms are randomly distributed across the various sites of the lattice; (ii) *ordered substitutional* – the atoms are arranged in a regular way (the atoms of the solute occupy certain preferred sites in the lattice of the solvent); (iii) *substitutional solid solutions with atomic assemblies* – the atoms of the solute tend to aggregate forming simple to complex clusters (dimers, multimers).

The criteria for the existence of substitutional solid-solutions between two parents are given by *the Hume-Rothery rules*:

- The solubility is possible if the crystal structures of the solute and solvent are identical.
- The atomic radius of the solute and solvent atoms must differ by no more than 15%.
- Complete solubility occurs when the solvent and solute have the same valency.
- The solute and solvent should have similar electronegativity (typically within ±0.4).

There is no universal definition for the x parameter in substitutional solid solutions $A_{1-x}B_x$ to separate the term "doping" from the "mixed" crystal or solid-solution. This separation becomes especially relevant for heavily doped materials. From the point of view of optical applications, it can be treated as there is a minimum value inducing a noticeable change of the spectroscopic properties. Indeed, for crystals with high doping levels (about tens of at.%), the introduction of the dopant may notably change the lattice parameter of the compound and the crystal-field strength around the active ions, in a similar way that in solid-solution host matrices.

One classical example is cubic rare-earth sesquioxides. Let us first consider only compounds based on optically passive cations, Y_2O_3, Lu_2O_3 and Sc_2O_3. We will verify the applicability of the Hume-Rothery rules: (i) all three components are isostructural (cubic, bixbyite-type structure); (ii) the ionic radii of Y^{3+} (0.90 Å), Lu^{3+} (0.861 Å) and Sc^{3+} (0.745 Å), (all the values are given for VI-fold oxygen coordination) differ by less than 17%; (iii) the ions have the same valence (+3) and (iv) the Poling electronegativities of Y (1.22), Lu (1.36) and Sc (1.49) differ by no more than ±0.3. As a result, binary and ternary substitutional solid-solutions with complete solubility exist in the Y_2O_3 - Lu_2O_3 - Sc_2O_3 system. Note that many cubic rare-earth sesquioxides based on optically active ions, such as Er_2O_3, Yb_2O_3, Ho_2O_3, etc., exhibit a similar behavior with the above-mentioned compounds. However, for laser applications, substitutional solid-solutions containing one (or several) laser-active ions and just one optically passive ion are still referred to as doped (codoped) materials.

"Mixed" host matrices are attractive for doping with trivalent rare-earth ions as they exhibit inhomogeneous spectral broadening of their absorption and emission bands. It arises from the composition variation of the nearest-neighbor cationic coordination sphere of the RE^{3+} ions. The broadband emission behavior of a material is of practical importance for the development of broadly tunable lasers and especially ultrafast (femtosecond) oscillators as much shorter laser pulses can be generated using RE^{3+}-doped "mixed" materials as compared to the corresponding parent ones. However, solid-solution compositions may suffer from reduced thermal conductivity and optical quality. Thus, it is of practical importance to search for solid-solution laser host matrices combining broadband emission properties of RE^{3+} dopants with reasonable thermal behavior.

The examples of such crystals are cubic Y_2O_3 – Lu_2O_3 – Sc_2O_3 [Kra22] solid-solutions.

It should be noted that there exist materials, which combine the features described above. The fluorite-type solid-solutions CaF_2 – SrF_2 – BaF_2 [Kam13] combine the effects of compositional disorder and heterovalent substitution involving different charge compensation mechanisms. "Mixed" $Ca(Gd,Lu)AlO_4$ crystals [Pan22] combine the effects of local structure disorder with compositional disorder.

I.4.G. Transparent ceramics for laser applications

Transparent ceramics are polycrystalline optical materials composed of closely packed single-crystalline grains. These grains can be of random or controlled orientation, providing weak light scattering at the grain boundaries. This weak scattering is ensured by a low density of pores and the absence of secondary phases.

Transparent ceramics can serve as laser host materials for doping with rare-earth ions. An effort to use ceramics as a laser gain medium began in 1964 with Dy:CaF_2 in cryogenic conditions [Hat64]. The research and technological development of transparent laser ceramics have progressed significantly since Ikesue *et al*. fabricated in 1995 a high-quality Nd:$Y_3Al_5O_{12}$ transparent ceramic by a solid-state reaction method [Ike95].

Figure I.73 shows the main scattering centers inducing losses which prohibit laser oscillations. These scattering centers in ceramics results from refractive index variations. They include [Ike08, Xia20]:

(1) Grains and grain boundaries. The control of the quality of grain boundaries allows to fabricate ceramics with high optical quality. (2) Residual pores. Near the surface of pores light is reflected and refracted by both trapped air and the ceramic material. Therefore, porous ceramics are not transparent, regardless of whether the pores are inter-grained or intra-grained. (3) Secondary phases formed from sintering aids (ZrO_2, LiF, La_2O_3), which are usually localized near grain boundaries [Yan16, Bal20, Bal21]. (4) Double refraction on the boundaries. (5) Impurities. (6) Surface scattering due to its roughness.

The formation of the scattering centers is mainly influenced by the synthesis process and the pureness of raw materials in powder form. The chosen method of preparation and sintering is crucial to obtain ceramics with extremely low scattering losses leading to efficient laser actions comparable to single-crystal laser oscillation or even superior.

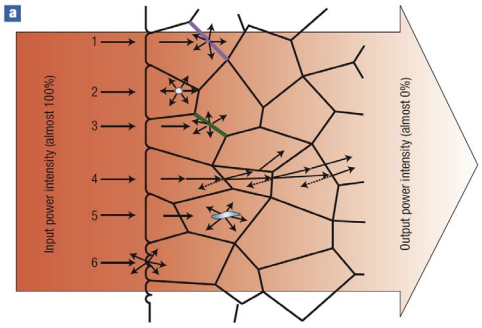

Figure I.73. A schematic showing the microstructure of transparent ceramics, light scattering and the attenuation of input power through the ceramic body. Strong scattering owing to (1) a grain boundary, (2) residual pores, (3) secondary phase, (4) double refraction, (5) inclusions and (6) surface roughness in ceramics prohibits applications in optics [Ike08].

To fabricate high optical quality ceramics for laser applications, precursor powders with a high reactivity and good dispersion are required to fabricate highly transparent ceramics with clean grain boundaries and narrowly distributed grain size. The quality of raw materials is crucial since a large particle size and hard aggregation may necessitate high sintering

temperatures and hence possibly cause exaggerated grain growth. The homogeneous distribution of dopant ions is also critical to laser performance.

The example of a laser quality Nd:YAG transparent ceramic is shown in Figure I.74 The microstructure of the ceramics shows no residual pores, secondary phases or optically inhomogeneous parts are observed. Only clean grain boundaries on the atomic scale were observed, as shown in Figure I.74(f,g). The numbers of point and line defects and dislocations were also at a minimum level in the grains.

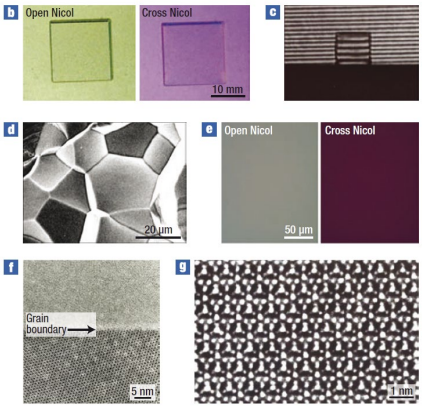

Figure I.74. Example of the microstructure of the laser quality Nd:YAG transparent ceramic: (b) polarized images the ceramic on the macroscopic scale viewed through a Nicol (*left*) and a crossed Nicol polarizing prism (*right*), showing no double refraction or refractive-index fluctuation. (c,) An interferometry image of the ceramic on the macroscopic scale. Stress-free and straight fringes can be seen throughout the whole position of the specimen. (d) Fracture surface and (e) polarized Nicol (*left*) and crossed Nicol (*right*) images of the ceramic on the microscopic scale. Perfect microstructure without pores and birefringence can be observed. (f) Transmission electron microscope image of a grain boundary and,(g) the lattice structure of the ceramic. Clean grain boundaries with no atomic defects can be seen. Taken from [Ike08].

Figure I.75(a) shows the example of the gradient distribution of Nd^{3+} ions in the length direction of the laser gain medium before and after sintering. The sintering significantly improves the distributions.

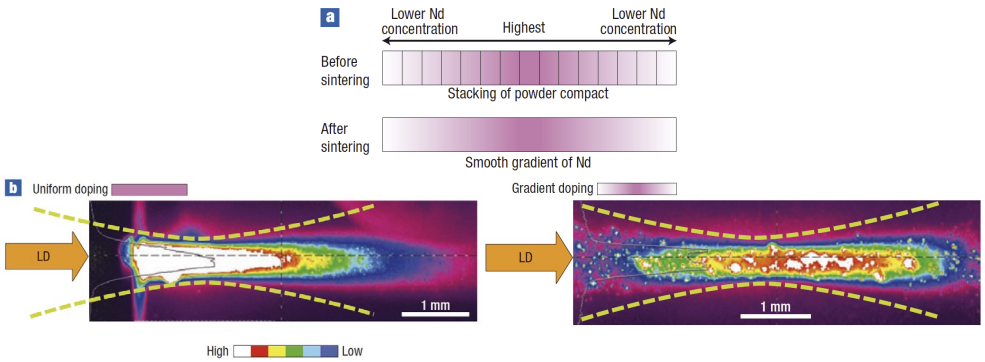

Figure I.75. Gradient-distribution of Nd:YAG ceramic: (a) a schematic showing the distribution of Nd before and after sintering; (b) a comparison of the thermal distribution during edge-pumped laser operation for uniform and gradient Nd distribution [Ike08].

Figure I.75(b) shows the comparison of the heat distribution of a laser diode pumped a conventional Nd:YAG single-crystal exhibiting uniform doping (*top panel*) and a Nd:YAG ceramic rod possessing a smooth gradient configuration (*bottom panel*). In the case of the single-crystal medium, very high heat generation was concentrated near the edge regions. In contrast, it was clear that the ceramic composite element suppressed such sudden heat generation due to the gradient distribution of Nd^{3+} ions. The control of the ion distribution is an important parameter to control the thermal lensing in the laser host media, which significantly affects the laser efficiency and the laser beam quality.

To fabricate ceramics with desirable properties for laser applications, many different techniques have been proposed [Ike95, Li13, Kim15, Xia20, Liu21]. Ceramic processing involves three main steps, see Figure I.76.

(i) *Powder preparation*. (ii) *Green body formation*. (iii) *Sintering*.

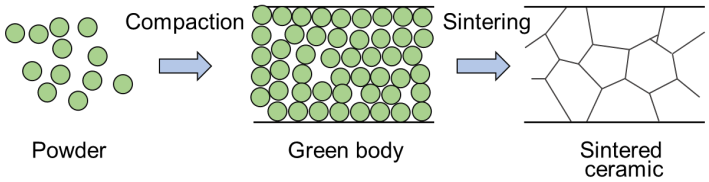

Figure I.76. Scheme of ceramic processing.

In the most common approach used for fabricating transparent laser ceramics, namely powder compact sintering, the raw materials in powder form are first processed, then formed into a green body (a shaped compact of the powder particles) and the significant porosity is then eliminated during sintering. The objective of sintering is to obtain a practically full porosity closure, namely, full densification, while keeping a minimal grain growth. Ceramic technologies also use various sintering additives to enhance the densification rate.

The solid-state reaction method is the widely used industrial method for the production of laser ceramics. This method involves the direct preparation of ceramics from precursor powders, including oxides, hydroxides, carbonates, and other salts. [Xia20]. Alternatively, powders can be prepared by different techniques: (i) chemical methods: chemical precipitation (for single oxides) or coprecipitation (for complex oxides), sol-gel processes, gel combustion, and hydrothermal reactions; (ii) laser-ablation method; (iii) combustion method; (iv) microwave-assisted method; (v) modified Pechini method.

The formation of the scattering centers is mainly influenced by the synthesis process. Transparent laser ceramics usually maintain the desirable spectroscopic and thermal properties of the corresponding single crystals.

The transparent ceramic technology offers several advantages compared to the single-crystal counterparts.

• The simplicity and cost effectivity of the fabrication due to shorter processing times and low temperature of synthesis.

The low temperature of synthesis is practically interesting for high melting point materials such as cubic sesquioxides (Y_2O_3, Lu_2O_3, Sc_2O_3). They possess a melting point around 2400 °C, whereas the corresponding transparent ceramics are fabricated at about 1800 °C.

• Easier and more controllable doping by RE^{3+} ions reaching higher concentrations, including much weaker segregation, which is often observed in single crystals.

• The possibility to fabricate compositionally "mixed" (solid-solution) compounds, such as $(Y_xLu_ySc_z)_2O_3$ (x + y + z = 1) with well-defined Y/Lu/Sc balances, as well as composite media with various geometries (layer, cylindrical, waveguide or gradient).

• Mass production.

Typically, cubic materials are selected for the development of transparent laser ceramics, avoiding additional scattering losses related to birefringence. Three cubic material families are mainly employed for transparent laser ceramics doped with rare-earth ions: (i) fluorite-type crystals (CaF_2) [Akc13]; (ii) rare-earth sesquioxides (Y_2O_3, Lu_2O_3, Sc_2O_3) [Tak05]; (iii) multicomponent garnets ($Y_3Al_5O_{12}$) [Yag07].

Conclusions of Chapter I

In this chapter, a detailed literature review on solid-state lasers and laser materials based on thulium and holmium ions emitting around 2 μm and beyond was conducted. The goal was to bridge the gap between laser development techniques and material engineering for laser active gain media. This study clearly indicates a gap in understanding the links between material properties, including material structure, and the spectroscopic and laser performance of solid-state oscillators. In particular, the information that is either insufficiently systematic or completely missing in the literature can be summarized as follows:

• There is no systematic study of the effect of compositional disorder in "mixed" materials on their emission properties.

• There is no direct comparison of different mechanisms of inhomogeneous spectral line broadening.

• No guidelines have been proposed for efficient material engineering for mode-locked solid-state lasers around 2 μm.

There is a need for novel, efficient, broadly emitting materials (crystals and ceramics) at 2 μm that potentially support few-optical-cycle generation. To address these existing challenges, we propose the following solutions, which will be presented in this PhD thesis:

Performing a detailed spectroscopic study to reveal materials exhibiting strong inhomogeneous spectral line broadening, leading to structureless and broad absorption and emission spectra of the dopant ions.

Considering different strategies to promote this effect, namely:

• Rare-earth ion clustering in fluorite-type crystals.

• Structural disorder, such as random site distribution for cations in $CaGdAlO_4$.

• Compositional disorder in solid-solution compounds, such as "mixed" $Y_2O_3 – Lu_2O_3 – Sc_2O_3$ sesquioxide ceramics.

Chapter II

Fluorite-Type Crystals with Rare-Earth Ion Clustering

Calcium fluoride (CaF_2) is a cubic crystal, where Ca^{2+} cations are bonded in a body-centered cubic geometry to eight F^- anions. Due to its broadband transparency, low refractive index and high thermal conductivity, CaF_2 is widely used in optical components. It is also very attractive for doping with laser-active trivalent RE^{3+} ions replacing Ca^{2+} cations. Even at moderate doping levels (>0.1 at.% RE^{3+}), calcium fluoride crystals exhibit RE^{3+} ion clustering resulting in a strong inhomogeneous broadening of absorption and emission bands (a "glassy-like" behavior) and enhancement of the energy-transfer processes. The broadband emission and good thermal properties of RE^{3+}-doped CaF_2 crystals determine their applications in high-power / high-energy ultrafast lasers and amplifiers.

In this chapter, the synthesis and spectroscopic study of Tm^{3+} and Ho^{3+} ions in cubic CaF_2 crystals as well as their efficient laser operation are reported. In Section II.1, the effect of different Tm/Ho-codoping ratios on the laser performance of Tm,Ho:CaF_2 crystals were studied. In Section II.2, the first laser operation of a Tm:CaF_2 waveguide laser produced by femtosecond laser writing was achieved.

II.1. Efficient broadly tunable Tm,Ho:CaF_2 laser at 2.1 µm

This section discusses the synthesis of Tm,Ho:CaF_2 crystals and their material characterization. The impact of Tm^{3+} co-doping on the spectroscopic properties of Ho:CaF_2 was investigated at both room and low temperatures. The Judd-Ofelt analysis was conducted for Ho^{3+} ions in CaF_2 to determine the intensity parameters. The formation of various types of ion clusters in Tm,Ho:CaF_2 was confirmed through the analysis of energy transfer between Tm^{3+} and Ho^{3+} ions. The first continuous-wave laser operation of the Tm,Ho:CaF_2 crystal was achieved with a broadly tunable range.

II.1.A. Crystal growth and material characterization

Single-crystals of CaF_2 codoped with 3-5 at.% Tm^{3+} and 0.3-0.5 at.% Ho^{3+} (with respect to Ca^{2+}) were grown by the Bridgman–Stockbarger technique using graphite crucibles (Φ8 mm, height: 40 mm) in our laboratory (CIMAP). The starting reagents were CaF_2, TmF_3 and HoF_3 powders (purity: 4N), the rare-earth fluorides were achieved by fluorination of the corresponding oxides. A special attention was paid to reduce the oxygen contamination: the growth chamber was sealed to vacuum (<10^{-5} mbar) and refilled with Ar + CF_4 gases. The starting reagents were mixed and placed into the crucible which was heated slightly above (~40 °C) the melting point (1418 °C) and the solution was homogenized for 3-4 h. The growth was ensured by translating the crucible in a vertical temperature gradient of 30-40 °C/cm. After the growth was completed, the crystals were slowly cooled down to room temperature within 48 h. The segregation coefficients for Tm^{3+} and Ho^{3+} ions in CaF_2 are 0.94 and 0.98, respectively. The actual ion

densities are N_{Tm} = 6.91 and N_{Ho} = 0.72 [10^{20} at/cm^3] for the 3 at.% Tm^{3+}, 0.3 at.% Ho^{3+}:CaF_2 crystal.

The as-grown crystals were transparent with a slight rose coloration due to Ho^{3+} doping, Figure II.1(a). A Schlieren photography of a polished cylindrical barrel cut from the central part of the crystal confirmed its high optical quality, Figure II.1(b).

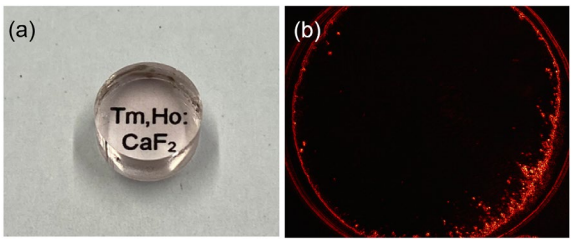

Figure II.1. (a) A photograph and (b) a Schlieren photography of a polished cylindrical barrel cut from the central part of an as-grown 3 at.% Tm^{3+}, 0.3 at.% Ho^{3+}:CaF_2 crystal.

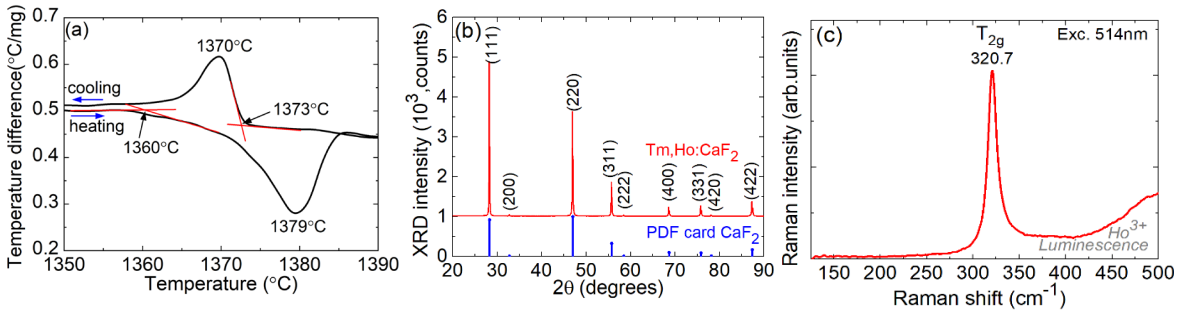

Figure II.2. Material characterization of the 3 at.% Tm, 0.3 at.% Ho:CaF_2 crystal: (a) a differential thermal analysis (DTA) curve, *blue arrows* indicate the direction of cooling and heating; (b) an X-ray powder diffraction (XRD) pattern, (*hkl*) – Miller's indices; (c) Raman spectrum, λ_{exc} = 514 nm, *number* – Raman frequency in cm^{-1}.

The differential thermal analysis (DTA) and X-ray powder diffraction (XRD) of the 3 at.% Tm^{3+}, 0.3 at.% Ho^{3+}:CaF_2 crystal were performed by our colleagues at the University of Tarragona, Spain.

Figure II.2(a) shows a DTA curve recorded during heating and cooling. The melting point of the crystal was determined to be 1360°C. The onset of crystallization temperature is determined to be 1373°C. An XRD pattern is shown in Figure II.2(b), revealing a single-phase nature with a cubic, fluorite-type crystal structure (sp. gr. $Fm\bar{3}m$). The Raman spectra of Tm,Ho:CaF_2 crystal contains only one peak characteristic of fluorite at 320.7 cm^{-1} (symmetry: T_{2g}).

In CaF_2 doped with RE^{3+} ions, the various methods of charge compensation for dopant RE^{3+} ions by F_i^- ions take place, as shown in Figure II.3.

- When RE^{3+} ions substitute for Ca^{2+} ions and the charge compensation does not occur locally, RE^{3+} ions are at the O_h site symmetry.
- If the nearest-neighbor charge compensation appears along the ⟨100⟩ crystal axis due to F_i^-, the point symmetry of the site is tetragonal C_{4v}.
- If a fluorine cube is located in the next-nearest-neighbor interstitial site, the symmetry is C_{3v}, with the ⟨111⟩ axis of the crystal host passing through RE^{3+} and F_i^- ions.

• If oxygen is present in the crystal, then an O^{2-} ion substituting for a lattice F_i^- adjacent to the RE^{3+} can provide the charge compensation, resulting in another possible C_{3v} site symmetry.

It has been shown that large dopant RE^{3+} ions tend to form centers with C_{4v} symmetry, while smaller ones give rise to sites with C_{3v} symmetry. However, the dominant symmetry of sites throughout the RE series with low doping concentrations (usually less than 0.05 at.%) in CaF_2 is C_{4v}.[Boo94, Wel96, Str96].

These centers can be distinguished by studying the absorption and emission spectra at low temperatures, including their shape, peaks, and relative intensities depending on the excitation wavelength [See79, Coc87, Str97,]. Additionally, the energy-level lifetimes of RE^{3+} associated with each incorporation site can provide valuable informations.

At RE^{3+} doping concentrations usually higher than 0.05 at.%, RE^{3+} ions are incorporated as clusters in CaF_2. They are no longer isolated and are located close to each other. Strong dipole-dipole interactions can occur, leading to enhanced nonradiative energy transfer processes.

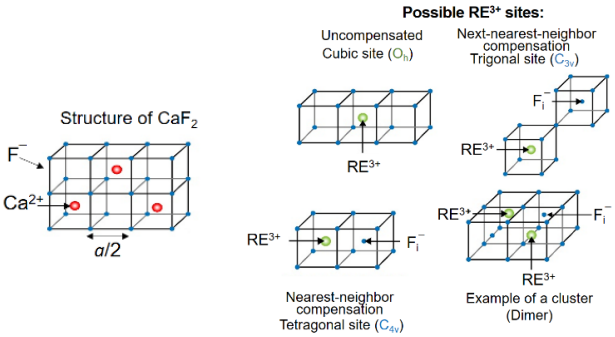

Figure II.3. The structure of CaF_2 and possible RE^{3+} sites, taken from [Pay91].

II.1.B. Transition cross-sections of Tm^{3+} and Ho^{3+} ions

The transmission spectra of the 3-5 at.% Tm^{3+} and 0.3-0.5 at.% Ho^{3+} codoped CaF_2 crystals were measured using a CARY 5000 spectrophotometer. The samples have a thickness of 4.1 mm and 5.1 mm for two of them. The room temperature (RT) absorption spectra of the 5 at.% Tm, 0.5 at.% Ho:CaF_2 crystal are plotted in Figure II.4 in terms of the absorption coefficient calculated using Eq. A.3.2, according to the Beer-Lambert law using the measured transmission spectra. The absorption bands of Tm^{3+} and Ho^{3+} excited-states overlap. It is thus challenging to assign the excited-states of Ho^{3+} ions because of the strong absorption of Tm^{3+} ions.

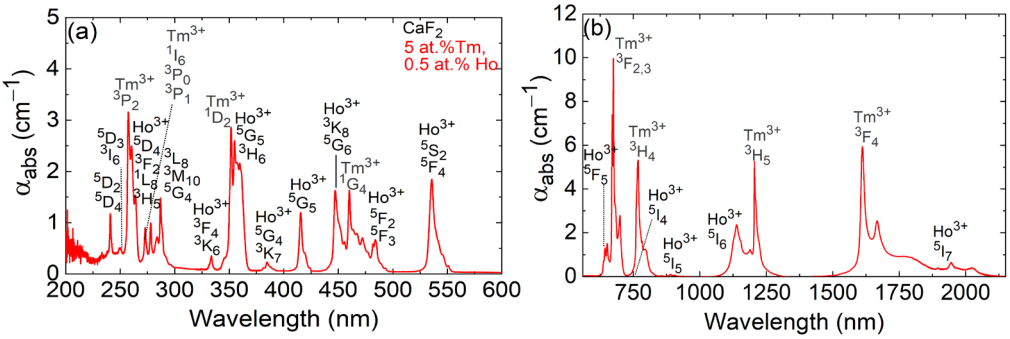

Figure II.4. Absorption spectra of the 5 at.% Tm, 0.5 at.% Ho:CaF_2 crystal in the 200 – 2150 nm spectral range.

The absorption bands of the $^5I_6$ and $^5I_4$ excited manifolds are obscured and indistinguishable due to strong Tm^{3+} absorption around 755 nm and 1150 nm, respectively. The rest of the excited manifolds up to $^5D_4$+$^5D_2$ (at 242 nm) were identified. The assignment of the excited manifolds of Tm^{3+} ions follows the one by Carnall *et al.* [Car68]. The absorption bands of Tm^{3+} ions are due to transitions from the $^3H_6$ ground-state to the excited-states ranging from $^3F_4$ (at 1.6 μm) up to $^3P_2$ (at 255 nm).

The absorption spectra of Tm,Ho:CaF_2 crystals corresponding to the $^3H_6 \rightarrow {}^3H_4$ Tm^{3+} pump transition are shown in Figure II.5(a). For the 5 at.% Tm, 0.5 at.% Ho:CaF_2 crystal, the peak absorption cross-section σ_{abs} is 0.46×10^{-20} cm^2 at 768 nm and the corresponding bandwidth (full width at half maximum, FWHM) is 12.6 nm, which is beneficial for diode-pumping. The absorption cross-section was calculated using Eq. I.18. For the 3 at.% Tm, 0.3 at.% Ho:CaF_2 crystal, the peak σ_{abs} is 0.38×10^{-20} cm^2 at 766 nm with a bandwidth of 12 nm. It should be noted that the small difference in absorption cross-sections is likely due to the cross-section calculation which takes into account the nominal doping level. The position of the σ_{abs} peak is slightly shifted to longer wavelengths and the bandwidth broadens when increasing the total doping concentration due to the formation of RE clusters.

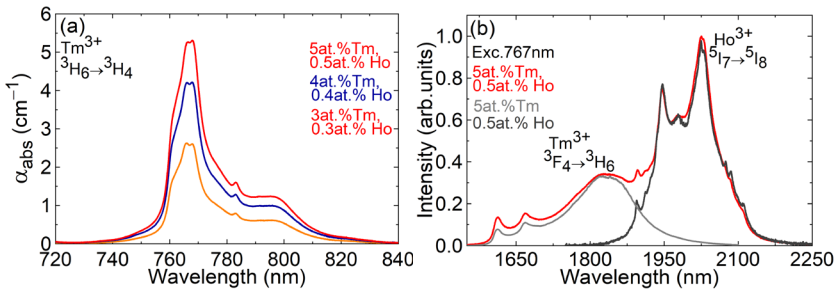

Figure II.5. Spectroscopy of Tm,Ho:CaF_2 crystals: (a) absorption spectra, the $^3H_6 \rightarrow {}^3H_4$ Tm^{3+} transition; (b) luminescence spectrum around 2 μm, 5 at.% Tm^{3+}, 0.5 at.% Ho^{3+} codoped crystal, the spectra for singly-doped crystals are given for comparison λ_{exc} = 767 nm.

Figure II.5(b) shows the luminescence spectrum of a codoped crystal around 2 μm. It is smooth and broad spanning from 1.55 to 2.25 μm due to two spectrally overlapping transitions, $^3F_4 \rightarrow {}^3H_6$ Tm^{3+} and $^5I_7 \rightarrow {}^5I_8$ Ho^{3+}, with the Ho^{3+} emission peaking at 2025 nm being more intense. As compared to singly Ho^{3+}-doped crystals, the Tm^{3+},Ho^{3+} codoping induces additional broadening of the Ho^{3+} emission band due to more profound ion clustering at higher total RE^{3+} doping levels.

To calculate the absorption and stimulated-emission cross-sections for the $^5I_8 \leftrightarrow {}^5I_7$ Ho^{3+} transitions, the contribution of Tm^{3+} ions to absorption and emission spectra was subtracted from those for 5 at.% Tm^{3+}, 0.5 at.% Ho^{3+} codoped CaF_2 crystal. The absorption, σ_{abs}, and stimulated-emission cross-section, σ_{SE}, spectra for the $^5I_8 \leftrightarrow {}^5I_7$ Ho^{3+} transitions are shown in Figure II.6(a). The maximum σ_{abs} for the $^5I_8 \rightarrow {}^5I_7$ Ho^{3+} transition is 0.38×10^{-20} cm^2 at 1945 nm.

The maximum σ_{SE} is 0.57×10^{-20} cm^2 at 2025 nm, as calculated using the Füchtbauer–Ladenburg formula, Eq. I.21. The $^5I_7$ radiative lifetime, τ_{rad} = 17.09 ms was determined using the Judd-Ofelt analysis, see Table II.1. According to the quasi-three-level nature of the Ho^{3+} laser scheme, the gain cross-sections for Ho^{3+} ions were calculated using $\sigma_{gain} = \beta\sigma_{SE} - (1-\beta)\sigma_{abs}$ for

different inversion ratios $\beta = N_7/N_{Ho}$, where N_7 is the population of the upper laser level ($^5I_7$), Figure II.6(b). The gain profiles are smooth and broad and their maximum experiences a blue-shift with increasing the inversion ratio, from 2130 nm ($\beta = 0.12$) to 2040 nm ($\beta = 0.30$). For an intermediate $\beta = 0.24$, the gain bandwidth (FWHM) is 77 nm.

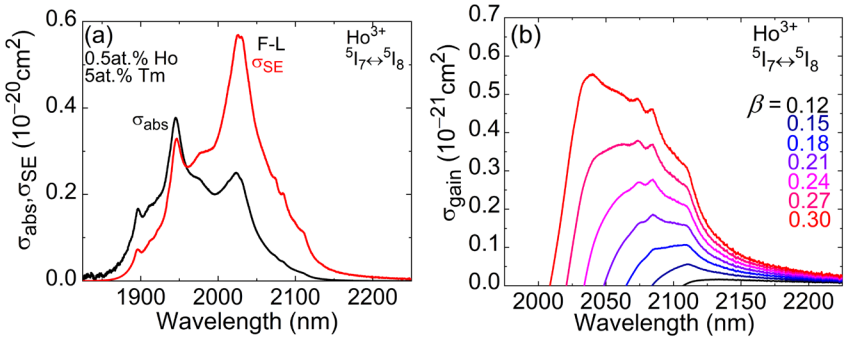

Figure II.6. $^5I_8 \leftrightarrow {}^5I_7$ Ho^{3+} transition in 5 at.% Tm^{3+}, 0.5 at.% Ho^{3+}:CaF_2: (a) absorption, σ_{abs}, and stimulated-emission, σ_{SE}, cross-sections, (b) gain cross-sections for Ho^{3+} ions, σ_{gain}, $\beta = N_7(^5I_7)/N_{Ho}$ – inversion ratio. F-L – Füchtbauer–Ladenburg.

II.1.C. Low-temperature spectroscopy of Ho^{3+} ions: effect of codoping

A low-temperature (LT, 12 K) the absorption spectrum of a 0.5 at.% Ho:CaF_2 crystal at ~2 μm is shown in Figure II.7(a). It shows sharp peaks assigned to isolated Ho^{3+} ions in trigonal (C_{3v}), tetragonal (C_{4v}) and cubic (O_h) sites, as well as intense and broader bands owing to Ho^{3+} clusters. The position of the isolated Ho^{3+} ions in different sites were taken from [Muj92, Pie20]. For a codoped crystal (5 at.% Tm^{3+}, 0.5 at.% Ho^{3+}), the LT absorption and emission spectra of Ho^{3+} ions for the $^5I_8 \leftrightarrow {}^5I_7$ transition, Figure II.7(a,b), exhibit broad bands which are different from those for single Ho^{3+} doping indicating the entering of Ho^{3+} ions into rare-earth (Tm-Ho) ion clusters.

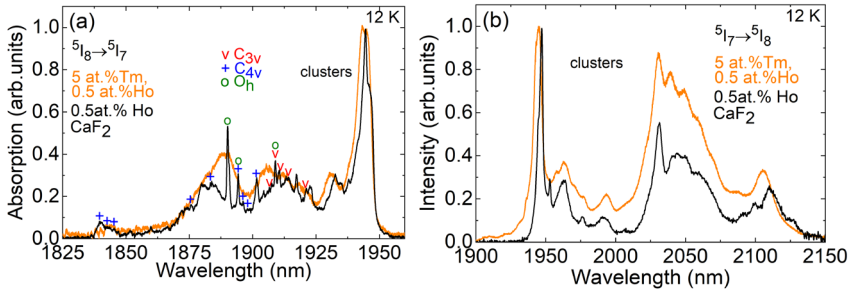

Figure II.7. LT (12 K) (a) absorption and (b) luminescence spectra of Ho^{3+} ions in CaF_2 ($^5I_8 \leftrightarrow {}^5I_7$ transition): a 5 at.% Tm^{3+}, 0.5 at.% Ho^{3+} codoped crystal and a 0.5 at.% Ho^{3+} singly-doped one.

II.1.D. Judd-Ofelt analysis for Ho^{3+} ions in CaF_2

To determine absorption oscillator strengths and emission probabilities for Ho^{3+} ions in CaF_2, we measured the absorption spectra of 0.5 at.% Ho:CaF_2 crystal. The spectra were measured in the 230 – 2150 nm spectral range, considering the excited manifolds from $^5I_7$ to $^5D_4$+ $^5D_2$, as shown in Figure II.8.

The measured absorption spectra were analyzed using the modified Judd-Ofelt (J–O) theory, see Chapter I, Section I.2.D. The set of reduced squared matrix elements $U(k)$ was taken from [Kor04]. The MD contributions to transition intensities (for transitions with $\Delta J = J - J' = 0, \pm 1$) were calculated within the Russell-Saunders approximation using the wave functions of the free Ho^{3+} ion. The refractive index of CaF_2 was calculated using dispersion curves [Mal63].

For calculating the absorption oscillator strengths, we have used the full Ho^{3+} ions density ($N_{Ho} = 1.23\times10^{20}$ at/cm^3).

Table II.1. Experimental and calculated absorption oscillator strengths for Ho^{3+} ions in CaF_2

Transition $^5I_8 \rightarrow {}^{2S+1}L_J$	$\langle\lambda_{abs}\rangle$, nm	$\langle E\rangle$, cm^{-1}	Γ, cm^{2}nm	$f^{\Sigma}_{exp}\times10^6$	$f^{\Sigma}_{calc}\times10^6$
$^5I_7$	2023	4943	58.412	1.386	1.451
$^5I_6$	1153	8674	12.285	0.831	0.829
$^5I_5$	889	11244	2.886	0.328	0.174
$^5I_4$	764	13085	0.201	0.032	0.016
$^5F_5$	637	15694	13.491	2.986	2.901
$^5S_2+^5F_4$	535	18676	12.983	4.128	4.131
$^5F_3+^5F_2+^3K_8+^5G_6$	490 447	20406 22359	16.190	7.036	6.970
$^5G_5$	415	24069	4.653	2.466	2.434
$^5G_4+^3K_7$	381	26223	1.153	0.711	0.593
$^3H_6+^5G2_5$	360	27799	3.278	2.315	2593
$^3L_9+^5G_3$	345	28975	0.890	0.686	1.215
$^3K_6+^3F_4$	334	29963	0.668	0.552	0.606
$^3L_8+^3M_{10}+^5G_4$	287	34848	2.788	3.073	3.036
$^5D_4+^3F_2$ +$^1L_8+^3H_5$	278	35962	1.786	2.134	2.234
$^3F2_4+^3I_7$	260	38459	0.443	0.602	0.139
$^5D_3+^3I_6$	250	39927	0.451	0.662	0.413
$^5D_4+^5D_2$	242	41398	1.492	2.360	2.249
Δ_{rms}					*0.125*

[a] $\langle\lambda_{abs}\rangle$ – "center of gravity" of the absorption band, $\langle E\rangle$ – energy barycenter of the multiplet, Γ – integrated absorption coefficient, f^{Σ}_{exp} and f^{Σ}_{calc} – experimental and calculated absorption oscillator strengths, respectively.

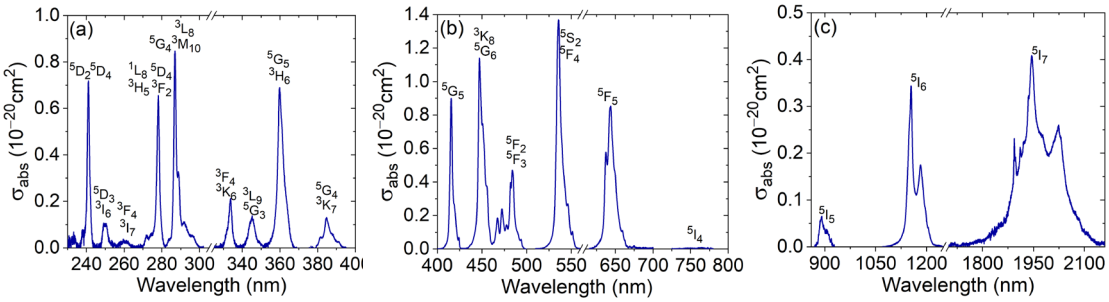

Figure II.8. Absorption cross-sections for different transitions of Ho^{3+} ions in CaF_2 in the 230 – 2150 nm spectral range.

Table II.1 contains the experimental (f^{Σ}_{exp}) and calculated (f^{Σ}_{calc}) absorption oscillator strengths. Here, the superscript "Σ" indicates a total value (ED + MD). The root mean square (r.m.s.) deviation (see Chapter I.2.D) between the f^{Σ}_{exp} and f^{Σ}_{calc} values is $\Delta_{rms} = 0.125$, mainly

due to the transitions to thermally coupled levels in UV and visible spectral ranges. For the lowest-lying excited-state ($^5I_7$), a relatively good agreement is observed. The J–O intensity parameters Ω_2, Ω_4, and Ω_6 amount to 0.262, 1.459, and 4.650 × 10^{-20} cm^2, respectively. These values agree well with those reported recently for another Ho^{3+}-doped fluoride crystals, i.e. BaF_2, see Table II.3. Using the determined J–O parameters, the probabilities (ED + MD) of spontaneous radiative transitions for the different emission channels $J \rightarrow J'$ $A_\Sigma^{calc}(JJ')$, the total probabilities of radiative transitions from each excited-state A_{tot}, the luminescence branching ratios $B(JJ')$ and the radiative lifetimes τ_{rad} were calculated using Eqs. I.28-30 from Chapter I.2.D, as summarized in Table II.2. The mean emission wavelengths $\langle\lambda_{em}\rangle$ were estimated using the barycenter energies of Ho^{3+} multiplets $\langle E\rangle$ from Table II.1. For the $^5I_7$ state, τ_{rad} amounts to 17.09 ms.

Table II.2. Calculated emission probabilities for Ho^{3+} ions in CaF_2

Excited state	Terminal state	$\langle\lambda_{em}\rangle$, nm	$A_\Sigma^{calc}(JJ')$, s^{-1}	$B(JJ')$, %	A_{tot}, s^{-1}	τ_{rad}, ms
$^5I_7$	$^5I_8$	1948.9	$41.20^{ED} + 17.31^{MD}$	100	58.51	17.09
$^5I_6$	$^5I_7$	2914.6	$12.54^{ED} + 8.58^{MD}$	16.4	129.08	7.75
	$^5I_8$	11168.0	107.96^{ED}	83.6		
$^5I_5$	$^5I_6$	3882.0	$5.18^{ED} + 4.15^{MD}$	7.4	125.44	7.97
	$^5I_7$	1664.7	70.62^{ED}	56.3		
	$^5I_8$	897.8	45.49^{ED}	36.3		
$^5I_4$	$^5I_5$	4777.8	$5.19^{ED} + 1.84^{MD}$	7.7	90.81	11.01
	$^5I_6$	2141.8	36.28^{ED}	40.0		
	$^5I_7$	1234.6	40.08^{ED}	44.1		
	$^5I_8$	755.8	7.42^{ED}	8.2		
$^5F_5$	$^5I_4$	4315.9	$0.05^{ED} + 0.02^{MD}$	0.0	1948.19	0.513
	$^5I_5$	2267.6	$7.76^{ED} + 0.39^{MD}$	4.0		
	$^5I_6$	1431.4	$93.41^{ED} + 1.3^{MD}$	4.9		
	$^5I_7$	960.0	363.28^{ED}	18.6		
	$^5I_8$	643.2	1481.97^{ED}	76.1		
$^5S_2+^5F_4$	$^5F_5$	3380.7	$1.85^{ED} + 2.86^{MD}$	0.0	6169.56	0.162
	$^5I_4$	1895.7	$76.61^{ED} + 0.03^{MD}$	1.2		
	$^5I_5$	1357.2	$197.08^{ED} + 0.11^{MD}$	3.2		
	$^5I_6$	1005.6	401.35^{ED}	6.6		
	$^5I_7$	747.7	1229.08^{ED}	19.9		
	$^5I_8$	540.4	4260.59^{ED}	69.1		

[a]$\langle\lambda_{em}\rangle$ – mean emission wavelength, $A_\Sigma^{calc}(JJ')$ – probability of spontaneous transitions, $B(JJ')$ – luminescence branching ratio, A_{tot} – total probability of spontaneous transitions from an excited-state, τ_{rad} – radiative lifetime.

Table II.3. Comparison of the J–O intensity parameters (×$10^{-20}$$cm^2$) of Ho^{3+} ions in CaF_2 with other fluorites

Materials	Ω_2	Ω_4	Ω_6	Ref.
CaF_2	0.262	1.459	4.650	This work
CaF_2	0.018	0.570	0.587	[Bul97]
BaF_2	0.298	1.784	1.491	[Bro20]
LaF_3	1.030	0.980	0.310	[Hon16]

II.1.E. Energy-transfer between Tm^{3+} and Ho^{3+} ions

In Chapter I.3, we discussed different approaches to quantify the energy-transfer parameters. Here, we employed the dynamical model, Eqs. I.67-68, based on luminescence lifetime measurements.

First, the luminescence decay curves from the $^3F_4$ Tm^{3+} and $^5I_7$ Ho^{3+} levels were measured under Tm^{3+} excitation into the $^3H_4$ level for singly-doped 4 at.% Tm:CaF_2 and under resonant Ho^{3+} excitation into the $^5I_7$ level for 0.5 at.% Ho:CaF_2 crystals, Figure II.9(a). The samples were finely powdered before the measurements to avoid reabsorption leading to longer lifetimes. The decay curves for both crystals are nearly single exponential yielding luminescence lifetimes τ_{lum} of 13.75 ms and 14.07 ms, respectively. This long luminescence lifetimes are characteristic of the low phonon energy nature of CaF_2 leading to low threshold laser behavior due to accumulation of more excited ions in the laser level.

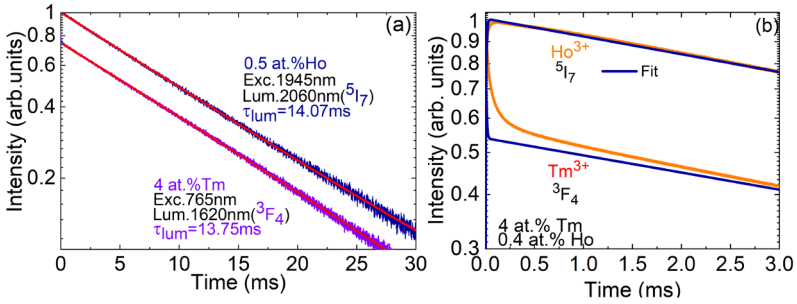

Figure II.9. Luminescence decay from the $^3F_4$ Tm^{3+} and $^5I_7$ Ho^{3+} states in CaF_2: (a) singly-doped crystals (4 at.% Tm^{3+} and 0.5 at.% Ho^{3+}), *solid red lines* – exponential fit; (b) a codoped crystal (4 at.% Tm^{3+}, 0.4 at.% Ho^{3+}).

The luminescence dynamics were studied for a 4 at.% Tm, 0.4 at.% Ho:CaF_2 crystal under resonant Tm^{3+} excitation, see Figure II.9(b). The decay curves are typical for the Tm^{3+},Ho^{3+} coupled systems indicating an efficient and predominantly unidirectional $^3F_4(Tm^{3+}) \rightarrow {}^5I_7(Ho^{3+})$ energy-transfer. The observation of two different time scales for the rise of Ho^{3+} luminescence and the beginning of the Tm^{3+} decay indicates the presence of two ion cluster compositions: (i) those containing both dopants and (ii) those being composed of only Tm^{3+} ions. One can see that the shape of the luminescence decay curve of Ho^{3+} ions is well-fitted using the Walsh model, but in case of Tm^{3+} ions, the decay curve is not well-fitted indicating an addition interaction within the Tm-Tm clusters. Consequently, the parameter of direct energy-transfer can be determined. The corresponding energy-transfer parameter is $P_{28} = 127 \times 10^{-23}$ cm^{3}μs^{-1} and the thermal equilibrium time is 11.0±0.5 ms.

II.1.F. Continuous-wave broadly tunable Tm,Ho:CaF_2 laser at 2.1 μm

To perform the first continuous-wave laser operation of Tm,Ho:CaF_2 crystals, we employed the laser set-up that is depicted in Figure II.10. Cylindrical laser elements (Φ8 mm, thickness: 4.1 mm) were cut from the central parts of the as-grown Tm,Ho:CaF_2 crystal boules with three doping levels, 5/0.5, 4/0.4 and 3/0.3 at.% Tm^{3+}/Ho^{3+}. They were polished to laser-quality on both sides and left uncoated. The elements were mounted on a Cu-holder using a silver paste

for better heat removal. The crystals were passively cooled to benefit from the good thermal properties of CaF_2. The hemispherical laser cavity was formed by a flat pump mirror (PM) coated for high transmission (HT, T = 93%) at 0.77 μm and high reflection (HR) at 1.9 – 2.3 μm, and a set of concave output couplers (OCs) with a radius of curvature (RoC) of 100 mm and a transmission at the laser wavelength T_{OC} in the range of 0.05% – 5%. The cavity length was ~99 mm.

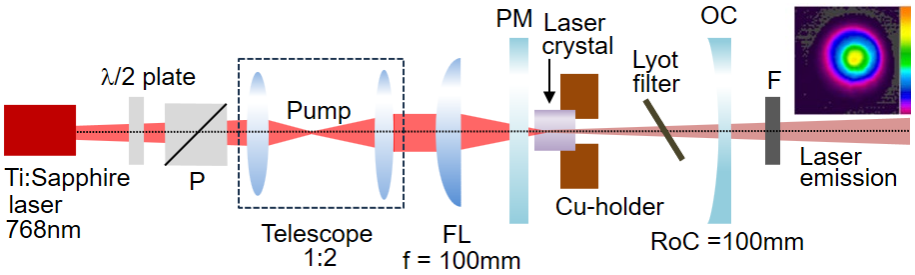

Figure II.10. Set-up of the tunable Tm,Ho:CaF_2 laser: P – Glan-Taylor polarizer FL – aspherical focusing lens, PM – pump mirror, OC – output coupler, F – long-pass filter, *insert* – a typical far-field mode profile.

The laser crystal was placed near the PM with a separation <1 mm. The pump source was a CW Ti:Sapphire laser (3900S, Spectra Physics) emitting up to 4.0 W at 768.0 nm with a nearly diffraction limited beam ($M^2 \approx 1$). To adjust the incident pump power, a half-wave plate and a Glan-Taylor polarizer was used. The pump beam was expanded by a telescope with a reimaging ratio of 1:2 and focused into the crystal through the PM using an antireflection (AR) coated aspherical lens (focal length, f = 100 mm). The pump spot size in the focus was $2w_P = 70 \pm 10$ μm. The pumping was in double pass owing to a high reflectivity of the OCs at the pump wavelength. *E.g.*, for the 3 at.% Tm^{3+}, 0.3 at.% Ho^{3+} codoped crystal, the total pump absorption, determined by a pump-transmission experiment conducted under lasing conditions, was approximately 76%, exhibiting a weak dependence on the output coupling. Optionally, the pump beam was modulated using a mechanical chopper (duty cycle: 1:4) to the heat loading in the crystal. A long-pass filter (FEL1000, Thorlabs) was placed after the OC to filter out the residual pump. The laser spectra were recorded using an optical spectrum analyzer (AQ6376, Yokogawa) and a ZrF_4 fiber. The laser mode profile was captured using a Pyrocam IIIHR camera (Ophir-Spiricon).

The best laser performance was achieved for the 3 at.% Tm^{3+}, 0.3 at.% Ho^{3+}:CaF_2 crystal. In the CW regime, the Tm,Ho:CaF_2 laser generated a maximum output power of 737 mW at 2062-2088 nm with a slope efficiency η of 28.0% (vs. the absorbed pump power) and a low laser threshold P_{th} of 133 mW (for T_{OC} = 1%), as shown in Figure II.11(a). For higher output coupling (T_{OC} > 1%), the laser performance deteriorated which is attributed to the detrimental effect of ETU at increased populations of the upper laser level. For these OCs, a thermal roll-over was observed for P_{abs} > 2.2 W. With reducing the output coupling, the laser threshold gradually decreased from P_{th} = 312 mW (5% OC) to 65 mW (0.05% OC). Power scaling was limited by the available pump power.

The typical spectra of laser emission are shown in Figure II.11(b). The laser operated solely on the $^5I_7 \rightarrow {}^5I_8$ Ho^{3+} transition and no Tm^{3+} colasing was observed. The laser wavelength experienced a blue-shift with increasing T_{OC}, from 2090-2116 nm (0.05% OC) to 2032-2039 nm (5% OC). This behavior is due to the quasi-three-level nature of the Ho^{3+} laser scheme with reabsorption and it agrees well with the gain spectra of Ho^{3+} ions in CaF_2, see Figure II.6(b). The laser emission was unpolarized. The Tm,Ho:CaF_2 laser operated on the fundamental transverse mode, Figure II.10, with a measured beam quality factor $M^2 < 1.1$ at the highest output power. The laser mode profile was measured at 15 cm from the OC.

For the wavelength tunable operation, a Lyot filter was inserted into the laser cavity at Brewster angle close to the laser crystal. It was made of a 2 mm-thick quartz plate with an optical axis lying in the surface plane. When using T_{OC} = 1%, the laser wavelength was continuously tunable from 1985 to 2114 nm (tuning range: 129 nm at the zero-power level), Figure II.11(c).

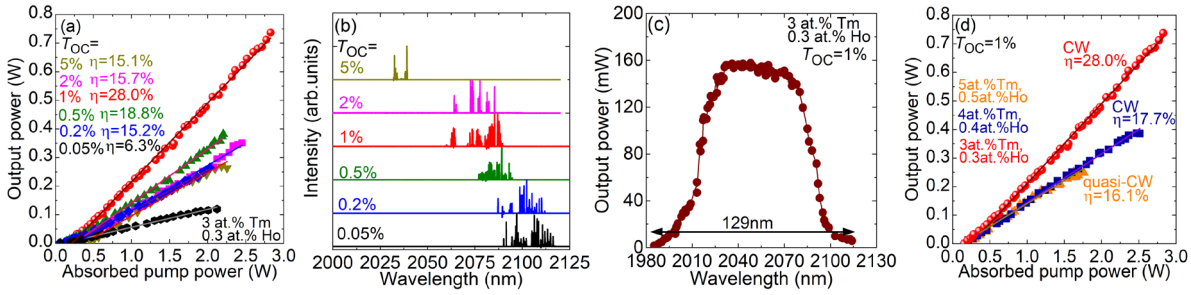

Figure II.11. CW Tm,Ho:CaF_2 lasers: (a-b) a 3 at.% Tm^{3+}, 0.3 at.% Ho^{3+} codoped crystal: (a) input-output dependences, η – slope efficiency; (b) typical laser emission spectra; (c) tuning curve, T_{OC} = 1%; (d) effect of the Tm^{3+} / Ho^{3+} doping level on the laser performance.

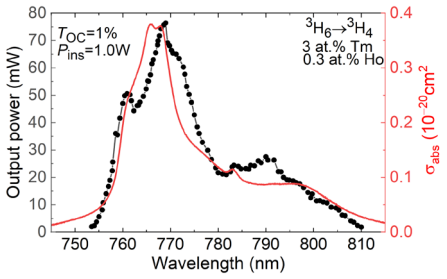

Figure II.12. Laser excitation curve of the 3 at.% Tm, 0.3 at.% Ho:CaF_2 laser. The absorption cross-section for the $^3H_6 \rightarrow {}^3H_4$ transition are added for comparison (*red solid curve*). The incident pump power (P_{ins}) was 1.0 W.

The laser performance of Tm,Ho:CaF_2 crystals with different doping levels is compared in Figure II.11(d) (for the same T_{OC} = 1%). With increasing the doping level, despite the increased pump absorption, the maximum output power and the slope efficiency decreased to 386 mW at 2070-2086 nm with η = 17.7% (4 at.% Tm^{3+}, 0.4 at.% Ho^{3+}:CaF_2) and 249 mW at 2083-2087 nm with η = 16.1% (5 at.% Tm^{3+}, 0.5 at.% Ho^{3+}:CaF_2). For these crystals, a thermal roll-over in the output dependences was observed for absorbed pump powers above 2.5 W and 1.75 W, respectively (for the latter crystal, the laser was operated in quasi-CW regime). The observed deterioration of the laser performance is ascribed to a drop in the thermal conductivity of CaF_2

crystals upon rare-earth doping increase. The CaF_2 thermal conductivity drops from 9.7 to 4 Wm^{-1} K^{-1} between an undoped CaF_2 and a CaF_2 doped with 5.5 % RE^{3+} ions, respectively [Nor17].

In Figure II.12, we show the laser excitation spectrum as the output power *vs*. the pump wavelength. The absorption cross-section for the $^3H_6 \rightarrow {}^3H_4$ transition of Tm^{3+} ions are plotted for comparison. The laser operation was achieved in the range of pump wavelengths of 753.5 – 810 nm. The maximum output power was detected at 769 nm.

To conclude, we obtained the first continuous-wave Tm,Ho:CaF_2 laser delivering an output power up to 737 mW at 2062-2088 nm with a maximum slope efficiency of 28.0% and a laser threshold down to 65 mW, operating on the fundamental transverse mode. A continuous wavelength tuning over a broad range of 129 nm (1985 - 2114 nm) was demonstrated. These results are superior to the previous reports on Tm,Ho:CaF_2 ceramic lasers (operating in free-running / quasi-CW regimes) [Sul13, Sul14], mainly due to the better optical and thermal properties of Tm,Ho:CaF_2 single-crystals. In the present work, the crystal quality was improved by carefully controlling the growth atmosphere. The spectroscopic properties of Ho^{3+} ions in Tm,Ho:CaF_2 crystals were also studied. They exhibit inhomogeneously broadened emission spectra extending above 2 µm (up to at least 2.25 µm) owing to the profound rare-earth ion clustering, an efficient $Tm^{3+} \rightarrow Ho^{3+}$ energy-transfer and a relatively long thermal equilibrium decay time. The evidence of the existence of two cluster compositions (Tm and Tm/Ho clusters) is suggested.

Thanks to its low melting point and good thermal properties, Tm,Ho:CaF_2 appears as an attractive competitor to other recently studied Tm^{3+},Ho^{3+}-codoped laser crystals with broadband emission properties, Tm,Ho:$CaGaAlO_4$ [Wan22] and Tm,Ho:CNGG [Pan21a]. Further improvement of the laser efficiency for Tm,Ho:CaF_2 is possible by: optimizing the Ho^{3+}/Tm^{3+} codoping ratio to suppress the Ho-free Tm-clusters which do not contribute significantly to laser emission >2 µm, and implementing a Tm resonant pumping, *e.g.*, by Raman-shifted Erbium fiber lasers [Loi22]. Further power scaling is expected under pumping at ~0.8 µm using AlGaAs laser diodes and applying active cooling. In this case, lower total Tm+Ho doping levels are preferable for maintaining better thermal properties of Tm,Ho:CaF_2 crystals, as evidenced by the present work.

II.2. First Tm^{3+}:CaF_2 waveguide laser at 1.9 µm produced by femtosecond laser writing

Waveguide (WG) lasers are an important component of integrated photonics. They are compatible with optical fibers and various on-chip devices, enabling applications in optical sensing, on-chip spectroscopy, microfluidics, telecommunications, medicine, and soft materials processing. In this section, the principles of the technique of waveguide production by femtosecond laser writing are discussed. The modifications induced by the femtosecond radiation within the materials were investigated by µ-Raman and µ-luminescence mapping. The first laser operation of Tm:CaF_2 channel WG is presented in this section.

II.2.A. Spectroscopy of $Tm^{3+}:CaF_2$ crystal

The spectroscopic properties of 3 at.% CaF_2 crystal (N_{Tm} = 11×10^{20} at/cm^3) related to the 1.9 μm laser emission were studied. The absorption cross-sections for the $^3H_6 \rightarrow {}^3H_4$ and $^3H_6 \rightarrow {}^3F_4$ transitions, stimulated-emission cross-section for the $^3F_4 \rightarrow {}^3H_6$ transition and the $^3F_4$ luminescence decay curve are plotted in Figure II.13(a).

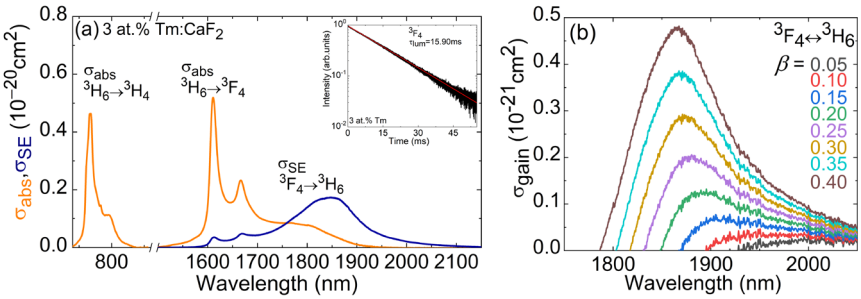

Figure II.13. Spectroscopic study of 3 at.% Tm:CaF_2 waveguide: (a) stimulated-emission and absorption cross-sections for the $^3F_4 \rightarrow {}^3H_6$ and $^3H_6 \rightarrow {}^3H_4$, $^3H_6 \rightarrow {}^3F_4$ transitions, *insert* – luminescence decay curve, τ_{lum} – luminescence lifetime; (b) gain cross-section as a function of inversion ratio.

The $^3F_4$ radiative lifetime τ_{rad} = 21.3 ms obtained from J-O analysis [Loi21b] is used to calculate the SE cross-sections. The peak σ_{abs} equals 0.46×10^{-20} cm^2 at 768 nm and 0.52×10^{-20} cm^2 at 1611 nm with a bandwidth (FWHM) of 18 nm. Both absorption bands are suitable for pumping by AlGaAs laser diodes around 770 nm and Raman fiber lasers or Er^{3+}-lasers around 1.7 μm. The luminescence lifetime of the $^3F_4$ manifold is 15.9 ms, while Figure II.13(b) shows the Tm:CaF_2 crystal gain cross-section spectra where the peak σ_{gain} shifts to the shorter wavelength from 1920 to 1860 nm when β increases from 0.05 to 0.30, respectively. For β = 0.15, the bandwidth is 110 nm indicating that Tm:CaF_2 is a potential candidate for mode-locked waveguide lasers.

II.2.B. Inscription of depressed cladding waveguides in $Tm^{3+}:CaF_2$

For the fabrication of Tm channel WG lasers, various methods can be employed, such as Liquid Phase Epitaxy with different types of subsequent microstructuring by reactive ion (Ar^+) beam etching or by diamond-saw dicing. In recent years, another method for fabricating photonic microstructures in transparent dielectric materials has emerged, the femtosecond Direct Laser Writing. Figure II.14(a) shows a photograph of a sample under fs-DLW.

In the present work, the depressed cladding (type III) buried WGs with a circular profile (Φ30 – 50 μm) were inscribed by our colleagues at the Aplicaciones del Láser y Fotónica, University of Salamanca, Spain, using fs-DLW in a 3 at.% $Tm^{3+}:CaF_2$ crystal grown by the Bridgman-Stockbarger method in Ar + CF_4 atmosphere, see Chapter II.1. A Ti:Sapphire regenerative amplifier delivering 120 fs pulses at 795 nm at a repetition rate of 1 kHz was employed for this aim. The incident pulse energy on the crystal was 0.246 μJ and the scanning speed was 500 μm/s. The femtosecond laser radiation into the crystal through the polished top face was focused by a 20× microscope objective (numerical aperture: N.A. 0.75). The WG was

written along the [111] direction, as shown in Figure II.14(b). The damage tracks were continuous and they were written through the entire sample length thus reaching the polished input and output surfaces. No repolishing of the sample end-facets was applied after completing the fs-DLW process. The refractive index variation Δn mentioned earlier was estimated to be -3×10^{-4}. This variation was estimated from the numerical aperture of the waveguide.

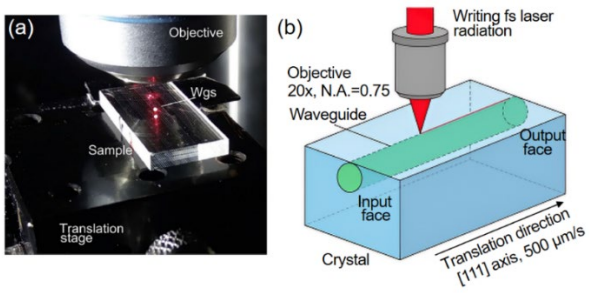

Figure II.14. (a) Photograph of a sample under femtosecond Direct Laser Writing, the red laser serves as a laser pointer, taken from [Kif20]; (b) fs-DLW of channel buried waveguide in a bulk Tm:CaF_2 crystal.

II.2.C. Confocal laser microscopy

The WG geometry was revealed using confocal laser microscopy by our colleagues at the University of Salamanca. The confocal laser scanning microscope (model Zeiss LSM 710,) is equipped with a blue GaN laser diode (λ = 405 nm) and possesses a spatial resolution of 0.24 μm. The examination was performed in transmission mode using linearly polarized light. The confocal laser microscope images of the end-facet and top-surface of the Tm^{3+}-doped CaF_2 crystal are shown in Figure II.15(a,b).

The cladding can be clearly seen as the dark ellipses of damage tracks forming the core of a waveguide below the crystal surface, see Figure II.15(a). Quasi-continuous cladding along the entire crystal length (5.0 mm) were fabricated. Possible additional cracks surrounding the cladding were not observed. The inner part of the WG is darker due to light scattering at the damage track's location. The dark barrel-shaped cladding is visible in the unmodified bulk volume. A similar picture was observed from the top crystal surface, as shown in Figure II.15(b). The damage track size is 1 μm along the *x*-axis and 4 μm along the *y*-axis. The diameter of the WG is 50 μm and the WG axis is at 50 μm beneath the surface.

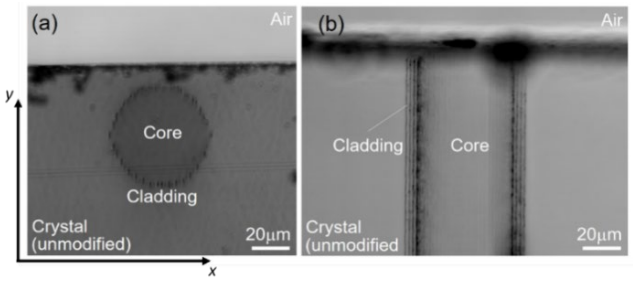

Figure II.15. Confocal laser microscope images of a buried channel WG in Tm:CaF_2 produced by fs-DLW: (a) end-facet view; (b) top view. Transmission mode, light source – 405 nm GaN laser diode, spatial resolution – 0.24 μm. Polarization of light is linear.

II.2.D. μ-Raman mapping

To examine the alterations in the crystal within the irradiated regions, μ-Raman mapping spectroscopy was used, as illustrated in Figure II.16. Comprehensive details about this technique are provided in the Supplemental Materials, Appendix A.3. This approach is highly effective for characterizing the structural modifications induced by femtosecond pulses and for assessing the integrity of the intrinsic crystal structure at the waveguide core.

The overview μ-Raman spectra from core, cladding and bulk areas are plotted in Figure II.16(a). They demonstrate that a typical fluorite type structure exhibiting one Raman-active mode at the center of the Brillouin zone with T_{2g} symmetry being preserved in the WG structures. No changes in the emission properties of Tm^{3+} ions in the core region were observed with respect to the unmodified bulk regions.

For the μ-Raman mapping, the Raman peak at 320 cm^{-1} was selected. The results of the analysis are shown in Figure II.17. In the optical image, the selected WG is shown. No cracks in the WG core nor in the surrounding bulk areas were observed, see Figure II.17(a). In the irradiated areas the Raman peak intensity decreases, the Raman peaks are broadened and a slight shift of the Raman peak position is observed. These apparent loss of crystallinity in the irradiated areas can be due to a partial amorphization under the high-power femtosecond radiation while the crystalline structure is well-preserved in the WG core.

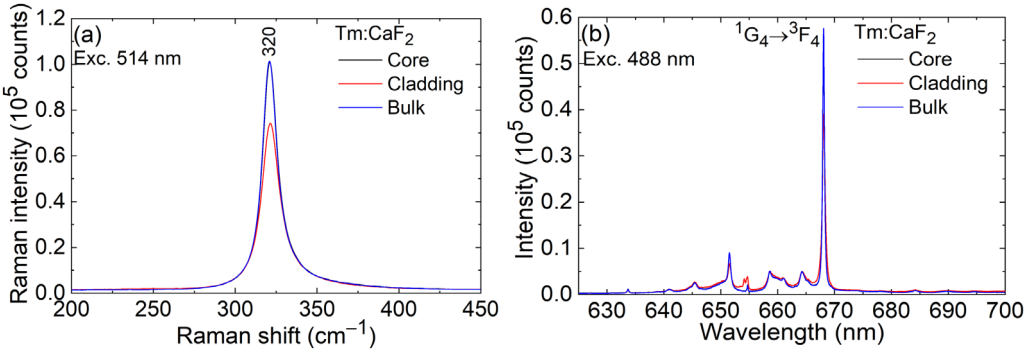

Figure II.16. (a) Examination of the WG structures (core and cladding) and bulk $Tm:CaF_2$ crystal by: (a) μ-Raman spectroscopy, λ_{exc} = 514 nm, and (b) μ-luminescence spectroscopy, λ_{exc} = 488 nm.

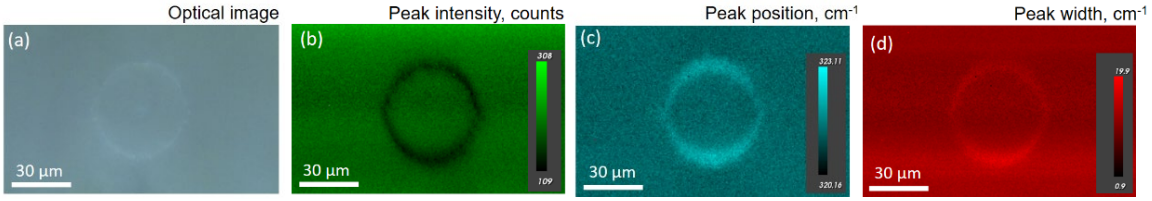

Figure II.17. μ-Raman mapping of a polished end-facet of the depressed cladding buried WG in $Tm:CaF_2$: (a) optical image; (b) peak intensity; (c) peak position; (d) peak width (FWHM), λ_{exc} = 514 nm. WG diameter is 50 μm.

II.2.E. Waveguiding behavior of inscribed microstructures

In Figure II.18(a,b) shows the near-field modal profiles of the guided pump radiation (at 0.77 μm) and laser emission (at 1.88 μm). The white circles indicate the cladding area. The

pump mode is well confined within the cladding, but it is multimode because of the 50 μm diameter of the WG. There is a weak leakage of the pump mode though the ring of the cladding, see Figure II.18(a). The laser mode is confined within the cladding and is slightly multimode, see Figure II.18(b). It has an asymmetric shape extended along the horizontal direction and it is not localized symmetrically with respect to the WG cladding. This could be explained by the asymmetric stress field, which is induced in the laser crystal by the femtosecond irradiation or spatial inhomogeneous losses through the length of the waveguide.

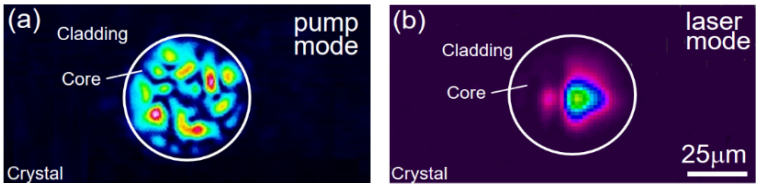

Figure II.18. Near-field profiles of (a) the pump and (b) laser modes, *white circle* – WG cladding.

II.2.F. Efficient Tm:CaF_2 channel waveguide laser at 1.9 μm

For the laser operation of 3 at.% Tm:CaF_2 crystal, a linear Fabry-Perot type laser cavity was formed by a plane PM coated for high transmission at 0.77 μm and high reflection at 1.87-2.35 μm, and a set of plane output couplers with a transmission T_{OC} of 0.2% – 17% at the laser wavelength. The scheme of laser set-up is shown in Figure II.19(a). The PM and OCs were placed close to the WG end-facets without any index-matching liquid. The total cavity length was 5 mm. The crystal was mounted on a passively cooled Cu-holder using a silver paint.

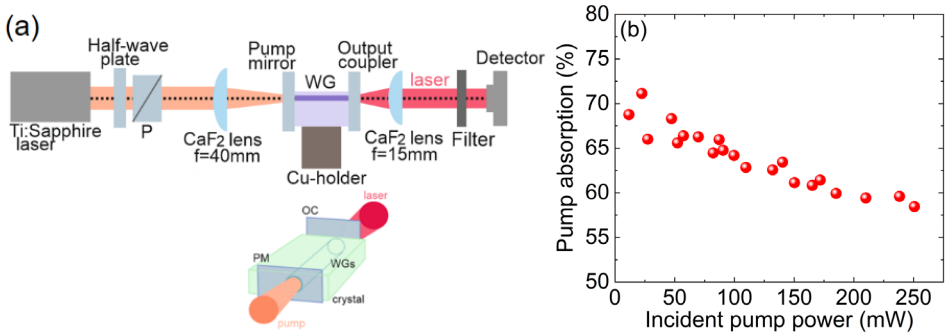

Figure II.19. (a) Scheme of the Tm:CaF_2 channel WG laser; (b) measured single-pass pump absorption in the WG (non-lasing conditions).

The pump source was a Ti:Sapphire laser. The pump radiation at 768.2 nm was focused and coupled into the WG using an AR coated achromatic CaF_2 lens (f = 40 mm) resulting in a pump spot diameter of 18 ± 5 μm. The residual (non-absorbed) pump after the OC was filtered out using a long-pass filter. To capture the near-field modal profiles, a spherical CaF_2 lens (f = 15 mm) and a Pyrocam IIIHR camera were used. The laser emission spectra were measured using a spectrum analyzer (AQ6376, Yokogawa) with a resolution of 0.2 nm. The pump coupling efficiency including the propagation loss was estimated to be 69.7% (measured at 875 nm). The pump absorption under lasing conditions decreased from 67.1% to 60.3%, see Figure II.19(b).

The Tm:CaF_2 WG laser generated a maximum output power of 385 mW at 1851-1884 nm with a slope efficiency η of 41.1% (with respect to the absorbed pump power) and a laser threshold P_{th} of 265 mW (T_{OC} = 10%), Figure II.20(a). The lowest P_{th} was 100 mW (for small T_{OC} = 0.2%). The laser emission occurred at ~1.88 μm and the spectra were very broad due to the broadband gain properties of Tm^{3+}:CaF_2, cf. Figure II.13(b). The laser emission was unpolarized, as shown in Figure II.20(b).

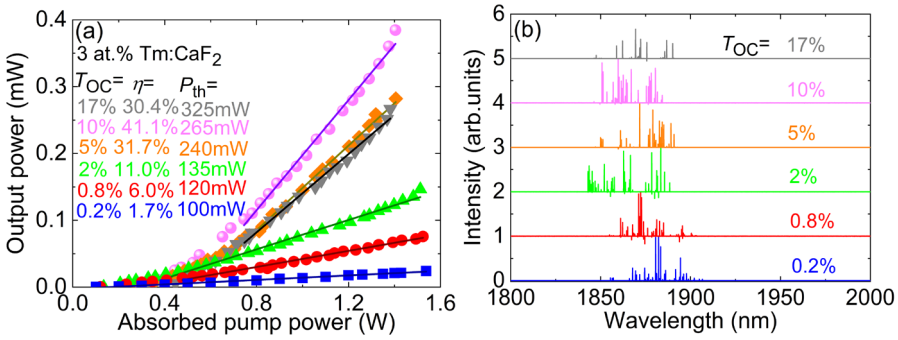

Figure II.20. CW laser performance of Tm:CaF_2 channel WG laser: (a)output-input dependences; (b) typical laser emission spectra.

The WG propagation loss was estimated using the Caird analysis [Cai88] modified for the case of a high output coupling transmission [Mor17]:

$$\frac{1}{\eta}=\left(\frac{1}{\eta_0}\right)\left(1+\frac{2\gamma}{\gamma_{OC}}\right), \tag{II.1}$$

$$\gamma=-\ln(1-L), \tag{II.2a}$$

$$\gamma_{OC}=-\ln\left(1-T_{OC}\right), \tag{II.2b}$$

where η is the limiting slope efficiency, γ and γ_{OC} are the logarithmic internal loss of the cavity per pass and logarithmic loss of the output coupler respectively, L represents the internal losses, and η_0 is the intrinsic slope efficiency. The Caird analysis uses the relationship between the measured slope efficiencies and the known output coupling to determine the cavity losses. In the case of large transmission of OC and, consequently, loss per pass, the analysis is modified to contain logarithmic arguments in Eqs. II.2(a,b).

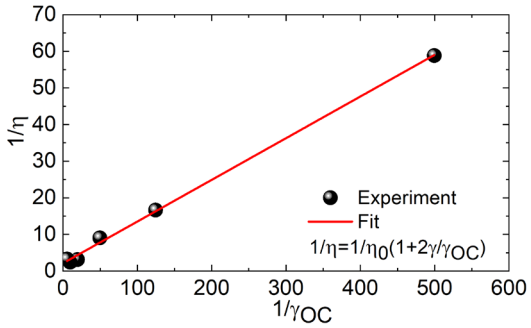

Figure II.21. Fitting the experimental slope efficiency by Eq. II.1.

Figure II.21 shows the linear dependence between the measured inverse slope efficiencies values and 1/ γ_{OC} . From this fit one can derive the propagation losses at the laser wavelength

(λ = 1.89 μm) estimated here to be 0.3±0.1 dB/cm and the intrinsic slope efficiency, in this case η_0 = 46.4±5%.

Table II.4 summarizes the output characteristic of Tm channel waveguides fabricated by the fs-DLW technique. The highest slope efficiency and output power are achieved using in-band pumping scheme at 1.68 μm (Raman fiber laser as a pump source) which appears to be a great approach to increase the waveguide laser performance.

Table II.4. Output characteristics of thulium channel waveguide lasers fabricated in fluorites, oxides crystals and glasses by fs-DLW on the $^3F_4 \rightarrow {}^3H_6$ transition. (RFL stands for Raman Fiber Laser).

Material	Pump	λ_p, nm	C_{Tm} at. %	P_{th}, mW	P_{out}, W	η, %	λ_L, μm	δ_{loss}, dB/cm	Ref.
Tm:CaF_2	*Ti:Sa*	*768*	*3.0*	*265*	*0.38*	*41*	*1851-1884*	*0.3*	*This work*
Tm:SrF_2	Ti:Sa	797	5.2	120	0.15	64	1868-1878		[Lla20]
Tm:BaY_2F_8	Ti:Sa	781	8.0	23	0.07	13	1861	0.2	[Mor22]
Tm:$LiYF_4$	Ti:Sa	779	3.0		0.107	19	1877		[Xio23]
Tm:$KLu(WO_4)_2$	Ti:Sa	802	3.0	170	1.07	62	1828-1865	0.2	[Kif20]
	RFL	1679		17	1.37	83	1915-1923		
Tm:$Y_3Al_5O_{12}$	Ti:Sa	800	1.0	312	0.09	27	1985		[Ren12]
Tm:Lu_2O_3	Ti:Sa	796		50	0.08	7	1940	0.7	[Mir17]
Tm:$CaGdAlO_4$	Ti:Sa	798	3.5	92	0.27	50	1824-1832		[Lla20a]
	RFL	1679		200	0.81	71	1866-1947	0.3	
Tm:YVO_4	Ti:Sa	797	3.0	213	0.27	36	1806		[Don23]
Tm:ZBLAN	Ti:Sa	792		12	0.21	67	1890	0.4	[Lan12]
Tm:GPNG	Ti:Sa	791	2.0	80	0.03	6	1930		[Fus11]

To conclude this section, thulium doped CaF_2 crystals are potential laser materials for fabrication of low-loss single-transverse-mode channel waveguides by femtosecond-direct laser writing. This first femtosecond-laser-written waveguide laser in Tm:CaF_2 generates 385 mW at 1.88 μm with a slope efficiency of 41.1%. The waveguide exhibits well-preserved crystallinity in the core region, moderate propagation losses ~0.3 dB/cm. Strong ion clustering in these crystals leads to efficient CR enhancing the laser slope efficiency, as well as a strong inhomogeneous spectral line broadening that makes them promising for mode-locked waveguide laser development. Moreover, the long lifetime of the $^3F_4$ level leads to good energy storage capabilities of Tm:CaF_2 crystals making them attractive for passively Q-switched WG lasers. Further power scaling can be achieved, *e.g.*, by in-band pumping directly into the $^3F_4$ upper laser level using Raman fiber lasers at 1.7 μm.

Conclusions of Chapter II

Thulium and holmium codoped CaF_2 crystals feature long luminescence lifetimes of the first excited states ($^3F_4$ for Tm^{3+} and $^5I_7$ for Ho^{3+}) due to their low-phonon-energy behavior. Additionally, they exhibit "glassy-like" spectroscopic behavior and efficient energy transfers between $Tm^{3+} \rightarrow Tm^{3+}$ ions or $Tm^{3+} \rightarrow Ho^{3+}$ ions. This is attributed to the profound clustering of RE^{3+} ions, which becomes more pronounced as doping concentrations increase. The formation of two cluster compositions (Tm and Tm/Ho clusters) was confirmed by luminescence dynamic studies and it presents the dominantly direct Tm → Ho energy transfer.

All these features allowed to achieve the first truly continuous-wave and broadly tunable laser operation of a Tm,Ho:CaF_2 crystal. Further improvement of the laser efficiency of Tm,Ho:CaF_2 is possible by optimizing the Ho^{3+}/Tm^{3+} codoping ratio to suppress the Ho-free Tm clusters, which do not contribute significantly to laser emission at >2 μm, and by implementing Tm resonant pumping. Further power scaling is expected under pumping at ~0.8 μm using AlGaAs laser diodes and by applying active cooling. In this case, lower total Tm + Ho doping levels are preferable for maintaining better thermal properties of Tm,Ho:CaF_2 crystals, as evidenced by the present work.

Thanks to its low melting point and good thermal properties, Tm,Ho:CaF_2 appears to be an attractive competitor to other recently studied Tm^{3+},Ho^{3+}-codoped laser crystals with broadband emission properties, Tm,Ho:$CaGaAlO_4$ and Tm,Ho:$Ca_3Nb_{1.5}Ga_{3.5}O_{12}$.

Moreover, the first laser operation of a femtosecond-laser-written waveguide laser in Tm:CaF_2 crystal was achieved. The laser generated high output power and had a high efficiency due to the formation Tm clusters enhancing the cross-relaxation energy-transfer. The broadband emission properties of Tm^{3+} ions in CaF_2 are promising for mode-locked waveguide lasers. CaF_2 crystals represent suitable materials for the fabrication waveguide structures by femtosecond direct laser writing and then for developing waveguide lasers.

Chapter III

Structurally Disordered Aluminate, Scandate, and Garnet crystals with Ho^{3+} ions

Structurally disordered aluminate, scandate, and garnet crystals, namely tetragonal calcium gadolinium aluminate ($CaGdAlO_4$, known as CALGO), cubic calcium niobium gallium garnet ($Ca_3Nb_{1.5}Ga_{3.5}O_{12}$), and orthorhombic gadolinium scandate ($GdScO_3$), are well-known host matrices for doping with laser-active RE^{3+} ions. They are attracting attention for laser development due to their moderate thermal conductivity and relatively low phonon energies (among oxides), which help suppress nonradiative decay paths from excited states of RE^{3+} ions. Especially, they are widely used for developing broadly tunable and mode-locked lasers due to their broadband gain profiles, enhanced by different mechanisms that introduce disorder in their structure. In particular, when doped with Ho^{3+} ions, these host matrices can emit around 2.1 μm, allowing to avoid the strong water absorption in the atmosphere around 1.9 μm. This has a favorable effect on mode-locked lasers.

This chapter is divided as follows: in Section III.1, polarized spectroscopic properties of Ho:$CaGdAlO_4$ crystals are studied with the goal to interpret the results achieved in mode-locked lasers; in Section III.2, highly efficient laser operation of Tm,Ho:$GdScO_3$ crystal at 2.1 μm are reported and the nature of the structure disorder is discussed; in Section III.3, the structure refinement, detailed spectroscopic study, and effect of Yb^{3+},Eu^{3+}-codoping on the emission properties of Ho:$Ca_3Nb_{1.5}Ga_{3.5}O_{12}$ crystal are reported.

III.1. Ho^{3+}-doped calcium gadolinium aluminate crystal

This section deals with the systematic study of the polarization-resolved spectroscopic properties of Ho^{3+} ions in $CaGdAlO_4$ crystals grown by the Czochralski method. In particular, we focus on interpreting the results on mode-locked Ho:$CaGdAlO_4$ lasers emitting beyond 2.1 μm and evaluation of the suitability of Ho:$CaGdAlO_4$ crystals for laser operation at 2.9 μm.

III.1.A. Crystal growth

The studied 1 at.% and 3.1 at.%Ho^{3+}-doped CALGO crystals come from our colleagues from the Ruhr Universität in Bochum, Germany and were grown by using the Czochralski method at the OT GmbH, Germany. CALGO is a congruently melting crystal. An Iridium crucible with a diameter of 80 mm is used in a standard thermal insulation setup. The growth process takes place at a temperature of approximately 1750°C. In the vicinity of the melting point, the temperature gradient was measured to be approximately 7°C/mm. The seeds used in the process were oriented along an a-axis. The growth atmosphere is made of nitrogen. The seed rotation and pulling parameters were 12 rpm (revolutions per minute) and 1 mm/h, respectively. The resulting boules had masses around 250 grams, corresponding to diameters

close to 25 mm and usable cylinder lengths near 60 mm. The growth interfaces appear to be slightly convex, with small {101} facets sometimes present near the center of the boule. When the cone angles on the seed end of the boules are too wide, occasional cleaving of the boules along planes parallel to {001} faces may occur across the entire boule, with only a marginal impact on the fraction of usable volume.

Figure III.1. An as-grown crystal boule, the growth direction is along the [100] axis.

III.1.B. Polarized Raman spectroscopy

For the tetragonal $CaREAlO_4$ crystals with the primitive cell of the D^{17}_{4h} symmetry, the factor group analysis predicts the following irreducible representations for the optical and acoustical modes at the center of the Brillouin zone ($\boldsymbol{k} = 0$) [Rou81]:

$\Gamma = 2A_{1g} + 2E_g + 4A_{2u} + 5E_u + B_{2u}$,

where $A_{1g} + E_g$ modes of Ca|RE and $A_g + E_g$ modes of oxygen are Raman active, $3A_{2u} + 4E_u$ are IR-active modes, $A_{2u} + E_u$ are acoustic modes and B_{2u} is a silent mode [Had97,Kam12].

The polarized Raman spectra of the Ho^{3+}-doped $CaGdAlO_4$ crystal ($\boldsymbol{a}$-cut) are plotted in Figure III.2. To identify vibrational modes of different symmetry, we used the Porto's notations: $m(nk)\bar{l}$ where m and l are the directions of propagation of the incident and scattered light, respectively (in our case for the confocal geometry, $m \equiv l$), and n and k are the polarization states of the incident and scattered light, respectively [Dam66]. The four spectra were measured for four polarization configurations, $\boldsymbol{a}(ij)\bar{\boldsymbol{a}}$, $i, j = \pi, \sigma$.

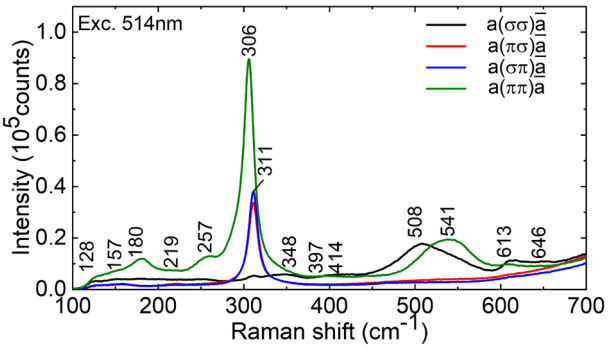

Figure III.2. Polarized Raman spectra of the a-cut Ho:CALGO crystal. $a(ij)\bar{\boldsymbol{a}}$, $i, j = \pi, \sigma$ geometries, $\lambda_{exc} = 514$ nm, *numbers* indicate the Raman frequencies in cm^{-1}.

The spectra are strongly polarized. The E_g modes occurred in the $\boldsymbol{a}(\sigma\pi)\bar{\boldsymbol{a}}$ and $\boldsymbol{a}(\pi\sigma)\bar{\boldsymbol{a}}$ geometries at 157 and 311 cm^{-1}. The low-frequency mode is attributed to Ca|RE vibrations in the $\boldsymbol{a}$-$\boldsymbol{b}$ plane, while the high-frequency one corresponds to similar O vibrations. In the $\boldsymbol{a}(\sigma\sigma)\bar{\boldsymbol{a}}$ A_{1g} geometry, an additional band at higher frequencies at 508 and 541 cm^{-1} attributed to O vibrations. In the $\boldsymbol{a}(\pi\pi)\bar{\boldsymbol{a}}$ A_{1g} geometry, the spectrum exhibits the most intense band at 306 cm^{-1} and a weaker broad band at around 541 cm^{-1}. The band at approximately 306 cm^{-1} is thus

assigned to A_{1g} symmetry (Ca|RE vibrations along the ***c***-axis), and the band with a complex structure (evident for the $\boldsymbol{a}(\sigma\sigma)\bar{\boldsymbol{a}}$ geometry) with two peaks at around 508 and 541 cm^{-1} is attributed to O vibrations. All four Raman-active modes are identified. The bands at approximately 613 and 646 cm^{-1} can be due to defect-induced modes [Had97].

III.1.C. Polarization-resolved study of gain profiles: Application to interpreting the results on mode-locked Ho:CALGO lasers

$CaGdAlO_4$ crystal doped with RE^{3+} ions are promising for the generation of femtosecond pulses in mode-locked lasers due to a strong inhomogeneous spectral line broadening of the RE^{3+} emission spectra. This effect originates from the disorder of the second coordination sphere of the RE^{3+} ions due to the charge difference between the Ca^{2+} and RE^{3+} cations and the large difference in the metal-to-metal distances [Pan22]. Yao *et al.* demonstrated the first mode-locked laser operation of 3.1 at.% Ho:CALGO crystal with a SESAM achieving a maximum output power of 8.7 W and a pulse duration of 369 fs [Yao22]. Shorter pulses of 92 fs and a maximum output power of 1.68 W were more recently achieved [Yao24]. This result is made possible by mode-locking at wavelengths longer (2151 nm) than the longest electronic transition (2130 nm). This laser long wavelength is most likely assisted by vibronic transitions. To confirm this, we studied the polarized spectroscopic properties of the 3.1 at.% Ho:CALGO crystal beyond 2 µm.

Since the $^5I_7 \rightarrow {}^5I_8$ transition is a quasi-three-level laser system with reabsorption at the laser wavelength, we studied the absorption and stimulated-emission cross-sections of the $^5I_8 \rightarrow {}^5I_7$ and $^5I_7 \rightarrow {}^5I_8$ transitions of Ho^{3+} ions in the 3.1 at.% Ho:CALGO crystal. Ho^{3+} ions in CALGO exhibit inhomogeneously broadened spectral bands and a polarization anisotropy of absorption and emission properties (CALGO is an optically uniaxial crystal). The absorption cross-sections, σ_{abs}, for the $^5I_8 \rightarrow {}^5I_7$ transition are shown in Figure III.3. For π-polarization, three maxima of σ_{abs} are ranging from 0.68 – 0.65×10^{-20} cm^2 at 1998 – 1950 nm. For σ-polarization, the peak σ_{abs} is 0.69×10^{-20} cm^2 at 1922 nm. These wavelengths can be used within an in-band pumping scheme and can be addressed by commercial Tm-fiber lasers.

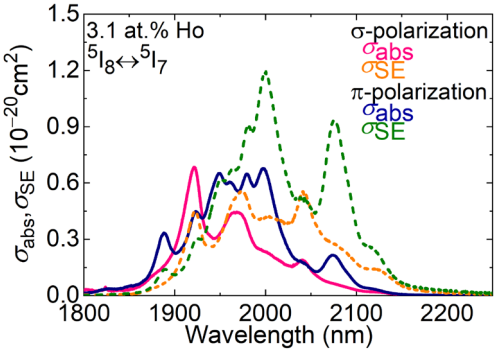

Figure III.3 RT polarized absorption, σ_{abs}, and stimulated-emission, σ_{SE}, cross-sections for the $^5I_8 \leftrightarrow {}^5I_7$ transitions of Ho:CALGO crystals for ultrafast 2.1-µm lasers.

The stimulated-emission cross-sections around 2 µm were calculated using a combination of the reciprocity method and the Füchtbauer-Ladenburg formula, Figure III.3. For this

calculation, we used the experimental crystal-field splitting of the $^5I_7$ and $^5I_8$ Ho^{3+} manifolds determined by low-temperature (12 K) spectroscopy. The zero-phonon line energy for the $^5I_7 \rightarrow {}^5I_8$ transition is 5133 cm^{-1} and the partition functions are $z_8(^5I_8) = 8.315$ and $z_7(^5I_7) = 8.966$ (at RT). The total Stark splitting of the ground-state, $\Delta E(^5I_8)$, is relatively large, 438 cm^{-1}, which explains the broadband emission from Ho^{3+} ions extending beyond 2.1 μm. Adjusting the Füchtbauer-Ladenburg to the reciprocity method results leads to a radiative lifetime of 5.7±0.5 ms for the $^5I_7$ state. This lifetime reasonably agrees with that obtained from J-O analysis 3.32 ms in Ho:Ca(Gd,Lu)AlO_4 [Pan22] and 6.35 ms in Ho:$CaYAlO_4$ [Yao21]. The refractive indices were taken from [Loi17], i.e., $n_o = 1.901$ and $n_e = 1.924$ at 2 μm.

At the wavelengths where laser operation is expected, σ_{SE} is 1.19×10^{-20} cm^2 at 2000 nm, 0.94×10^{-20} cm^2 at 2076 nm and 0.25×10^{-20} cm^2 at 2120 nm (for π-polarized light). For the σ-polarization, σ_{SE} is 0.55×10^{-20} cm^2 at 1973 nm and 2041 nm, 0.14×10^{-20} cm^2 at 2126 nm. Thus, the polarization anisotropy of the stimulated-emission properties of Ho^{3+} ions in CALGO is expected to favor laser operation on π-polarization. Due to the quasi-three-level nature of the Ho-lasers with reabsorption, the laser generation is expected to occur in the longer wavelength part of the emission spectrum.

Luminescence lifetimes of the $^5I_7$ and $^5I_6$ states were estimated from the fit of the luminescence decay curves from these states, as shown in Figure III.4(a,b). For the measurements, finely powdered samples doped with 1 at.% and 3.1 at.% Ho^{3+} ions were used to avoid reabsorption effects. The luminescence decay from the $^5I_7$ level exciting at 1920 nm is a single-exponential yielding a reabsorption-free lifetime τ_{lum} of 5.27 ms (for 1 at.% Ho doping). This lifetime value of the $^5I_7$ manifold is close to the radiative one estimated by F-L formula and RM method. The decay from the $^5I_6$ level exciting at 533 nm deviates from the single-exponential law and can be explained by the rise at the beginning of the decay. The luminescence lifetime of the $^5I_6$ state is estimated to be 0.237 ms (for 1 at.% Ho doping).

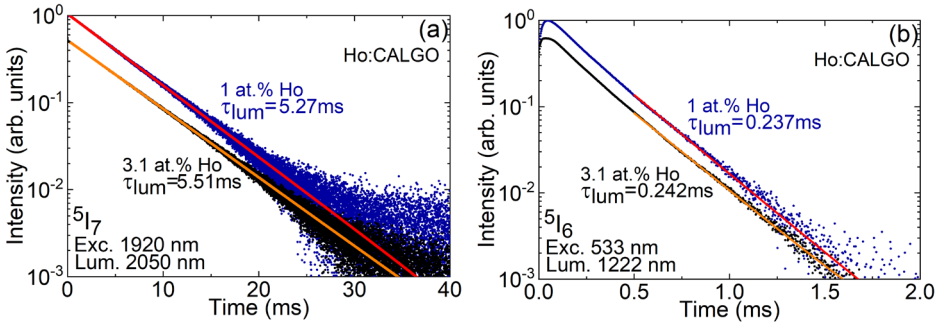

Figure III.4. RT luminescence decay curves for Ho^{3+} ions in 1 at.% and 3.1 at.% Ho^{3+}-doped CALGO crystal in a semi-log scale: (a) decay from the $^5I_7$ state, $\lambda_{exc} = 1920$ nm, $\lambda_{lum} = 2050$ nm; (b) decay from the $^5I_6$ state, $\lambda_{exc} = 533$ nm, $\lambda_{lum} = 1222$ nm. Powdered samples. The curves were shifted along the *y*-axis for better observation.

The $^5I_7 \rightarrow {}^5I_8$ Ho^{3+} gain cross-sections were then calculated to conclude about the potential laser wavelength and gain bandwidth. Two distinct operation regimes can be predicted:

i) a high-inversion regime ($0.25 < \beta < 0.5$) which is expected for low-doped (<1 at.% Ho) and short crystals should lead to a laser emission at 2.08 μm with an available gain bandwidth (FWHM) of ~35 nm, Figure III.5(a).

ii) a low inversion regime ($\beta < 0.2$) which can be observed for heavily doped (~3 at.% Ho) and relatively long crystals maximizing the pump absorption efficiency and gain, where the Ho:CALGO laser will tend to operate on the longest-wavelength electronic transition at ~2.12-2.13 μm with a non-negligible contribution of phonon sidebands, Figure III.5(b). In the latter case, the gain bandwidth is as broad as ~50 nm supporting generation of much shorter pulses in the mode-locked regime. Figure III.5(b) well explains the spectral behavior of the SESAM mode-locked 3.1 at.% Ho:CALGO laser reported by Yao *et al.* [Yao22].

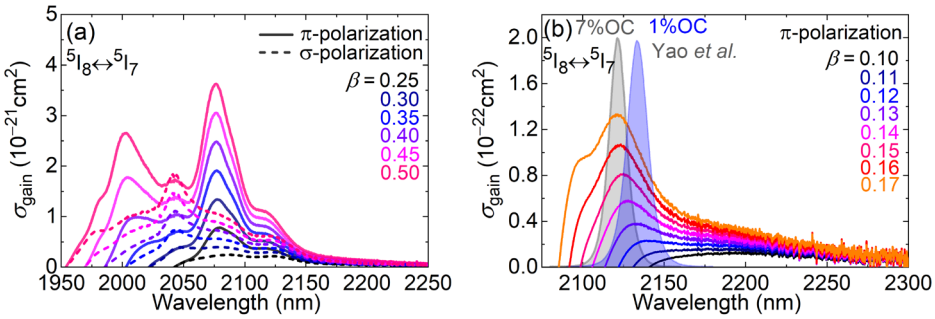

Figure III.5. RT gain cross-sections spectra: (a) high-inversion regime, π- and σ-polarized light; (b) low-inversion regime, π-polarized light. *Grey and blue curve* – laser spectra of the SESAM and mode-locked 3.1 at.% Ho:CALGO laser (7% and 1% output-coupling) [Yao22].

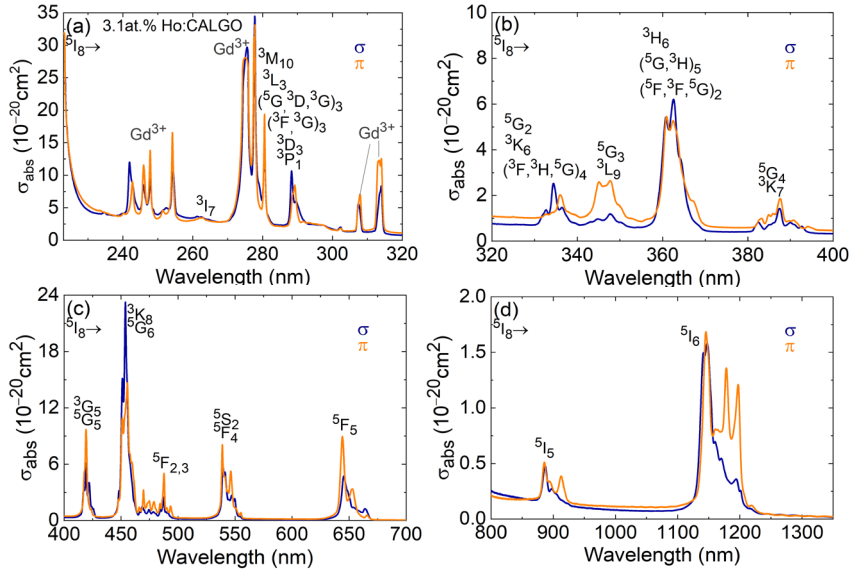

Figure III.6. RT absorption cross-section spectra of the 3.1 at.% Ho:CALGO crystal in different spectral ranges for σ and π light polarizations.

The absorption spectra were measured from 2300 to 220 nm at RT to observe the bands of excited state of Ho^{3+} ions in $CaGdAlO_4$ crystal and calculate absorption cross-section for the corresponding transitions. The cross-section spectra are shown in Figure III.6. The Ho^{3+} ion density is 3.78×10^{20} at/cm^3 for the 3.1 at.% Ho^{3+} doping. The peak positions of the Ho^{3+} excited states ions were taken from [Car68]. In the UV spectral range, the several intense absorption

peaks occur with groups of peaks between 242 and 254 nm, at 275 nm and two peaks at 308 and 314 nm. These peaks are assigned to Gd^{3+} excited states [Car71, Bin97]. They spectrally overlap with transitions of Ho^{3+} ions around 250 and 280 nm. An UV absorption edge is observed at 223 nm and is consistent with the absorption edge in undoped $CaGdAlO_4$ crystal and its bandgap energy [Mas14, Tal19].

Ho:CALGO exhibit high absorption cross-sections at 1150 nm ($^5I_6$) which is covered by commercially available Raman fiber lasers to achieve 2.9 µm Ho-laser emission. The maximum of σ_{abs} amounts to 1.68×10^{-20} cm^2 at 1145 nm with a bandwidth of 14 nm. Ho^{3+} ions possess higher absorption cross-sections in the visible spectral range, with bands at 455 nm ($^3K_8$, $^5G_6$), 550 nm ($^5S_2$, $^5F_4$) and 650 nm ($^5F_5$).

III.1.D. Polarized low-temperature spectroscopy of Ho^{3+} ions

To calculate the stimulated-emission at 2.1 µm ($^5I_7 \rightarrow {}^5I_8$ transition) and the excited-state absorption cross-section spectra at 3 µm ($^5I_7 \rightarrow {}^5I_6$ transition), by the reciprocity method, the partition function of the $^5I_8$, $^5I_7$ and $^5I_6$ manifolds have to assessed. The low-temperature measurements of the absorption of the $^5I_8 \rightarrow {}^5I_6$ and $^5I_8 \rightarrow {}^5I_7$ transitions, and emission spectra from the $^5I_7 \rightarrow {}^5I_8$ transition allows to determine the experimental crystal-field splitting of those manifolds and, then to calculate the partition functions. Since Ho^{3+} ions occupy a C_{4v} site symmetry in $CaGdAlO_4$, a total number of Stark sub-levels of 13, 11 and 10 for the $^5I_8$, $^5I_7$ and $^5I_6$ multiplets are expected, respectively.

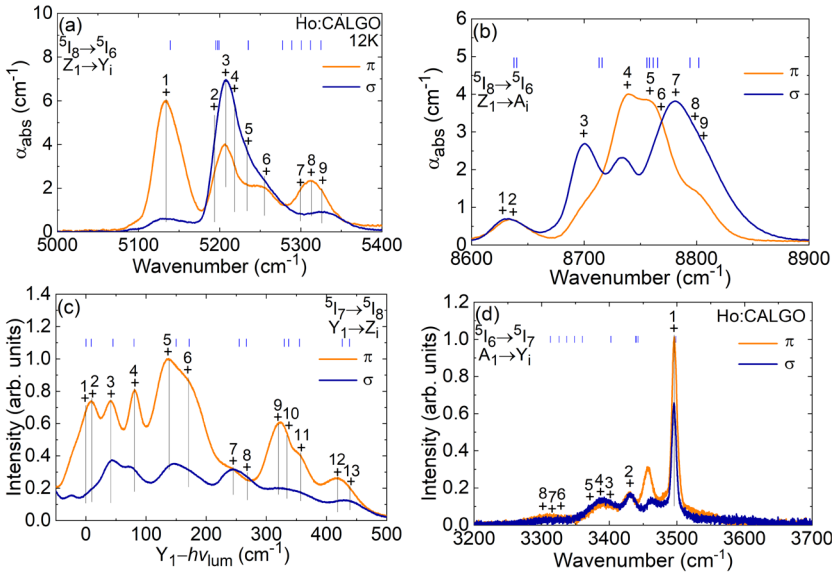

Figure III.7. Low-temperature (12 K) spectroscopy of Ho^{3+} ions in the CALGO crystal: (a,b) absorption spectra, ($^5I_8 \rightarrow {}^5I_7$, $^5I_8 \rightarrow {}^5I_7$ transitions); (c,d) luminescence spectra, ($^5I_7 \rightarrow {}^5I_8$, $^5I_6 \rightarrow {}^5I_7$ transitions) around 2 and 3 µm respectively, *blue vertical dashes* – theoretical crystal field splitting for $CaGdAlO_4$. λ_{exc} = 885 nm.

The measured absorption and emission spectra are shown in Figure III.7. The emission spectra were measured under the resonant excitation of the $^5I_5$ state (at 885 nm). The spectra exhibit an inhomogeneous spectral line broadening even at 12 K, evidence of the disorder in the

CALGO crystal structure. For labelling the electronic transitions, we used the following phenomenological notations for the Stark sub-levels: X_i Y_i, and Z_i for the $^5I_6$, $^5I_7$ and $^5I_8$ respectively [Lea82] where i = 1, 2, … 2J+1, counting from the lowest sub-level. For the assignment of the electronic transitions of Ho^{3+} ions in $CaGdAlO_4$, we followed the calculations of the Stark levels theoretical positions [unpublished results]. Two examples of the sub-levels assignment for the $^5I_8 \rightarrow {}^5I_7$ and $^5I_8 \rightarrow {}^5I_6$ transitions are shown in Figure III.7(a,b). The blue vertical dashes in Figure III.7 mark the positions of the calculated electronic transitions by crystal-field theory.

The total Stark splitting of the ground-state, $\Delta E(^5I_8)$ in Figure III.7(c), is relatively large, 440 cm^{-1}, which explains the broadband emission from Ho^{3+} ions extending beyond 2.1 µm.

III.1.E. Temperature dependences of the $^5I_6$ and $^5I_7$ Ho^{3+} lifetimes

Temperature-dependent unpolarized luminescence spectra of Ho:CALGO at 2.9 µm, (the $^5I_6 \rightarrow {}^5I_7$ transition), are shown in Figure III.8(a). When the temperature decreases, the emission intensity increases and the spectra become more structured due to the depopulation of the $^5I_6$ upper Stark sub-levels.

Cryogenic cooling can be a suitable approach to reduce non-radiative path from excited state with short lifetimes such as the Ho^{3+} $^5I_6$ manifold. We employed 1 at.% Ho-doped CAGLO bulk crystal with a thickness less than 1 mm. The excitation into the ($^5S_2$, $^5F_4$) manifolds (at 535 nm) was non-resonant with the $^5I_6$ level to reduce the contribution of the pump signal. The kinetics were fitted by an exponential law. The temperature-dependent luminescence lifetimes of the $^5I_6$ and $^5I_7$ states are shown in Figure III.8(b).

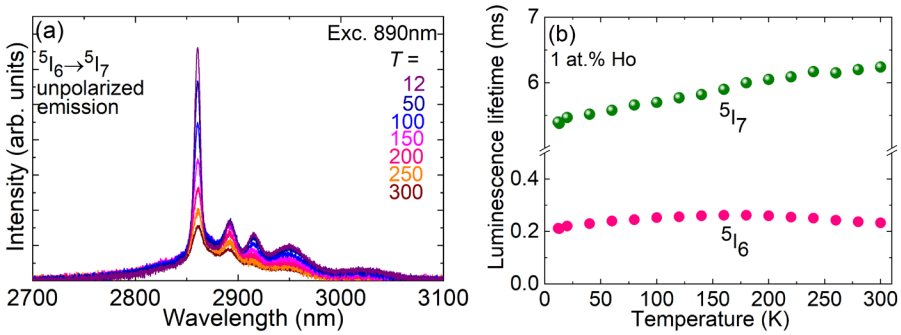

Figure III.8. Spectroscopic study of the temperature dependence of: (a) luminescence spectra at 3 µm, the $^5I_6 \rightarrow {}^5I_7$ transition, λ_{exc} = 890 nm; (b) luminescence lifetimes of the $^5I_6$ and $^5I_7$ manifolds, λ_{exc} = 535 nm.

The lifetime of the $^5I_7$ manifold decreases gradually from 6.3 ms at 300 K to 5.4 ms at 12 K. The lifetime of this level at 12 K becomes equal to that of the powdered (reabsorption-free) sample, as shown in Figure III.4(a). Therefore, the shortening of the lifetime of the $^5I_7$ manifold with decreasing temperature is most likely due to the reduced reabsorption effect. The lifetime of the $^5I_6$ manifold does not change significantly and almost stays the same with a slight deviation. It equals to 233 µs at 300 K, 262 µs at 180 K and 212 µs at 12 K.

III.1.F. Multiphonon-assisted long-wave emission

As discussed in Section I.2.I not all RE^{3+} ions exhibit the same electron-phonon interaction and some of them show a strong coupling with the host matrix vibrations and Ho^{3+} is one example.

We plotted the absorption and emission spectra of Ho^{3+} ions in CALGO beyond 2.1 µm in a semi-log scale, as shown in Figure III.9(a) for π-polarized light. Similar properties are observed for σ-polarized light. The longest wavelength electronic transition was determined by low-temperature spectroscopy in this work and is found at ~2130 nm. SE beyond this wavelength is assumed to be due to vibronic transitions.

Figure III.9(a) shows that Ho^{3+} ions in CALGO experience a strong electron-phonon interaction leading to a temperature broadening of their spectral lines and the appearance of an exponential multi-phonon sideband in the long-wave part of the emission spectrum extending up to 2.35 µm. This RE^{3+} multiphonon sideband is illustrated in Figure III.9(a) by the orange solid line for the Stokes sideband and the red line for the anti-Stokes sideband. This exponential dependence is characteristic of a weak-coupling ion-lattice interaction which is typical for 4f shells. The values of the α_S and α_{AS} were obtained by fitting the sideband and equal $7\pm0.5\times10^{-3}$ cm and $12\pm0.5\times10^{-3}$ cm, respectively. These values are slightly smaller than those reported for Er:$LiYF_4$, $\alpha_S = 9.2\times10^{-3}$ cm $\alpha_{AS} = 14.5\times10^{-3}$ cm [Auz95] in agreement with higher phonon energies in Ho:CALGO compared to $LiYF_4$.

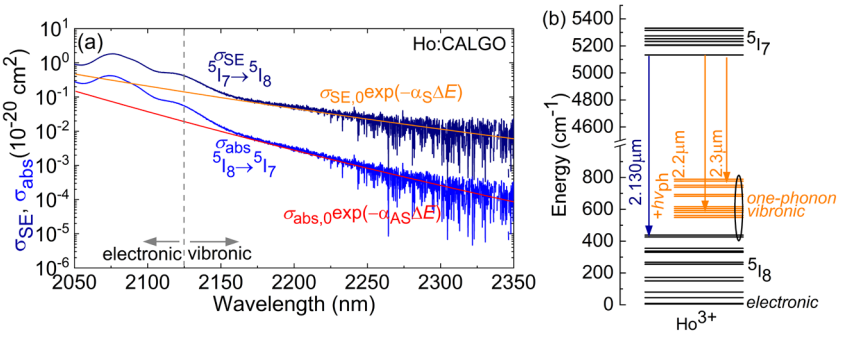

Figure III.9. Observation of the vibronic properties of the Ho:CALGO crystal: (a) long-wave phonon-assisted emission (π light polarization) in a semi-log scale; (b) the Stark splitting of the $^5I_7$ and $^5I_8$ multiplets showing the longest electronic transition by the blue arrow and assignment of the possible laser lines (orange arrows) relevant to the vibronic transitions.

These long-wave emission and absorption can be explained by considering vibronic energy-levels, as shown in Figure III.9(b). Their positions are obtained by adding the energies of phonons in CALGO to the highest Stark sub-level of the $^5I_8$ manifold. The consideration of these phonon sidebands is essential, *e.g.*, for the design of Kerr-lens mode-locked Ho:CALGO lasers.

III.1.G. Assessing the suitability of Ho:CALGO crystals for laser operation at 3 µm

As shown, Ho:CALGO exhibits relatively low phonon energy (among oxides), the non-radiative path from the $^5I_6$ manifold is expected to be weak, and the absorption cross-section for the $^5I_8 \rightarrow {}^5I_6$ transition is rather large. These characteristics make Ho:CALGO crystals a potential gain medium for 2.9 µm lasers. To conclude about the suitability and expected laser

wavelengths, the gain cross-sections are calculated for the $^5I_6 \rightarrow {}^5I_7$ transition at 2.9 μm since this transition represents a quasi-four-level laser system with reabsorption.

For this gain cross-sections calculation, we calculated first the stimulated-emission cross-section spectra for the $^5I_6 \rightarrow {}^5I_7$ transition and then the excited-state absorption cross-section for the $^5I_7 \rightarrow {}^5I_6$ transition using the partition functions obtained from the crystal field data, as shown in Figure III.10(a,b). The peak σ_{SE} amounts to 5.0×10^{-20} cm^2 at 2861 nm for the π-polarization and 2.7×10^{-20} cm^2 at 2862 nm for the σ-polarization.

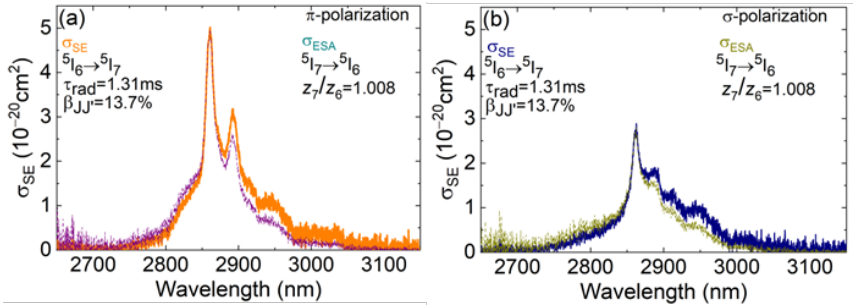

Figure III.10. RT SE cross-section and excited-state absorption cross-sections for the $^5I_6 \rightarrow {}^5I_7$ and $^5I_7 \rightarrow {}^5I_6$ transitions of Ho^{3+} ions in CALGO crystal, respectively: (a) for π light polarization; (b) for σ light polarization. λ_{exc} = 885 nm.

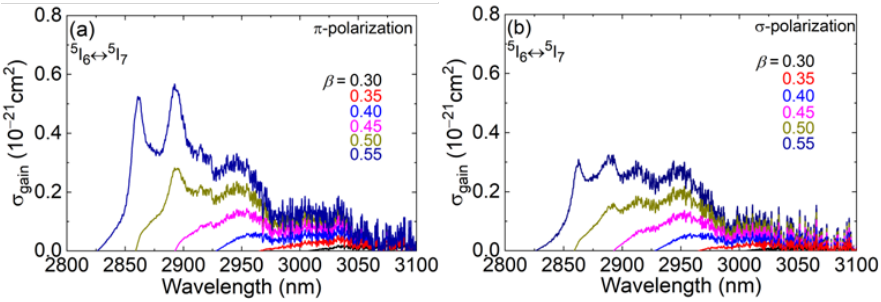

Figure III.11. Gain cross-section spectra around 3 μm: (a) for π light polarization; (b) for σ light polarization.

Then, the gain cross-sections were derived and plotted in Figure III.11. The gain becomes positive when the inversion ratio reaches more than 30%. For this inversion, the laser operation is expected at 3035 nm. For higher β values, the maximum shifts to shorter wavelengths at 2950 nm and 2895 nm. The gain profile is broad and can reach a 100 nm bandwidth for the σ polarization.

As discussed in Chapter I.3, to achieve Ho laser operation in continuous-wave regime at 2.9 μm is a real challenge. One of the most appropriate methods could be the codoping with Pr^{3+} ions to quench the luminescence lifetime of the $^5I_7$ terminal laser level.

To conclude, heavily doped Ho:CALGO crystals are attractive for femtosecond pulse generation around 2.1 μm in the "small-inversion" regime featuring a broad gain bandwidth of ~50 nm (for π-polarized light) supported by the inhomogeneous spectral line broadening in this structurally disordered material and a strong electron-phonon interaction. Furthermore, Ho:CALGO crystals appear to be promising materials for lasers emitting at 2.9 μm.

III.2. Tm^{3+},Ho^{3+}-codoped gadolinium scandate crystal

In this chapter we are going to investigate the polarized spectroscopic properties and luminescence dynamics of $GdScO_3$ a perovskite type crystal doped with Tm^{3+} and Ho^{3+} ions, with the aim of using it for ultrafast laser development in the near-infrared region since dopant ions exhibit in this crystal broad and structureless emission spectra. It will be shown that the spectral line broadening is not due to the same inhomogeneous mechanisms observed in the previously considered disordered crystals.

III.2.A. Crystal growth

The Tm,Ho:$GdScO_3$ crystal melts congruently at a high temperature of ~2100°C and can be grown by the standard Cz method. For this work, the crystal was grown by the Cz method in an induction heating furnace by our colleagues at the SIOM CAS in China. The raw materials were oxide powders of Gd_2O_3, Sc_2O_3, Tm_2O_3, and Ho_2O_3 with a purity of 99.99%. The raw materials were accurately weighed in stoichiometric ratios with doping concentrations of Tm^{3+} and Ho^{3+} ions at 5 at.% and 0.5 at.% (respectively, with respect to Gd^{3+}) in $GdScO_3$. The total weighed mass was 75% of the total mass that the crucible could hold, considering that the growth charge expands as it melts. After thorough mixing, the raw materials were pressed into tablets with a diameter of 60 mm. Then, the tablets were sintered in air at 1500°C for 10 h. The crystal growth took place in an iridium crucible, with ZrO_2 as an isolator in an argon atmosphere. The power used for crystal growth was approximately 8 kW, corresponding to the melting point of Tm,Ho:$GdScO_3$ of about 2100°C. The single crystal was grown using a [110] oriented seed from an undoped $GdScO_3$ crystal. The complete process included the following steps: furnace loading, vacuuming, argon charging, heating, melting, crystal growth, and slow cooling down to room temperature for 20 h. The pulling rate was 1.0 mm/h, and the rotation speed was 10 rpm.

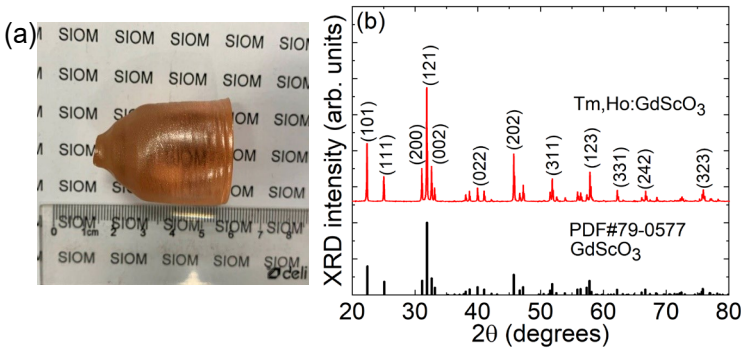

Figure III.12. Tm, Ho:$GdScO_3$ crystal: (a) a photograph of the as-grown crystal, the growth direction is along the [110] orientation; (b) X-ray powder diffraction (XRD) pattern, *numbers* denote the Miller's indices, (*hkl*), *black lines* – the reference pattern of $GdScO_3$.

A photograph of an as-grown Tm,Ho:$GdScO_3$ crystal is shown in Figure III.12(a). The boule had a cylindrical shape with dimensions of Φ30 × 30 mm^3. It was free of cracks, inclusions, and bubbles and had a yellow-brown coloration due to colour centers formed during growth in an oxygen-deficient atmosphere. This coloration was subsequently removed by annealing in air.

The phase purity and crystal structure of Tm,Ho:$GdScO_3$ were confirmed by X-ray powder diffraction (XRD), as seen in Figure III.12(b). All the reflections in the diffraction pattern were assigned to the orthorhombic phase isostructural to undoped $GdScO_3$ (PDF card No. 79-0577). The characteristic $GdFeO_3$-type structure has four distorted perovskite units in the crystallographic cell (space group *Pnma* – D162h, No. 62). According to previous studies, it is expected that the dopant Tm^{3+} and Ho^{3+} ions replace the host-forming Gd^{3+} cations in C_s symmetry sites (Wyckoff: 4c).

The actual composition of the grown crystal was studied by Inductively Coupled Plasma Atomic Spectroscopy (ICP-AS). The RE doping levels were 3.76 at.% Tm and 0.35 at.% Ho (corresponding to ion densities of $N_{Tm} = 6.25 \times 10^{20}$ at/cm^3 and $N_{Ho} = 0.58 \times 10^{20}$ at/cm^3). The RE ion segregation coefficients are $K_{Tm} = 0.75$ and $K_{Ho} = 0.70$.

III.2.B. Nature of the structure disorder

Before determining the nature of the structure disorder in $GdScO_3$, the crystal structure should be considered with a small introduction on perovskite type materials.

Perovskites are materials with a chemical formula of ABX_3, where A and B are cations, often of rather different sizes, and X is an anion. This class of materials is named after the mineral perovskite, calcium titanium oxide $CaTiO_3$. The perovskite structure is known for permitting diverse ionic substitutions at both cationic sites due to its high tolerance to structural distortions. Perovskites exhibit exciting compositionally driven ferro-, piezo-, and pyro-electrical properties, as well as electro-optical effects, and they have been used as electric, magnetic, optical, and catalytic materials in various applications [Hwa17, Qua19].

Perovskite oxides, ABO_3, are relevant as host materials for doping with trivalent rare-earth ions for luminescent and laser materials [Yam02]. In ABO_3 crystals, cations with a large ionic radius occupy A-sites and coordinate to XII oxygen atoms, and those with a small ionic radius reside in VI-fold coordinated B-sites. The idealized form of ABO_3 compounds is cubic ($Pm\bar{3}m$), *e.g.*, $SrTiO_3$ and $BaTiO_3$. More often, the structure is modified by cation displacement or by tilting of octahedra, lowering the crystal symmetry. The orthorhombic $CaTiO_3$ phase (space group *Pnma*) is among the most common non-cubic variants. Orthorhombic yttrium aluminium perovskite, $YAlO_3$, is a well-known example of laser host materials.

Among the ABO_3 perovskites, RE orthoscandates $REScO_3$ with RE = La to Ho have attracted a lot of attention in recent years. Their structures have been known since 1957 when they were presented by Geller [Gel57] and further described by other authors [Cla78, Ama87, Lif04, Vel07]. For predicting the stability of ABO_3 perovskite structures, the Goldschmidt tolerance factor *t* is used [Gol26]. The *t* factors for $REScO_3$ crystals are lower compared to other $REBO_3$ compounds, suggesting that orthoscandates form highly distorted structures [Lif04]. Gadolinium orthoscandate, $GdScO_3$, adopts the $GdFeO_3$ type structure (orthorhombic, sp. gr. *Pnma*, lattice constants: $a = 5.745(1)$ Å, $b = 7.929(2)$ Å, $c = 5.481(1)$ Å [Vel07]). Its Goldschmidt tolerance factor is relatively low, 0.808, but well within the range of stable orthorhombic perovskites [Lif04].

The structure of $GdScO_3$ is composed of a framework of corner-connected $[ScO_6]$ octahedra and Gd^{3+} in interstices surrounded by eight $[ScO_6]$ octahedra, see Figure III.13. The orthorhombic structure is derived from the ideal ABO_3 cubic (sp. gr. $Pm\bar{3}m$) aristotype by tilting about the axes of the cubic unit cell running parallel to the edges of the cubes formed by eight $[ScO_6]$ octahedra in an $a^-b^+a^-$ pattern (Glazer notation [Gla72]) as a response to the occupancy of the A-site by a cation which is smaller than that required to form the ideal cubic structure [Lif04]. The octahedron tilting results in a symmetry reduction. It is also known that for rare-earth orthoscandates, the RE^{3+} coordination polyhedron in the A-site is best regarded as $[REO_8]$ rather than $[REO_{12}]$, i.e., a four-fold anti-prism [Lif04].

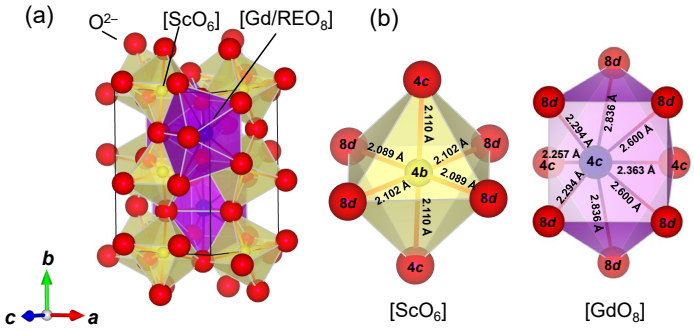

Figure III.13 The crystal structure of an orthorhombic $GdScO_3$ crystal: (a) a fragment of the structure, black lines marking the unit cell; (b) schematic of the $[ScO_6]$ (*left*) and $[GdO_8]$ (*right*) polyhedra showing the metal-to-oxygen (M–O) interatomic distances. The atomic coordinates reported by Veličkov *et al.* [Vel07] are used.

As already discussed, and shown previously, the broad and smooth absorption and emission spectra of Tm^{3+} and Ho^{3+} ions in the CaF_2 and $CaGdAlO_4$ crystals are due to different inhomogeneous broadening mechanisms, either related to the doping for CaF_2 or to structural disorder for $CaGdAlO_4$. In the case of $GdScO_3$, Amanyan *et al.* studied Nd^{3+}-doped $GdScO_3$ crystals and indicated that for this compound, the spectral linewidths at room temperature were substantially larger than those for ordered $YAlO_3$ and $Y_3Al_5O_{12}$ crystals [Ama83]. These authors also suggested that the relatively large Stark splitting of RE^{3+} multiplets in $GdScO_3$ comes from the low-symmetry component in the crystal-field potential expansion, indicating a strong low-symmetry distortion in the local symmetry of the activator centre [Ama83]. Guo *et al.* studied the LT fluorescence of Yb^{3+} ions in $GdScO_3$ and indicated that the energy transitions of Yb^{3+} were almost independent of the excitation wavelength, revealing a single type of Yb^{3+} species [Guo23]. Zhang *et al.* indicated that although the shape of $[Gd|REO_8]$ polyhedra is the same throughout the $GdScO_3$ unit-cell, their orientations are different, which may contribute to additional inhomogeneous spectral line broadening [Zha21]. However, no evidence of the latter effect was provided.

In the $GdScO_3$ crystal, there are two possible sites for RE substitution, namely A-sites (Gd ones, C_s symmetry) and B-sites (Sc ones, C_i symmetry). The entry of RE^{3+} ions such as Tm^{3+} and Ho^{3+} into Sc sites seems very improbable due to the large difference in their ionic radii (R_{Tm} = 0.88 Å, R_{Ho} = 0.901 Å, and R_{Sc} = 0.745 Å for VI-fold oxygen coordination), as pointed out by Piotrowski *et al.* [Pio22]. Moreover, electric dipole transitions are forbidden for sites with a

centre of inversion, so that even if a small amount of RE^{3+} dopant ions is found in the Sc sites, they will not appear in the optical spectra (except for transitions with a magnetic dipole component of the transition intensity). This situation is similar to the case of multi-site cubic sesquioxides (*e.g.*, Y_2O_3) featuring a distribution of the dopant ions over C_2 and C_{3i} symmetry sites. However, since both sites in the latter are occupied by the same host cations, 25% of the dopant ions remain optically inactive.

In the present work, no signs of multi-site behaviour for either Tm^{3+} or Ho^{3+} ions were revealed by LT spectroscopy and the measured LT emission spectra at 2 μm were almost independent of the excitation wavelength, see below. To get further insight into this topic, we compared the low-temperature absorption spectra of Ho^{3+} ions ($^5I_8 \rightarrow {}^5I_7$ transition) for three crystals: ordered $YAlO_3$ (Y site symmetry: C_s), $GdScO_3$ (Gd site symmetry: C_s), and Y_2O_3 (Y site symmetry: C_2 and C_{3i}), as shown in Figure III.14. At 12 K, the spectral lines temperature broadening is greatly reduced. As seen from the figure, the spectral linewidths for all three crystals are comparable, and they are much narrower than those for crystals with a structure and/or compositional disorder featuring strong inhomogeneous spectral line broadening, such as $CaGdAlO_4$ crystal or solid-solution sesquioxides $(Lu,Sc)_2O_3$.

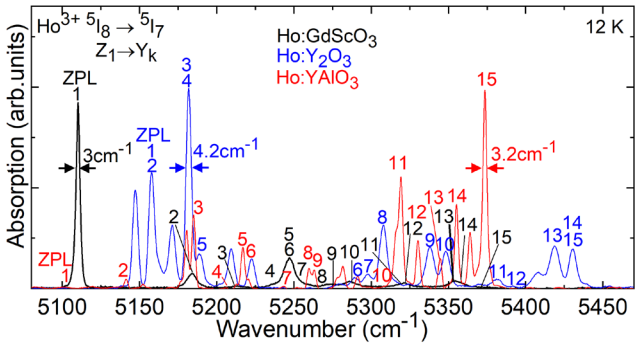

Figure III.14. LT (12 K) absorption spectra of Ho^{3+}-doped $GdScO_3$, Y_2O_3 and $YAlO_3$ crystals, the $^5I_8 \rightarrow {}^5I_7$ transition.

From the above-mentioned considerations, we conclude that the main reasons for the observation of broad and structureless spectra of RE^{3+} ions in $GdScO_3$ are (i) low-symmetry component in the crystal-field potential expansion leading to a large Stark splitting of RE^{3+} multiplets, and (ii) a strong electron-phonon interaction leading to large homogeneous thermal line widths at room temperature. The latter is consistent with the fact that the spectral broadening is more pronounced for Tm^{3+} ions than for Ho^{3+} ions, as evidenced by the luminescence spectra at 2 μm (see Figure 17(b)). Indeed, it is known that the strength of the lattice-orbit interaction is not homogeneous across the lanthanide series and increases at its beginning and end, being particularly strong for Tm^{3+} ions.

III.2.C. Polarized Raman spectroscopy

The room-temperature polarized Raman spectra of the Tm,Ho:$GdScO_3$ crystal are presented in Figure III.15. As in the case of the CALGO crystal, four polarization configurations were used to identify vibration modes of different symmetry. For orthorhombic RE scandates (sp. gr. *Pnma*),

according to the factor group analysis, four formula units consisting of 20 atoms per unit cell give rise to 60 vibrational modes at the centre of the Brillouin zone ($k = 0$):

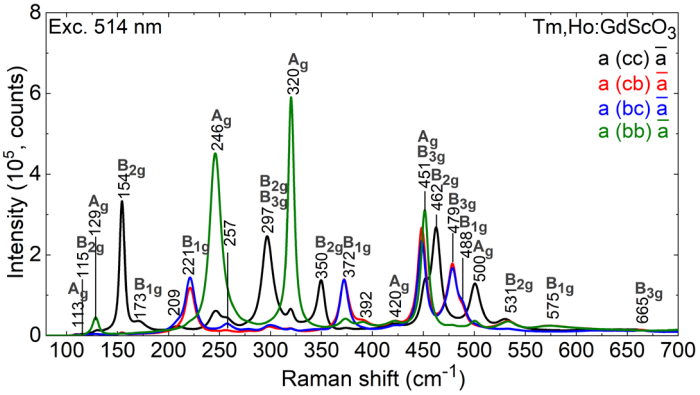

Figure III.15. Polarized Raman spectra of an *a*-cut Tm,Ho:$GdScO_3$ crystal, $\lambda_{exc} = 514$ nm, *numbers* - Raman frequencies in cm^{-1}.

$\Gamma_{op} = 7A_g + 5B_{1g} + 7B_{2g} + 5B_{3g} + 8A_u + 9B_{1u} + 7B_{2u} + 9B_{3u}$,
of which 24 modes are Raman-active (A_g, B_{1g}, B_{2g}, and B_{3g}), 25 modes are IR-active (B_{1u}, B_{2u}, and B_{3u}) and 8 modes are silent (A_u), and $\Gamma_{ac} = B_{1u} + B_{2u} + B_{3u}$ [Cha09]. The Raman spectra of Tm,Ho:$GdScO_3$ are typical for orthorhombic perovskites and are strongly polarized. 22 active Raman modes were found and assigned out of 24 predicted ones. Note that to date, none of the perovskites has shown all the modes. The number of modes depends on the degree of distortion of the ideal perovskite structure. In the low-frequency range (below 200 cm^{-1}), the Raman modes are due to A-site (Gd^{3+}) translations, while those at higher energies (above 200 cm^{-1}) are due to oxygen motions (bending, stretching, and tilting) in the [AO_8] units [Cha11]. In orthorhombic symmetry, the B cation (Sc^{3+}) occupies a site of inversion symmetry (C_i) and thus, the Raman spectra of such perovskites should not have modes which are due to B cation translations or vibrations [Gro12]. The dominant Raman peak appears at 320 cm^{-1} (A_g) and the maximum phonon energy is 665 cm^{-1} (B_{3g}). The relatively low maximum phonon energy of $GdScO_3$ is beneficial for reducing the multiphonon non-radiative relaxation rate from the $^5I_6$ Ho^{3+} state

III.2.D. Polarized absorption and emission properties

The orthorhombic $GdScO_3$ crystal is optically biaxial, and its optical indicatrix frame aligns with the crystallographic axes. The spectroscopic properties of Tm^{3+},Ho^{3+}-codoped $GdScO_3$ were studied for the principal light polarizations $\boldsymbol{E} \parallel \boldsymbol{a}, \boldsymbol{b}, \boldsymbol{c}$.

The room-temperature polarized absorption spectrum of Tm,Ho:$GdScO_3$ is presented in Figure II.16(a-c) in terms of absorption coefficient α_{abs}. The assignment of electronic transitions of Tm^{3+} and Ho^{3+} ions follows that by Carnall *et al.* [Car68]. The broad absorption in the visible (320 – 500 nm) is assigned to color centers that are not entirely removed upon annealing in air [Li22]. Absorption bands related to transitions from the $^3H_6$ Tm^{3+} and $^5I_8$ Ho^{3+} ground states to the excited states ranging from $^3F_4$ Tm^{3+} and $^5I_7$ Ho^{3+} up to $^1D_2$ Tm^{3+} and $^3L_9 + {}^5G_3$ Ho^{3+}

(wavelength range: 320 – 2150 nm) are observed. For undoped $GdScO_3$, the optical bandgap E_g is 5.8 eV (~213 nm)[Der12].

The absorption cross-sections for the $^3H_6 \rightarrow {}^3H_4$ Tm^{3+} transition around 0.8 μm are shown in Figure II.16(d). This band is suitable for pumping Tm^{3+},Ho^{3+}-codoped crystals by high-brightness Ti:Sapphire lasers or commercial high-power spatially multimode AlGaAs laser diodes. The maximum σ_{abs} value reaches 1.52×10^{-20} cm^2 at 794.2 nm and the absorption bandwidth is as large as 8.0 nm (for light polarization $\boldsymbol{E} \parallel \boldsymbol{b}$). For the other two polarizations, the absorption is weaker, $\sigma_{abs} = 0.93 \times 10^{-20}$ cm^2 at 792.4 nm (for $\boldsymbol{E} \parallel \boldsymbol{a}$) and $\sigma_{abs} = 0.75 \times 10^{-20}$ cm^2 at 801.5 nm (for $\boldsymbol{E} \parallel \boldsymbol{c}$). The relatively broad absorption of Tm^{3+} ions around 0.8 μm is beneficial for suppressing the effect of the temperature drift of the pump diode wavelength.

Recently, resonant (in-band) Tm^{3+} pumping was considered as a viable way for power scaling of Tm,Ho lasers. It corresponds to the $^3H_6 \rightarrow {}^3F_4$ Tm^{3+} absorption transition. Raman-shifted Er-fiber lasers emitting at 1.68 μm can address this absorption band. For Tm^{3+} ions in $GdScO_3$, the maximum σ_{abs} value is 0.98×10^{-20} cm^2 at 1673.6 nm for light polarization $\boldsymbol{E} \parallel \boldsymbol{b}$. For the other two polarizations, the absorption is weaker, $\sigma_{abs} = 0.61 \times 10^{-20}$ cm^2 at 1670.7 nm (for $\boldsymbol{E} \parallel \boldsymbol{a}$) and $\sigma_{abs} = 0.67 \times 10^{-20}$ cm^2 at 1670.6 nm (for $\boldsymbol{E} \parallel \boldsymbol{c}$).

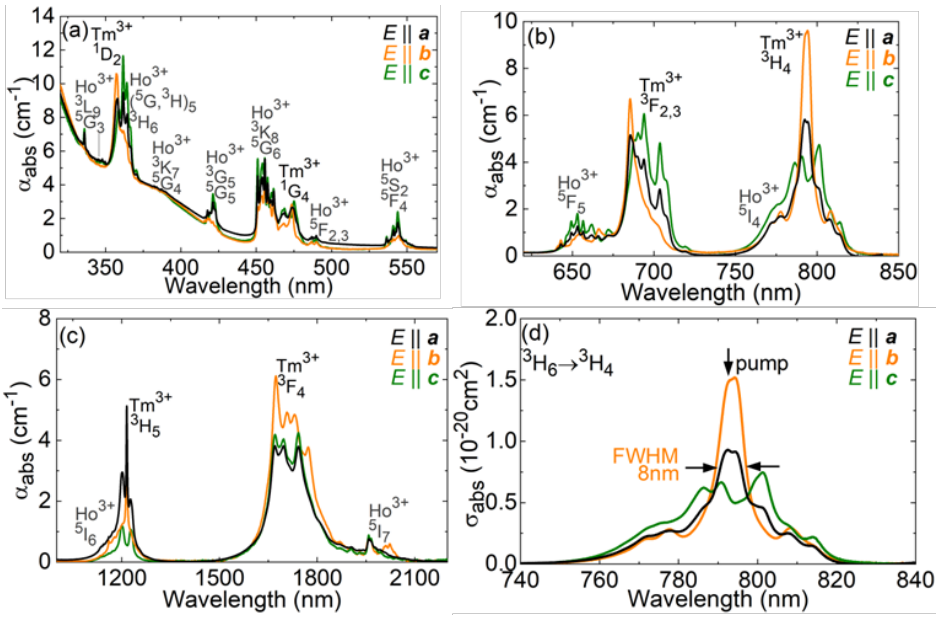

Figure III.16. Polarized absorption properties of the Tm,Ho:$GdScO_3$ crystal: (a-c) absorption spectra; (d) absorption cross-sections, σ_{abs}, for the $^3H_6 \rightarrow {}^3F_4$ Tm^{3+} transition, arrow indicates the pump wavelength.

The luminescence spectra of the Tm,Ho:$GdScO_3$ crystal in the near-IR are shown in Figure III.17(a), measured for the three principal light polarizations $\boldsymbol{E} \parallel \boldsymbol{a}, \boldsymbol{b}, \boldsymbol{c}$ under excitation at 794 nm. The spectra are strongly polarized and exhibit a notable spectral line broadening which is attributed to the strong electron-phonon coupling for this host crystal (note that homogeneous thermal line broadening is expected to be stronger for Tm^{3+} ions than for Ho^{3+} ones in line with the measured spectra). The weak band at 1.37 – 1.53 μm is due to the $^3H_4 \rightarrow {}^3F_4$ Tm^{3+} transition, and a broad band spanning from 1.55 to 2.3 μm is assigned to two spectrally overlapping transitions, namely $^3F_4 \rightarrow {}^3H_6$ Tm^{3+} and $^5I_7 \rightarrow {}^5I_8$ Ho^{3+}. The latter emission is more

intense despite the low Ho:Tm codoping ratio (1:10.7, according to the actual rare-earth ion densities), indicating an efficient $Tm^{3+} \rightarrow Ho^{3+}$ energy transfer. In the spectral range where laser operation is expected, the highest emission intensity corresponds to the light polarization $\boldsymbol{E} \parallel \boldsymbol{c}$ and several local peaks are found in the luminescence spectra centered at 2022, 2064, 2098, and 2111 nm.

Benefiting from the combined gain bandwidth of Tm^{3+} and Ho^{3+} ions and the homogeneous thermal line broadening in a $GdScO_3$ crystal, Liu *et al.* achieved a broadly tunable laser operation from 1914 to 2125 nm (with a broad range of 215 nm) and a pulse duration of 72 fs for the $\boldsymbol{E} \parallel \boldsymbol{b}$ light polarization [Liu24].

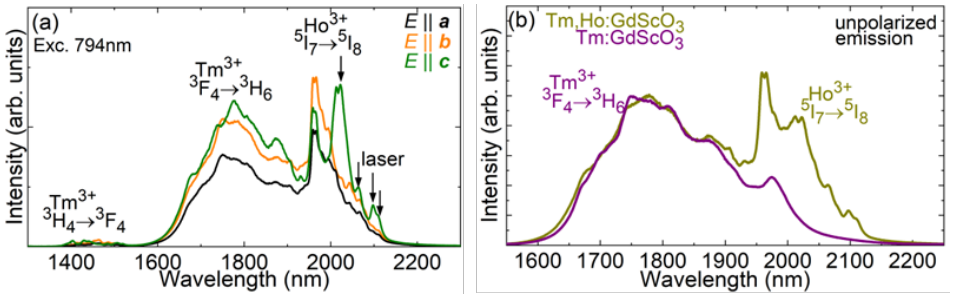

Figure III.17. Emission properties of Tm,Ho:$GdScO_3$: (a) polarized luminescence spectra in the near-IR, light polarizations: $\boldsymbol{E} \parallel \boldsymbol{a}, \boldsymbol{b}, \boldsymbol{c}$, arrows indicate the observed laser wavelengths (for light polarization $\boldsymbol{E} \parallel \boldsymbol{c}$); (b) a comparison of unpolarized emission spectra of Tm^{3+},Ho^{3+}-codoped and singly Tm^{3+}-doped $GdScO_3$ crystals around 2 μm, λ_{exc} = 794 nm.

III.2.E. Tm ↔ Ho energy-transfer

The luminescence dynamics from the lower-lying excited states of Tm^{3+} and Ho^{3+} ions in Tm,Ho:$GdScO_3$, which are responsible for the laser emission around 2 μm, were studied under resonant Tm^{3+} excitation (pumping to the $^3F_4$ state). The luminescence was detected at two wavelengths corresponding to almost pure Tm^{3+} and Ho^{3+} emissions. The measured luminescence decay curves from the $^3F_4$ Tm^{3+} and $^5I_7$ Ho^{3+} manifolds plotted on a semi-log scale are shown in Figure III.18. In the initial time frame, a rapid rise of the Ho^{3+} emission intensity and, at the same time, a corresponding fast drop in the Tm^{3+} luminescence intensity are observed within a few hundred of microseconds, as mentioned in Chapter I.3.

The parameters of the bidirectional $^3F_4(Tm^{3+}) \leftrightarrow {}^5I_7(Ho^{3+})$ energy-transfer were estimated using the dynamical model developed by [Wal00]. The luminescence decay curves were fitted using Eqs. I.67-68. The best-fit curves are shown in Figure III.18. The corresponding fit parameters are $\tau = 3.5 \pm 0.5$ ms, $P_{28} = 1.30 \pm 0.03 \times 10^{-22}$ $cm^3 \mu s^{-1}$ and $P_{71} = 0.99 \pm 0.03 \times 10^{-23}$ $cm^3 \mu s^{-1}$. The ratio of the energy-transfer parameters, Eq. I.65, amounts to 0.076 confirming the predominantly direct $Tm^{3+} \rightarrow Ho^{3+}$ energy-transfer. The Θ value for the Tm,Ho:$GdScO_3$ crystal is close to the one for Tm,Ho:$LiYF_4$ (Θ = 0.076) [Wal00], another well-known crystal for 2.1-μm lasers, and is lower than for Tm,Ho:$Y_3Al_5O_{12}$ (Θ = 0.120) [Wal00].

The equilibrium constant for a Tm^{3+},Ho^{3+}-codoped crystal can be independently estimated from the crystal-field splitting of Tm^{3+} and Ho^{3+} multiplets involved in the energy-transfer using Eq. I.76. The partition functions used in this equation were calculated using the experimental Stark splitting for Tm^{3+} and Ho^{3+} in $GdScO_3$ determined in the present work (see below):

$z_1 = 4.967$, $z_2 = 5.213$ (Tm^{3+}) and $z_7 = 7.249$, $z_8 = 7.530$ (Ho^{3+}). From Eq. I.66, we arrive at $\Theta = 0.054$ which is smaller than the value determined from the luminescence decay studies. Eq. I.76 considers only energy transfers between nearly resonant Stark sub-levels, while the Θ value obtained from the measured luminescence decay curves also encompasses phonon-assisted processes where phonons bridge the energy gap for non-resonant energy transfer.

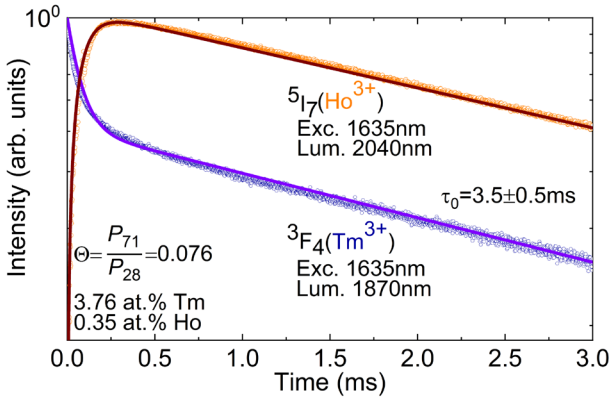

Figure III.18. Luminescence decay curves from the $^3F_4$ Tm^{3+} and $^5I_7$ Ho^{3+} manifolds measured under resonant Tm^{3+} excitation ($\lambda_{exc} = 1635$ nm), *circles* – experimental data, *curves* – their fits using Eqs. I.67-68, τ_0 – thermal equilibrium decay time.

III.2.F. Polarized low-temperature spectroscopy of Tm^{3+} and Ho^{3+} ions

The dopant trivalent RE ions (Tm^{3+} and Ho^{3+}, in our case) in $GdScO_3$ predominantly substitute for the Gd^{3+} host-forming cations in C_s symmetry sites with an VIII-fold oxygen coordination (Wyckoff: 4*c*). The corresponding ionic radii are $R_{Gd} = 1.053$ Å, $R_{Tm} = 0.994$ Å and $R_{Ho} = 1.015$ Å. The Sc^{3+} sites (Wyckoff: 4*b*) feature a VI-fold oxygen coordination ($R_{Sc} = 0.745$ Å). The $^{2S+1}L_J$ multiplets with an integer total angular momentum J are split into $2J + 1$ Stark components within the C_s monoclinic crystal-field symmetry. In the present work, we determined the crystal-field splitting of the two lowest multiplets of Tm^{3+} ($^3H_6$ and $^3F_4$) and Ho^{3+} ($^5I_8$ and $^5I_7$) in $GdScO_3$ as they are relevant for describing the laser emission properties around 2 μm and energy-transfer between these two dopant ions.

The low-temperature (LT, 12 K) absorption and luminescence spectra corresponding to the $^3H_6 \leftrightarrow {}^3F_4$ Tm^{3+} and $^5I_8 \leftrightarrow {}^5I_7$ Ho^{3+} transitions were measured for singly Tm^{3+}-doped and Tm^{3+},Ho^{3+}-codoped $GdScO_3$ crystals, respectively, using linearly polarized light, as shown in Figure III.19. The LT absorption spectra were used to resolve the crystal-field splitting of the RE^{3+} excited-states and they are plotted vs. the photon energy (expressed in cm^{-1}). The LT emission spectra were measured to determine the Stark sub-level energies of the RE^{3+} ground-states and they are plotted as a function of (E_{ZPL} – photon energy), expressed in cm^{-1}. For labelling electronic transitions, we used the following phenomenological notations for Stark sub-levels: Y_i, Z_j, Y_k, Z_l for the $^3F_4$ ($I = 1$ - 9), $^3H_6$ ($j = 1$ - 13), $^5I_7$ ($k = 1$ - 15), and $^5I_8$ ($l = 1$ - 17) multiplets, respectively [Gru64, Raj67]. For the assignment of the electronic transitions of Tm^{3+} and Ho^{3+} ions in $GdScO_3$, we followed the previous work on the isostructural $GdAlO_3$ crystal (sp. gr. *Pnma*) doped with Tm^{3+} and Ho^{3+} ions (Gd^{3+} site symmetry: C_s). The vertical dashes in Figure III.19 mark the electronic transitions for these reference crystals.

Figure III.20 presents the determined experimental crystal-field splitting of the ($^3H_6$ and $^3F_4$) Tm^{3+} and ($^5I_8$ and $^5I_7$) Ho^{3+} multiplets in $GdScO_3$. The ZPL energies E_{ZPL} are 5712 cm^{-1} (Tm^{3+}) and 5110 cm^{-1} (Ho^{3+}). The total Stark splitting of the ground-state amounts to $\Delta E(^3H_6)$ = 681 cm^{-1} (Tm^{3+}) and $\Delta E(^5I_8)$ = 382 cm^{-1} (Ho^{3+}). Table III.1 lists the experimental Stark sub-level energies for the considered multiplets.

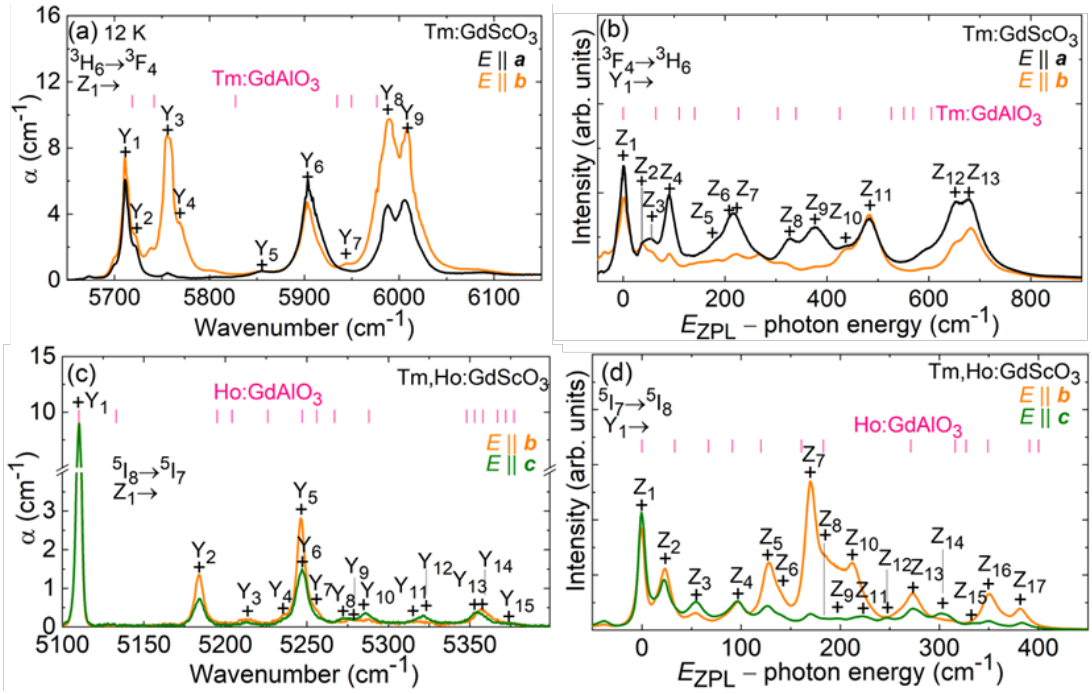

Figure III.19. Low-temperature (12 K) spectroscopy of Tm^{3+} and Ho^{3+} ions in the $GdScO_3$ crystal: (a,c) absorption spectra: (a) the $^3H_6 \rightarrow {}^3F_4$ Tm^{3+} transition; (c) the $^5I_8 \rightarrow {}^5I_7$ Ho^{3+} transition; (b,d) luminescence spectra: (c) the $^3F_4 \rightarrow {}^3H_6$ Tm^{3+} transition; (d) the $^5I_7 \rightarrow {}^5I_8$ Ho^{3+} transition, "+" indicate the assigned electronic transitions. *Vertical dashes* – experimental Stark splitting for Tm^{3+} and Ho^{3+} ions in C_s sites in the $GdAlO_3$ crystal (after [Ars72, Ars72a]).

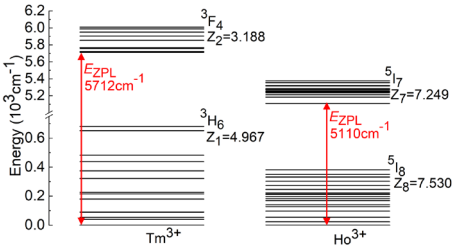

Figure III.20. Experimental crystal-field splitting of two lowest multiplets of Tm^{3+} and Ho^{3+} ions in the $GdScO_3$ crystal. E_{ZPL} – zero-phonon line, z_1, z_2, z_7 and z_8 are the partition functions of the $^3H_6$, $^3F_4$ Tm^{3+} and $^5I_7$, $^5I_8$ Ho^{3+} multiplets, respectively.

Table III.1. Experimental Crystal-Field Splitting of the $^3H_6$, $^3F_4$,Tm^{3+} and $^5I_8$, $^5I_7$ Ho^{3+} Multiplets in the $GdScO_3$ crystal

Ion	$^{2S+1}L_J$	Energy E, cm^{-1}
Tm^{3+}	$^3H_6$	0; 40; 54; 90; 180; 216; 226; 321; 374; 438; 482; 652; 681
	$^3F_4$	5712; 5721; 5756; 5767; 5853; 5904; 5950; 5988; 6009
Ho^{3+}	$^5I_8$	0; 23; 55; 97; 128; 140; 170; 183; 197; 212; 222; 246; 273; 303; 332; 350; 382
	$^5I_7$	5110; 5184; 5212; 5236; 5246; 5247; 5256; 5273; 5276; 5285; 5316; 5321; 5354; 5356; 5375

III.2.G. Efficient Tm,Ho:$GdScO_3$ laser at 2.1 μm

The 3.76 at.% Tm and 0.35 at.% Ho crystal was placed within a laser cavity to assess its laser performance at 2.1 μm. For this laser experiment, the same laser set-up was used as in Chapter II.1. The transmission of the PM was 80% at the pump wavelength of 790 nm. A series OCs with a transmission at the laser wavelength T_{OC} ranging from 0.1% to 10% was used. The rectangular laser element was cut from the 3.76 at.% Tm, 0.35 at.% Ho:$GdScO_3$ crystal for light propagation along the ***a***-axis (***a***-cut) with a thickness of 3.1 mm and an aperture of 3.0(***b***) × 3.0(***c***) mm^2. It was polished to laser quality on both sides, with good parallelism, and left uncoated. The crystal was placed near the PM with a small air gap of less than 1 mm. The geometric cavity length was ~99 mm. The pump power was adjusted by a half-wave plate with the polarization fixed by a polarizer to be ***E*** || ***b*** in the crystal. The pump radiation was focused into the crystal AR-coated aspherical lens with a focal length f of 75 mm. The diameter of the pump spot $2\omega_p$ was 70 ± 10 μm. The pumping was done in a double-pass configuration due to the non-negligible reflectance of the OCs at 0.79 μm. The pump absorption efficiency under lasing conditions was weakly dependent on the output coupling and amounted to ~82%.

The Tm,Ho:$GdScO_3$ laser generated a maximum output power of 1.16 W at ~2067 and 2099 nm (dual-band emission) with a slope efficiency η of 50.5% (relative to the absorbed pump power) at the maximum absorbed pump power of 2.60 W for an intermediate T_{OC} of 5%, as illustrated in Figure III.21(a). The optical efficiency was 29.1% (relative to the pump power incident on the crystal). Upon increasing the output coupling from 0.1% to 10%, there was a gradual rise in the laser threshold from 52 to 290 mW. The input-output dependences were linear within the investigated range of pump powers, and no indications of unwanted thermal effects or thermal fracture of the crystal were detected.

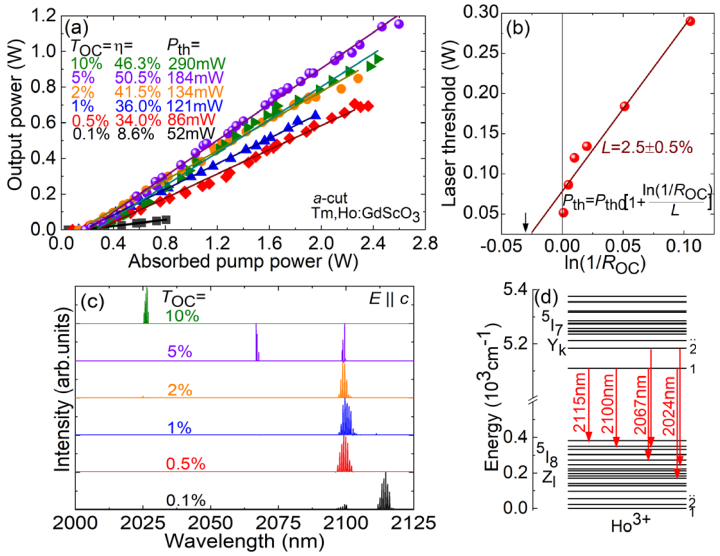

Figure III.21. Tm,Ho:$GdScO_3$ laser: (a) input-output dependences for various output coupling, ***a***-cut crystal, η – slope efficiency, P_{th} – threshold pump power; (b) Findlay-Clay analysis for evaluating the round-trip passive losses L; (c) typical spectra of laser emission measured well above the laser threshold, the laser polarization is ***E*** || ***c***; (d) experimental crystal-field splitting of the $^5I_7$ and $^5I_8$ Ho^{3+} manifolds, *arrows* indicate the observed laser transitions.

The round-trip passive losses L in the Tm,Ho:$GdScO_3$ laser were evaluated by the Findlay-Clay analysis, i.e., by plotting the laser threshold power P_{th} vs. $\ln(1/R_{OC})$ where $R_{OC} = 1 - T_{OC}$ is the OC reflectivity, see Figure III.21(b). This yields $L = 2.5 \pm 0.5\%$, well below the Fresnel loss at the uncoated crystal surfaces owing to etalon effects. The theoretical slope efficiency of the Ho laser is calculated as $\eta = \eta_{St,L} \times \eta_q \times \eta_{OC} \times \eta_{mode}$, where $\eta_{St,L} = \lambda_P/\lambda_L$ is the Stokes efficiency under lasing conditions, λ_P and λ_L are the pump and laser wavelengths, respectively, η_q is the quantum efficiency which can reach 2 assuming a very efficient cross-relaxation for Tm^{3+} ions and efficient $Tm^{3+} \rightarrow Ho^{3+}$ energy transfer, $\eta_{OC} = \ln(1 - T_{OC})/\ln[(1 - T_{OC})\times(1 - L)]$ is the output-coupling efficiency and η_{mode} is the mode-matching efficiency. For $T_{OC} = 5\%$, the result is $\eta = 51.2\%$ which is just above the measured slope efficiency.

Typical laser emission spectra measured well above the laser threshold, are depicted in Figure III.21(c). For a very low T_{OC} of 0.1%, the laser operated across a wide spectral range of 2097 – 2117 nm. For T_{OC} between 0.5% and 2%, the emission occurred at ~2.10 µm. Upon increasing T_{OC} to 5% and 10%, the laser wavelength switched to 2.066 and 2.026 µm, respectively. For all studied OCs, the laser operated solely on the $^5I_7 \rightarrow {}^5I_8$ Ho^{3+} transition without Tm^{3+} colasing confirming the properly selected Ho/Tm codoping ratio. The observed progressive blue-shift in the laser spectra can be attributed to the quasi-three-level nature of the $^5I_7 \rightarrow {}^5I_8$ Ho^{3+} laser transition. For all the studied OCs, the laser emission was linearly polarized ($\boldsymbol{E} \parallel \boldsymbol{c}$), and the polarization state was naturally determined by the anisotropy of the gain, as shown in Figure III.17(a). Based on the determined crystal-field splitting of the $^5I_7$ (Y_k) and $^5I_8$ (Z_l) Ho^{3+} multiplets, we assigned the observed laser lines to the $Y_1 \rightarrow Z_{17}$ (2115 nm), Z_{16} (2100 nm), Z_{13} (2067 nm) and Z_7 (2024 nm) electronic transitions, as illustrated in Figure III.21(d).

The polarization behavior of the Tm,Ho:$GdScO_3$ laser was studied in more detail in Figure III.22. By using a rotatory Glan-Taylor prism placed after the OC and the long-pass filter, we measured the polarization state of the output. The polar plot of the normalized laser power transmitted through the polarizer P vs. its orientation θ ($\theta = 0$ for horizontal polarization, along the $\boldsymbol{b}$-axis) is well fitted using the formula $P_{trans}(\theta) = P_u/2 + P_p\cos^2(\theta - \varphi)$, see Figure III.22(a), where P_u and P_p are the unpolarized and polarized power fractions, respectively, and φ is the preferential orientation of the electric field vector $\boldsymbol{E}$, with $P_u<0.001$ and $\varphi = 90°$ suggesting a linearly polarized light along the $\boldsymbol{c}$-axis. The polarization degree $P = P_p/(P_p + P_u)>99.9\%$. Then, by inserting another AR-coated half-wave plate before the focusing lens, the orientation of the pump polarization E_P was changed between $\boldsymbol{E} \parallel \boldsymbol{b}$ and $\boldsymbol{E} \parallel \boldsymbol{c}$.

The output power of the Tm,Ho:$GdScO_3$ laser was monitored as a function of E_P at a fixed incident pump power and fitted by the formula, $P_{pump}(\theta) = P_{abs//b}\cos^2(\theta - \varphi) + P_{abs//c}\sin^2(\theta - \varphi)$, see Figure III.22(b). The strong absorption anisotropy of Tm^{3+} in $GdScO_3$ at the pump wavelength of 791 nm, as shown in Figure III.16(d), leads to a notable variation of the pump absorption efficiency when rotating the pump polarization and, consequently, a change in the output power of the laser. This analysis confirms the preferential pumping with the $\boldsymbol{E}_P \parallel \boldsymbol{b}$ polarization.

The Tm,Ho:$GdScO_3$ laser generated a nearly circular output beam even at high pump powers. The corresponding 1D intensity distributions were well fitted by a Gaussian profile, as illustrated in Figure III.23(a,b). The laser was operating on the fundamental transverse mode (measured beam quality factors $M^2_{x,y} < 1.05$), leading to good mode-matching efficiency.

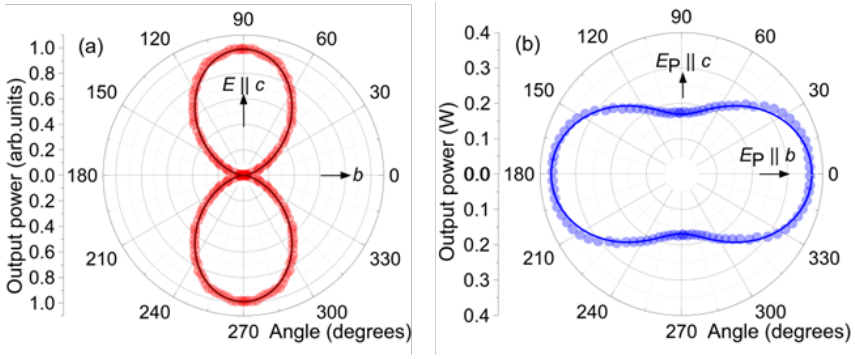

Figure III.22. Polarization behavior of the Tm,Ho:$GdScO_3$ laser based on an ***a***-cut crystal: (a) study of the polarization state of the laser emission (***E*** || ***c***); (b) dependence of output power on the pump polarization E_P in the ***b***-***c*** plane, T_{OC} = 5%, P_{inc} = 1.1 W.

A typical oscilloscope trace of the output emission from the Tm,Ho:$GdScO_3$ laser is shown in Figure III.23(c). It reveals a highly stable CW operation after the spiking following switching on of the pump, and no relaxation oscillations are observed.

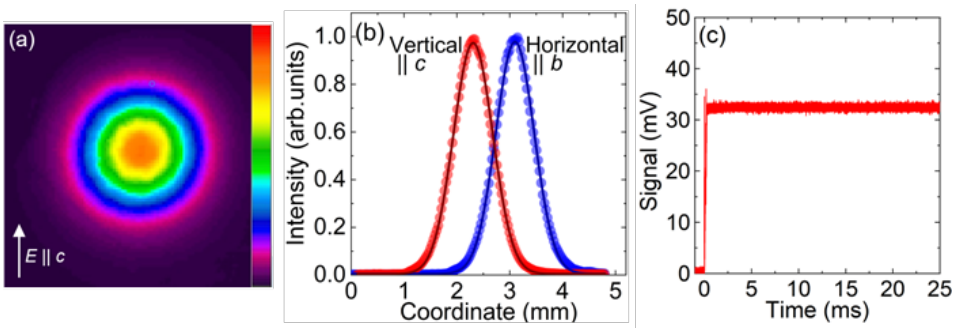

Figure III.23. Spatial and temporal emission characteristics of the Tm,Ho:$GdScO_3$ laser: (a) a typical far-field beam profile; (b) the corresponding 1D intensity distributions (*symbols*) and their Gaussian fits (*curves*); (c) a typical switch-on oscilloscope trace, T_{OC} = 5%, P_{abs} = 2.0 W.

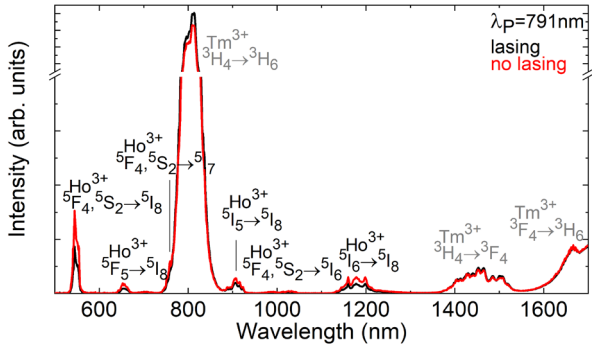

Figure III.24. Spectra of visible and near-IR luminescence (unpolarized emission) from the Tm,Ho:$GdScO_3$ crystal under lasing and non-lasing conditions, λ_P = 791 nm.

The unpolarized spectra of visible and near-IR luminescence from the Tm,Ho:$GdScO_3$ crystal were measured under lasing and non-lasing conditions, see Figure III.24. The spectra are dominated by intense Tm^{3+} emission from the pump manifold according to the $^3H_4 \rightarrow {}^3H_6$ transition, observed at 0.8 μm. The upconversion emissions are solely attributed to Ho^{3+} ions indicating an efficient $Tm^{3+} \rightarrow Ho^{3+}$ energy transfer draining the population of the Tm^{3+} metastable state ($^3F_4$). In the visible, intense upconversion luminescence is observed in the green (the $^5F_4 + {}^5S_2 \rightarrow {}^5I_8$ transition, at 544 nm) and red (the $^5F_5 \rightarrow {}^5I_8$ transition, at 654 nm). Under lasing conditions, the intensity of Ho^{3+} upconversion luminescence is notably decreased compared to the case without lasing due to the rapid depopulation of the metastable $^5I_7$ Ho^{3+} state by the lasing process ($^5I_7 \rightarrow {}^5I_8$). In contrast, the intensity of Tm^{3+} emissions changes only marginally.

Diode-pumped laser operation. For the diode-pumped laser performance, the same cavity was employed and the crystal was passively cooled like for the Ti:Sapphire pumped laser study. A fiber-coupled (core diameter: 105 μm, numerical aperture: 0.22) AlGaAs laser diode module from DILAS was used as pump source. The pump laser wavelength was at ~786 nm at low power and ~788 nm at high power (6 W). The emission wavelength of the laser-diode was stabilized by fixing the diode temperature with circulating water. The laser pump beam was focused into the crystal through the PM with an AR coated lens assembly (reimaging ratio 1:1, focal length of 50 mm). The pump spot size in the focus amounted to $2w_p = 105 \pm 10$ μm. To reduce the thermal detrimental effects within the crystal, the pump beam was modulated using a mechanical chopper with a duty cycle: 1:4. The total cavity length was 100.5 mm.

The input-output dependences and typical laser emission spectra are shown in Figure III.25. The Tm,Ho:$GdScO_3$ laser generated a maximum output power of 679 mW at ~2097 nm with a slope efficiency η of 15.8% (relative to the absorbed pump power) at the maximum absorbed pump power of 4.54 W for an intermediate T_{OC} of 1%, as illustrated in Figure III.25(a). Upon increasing the output coupling from 0.1% to 5%, there was a gradual rise in the laser threshold from 40 to 680 mW. The input-output dependences were linear within the investigated range of pump powers, and no indications of unwanted thermal effects or thermal fracture of the crystal were detected.

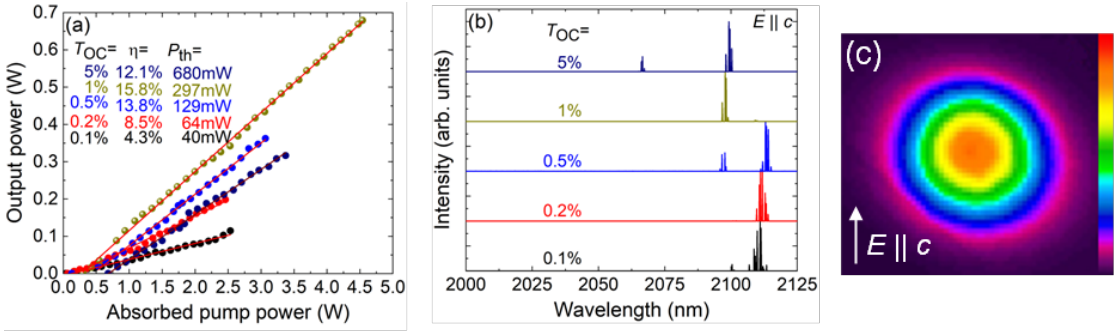

Figure III.25. Diode-pumped Tm,Ho:$GdScO_3$ laser: (a) input-output dependences; (b) typical spectra of laser emission measured well above laser threshold, the laser polarization is $E \parallel c$; (c) a typical far-field beam profile.

Typical laser emission spectra measured well above the laser threshold, are depicted in Figure III.25(b). When T_{OC} increases from 0.2% to 0.5%, the laser emission is experienced a red-shift. Upon increasing T_{OC} to 1% and 5% the emission shifted to shorter wavelengths. For 5% OC, the laser operated in the wide range from 2099 nm to 2066 nm. For all studied OCs, the laser operated solely on the $^5I_7 \rightarrow {}^5I_8$ Ho^{3+} transition without Tm^{3+} colasing

The Tm,Ho:$GdScO_3$ laser generated a nearly circular output beam even at high pump powers. Figure III.25(c) shows typical far-field beam profile. The laser was operating on the fundamental transverse mode, leading to good mode-matching efficiency.

To summarize, Tm^{3+},Ho^{3+}-codoped gadolinium orthoscandate ($GdScO_3$) perovskite-type crystals are promising candidates as laser sources emitting around 2.1 μm due to their intense and broad absorption around 0.8 μm, broadband and polarized emission properties, predominantly unidirectional $Tm^{3+} \rightarrow Ho^{3+}$ energy transfer, and a relatively large Stark splitting of the Tm^{3+} and Ho^{3+} ground manifolds attributed to the low-symmetry distortion in the local symmetry of the activator center. Through low-temperature absorption and fluorescence spectroscopy, we fully resolved the crystal-field splitting of the two lowest manifolds of Tm^{3+} and Ho^{3+} ions. Our studies suggest that both rare-earth ions reside in a single type of site (A-sites of the perovskite structure, C_s symmetry), and indicate that the spectral line broadening at room temperature mainly originates from homogeneous (thermal) broadening due to the electron-phonon interaction rather than some inhomogeneous mechanism. Highly efficient, low-threshold, and power-scalable continuous-wave laser operation of the Tm,Ho:$GdScO_3$ crystal was achieved. Given their attractive spectroscopic properties, Tm,Ho:$GdScO_3$ crystals hold promise for sub-100 fs pulse generation from mode-locked lasers

III.3. Triply doped (Yb^{3+}, Ho^{3+}, Eu^{3+}) calcium niobium gallium garnets

In the previous sections of this chapter, we considered different pumping scheme to achieve Ho laser emission at 2 µm, *e.g.*, in-band pumping directly into the $^5I_7$ laser level and through an energy transfer between Tm and Ho ions. Another way to enhance not only the 2.1 µm laser emission but also the 2.9 µm one exists through an energy-transfer between Yb and Ho ions. Therefore, in this section, we studied the structure and spectroscopic properties of Yb^{3+},Ho^{3+} and Yb^{3+},Ho^{3+},Eu^{3+} codoped calcium niobium gallium garnet crystals with the goal of developing materials with broadband emission properties around 2.1 µm and 2.9 µm. We also present the first laser operation of Yb,Ho:CNGG crystals on the $^5I_7 \rightarrow {}^5I_8$ transition. The influence of Eu^{3+} doping on the luminescence lifetime of the $^5I_6$ and $^5I_7$ laser levels is also discussed.

III.3.A. Crystal growth

A series of Yb^{3+},Ho^{3+},Eu^{3+}-codoped calcium niobium gallium garnet crystals (shortly Yb,Ho,Eu:CNGG) was grown by the Cz method, as summarized in Table III.2 for the initial doping levels. The growth was performed at the College of Physics, Qingdao University, Qingdao in China. We describe the growth of a 10 at.% Yb^{3+}, 1 at.% Ho^{3+}, 0.075 at.% Eu^{3+}-codoped crystal (nominal composition, the atomic fractions are indicated with respect to the Ca^{2+} cations). The starting materials, $CaCO_3$ (purity: 4N), Nb_2O_5 (4N), Ga_2O_3 (5N) and RE_2O_3 (RE = Yb, Ho, Eu, 5N) were weighed according to the following chemical formula:

$$3CaCO_3 + 0.84375Nb_2O_5 + 1.8875Ga_2O_3 + 0.15Yb_2O_3 + 0.015Ho_2O_3 + 0.01125Eu_2O_3 =$$

$$Ca_3Nb_{1.6875}Ga_{3.1875}O_{12}\cdot 0.1Yb_3Ga_5O_{12}\cdot 0.01Ho_3Ga_5O_{12}\cdot 0.0075Eu_3Ga_5O_{12} + 3CO_2\uparrow.$$

To compensate the volatilization of Ga_2O_3 during the synthesis of the polycrystalline material and the crystal growth, an excess of 1.0 wt% Ga_2O_3 was added. The raw materials were first mixed during 24 h and heated at 1173 K in a Pt crucible for 10 h to decompose $CaCO_3$. After cooling to room temperature (RT, 293 K), the mixture was ground to powder, mixed for 24 h and pressed into pellets and reheated at 1373 K for 15 h to synthesize the Yb,Ho,Eu:CNGG polycrystalline material. The growth process was performed with a Pt crucible in ambient atmosphere. The seed was cut from an Yb:CNGG crystal along the [111] crystallographic direction. The pulling rate was 0.5 - 3.0 mm/h and the rotation speed was 5 - 20 rpm. For comparison, we have also used two Yb^{3+},Ho^{3+}-codoped crystals (Table III.2). The description of the crystal growth can be found elsewhere [Zho21].

A photograph of an as-grown Yb,Ho,Eu:CNGG crystal boule is shown in Figure III.26. It has a cylindrical shape with a uniform cross-section in the central part of the boule (diameter: 25 mm, length: 30 mm). The cross-section is circular, which is typical for the Cz method. The crystal boule is transparent and neither cracks nor inclusions are observed. The as-grown crystal shows a slight yellow coloration due to the absorption of color centers in the visible related to cationic vacancies, a typical behavior for CNGG-type crystals [Pan21a].

The actual concentrations of Yb^{3+} and Ho^{3+} ions were measured using Inductively-Coupled Plasma Mass Spectrometry (ICP-MS, Agilent), Table III.2. The Eu^{3+} doping level was below the sensitivity limit of the used equipment. For the above-described crystal, the actual doping levels

are 11.5 at.% Yb^{3+} and 1.25 at.% Ho^{3+} corresponding to the ion densities $N_{Yb} = 14.1\times10^{20}$ cm^{-3} and $N_{Ho} = 1.54\times10^{20}$ cm^{-3}, respectively. The segregation coefficients for Yb^{3+} and Ho^{3+} ions, $K_{RE} = C_{crystal}/C_{melt}$, amount to 1.15 and 1.25, respectively. The determined K_{RE} values are almost independent of the initial crystal composition.

Figure III.26. A photograph of an as-grown Yb,Ho,Eu:CNGG crystal (11.5 at.% Yb^{3+}, 1.25 at.% Ho^{3+}, 0.075 at.% Eu^{3+}), the growth direction is along the [111] axis.

Table III.2. Initial (C_{melt}) and actual ($C_{crystal}$) doping concentrations of rare-earth ions and their segregation coefficients (K_{RE}) for the studied Yb,Ho:CNGG and Yb,Ho,Eu:CNGG crystals.

C_{melt}, at.%			$C_{crystal}$, at.%		K_{RE}	
Yb	Ho	Eu	Yb	Ho	K_{Yb}	K_{Ho}
10	0.75	-	11.5	0.94	1.15	1.25
10	0.75	0.2	11.5	0.94	1.15	1.25
10	1	-	11.5	1.25	1.15	1.25
10	1	0.075	11.5	1.25	1.15	1.25
10	1	0.2	11.5	1.25	1.15	1.25

III.3.B. Crystal structure and vibronic properties

The phase purity and the crystal structure were confirmed by our colleagues using powder XRD. The measured XRD pattern of the Yb,Ho,Eu:CNGG crystal (11.5 at.% Yb^{3+}, 1.25 at.% Ho^{3+}, 0.075 at.% Eu^{3+}) is shown in Figure III.27, together with the results of the structure refinement by the Rietveld method using the Match3 software (the crystal structure of undoped CNGG [Cas16] was taken as a starting model). Only one phase with a cubic garnet structure (sp. gr. O^{10}_h - $Ia\bar{3}d$, No. 230) is identified. The determined lattice constant equals a = 12.4748(2) Å, the volume of the unit-cell V = 1941.34(4) $Å^3$ (number of the formula units per unit-cell: Z = 2) and the calculated crystal density ρ_{calc} = 5.309 g/cm^3. The following refinement R-factors were obtained: R_{exp} = 2.10% R_{wp} = 6.35%, and the reduced khi-squared $\chi^2 = (R_{wp}/R_{exp})^2$ = 9.18 indicating a relatively good convergence of the fit.

As mentioned above, CNGG is an example of a multicomponent garnet with a chemical formula $Ca_3Nb_{1.5}Ga_{3.5}O_{12}$ = {Ca_3}[$Nb_{1.5}Ga_{0.5}$](Ga_3)O_{12}. For any real doped or undoped crystal, its composition deviates from the stoichiometry. The determined fractional atomic coordinates (x, y, z), the site occupancy factors (O.F.) and the isotropic displacement parameters (B_{iso}) for the Yb,Ho,Eu:CNGG crystal are listed in Table III.3. The dodecahedral sites are occupied by the Ca^{2+} and Yb^{3+}|Ho^{3+}|Eu^{3+} cations (the corresponding O.F. were taken according to the results of the ICP-MS analysis, cf. Table III.2). The Ga^{3+} and Nb^{5+} cations are randomly distributed over two

non-equivalent sites (the octahedral and tetrahedral ones, respectively) that determine the structure disorder.

According to the determined atomic coordinates, we draw a fragment of the crystal structure, Figure III.28. The unit-cell of Yb,Ho,Eu:CNGG contains 160 atoms. The dodecahedral {A} sites are occupied by Ca^{2+} and RE^{3+} ions. When the dopant RE^{3+} ions are incorporated into the CNGG lattice, they are supposed to replace for the Ca^{2+} ones because of the closeness of the corresponding ionic radii for VIII-fold oxygen coordination (R_{Yb} = 0.985 Å, R_{Ho} = 1.015 Å, and R_{Eu} = 1.066 Å, compared with R_{Ca} = 1.12 Å). There are 4 shorter (2.3932(9) Å) and four longer (2.5179(8) Å) interatomic distances in the [Ca|REO_8] polyhedra indicating a distorted dodecahedral coordination. For the [Nb1|$Ga1O_6$] and [Nb2|$Ga2O_4$] polyhedra, the metal-oxygen interatomic distances are 1.9960(2) Å (×6) and 1.8547(8) Å (×4), respectively. In the CNGG structure, each [Nb1|$Ga1O_6$] octahedron is connected with six [Nb2|$Ga2O_4$] tetrahedra, and each [Nb2|$Ga2O_4$] tetrahedron is connected with four [Nb1|$Ga1O_6$] octahedra, and these polyhedra are linked by corner-sharing, which results in the formation of a dodecahedron void, Figure III.28. The Ca^{2+}|RE^{3+} cations occupy the centers of these voids.

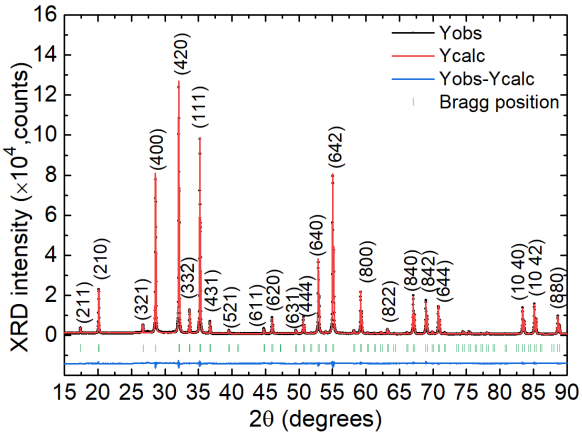

Figure III.27. Rietveld structure refinement of the XRD pattern of the Yb,Ho,Eu:CNGG crystal (11.5 at.% Yb^{3+}, 1.25 at.% Ho^{3+}, 0.075 at.% Eu^{3+}): measured (Y_{obs}, *black*), calculated (Y_{calc}, *red*) and residual ($Y_{obs} - Y_{calc}$, *blue*) patterns, *green dashes* – Bragg reflections, *numbers* denote the Miller's indices, (*hkl*).

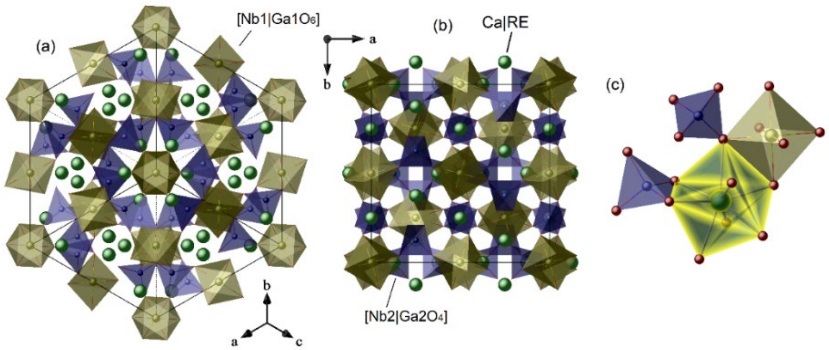

Figure III.28. Crystal structure of Yb,Ho,Eu:CNGG: (a) [111] view; (b) a projection on the *a-b* crystallographic plane; (c) the connection between the polyhedra [Ca|REO_8], [Nb1|$Ga1O_6$] and [Nb2|$Ga2O_4$].

The vibrational properties of Yb,Ho: and Yb,Ho,Eu:CNGG crystals were studied by Raman spectroscopy, Figure III.29. In the range of frequencies from 700 to 900 cm^{-1}, the Raman spectra of CNGG-type crystals show two groups of vibrations usually assigned to symmetric stretching modes (ν_s) of isolated metal-oxygen tetrahedra [$M2O_4$]. The tetrahedral M2 sites are occupied by both Nb^{5+} and Ga^{3+} cations. The peaks at higher frequencies are related to the [$Nb2O_4$] groups and those at lower frequencies – to the [$Ga2O_4$] ones [Vor02, Ser17]. There are two peaks at 827 cm^{-1} (C_4, undistorted [$Nb2O_4$] tetrahedra) and 846 cm^{-1} (C_5, vacancies) and two other peaks at 787 cm^{-1} (C_2, undistorted [$Ga2O_4$] tetrahedra) and 767 cm^{-1} (C_1, vacancies). The structural distortion of the [$M2O_4$] tetrahedra is evidenced by the appearance of satellite peaks due to a nearby cationic vacant position. However, the relative intensity of the satellite C_5 and C_1 peaks is weak indicating a moderate distortion of the [$M2O_4$] tetrahedra. The Raman spectra are weakly dependent on the concentration of Ho^{3+} and Eu^{3+} ions which are relatively low compared to the Yb^{3+} concentration. Compared to undoped CNGG crystals (C_4 = 832 cm^{-1}, C_2 = 763 cm^{-1}), the Yb^{3+} doping induces a frequency shift for both the C_4 and C_2 characteristic peaks.

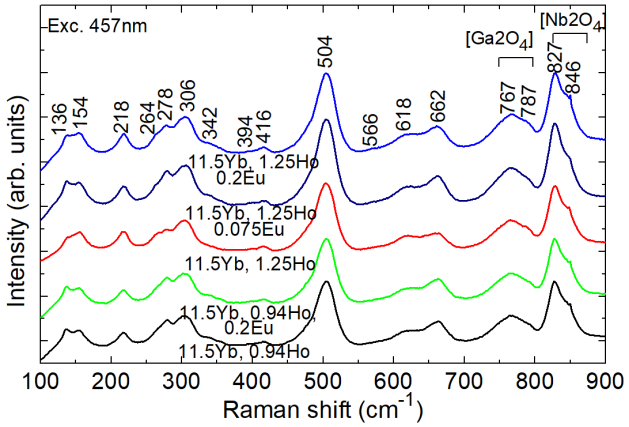

Figure III.29. Unpolarized Raman spectra of Yb,Ho: and Yb,Ho,Eu:CNGG crystals, *numbers* denote the phonon energies in cm^{-1}, λ_{exc} = 457 nm.

Table III.3. Fractional atomic coordinates (*x*, *y*, *z*), occupancy factors (O.F.) and isotropic displacement parameters (B_{iso}) for the Yb,Ho,Eu:CNGG crystal.

Atom	Wyckoff	*x*	*y*	*z*	O.F.	B_{iso}, Å^2
Ca	24*c*	0.1250(0)	0.0000	0.2500(0)	0.872	1.675(0)
Yb	24*c*	0.1250(0)	0.0000	0.2500(0)	0.115	1.675(0)
Ho|Eu	24*c*	0.1250(0)	0.0000	0.2500(0)	0.012|0.001	1.675(0)
Ga1	16*a*	0.0000	0.0000	0.0000	0.3000	0.388(4)
Nb1	16*a*	0.0000	0.0000	0.0000	0.6900	0.388(4)
Nb2	24*d*	0.3750(0)	0.0000	0.2500(0)	0.0970	0.596(0)
Ga2	24*d*	0.3750(0)	0.0000	0.2500(0)	0.9091	0.596(0)
O	96*h*	0.4483(0)	0.1485(4)	1.0294(0)	1.0000	1.851(0)

III.3.C. Absorption and stimulated-emission cross-sections

The absorption spectra of two CNGG crystals both codoped with 11.5 at.% Yb^{3+}, 1.25 at.% Ho^{3+} and containing no Eu^{3+} or 0.075 at.% Eu^{3+} are shown in Figure III.30. The most intense absorption band at ~1 μm is related to the $^2F_{7/2} \rightarrow {}^2F_{5/2}$ transition of Yb^{3+} ions. The narrow peak

at 972.2 nm corresponding to the ZPL has a bandwidth of 2.9 nm and a peak $\sigma_{abs} = 1.48 \times 10^{-20}$ cm^2. At shorter wavelengths, several overlapping broad peaks with maxima at 944.0, 933.4, 927.8 and 920.9 nm appear. The corresponding σ_{abs} is in the range of 0.48 – 0.60 × 10^{-20} cm^2.

The absorption spectrum also contains multiple bands assigned to Ho^{3+} transitions from the ground-state ($^5I_8$) to the excited-states ranging from $^5I_7$ to $^3K_6$. Here, the assignment is according to Carnall *et al.* [Car68]. In particular, the broad absorption band spanning from 1.82 to 2.12 µm is related to the $^5I_8 \rightarrow {}^5I_7$ Ho^{3+} transition. The maximum absorption cross-section for this transition $\sigma_{abs} = 0.51 \times 10^{-20}$ cm^2 lies at 1918 nm.

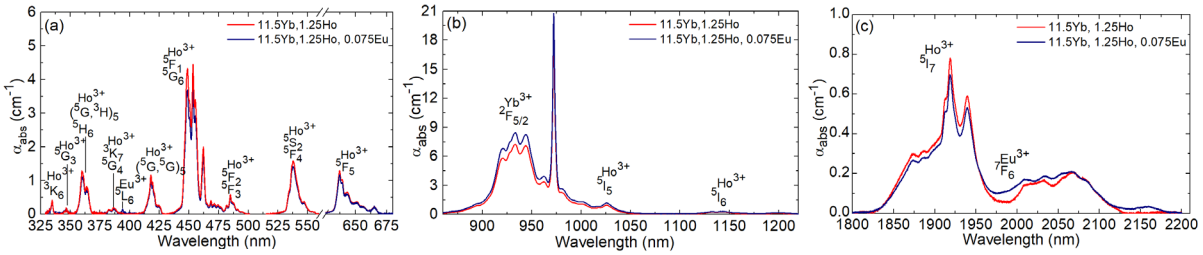

Figure III.30. RT absorption spectra of Yb,Ho: and Yb,Ho,Eu:CNGG crystals: spectral range (a) 325 – 680 nm, (b) 860 – 1220 nm, (c) 1800 – 2200 nm.

A careful comparison of the absorption spectra of the crystals with and without Eu^{3+} ions reveals their spectroscopic signatures. The band in the blue corresponds to the $^7F_{0,1} \rightarrow {}^5L_6$ transition, Figure III.30(a), and a rise of the absorption intensity at 2 – 2.2 µm – to the $^7F_{0,1} \rightarrow {}^7F_6$ one, Figure III.30(c). This indicates the possibility of the $Ho^{3+}(^5I_7) \rightarrow Eu^{3+}(^5F_6)$ energy transfer.

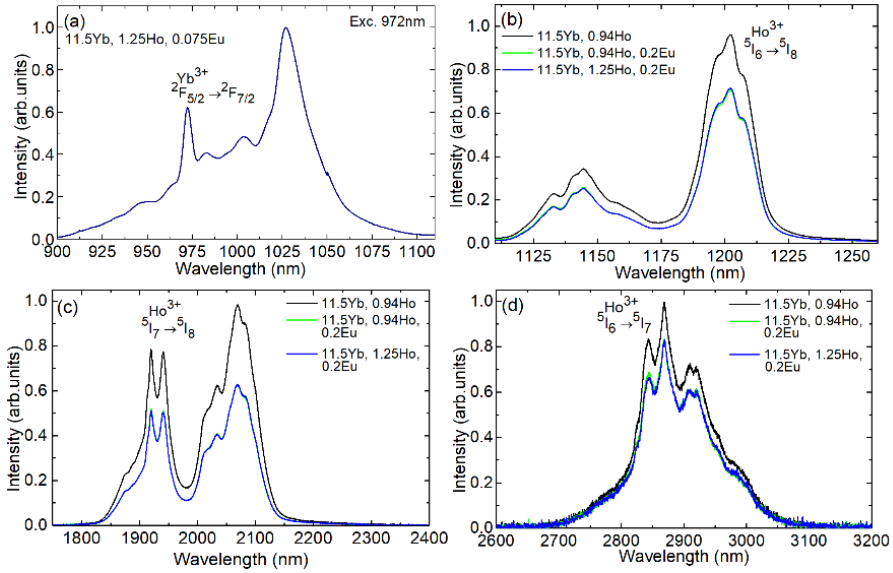

Figure III.31. RT luminescence spectra of Yb,Ho: and Yb,Ho,Eu:CNGG crystals: (a) Yb^{3+} ions, the $^5F_{5/2} \rightarrow {}^5F_{7/2}$ transition, (b) Ho^{3+} ions, the $^5I_6 \rightarrow {}^5I_8$ transition, (c) Ho^{3+} ions, the $^5I_7 \rightarrow {}^5I_8$ transition, (d) Ho^{3+} ions, the $^5I_6 \rightarrow {}^5I_7$ transition, $\lambda_{exc} = 972.1$ nm.

The luminescence spectra of Yb^{3+} and Ho^{3+} ions in the CNGG crystal were measured under excitation at 972 nm (to the $^2F_{5/2}$ Yb^{3+} manifold) as shown in Figure III.31. Figure III.32 shows a scheme of energy-levels of Yb^{3+}, Ho^{3+} and Eu^{3+} ions indicating the relevant spectroscopic processes for the emissions of these species. Yb^{3+} ions exhibit a broad emission band spanning

from 0.9 to 1.1 μm related to the $^2F_{5/2} \rightarrow {}^2F_{7/2}$ transition with a maximum at 1027 nm, Figure III.31(a). The narrow peak at 972.2 nm is related to the ZPL transition in emission.

Three Ho^{3+} emission bands in the IR are observed. The emissions at 1.11 – 1.25 μm with a maximum at 1202 nm and at 2.65 – 3.15 μm with a maximum at 2868 nm originate from transitions from the $^5I_6$ intermediate level to the ground-state ($^5I_8$) and the first excited-state ($^5I_7$), respectively, Figure III.31(b,d). This manifold is populated by a phonon-assisted energy-transfer process from Yb^{3+} ($^2F_{5/2}$) to Ho^{3+}($^5I_6$). The emission at 1.8 – 2.25 μm with a maximum at 2069 nm is assigned, as mentioned before, to the $^5I_7 \rightarrow {}^5I_8$ Ho^{3+} transition, Figure III.31(c).

The luminescence spectra are smooth and broad due to a significant inhomogeneous spectral broadening for the dopant ions (Yb^{3+} and Ho^{3+}) owing to the disordered nature of the CNGG host matrix. The shape of the luminescence spectra of Ho^{3+} ions does not depend on the Eu^{3+} codoping. The intensity of Ho^{3+} luminescence at ~2 μm (the $^5I_7 \rightarrow {}^5I_8$ transition) notably decreases upon the presence of Eu^{3+}, Figure III.31(c), due to its quenching effect on the $^5I_7$ Ho^{3+} manifold. A certain reduction of the luminescence intensity for Eu^{3+}-containing crystals is also observed at ~2.9 μm ($^5I_6 \rightarrow {}^5I_7$ transition), Figure III.31(d), but it is much weaker than in the former case. These observations are in line with lifetime measurements (see below).

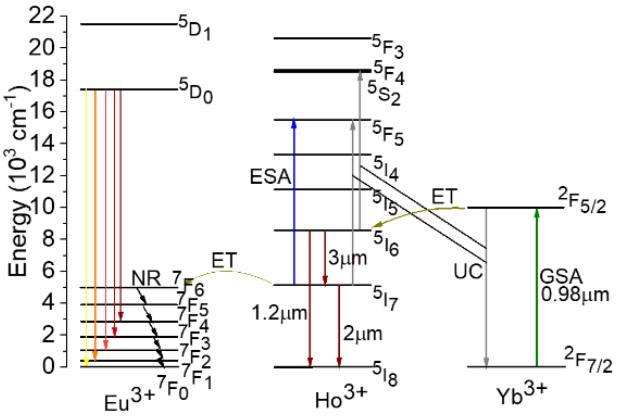

Figure III.32. A simplified scheme of energy-levels of Yb^{3+}, Ho^{3+} and Eu^{3+} ions showing different spectroscopic processes: ET – energy-transfer, GSA and ESA – ground-state and excitation-state absorption, respectively, NR – non-radiative transitions, UC – upconversion.

The luminescence spectra of Eu^{3+} ions in the codoped CNGG crystals are shown in Figure III.33(a), measured under excitation in the blue at 395 nm (to the $^5L_6$ manifold). They contain several bands peaking at 579, 588-594, 610, 653 and 706 nm related to transitions from the metastable state $^5D_0$ to the group of closely located ^7F_J states (where J = 0...4, respectively, $^7F_0$ being the Eu^{3+} ground-state). The most intense emission band at 610 nm is due to the $^5D_0 \rightarrow {}^7F_2$ transition and it corresponds to the well-known red color of Eu^{3+} luminescence. The emission bands are also inhomogeneously broadened. The emission properties of Eu^{3+} ions are known to be sensitive to the site symmetry and its distortion and can be considered as a "structural probe". In particular, the ratio of integrated intensities of the purely electric-dipole (ED) $^5D_0 \rightarrow {}^7F_2$ transition and the purely magnetic-dipole $^5D_0 \rightarrow {}^7F_1$ one, called the asymmetry parameter, R, for Eu^{3+} ions in CNGG is determined to be 2.45. A R value well above 1 indicates

that the Eu^{3+} sites have no center of inversion. This agrees with the structural analysis: the Eu^{3+} ions are expected to replace Ca^{2+} cations in sites with a local symmetry D_2 or lower.

Another interesting feature of Eu^{3+} ions is the $^5D_0 \rightarrow {}^7F_0$ transition which is both ED and MD forbidden. For the studied crystals, only one peak at 579.44 nm is observed in line with a single type of sites for rare-earth ions in CNGG. However, this peak is notably broadened as compared to ordered crystals. This was previously explained by the different ways of arrangements of Nb^{5+} and Ga^{3+} in the nearest to Eu^{3+} tetrahedral and octahedral nodes of the lattice [Vor94].

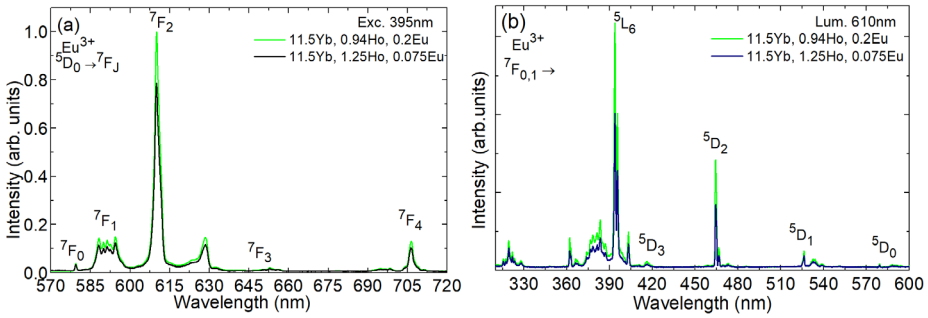

Figure III.33. (a) Luminescence (λ_{exc} = 395 nm) and (b) excitation (λ_{lum} = 610 nm) spectra of Eu^{3+} ions in Yb,Ho,Eu:CNGG crystals at RT.

The excitation spectra for Eu^{3+} ions were also measured, Figure III.33(b). It contains bands related to transitions from the $^7F_{0,1}$ states to different excited-states: $^5D_0$ (~579 nm), $^5D_1$ (~526 nm), $^5D_2$ (~464 nm), $^5D_3$ (416 nm) and $^5L_6$ (394 nm). At shorter wavelengths, the assignment of the absorption peaks is complicated due to the overlapping of several higher-lying ^5L_J, ^5H_J and ^5G_J multiplets. The most intense band in the excitation spectrum centered at 394 nm corresponds to transitions to the $^5L_6$ state in agreement with the absorption spectrum, Figure III.30(a). Note that no Eu^{2+} signatures are observed in the spectra.

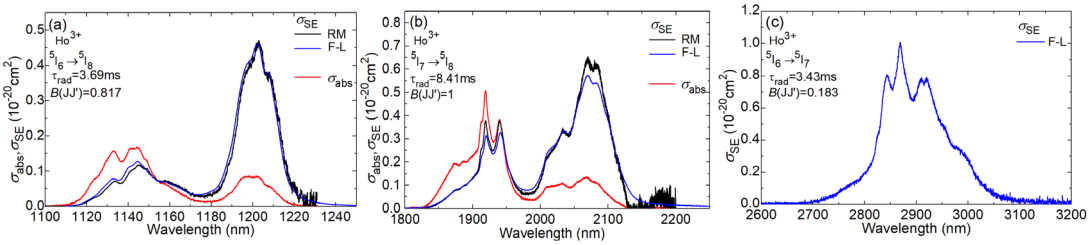

Figure III.34. RT transition cross-section of Ho^{3+} ions in the CNGG crystal: (a,b) absorption, σ_{abs}, and stimulated-emission (SE), σ_{SE}, cross-sections, for the (a) $^5I_6 \rightarrow {}^5I_8$ and (b) $^5I_7 \rightarrow {}^5I_8$ transitions; (c) SE cross-sections, σ_{SE}, for the $^5I_6 \rightarrow {}^5I_7$ transition. RM - reciprocity method, F-L - Füchtbauer-Ladenburg formula, τ_{rad} – radiative lifetime of the emitting state, B(JJ') – luminescence branching ratio [Pan21].

The SE cross-sections, σ_{SE}, for transitions of Ho^{3+} ions in the near- and mid-IR were calculated using the F-L formula, Eq. I.21 and RM, Eq. I.19, methods. To apply these methods several spectroscopic parameters are needed as discussed previously in Chapter I and II. The refractive index of the crystal at the mean emission wavelength is calculated using the dispersion data from [Ser17] while τ_{rad} of the emitting state and B(JJ') were taken from the Judd-Ofelt calculations for Ho^{3+} ions in CNGG [Pan21a]. The measured luminescence spectra were

corrected for the response of the set-up. For the RM method, due to the impossibility to fully resolve the crystal-field splitting for Ho^{3+} ions in CNGG (see below), the crystal-field data of another Ho^{3+} doped gallium garnet, Ho:YGG [Gru09], were used.

For the $^5I_6 \rightarrow {}^5I_8$ Ho^{3+} transition, the maximum SE cross-section is 0.46×10^{-20} cm^2 at 1202 nm, as calculated by the F-L formula using $\tau_{rad}(^5I_6) = 3.69$ ms and $B(JJ') = 81.7\%$, Figure III.34(a). This value agrees very well with that obtained via the RM.

For the $^5I_7 \rightarrow {}^5I_8$ Ho^{3+} transition interesting for laser operation slightly above 2 μm, the maximum σ_{SE} is 0.57×10^{-20} cm^2 at 2070 nm and another intense peak appears at a slightly longer wavelength with $\sigma_{SE} = 0.54 \times 10^{-20}$ cm^2 at 2082 nm, as calculated using the F-L formula with $\tau_{rad}(^5I_7) = 8.41$ ms, Figure III.34(b). Again, a reasonable agreement with the RM is observed considering the effect of reabsorption on the measured luminescence spectrum visible at shorter wavelengths. The emission bandwidth of the band at 2.08 μm is as broad as 83 nm.

For the mid-infrared emission interesting for laser operation at ~3 μm owing to the quasi-four-level $^5I_6 \rightarrow {}^5I_7$ Ho^{3+} transition, the maximum σ_{SE} is 1.01×10^{-20} cm^2 at 2869 nm and at longer wavelengths another two peaks appear at 2910 and 2920 nm corresponding to $\sigma_{SE} = 0.78 \times 10^{-20}$ cm^2, Figure III.34(c). Here, the calculated value is based on the F-L formula with $\tau_{rad}(^5I_6) = 3.69$ ms and $B(JJ') = 18.3\%$.

III.3.D. Luminescence dynamics: revealing the Yb → Ho energy transfer and the quenching mechanism of Eu^{3+} ions

For the luminescence dynamics studies, the crystal samples were finely powdered to avoid the effect of reabsorption (luminescence trapping) on the measured lifetimes. The measured luminescence decay curves for the metastable states of Yb^{3+}, Ho^{3+} and Eu^{3+} ions are shown in Figure III.35 and the corresponding mean luminescence lifetimes τ_{lum} are given in Table III.4. For Yb^{3+} ions, the decay from the $^2F_{5/2}$ excited-state was studied. For singly Yb^{3+}-doped CNGG studied for comparison, $\tau_{lum,0} = 0.978$ ms. For Ho^{3+} codoping with an increased Ho^{3+} content, the $^2F_{5/2}$ lifetime is shortened due to the enhanced efficiency of the $Yb^{3+}(^2F_{5/2}) \rightarrow Ho^{3+}(^5I_6)$ energy-transfer. For 11.5 at.% Yb^{3+}, 1.25 at.% Ho^{3+}, the ET efficiency is estimated as $\eta_{ET} \approx 1 - \tau_{lum}(Yb,Ho)/\tau_{lum,0}(Yb) = 46.5\%$. For the same doping levels of Yb^{3+} and Ho^{3+}.

For Ho^{3+} ions, the luminescence decay from the two lowest lying excited-states, $^5I_6$ and $^5I_7$, was studied under Yb^{3+} excitation. Because of this, the measured kinetics contain both a luminescence rise and a decay. The rise time agrees with the lifetime of the $^2F_{5/2}$ Yb^{3+} state. For the Yb^{3+},Ho^{3+} codoped crystals (without Eu^{3+}), the $^5I_6$ and $^5I_7$ Ho^{3+} lifetimes are weakly dependent on the Ho^{3+} content in the range 0.94 – 1.25 at.% and amount to 0.30 ms and 7.24 ms, respectively. With adding Eu^{3+}, the $^5I_7$ Ho^{3+} lifetime is notably quenched as it amounts only to 3.24 ms for the sample with 1.25 at.% Ho^{3+} and 0.2 at.% Eu^{3+}. This is because of the $Ho^{3+}(^5I_7) \rightarrow Eu^{3+}(^7F_6)$ energy transfer promoted by the resonant location of the corresponding manifolds of the two ions, followed by multiple non-radiative relaxation steps in the system of closely located lower-lying ^7F_J (J = 0 – 6) Eu^{3+} multiplets.

The efficiency of this ET process can be estimated as $\eta_{ET} \approx 1 - \tau_{lum}(Ho,Eu)/\tau_{lum,0}(Ho) = 55.2\%$. Note that even a small addition of Eu^{3+} ions (0.2 at.%) is enough to induce a significant effect on

the $^5I_7$ Ho^{3+} lifetime as the absorption cross-sections for the spin-allowed $^7F_{0,1} \rightarrow {}^7F_6$ Eu^{3+} transitions are relatively high compared to spin-forbidden transitions of Eu^{3+} in the visible spectral range. With Eu^{3+} addition, the lifetime of the $^5I_6$ Ho^{3+} level is also quenched but this effect is much weaker than for its $^5I_7$ counterpart. The lifetime reduction for Ho^{3+} ions upon Eu^{3+} codoping explains the drop in the luminescence intensity from these manifolds as shown in Figure III.31(b-d). Thus, the addition of Eu^{3+} is beneficial for potential laser operation of Yb,Ho,Eu:CNGG crystals at 2.9 μm as it helps to balance the lifetimes of the upper and lower laser levels.

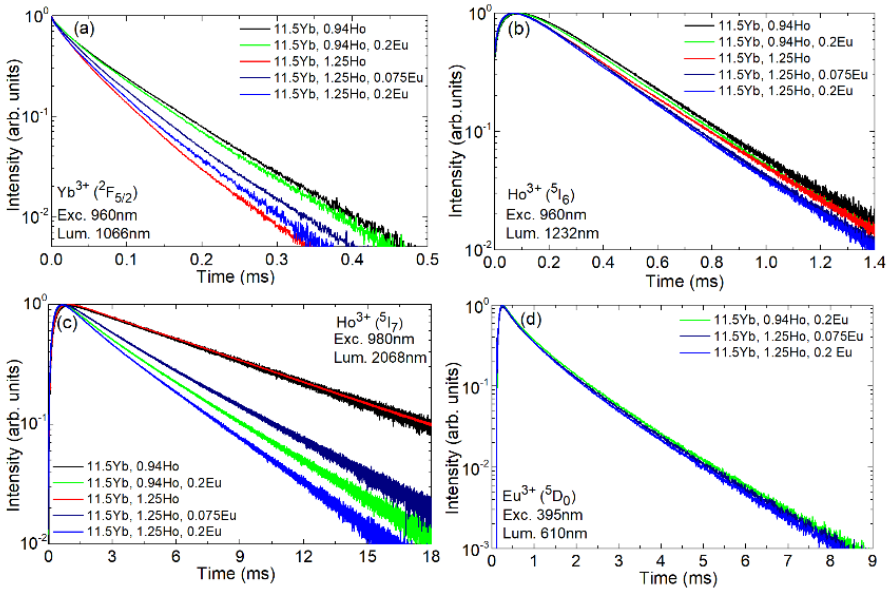

Figure III.35. RT luminescence decay curves for Yb^{3+}, Ho^{3+} and Eu^{3+} ions in the CNGG crystals: (a) the $^2F_{5/2}$ Yb^{3+} state, λ_{exc} = 960 nm, λ_{lum} = 1066 nm, (b) the $^5I_6$ Ho^{3+} state, λ_{exc} = 960 nm, λ_{lum} = 1232 nm, (c) the $^5I_7$ Ho^{3+} state, λ_{exc} = 980 nm, λ_{lum} = 2068 nm and (d) the $^5D_0$ Eu^{3+} state, λ_{exc} = 395 nm, λ_{lum} = 610 nm.

For the Eu^{3+} ions, the lifetime of the metastable $^5D_0$ state was measured under excitation to the higher-lying $^5L_6$ manifold, Figure III.35(d). The luminescence decay curve deviates from a single-exponential law probably due to $Eu^{3+} \rightarrow Ho^{3+}$ and $Eu^{3+} \rightarrow 2Yb^{3+}$ energy-transfers. The mean luminescence lifetime $^5D_0$ $<\tau_{lum}>$ amounts to 0.90 – 0.92 ms.

Table III.4. Measured luminescence lifetimes τ_{lum} of selected excited-states of Yb^{3+}, Ho^{3+} and Eu^{3+} ions in CNGG crystals.

Concentration, at.%			τ_{lum}, ms			
Yb	Ho	Eu	Yb ($^2F_{5/2}$)	Ho ($^5I_6$)	Ho ($^5I_7$)	Eu ($^5D_0$)
11.9	-	-	0.978	-	-	-
11.5	0.94	-	0.80	0.30	7.24	-
11.5	1.25	-	0.52	0.29	7.24	-
11.5	0.94	0.2	0.74	0.29	3.68	0.92
11.5	1.25	0.075	0.63	0.28	4.21	0.91
11.5	1.25	0.2	0.57	0.27	3.24	0.90

III.3.E. Low-temperature spectroscopy of Ho^{3+} ions

The spectroscopic properties of Ho^{3+} ions were studied at LT to resolve the crystal-field splitting of the multiplets involved in the studied near- and mid-IR emissions. The LT absorption spectra for the $^5I_8 \rightarrow {}^5I_7$ and $^5I_6$ transitions are shown in Figure III.36(a,b) giving access to the splitting of the $^5I_7$ and $^5I_6$ excited-states. The LT luminescence spectra for the $^5I_6 \rightarrow {}^5I_8$ and $^5I_7 \rightarrow {}^5I_8$ are shown in Figure III.36(c). Both of them are plotted vs. (photon energy – E_{ZPL}) thus directly giving access to the splitting of the ground-state, $^5I_8$. For the assignment of electronic transitions for Ho^{3+} ions in CNGG, we used the crystal-field data for Ho^{3+} ions in the isostructural YGG garnet [Gru09]. The vertical dashes in Figure III.36 mark the positions of electronic transitions for this reference crystal.

Even at 12 K, the absorption and luminescence spectra of Ho^{3+} ions in CNGG are rather broad revealing a significant inhomogeneous spectral broadening. Note that almost no effect of the excitation wavelength on the measured LT emission spectra was observed. An attempt to determine the energies of individual Stark sub-levels for the $^5I_8$, $^5I_7$ and $^5I_6$ Ho^{3+} multiplets was made, cf. Table III.5. It was assumed that each $^{2S+1}L_J$ multiplet is split into 2J + 1 sub-levels. Still, some experimental energy-levels are missing.

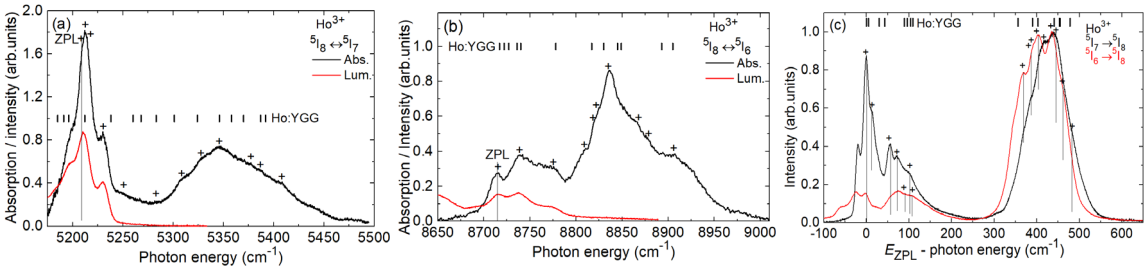

Figure III.36. Low-temperature (LT, 12 K) spectroscopy of Ho^{3+} ions in the CNGG crystal: (a,b) absorption spectra: the $^5I_8 \rightarrow {}^5I_7$ transition; (b) the $^5I_8 \rightarrow {}^5I_6$ transition; (c) luminescence spectra, the $^5I_7 \rightarrow {}^5I_8$ and the $^5I_6 \rightarrow {}^5I_8$ transitions, ZPL – zero-phonon-lines, "+" indicate the assigned electronic transitions, *vertical dashes* – crystal-field splitting for Ho^{3+} ions in the YGG crystal [Gru09].

Table III.5. Energies of Stark sub-levels of the $^5I_8$, $^5I_7$ and $^5I_6$ Ho^{3+} multiplets in CNGG.

Multiplet	Energy, cm^{-1}
$^5I_8$	0; 15; 55; 73; 90; 103; 110; 368; 382; 389; 401; 418; 434; 447; 461; 485 (*1 missing*)
$^5I_7$	5408; 5385; 5376; 5348; 5328; 5311; 5283; 5252; 5206; 5214; 5211; 5208 (*3 missing*)
$^5I_6$	8913; 8881; 8865; 8842; 8826; 8818; 8811; 8780; 8741; 8711 (*3 missing*)

The joint analysis of LT absorption and luminescence spectra as shown in Figure III.36(a) allowed us to determine the positions of the ZPL for the $^5I_8 \rightarrow {}^5I_7$ and $^5I_6$ transitions, namely E_{ZPL} = 5408 cm^{-1} ($^5I_8 \rightarrow {}^5I_7$) and E_{ZPL} = 8913 cm^{-1} ($^5I_8 \rightarrow {}^5I_6$). These values were used for calculating the SE cross-sections via the RM (see above).

III.3.F. Yb,Ho:CNGG laser at 2.1 μm

The laser operation of the Yb,Ho:CNGG crystal on the $^5I_7 \rightarrow {}^5I_8$ Ho^{3+} transition was studied. The crystal codoped with 11.5 at.% Yb^{3+}, 1.25 at.% Ho^{3+} was used. A rectangular sample (thickness:

5.5 mm, aperture: 3.0×3.0 mm^2) was cut along the [111] crystallographic axis. It was double-side polished and left uncoated. A hemispherical laser cavity was used. It was formed by a flat dichroic mirror coated for high transmission (T = 92.5%) at 0.95 μm and high reflection at 1.85 – 2.3 μm and a set of concave OCs having a radius of curvature of -100 mm and a transmission T_{OC} in the range of 0.5% - 10% at 1.95 – 2.1 μm. The cavity length was ~100 mm. The pump source was a Ti:Sapphire laser emitting up to 2.5 W at 950 nm with a nearly diffraction limited beam ($M^2 \sim 1$). The pump radiation was focused into the crystal using an AR-coated lens (f = 75 mm). The pumping was in single pass. The measured pump absorption under lasing conditions was 71.2%. The residual pump was filtered out using a long-pass filter (LP1400, Spectrogon).

The input-output dependences of the Yb,Ho:CNGG laser are shown in Figure III.37(a). The laser generated a maximum output power of 19 mW at 2083-2089 nm with a slope efficiency η of 1.8% (with respect to the absorbed pump power) and a laser threshold of 0.52 W (for T_{OC} = 5%). With increasing the output coupling, the laser threshold gradually increased from 0.29 W (T_{OC} = 0.5%) to 0.63 W (T_{OC} = 10%). The input-output dependences were linear in the studied range of pump powers.

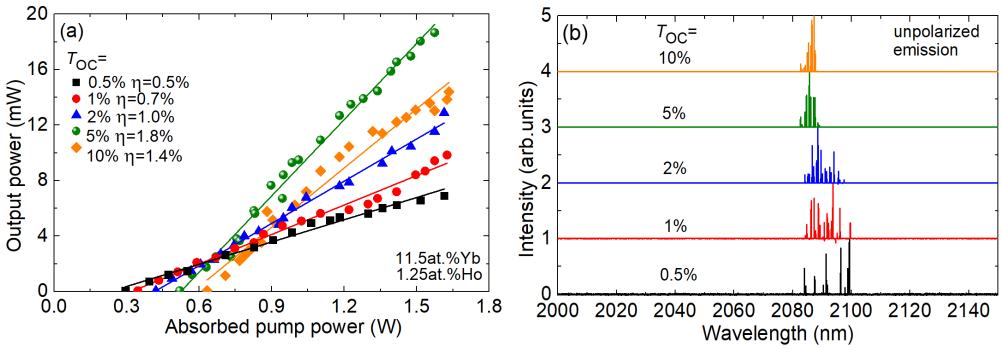

Figure III.37. Yb,Ho:CNGG laser operating on the $^5I_7 \rightarrow {}^5I_8$ Ho^{3+} transition: (a) input-output dependences, η – slope efficiency; (b) typical spectra of unpolarized laser emission. 11.5 at.% Yb^{3+}, 1.25 at.% Ho^{3+}:CNGG crystal, pump wavelength: 950 nm.

The typical spectra of the laser emission are shown in Figure III.37(b). The laser operated at ~2.09 μm (the $^5I_7 \rightarrow {}^5I_8$ Ho^{3+} transition) and the spectra experienced a slight blue shift with increasing the output coupling, from 2083 – 2099 nm (T_{OC} = 0.5%) to 2082 – 2087 nm (T_{OC} = 10%). The laser emission was unpolarized. The CW laser exhibits relaxation oscillations typical for ~2 μm Tm^{3+} and Ho^{3+} lasers. The laser operated on the fundamental transverse mode.

To conclude, Yb^{3+},Ho^{3+} and Yb^{3+},Ho^{3+},Eu^{3+} codoped CNGG crystals are attractive as broadband gain media for laser emitting at 2.1 μm (the $^5I_7 \rightarrow {}^5I_8$ Ho^{3+} transition) and 2.9 μm (the $^5I_6 \rightarrow {}^5I_7$ Ho^{3+} transition). A significant inhomogeneous broadening of absorption and emission bands of rare-earth ions in these crystals well preserved even at low temperatures (12 K) is due to the structure disorder originating from a random distribution of Ga^{3+} and Nb^{5+} cations over two different lattice sites, octahedral and tetrahedral ones. The Ho^{3+} ions in CNGG crystals exhibit relatively long luminescence lifetimes of the two lowest excited-states interesting for laser operation, namely 7.24 ms ($^5I_7$) and 0.30 ms ($^5I_6$). The Yb^{3+},Ho^{3+} codoping promotes the $Yb^{3+}(^2F_{5/2}) \rightarrow Ho^{3+}(^5I_6)$ energy transfer but its efficiency ($\eta_{ET} \approx 46.5\%$ for 11.5 at.% Yb^{3+}, 1.25 Ho^{3+}) can be further optimized by adjusting the Yb^{3+}/Ho^{3+} ratio. The Eu^{3+} codoping leads to the

quenching of the $^5I_7$ Ho^{3+} lifetime due to the $Ho^{3+}(^5I_7) \rightarrow Eu^{3+}(^7F_6)$ energy-transfer followed by multiphonon non-radiative relaxation between the group of closely located ^7F_J (J = 0 – 6) Eu^{3+} manifolds which is favorable for laser operation on the $^5I_6 \rightarrow {}^5I_7$ Ho^{3+} transition impaired by its self-terminating nature. We report on the first laser operation of an Yb^{3+},Ho^{3+} codoped CNGG crystal at 2.1 μm (the $^5I_7 \rightarrow {}^5I_8$ Ho^{3+} transition): pumping at 950 nm, a maximum continuous-wave output power of 19 mW is achieved at 2083-2089 nm with a laser threshold of 0.52 W. Further power scaling is expected via (i) optimizing the Yb^{3+}/Ho^{3+} codoping ratio for better $Yb^{3+} \rightarrow Ho^{3+}$ ET and (ii) using diode-pumping.

Conclusions of Chapter III

In this chapter, we presented a detailed spectroscopic study and characterization of the laser properties of several disordered crystals. These include aluminate $CaGdAlO_4$, multicomponent garnet $Ca_3Nb_{1.5}Ga_{3.5}O_{12}$, and gadolinium scandate $GdScO_3$, all doped with Ho^{3+} ions. Our findings indicate that these crystals are attractive gain materials for broadly tunable and mode-locked lasers emitting at 2.1 μm. The conclusions are as follows.

• $CaGdAlO_4$ crystals doped with Ho^{3+} ions demonstrate a significant inhomogeneous broadening of the spectral bands induced by the structure disorder, a strong polarization-anisotropy of emission properties of dopant ions. The combination of high Ho^{3+} doping concentrations and the relatively long length of the crystal enhances laser performance in a low-inversion regime, maximizing the absorption efficiency and gain, when Ho:$CaGdAlO_4$ laser tends to operate on the longest-wavelength electronic transition with a non-negligible contribution of the phonon-terminating mechanism. In the latter case, the gain bandwidth is as broad as ~50 nm supporting generation of much shorter pulses in the mode-locked regime.

Moreover, Ho:$CaGdAlO_4$ crystals have the potential for 3-μm lasers since they possess high stimulated-emission cross-sections and relatively low phonon energies (among oxide crystals), which leads to a weak non-radiative path from the $^5I_6$ upper laser level. Codoping with Pr^{3+} ions will result in the quenching of the long luminescence lifetime of the $^5I_7$ lower laser level, thereby supporting the generation of 3 μm lasers.

• Tm^{3+},Ho^{3+}-codoped $GdScO_3$ perovskite-type crystals are attractive for laser sources emitting around 2.1 μm due to their intense and broad absorption around 0.8 μm, broadband and polarized emission properties, predominantly unidirectional $Tm^{3+} \rightarrow Ho^{3+}$ energy transfer, and relatively large Stark splitting of the Tm^{3+} and Ho^{3+} ground manifolds due to low-symmetry distortion in the local symmetry of the activator center. By employing low-temperature absorption and emission spectroscopy, the crystal-field splitting of the two lowest manifolds of Tm^{3+} and Ho^{3+} ions were fully resolved. Our studies suggest that both rare-earth ions reside in a single type of site and that spectral line broadening at room temperature mainly originates from homogeneous (thermal) broadening due to electron-phonon interaction rather than an inhomogeneous mechanism. Highly efficient, low-threshold, and power-scalable to Watt-level continuous-wave laser operation of the Tm,Ho $GdScO_3$ crystal was achieved.

• $Ca_3Nb_{1.5}Ga_{3.5}O_{12}$ crystals: Ho^{3+} emission at 2.1 μm was enhanced by codoping with Yb^{3+} ions through $Yb^{3+} \rightarrow Ho^{3+}$ energy transfer. Due to the energy transfer, the first laser operation of an Yb^{3+},Ho^{3+} codoped $Ca_3Nb_{1.5}Ga_{3.5}O_{12}$ crystal at 2.1 μm was achieved, but with low maximum output power. Further power scaling is expected via diode-pumping and optimization of the Yb^{3+}/Ho^{3+} codoping ratio for better $Yb^{3+} \rightarrow Ho^{3+}$ energy transfer, as its efficiency was about 50%. Additionally, Yb,Ho:$Ca_3Nb_{1.5}Ga_{3.5}O_{12}$ crystals can be used for lasers emitting at 3 μm when additionally doped with Eu^{3+}, as the luminescence lifetime of $^5I_6$ is relatively long and Eu^{3+} ions lead to the quenching of the $^5I_7$ lifetime due to the $Ho^{3+} \rightarrow Eu^{3+}$ energy transfer.

Chapter IV

Parent and Solid-Solution Cubic Rare-Earth Sesquioxides

Cubic rare-earth sesquioxides R_2O_3, where R stands for Y, Lu and Sc (referred to as yttria, lutecia and scandia, respectively), or their mixture, are well-known host matrices for doping with laser-active RE^{3+} ions, particularly thulium and holmium ones. From the material point of view, they exhibit strong crystal strength, which results in broadband emission properties and a relatively long luminescence lifetime. Due to the ability to form substitutional solid-solutions in the system Y_2O_3–Lu_2O_3–Sc_2O_3. For a full range of yttria, lutecia and scandia content, they offer a great flexibility for material engineering. Moreover, they are rather attractive for laser development due to the ability of the host matrices, namely: a high thermal conductivity, enabling efficient heat extraction even in high-power laser operation; low phonon energies (among oxides) that suppress non-radiative decay paths from excited states of RE^{3+} ions. In this way, they are of great interest for lasers emitting beyond 2 μm.

In this chapter, the spectroscopic study of Tm^{3+} and Ho^{3+} ions in stoichiometric cubic sesquioxide ceramics and crystals $(Y_xLu_ySc_z)_2O_3$ (x + y + z =1) as well as efficient laser operation are reported. In Section IV.1, a systematic study of the variation of crystal field strength, absorption and emission bandwidth of Tm^{3+} ions over the cubic rare-earth sesquioxides were presented. In Section IV.2, the particular case of the Tm^{3+}-doped $(Y,Lu)_2O_3$ "mixed" laser ceramic is considered. In Section IV.3, the effect of Sc-addition into the Tm^{3+}-doped Y_2O_3 laser ceramic on its spectroscopic, thermal properties is demonstrated. Moreover, an efficient Tm laser based on the Y_2O_3 and $(Y,Sc)_2O_3$ ceramics. In Section IV.4, the first study of the Tm^{3+},Ho^{3+}-codoped mixed sesquioxide based on $(Y,Sc)_2O_3$ ceramic is reported. This study particularly focuses on the energy-transfer between Tm and Ho ions and presents the first efficient and broadly tunable the Tm^{3+},Ho^{3+}-codoped sesquioxide ceramic laser. In Section IV.5, emission of Tm^{3+} ions around 2.3 μm and excited-state absorption spectra in sesquioxides were demonstrated. Moreover, the first laser operation of the Tm-doped Lu_2O_3 around 2.3 μm was performed. The electron-phonon interaction of Tm^{3+} ions in sesquioxides is discussed.

IV.1. Tailoring crystal-field strength and emission bandwidth of Tm^{3+}-doped sesquioxide ceramics in the ternary system Y_2O_3-Lu_2O_3-Sc_2O_3

This section deals with the systematic study of the spectroscopic properties of Tm^{3+} ions in cubic rare-earth sesquioxides, including parent compounds (yttria, lutecia and scandia), as well as their binary and ternary solid-solutions in the Y_2O_3–Lu_2O_3–Sc_2O_3 system. Such a systematic study for serials of samples fabricated under identical conditions with the same Tm doping level was performed for the first time. In particular, we focus on the effects of

inhomogeneous spectral line broadening for Tm^{3+} ions and how crystal field splitting of Tm^{3+} manifolds vary with different host-forming cations. Additionally, we provide the first evidence of C_{3i} Tm^{3+} sites in cubic sesquioxides.

IV.1.A. Synthesis of ceramics

A series of sesquioxide ceramics, including stoichiometric Y_2O_3, Lu_2O_3, Sc_2O_3, and binary / ternary solid-solutions with an equal molar ratio of the metals $(Lu,Y)_2O_3$, $(Lu,Sc)_2O_3$, and $(Y,Lu,Sc)_2O_3$, doped with 3.0 at.% Tm^{3+}, and the other series 0.3 at.% Tm^{3+} parent compounds were fabricated at the G. G. Devyatykh Institute of Chemistry of High-Purity Substances of RAS, Nizhny Novgorod, Russia (see Figure IV.1).

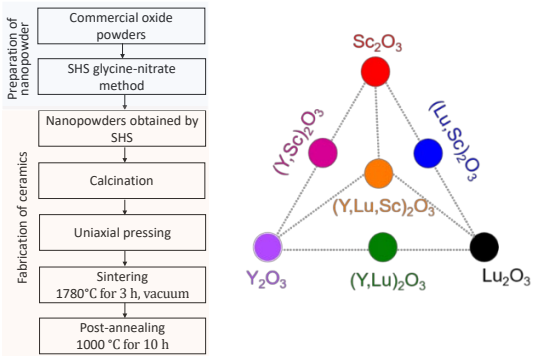

Figure IV.1. (a) Scheme of the ceramic fabrication process and (b) a diagram showing list of Tm^{3+} doped R_2O_3 and their mixture ceramics.

The initial nanopowders were prepared by the glycine-nitrate method. First, commercial powders of Tm_2O_3 (purity: 4N), Y_2O_3, (5N), Lu_2O_3 (4N), Sc_2O_3 (4N) from Polirite, Russia were dissolved in nitric acid (6N, Khimreaktiv, Russia), the corresponding nitrates were mixed, and glycine (3N, Khimreaktiv, Russia) was added in a 1:1 mole ratio. After drying the solution, the precursor was placed in a furnace heated up to 500°C. The self-propagating synthesis resulted in the formation of nanodispersed powders of $Tm:R_2O_3$. The powders were calcined at 900°C for 5 h in air and compacted in a steel mold with a diameter of 13 mm at a pressure of 250 MPa. The green bodies were sintered at 1780 °C for 3 h in an oil vacuum lower than 1×10^{-2} Pa. The furnace was equipped with a tungsten rod as a heating element and graphite thermal insulation. The samples were then annealed in air at 1000°C for 10 h to restore the oxygen stoichiometry. The obtained transparent ceramics had a slight coloration due to the Tm^{3+} doping.

The Tm^{3+} ion density N_{Tm} was 8.06, 8.55 and 9.92 [10^{20} at/cm^3] for the parent compounds (Y_2O_3, Lu_2O_3 and Sc_2O_3, respectively) and 8.37, 8.92 and 8.67 [10^{20} at/cm^3] for the "mixed" ones ($(Y,Lu)_2O_3$, $(Lu,Sc)_2O_3$ and $(Y,Lu,Sc)_2O_3$, respectively).

IV.1.B. Formation of solid solutions: X-ray diffraction and Raman spectroscopy study

Now let us discuss in detail the structure of cubic sesquioxides. Cubic R_2O_3 sesquioxides (R = Y, Lu and Sc) adopt the bixbyite structure (bixbyite is the $(Fe,Mn)_2O_3$ mineral), VI[R_2]IV[O_3], where VI[] and IV[] are octahedral and tetrahedral sites, respectively [Pau30, Han84]. The

corresponding lattice constants are a = 10.596 Å, 10.391 Å and 9.857 Å. Since two out of five ions in the chemical formula are RE^{3+} cations, it leads to cation densities around 3×10^{22} cm^{-3}, which is about twice as high as, *e.g.*, in $Y_3Al_5O_{12}$. This means that the doping density of a 1% doped sesquioxide roughly corresponds to that of a 2% doped YAG crystal [Kra15].

This structure is derived from the fluorite lattice by doubling the lattice parameter and leaving 1/4 of the anion sites vacant in an ordered way. A fragment of the crystal structure of yttria [Fau80] is shown Figure IV.2 The unit-cell contains 32 cation sites of which 24 exhibit the C_2 symmetry (Wyckoff: 24d) and the remaining 8 ones – the C_{3i} symmetry (Wyckoff 8b) Figure IV.2(b).

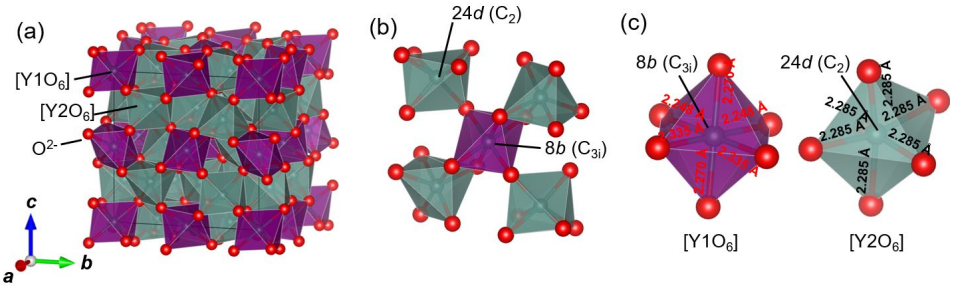

Figure IV.2. The crystal structure of C-type Y_2O_3: (a) a fragment of the crystal structure, black lines – unit-cell; (b) the connection between the $[Y1O_6]$ and $[Y2O_6]$ polyhedra; (c) the local geometry of the C_2 and C_{3i} symmetry sites.

For both sites, the R^{3+} cations are VI-fold coordinated by oxygens, Figure IV.2(c). The bonding is different for the two R^{3+} sites of the C-type structure: the oxygens around R1 form a regular octahedron with 6 equal R–O distances (2.285 Å), while those around R2 form an irregular octahedron with three different R–O distances (2.248, 2.270, 2.335 Å, all the values are specified for Y_2O_3). Each $[R2O_6]$ polyhedron is linked to four $[R1O_6]$ ones via edge-sharing. For the C_{3i} sites, the ED transitions are forbidden due to the presence of a center of inversion, and only MD transitions are allowed. Thus, rare-earth ions residing in these sites do not contribute to transition intensities. For the C_2 sites, both ED and MD transitions are allowed.

X-ray diffraction study was performed by our colleagues from the G. G. Devyatykh Institute of Chemistry of High-Purity Substances of RAS. All the ceramics were of single-phase nature (C-type, sp. gr. $Ia\bar{3}$) as confirmed by X-ray powder diffraction (XRD), Figure IV.3(a).

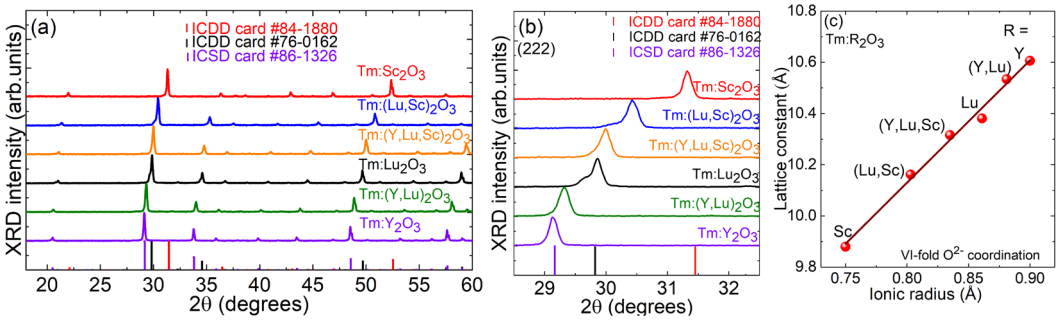

Figure IV.3. XRD study of $Tm:R_2O_3$ ceramics (R = Y, Lu, Sc or their mixture): (a) XRD patterns; (b) a close look at the (222) diffraction peak; (b) the lattice constant a as a function of the average ionic radius of the host-forming cation R^{3+} (for VI-fold oxygen coordination), (*hkl*) – Miller's indices.

The bixbyite-type structure of sesquioxides is well documented [Pau30]. In Figure IV.3(b), a close look at the most intense diffraction peak related to the (222) Bragg reflection is shown. For the parent compounds, the position of the most intense diffraction peak related to the (222) Bragg reflection, see Figure IV.3(b), progressively shifts to higher diffraction angles 2θ in the R = Y → Lu → Sc series. For the "mixed" compounds, this diffraction peak takes an intermediate position between those for the corresponding parents. This behavior is due to a nearly linear relation between the average ionic radius of the host-forming cation R^{3+} (for VI-fold oxygen coordination) [Sha76] and the lattice constant *a*, expressed by the Vegard's law [Veg21], see Figure IV.3(c).

Raman spectroscopy is a sensitive tool for studying material structures and their possible alteration. The vibronic properties of parent R_2O_3 sesquioxides (R = Y, Sc, Nd – Lu) are well known [Abr14]. In the present work, Raman spectroscopy was employed to confirm the formation of substitutional solid-solutions for "mixed" sesquioxide ceramics. The Raman spectra of parent Tm:R_2O_3 ceramics (for R = Y, Lu and Sc) are shown in Figure IV.4(a). They agree with the spectra reported previously by Abrashev *et al.* for powders of undoped Y_2O_3, Lu_2O_3 and Sc_2O_3 [Abr14]. For cubic (C-type) sesquioxides with a body-centered structure, the factor group analysis predicts the following set of irreducible representations for the optical and acoustical modes at the center of the Brillouin zone Γ (***k*** = 0):

$\Gamma_{op} = 4A_g + 4E_g + 14F_g + 5A_{2u} + 5E_u + 16F_u$ *and* $\Gamma_{ac} = F_u$,

of which 22 *gerade* modes (A_g, E_g and F_g) are Raman-active, 16 modes (F_u) are IR-active and the rest are silent [Rep95, Tod13].

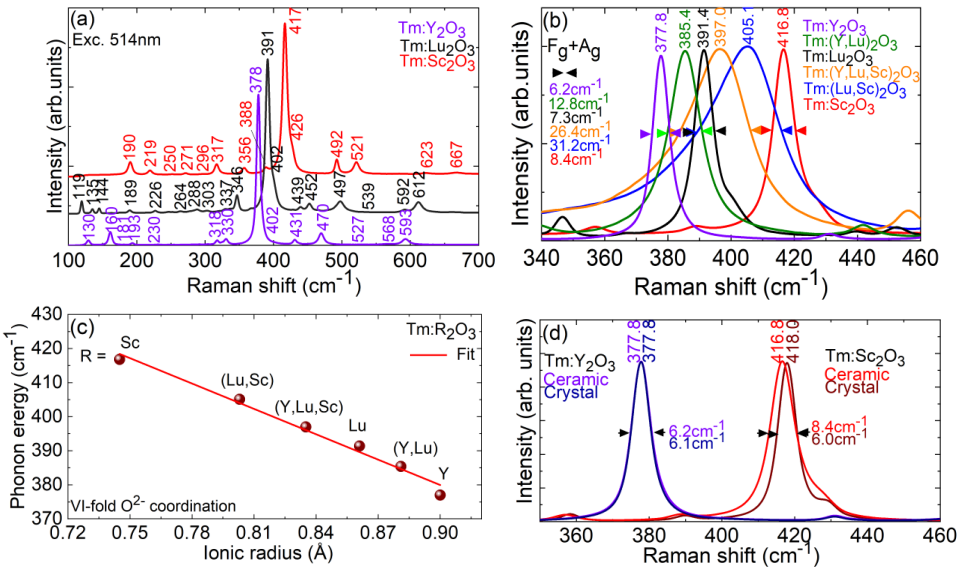

Figure IV.4. Raman spectroscopy of 3 at.% Tm:R_2O_3 ceramics (R = Y, Lu, Sc or their mixture): (a) overview Raman spectra of Tm:Y_2O_3, Tm:Lu_2O_3 and Tm:Sc_2O_3 ceramics; (b) a close look at the most intense mode ($F_g + A_g$); (c) its phonon energy vs. the ionic radius of the host-forming R^{3+} cation (VI-fold oxygen coordination); (d) a comparison of the Raman spectra of Tm:Y_2O_3 and Tm:Sc_2O_3 single-crystals and ceramics. λ_{exc} = 514 nm.

The measured spectra are characteristic of cubic sesquioxides. The vibration spectra exhibit two distinct frequency ranges. The range below 300 cm^{-1} corresponds to the square root ration

of the atomic masses of R atoms, affecting by the motions of R atoms in their [RO_6]. Whereas, the relative position and intensities of the modes above 300 cm^{-1} are rather similar for different ceramic compositions, indicating that they are most probably related to oxygen motions and deformations of [RO_6] octahedrons [Rep95]. The most intense Raman peak is assigned to A_g + F_g vibrations. In the R = Y → Lu → Sc series, its position shifts to higher energies (377.8 → 391.4 → 416.8 cm^{-1}) and its width broadens (full width at half maximum, FWHM: 6.2 → 7.3 → 8.4 cm^{-1}). A similar tendency is observed for all the assigned Raman peaks, in particular, for the maximum phonon energy (F_g vibrations [Abr14], 593 → 612 → 667 cm^{-1}).

Figure IV.4(b) shows a close look at the dominant Raman peak for all six studied compounds. For the "mixed" ceramics, it takes an intermediate position between those for the parent ones and notably broadens. Continuous changes of band position with composition are typical for substitutional solid solutions and often the linewidth observed for such systems exhibit a local maximum at equal fractions of the parent compounds [Bar75]. The broadening effect is more pronounced for Sc^{3+}-containing ceramics due to the smaller ionic radius of Sc^{3+} (0.745 Å) as compared to those of Y^{3+} (0.90 Å) and Lu^{3+} (0.861 Å, all values correspond to a VI-fold coordination by oxygen). For example, for Tm:$(Y,Lu)_2O_3$ and Tm:$(Lu,Sc)_2O_3$, the dominant Raman peak is found at 385.4 and 405.1 cm^{-1} and its FWHM is as broad as large as 12.8 and 31.2 cm^{-1}, respectively. This confirms the formation of a substitutional solid-solution.

Even for parent compounds, the substitution of the host-forming cations (R = Y, Lu or Sc) by the dopant Tm^{3+} ions is expected to induce an additional broadening of the Raman peaks [Pan00]. Note that cubic Tm_2O_3 oxide exhibits a very broad dominant Raman peak at 383 cm^{-1} [Uba08]. The different broadening for various R cations is due to the different degree of the contraction of the unit cell [Gou79] and subtle changes in the chemical bonding [Pan00]. A similar trend for the R = Y → Ho → Dy → Yb, namely an increase of the linewidth of the most intense band and a decrease in its position, was observed previously [Pan00].

The dependence of the dominant Raman peak energy with the average ionic radius of the host-forming cation R^{3+} in Tm:R_2O_3 is shown in Figure IV.4(c). The experimental points are well fitted with a linear law.

The comparison of the Raman spectra of Tm^{3+}-doped yttria and scandia single-crystals and polycrystalline ceramics is shown in Figure IV.4(d). For yttria compounds, the spectra are very close, while for the scandia ones, the dominant Raman band in ceramic slightly broadens and experiences a minor shift to lower energies as compared to the corresponding single crystal. This particular behavior of the Tm:Sc_2O_3 ceramic is assigned to the large difference of the ionic radii of the dopant and host-forming cations. This is expected to induce additional disorder of the crystalline structure of the ceramic grains, including a possible variation of the doping level between them. A similar effect is known for Er^{3+}-doped Sc_2O_3 single crystals featuring a strong gradient of the dopant concentration [Uva23].

IV.1.C. Optical spectroscopy of Tm^{3+} ions

The absorption spectra of Tm^{3+} ions in the parent sesquioxide *crystals* Y_2O_3, Lu_2O_3 and Sc_2O_3 were reported [Loi18a]. In the present work, we focus on the spectral line broadening for Tm^{3+}

ions in "mixed" sesquioxide ceramics, while the spectra for parent ceramics are mainly provided for comparison.

Two transitions were considered, $^3H_6 \rightarrow {}^3H_4$ and $^3H_6 \rightarrow {}^3F_4$. The first one is commonly used for pumping Tm^{3+} ions, as already mentioned, by commercial high-power AlGaAs laser diodes emitting around 0.8 μm. The second one is promising for in-band pumping (directly to the upper laser level), *e.g.*, by Raman-shifted Erbium fiber lasers operating at 1.68 μm.

The σ_{abs} spectra for the parent compounds are shown in Figure IV.5(a,c). In the R = Y → Lu → Sc series, the peak absorption cross-sections slightly increase, the absorption bands (as a whole) broaden while the individual peaks related to particular electronic transitions become narrower. For the $^3H_6 \rightarrow {}^3H_4$ transition, the peak σ_{abs} is 0.37×10^{-20} cm² at 796.7 nm ($Tm:Y_2O_3$), 0.38×10^{-20} cm² at 796.2 nm ($Tm:Lu_2O_3$) and 0.40×10^{-20} cm² at 795.8 nm ($Tm:Sc_2O_3$) and the absorption linewidth (FWHM) is 4.2, 3.5 and 3.4 nm, respectively. These data agree well with the previous study for Tm^{3+}-doped Y_2O_3, Lu_2O_3 and Sc_2O_3 single-crystals [Loi18a, Kra22].

For "mixed" compounds, cf. Figure IV.5(b,d), the absorption spectra become less structured and this effect is stronger for Sc^{3+}-containing ceramics. The spectra of solid-solutions cannot be obtained simply as a linear combination of the spectra of the two corresponding parents (as shown in Figure IV.5(b) by a dashed curve for the case of Lu_2O_3 – Sc_2O_3). As a result, the peak σ_{abs} values decrease while the corresponding absorption linewidths increase (in part because of the merging of several individual absorption peaks). This behavior is favorable for reducing the sensitivity to the temperature drift of the emission wavelength of AlGaAs diode lasers. For the $^3H_6 \rightarrow {}^3H_4$ transition, the peak σ_{abs} amounts to 0.33×10^{-20} cm² at 796.2 nm ($Tm:(Y,Lu)_2O_3$) and 0.29×10^{-20} cm² at 792.2 nm ($Tm:(Lu,Sc)_2O_3$) and the absorption linewidth is ~21 nm. It is worth noting that the ternary ceramic $Tm:(Y,Lu,Sc)_2O_3$ does not provide much smoother spectra than the $Tm:(Lu,Sc)_2O_3$ one.

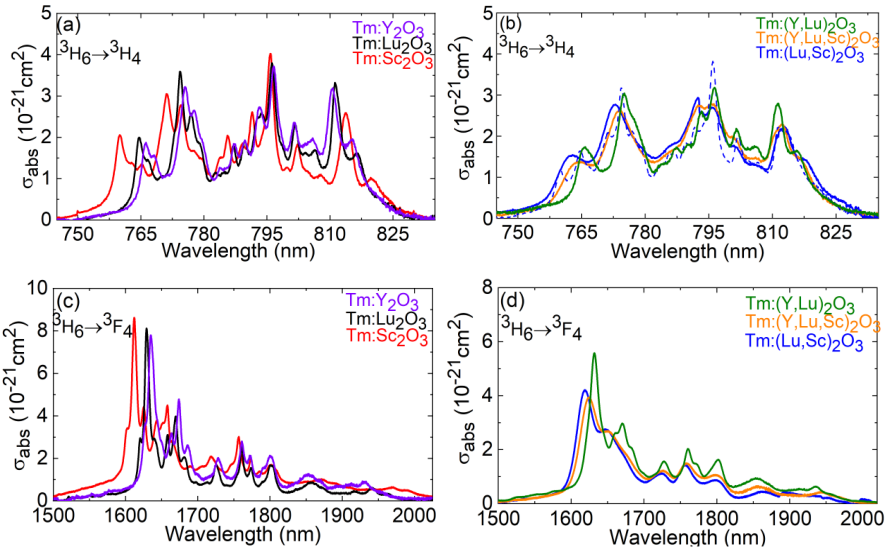

Figure IV.5. RT absorption cross-sections, σ_{abs}, for (a) the $^3H_6 \rightarrow {}^3H_4$ transition and (b) the $^3H_6 \rightarrow {}^3F_4$ transition of Tm^{3+} ions in the R_2O_3 ceramics (R = Y, Lu, Sc or their mixture). *Dashed curve* in (b) – linear superposition of absorption spectra of Tm^{3+} in Lu_2O_3 and Sc_2O_3.

The broadening degree of the absorption spectra correlates adequately with the difference between the ionic radius of Tm^{3+} (0.88 Å) and the mean ionic radius of the host-forming R^{3+} cations (0.881, 0.835 and 0.803 Å for R = (Y,Lu), (Y,Lu,Sc) and (Lu,Sc), respectively).

The results on the peak absorption cross-sections for the $^3H_6 \rightarrow {}^3H_4$ Tm^{3+} transition in all six studied ceramics are summarized in Table IV.1.

The stimulated-emission (SE) cross-sections, σ_{SE}, for the $^3F_4 \rightarrow {}^3H_6$ transition of Tm^{3+} ions in the parent sesquioxide crystals, Y_2O_3, Lu_2O_3 and Sc_2O_3, were reported [Loi18a]. Recently, Kränkel et al. [Kra22] and Moncorgé et al. [Mon22] overviewed the emission properties of Tm^{3+}-doped binary "mixed" sesquioxides. In the present work, the σ_{SE} spectra for the $Tm:R_2O_3$ ceramics (R = Y, Lu, Sc or their mixture) were calculated using a combination of the reciprocity method and the Füchtbauer – Ladenburg formula. The refractive indices were calculated using dispersion formulas from [Zel13]. The data on the crystal-field splitting from Section IV.1.C was used.

The F-L method relying on the measured luminescence spectrum can be inaccurate at shorter wavelengths, in the spectral range with a stronger overlap with the reciprocal absorption band, due to the effect of reabsorption. The calculation via RM fails at longer wavelength due to the exponential term in Eq. I.19. The radiative lifetime of the $^3F_4$ state was adjusted until a good matching between the spectra calculated by both methods was observed.

The resulting σ_{SE} spectra of Tm^{3+} ions in the parent compounds are shown in Figure IV.6(a). In the R = Y → Lu → Sc series, the stimulated-emission cross-section peak increases, and the emission bandwidth increases. The maximum σ_{SE} amounts to 0.92×10^{-20} cm^2 at 1933.5 nm ($Tm:Y_2O_3$), 0.94×10^{-20} cm^2 at 1943.0 nm ($Tm:Lu_2O_3$) and 1.01×10^{-20} cm^2 at 1990.1 nm ($Tm:Sc_2O_3$). The $^3F_4 \rightarrow {}^3H_6$ Tm^{3+} transition represents a quasi-three-level laser scheme with reabsorption. Consequently, the laser emission will occur at wavelengths longer than the ZPL position, i.e., in the long-wave part of the σ_{SE} spectrum, above 2 μm. All three parent sesquioxides present a distinct emission peak in this spectral range. The corresponding SE cross-sections are 0.35×10^{-20} cm^2 at 2051.6 nm ($Tm:Y_2O_3$), 0.32×10^{-20} cm^2 at 2064.4 nm ($Tm:Lu_2O_3$) and 0.39×10^{-20} cm^2 at 2113.7 nm ($Tm:Sc_2O_3$). These results are in line with the previous study for Tm^{3+}-doped Y_2O_3, Lu_2O_3 and Sc_2O_3 single-crystals [Loi18a].

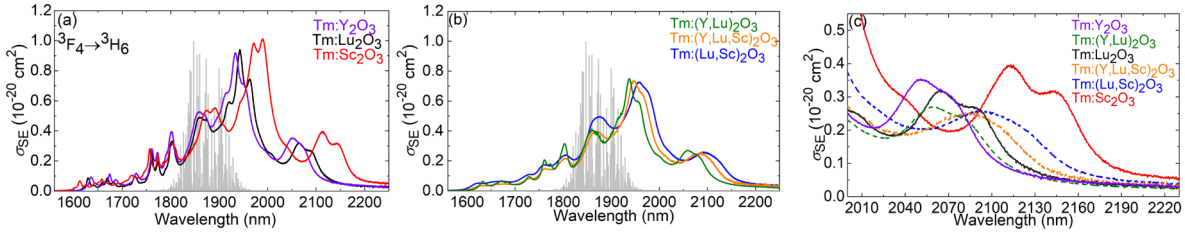

Figure IV.6. RT stimulated-emission (SE) cross-section, σ_{SE}, spectra for the $^3F_4 \rightarrow {}^3H_6$ transition of Tm^{3+} ions in the R_2O_3 ceramics (R = Y, Lu, Sc or their mixture): (a) parent compounds; (b) solid-solution compositions; (c) a close look at the 2000-2250 nm range. *Grey lines* – water absorption according to the HITRAN database [arb.units].

For "mixed" sesquioxides, the emission spectra become less structured (similar to that observed for the absorption spectra), see Figure IV.6(b). This effect is most pronounced for Tm:(Lu,Sc)$_2$O$_3$. The SE cross-sections relevant for laser operation are listed in Table IV.1.

Figure IV.6(c) shows a close look at the long-wave emission peak (at wavelengths above 2 μm) of Tm^{3+} ions in all six sesquioxide ceramics.

This part of the spectrum is particularly attractive for the development of mode-locked lasers delivering femtosecond pulses. This is because multiple narrow absorption lines of water in the atmosphere which appear at shorter wavelengths prevent the generation of such broadband pulses [Wan16a]. By selecting the proper host-forming cation R^{3+} (for parent compounds) or their combination (for "mixed" ones), it is possible to tailor both the peak position and the emission bandwidth. For "mixed" compounds, the peak emission wavelength takes an intermediate position between those for the corresponding parents while the spectral profile of the emission peak broadens. For example, for Tm:(Lu,Sc)$_2$O$_3$, σ_{SE} is 0.26×10^{-20} cm^2 at 2095.7 nm and the corresponding emission bandwidth (FWHM) is 69.8 nm, compared with 58.1 nm (Tm:Lu$_2$O$_3$) and 64.1 nm (Tm:Sc$_2$O$_3$).

Sc^{3+}-containing sesquioxides provide emission around 2.1 μm, in the spectral range typically addressed by Holmium (Ho^{3+}) ions (the $^5I_7 \rightarrow {}^5I_8$ electronic transition) in various oxide and fluoride crystals. Singly Tm^{3+}-doped parent and solid-solution scandia ceramic can be thus considered as viable alternatives to Ho^{3+}-doped and Tm^{3+},Ho^{3+} codoped laser materials.

The long-wave emission of Tm^{3+} ions in cubic sesquioxides extending until at least 2.2 μm is most likely due to multiphonon-assisted processes [Auz76, Zha21a].

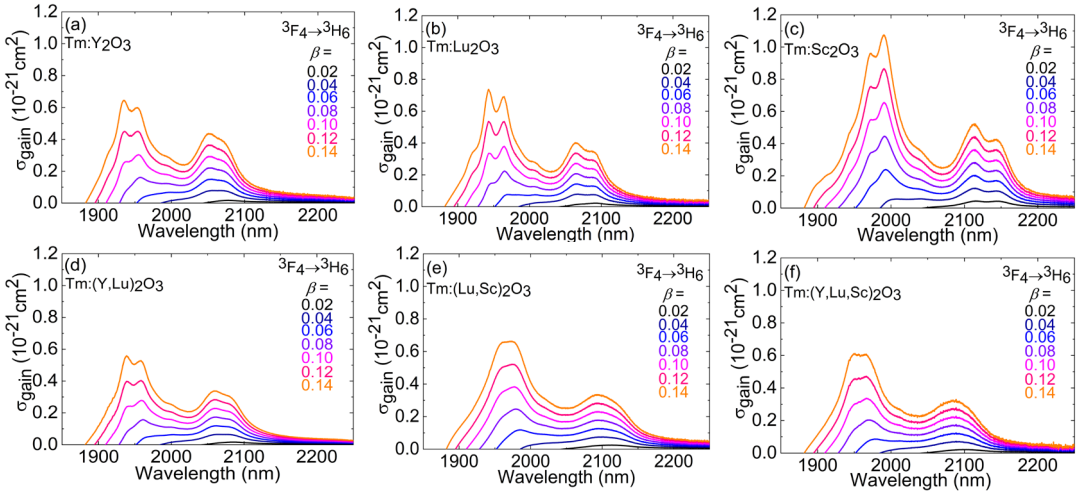

Figure IV.7. (a-f) Gain cross-section spectra for Tm^{3+} ions in the R_2O_3 ceramics (R = Y, Lu, Sc or their mixture), plotted for different inversion ratios.

The gain cross-sections were calculated as shown in Figure IV.7. For all the sesquioxide ceramics, the gain profiles are broad and naturally extend beyond 2 μm. The position of the long-wave maximum in the gain spectra shifts to longer wavelengths in the R = Y → Lu → Sc series. As expected for the "mixed" ceramics, the spectra become less structured. For small inversion ratios, a local peak above 2 μm dominates in the gain spectra and when increasing β

above 0.06–0.08 (depending on the composition), another peak at shorter wavelengths (<2 μm) appears.

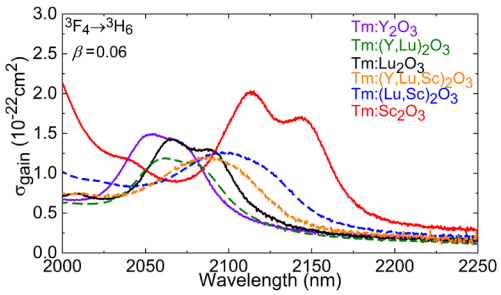

Figure IV.8. A comparison of gain profiles of Tm^{3+} ions in the R_2O_3 ceramics (R = Y, Lu, Sc or their mixture) in the spectral range of 2000 – 2250 nm, for a fixed inversion ratio $\beta = 0.06$.

The gain bandwidth can be increased for the "mixed" compounds. Figure IV.8 presents a direct comparison of the gain profiles of Tm^{3+} ions in the R_2O_3 ceramics for the same inversion ratio ($\beta = 0.06$) focusing on the spectral range of 2000-2250 nm relevant for the development of femtosecond lasers.

Table IV.1. Peak absorption and stimulated-emission cross-sections for Thulium ions in R_2O_3 crystals (after [Loi18a]) and ceramics, Z_1 and Z_2 are partition function of the $^3H_6$ and $^3F_4$ Tm^{3+} manifolds.

R_2O_3	σ_{abs}, 10^{-20} cm^2	λ_{abs}, nm	$\Delta\lambda_{abs}$, nm	σ_{SE}, 10^{-20} cm^2	λ_{em}, nm	$\Delta\lambda_{em}$, nm	Z_1/Z_2
Crystals							
Y_2O_3	0.32	796.5	3.5	0.28	2051.6	54.3	1.445
Lu_2O_3	0.38	796.2	2.7	0.32	2065.5	52.4	1.450
Sc_2O_3	0.42	795.8	2.4	0.35	2115.0	64.6	1.436
Ceramics							
Y_2O_3	0.36	796.7	4.2	0.35	2051.6	50.2	1.429
Lu_2O_3	0.38	796.2	3.5	0.32	2064.4	58.1	1.445
Sc_2O_3	0.40	795.8	3.4	0.39	2113.7	64.1	1.447
$(Y,Lu)_2O_3$	0.33	796.2	~21	0.27	2059.0	54.7	
$(Y,Lu,Sc)_2O_3$	0.28	796.0	~21	0.25	2087.9	63.0	
$(Lu,Sc)_2O_3$	0.29	792.2	~21	0.26	2095.7	69.8	

The RT luminescence decay curves from the $^3F_4$ state of Tm^{3+} ions in the Tm^{3+}-doped R_2O_3 ceramics (R = Y, Lu, Sc or their mixture) were measured under resonant excitation, as shown in Figure IV.9. The $^3F_4 \rightarrow {}^3H_6$ transition is of purely electric dipole nature and thus only Tm^{3+} ions residing in C_2 sites contribute to the observed emission. The decay curves for 3 at.% Tm^{3+}-doped ceramics deviate from a single-exponential law, Figure IV.9(a), due to the phonon-assisted energy-transfer upconversion (ETU) processes from the $^3F_4$ state, $^3F_4 + {}^3F_4 \rightarrow {}^3H_6 + {}^3H_4$ (ETU_1) and $^3F_4 + {}^3F_4 \rightarrow {}^3H_6 + {}^3H_5$ (ETU_2) [Loi16]. The ETU rates are concentration-dependent, and they are enhanced with the Tm doping considering the high rare-earth ion density in cubic sesquioxides.

For low-doped (0.3 at.% Tm^{3+}) parent sesquioxides, the intrinsic luminescence lifetimes $\tau_{lum,0}$ are 3.73 ms ($Tm:Lu_2O_3$), 3.58 ms ($Tm:Y_2O_3$) and 3.44 ms ($Tm:Sc_2O_3$), Figure IV.9(b). For ceramics with 3 at.% Tm, the luminescence lifetimes are shortened due to concentration-

quenching. With increasing the Sc^{3+} content in the ceramics, τ_{lum} is shortened which is assigned to increased non-radiative path owing to the higher phonon energy of scandia.

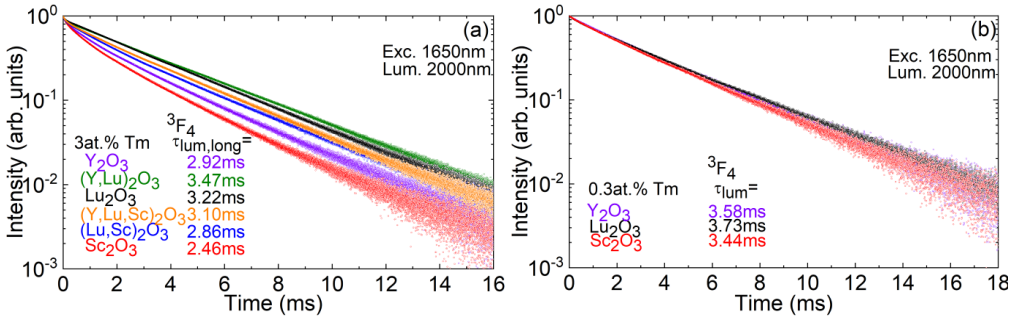

Figure IV.9. RT luminescence decay curves from the $^3F_4$ Tm^{3+} state in $Tm:R_2O_3$ ceramics (R = Y, Lu, Sc or their mixture): (a) 3 at.% Tm, all compositions; (b) 0.3 at.% Tm, parents, λ_{exc} = 1650 nm, λ_{lum} = 2000 nm. Powdered samples.

Table IV.2 summarizes the intrinsic luminescence lifetimes ($\tau_{lum,0}$) obtained for ceramic and crystals [Loi18a] with a low doping level of ≤ 0.3 at.% Tm, as well as the radiative lifetimes (τ_{rad}) calculated using the Judd-Ofelt theory assuming that only ions residing in C_2 sites (3/4 of ions) contribute to optical absorption [Mon22].

Table IV.2. Intrinsic luminescence ($\tau_{lum,0}$) and radiative (τ_{rad}) lifetimes of the $^3F_4$ Tm^{3+} multiplet in 0.3 at. % $Tm:R_2O_3$, (R = Y, Lu, Sc).

Compound	$\tau_{lum,0}$, ms ceramic	$\tau_{lum,0}$, ms [Loi18a] crystal	τ_{rad}, ms [Mon22]
$Tm:Y_2O_3$	3.58	3.54	3.79
$Tm:Lu_2O_3$	3.73	3.38	3.84
$Tm:Sc_2O_3$	3.44	3.57	3.80

The $^3F_4$ Tm^{3+} manifold for the parent sesquioxides, Y_2O_3, Lu_2O_3 and Sc_2O_3, is considered. The intrinsic lifetimes for ceramics and single-crystals are in good agreement with each other indicating an almost negligible effect of possible defects and impurity centers in ceramics. They are also in line with the radiative ones evaluated recently by Moncorgé *et al.* [Mon22].

IV.1.D. Low-temperature spectroscopy of Tm^{3+} ions in parent sesquioxides

Tm^{3+} ions in cubic sesquioxides can reside in two non-equivalent sites with symmetry C_2 (24*d*, 3/4 of cationic positions in the unit-cell) and C_{3i} (8*b*, 1/4 of the cationic positions) [Lea82, Gru85]. Both sites have a VI-fold oxygen coordination. For both sites, each $^{2S+1}L_J$ multiplet with an integer J is split into a total of 2J + 1 Stark sub-levels. The spectroscopic signatures of the C_{3i} sites are expected only for transitions with a MD contribution. We use the phenomenological notations for Tm^{3+} multiplets proposed by Gruber *et al.* [Gru64], namely Z, Y, X and A for the $^3H_6$, $^3F_4$, $^3H_5$ and $^3H_4$ manifolds, respectively. Each Stark sub-level is designated as Z_i, Y_i, X_i and A_i, where i = 1, 2, ... 2J + 1, counting from the lowest sub-level. The assignment of electronic transitions takes into consideration the previous studies [Gru64].

The experimental crystal-field splitting for Tm^{3+} ions in three parent sesquioxides, Y_2O_3, Lu_2O_3 and Sc_2O_3, was reported in PhD theses from the University of Hamburg [For99, Koo12],

however, without providing the low-temperature spectra and their assignment. Moreover, the possible spectroscopic signatures of C_{3i} sites were not analyzed.

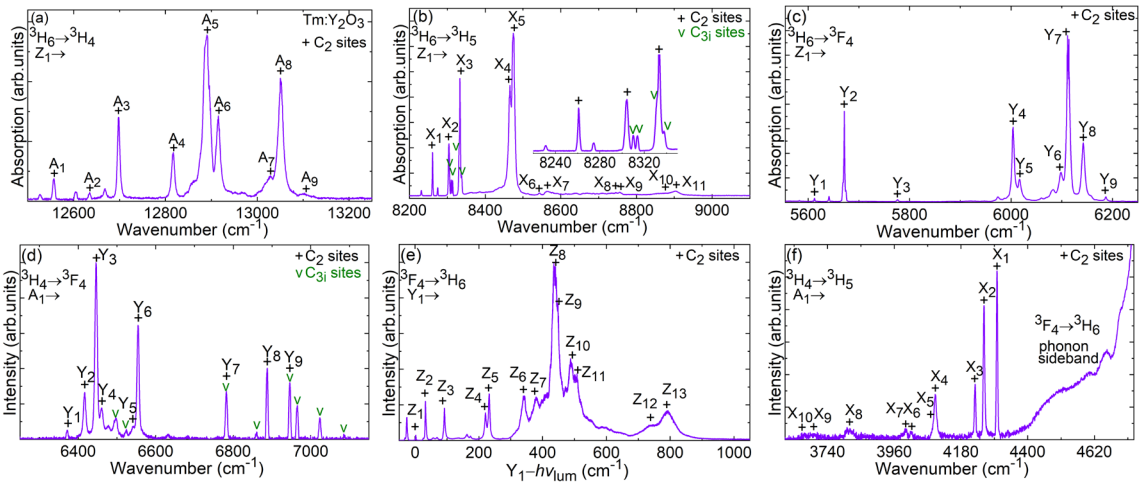

Figure IV.10. LT (12 K) absorption spectra (a,b,c) and luminescence spectrum (d,e,f) of Tm^{3+} ions in Y_2O_3 crystal: (a) the $^3H_6 \rightarrow {}^3H_4$ transition; (b) the $^3H_6 \rightarrow {}^3H_5$ transition; (c) the $^3H_6 \rightarrow {}^3F_4$ transition; (d) the $^3H_4 \rightarrow {}^3F_4$ transition, (e) the $^3F_4 \rightarrow {}^3H_6$ transition, (f) the $^3H_4 \rightarrow {}^3H_5$ transition. + – C_2 sites, v – C_{3i} sites, A_i, X_i, Y_i and Z_i – the phenomenological notations.

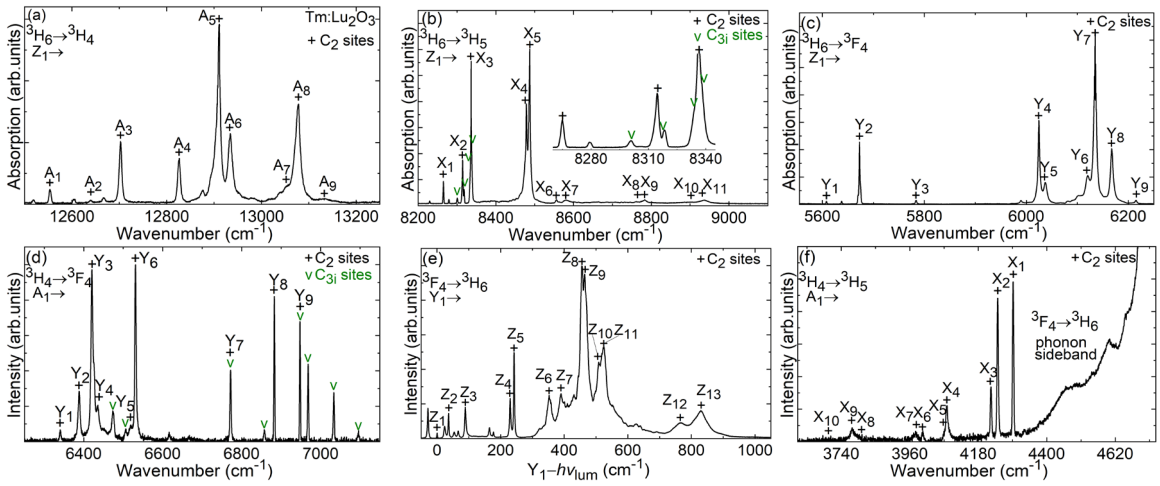

Figure IV.11. LT (12 K) absorption spectra (a,b,c) and luminescence spectrum (d,e,f) of Tm^{3+} ions in Lu_2O_3 crystal: (a) the $^3H_6 \rightarrow {}^3H_4$ transition; (b) the $^3H_6 \rightarrow {}^3H_5$ transition; (c) the $^3H_6 \rightarrow {}^3F_4$ transition; (d) the $^3H_4 \rightarrow {}^3F_4$ transition, (e) the $^3F_4 \rightarrow {}^3H_6$ transition, (f) the $^3H_4 \rightarrow {}^3H_5$ transition. + – C_2 sites, v – C_{3i} sites, A_i, X_i, Y_i and Z_i – the phenomenological notations.

First, the low-temperature (LT, 12 K) absorption and emission spectra of Tm^{3+} ions in the three parent sesquioxides (Y_2O_3, Lu_2O_3 and Sc_2O_3) were measured focusing on the four lower-lying multiplets ($^3H_6$, $^3F_4$, $^3H_5$ and $^3H_4$), see Figure IV.10, Figure IV.11, and Figure IV.12.

The LT absorption spectra for the $^3H_6 \rightarrow {}^3F_4$, $^3H_5$ and $^3H_4$ transitions are plotted versus the photon energy ($h\nu_{abs}$, in cm^{-1}). Assuming that only the lowest Stark sub-level of the ground-state is populated, the energies of assigned electronic transitions directly give the Stark sub-level energies. For these multiplets, all the 2J + 1 sub-levels of Tm^{3+} ions in C_2 sites were identified. Then, the LT $^3F_4 \rightarrow {}^3H_6$ emission spectra were measured to determine the splitting of the

ground-state and plotted versus E_{ZPL} – photon energy ($Y_1 - h\nu_{lum}$, in cm^{-1}). Again, all 2J + 1 sub-levels of the ground-state of Tm^{3+} ions in C_2 sites were identified. The positions of the Stark sublevels were determined for the $^3H_4 \rightarrow {}^3H_5$ transition by subtracting the positions of the $^3H_5$ Stark levels from the ZPL ($A_1 - X_j$) of the $^3H_4$ level.

Let us discuss the distribution of the dopant cations in the R_2O_3 sesquioxides over the C_2 and C_{3i} sites. As noted above, for ideal parent compounds, the host-forming cations R^{3+} are present in both sites with a proportion 3/4 (C_2) and 1/4 (C_{3i}). Gruber *et al.* indicated that due to the favorable size of Tm^{3+}, by isomorphic substitution, these ions can replace with perhaps equal probability the Y^{3+} cations in the two different sites of the Y_2O_3 lattice [Gru64].

A comparative study of optical spectra of Y_2O_3 crystals containing different concentrations of Tm^{3+} indicated that increased amounts of Tm does not appreciably distort the lattice in the neighbourhood of the cation sites. The proportion of ions residing in both sites does not seem to change with the Tm doping level up to the Tm_2O_3 composition. Blanusa *et al.* concluded about a nearly random cationic distribution for Tm^{3+} dopant ions in $(Y_{1-x}Tm_x)_2O_3$ solid-solutions based on the Rietveld refinement data [Bla00]. A similar conclusion was made by Mitric *et al.* Yb^{3+} in $(Y_{1-x}Yb_x)_2O_3$ solid-solutions and Rodic *et al.* for Gd^{3+}, Er^{3+}, Ho^{3+} and Dy^{3+} ions in Y_2O_3 [Mit97, Rod95]. According to the findings of the present work, due to the closeness of integrated absorption cross-sections for Tm^{3+} transitions in all the studied parent and "mixed" sesquioxides, a similar distribution of dopants over the two lattice sites is expected.

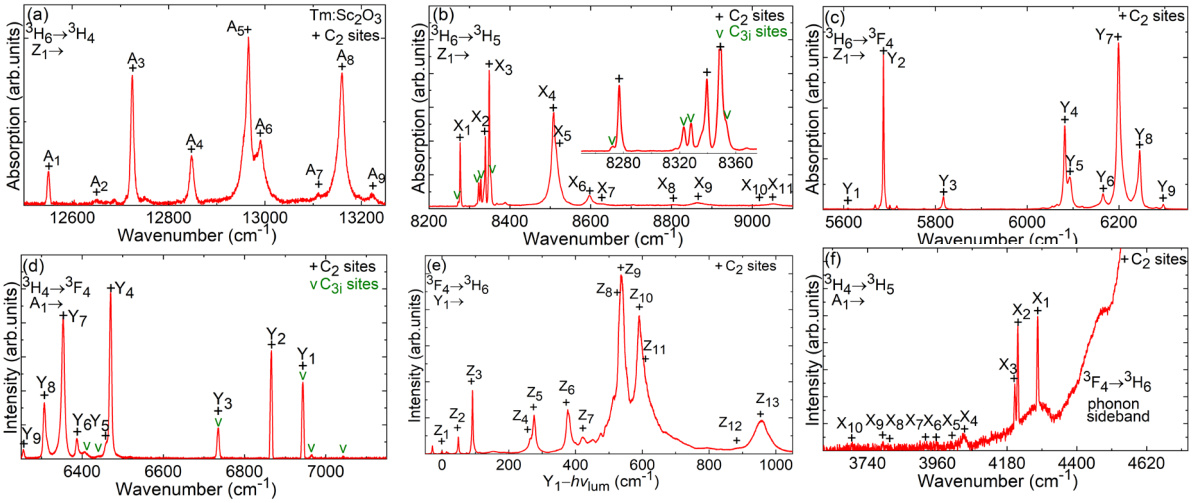

Figure IV.12. LT (12 K) absorption spectra (a,b,c) and luminescence spectrum (d,e,f) of Tm^{3+} ions in Sc_2O_3 crystal: (a) the $^3H_6 \rightarrow {}^3H_4$ transition; (b) the $^3H_6 \rightarrow {}^3H_5$ transition; (c) the $^3H_6 \rightarrow {}^3F_4$ transition; (d) the $^3H_4 \rightarrow {}^3F_4$ transition, (e) the $^3F_4 \rightarrow {}^3H_6$ transition, (f) the $^3H_4 \rightarrow {}^3H_5$ transition. + – C_2 sites, v – C_{3i} sites, A_i, X_i, Y_i and Z_i – the phenomenological notations.

We also compared the LT spectra of Tm^{3+} ions in parent single-crystals and ceramics. The LT $^3H_6 \rightarrow {}^3F_4$ absorption was analyzed for $Tm:Y_2O_3$ and $Tm:Sc_2O_3$, similarly to the analysis performed for the Raman spectra. Figure IV.13 shows a close look at the part of the LT absorption spectrum related to transitions from the $Z_1(^3H_6)$ sub-level to the Y_4 to $Y_9(^3F_4)$ ones. For both compounds, the peak positions are very close (within the measurement error) while the peak width is different. It almost does not change between the $Tm:Y_2O_3$ single crystal and

ceramic while it notably increases between the Tm:Sc_2O_3 ones. We assume that it can be caused by a gradient of the dopant ion concentration in rare-earth-doped Sc_2O_3 by a large difference of the ionic radii of the dopant and host-forming cations [Uva23].

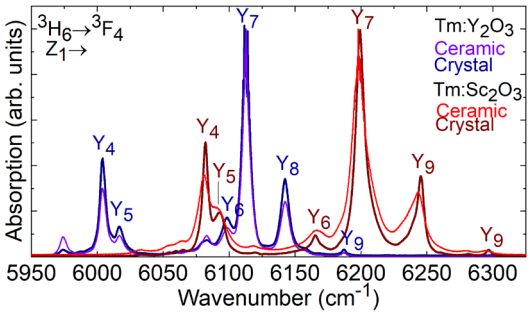

Figure IV.13. A comparison of LT (12 K) absorption spectra of Tm^{3+} ions (the $^3H_6 \rightarrow {}^3F_4$ transition) in Y_2O_3 and Sc_2O_3 single crystals and ceramics. Y_i denotes electronic transitions to the Stark sub-levels of the $^3F_4$ multiplet.

Table IV.3. Experimental crystal-field splitting of Tm^{3+} multiplets in Y_2O_3, Lu_2O_3 and Sc_2O_3 (C_2 and C_{3i} sites)

R_2O_3	$^{2S+1}L_J$	Notation	*E*, cm^{-1}
Y_2O_3	$^3H_6$	Z	0; 30; 89; 217; 229; 338; 376; 432; 439; 486; 503; 732; 788 (C_2) 0; 37; 130; 213; 384; 519; 709; 761; 762 (C_{3i}) [Gru85]
	$^3F_4$	Y	5612; 5672; 5776; 6003; 6016; 6099; 6112; 6142; 6187 (C_2) 5472; 5535; 5593; 5612; 5696; 5776; 6034; 6060 (C_{3i})
	$^3H_5$	X	8261; 8304; 8333; 8466; 8474; 8542; 8562; 8742; 8755; 8875; 8905 (C_2) 8310; 8314; 8331; 8338 (C_{3i})
	$^3H_4$	A	12557; 12634; 12698; 12817; 12890; 12915; 13028; 13051; 13103 (C_2)
Lu_2O_3	$^3H_6$	Z	0; 35; 88; 229; 241; 352; 388; 455; 463; 508; 523; 764; 828 (C_2)
	$^3F_4$	Y	5607; 5673; 5784; 6025; 6037; 6120; 6135; 6167; 6214 (C_2) 5461; 5522; 5588; 5608; 5698; 5784; 6050; 6082; 6130 (C_{3i})
	$^3H_5$	X	8265; 8315; 8336; 8479; 8487; 8556; 8580; 8761; 8783; 8900; 8937 (C_2) 8301; 8318; 8334; 8339 (C_{3i})
	$^3H_4$	A	12553; 12640; 12703; 12826; 12910; 12934; 13016; 13078; 13135 (C_2)
Sc_2O_3	$^3H_6$	Z	0; 49; 91; 265; 275; 377; 422; 529; 537; 590; 607; 882; 955 (C_2)
	$^3F_4$	Y	5609; 5687; 5818; 6082; 6093; 6166; 6199; 6245; 6296 (C_2) 5510; 5587; 5609; 5818; 6111; 6143 (C_{3i})
	$^3H_5$	X	8278; 8339; 8349; 8508; 8515; 8598; 8632; 8809; 8863; 9020; 9052 (C_2) 8272; 8323; 8328; 8353 (C_{3i})
	$^3H_4$	A	12550; 12650; 12725; 12848; 12966; 12991; 13111; 13160; 13222 (C_2)

IV.1.E. Evidence of C_{3i} Tm^{3+} species

To reveal the spectroscopic evidence of Tm^{3+} ions in C_{3i} sites, we additionally studied two emissions with a MD contribution, namely $^3H_4 \rightarrow {}^3F_4$ (at ~1.5 μm) and $^3H_4 \rightarrow {}^3H_5$ (at ~2.3 μm). The corresponding LT emission spectra gave access to the Stark splitting of the terminal levels,

$^3F_4$ and $^3H_5$, for ions located in both C_2 and C_{3i} sites, Figure IV.14-16. The LT emission spectra were plotted versus E_{ZPL} – photon energy (A_1 – $h\nu_{lum}$, in cm^{-1}).

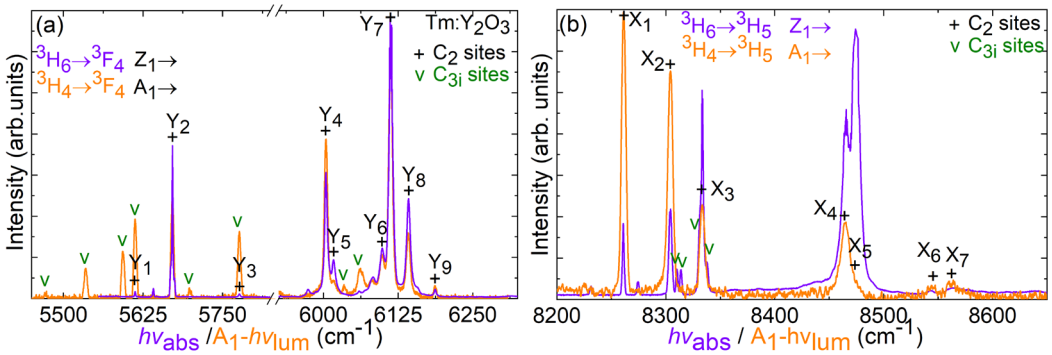

Figure IV.14. A comparison of the $^3H_6 \rightarrow {}^3H_5$ LT absorption and $^3H_4 \rightarrow {}^3H_5$ emission spectra evidencing the presence of C_{3i} species of Tm^{3+} ions in Y_2O_3. + – C_2 sites, v – C_{3i} sites.

Let us first discuss the $^3H_4 \rightarrow {}^3F_4$ emission representing the fingerprints of both the C_2 and C_{3i} sites. By overlapping it with the $^3H_6 \rightarrow {}^3F_4$ transition in absorption (related exclusively to C_2 sites), one can observe narrow extra lines due to the C_{3i} sites. Note that their energy is determined assuming that the lowest Stark sub-level of the $^3H_4$ manifold (A_1) has the same energy for both sites. The experimental crystal-field splitting for the Tm^{3+} C_{3i} species in cubic sesquioxides has never been reported. As a figure of merit to support the above-mentioned assumption, we compare the position of the lowest-lying Stark sub-level for the $^4I_{13/2}$ Er^{3+} multiplet in cubic Y_2O_3, namely 6510 cm^{-1} (C_2 sites) and 6514 cm^{-1} (C_{3i} sites) indicating a small energy difference [Gru85]. The full set of 9 sub-levels of the $^3F_4$ state (C_{3i} sites) is determined only for Tm^{3+} ions in Lu_2O_3 and for other compounds, less lines are identified, namely 8 ($Tm:Y_2O_3$) and 6 ($Tm:Sc_2O_3$).

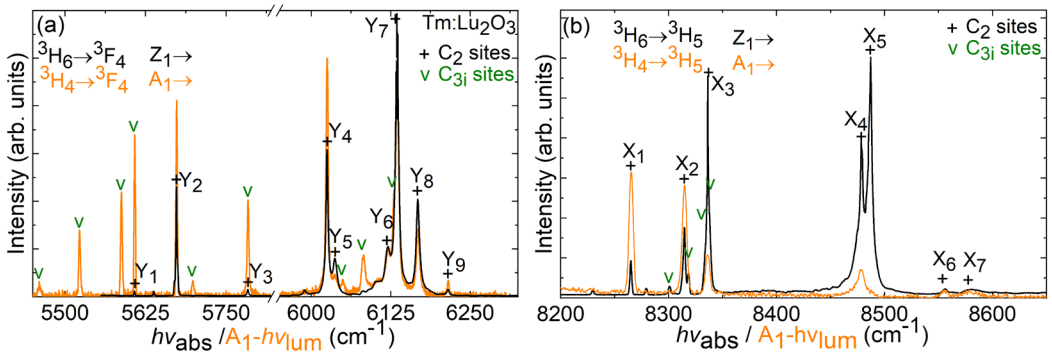

Figure IV.15. A comparison of the $^3H_6 \rightarrow {}^3H_5$ LT absorption and $^3H_4 \rightarrow {}^3H_5$ emission spectra evidencing the presence of C_{3i} species of Tm^{3+} ions in Lu_2O_3. + – C_2 sites, v – C_{3i} sites.

Now, let us discuss the $^3H_4 \rightarrow {}^3H_5$ emission. It is of both ED and MD nature and thus Tm^{3+} ions located in both the C_2 and C_{3i} sites contribute to it. The transition in absorption giving access to the $^3H_5$ state is also allowed for both sites. By comparing the spectra, one can identify the extra lines owing to the C_{3i} sites. Moreover, their energy is unambiguously determined from the LT absorption spectrum. A total of 4 extra lines (out of 9 possible Stark sub-levels) are identified in all three compounds. This is the first direct observation of C_{3i} species for Tm^{3+}-

doped sesquioxides. Gruber *et al.* calculated the position of Stark sub-levels of the Tm^{3+} ground-state ($^3H_6$) in Y_2O_3 based on the phenomenological crystal-field parameters [Gru85]. However, they were accessed experimentally as the only possible suitable transition, $^3H_5 \rightarrow {}^3H_6$, corresponds to a very weak emission due to the short lifetime of the $^3H_5$ state quenched as a result of the non-radiative relaxation. Table IV.3 summarizes the determined energies of Stark sub-levels for Tm^{3+} ions in C_2 sites (full set) and C_{3i} sites (only $^3F_4$ and $^3H_5$ multiplets, partially) for the parent sesquioxides.

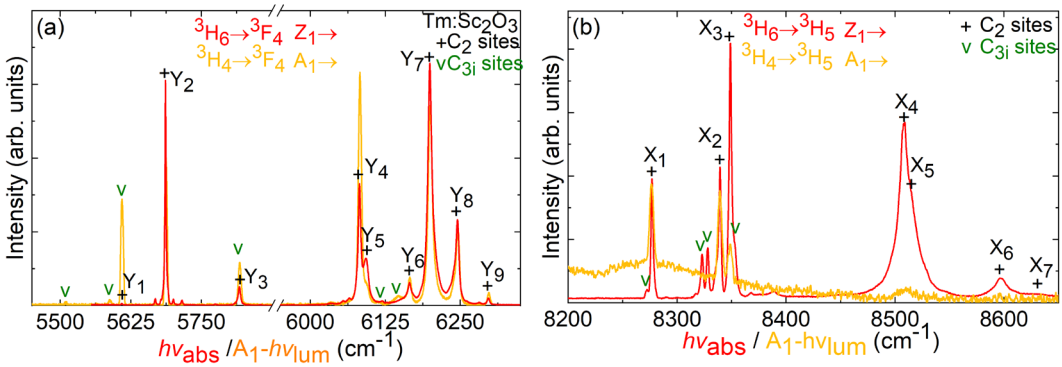

Figure IV.16. A comparison of the $^3H_6 \rightarrow {}^3H_5$ LT absorption and $^3H_4 \rightarrow {}^3H_5$ emission spectra evidencing the presence of C_{3i} species of Tm^{3+} ions in Sc_2O_3. + – C_2 sites, v – C_{3i} sites.

IV.1.F. Inhomogeneous spectral broadening in solid-solution sesquioxides

The LT absorption / emission spectra of Tm^{3+} ions in "mixed" ceramics were studied to reveal the inhomogeneous spectral line broadening induced by the compositional disorder. For the sake of brevity, we focus here on one transition relevant for the development of 2 μm lasers, namely the $^3H_6 \leftrightarrow {}^3F_4$ transition, both in absorption and emission, see Figure IV.17 and 18. In this section, for describing the spectroscopic properties and, in particular, the crystal-field splitting for "mixed" ceramics, we will use the concept of an activator *quasicenter* first introduced by Kaminski [Kam13] to generalize the optical properties of disordered laser materials.

By a quasicenter, we mean an ensemble-averaged structure that generalizes properties of several local activator centers that only slightly differ in structure and have very similar Stark splitting of their energy states. In general, the structure and number of separate activator centers depend on the permissible disorder of a crystalline system and on the concentration of its components, including the activator. For compositionally "mixed" (solid-solution) compounds, a quasicenter can be determined with its crystal-field splitting representing a macroscopic average of multiple local activator centers which differ by the actual composition of the second coordination sphere (which, in turn, depends on the concentration of components constituting the solid-solution). It thus represents an intermediate case between the two parent compounds. At 12 K, the spectral lines assigned to electronic transitions of Tm^{3+} ions in solid-solution ceramics take an intermediate position between those for the corresponding parents while they significantly broaden. Indeed, for the transition between the Stark components $Z_1 \rightarrow Y_2$ (the $^3H_6 \rightarrow {}^3F_4$ intermanifold transition in absorption), Figure IV.17(a-c), the spectral

linewidth (defined as FWHM) at 12 K is just 2.0, 2.1 and 6.4 cm^{-1} for the parent compounds $Tm:R_2O_3$ (for R = Y, Lu, Sc, respectively), while it increases to 20.0 and 62.0 cm^{-1} for the solid-solutions $Tm:(Y,Lu)_2O_3$ and $Tm:(Lu,Sc)_2O_3$, respectively. For the Sc^{3+}-containing ceramic, this value includes two electronic transitions, $Z_1 \rightarrow Y_{1,2}$, and associated phonon sidebands. As a result of such broadening, not all of the possible electronic transitions can be unambiguously assigned.

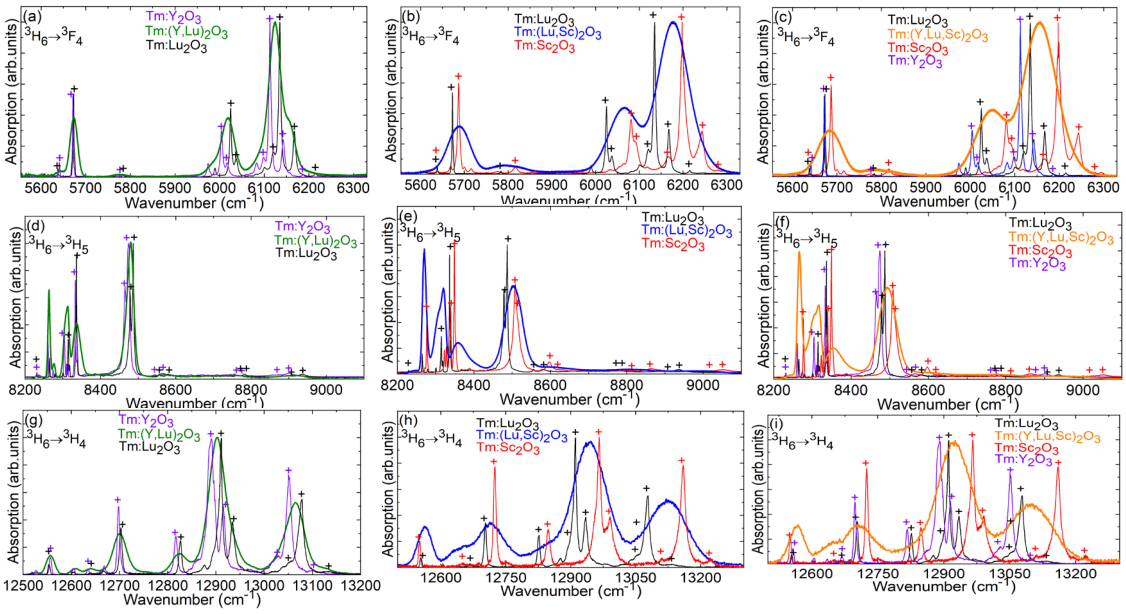

Figure IV.17. Inhomogeneous spectral broadening at 12 K for Tm^{3+} ions in "mixed" sesquioxide ceramics: (a,d,g) Y_2O_3 – Lu_2O_3 binary system; (b,e,h) Lu_2O_3 – Sc_2O_3 binary system; (c,f,i) Y_2O_3 – Lu_2O_3 – Sc_2O_3 ternary system, the $^3H_6 \rightarrow {}^3F_4$, $^3H_5$, $^3H_4$ transitions in absorption.

A similar behavior is also observed for the LT luminescence spectra, Figure IV.18(a-c). For the $Y_1 \rightarrow Z_{13}$ intermanifold transitions in emission, the spectral linewidth is 61, 52 and 73 cm^{-1} for R = Y, Lu, Sc, respectively, and it increases up to 69 and 200 cm^{-1} for the "mixed" $Tm:(Y,Lu)_2O_3$ and $Tm:(Lu,Sc)_2O_3$ ceramics, respectively (for the latter compositions, the linewidth includes

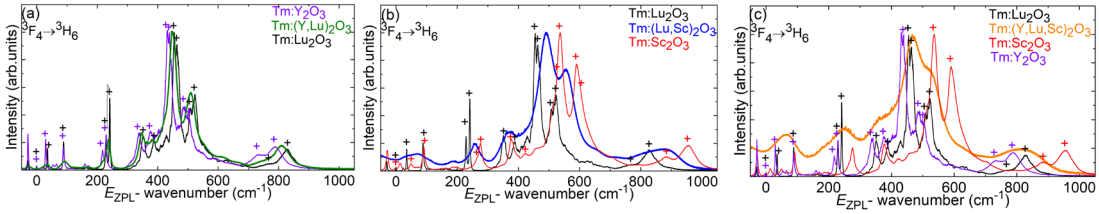

Figure IV.18. Inhomogeneous spectral broadening at 12 K for Tm^{3+} ions in "mixed" sesquioxide ceramics: (a) Y_2O_3 – Lu_2O_3 binary system; (b) Lu_2O_3 – Sc_2O_3 binary system; (c) Y_2O_3 – Lu_2O_3 – Sc_2O_3 ternary system, the $^3F_4 \rightarrow {}^3H_6$ transition in emission.

both the $Y_1 \rightarrow Z_{12,13}$ transitions). For the studied solid-solution ceramics, the LT spectroscopy did not reveal any signatures of non-equivalent Tm^{3+} spectroscopic species (*e.g.*, the presence of "twinned" absorption or emission lines which could be associated with Tm^{3+} ions sitting in different local environments preferentially composed of one type of the host-forming cations R^{3+}, or profound dependence of the LT luminescence spectra on the excitation wavelength

which was tuned across the entire $^3H_6 \rightarrow {}^3H_4$ absorption band with a laser linewidth of <0.1 nm). This confirms the formation of binary and ternary substitutional solid-solutions $(R1,R2)_2O_3$ and $(R1,R2,R3)_2O_3$ with mixing of the host-forming cations R^{3+} at the atomic level. The compositional disorder originated from the second coordination sphere of Tm^{3+} ions formed by different sets of $R1^{3+}$ and $R2^{3+}$ ($R3^{3+}$) cations with different masses and ionic radii. These observations confirm the validity of the quasicenter model described above.

To illustrate the inhomogeneous spectral broadening in solid-solution sesquioxides, the diagram of the crystal-field splitting of the ground-state $^3H_6$ and the first excited-state $^3F_4$ of Tm^{3+} ions accounting both for the Stark sub-level position and the spectral line broadening (FWHM) was constructed, Figure IV.19.

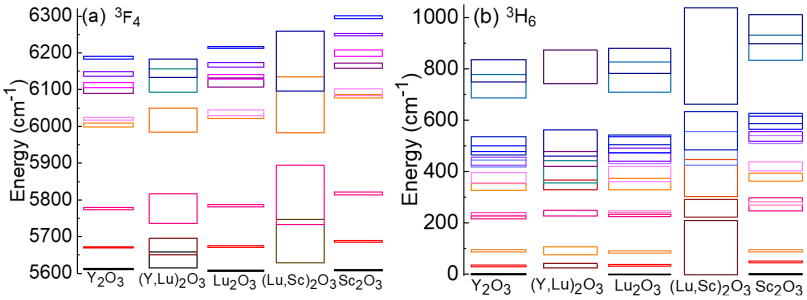

Figure IV.19. Inhomogeneous broadening of the energy-levels of the ground-state $^3H_6$ and the first excited-state $^3F_4$ of Tm^{3+} ions in $Tm:R_2O_3$ (R = Y, Lu, Sc or their mixture) ceramics (at 12 K) by the crystal field. The height of each rectangle corresponds to the FWHM of the absorption / emission peaks corresponding to individual electronic transitions.

IV.1.G. Barycenter plot and effect of the cation radius on the crystal-field strength

Antic-Fidancev *et al.* proposed the so-called barycenter plot: a plot of the barycenter energy of one $^{2S+1}L_J$ $4f^n$ multiplet of a rare-earth ion vs. that of another multiplet of the same ion, and applied it to the case of several rare-earth ions, namely Nd^{3+} ($4f^2$), Pr^{3+} ($4f^3$), Eu^{3+} ($4f^6$) and Yb^{3+} ($4f^{13}$) ions [Hau01, Ant00]. We applied it here to the case of Tm^{3+} ions, Figure IV.20. The separation between the $^3H_6$ (ground-state) and $^3F_4$ (first excited-state) manifolds results from the spin–orbit interaction. For Tm^{3+} ions embedded in a crystalline lattice, two different effects can potentially affect this energy separation: (i) the modification of the spin–orbit coupling constant which is weak for 4f transitions of rare-earth ions, and (ii) *J*-mixing (mixing of states with different total angular momentum *J* by the crystal-field) increasing the energy separation between the two manifolds. For Tm^{3+} ions, due to the large energy difference between the $^3H_6$ and $^3F_4$ states (about 5600 cm^{-1}), the *J*-mixing can be neglected. Consequently, we can consider that the energy separation between the Tm^{3+} ground and first excited states is nearly constant for different hosts, and equal to the spin–orbit splitting for the free ion. The barycenter plot can serve as a verification tool for the determined crystal-field splitting. In the present work, we have used this concept to position the determined experimental Stark splittings for Tm^{3+} ions in C_2 sites in R_2O_3 sesquioxides with respect to other materials accommodating Tm^{3+} ions, see Figure IV.20.

Auzel et al. proposed a scalar crystal field strength parameter N_v to compare different materials in terms of Stark splitting (ΔE) of $4f^n$ multiplets of rare-earth ions $^{2S+1}L_J$, as $\Delta E(^{2S+1}L_J) \sim N_v$ [Auz83]. Thus, by plotting the total Stark splitting of one manifold of a particular rare-earth ion vs. that of another manifold of the same ion, one can compare the crystal-field strength for different crystalline materials. Such an analysis is performed in Figure IV.21 for the case of Tm^{3+} ions, by plotting ΔE of the first excited-state ($^3F_4$) vs. that of the ground-state ($^3H_6$). One can see that for oxide matrices, the crystal-field strengths and the corresponding Stark splittings are in general higher. Among the oxide hosts, the cubic R_2O_3 crystals feature one of the largest crystal-field strengths and, more remarkably, a pronounced sensitivity to the nature of the host-forming cation R^{3+} (the total Stark splitting gradually increases in the R = Gd → Y → Lu → Sc series). Thus, they are indeed among the best candidates for achieving broadband emission using the $^3F_4 \rightarrow {}^3H_6$ transition by engineering their composition.

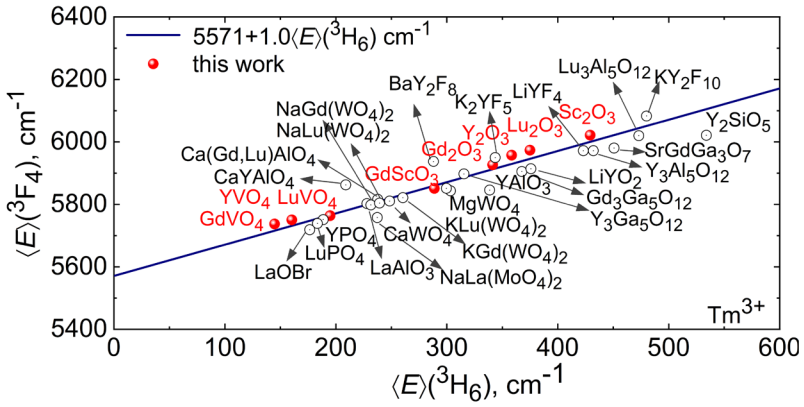

Figure IV.20. A barycenter plot of the crystal-field splitting for Tm^{3+} ions in various hosts: the barycenter energy ⟨E⟩, of the $^3F_4$ excited-state versus that of the $^3H_6$ ground-state, plotted along the nephelauxetic scale. symbols – experimental/calculated data, *line* – their phenomenological fit. *Red circles* – experimental data for crystals obtained in this work.

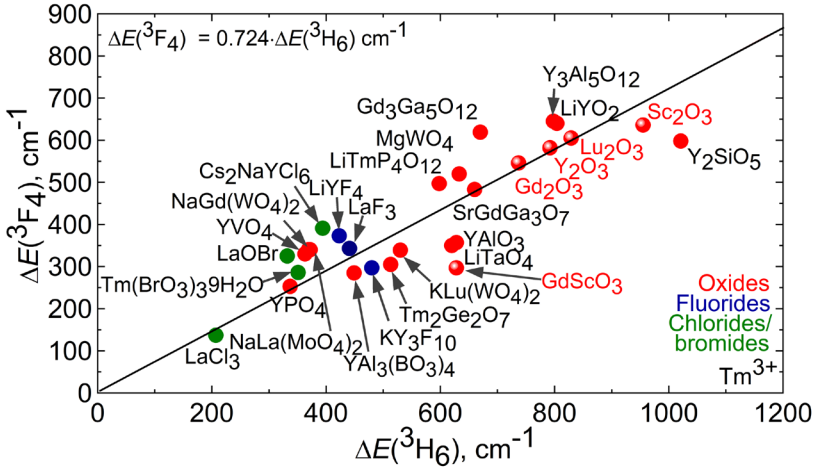

Figure IV.21. Total Stark splitting of the first excited-state ($^3F_4$) vs. that of the ground-state ($^3H_6$) for Tm^{3+} ions in various crystals (oxide (*red*), fluoride (*blue*) and chloride/bromide (*green*)), *symbols* – experimental data from the literature, *line* – their linear fit. For cubic sesquioxides, C_2 sites are considered.

For applications of Tm^{3+}-doped sesquioxides in mode-locked lasers, it is relevant to look at the spectral range of the $^3F_4 \rightarrow {}^3H_6$ emission and, in particular, on its long-wave part extending above 2 µm in sesquioxides. It is determined by the total Stark splitting of the Tm^{3+} ground-state, $\Delta E(^3H_6)$. Figure IV.22(a) summarizes the experimental crystal-field splitting of the $^3H_6$ Tm^{3+} multiplet in the parent $Tm:R_2O_3$ (R = Y, Lu, Sc) sesquioxide ceramics, as well as tentatively determined Stark sub-level energies for Tm^{3+} ions in the solid-solution compositions. Due to the strong inhomogeneous spectral broadening, even at 12 K, we were unable to determine the full set of Stark sub-level energies for the "mixed" ceramics, so that the number of experimental levels is less than the theoretical one.

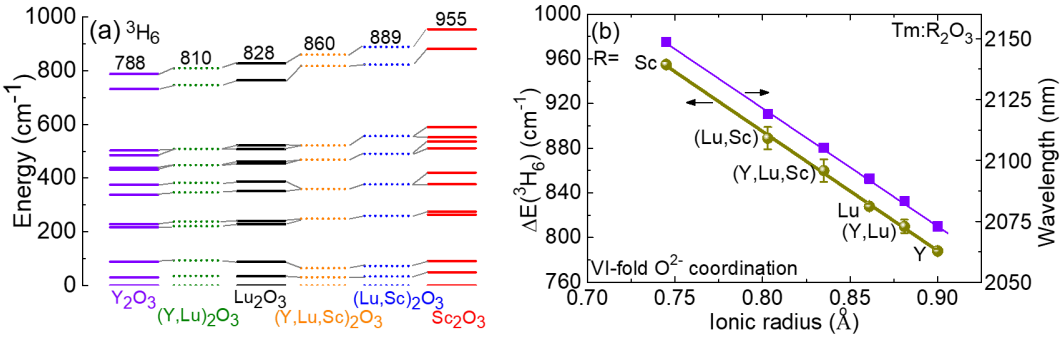

Figure IV.22. (a) The experimental crystal-field splitting of the $^3H_6$ Tm^{3+} multiplet in 3 at.% $Tm:R_2O_3$ (R = Y, Lu, Sc or their mixture); (b) the total ground-state Stark splitting and the longest wavelength of the purely electronic transition $^3F_4 \rightarrow {}^3H_6$ vs. the average R^{3+} ionic radius for VI-fold oxygen coordination.

The energy of each individual sub-level, the barycenter energy of the whole multiplet and its total Stark splitting tend to increase with decreasing the average radius of the host-forming cation R^{3+}, i.e., in the R = Y → Lu → Sc series for the parent compounds. As a result, the longest wavelength of the purely electronic $^3F_4 \rightarrow {}^3H_6$ transition experiences a progressive red-shift for smaller R^{3+} cations, Figure IV.22(b). It is deduced from the energy of the transition between the Stark sub-levels $Y_1 \rightarrow Z_{13}$ and amounts to 2073 nm ($Tm:Y_2O_3$), 2093 nm ($Tm:Lu_2O_3$) and 2149 nm ($Tm:Sc_2O_3$).

Antic-Fidancev *et al.* reported on a linear variation of the crystal-field strength with the ionic radius of the host-forming cation along the lanthanide series (the crystal-field strength increases for smaller cations) for several isostructural crystal families, including orthovanadates $Pr^{3+}:RVO_4$, sesquioxides $Eu^{3+}:R_2O_3$, garnets $Pr^{3+}:R_3Ga_5O_{12}$ [Ant02, Ant98], and Hölsä *et al.* performed a similar theoretical study for oxychlorides ROCl [Hol00]. In the present work, we extend this concept to both parent and solid-solution sesquioxides doped with Tm^{3+} ions with the goal of more flexible control of their emission properties.

In Figure IV.23, we compare the longest wavelength of a purely electronic transition $^3F_4 \rightarrow {}^3H_6$ (corresponding to transitions from the lowest Stark sub-level of the $^3F_4$ manifold to the highest sub-level of the $^3H_6$ one) for Tm^{3+} ions in various crystals considered for the development of ultrashort-pulse lasers at ~2 µm [Loi18c]. Only a few crystal families exhibit strong enough crystal-fields leading to emission peaks owing to electronic transitions extending above 2 µm (while the long-wave phonon sideband of the $^3F_4 \rightarrow {}^3H_6$ emission band

can extend well beyond the range of electronic transitions) thus avoiding the structured water vapor absorption in the atmospheric air, namely garnets, sesquioxides, monotungstates and silicates. Compared to other isostructural series, cubic sesquioxides R_2O_3 show the strongest variation of the emission wavelength with the host-forming cation R^{3+}, and the emission wavelength of Tm^{3+} ions in Sc_2O_3 reaches well beyond 2 μm being exceptionally long among other analyzed compounds.

The analysis performed allowed us to draw several conclusions regarding the material engineering and laser potential of different crystal families for the development of gain media for ~2 μm lasers with broadband emission properties:

(i) For shifting the $^3F_4 \rightarrow {}^3H_6$ Tm^{3+} emission spectra towards longer wavelengths, host matrices with small host-forming cations, leading to stronger crystal-fields, shall be selected. For stronger inhomogeneous spectral broadening in solid-solution compositions, it is necessary to select two parents with rather different sizes of their host-forming cations;

(ii) For achieving emission above 2 μm, the most promising parent compounds are cubic sesquioxides (Y_2O_3-type), cubic ordered ($Y_3Al_5O_{12}$-type) and disordered ($Ca_3Nb_{1.5}Ga_{3.5}O_{12}$-type) garnets, tetragonal disordered melilites ($SrGdGa_3O_7$-type), and monoclinic disordered orthosilicates (Y_2SiO_5-type). Note that the latter two compounds have been barely studied for femtosecond lasers at ~2 μm. The spectral broadening in these systems can be enhanced in "mixed" compositions based on small cations as explained above;

(iii) In the garnet family, it is more promising to study "mixed" compounds of the type $A_3(B1,B2)_5O_{12}$ rather than $(A1,A2)_3B_5O_{12}$ due to the larger variation of the crystal-field strength across the isostructural series in the former case.

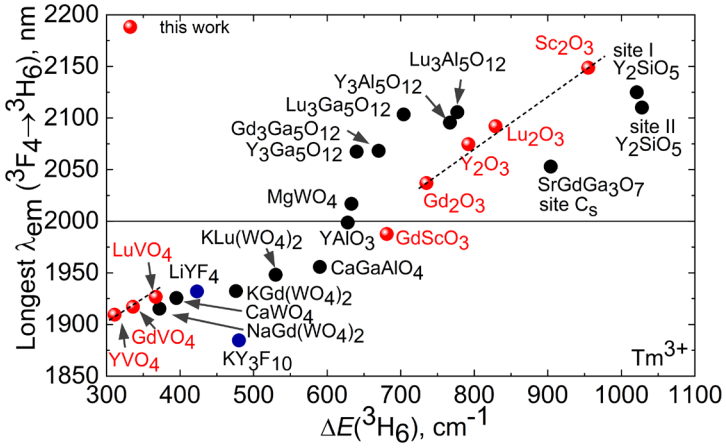

Figure IV.23. The longest wavelength corresponding to the purely electronic transition $^3F_4 \rightarrow {}^3H_6$ vs. the total Stark spitting ΔE of the $^3H_6$ ground-state for Tm^{3+} ions in various crystalline matrices considered for mode-locked lasers at ~2 μm.

To conclude this section, cubic rare-earth sesquioxides R_2O_3 (where R stands for the host-forming cation, R = Y, Lu, Sc, or their mixture) are highly attractive hosts for doping with thulium ions in lasers emitting slightly above 2 μm. They are particularly suitable for generating ultrashort pulses in this spectral range. Sesquioxides are available in the form of single crystals

and transparent polycrystalline ceramics, which exhibit relatively similar spectroscopic properties.

Based on a detailed spectroscopic study of stoichiometric and binary/ternary solid-solution sesquioxides doped with Tm^{3+} ions, the following conclusions are drawn:

(1) Cubic R_2O_3 sesquioxides exhibit strong crystal fields for Tm^{3+} dopant ions in C_2 symmetry sites. These crystal fields mainly determine their optical properties, resulting in remarkably high total Stark splitting of their ground-state ($^3H_6$). The splitting ranges from 788 cm^{-1} (Y_2O_3) to 955 cm^{-1} (Sc_2O_3). Consequently, they produce broadband emission due to the electronic $^3F_4 \rightarrow {}^3H_6$ transition, which extends well beyond 2 μm, effectively avoiding structured water vapor absorption in the atmosphere. For Tm:Sc_2O_3, the longest wavelength of a purely electronic transition is 2149 nm. Thus, Tm^{3+}-doped sesquioxides can effectively compete with other Ho^{3+}-doped materials.

(2) The crystal-field strength for the R_2O_3 isostructural series is highly sensitive to the nature of the host-forming cation R^{3+}. It increases linearly with decreasing ionic radius, leading to corresponding changes in the Stark splitting of Tm^{3+} multiplets. This allows for tuning the emission peaks of Tm^{3+} ions around 2 μm. This trend holds true for both parent and "mixed" compounds.

(3) Experimental crystal-field splitting for Tm^{3+} ions in C_2 symmetry sites in parent sesquioxides (Y_2O_3, Lu_2O_3, and Sc_2O_3) is determined for several relevant multiplets for laser applications (from $^3H_6$ to $^3H_4$) and validated using the barycenter plot. Additionally, the first experimental evidence of C_{3i} Tm^{3+} species for sesquioxides is presented. These species are revealed in transitions with a magnetic dipole contribution ($^3H_6 \rightarrow {}^3H_5$ for absorption and $^3H_4 \rightarrow {}^3H_5$ for emission). However, C_{3i} centers do not contribute to the lifetime of the $^3F_4$ upper laser level.

(4) Based on X-ray diffraction, Raman spectroscopy, and low-temperature absorption/emission spectroscopy, it is confirmed that "mixed" sesquioxide ceramics of the Y_2O_3–Lu_2O_3–Sc_2O_3 ternary system represent substitutional solid solutions with a mixing of the host-forming cations at the atomic level. This results in significant inhomogeneous spectral broadening of the absorption and emission lines of Tm^{3+} ions, even at 12 K. Spectral linewidths for "mixed" sesquioxides notably exceed those for the corresponding parent compounds. At room temperature, an appropriate combination of the host-forming cations R^{3+} enables the design of the gain bandwidth around 2 μm, which is crucial for further pulse shortening in mode-locked lasers. The strongest broadening is observed for Sc^{3+}-containing materials.

(5) Further work in this direction should involve a combination of materials with structural and/or compositional disorder to enhance inhomogeneous spectral broadening, leading to a "glassy-like" spectroscopic behavior characterized by smooth and structureless spectral bands. Additionally, materials with high crystal-field strength should be utilized for broadband emission naturally extending beyond 2 μm. Efficient electron-phonon coupling should also be ensured to utilize long-wave phonon sidebands, contributing to the extension of the gain bandwidth.

IV.2. Spectroscopy of Tm:$(Y,Lu)_2O_3$ laser ceramic

In the previous section, we overviewed the spectroscopy properties of Tm^{3+} ions in parent and solid-solution cubic rare-earth sesquioxide ceramics and identified the potential sesquioxides for engineering the emission wavelengths slightly above 2 μm. In Section IV.2 and Section IV.3, two particular compositions of mixed sesquioxide ceramics are studied. Both of them showed great potential for laser development. This section deals with Tm^{3+}-doped "mixed" $(Y,Lu)_2O_3$ laser ceramic fabricated using hot isostatic pressing. This ceramic has demonstrated broadly tunable laser operation in the continuous-wave regime as well as the capability to support femtosecond pulse generation in mode-locked lasers emitting at 2 μm. However, the relevant information about spectroscopic properties is still missing.

IV.2.A. Synthesis of ceramics

The fabrication of the ceramic was carried at the Shanghai Institute of Ceramics. Commercial powders of rare-earth oxides, Lu_2O_3 (purity: 4N), Y_2O_3 (5N) and Tm_2O_3 (4N) were used as raw materials. The synthesis scheme if the ceramics is shown in Figure IV.24. They were weighed according to the composition of 3.0 at.% Tm:$(Lu_{0.5}Y_{0.5})_2O_3$. The mixed powders were ball-milled in ethanol for 24 h with 1.0 at % monoclinic ZrO_2 powder serving as a sintering aid. The milled slurries were dried in an oven at 70°C for 24 h and then sieved through a 100-mesh screen. After that, the powders were dry-pressed into pellets by a 12 mm-diameter mold and cold isostatically pressed at 200 MPa for 5 min. All the green bodies were calcined at 850 °C for 4 h to remove the residue organics. After that, the samples were first pre-sintered at 1650 °C for 4 h in vacuum under a pressure lower than 1.0×10^{-3} Pa, equipped with a tungsten mesh as the heating element. Then, the pre-sintered ceramics were treated by hot isostatic pressing (HIPing) at 1600 °C for 3 h in 190 MPa argon pressure to eliminate residual pores. Finally, the HIP-treated samples were annealed at 1200 °C for 24 h in a muffle furnace in air to compensate the oxygen loss during the vacuum pre-sintering and the following HIP treatment. Then, the ceramic disks were polished on both sides to laser quality, see Figure IV.25(c). The obtained ceramic disks were transparent and slightly yellow colored due to the Tm^{3+} doping. The calculated Tm^{3+} ion density in the "mixed" ceramic was $N_{Tm} = 8.34 \times 10^{20}$at/cm^3.

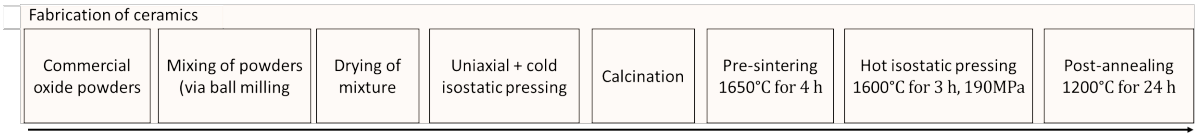

Figure IV.24. A synthesis scheme of the 3.0 at.% Tm:$(Lu_{0.5}Y_{0.5})_2O_3$ ceramic.

To observe the microstructure of the ceramic, its polished surface was thermally etched at 1400°C for 2 h in a muffle furnace in air. The thermally etched surfaces of the 3.0 at.% Tm:$(Y,Lu)_2O_3$ ceramics before and after HIPing were characterized using a Scanning Electron Microscope (SEM, TM3000, Hitachi, Japan). The pre-sintered ceramic has an average grain size of 1 μm and it contains sub-μm sized pores localized at the grain boundaries, Figure IV.25(a).

After HIPing, the mean grain size increases to 2.4 μm. The ceramic exhibits a close-packed microstructure with clean grain boundaries, Figure IV.25(b).

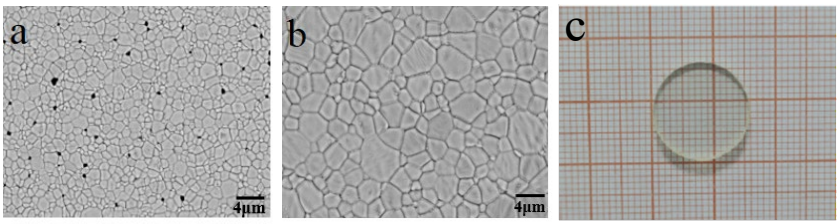

Figure IV.25. SEM images of the thermally etched surface of the Tm:$(Y,Lu)_2O_3$ ceramics: (a) a pre-sintered sample and (b) a sample after HIPing; (c) a photograph of annealed and polished ceramic disk.

IV.2.C. Absorption spectra and Judd-Ofelt analysis

Absorption spectra of Tm:$(Y, Lu)_2O_3$ laser ceramic in different spectral ranges are plotted in Figure IV.26. Tm:Y_2O_3 and Tm: Lu_2O_3 ceramics are placed for comparison. The Tm:$(Y, Lu)_2O_3$ ceramic exhibited a relatively high linear transmission of 81.5% at 2.2 μm (out of the Tm^{3+} absorption bands), close to the theoretical limit, $T_0 = 2n/(n_2 + 1) = 82.0\%$ (a formula accounting for multiple light reflections, n = 1.918 is the estimated refractive index of $(Y,Lu)_2O_3$ [Zel13]). Bands related to transitions from the ground-state ($^3H_6$) to the excited-states ranging from $^3F_4$ up to $^3P_{0-2}$ are observed. The UV absorption edge is observed at ~250 nm (for undoped Lu_2O_3, the optical bandgap E_g is 5.6 eV [Zha21b] or ~221 nm).

The measured absorption spectra of the Tm:$(Y,Lu)_2O_3$ laser ceramic were analyzed using the standard J–O theory see Chapter I, Section I.2.D. Eight Tm^{3+} transitions were considered. The set of reduced squared matrix elements $U_{(k)}$ was taken from [Kor04]. The magnetic-dipole contributions to transition intensities (for transitions with $\Delta J = J - J' = 0, \pm 1$) were calculated within the Russell-Saunders approximations using the wave functions of the free Tm^{3+} ion. The refractive index of the "mixed" ceramic $(Y,Lu)_2O_3$ was calculated using the dispersion curves of the parent compounds [Zel13].

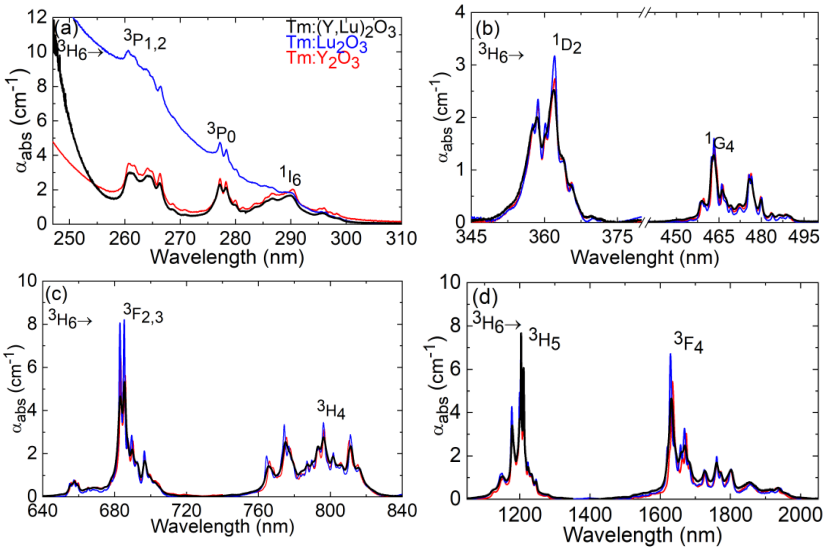

Figure IV.26. Absorption spectra of the 3 at.% Tm:$(Y,Lu)_2O_3$, Y_2O_3 and Lu_2O_3 ceramics.

Table IV.4. Experimental and calculated absorption oscillator strengths for Tm^{3+} ions in $LuYO_3$

Transition	$\langle\lambda_{abs}\rangle$, nm	$\langle E\rangle$, cm^{-1}	$\langle n\rangle$	Γ, $cm^{-1}nm$	$f^{\Sigma}_{exp}\times10^6$	$f^{\Sigma}_{calc}\times10^6$
$^3H_6\rightarrow{}^3F_4$	1763	5672	1.912	444.25	2.038	2.126^{ED}
$^3H_6\rightarrow{}^3H_5$	1206	8292	1.921	243.02	2.308	$1.458^{ED}+0.530^{MD}$
$^3H_6\rightarrow{}^3H_4$	795	12585	1.933	101.29	2.192	2.562^{ED}
$^3H_6\rightarrow{}^3F_2+{}^3F_3$	684	14616	1.939	68.308	1.977	3.216^{ED}
$^3H_6\rightarrow{}^1G_4$	473	21155	1.964	14.359	0.881	0.753^{ED}
$^3H_6\rightarrow{}^1D_2$	361	27738	2.009	20.231	2.117	2.114^{ED}
$^3H_6\rightarrow{}^1I_6+{}^3P_0+{}^3P_1$	284	35178	2.084	24.788	4.131	$1.778^{ED}+0.029^{MD}$
$^3H_6\rightarrow{}^3P_2$	263	37968	2.126	13.235	2.585	2.411^{ED}
Δ_{rms}						*1.202*

Table IV.5. Calculated emission probabilities for Tm^{3+} ions in $(Y,Lu)_2O_3$

Excited state	Terminal state	$\langle\lambda_{em}\rangle$, nm	$A_{\Sigma}^{calc}(JJ')$, s^{-1}	$B(JJ')$, %	A_{tot}, s^{-1}	τ_{rad}, ms
$^3F_4$	$^3H_6$	1763.0	239.36^{ED}	100	239.36	4.18
$^3H_5$	$^3F_4$	3816.8	$9.69^{ED} + 0.26^{MD}$	2.5	406.09	2.46
	$^3H_6$	1206.0	$291.03^{ED} + 105.11^{MD}$	97.5		
$^3H_4$	$^3H_5$	2329.4	$25.20^{ED} + 10.48^{MD}$	2.2	1649.2	0.606
	$^3F_4$	1446.5	$122.23^{ED} + 27.27^{MD}$	9.1		
	$^3H_6$	794.6	1464.01^{ED}	88.7		
$^3F_2+{}^3F_3$	$^3H_4$	4923.7	$20.48^{ED} + 0.39^{MD}$	0.4	4898.3	0.204
	$^3H_5$	1581.3	590.23^{ED}	12.0		
	$^3F_4$	1118.1	$818.81^{ED} + 72.33^{MD}$	18.2		
	$^3H_6$	684.2	3396.12^{ED}	69.4		
$^1G_4$	$^3F_2+{}^3F_3$	1529.3	$86.00^{ED} + 4.64^{MD}$	3.1	2867.8	0.349
	$^3H_4$	1166.9	$257.70^{ED} + 39.56^{MD}$	10.4		
	$^3H_5$	777.4	$845.70^{ED} + 161.92^{MD}$	35.1		
	$^3F_4$	645.9	$215.47^{ED} + 13.49^{MD}$	8.0		
	$^3H_6$	472.7	1243.3^{ED}	43.4		
$^1D_2$	$^1G_4$	1519.1	188.17^{ED}	3.7	34688	0.029
	$^3F_2+{}^3F_3$	762.1	$2320.43^{ED} +185.66^{MD}$	4.0		
	$^3H_4$	659.9	2010.27^{ED}	5.8		
	$^3H_5$	514.2	135.03^{ED}	0.4		
	$^3F_4$	453.2	18445.5	53.2		
	$^3H_6$	360.5	11403.4	32.9		

For calculating the absorption oscillator strengths, we have used the full Tm^{3+} ions density, although some authors suggest to account only for ions located in C_2 sites [$\sim(3/4)N_{Tm}$] [Mon39]. However, for a "mixed" ceramic, the actual distribution of dopant ions over the C_2 and C_{3i} sites may significantly differ from that for the parent material. Tables IV.4 and 5 contain the results of J-O analysis. The Δ_{rms} value equals 1.202 due to the transitions to thermally coupled levels $^3F_2$ + $^3F_3$ and $^1I_6$ + $^3P_0$ + $^3P_1$. For the lowest-lying excited-state ($^3F_4$), a relatively good agreement is observed. The corresponding J–O parameters are Ω_2 = 2.537, Ω_4 = 1.156 and Ω_6 = 0.939 [10^{20} cm^2]. These values agree well with those reported recently for another Tm^{3+}-doped "mixed" sesquioxide ceramic with a composition $(Lu,Sc)_2O_3$, Table IV.6, [Jin17]. The probabilities (ED + MD) of spontaneous radiative transitions, the total probabilities of radiative transitions from excited-states, the luminescence branching ratios and the radiative lifetimes

were calculated, cf. Table IV.5. The mean emission wavelengths $\langle\lambda_{em}\rangle$ were estimated using the barycenter energies of Tm^{3+} multiplets $\langle E\rangle$ from Table IV.4. For the $^3F_4$ and $^3H_4$ states, τ_{rad} amounts to 4.18 ms and 0.61 ms, respectively.

Table IV.6. Comparison of the J–O intensity parameters (× 10^{-20} cm^2) of Tm^{3+} ions in $(Y,Lu)_2O_3$ with another cubic sesquioxides

Materials	Ω_2	Ω_4	Ω_6	Ref.
Crystals				
Y_2O_3	3.17	1.43	0.48	[For99]
	2.51	0.85	0.49	[Mon22]
	4.07	1.46	0.61	[Cai75]
Lu_2O_3	2.87	1.38	0.46	[For99]
	2.29	0.89	0.55	[Mon22]
Sc_2O_3	2.58	0.88	0.67	[For99]
	1.98	0.85	0.52	[Mon22]
$(Y,Lu)_2O_3$	5.44	3.37	1.57	[Che20]
Ceramics				
Sc_2O_3	2.92	1.30	0.90	[Che11]
$(Y,Lu)_2O_3$c	2.58	1.16	0.94	This work
$(Lu,Sc)_2O_3$	2.43	1.08	0.65	[Jin17]

IV.2.B. Transition cross-sections for Tm^{3+} ions

The absorption cross-sections σ_{abs} for the $^3H_6 \rightarrow {}^3H_4$, $^3F_4$ transitions of Tm^{3+} in the "mixed" $(Y,Lu)_2O_3$ laser ceramic, and in Y_2O_3 and Lu_2O_3 ceramic are shown in Figure IV.27(a,b). The absorption band, the $^3H_6 \rightarrow {}^3H_4$ transition, is suitable for pumping Tm-lasers using commercially available AlGaAs diode lasers emitting around 0.8 µm, Figure IV.27(a). For the "mixed" ceramic, the absorption spectrum is broadened as compared to both parent compounds; the maximum σ_{abs} is 0.33×10^{-20} cm^2 at 796.2 nm corresponding to an absorption bandwidth $\Delta\lambda_{abs}$ of ~21 nm (combining several peaks), compared with $\sigma_{abs} = 0.37\times10^{-20}$ cm^2 at 796.7 nm with $\Delta\lambda_{abs}$ of ~7 nm for the $Tm:Y_2O_3$ ceramic.

The second absorption band, the $^3H_6 \rightarrow {}^3F_4$ transition, is promising for in-band pumping by Raman-shifted Erbium fiber lasers operating at 1.68 µm, Figure IV.27(b). The peak σ_{abs} amounts to 0.56×10^{-20} cm^2 at 1632.0 nm ($Tm:(Y,Lu)_2O_3$), 0.69×10^{-20} cm^2 at 1635.0 nm ($Tm:Y_2O_3$) and 0.78×10^{-20} cm^2 at 1629.3 nm ($Tm:Lu_2O_3$) corresponding to absorption bandwidths (FWHM) $\Delta\lambda_{abs}$ of ~21, ~11 and ~10 nm, respectively.

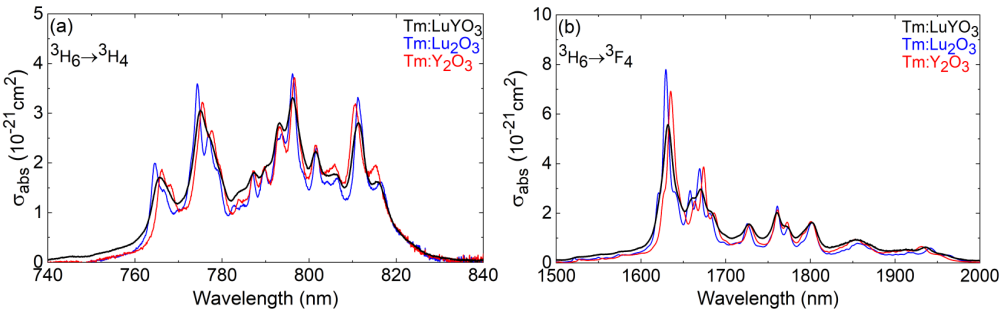

Figure IV.27. Absorption cross-sections, σ_{abs}, for (a) the $^3H_6 \rightarrow {}^3H_4$ transition (b) and the $^3H_6 \rightarrow {}^3F_4$ transition of Tm^{3+} ions in the $(Y,Lu)_2O_3$, Y_2O_3 and Lu_2O_3 ceramics.

The stimulated-emission (SE) cross-sections, σ_{SE}, for the $^3F_4 \rightarrow {}^3H_6$ transition of Tm^{3+} ions in the $(Y,Lu)_2O_3$ ceramic were calculated using the reciprocity method and the F–L formula, Figure IV.28.

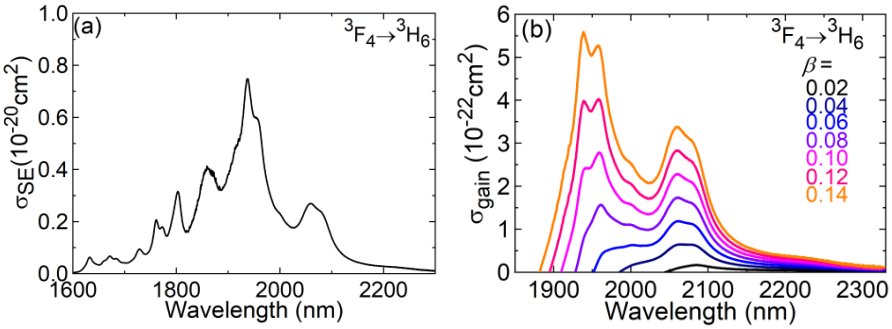

Figure IV.28. Transition cross-section of Tm^{3+} ions in the $(Y,Lu)_2O_3$ ceramic: (a) absorption, σ_{abs}, and stimulated-emission (SE), σ_{SE}, cross-sections for $^3H_6 \rightarrow {}^3F_4$ and $^3F_4 \rightarrow {}^3H_6$ transitions; (b) σ_{abs} for $^3H_6 \rightarrow {}^3F_4$ and combined σ_{SE} for $^3F_4 \rightarrow {}^3H_6$ transitions. F-L – Füchtbauer-Ladenburg, RM – reciprocity method. The gain cross-sections of Tm^{3+} ions in the $(Y,Lu)_2O_3$ ceramic, the $^3F_4 \rightarrow {}^3H_6$ transition.

The σ_{SE} spectra obtained by both methods were in good agreement with each other, considering the effect of reabsorption on the measured emission spectrum. In the F-L formula, we have used a radiative lifetime of the $^3F_4$ state $\tau_{rad} = 3.85 \pm 0.1$ ms to fit the two methods which reasonably agrees with that determined using the J–O theory (4.18 ms). The maximum σ_{SE} is 0.75×10^{-20} cm^2 at 1937 nm and at longer wavelengths where the laser operation is expected, $\sigma_{SE} = 0.27 \times 10^{-20}$ cm^2 at 2059 nm.

The gain profiles of "mixed" ceramic are shown in Figure IV.28(b).The spectra are smooth and broad extending until 2.35 μm. For small inversion ratios ($\beta < 0.10$), two local maxima appear in the spectra, centered at ~2085 and 2059nm. For $\beta = 0.04$, the gain bandwidth (FWHM) is as broad as 75 nm. For higher $\beta > 0.10$, the gain maxima experience a blue-shift to ~1960 and 1938 nm. The observed broadband gain properties indicate the high suitability of this ceramic for generation of sub-100 fs pulses. The existence of gain at long wavelengths well above 2.1 μm due to the multiphonon-assisted transitions is an important prerequisite for generation of ultrashort pulses from mode-locked Tm sesquioxide lasers. Indeed, the emission spectra of such lasers delivering pulses in the sub-100 fs time domain contained spectral components extending up to 2.3 μm [Zha20, Zha21a].

It should be noted that the absorption cross-sections for the studied Tm:$(Y,Lu)_2O_3$ ceramic is almost similar to those for the ceramics studied in Chapter IV.1.

For the $^3F_4$ Tm^{3+} state, the decay curves are well described by a single-exponential law, Figure IV.29(a), yielding τ_{lum} = 3.470 ms for the Tm:$(Y,Lu)_2O_3$ ceramic. This value is slightly longer compared to the parent compounds, 3.224 ms (Tm:Lu_2O_3) and 2.919 ms (Tm:Y_2O_3). Note that the measured luminescence lifetimes of the $^3F_4$ state for the studied sesquioxide ceramics are close to those obtained for single-crystals with low Tm^{3+} doping levels (<0.3 at.%), i.e., 3.38 ms (Tm:Lu_2O_3) and 3.54 ms (Tm:Y_2O_3) [Loi18a], indicating a relatively weak concentration quenching.

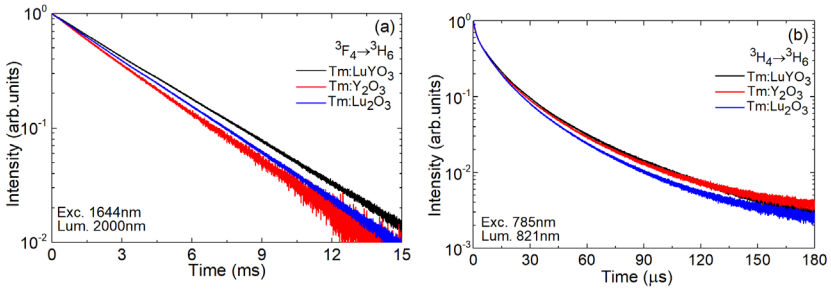

Figure IV.29. Luminescence decay curves for Tm^{3+} ions in the $(Y,Lu)_2O_3$, Y_2O_3, and Lu_2O_3 ceramics: (a) decay from the $^3F_4$ state, λ_{exc} = 1644 nm, λ_{lum} = 2000 nm; (b) decay from the $^3H_4$ state, λ_{exc} = 785 nm, λ_{lum} = 821 nm. Powdered samples.

Table IV.7. Measured luminescence lifetimes of the $^3F_4$ and $^3H_4$ Tm^{3+} states in the $(Y,Lu)_2O_3$, Y_2O_3 and Lu_2O_3 ceramics.

Ceramic	τ_{lum}, ms	
	$^3H_4$	$^3F_4$
$(Y,Lu)_2O_3$	0.024	3.47
Y_2O_3	0.025	2.92
Lu_2O_3	0.022	3.22

For the $^3H_4$ pump level, the decay is clearly not single-exponential, Figure IV.29(b), owing to the efficient cross-relaxation (CR) process, $^3H_4 + {}^3H_6 \rightarrow {}^3F_4 + {}^3F_4$. For the Tm:$(Y,Lu)_2O_3$ ceramics, the mean luminescence lifetime of the $^3H_4$ state $\langle\tau_{lum}\rangle$ is only 24 μs. It is much shorter than the so-called intrinsic lifetime (measured at a very low Tm^{3+} doping level, i.e., unaffected by the CR process), $\tau_{lum,0}$ = 350 μs for Tm:Lu_2O_3 [Loi18a]. Thus, the estimated CR rate, $W_{CR} = (1/\tau_{lum}) - (1/\tau_{lum,0})$, is about 3.88×10^4 s^{-1} (for 3 at.% Tm^{3+} doping). The CR rate is quadratically proportional to the doping concentration, $W_{CR} = C_{CR}(N_{Tm})^2$ [Loi16], where $C_{CR} = 0.56 \times 10^{-37}$ cm^6s^{-1} is the concentration-independent CR parameter. Table IV.7 summarizes the measured luminescence lifetimes.

IV.3. Spectroscopy and laser operation of Tm:$(Y,Sc)_2O_3$ ceramics produced from laser-ablated nanoparticles

In Section IV.1, we overview the spectroscopic properties of Tm-doped parent and solid-solution cubic rare-earth sesquioxide ceramics. It was shown that additional scandia is the most efficient way to alter the spectroscopic properties of Tm ions due to the great difference between the ionic radius of Y^{3+} or Lu^{3+} and Sc^{3+} cations. On the other hand, one can expect a detrimental effect of the solid-solution on the thermal properties of ceramics. In this section, we focus on a particular case of Tm^{3+}-doped "mixed" $(Y,Sc)_2O_3$ ceramics to demonstrate the effect of scandia addition on the broadband emission properties as well as their thermal conductivity. The specific feature of these ceramic samples resides in the original method of synthesis of the starting nanopowders, by laser ablation. This method greatly improves the optical quality of the ceramics as evidenced by the efficient continuous-wave laser operation of these materials [Pir21, Mak23].

IV.3.A. Synthesis of ceramics and structural study

Transparent Tm:$(Y_{1-x}Sc_x)_2O_3$ ceramics were fabricated by solid-state consolidation of nanoparticles synthesized by laser ablation of a solid target material [Osi13]. The ceramics were fabricated by our colleagues at the Institute of Electrophysics, Ural Branch of the RAS, Ekaterinburg, Russia. The synthesis scheme of the ceramics is shown in Figure IV.30. To prepare the targets, commercial high-purity R_2O_3 (R =Y, Sc, Tm) powders were dry-mixed for 24 h in the proportion $Tm_{0.05}(Y_{1-x}Sc_x)_{1.95}O_3$ (x = 0, 0.125, 0.25). A small amount (1.7 mol%) of zirconium dioxide (ZrO_2) was used in the mixtures as a sintering additive. ZrO_2 was employed to reduce the grain boundary mobility and prevent the formation of pores trapped within grains caused by rapid grain growth during the pressureless sintering stage of sesquioxides powders [Mak23]. The mixtures were compacted and sintered at 1100°C for 5 h in air to reach the mechanical strength sufficient for laser ablation. The vapor phase above the target surface, formed under irradiation by a pulsed CO_2 laser, was cooled by an airflow to condense and crystallize as nanoparticles. The details of the experimental setup and the main laser parameters can be found in [Osi13, Pir21]. The coarse particles such as fragments of the solid target and μm-sized melt droplets were extracted from the obtained nanopowder by sedimentation in ethyl alcohol. Their composition was $(Tm_{0.05}Y_{0.95})_2O_3$, $(Tm_{0.05}Y_{0.829}Sc_{0.121})_2O_3$, and $(Tm_{0.05}Y_{0.698}Sc_{0.252})_2O_3$ according to the inductively coupled plasma mass spectrometry analysis. To complete the phase transition from structure type B to structure type C, they were calcined at 1050°C and uniaxially pressed in a stainless-steel die at 200 MPa to form green bodies with a diameter of 15 mm and a thickness of ~3 mm. To fabricate the ceramics, the green bodies were sintered at 1750 °C for 5 h under a residual gas pressure of 10^{-3} Pa. The sintered ceramics were annealed at 1400 °C for 2 h in air to eliminate color centers. The ceramic disks (Ø12 mm, ~1.8–1.9-mm-thick) were polished to laser-grade quality on both sides. A photograph of annealed polished ceramic disks is shown in Figure IV.30. The samples were transparent with a slight yellow coloration attributed to Tm^{3+} doping.

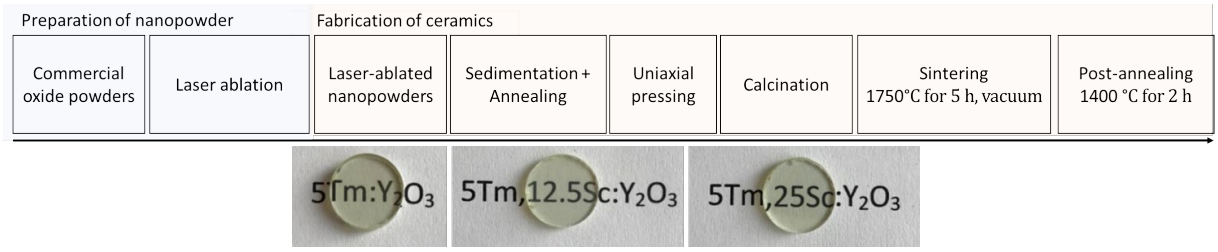

Figure IV.30. A synthesis scheme of the $Tm_{0.05}(Y_{1-x}Sc_x)_{1.95}O_3$ and a photograph of annealed and laser-grade polished ceramic disks.

A typical Scanning Electron Microscope (SEM) images of a thermally etched surface and a fracture surface of the $(Tm_{0.05}Y_{0.95})_2O_3$ and $(Tm_{0.05}Y_{0.829}Sc_{0.121})_2O_3$ ceramics are shown in Figure IV.31. The samples consisted of polyhedral-shaped micro-crystallites separated by well-defined and clean boundaries. Partial substitution of Y^{3+} by Sc^{3+} accelerated the diffusion processes and caused a notable increase in the grain size (D_{grain} = 6.8, 21.2, and 28.2 μm for 0, 12.1, and 25.2 at.% Sc^{3+}). The content of μm-sized pores progressively increased, X_{pore} = 0.6,

25.9, and 46.1 ppm, respectively, as shown in Figure IV.31(c). It is likely that the accelerated grain growth led to the entrapment of a considerable fraction of pores. In Figure IV.31(a,b), the lines present polishing defects. All studied ceramics were re-polished to induce those defects.

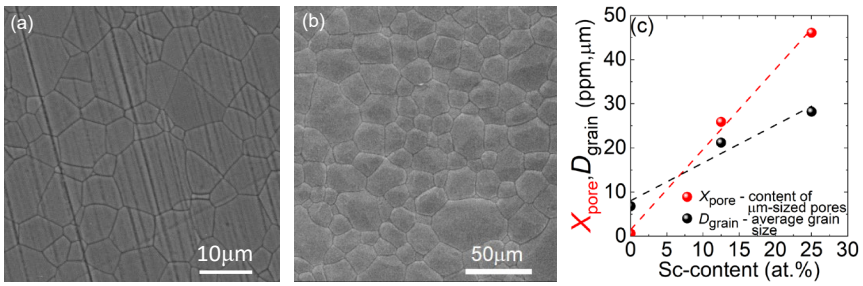

Figure IV.31. Scanning Electron Microscope (SEM) images of the 5 at.% Tm:$(Y,Sc)_2O_3$ ceramic: (a) the thermally etched and polished surface of the $(Tm_{0.05}Y_{0.95})_2O_3$ ceramic; (b) an etched surface of $(Tm_{0.05}Y_{0.698}Sc_{0.121})_2O_3$ ceramic; (c) Sc-content dependence of the average grain size (D_{grain}) and content of μm-sized pores (X_{pore}). The lines in (a,b) are the polishing defects.

IV.3.B. Thermal properties of ceramics

The thermophysical characteristics of ceramics were studied by the laser flash method using a NETZSCH LFA 467 Hyper- Flash at 25–350°C under Ar atmosphere by our colleagues from North-Caucasus Federal University, Stavropol, Russia. The samples were covered with a graphite layer. The thermal conductivity was calculated as follows:

$$\kappa = \alpha C_p \rho \qquad \text{(IV.1)}$$

where α is the thermal diffusivity, C_p is the specific heat, and ρ is the density evaluated from the XRD analysis, see Figure IV.32(a-c). At room temperature (RT), κ gradually decreases from 5.93 to 4.48 W m^{-1} K^{-1} when raising the Sc^{3+} content from 0 to 25.2 at.%, as expected for solid solution compositions, see Figure IV.32(c).

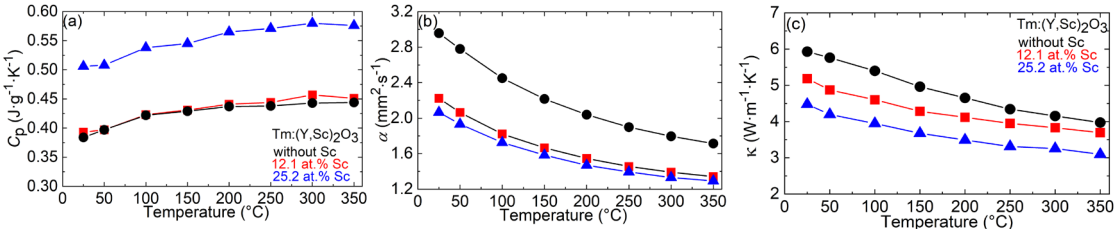

Figure IV.32. 5 at.% Tm:$(Y_{1-x}Sc_x)_2O_3$ ceramics (x = 0 – 0.252): temperature dependence of (a) specific heat C_p, (b) thermal diffusivity α, and (c) thermal conductivity κ.

Considering the presence of ~1.7 mol.% ZrO_2 in the fabricated ceramic, a κ value of 5.93 W m^{-1} K^{-1} for the $(Tm_{0.05}Y_{0.95})_2O_3$ ceramic is comparable to the previously reported values of 7.46 W m^{-1} K^{-1} for a $(Tm_{0.05}Y_{0.95})_2O_3$ single crystal and 6.39 W m^{-1} K^{-1} for a $(Yb_{0.05}Y_{0.92}Zr_{0.03})_2O_3$ ceramic [Mun11, Hou11]. Since the atomic mass and the ionic radius of Tm^{3+} (169 u and 0.880 Å) and Yb^{3+} (173 u and 0.868 Å) are close to each other, a similar level of distortion and effect on the thermal properties is expected when Y^{3+} cations are partially substituted by Tm^{3+} or Yb^{3+} ones. For mixed ceramics, the maximum κ amounts to 5.18

($(Tm_{0.05}Y_{0.829}Sc_{0.121})_2O_3$) and 4.48 W m^{-1} K^{-1} ($(Tm_{0.05}Y_{0.698}Sc_{0.252})_2O_3$). These values are close to those in undoped $(Y_{0.833}Sc_{0.167})_2O_3$ and $(Y_{0.767}Sc_{0.231})_2O_3$, 7.20 and 5.53 W m^{-1} K^{-1}, respectively, [Yan22] considering the additional Tm^{3+} and ZrO_2 doping.

To describe the change in thermal conductivity of the ceramics when Y^{3+} is substituted by Sc^{3+} we used the Gaume model [Gau03] which can be described as follows:

$$\kappa = \frac{1}{\pi a_o}\sqrt{\frac{2k_B\nu\kappa_o}{\delta}}A\tan\left(\pi a_o\sqrt{\frac{\kappa_o\delta}{2k_B\nu}}\right), \quad \text{(IV.2)}$$

with

$$\delta = \sum_i c_i\left(\frac{M_i - M}{M}\right)^2 \quad \text{(IV.2)}$$

and

$$M = \sum_i c_i M_i \quad \text{(IV.3)}$$

with a_o is the average interatomic distance, k_B is the Boltzmann's constant, κ_o is the undoped thermal conductivity value, ν is the sound velocity of longitudinal acoustic modes in solid material, δ is the mass variance of the lattice substitution sites of average mass M that have an occupation probability c_i to be occupied with ions i with mass M_i.

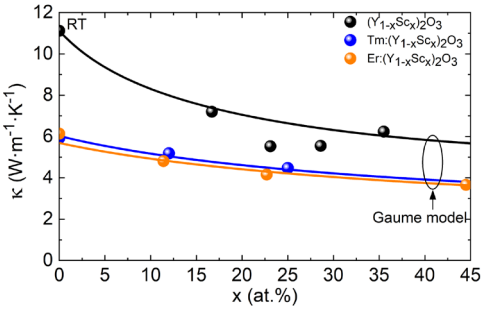

Figure IV.33. Room temperature (RT) thermal conductivity as a function of dopant concentration for $(Tm_{0.05}Y_{1-x}Sc_x)_2O_3$, $(Er_{0.07}Y_{1-x}Sc_x)_2O_3$ [Mak23] and $(Y_{1-x}Sc_x)_2O_3$ [Yan22] ceramics, *points* are experimental values, *curves* are simulations following the Gaume model.

Figure IV.33 illustrates the comparison of the experimental and calculated concentration dependence of κ for $(Tm_{0.05}Y_{1-x}Sc_x)_2O_3$, $(Er_{0.07}Y_{1-x}Sc_x)_2O_3$ [Mak23] and $(Y_{1-x}Sc_x)_2O_3$ [Yan22] ceramics. A good agreement between our data and the literature is observed. As shown in [Mun11], the thermal conductivity of Y_2O_3 significantly decreases as the content of heavy RE^{3+} ions increases, *e.g.*, from 16 W m^{-1} K^{-1} (undoped Y_2O_3 single crystal) to 7.5 W m^{-1} K^{-1} (5 at.% $Tm:Y_2O_3$). In the presence of light Sc^{3+} addition, thermal conductivity decreases smoothly from 11 to 6.2 W m^{-1} K^{-1} for 0 at.% and 35.5 at.% Sc^{3+}, respectively, as shown in Figure IV.33. These facts indicate that the influence of the cation atomic mass difference on thermal conductivity is more pronounced than the difference in ionic radius.

As mentioned before, the measured value of $(Tm_{0.05}Y_{0.95})_2O_3$ ceramic is slightly lower than for the single crystal with the same composition without ZrO_2 doping. This fact indicates slightly higher concentration of lattice defects in the sintered ceramics. Oxygen vacancies formed for charge compensation due to the introduction of tetravalent Zr^{4+} into Y^{3+} sites could be

responsible for the additional drop-off in thermal conductivity. In general, the phonon propagation determines the heat transport in dielectric materials and the mean phonon free path is the most important parameter controlling the thermal conductivity. The addition of Sc_2O_3 and ZrO_2 to Tm:Y_2O_3 induces a structural distortion because of a mismatch in the atomic mass and the ionic radius between Sc^{3+}, Zr^{4+} and Y^{3+}. The introduction of those cations can be considered as substitutional defects causing additional phonon scattering that shortens their mean free path and deteriorates the thermal properties [Kle60].

In order to keep κ at its highest value a cationic substitution in a crystal lattice (ions with the same size and charge), dopant ions must substitute cations with a comparable atomic weight [Gau03]. An example can be found in cubic sesquioxides such as RE^{3+}-doped Lu_2O_3. [Koo11] for which the κ reported values with an increase of Tm^{3+} concentrations range from 12.8 (0 at.% Tm) to 11.3 W m^{-1} K^{-1} (5 at.% Tm).

IV.3.C. Effect of Sc^{3+} addition on the spectroscopic properties of Tm^{3+} ions in the $(Y_{1-x}Sc_x)_2O_3$ isostructural series

The formation of a substitutional solid-solution for Sc-containing ceramics was confirmed by Raman spectroscopy, see Figure IV.34. For Tm:Y_2O_3 ceramic, a total of 12 Raman modes out of 22 possible are observed. The most intense Raman band assigned to F_g +A_g modes of the cubic bixbyite structure broadens and experiences a progressive shift towards higher frequencies with increasing Sc^{3+} content from 377 to 390 cm^{-1}. For 25.2 at.% Sc^{3+}, it is centered at 390 cm^{-1} (bandwidth, 31 cm^{-1}) and the highest phonon energy is 614 cm^{-1}. This behaviour well agrees with the phonon spectra of the parent compounds showing the most intense peaks at 377 cm^{-1} (Y_2O_3) and 419 cm^{-1} (Sc_2O_3).

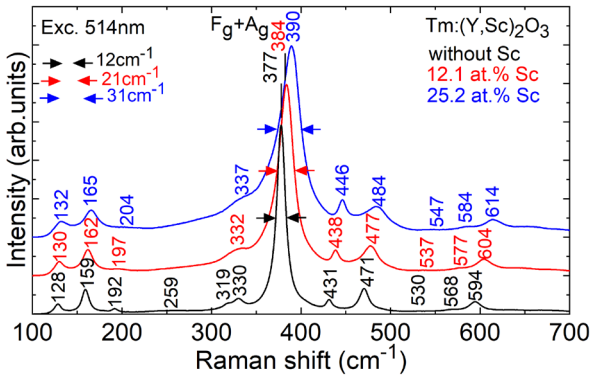

Figure IV.34. Raman spectra of 5 at.% Tm:$(Y_{1-x}Sc_x)_2O_3$ ceramics, λ_{exc} = 514 nm, *numbers* – Raman frequencies in cm^{-1}.

The in-line transmission spectra of the annealed ceramics from 230 to 1100 nm are plotted in Figure IV.35. The transmission at ~1 µm was T = 81.5%, 81.0%, and 80.5%, respectively. Those values are close to the theoretical limit set by Fresnel losses at the polished surfaces of the ceramic disks which is 82.7% (Y_2O_3) and 81.0% (Sc_2O_3) [Bas23]. The drop-off in transmission in the visible and UV spectral ranges with increasing Sc^{3+} content in the ceramics could be due to a combination of light scattering by pores and uncontrolled impurities. Undoped Y_2O_3 and Sc_2O_3 have a broad transparency range from around 0.22 µm to 8 µm. The

spectra contain typical Tm^{3+} absorption bands in that region and additional bands around 420 and 450 nm indicating the presence of a small amount of Ho^{3+} ions.

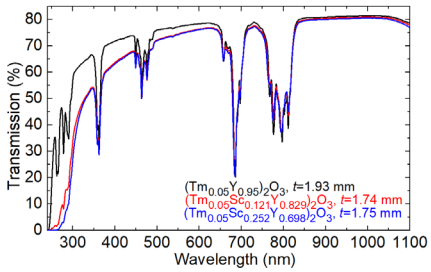

Figure IV.35. Transmission spectra of Tm:$(Y_{1-x}Sc_x)_2O_3$ ceramics from 1100 to 220 nm.

The absorption spectra of Tm^{3+} ions in three ceramics for different spectral range were measured and plotted in terms of absorption cross-section, σ_{abs}, in Figure IV.36. The Tm^{3+} ion density N_{Tm} was 1.35, 1.38, and 1.42 [10^{21} at./cm^3] for 0, 12.1, and 25.2 at.% Sc^{3+}, respectively. All Tm^{3+} absorption bands from $^3H_6$ are observed and assigned following [Gru64].

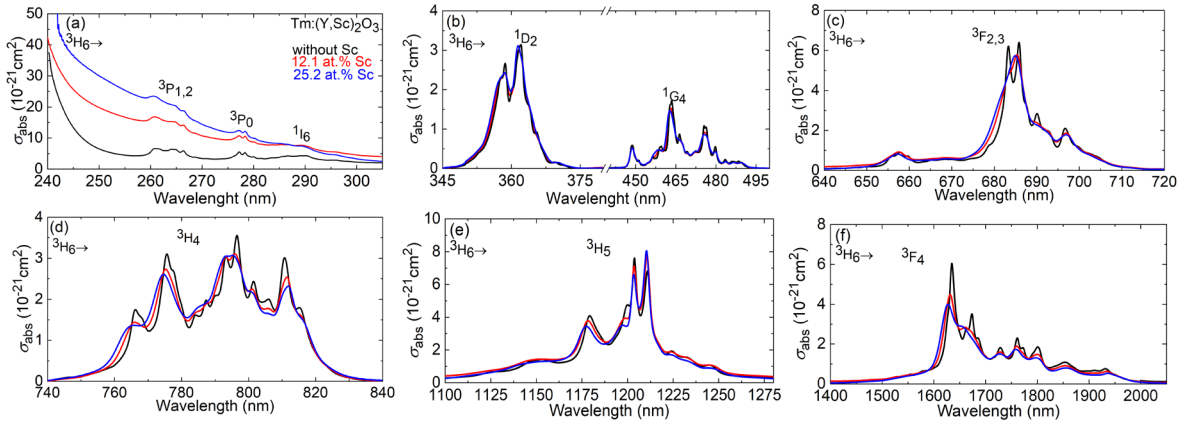

Figure IV.36. RT absorption cross-section spectra of Tm:$(Y_{1-x},Sc_x)_2O_3$ ceramics in different spectral ranges.

By adding Sc^{3+}, the absorption spectra become less structured as shown in Figure IV.36 and the σ_{abs} peaks slightly decrease. For the $^3H_6 \rightarrow {}^3H_4$ transition, the σ_{abs} peak value amounts to 0.36×10^{-20} cm^2 at 797 nm (0 at.% Sc), 0.31×10^{-20} cm^2 at 796.0 nm (12.1 at.% Sc) and 0.30×10^{-20} cm^2 at 795 nm (25.2 at.% Sc). The corresponding absorption linewidth (FWHM) is about 7, 15 and 17 nm. For the $^3H_6 \rightarrow {}^3F_4$ transition, the maximum σ_{abs} decreases from 0.61×10^{-20} cm^2 at 1635 nm (0 at.% Sc) to 0.4×10^{-20} cm^2 at 1627 nm (25.2 at.% Sc). The linewidth of those bands increases from 21 nm to 71 nm, respectively. For the ($Tm_{0.05}Y_{0.698}Sc_{0.252}$)$_2O_3$) ceramic, the observed σ_{abs} peaks are comparable to those reported by [Suz22] for a ($Tm_{0.02}Y_{0.49}Sc_{0.49}$)$_2O_3$ crystal. They are 0.21×10^{-20} cm^2 and 0.36×10^{-20} cm^2 at 794 and 1620 nm, respectively.

The stimulated-emission (SE) cross-section, σ_{SE}, spectra for the $^3F_4 \rightarrow {}^3H_6$ transition are shown in Figure IV.37. The calculations were performed as in Section IV.1 of this chapter, using the same methods. The σ_{SE} spectra obtained by the reciprocity and the F-L methods were in good agreement with each other, considering the effect of reabsorption on the measured

emission spectra. The adjusted radiative lifetimes of the $^3F_4$ manifold were 3.5, 3.6 and 4.0 ms of Tm^{3+} ions in $(Tm_{0.05}Y_{0.95})_2O_3$, $(Tm_{0.05}Y_{0.829}Sc_{0.121})_2O_3$ and $(Tm_{0.05}Y_{0.698}Sc_{0.252})_2O_3$ ceramics. For the mixed ceramics, the average refractive index of Y_2O_3 and Sc_2O_3 was used.

The peak σ_{SE} decreases from 0.82×10^{-20} cm² at 1933 nm to 0.67×10^{-20} cm² at 1941 nm when the Sc^{3+}-content increases. In the spectral range where the laser operation is expected, σ_{SE} is 0.32×10^{-20} cm² at 2050 nm (0 at.% Sc) and 0.24×10^{-20} cm² at 2075 nm (25.2 at.% Sc). For the $(Tm_{0.02}Y_{0.49}Sc_{0.49})_2O_3$ single crystal, the maximum σ_{SE} is 0.68×10^{-20} cm² and 0.22×10^{-20} cm² at 1949 nm and 2099 nm, respectively.

The spectra are very broad, spanning from 1.55 µm to 2.55 µm. By replacing Y^{3+} cations (R_Y = 0.9 Å for VI-fold O^{2-} coordination) with much smaller Sc^{3+} ones (R_{Sc} = 0.745 Å), the emission spectra of Tm^{3+} ions broadened and shifted toward longer wavelengths due to an increased crystal field strength in scandia as compared to yttria. A close look at the long-wave part of the spectra of all the studied ceramics in Figure IV.37(b) shows the long-wave emission plotted on a semi-log scale, indicating that the emission extends up to 2.55 µm. This part of the spectrum is structured and follows an exponential law at wavelengths greater than 2.25 µm. A more detailed explanation about the physics of this behavior will be given in section 6 of this chapter.

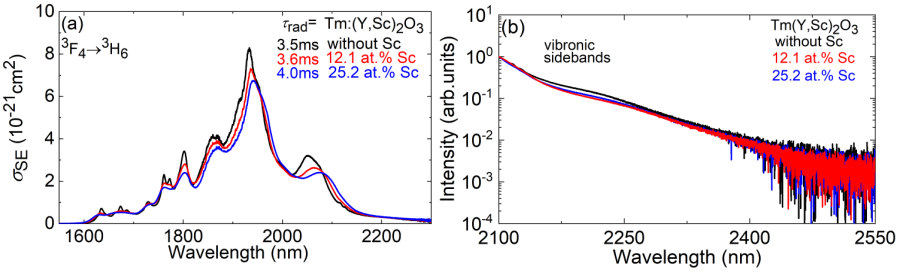

Figure IV.37. RT combined stimulated-emission cross-section spectra for the $^3F_4 \rightarrow {}^3H_6$ transition of Tm^{3+} ions in the $(Y_{1-x}Sc_x)_2O_3$ ceramics, taking into account reabsorption; (b) phonon-assisted emission above 2.1 µm.

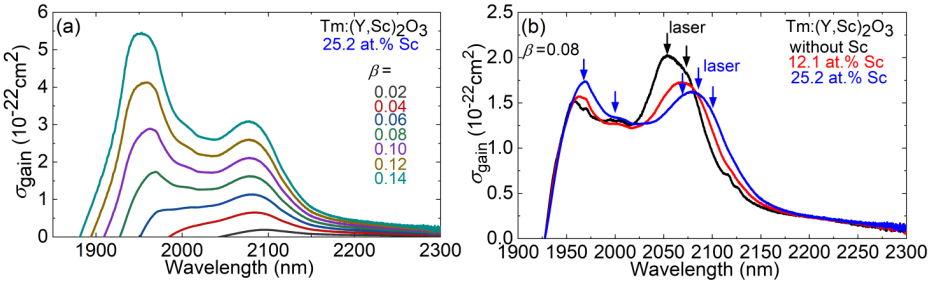

Figure IV.38. RT gain cross-sections spectra: (a) the $(Tm_{0.05}Y_{0.698}Sc_{0.252})_2O_3$ ceramic plotted for different inversion ratios; (b) a comparison of the gain profiles of the Tm:$(Y_{1-x}Sc_x)_2O_3$ ceramics for the same inversion ration (β = 0.08). The *black* and *red arrows* indicate the laser wavelengths for $(Tm_{0.05}Y_{0.95})_2O_3$ and $(Tm_{0.05}Y_{0.698}Sc_{0.252})_2O_3$ ceramic lasers.

The gain cross sections for the $^3F_4 \leftrightarrow {}^3H_6$ transition were calculated and plotted in Figure IV.38. For all ceramics, the gain profiles are broad and extended beyond 2 µm. For $(Tm_{0.05}Y_{0.698}Sc_{0.252})_2O_3$, for small inversion ratios $\beta < 0.06$, a local peak at ~2.09 µm dominates in the spectra and for higher β, another peak at ~1.95 µm appears. For small β = 0.06, the gain

bandwidth (FWHM) reaches 167 nm indicating a great potential for ultrashort (sub-100 fs) pulse generation [Suz23], as shown in Figure IV.38(a).

Figure IV.38(b) shows the comparison between the gain profiles of the different ceramics plotted for β = 0.08. As expected, the addition of Sc^{3+} shifts the position of the long-wave maximum in the gain spectra to longer wavelengths and induces a broadening of the gain spectra from 78 nm to 109 nm.

For the luminescence dynamic study, we employed finely powdered samples to avoid the effect of reabsorption on the measured lifetimes. The RT luminescence decay curves from the $^3F_4$ upper laser level of Tm^{3+} ions in the studied ceramics were measured under resonant excitation, as shown in Figure IV.39. They are well described by a single-exponential law and the $^3F_4$ lifetime was weakly dependent on the Sc^{3+} content, τ_{lum} = 2.41 – 2.55 ms.

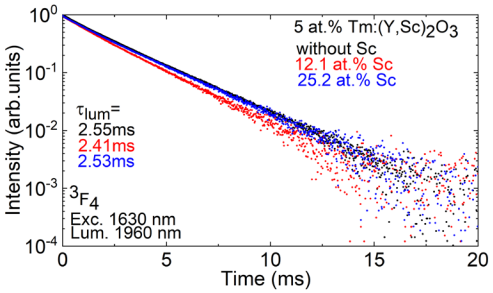

Figure IV.39. RT luminescence decay curves of the 5 at.% Tm:$(Y_{1-x}Sc_x)_2O_3$ ceramics from the $^3F_4$ manifold, λ_{exc} = 1630 nm, λ_{lum} = 1960 nm. Powder samples.

The inhomogeneous spectral broadening of Tm^{3+} absorption / emission bands in "mixed" (solid-solution) ceramics was confirmed by low-temperature (12 K) spectroscopy of the $^3F_4 \leftrightarrow {}^3H_6$ transitions, see Figure IV.40. An additional spectral broadening of the studied ceramics as compared to Tm:Y_2O_3 single crystals was induced by ZrO_2. [Pir21] reported on the same spectral broadening caused by the addition of ZrO_2. The linewidth of the peak at 1636 nm is 8 nm for the Tm:Y_2O_3 ceramic whereas for the ceramics doped with 12 at.% and 25 at.% Sc the linewidth is 20 and 30 nm, respectively.

An additional band in the LT absorption spectra appears below 1600 nm which is due to vibronic sidebands. In the emission spectrum, additional peaks around 2.1 μm and one around 1.9 μm are caused by a small amount of Ho^{3+} ion impurities in the ceramics.

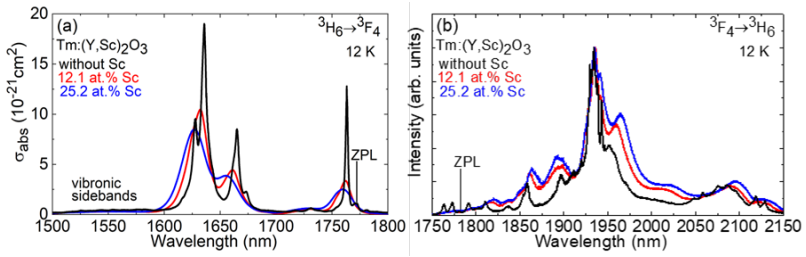

Figure IV.40. Low-temperature (LT, 12 K) spectroscopy of Tm^{3+} ions in the Y_2O_3 and $(Y,Sc)_2O_3$ ceramics: (a) the $^3H_6 \rightarrow {}^3F_4$ transition in absorption; (b) the $^3F_4 \rightarrow {}^3H_6$ transition in emission. ZPL – zero-phonon line.

IV.3.D. Efficient $Tm:Y_2O_3$ and $Tm:(Y,Sc)_2O_3$ ceramic lasers

For laser experiment, the $(Tm_{0.05}Y_{0.95})_2O_3$ and $(Tm_{0.05}Y_{0.698}Sc_{0.252})_2O_3$ ceramics were employed using the same laser set-up as in Chapter II.2.

The laser elements were cut from the central part of the ceramic disks; they were double-side polished to laser-grade quality with good parallelism and left uncoated. A hemispherical cavity was formed by a flat pump mirror coated for high transmission (HT, T = 78.7%) at 0.81 μm and high reflection (R > 99.9%) at 1.86 – 2.33 μm and concave OCs with a transmission T_{OC} in the range of 0.2% - 3.5% at the laser wavelength. The total cavity length was ~102 mm. The pump wavelength was 811 nm. The pump radiation was focused into the ceramic using an AR-coated aspherical lens (focal length: f = 75 mm). The pump spot diameter in the focus was 50±10 μm. The pumping was in double-pass due to a back-reflection from the OCs at the pump wavelength (R ~80%). For the $(Tm_{0.05}Y_{0.95})_2O_3$ ceramic and the optimum T_{OC} = 3.5%, the total pump absorption under lasing conditions was 51.0% representing a certain ground-state ($^3H_6$) bleaching. The radius of the laser mode in the ceramic was calculated using the ABCD method accounting for the thermal lens in $Tm:Y_2O_3$, w_L = 57±5 μm, indicating a good mode-matching.

The $(Tm_{0.05}Y_{0.95})_2O_3$ ceramic delivered a maximum output power of 812 mW with a high slope efficiency η of 70.2% (vs. the absorbed pump power) for T_{OC} = 3.5%, Figure IV.41(a). With increasing the output coupling, the laser threshold gradually increased from 90 mW (T_{OC} = 0.2%) to 393 mW (T_{OC} = 3.5%). The emission wavelength experienced a slight blue-shift with increasing the output coupling, from 2061–2085 nm (T_{OC} = 0.2%) to 2048–2063 nm (T_{OC} = 3.5%), see Figure IV.41(b). Comparing with the laser gain spectrum (Figure IV.38(b), one can assess that the laser operated at small inversion ratios below β = 0.08 since no shift of the emission wavelength to values below 2.0 μm was observed. The obtained laser slope efficiency exceeds the Stokes limit, $\eta_{St,L} = \lambda_P/\lambda_L$ = 39.6%, owing to an efficient CR among adjacent Tm^{3+} ions. After Loiko *et al.* [Loi18a], for 5 at.% Tm^{3+} doping in Y_2O_3, the quantum efficiency of excitation into the $^3F_4$ manifold is η_q = 1.97±0.03 (almost ideal one-to-two process). The upper limit for the slope efficiency is then [Dal14] $\eta < \eta_{St,L}\eta_q\eta_{mode}\eta_{OC}$ = 69±3%, where $\eta_{OC} = \ln[1 - T_{OC}]/\ln[(1 - T_{OC})(1 - L)]$ = 87±3% is the output-coupling efficiency (L is the round-trip passive loss, see below) and $\eta_{mode} \approx 1$ is the mode-matching one.

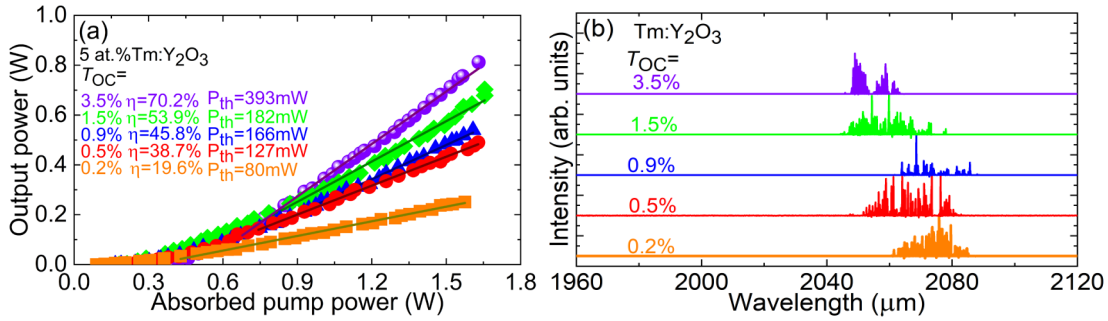

Figure IV.41. ~2 μm laser performance of the $(Tm_{0.05}Y_{0.95})_2O_3$ ceramic: (a) input-output dependences, η – slope efficiency; (b) typical spectra of laser emission.

For the yttria-scandia $(Tm_{0.05}Y_{0.698}Sc_{0.252})_2O_3$ ceramic, the laser generated 523 mW at 2065–2097 nm with a lower η of 44.7% and a laser threshold of 275 mW (for a smaller T_{OC} = 1.5%), Figure IV.42(a). The laser threshold was in the range 165 – 484 mW for output coupler transmissions between 0.3% and 3.5%. The deterioration of the slope efficiency for the Sc-containing ceramic is mainly related to higher passive losses caused by the residual porosity. The laser emission spectra for the "mixed" ceramic are shown in Figure IV.42(b). For $T_{OC} \leq 1.5\%$, the laser operated at 2.08 μm and for higher output coupling, additional lines at 1.96 and 1.99 μm appeared. This behavior agrees with the gain spectra for increased inversion ratios, cf. Figure IV.38(b). A clear red-shift of the laser wavelength due to the Sc^{3+} effect on the emission spectra was observed.

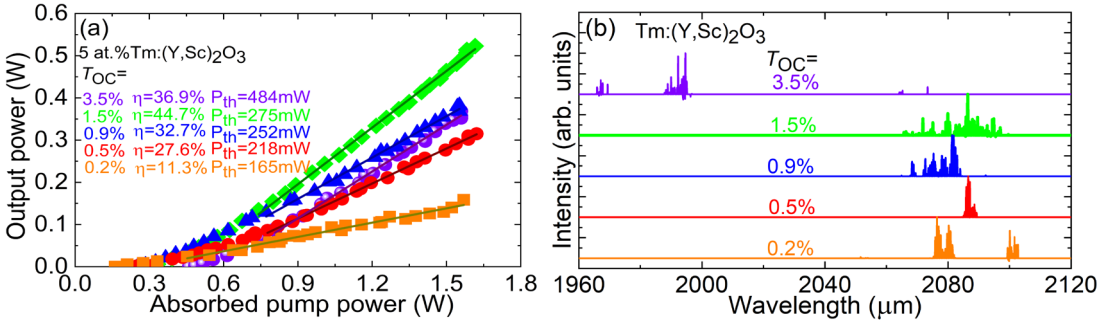

Figure IV.42. ~2 μm laser performance of the $(Tm_{0.05}Y_{0.698}Sc_{0.252})_2O_3$ ceramic: (a) input-output dependences, η – slope efficiency; (b) typical spectra of laser emission.

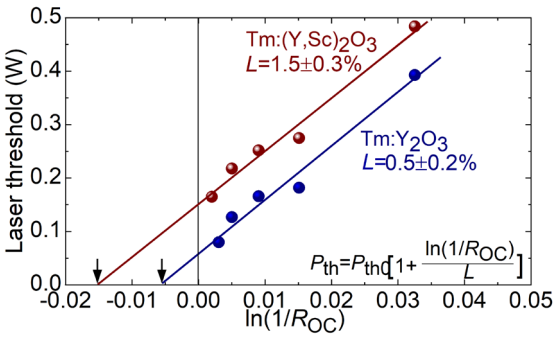

Figure IV.43. The Findlay-Clay analysis for estimating the round-trip passive loss L for $(Tm_{0.05}Y_{0.95})_2O_3$ and $(Tm_{0.05}Y_{0.698}Sc_{0.252})_2O_3$ ceramics

The round-trip passive losses in the ceramics were evaluated using the Findlay-Clay analysis [Cai88] by plotting the laser threshold P_{th} versus $\ln(1/R_{OC})$ where $R_{OC} = 1 - T_{OC}$ is the output coupler reflectivity, Figure IV.43. This analysis yielded L = 0.5±0.2% and 1.5±0.3% for the yttria and yttria-scandia ceramics, respectively. The rapid increase in the passive losses for the Sc-containing ceramic agrees with the higher content of pores for this material.

Suzuki *et al.* studied $(Tm_{0.031}Y_{0.474}Sc_{0.495})_2O_3$ single-crystals grown by the Czochralski method at a reduced temperature of 2100 °C. Under diode-pumping at 780 nm, an output power of 422 mW was generated at 2.11 μm with η = 45% [Suz22]. Jing *et al.* reported on a diode-pumped $(Tm_{0.048}Lu_{0.635}Sc_{0.317})_2O_3$ ceramic laser delivering 1.01 W at 2.10 μm with lower η = 24% [Jin17]. Pirri *et al.* reported on a quasi-CW diode-pumped $(Tm_{0.05}Sc_{0.252}Y_{0.698})_2O_3$ ceramic laser generating 1.24 W at 2.08 μm with lower η =9.5% [Pir21]. Our results for the

Tm:$(Y,Sc)_2O_3$ ceramic in terms of laser slope efficiency are superior to all previously studied Tm^{3+}-doped "mixed" sesquioxide ceramics and close to the best results for single-crystals.
The best result for the parent Tm:Y_2O_3 ceramic was achieved by Wang *et al.*: a diode-pumped $(Tm_{0.02}Y_{0.98})_2O_3$ laser generated 7.25 W at 2.05 μm with η = 40% [Wan17a]. The slope efficiency achieved in this work with the Tm:Y_2O_3 ceramic is close to the best results reported for single-crystalline Tm^{3+}-doped sesquioxides [Loi18a, Koo11a]. Table IV.8 summarize output characteristics of thulium cubic sesquioxides on the $^3F_4 \rightarrow {}^3H_6$ transition.

Table IV.8. Output characteristics of thulium-doped cubic sesquioxides on the $^3F_4 \rightarrow {}^3H_6$ transition.

R_2O_3	Pump	λ_p, nm	C_{Tm} at. %	P_{th}, W	P_{out}, W	η, %	λ_L, μm	Ref.
$(Y,Sc)_2O_3$ ceramic	Ti:Sap	810	5.0	0.27	0.52	44	2.09	This work
$(Y,Sc)_2O_3$ ceramic	LD	793	5.0	3.49	1.24	9	2.08	[Pir21a]
$(Lu,Sc)_2O_3$ ceramic	LD	780	4.8	0.86	1.01	24	2.10	[Jin17]
$(Y,Sc)_2O_3$ crystal	LD	780	3.1	0.30	0.42	45	2.11	[Suz22]
$(Lu,Sc)_2O_3$ crystal	LD	800	1.0		0.71	**55**	2.15	[Koo12]
Y_2O_3 ceramic	Ti:Sap	810	5.0	0.39	0.81	**70**	2.05	This work
Lu_2O_3 crystal	Ti:Sap	796	5.0	0.027	1.50	68	2.08	[Koo11a]
Y_2O_3 ceramic	LD	785	2.0	1.90	7.25	40	2.05	[Wan17]

In this section, we report on highly-efficient ~2 μm laser operation of Tm:Y_2O_3 and Tm:$(Y,Sc)_2O_3$ transparent sesquioxide ceramics. For both parent and solid-solution ceramics, the achieved laser slope efficiencies (70.2% and 44.7%) represent record-high values for any Tm^{3+}-doped sesquioxide ceramics being comparable with the best results for the corresponding single-crystals. It is due to an efficient cross-relaxation under high Tm^{3+} doping level (5 at.%) and relatively low passive losses even for "mixed" compounds owing to an optimized synthesis procedure involving Tm:$(Y_{1-x}Sc_x)_2O_3$ laser-ablated nanoparticles with a mixture of cations at the atomic level and ZrO_2 as a grain growth inhibitor. The high thermal conductivity of ceramics paves the way towards power scaling under pumping by AlGaAs laser diodes at 0.8 μm or Raman-shifted Erbium fiber lasers at 1.68 μm (in-band pumping). The laser efficiency for "mixed" ceramics could be improved by reducing their residual porosity through optimization of the processing conditions and purification of the Sc_2O_3 raw powder. The solid-solution Tm:$(Y,Sc)_2O_3$ ceramics feature inhomogeneously broadened emission spectra extending up to 2.4 μm making them promising for sub-100 fs pulse generation from SESAM or Kerr-lens mode-locked lasers.

IV.4. First laser operation of a Tm^{3+},Ho^{3+}-codoped sesquioxide

So far, the majority of studies on cubic rare-earth sesquioxides have focused on the single doping with Tm^{3+} or Ho^{3+} ions for laser emission at wavelengths slightly above 2 μm. However, it is known that the Tm,Ho-codoping scheme is beneficial for the development of ultrafast lasers. It facilitates the excitation of Ho^{3+} ions via Tm → Ho energy-transfer and benefits from the combined gain bandwidths of both ions above 2 μm. Therefore, ultrashort pulses can be envisioned from mode-locked lasers. In this section, the first results on the spectroscopy, continuous-wave and broadly tunable laser operation of a Tm,Ho-codoped rare-earth sesquioxide, namely a thulium and holmium codoped "mixed" yttria-scandia laser ceramic are presented. This ceramic represents a significant advance compared to the ceramics presented in the previous section by implementing the Tm,Ho-codoping scheme.

IV.4.A. Synthesis of ceramics and structural study

The studied ceramics were fabricated using the method described in Section IV.3 with minor modifications. To prepare solid targets, commercial high-purity powders (R_2O_3, R = Y, Sc, Tm and Ho) were dry mixed in the following proportion: $Tm_{0.031}(Y_{0.854}Sc_{0.115})_2O_3$, $Tm_{0.031}Ho_{0.006}(Y_{0.848}Sc_{0.115})_2O_3$ 5 mol.% ZrO_2 acting as a sintering additive was added. To irradiate the solid target, a 1070 nm Yb-fiber laser [Saf12] was employed.

According to the transmission electronic microscopy (TEM) observations (Figure IV.44(a)), the obtained powder composition, $Tm_{0.031}Ho_{0.006}(Y_{0.848}Sc_{0.115})_2O_3$, consists of nanosized spherical particles having an average size of about 19 nm assembled into loosely bound aggregates. The sintered ceramic featured a uniform and dense internal structure composed of tightly packed grains with an average size of 20.7 μm, and no precipitated phases were observed around grain boundaries, as demonstrated in Figure IV.44(b).

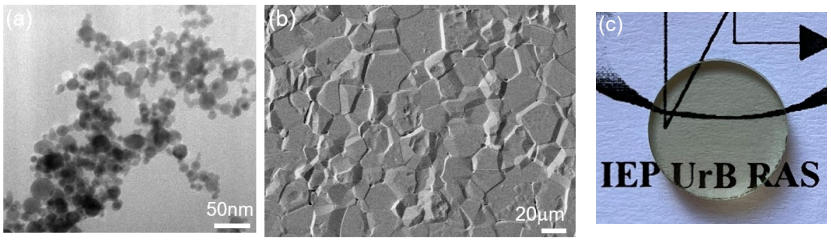

Figure IV.44. $Tm_{0.031}Ho_{0.006}(Y_{0.848}Sc_{0.115})_2O_3$ ceramic: (a) a TEM image the morphology of the as-synthesized nanopowder; (b) a SEM image of chemically etched surface of the ceramic; (c) a photograph of laser-grade polished ceramic disk.

Figure V.45 shows the X-ray diffraction pattern of the $Tm_{0.031}Ho_{0.006}(Sc_{0.115}Y_{0.848})_2O_3$ transparent ceramic. The positions and relative intensities of the observed peaks more closely match the Y_2O_3 phase with a cubic bixbyite structure (C-type, sp. gr. $Ia\bar{3}$, PDF No. 00-041-1105). No evidence of additional crystalline phases attributed to the presence of Sc_2O_3 or ZrO_2 were detected. The addition of Sc_2O_3 into Y_2O_3 lattice induces a small shift of peaks toward the high-angle side due to the ionic radius of Sc^{3+} (0.745 Å), for IV-fold oxygen coordination, which is much smaller than that of Y^{3+} (0.900 Å). The lattice constant of the formed solid solution was

determined to be a = 10.510 Å with the corresponding Tm^{3+} and Ho^{3+} ion densities of 8.55×10^{20} cm^{-3} and 1.65×10^{20} cm^{-3}, respectively.

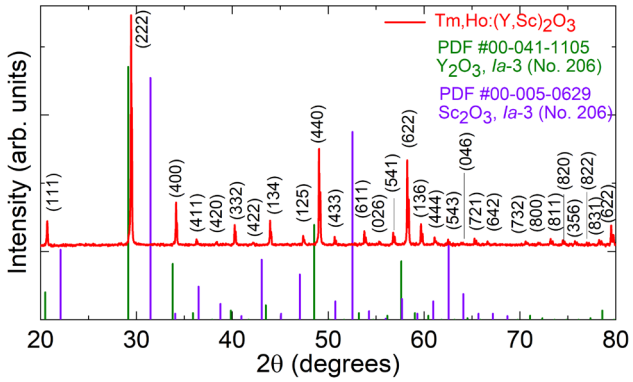

Figure IV.45. An X-ray powder diffraction (XRD) pattern of 3 at.% Tm, 0.6 at.% Ho:$(Y,Sc)_2O_3$ ceramic.

IV.4.B. μ-Raman and μ-luminescence mapping of codoped ceramics

To confirm a uniform distribution of host-forming cations (Y^{3+}, Sc^{3+}) and dopant ions (Tm^{3+}, Ho^{3+}), μ-Raman and μ-luminescence studies were employed, Figures IV.46 and 47. More details about these methods can be found in the Supplemental Materials, Appendix A.3.

For μ-Raman study, we analyzed the most intense Raman mode (F_g + A_g) at 384 cm^{-1}, as shown in Figure IV.46(a), which is related to oxygen motions and deformations of the [RO_6] octahedrons, where R refers to Y, Lu, Sc. The shape of the Raman spectrum confirms the formation of the single-phase cubic sesquioxide. As demonstrated in the previous sections, this peak is sensitive to changing host-forming cations and shifts to higher frequencies in the R = Y → Lu → Sc series, as illustrated in Figure IV.6(b,c). The μ-Raman analysis results are summarized for the 3 at.% Tm, 0.6 at.% Ho:$(Y,Sc)_2O_3$ ceramic in Figure IV.46(b-c).

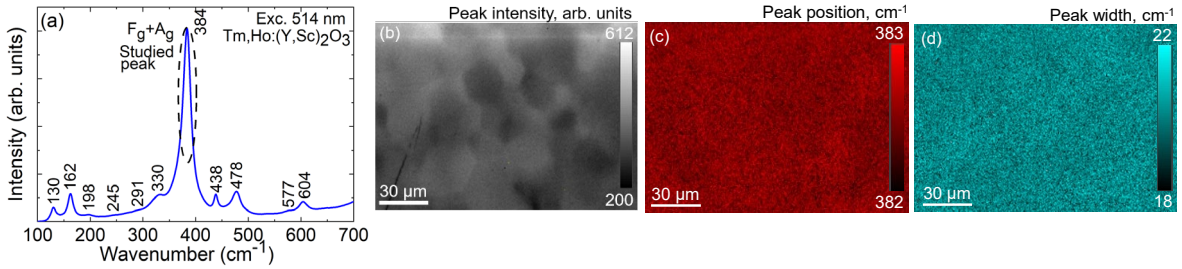

Figure IV.46. μ-Raman study of the 3 at. % Tm^{3+}, 0.6 at. % Ho^{3+} codoped $(Y,Sc)_2O_3$ ceramic: (a) a unpolarized Raman spectrum, λ_{exc} = 514 nm; (b) μ-Raman mapping, of the ceramic surface: measuring the main Raman mode (F_g + A_g) at 384 cm^{-1}, peak intensity; (c) peak position; (d) peak width (FWHM).

The peak intensity, peak position and full width at half maximum for the 384 cm^{-1} Raman band were analyzed. The μ-Raman image shows that the peak intensity of the Raman band is inhomogeneous. It allows us to observe significant variations between individual grains and at the grain boundaries, as shown in Figure IV.46(b). This μ-Raman image looks almost similar to the SEM image shown in Figure IV.44(b). The minima (black color) and maxima (green color)

in the F_g + A_g intensity reveal the differences in crystallographic orientation of the grains in the ceramic. [Mas18] demonstrated the variation of the peak intensity of the T_{2g} Raman mode within a UO_2 ceramic sample and calculated the crystallographic indices associated with the grains of the ceramic sample. It was concluded that grains with minimum T_{2g} intensities have a {100} orientation type whereas grains corresponding to the maximum T_{2g} intensities exhibit {111} and {110} orientations.

The F_g + A_g peak position and peak width maps are shown in Figure IV.46(c,d). The maps demonstrate homogeneous variations in the maximum and minimum of the peak positions and peak bandwidths. This confirms the uniform distribution of the host-forming cations yttrium and scandium within the ceramic.

To study the distribution of thulium and holmium ions in the ceramic, μ-luminescence mapping was used. We compared the peak intensities of Tm^{3+} ($^3H_4 \rightarrow {}^3H_6$ transition) and Ho^{3+} ($^5F_4$, $^5S_2 \rightarrow {}^5I_7$ transition) emissions, as depicted in Figure IV.47(a). The variation of the ratio of peak intensities slightly changes, indicating a uniform distribution of Tm^{3+} and Ho^{3+} ions throughout the Tm:Ho:$(Y,Sc)_2O_3$ ceramic, as shown in Figure IV.47(b).

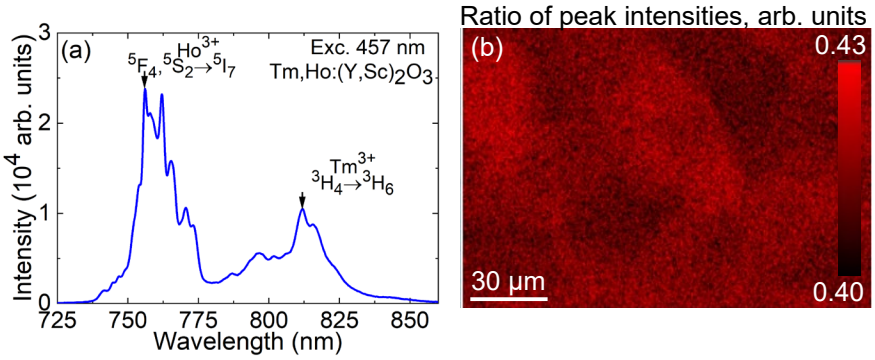

Figure IV.47. μ-luminescence study of the 3 at. % Tm^{3+}, 0.6 at. % Ho^{3+} codoped $(Y,Sc)_2O_3$ ceramic: (a) a luminescence spectrum of Tm^{3+} and Ho^{3+} ions, *arrows indicate to selected peaks for the ratio of peak intensities*, λ_{exc} = 457 nm; (b) μ-luminescence mapping of the ceramic surface: $^5F_4$, $^5S_2 \rightarrow {}^5I_7$ Ho^{3+} and $^3H_4 \rightarrow {}^3H_6$ Tm^{3+} emissions.

IV.4.C. Optical spectroscopy of Tm,Ho:$(Y,Sc)_2O_3$ ceramic

The in-line transmission spectra of the Tm:$(Y,Sc)_2O_3$ and Tm,Ho:$(Y,Sc)_2O_3$ ceramics with a thickness of ~1.7 mm are plotted in Figure IV.48. The spectrum of the Tm:$(Y,Sc)_2O_3$ ceramic is given for comparison. The ceramics exhibit a maximum optical transmittance at 2200 nm, beyond absorption lines of Tm^{3+} and Ho^{3+} ions. The transmission maximum was 81% and 79.7% for the undoped and codoped ceramics, respectively. These values are close to the theoretical transmission of pure Y_2O_3 and Sc_2O_3 ceramics, which are 83% and 81.4% at 2200 nm, respectively.

The absorption spectra of Tm^{3+} and Ho^{3+} ions in the ceramics were calculated from transmission spectra and plotted in Figure IV.49 in terms of absorption coefficient. The assignment of the excited multiplets follows the one by [Car68]. All absorption bands from the ground state $^3H_6$ Tm^{3+} were assigned from $^3F_4$ to $^3P_{1,2}$. Whereas, absorption bands of excited-states of Ho ions are assigned only up to $^3M_{10}$ + $^3L_3$ + (^5G, ^5D, $^3G)_3$ + (^3F, $^3G)_3$ (around 285 nm).

This is due to transitions, which are located deeper in the UV, spectrally overlapping with each other and Tm^{3+} absorption bands, and are superimposed with the UV absorption edge. However, some bands at ~ 250 nm, 243 nm are not assigned. In the same way, the absorption band of the $^5I_4$ Ho^{3+} excited-state was not identified due to spectral overlapping with the $^3H_4$ absorption band of Tm^{3+} ions.

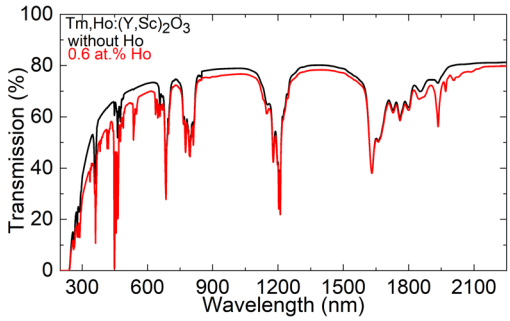

Figure IV.48. Transmission spectra of the single 3 at.% Tm-doped and 3 at.% Tm, 0.6 at.% Ho-codoped $(Y,Sc)_2O_3$ ceramics from 2250 to 200 nm.

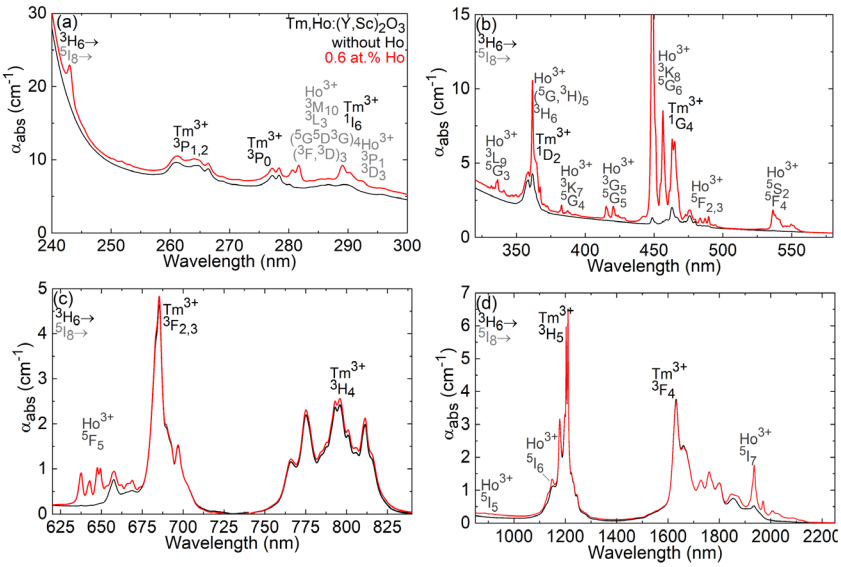

Figure IV.49. RT absorption spectra of $Tm:(Y,Sc)_2O_3$ and $Tm,Ho:(Y,Sc)_2O_3$ ceramics in different spectral ranges.

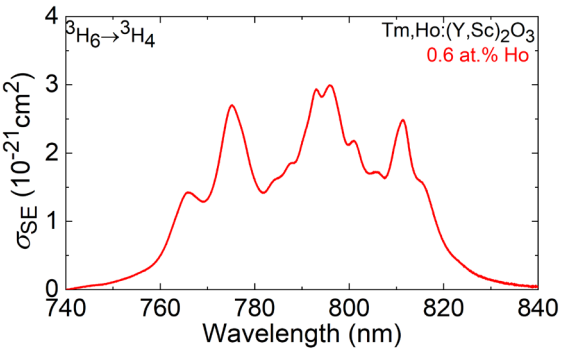

Figure IV.50. RT absorption cross sections, σ_{abs}, for the $^3H_6 \rightarrow {}^3H_4$ Tm^{3+} in 3 at.% Tm,0.6 at.% $Ho:(Y,Sc)_2O_3$ ceramic.

The absorption (σ_{abs}) cross-section spectrum for the $^3H_6 \rightarrow {}^3H_4$ Tm^{3+} transition in the Tm,Ho-codoped $(Y,Sc)_2O_3$ ceramic is shown in Figure IV.50. The spectrum exhibits broadening due to added Sc^{3+}. The maximum σ_{abs} is 0.30×10^{-20} cm^2 at 796 nm associated with an absorption bandwidth (FWHM) of ~20 nm. The value of σ_{abs} is comparable with that in scandium-containing ceramics from the previous section.

Figure IV.51(a) shows the luminescence spectra of the Tm,Ho:$(Y,Sc)_2O_3$ ceramic. Under excitation at 790 nm, the Tm,Ho:$(Y,Sc)_2O_3$ ceramic exhibits intense emission and a broad spectrum, spanning from 1.6 μm to 2.2 μm due to the spectrally overlapping $^3F_4 \rightarrow {}^3H_6$ Tm^{3+} and $^5I_7 \rightarrow {}^5I_8$ Ho^{3+} transitions. To illustrate this effect, the luminescence spectrum for $^3F_4 \rightarrow {}^3H_6$ Tm^{3+} transition in the 3 at.% Tm in the $(Y,Sc)_2O_3$ ceramic is also shown.

The spectrum of the codoped ceramic reveal intense local peaks at 1935 and 1970 nm, as well as, at 2090 and 2120 nm, where the laser emission is expected.

The long-wave phonon-assisted emission of the Tm,Ho:$(Y,Sc)_2O_3$ and Tm:$(Y,Sc)_2O_3$ ceramics is pictured in Figure IV.51(b) in semi-log scale. The figure shows that the long-wave emission of Tm,Ho-codoped ceramic exhibits similar behavior as in Tm-doped ceramic and extends up to 2550 nm. However, the local maximum shifts from ~2225 to 2250 nm. Further details about these phonon sidebands are given in the Section IV.6 of this chapter.

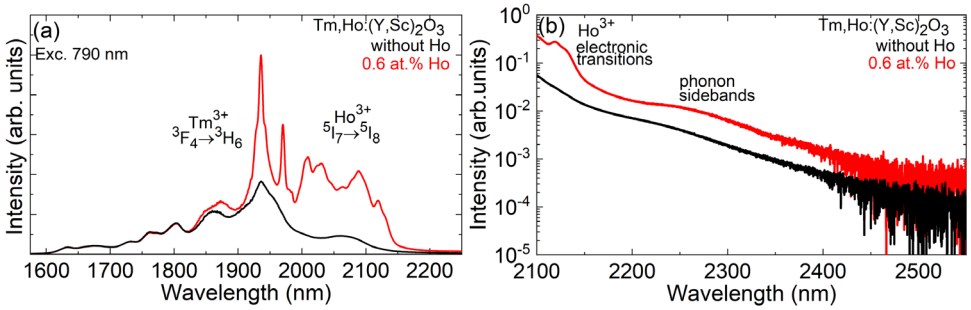

Figure IV.51. RT luminescence spectra of Tm,Ho:$(Y,Sc)_2O_3$ and Tm:$(Y,Sc)_2O_3$ ceramics: (a) around 2 μm; (b) long-wave phonon-assisted emission in semi-log scale.

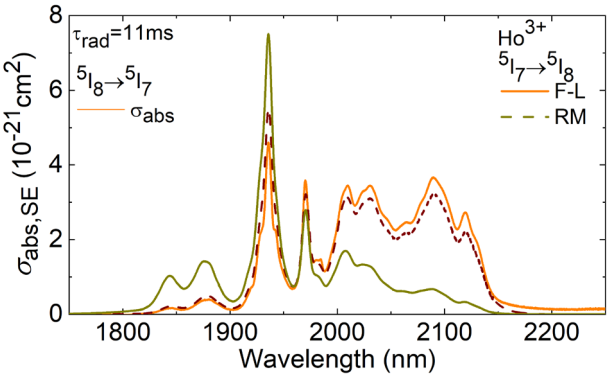

Figure IV.52. RT absorption , σ_{abs}, and stimulated-emission, σ_{SE}, cross-sections for $^5I_8 \leftrightarrow {}^5I_7$ Ho^{3+} transitions. τ_{rad} – radiative lifetime, F-L and RM – Füchtbauer-Ladenburg and Reciprocity method, respectively.

Figure IV.52 shows the stimulated-emission and absorption cross-section spectra for the $^5I_8 \leftrightarrow {}^5I_7$ Ho^{3+} transitions in 3 at.% Tm^{3+}. 0.6 at.% Ho^{3+} in $(Y,Sc)_2O_3$ ceramic. To obtain these spectra, the luminescence and absorption spectra of Tm were subtracted from those of

Tm,Ho:$(Y,Sc)_2O_3$. Afterward, the absorption cross-section for the $^5I_7 \rightarrow {}^5I_8$ Ho^{3+} transition was calculated using $N_{Ho} = 1.65\times10^{20}$ cm^{-3}. The maximum σ_{abs} is 0.75×10^{-20} cm^2 at 1936 nm with a bandwidth of 14 nm, indicating great potential for pumping with a high-power Tm^{3+}-fiber laser. The maximum σ_{SE} peaks are at 0.55×10^{-20} cm^2 at 1936 nm and 0.36×10^{-20} cm^2 and 0.27×10^{-20} cm^2 at 2090 and 2120 nm, respectively, where laser emission is expected.

Figure IV.53 shows the luminescence decay curves obtained for the $^3F_4$ Tm^{3+} and $^5I_7$ Ho^{3+} states in the 3 at. % Tm:$(Y,Sc)_2O_3$ and 1 at. % Ho doped Y_2O_3 ceramics, respectively, under resonant excitation. To avoid the effect of reabsorption on the measured luminescence lifetimes, finely powdered samples were used. For the Ho-doped ceramic, the decay curve exhibits single exponential behavior, resulting in luminescence lifetime τ_{lum} of 10.92 ms. For the Tm-doped ceramic, the decay curve slightly deviates from a single-exponential law due to the phonon-assisted energy-transfer upconversion process. The τ_{lum} is 3.35 ms.

Low-temperature (LT) spectroscopy enables the identification of inhomogeneous spectral broadening in "mixed" sesquioxides ceramics due to compositional disorder, as demonstrated in the previous sections of this chapter. Here, LT measurements confirm that Tm^{3+} and Ho^{3+} ions in $(Y,Sc)_2O_3$ ceramics exhibit an inhomogeneous spectral line broadening at 12 K. Additionally, the luminescence spectra of the Tm,Ho:$(Y,Sc)_2O_3$ ceramic were measured as a function of temperature from 300 to 13 K to demonstrate the effect of the energy-transfer between Tm and Ho ions on the emission properties of the codoped ceramic.

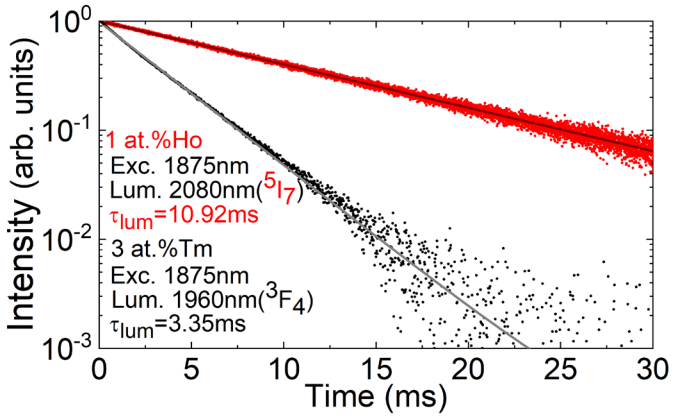

Figure IV.53. RT luminescence decay curves from the $^3F_4$ Tm^{3+} and $^5I_7$ Ho^{3+} states for the single 3 at.% Tm^{3+} and 1 at.% Ho^{3+} ceramics (powdered samples), τ_{lum} – luminescence decay time. *Solid lines* – fitting curves.

The temperature-dependant luminescence spectra of the Tm,Ho:$(Y,Sc)_2O_3$ ceramic for the $^3F_4 \rightarrow {}^3H_6$ Tm^{3+} and $^5I_7 \rightarrow {}^5I_8$ Ho^{3+} transitions, are depicted in Figure IV.54. With decreasing temperature, the intensity of the emission peaks, corresponding to the $^3F_4 \rightarrow {}^3H_6$ Tm^{3+} transition, decreases due to the thermal depopulation of the upper Stark levels of the $^3F_4$ manifold. At the same time the intensity of the Ho^{3+} emission peaks increases indicating a considerable drop in the stored population in $^3F_4$ state, which illustrates the fact that the rate of the direct Tm → Ho energy-transfer becomes faster.

Additionally, Figure IV.54(b) shows the evolution of the luminescence spectra of the Tm,Ho:$(Y,Sc)_2O_3$ ceramic at 2 μm as a function of temperature.

To study the luminescence dynamics of Tm^{3+} and Ho^{3+} ions in the $(Y,Sc)_2O_3$ ceramic as a function of temperature from 12 to 300 K, the luminescence decay curves were measured under resonant excitation of Tm^{3+} ions at 1630 nm. The luminescence was detected at 1900 and 2090 nm for Tm^{3+} and Ho^{3+} ions, respectively using a ceramic disk with a thickness of 2 mm was used. This thickness may affect the luminescence lifetimes due to reabsorption resulting from the partial overlap of the emission and absorption spectra of Tm,Ho: $(Y,Sc)_2O_3$ at 2 µm.

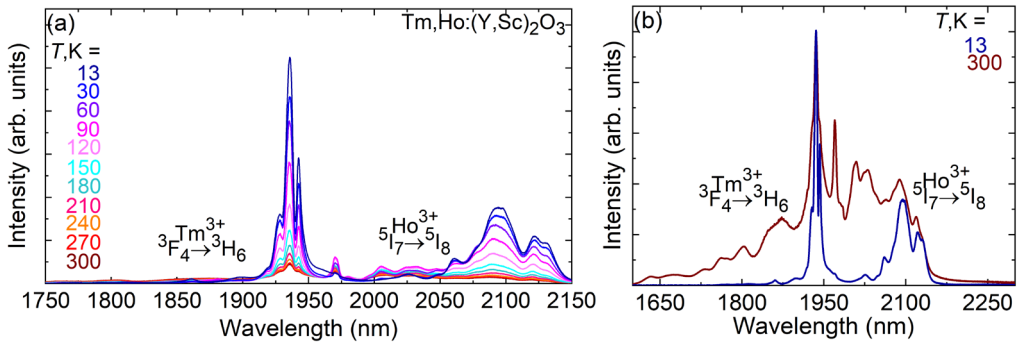

Figure IV.54. LT spectroscopy of the Tm,Ho:$(Y,Sc)_2O_3$ ceramic: (a) temperature-dependant luminescence spectra, the $^3F_4 \rightarrow {}^3H_6$ Tm^{3+} and $^5I_7 \rightarrow {}^5I_8$ Ho^{3+} transitions; (b) comparison of the luminescence spectra at LT and RT.

As mentioned in the previous chapters, one of the characteristics of the Tm → Ho energy transfer is the thermal equilibrium (τ_0) time during which the $^5I_7$ and the $^3F_4$ levels are expected to decay with the same time constant. To determine the equilibrium time, the measured decays were fitted starting from 10.5 ms after the excitation pulse, as shown in Figure IV.55(a). Wash et al. show that both Tm and Ho levels decay with the same time constant for temperatures above 250 K [Wal00]. We show in Figure IV.55(b) that this is also the case for lower temperatures down to 12 K. The equilibrium time gradually increases from 8.4 ms at 300 K and reaches a maximum of~11 ms at 100 K. For lower temperature, the equilibrium time stays almost the same.

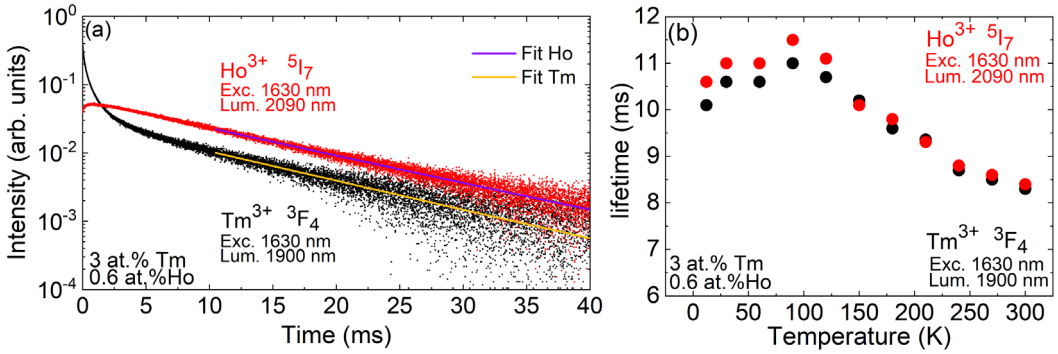

Figure IV.55. Low-temperature luminescence dynamic for $^3F_4$ Tm^{3+} and $^5I_7$ Ho^{3+} manifolds in 3 at. % Tm, 0.6 at.% Ho:$(Y,Sc)_2O_3$ ceramic: (a) luminescence decay curves at 12 K in semi-log scale; (b) temperature dependent luminescence equilibrium lifetimes of the $^3F_4$ Tm^{3+} and $^5I_7$ Ho^{3+} manifolds.

IV.4.D. Tm ↔ Ho energy-transfer: Comparison of different models for evaluating the energy-transfer parameters

The parameters of the bidirectional Tm ↔ Ho energy transfer in the $(Y,Sc)_2O_3$ ceramic were estimated using three approaches : (i) luminescence dynamics study, (ii) Stark levels energies and (iii) spectral overlap between emission and absorption cross-section spectra of Tm^{3+} and Ho^{3+} ions. These methods allow to derive the Tm ↔ Ho energy-transfer parameters which in turns can be used to assess the effective gain cross-section of these codoped laser materials and estimate the contribution of both ions to the laser operation.

Firstly, we measured the luminescence decay curves of both ions using finely powdered samples. The measured luminescence decay curves are shown in Figure IV.56 in a semi-log scale.

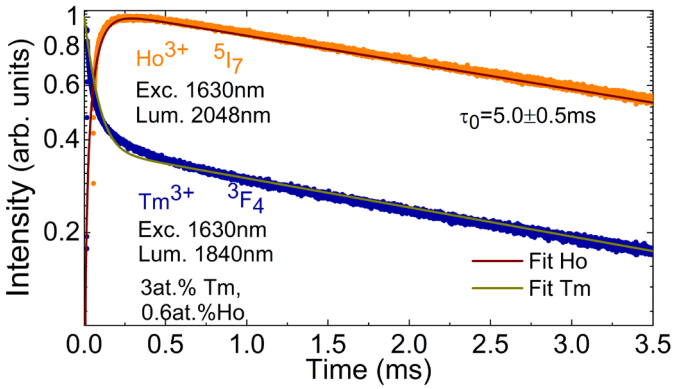

Figure IV.56. Luminescence dynamics of the 3 at.% Tm^{3+} and 0.6 at.% Ho^{3+}: $(Y,Sc)_2O_3$ ceramic: (a) decay curves from $^3F_4$ Tm^{3+} and $^5I_7$ Ho^{3+} states fitting using Walsh model. *Lines* – fit by the Eqs. I.67-68.

The decay curves of the Tm^{3+} and Ho^{3+} ions are non-exponential as expected (see Chapter I). The decay curves are well-fitted using the Walsh model, and the corresponding best parameters are $P_{28} = 0.58 \pm 0.03 \times 10^{-22}$ cm^{3}μs^{-1} and $P_{71} = 0.66 \pm 0.03 \times 10^{-23}$ cm^{3}μs^{-1} and $\tau_0 = 5.0 \pm 0.5$ ms. Θ amounts to 0.115. This value is the same as that for the Tm,Ho:YAG crystal, as shown in Table IV.9. The estimated energy-transfer parameters demonstrate the effective and dominant unidirectional energy-transfer from $^3F_4$ (Tm^{3+}) → $^5I_7$ (Ho^{3+}).

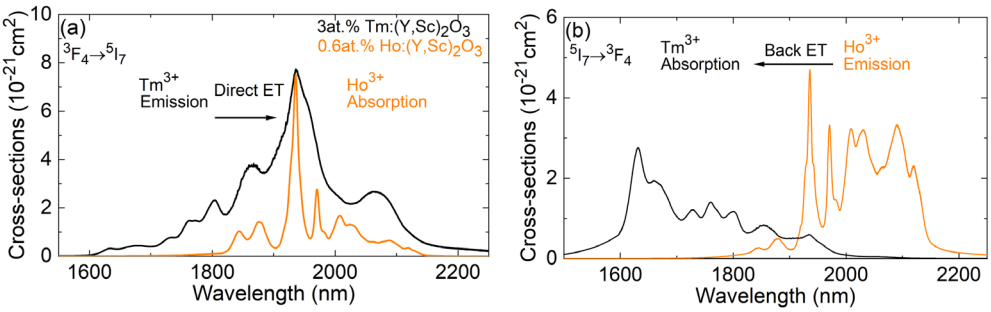

Figure IV.57. σ_{abs} and σ_{SE} cross-sections for Tm^{3+} and Ho^{3+} ions in $(Y,Sc)_2O_3$ ceramics around 2 μm demonstrate (a) direct and (b) back energy-transfers.

To give another estimate of the equilibrium constant Θ, Eq. I.66 was used. The energies of the Stark sub-levels obtained from the crystal-field splitting of the $^3F_4$ Tm^{3+} and $^5I_7$ Ho^{3+}

multiplets in singly doped Tm:Y_2O_3 and Ho:Y_2O_3 ceramics were used to calculate the $^3F_4$ Tm^{3+} and $^5I_7$ Ho^{3+} partition functions, see Table IV.3 and [Loi21a], respectively. We used these sub-levels from singly doped ceramics because the determination of all Stark sub-levels of the first excited levels of Tm and Ho ions in codoped "mixed" sesquioxides is not possible. The calculated value of the equilibrium constant Θ amounts to 0.086. This value is lower than the one estimated from the luminescence decay curves.

Table IV.9. Thulium-holmium energy-transfer parameters for various laser crystals obtained from luminescence dynamic studies

Crystal	P_{28}, 10^{-22} cm^{3}µs^{-1}	P_{71}, 10^{-23} cm^{3}µs^{-1}	$\Theta = P_{71}/P_{28}$	τ_0, ms	Ref.
$GdScO_3$	1.30	0.99	0.076	3.5	This work
$(Y,Sc)_2O_3$	0.58	0.66	0.115	5.0	This work
$Y_3Al_5O_{12}$	1.30	1.50	0.120		[Wal00]
CNGG	0.59	0.68	0.115	6.8	[Pan21a]
$Ca(Gd,Lu)AlO_4$	1.42	0.90	0.064	4.3	[Pan23]
$KY(WO_4)_2$	2.74	1.90	0.069	2.4	[Kur16]
$LiYF_4$	1.07	1.30	0.120	10.4	[Wal00]

The results obtained from the luminescence dynamics and crystal-field data were further supported by a third approach calculating microscopic interaction parameters according to the Förster-Dexter theory of resonant energy-transfer, see Eq. I.73. As described in Chapter I, energy transfer microparameters are determined by the overlap of absorption/emission and emission/absorption spectra of donor and acceptor ions, see Figure IV.57. The microparameters amount to 1.725×10^{-41} cm^{6}s^{-1} (direct energy-transfer, $c_{Tm\rightarrow Ho}$) and 1.001×10^{-42} cm^{6}s^{-1} (back energy-transfer, $c_{Tm\rightarrow Ho}$). The resulting equilibrium constant is 0.058 which takes an intermediate position between the values of equilibrium constants obtained from luminescence dynamic studies and crystal field data.

IV.4.E. Gain spectra of a codoped ceramic

The $\sigma_{gain,Tm}$ and $\sigma_{gain,Ho}$ cannot be calculated independently and used to explain the spectral behavior of wavelength tunable or mode-locked lasers. This is due to the fact that the populations of the excited-states of Tm^{3+} and Ho^{3+} ions are linked to each other within a thermal equilibrium regime by a bidirectional energy-transfer. The effective gain cross-section ($\sigma_{g,eff}$) spectra for Tm^{3+} and Ho^{3+} ions can be calculated for different inversion ratios of Tm^{3+} ions using the following equation [Pan21a]:

$$\sigma_{g,eff} = \left(\beta_{Ho}\sigma_{SE,Ho} - \left(1-\beta_{Ho}\right)\sigma_{abs,Ho}\right)\frac{N_{Ho}}{N_{tot}} + \left(\beta_{Tm}\sigma_{SE,Tm} - \left(1-\beta_{Tm}\right)\sigma_{abs,Tm}\right)\frac{N_{Tm}}{N_{tot}}. \quad \text{(IV.4)}$$

The $\sigma_{g,eff}$ is represented concerning the total thulium and holmium doping concentration, $N_{tot} = N_{Tm} + N_{Ho}$. Presuming the population of only the $^3H_6$, $^3F_4$ manifolds of Tm^{3+} ions and $^5I_8$, $^5I_7$ multiplets of Ho^{3+} ions, the condition of the thermal equilibrium established by the Tm ↔ Ho ET is defined as:

$$P_{28}\left(\mathrm{Tm}\rightarrow\mathrm{Ho}\right)\bullet N_2\left({}^3\mathrm{F}_4\right)\bullet\left(N_{\mathrm{Ho}}-N_7\left({}^5\mathrm{I}_7\right)\right)=P_{71}\left(\mathrm{Ho}\rightarrow\mathrm{Tm}\right)\bullet N_7\left({}^5\mathrm{I}_7\right)\bullet\left(N_{\mathrm{Tm}}-N_2\left({}^3\mathrm{F}_4\right)\right). \quad \text{(IV.5)}$$

From this equation, β_{Ho} is determined as follows:

$$\beta_{\mathrm{Ho}}=\frac{\Omega\beta_{\mathrm{Tm}}}{1+\left(\Omega-1\right)\beta_{\mathrm{Tm}}}, \quad \text{(IV.6)}$$

where, $\Omega = 1/\Theta$. For calculation, an average equilibrium constant Θ of 0.086 obtained by the three methods presented earlier was used.

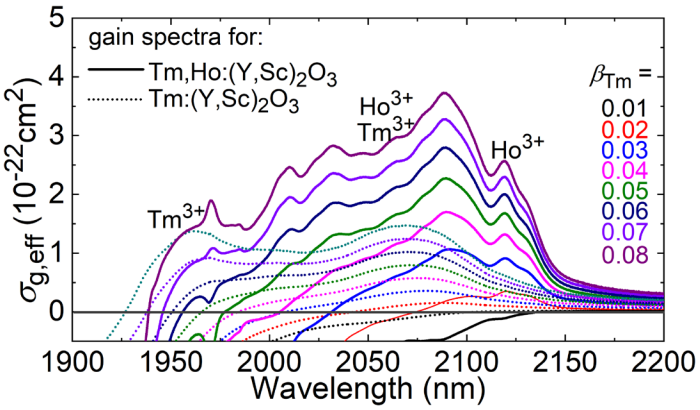

Figure IV.58. "Effective"' gain cross-section spectra account for the Tm^{3+}, Ho^{3+} absorption and stimulated-emission as well as the bidirectional energy transfer between them in the $(Y,Sc)_2O_3$ ceramic, calculated by the Eq. IV.4.

The calculated $\sigma_{g.eff}$ are plotted in Figure IV.58. The gain cross-section for Tm^{3+} ions in singly doped $(Y,Sc)_2O_3$ ceramic is shown for comparison. The gain spectra are smooth and broad. For small $\beta_{\mathrm{Tm}} < 0.03$, the spectra are almost flat and extend beyond 2.1 μm. With increasing the inversion ratio, the local maximum in the gain spectra experiences a blue-shift from 2120 nm to 2088 nm. The peak at 2088 nm, attributed the ${}^5I_7 \rightarrow {}^5I_8$ Ho^{3+} transition, dominates the spectra when the inversion ratio of Tm^{3+} is greater than 0.03. The gain around 2050 nm is due to the contribution of both ions and then, below approximately 2000 nm is mostly due to Tm^{3+}. For $\beta_{\mathrm{Tm}} = 0.08$, the gain bandwidth exceeds 135 nm.

IV.4.F. Efficient and broadly tunable Tm,Ho:$(Y,Sc)_2O_3$ ceramic lasers

For the laser operation of the Tm,Ho:$(Y,Sc)_2O_3$ ceramic, we employed the same laser set-up as in the previous chapters. The laser element was Φ12 mm, $t = 2.0$ mm and double-side polished to laser grade quality with good parallelism, and left uncoated. The ceramic disk was fixed on a passively cooled Cu-holder using a silver paint for better heat removal. A hemispherical laser cavity was formed by a flat PM coated for high transmission ($T = 68\%$) at 775 nm and high reflection at 1.86 – 2.33 μm and a concave (radius of curvature of -100 mm) OCs with a transmission T_{OC} of 0.05 – 3.5% at the laser wavelength. The total cavity length was ~102 mm. The pump beam was modulated using a mechanical chopper (duty cycle of 1:4) and the pump wavelength was 775 nm. A long-pass filter (FEL1400, Thorlabs) was placed after the OC to filter out the residual pump. The pump radiation was focused using an AR-coated aspherical lens with focal length of 75 mm. The pump spot diameter in the focus was 50±10 μm. The pumping

was in double-pass due to a back-reflection from the OCs at the pump wavelength (R ~80%). The total pump absorption under lasing conditions was in the range of 37% – 41%. The radius of the laser mode in the ceramic was calculated using the ABCD method accounting for the thermal lens, w_L = 57±5 μm, indicating a good mode-matching.

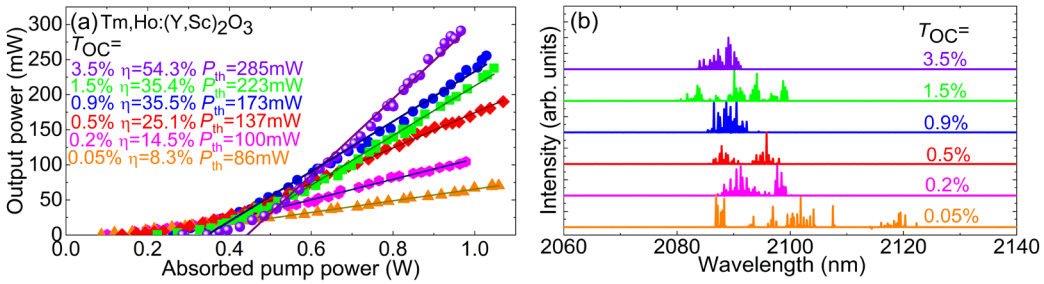

Figure IV.59. 3 at.% Tm, 0.6 at.% Ho:$(Y,Sc)_2O_3$ ceramic laser: (a) input-output dependences, η – slope efficiency; (b) spectra of laser emission.

In CW regime the ceramic laser generated an output power of 291 mW at 2.084 – 2.091 μm with a slope efficiency η of 54.3% (vs. the absorbed pump power) and a laser threshold P_{th} of 285 mW (for T_{OC} = 3.5%), Figure IV.59(a). With increasing the OCs, P_{th} gradually increased from 86 mW (T_{OC} = 0.05%) to 285 mW (T_{OC} = 3.5%) and the laser performance increased as well. Power scaling was limited by the available pump power.

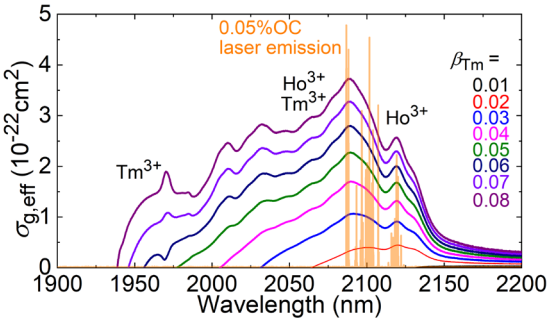

Figure IV.60. "Effective'" gain cross-section spectra of 3 at.% Tm, 0.6 at.% Ho:$(Y,Sc)_2O_3$ ceramic laser, *insert* – laser emission spectrum (T_{OC} = 0.05%).

Typical unpolarized laser emission spectra are shown in Figure IV.59(b). The laser operated on the $^5I_7 \rightarrow {}^5I_8$ Ho^{3+} transition and Tm^{3+} colasing was observed. The laser emission experienced a blue-shift with increasing the output coupling from 2087 – 2122 (T_{OC} = 0.05%) to 2084 – 2091 nm (T_{OC} = 3.5%). It agrees with the gain spectra of Tm^{3+} and Ho^{3+} ions in $(Y,Sc)_2O_3$, Figure IV.60.

The laser operated on the fundamental transverse mode with a measured beam quality factor M^2 < 1.1 at the highest output power, Figure IV.61(a). The round-trip passive losses in the ceramics were evaluated using the Findlay-Clay analysis [Cai88], Figure IV.61(b). This analysis yielded L = 1.4±0.3% for the Tm,Ho:$(Y,Sc)_2O_3$ ceramic laser.

A Lyot filter was used for wavelength-tunable operation. It was made of a 2-mm-thick quartz plate with an optical axis lying in the surface plate. The Lyot filter was inserted into the laser cavity at Brewster's angle close to the laser ceramic. The laser wavelength was CW tunable from 1937.6 to 2128.0 nm (a tuning range of 190.4 nm at the zero-power level) using an OC with T_{OC}

= 0.9%, Figure IV.62, indicating a high potential of this material for generation of femtosecond pulses from mode-locked lasers.

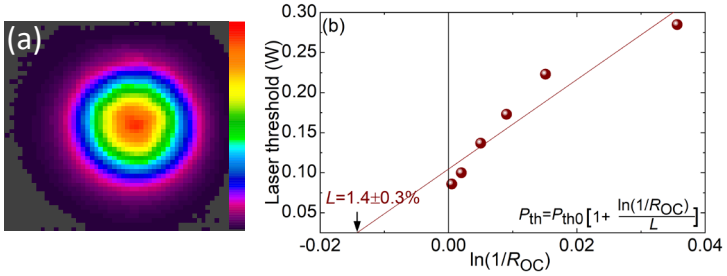

Figure IV.61. 3 at.% Tm, 0.6 at.% Ho:$(Y,Sc)_2O_3$ ceramic laser: (a) a typical far-field mode profile; (b) Findlay-Clay analysis for estimating the roundtrip passive loss *L*.

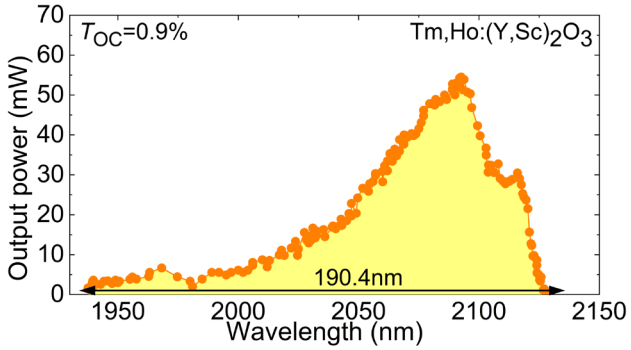

Figure IV.62. A tuning curve of 3 at. %, 0.6 at. % Ho:$(Y,Sc)_2O_3$ ceramic laser, T_{OC} = 0.9%. *the grey line* – the gain spectrum the ceramic for β = 0.07 in arbitrary units, *double arrow* indicates whole tuning range is 190.4 nm.

To conclude, the Tm,Ho-codoped $(Y,Sc)_2O_3$ laser ceramic fabricated from laser-ablated nanopowders demonstrates high potential for broadly tunable and mode-locked lasers emitting around 2 μm. This is because of the following spectroscopic features: a significant inhomogeneous spectral line broadening, induced both by the structure and compositional disorder; an efficient and predominantly direct Tm → Ho energy-transfer, expressed by the equilibrium constant; broad and smooth gain spectra (gain bandwidth of about 135 nm) extending well above 2 μm thus avoiding the unwanted strong water absorption due to the combined gain of both ions and a strong crystal field. In addition, the laser performance confirms a good laser quality of the ceramic.

IV.5. Excited-state absorption, energy-transfer upconversion and first 2.3 μm operation of Tm^{3+}-doped sesquioxides

In this section, we addressed various spectroscopic phenomena which are relevant for laser operation of Tm-doped cubic sesquioxides in the spectral range around 2.3 μm. Such laser emission can originate either from phonon-assisted processes or from the $^3H_4 \rightarrow {}^3H_5$ electronic transition. In order to have a complete understanding of these spectroscopic phenomena, we have studied excited-state absorption of Tm^{3+} ions in the near-infrared, derived the parameters of energy-transfer upconversion based on the measured excited-state absorption spectra, and demonstrated the first 2.3 μm laser operation of Tm-doped lutetium oxide crystal, as well as discussed the physical nature of this laser emission.

IV.5.A. Spectroscopy of the $^3H_4 \rightarrow {}^3H_5$ Tm^{3+} transition in sesquioxides

We start from deriving the stimulated-emission cross-sections for the $^3H_4 \rightarrow {}^3H_5$ electronic transition of Tm^{3+} ions in cubic sesquioxides R_2O_3, where R stands for Y, Lu and Sc.

The main complexity of measuring the luminescence spectra of Tm^{3+} ions around 2.3 μm originate from the strong self-quenching of the $^3H_4$ level lifetime by the cross-relaxation process. Thus, in this study, we employed low doped (0.3 at.% Tm^{3+}) Y_2O_3, Lu_2O_3 and Sc_2O_3 cubic sesquioxide ceramics for such measurements which were performed with a spectral resolution of 3 nm. The measured spectra are plotted in Figure IV.63(a). The spectra extend from 2.2 μm to 2.6 μm. Note that the longest wavelength of the $^3H_4 \rightarrow {}^3H_5$ transition amounts to 2.86 μm for $Tm:Sc_2O_3$. However, due to a technical limitation of the used spectral set-up, we were unable to resolve the emission at such a long wavelength. One needs to consider that the $^3H_4 \rightarrow {}^3H_5$ emission can spectrally overlap with the $^3F_4 \rightarrow {}^3H_6$ one, notably, its long-wave phonon sideband. In this way, one can argue that broad and structureless emission between 2.2 and 2.3 μm can partially originate from this phonon sideband.

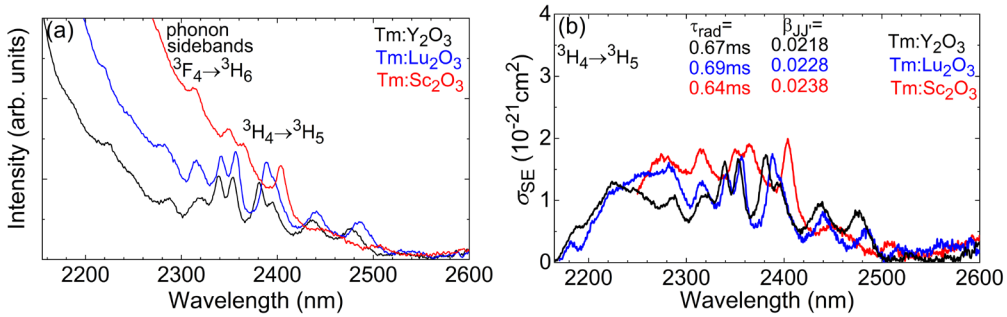

Figure IV.63. RT spectroscopy of 0.3 at.% Tm^{3+} doped Y_2O_3, Lu_2O_3 and Sc_2O_3 ceramics around 2.3 μm: (a) luminescence spectra in the 2155 nm to 2820 nm spectral range; (b) stimulated-emission cross-section for the $^3H_4 \rightarrow {}^3H_5$ transition.

Figure IV.63(b) shows the calculated emission cross-section spectra for the $^3H_4 \rightarrow {}^3H_5$ transition of Tm^{3+} ions in the studied ceramics. It should be noted that we tried to minimize the influence of the nearly exponential phonon sideband associated with the $^3F_4 \rightarrow {}^3H_6$ transition by subtracting it from the measured emission spectra. The stimulated-emission cross-sections were calculated using the Füchtbauer-Ladenburg formula. The radiative lifetimes of the $^3H_4$

level and branching ratios were taken from [For99, Mon22]. The values of the maximum σ_{SE} for the studied ceramics are compared in Table IV.10. For the Tm:Lu_2O_3 ceramic, it amounts to 0.18×10^{-20} cm^2 at 2388 nm.

Table IV.10. Peak stimulated-emission cross-section for the $^3H_4 \rightarrow {}^3H_5$, radiative lifetimes of the $^3H_4$ and branching ratio of thulium ions in the studied R_2O_3 ceramics.

Materials	σ_{SE}, 10^{-20} cm^2	λ_{em}, nm	[a]τ_{rad}, ms	[b]β(JJ'), %
Tm:Y_2O_3	0.17	2382	0.67	2.18
Tm:Lu_2O_3	0.18	2388	0.69	2.28
Tm:Sc_2O_3	0.20	2404	0.64	2.38

a – taken from [For99], *b* – taken from [Mon22].

To estimate the intrinsic luminescence lifetime of the $^3H_4$ upper level of Tm^{3+} ions in the studied ceramics, low doped samples were again used to reduce the effect of cross-relaxation on the measured lifetimes. The corresponding decay curves are plotted in Figure IV.64(a) in a semi-log scale. The kinetics for the 0.3 at.% Tm^{3+} doped ceramics slightly deviate from a single-exponential law at the beginning of the decay. Table IV.11 summarizes the intrinsic lifetimes obtained for the ceramics and single crystals [For99] with a low doping level of ≤ 0.3 at.% Tm. The intrinsic luminescence lifetimes for the ceramics and single crystals are in good agreement with each other, indicating an almost negligible effect of possible defects and impurity centres in the ceramics.

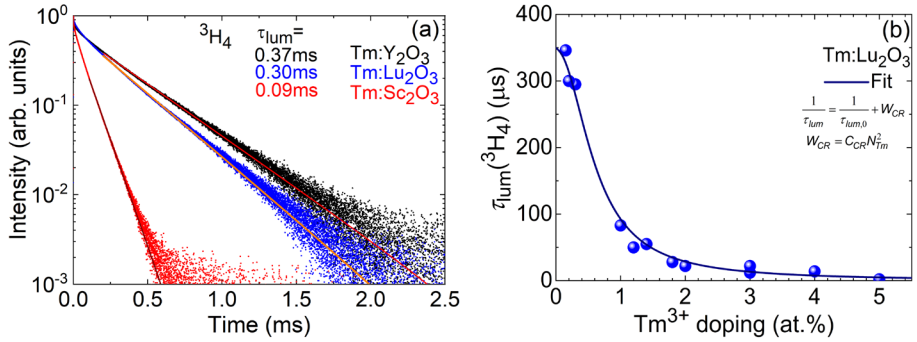

Figure IV.64. (a) RT luminescence decay curves from the $^3H_4$ level in the Ho:R_2O_3 ceramics, λ_{exc} = 785 nm, λ_{lum} = 821 nm. Bulk samples, *solid lines* – exponential fit. (b) Luminescence lifetime of the $^3H_4$ state as a function of Tm^{3+} doping level for Tm:Lu_2O_3, *points* – experimental data, *solid line* their fit.

Table IV.11. Intrinsic luminescence ($\tau_{lum,0}$) lifetimes of the $^3H_4$ Tm^{3+} multiplet in Tm:R_2O_3 doped with a low Tm concentration of ≤ 0.3 at. %.

Compound	$\tau_{lum,0}$, ms ceramic	$\tau_{lum,0}$, ms [For99] crystal
Tm:Y_2O_3	0.37	0.43
Tm:Lu_2O_3	0.30	0.35
Tm:Sc_2O_3	0.09	0.11

Figure IV.64(b) demonstrates the concentration dependence of the luminescence lifetime of the $^3H_4$ Tm^{3+} level in Lu_2O_3. The luminescence lifetime significantly decreases with increasing of Tm^{3+} doping due to the CR effect. Therefore, low Tm^{3+} doping level is preferable for

developing of 2.3 μm Tm-lasers. The experimental points in the figure were fitted using Eqs. I.69-70 to determine the microscopic concentration-independent C_{CR} parameter. For Tm:Lu_2O_3, the defined value of C_{CR} amounts to 1.25×10^{-37} cm^6 s^{-1} [Loi18a].

It should be noted that the difference between the intrinsic luminescence and radiative lifetimes of the $^3H_4$ state becomes greater from yttria to scandia due to the increased influence of non-radiative relaxation, which is significant for scandia.

IV.5.B. Excited-state absorption of Tm^{3+} ions in sesquioxides

It is well-known that the knowledge of excited-state absorption (ESA) properties of Tm^{3+} ions allows for the quantification of concentration-independent parameters of energy-transfer upconversion (ETU) processes [Gui22]. In the context of Tm lasers emitting at 2.3 μm, ETU can play a positive role by refilling the $^3H_4$ upper laser level in of favour the intermediate $^3F_4$ metastable state, and increasing the pump quantum efficiencies up to 2, representing a two-for-one pump process [Loi19a]. Thus, the ETU parameter is of particular importance for designing such lasers. In present work, we aimed to measure the spectra of excited-state absorption corresponding to the $^3F_4 \rightarrow {}^3H_4$ and $^3F_4 \rightarrow {}^3F_{2,3}$ transitions of Tm^{3+} ions in 2.5 at.% Tm:Y_2O_3, 1.8 at. % Tm:Lu_2O_3 and 2.0 at. % Tm:Sc_2O_3 single-crystals to evaluate the ETU parameters, namely K_{ETU} and C_{ETU}. The studied single-crystals were synthesized by our colleagues at the Leibniz-Institut für Kristallzüchtung.

To measure the ESA spectra of the three studied sesquioxide crystals, we employed the pump-probe method. The details of the set-up can be found in Supplemental Materials. The spectra were measured in the 980 – 1650 nm spectral range, where the $^3F_4 \rightarrow {}^3H_4$ and $^3F_4 \rightarrow {}^3F_{2,3}$ transitions are expected to occur. The measured spectra were scaled using the corresponding absorption cross-section spectra for each crystal. In Figure IV.65(a), we demonstrate the raw ESA spectrum, which was scaled, and the absorption cross-section spectra, σ_{GSA}, for the $^3H_6 \rightarrow {}^3F_4$ and $^3H_6 \rightarrow {}^3H_5$ transitions of the Tm:Y_2O_3 crystal as an example. Following state-of-the-art studies, the ESA spectrum is plotted in the range of negative cross-section, $-\sigma_{ESA}$ [Koe95].

We start from the particular case of Tm:Y_2O_3 crystal selected to illustrate the methodology of research regarding to ESA. First, the calibration of the ESA spectra and their assignment to electronic transitions are considered. Thereafter, we demonstrate the alternative approach to access the ESA spectra by RM method from the measured luminescence spectra at 1.5 μm.

In Tm-doped cubic sesquioxides, the ESA spectrum around 1050 nm cannot be precisely scaled due to the spectrally overlapping with the absorption at 1200 nm. Thus, the absorption cross-section from the ESA spectrum should be lower than that obtained from the classical absorption study. In the case of the ESA spectrum around 1400 nm, there is no contribution to the GSA from the ESA, thus, the σ_{ESA} can be precisely scaled. To confirm this, the full set of wavelengths corresponding to electronic transitions between the Stark sub-levels of the $^3F_{2,3}$ and $^3H_4$ Tm^{3+} multiplets was calculated. For the $^3H_4$ multiplet, the data on the crystal-field splitting for Tm^{3+} ions in the Tm:Y_2O_3, Tm:Lu_2O_3 and Tm:Sc_2O_3, obtained in this work, were used. For the $^3F_{2,3}$ multiplets, the data from [Gru64, For99] were used. The result of the calculation is shown in Figure IV.65(a) by the vertical dashes. Each line corresponds to the

possible electronic transitions from each Stark level of the $^3F_4$, $^3H_4$, $^3F_3$ and $^3F_2$ manifolds. It shows that the ESA transitions terminating at the closely located $^3F_2$ and $^3F_3$ manifolds are well resolved. For the ESA around 1400 nm, the transitions are also well resolved. However, we cannot observe the rest of the $^3F_4 \rightarrow {}^3F_3$ electronic transitions due to the absorption around 1150 nm. The same pattern is observed for the Tm:Lu_2O_3 and Tm:Sc_2O_3 crystals.

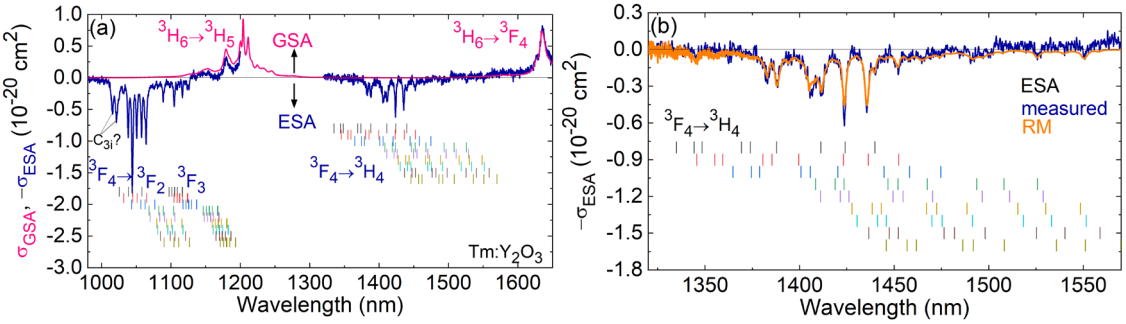

Figure IV.65. Evaluation and interpretation of the ESA cross-section spectra for the Tm:Y_2O_3 crystal: (a) raw ESA spectra scaled to the GSA cross-sections spectra: (b) comparison of the scaled and calculated ESA cross-section spectra using RM method. Dashes – ED electronic transitions of Tm^{3+} ions according to the crystal-field data.

It should be noted that there is a contribution from the transitions of Tm^{3+} ions in the C_{3i} sites corresponding to magnetic dipole transitions. The $^3F_4 \rightarrow {}^3H_4$ and $^3F_4 \rightarrow {}^3F_{2,3}$ transitions can have a MD contribution. The J-O calculations performed in this work for Tm^{3+} ions in (Y,Lu)$_2O_3$ laser ceramic predict the following ED and MD probabilities of spontaneous radiative transitions: A_{ED} = 122.23 s^{-1} and A_{MD} = 27.27 s^{-1} (for the $^3H_4 \rightarrow {}^3F_4$ transition) and A_{ED} = 818.81 s^{-1} and A_{MD} = 72.33 s^{-1} (for the $^3F_{2,3} \rightarrow {}^3F_4$ transition), see Chapter IV.2 of this chapter. Consequently, we expect a non-negligible MD contribution to the ESA probabilities, especially for the $^3F_{2,3} \rightarrow {}^3F_4$ transition. Therefore, spectral overlapping of these transitions is expected in the ESA spectra. For Figure IV.65(a), we can see two additional peaks at 1016 and 1021 nm, and the group at 1030, 1052, and 1058 nm that do not correspond to the transitions from C_2 sites. Hence, we assume that these peaks might be due to the transitions from the C_{3i} sites. For the Tm:Lu_2O_3 and Tm:Sc_2O_3 crystals, we also observed those extra peaks experiencing a blue-shift, *e.g.*, 1012, 1019, 1037, 1043 and 1047 nm for Tm:Lu_2O_3. For the ESA transition terminating at the $^3H_4$ state, the determining of the possible positions of the C_{3i} sites is complicated due to the low intensity of the raw ESA spectra.

Table IV.12. Excited-state absorption cross-sections for the $^3F_4 \rightarrow {}^3F_{2,3}$ and $^3F_4 \rightarrow {}^3H_4$ transitions.

	$^3F_4 \rightarrow {}^3F_{2,3}$			$^3F_4 \rightarrow {}^3H_4$
	σ_{ESA}, 10^{-20} cm^2	λ_{ESA}, nm	$\Delta\lambda$, nm	σ_{ESA}, 10^{-20} cm^2
Tm:Y_2O_3	1.83	1044.4	2.3	0.63 at 1423.7 nm
Tm:Lu_2O_3	1.97	1042.1	2.3	0.68 at 1421.9 nm
Tm:Sc_2O_3	0.87	1037.9	3.2	0.57 at 1419.8 nm

Figure IV.65(b) shows a comparison between the scaled σ_{ESA} and the σ_{ESA} spectra calculated by the RM method for the $^3F_4 \rightarrow {}^3H_4$ Tm^{3+} in Tm:Y_2O_3 crystal. They are in a good agreement

confirming of the pump-probe-based approach. Table IV.12 summarizes the peak σ_{ESA} for the studied crystals.

The high values of σ_{ESA} slightly above 1 μm corresponding to the $^3F_4 \rightarrow {}^3F_{2,3}$ transition indicate a great potential for upconversion pumping of Tm:Y_2O_3, Tm:Lu_2O_3 and Tm:Sc_2O_3 crystals for 2.3 μm lasers. No results on upconversion pumping of Tm-doped cubic sesquioxides have been reported so far. The σ_{ESA} spectra for the Tm:Y_2O_3, Tm:Lu_2O_3 and Tm:Sc_2O_3 crystals are plotted in Figure IV.66.

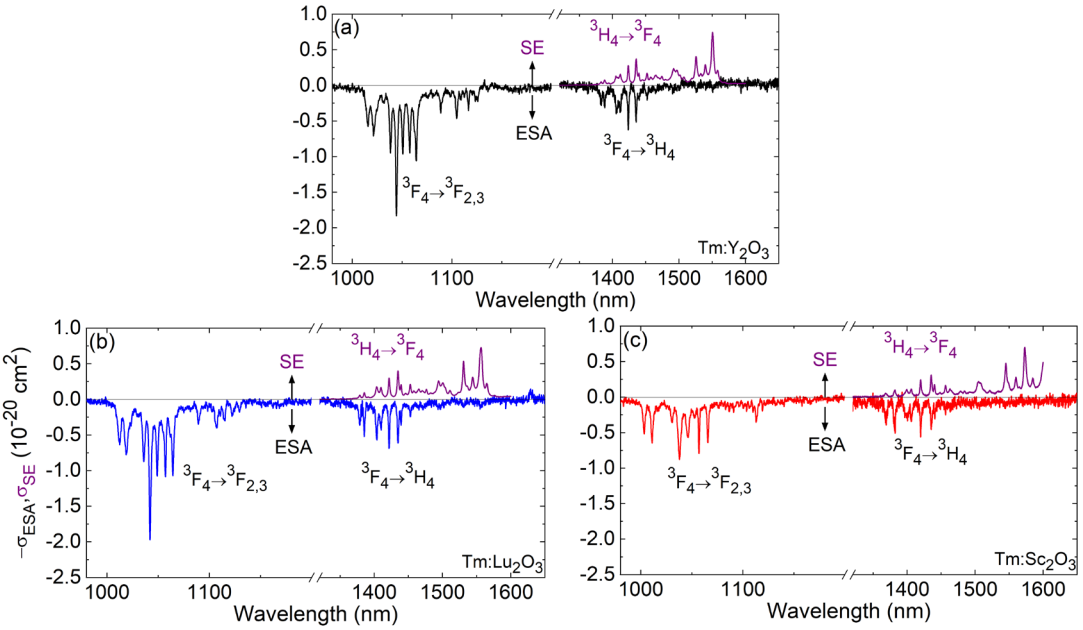

Figure IV.66. ESA cross-section spectra from the $^3F_4 \rightarrow {}^3F_{2,3}$ and $^3F_4 \rightarrow {}^3H_4$ transitions and SE cross-section spectra form the $^3H_4 \rightarrow {}^3F_4$ transition for Tm^{3+} ions in: (a) Tm:Y_2O_3, (b) Tm:Lu_2O_3 and (c) Tm:Sc_2O_3 single-crystals.

IV.5.C. Phonon sidebands for Tm^{3+} ions in sesquioxides

Further description of the long-wave emissions of Tm^{3+} ion in cubic sesquioxides requires a close look on the phonon sidebands of absorption and emission transitions.

To examine and interpretate the phonon sidebands, we measured the RT and LT (12 K) luminescence spectra of the Tm:R_2O_3 crystals, in the 1950-2500 nm spectral range with the spectral resolution of 1 nm. They are plotted in Figure IV.67(a,b) in a semi-log scale. The spectra were normalized and scaled along the *y*-axis for better visibility.

At RT, all spectra exhibit long-wave vibronic sidebands observed at the wavelengths exciding that of purely electronic transitions of Tm^{3+} ions. The longest wavelengths of such transitions amount to 2073 nm (Tm:Y_2O_3), 2092 nm (Tm:Lu_2O_3), and 2149 nm (Tm:Sc_2O_3). In the vibronic sidebands, the well-defined local maxima can be observed at the wavelengths of ~2220 nm, ~2250 nm and ~2300 nm for Tm-doped yttria, lutecia and scandia crystals, respectively. Wavelengths experience gradually red-shift in the series of the studied crystals which is assigned to increasing the crystal field strength for cubic sesquioxides and accordingly shifts the energy level position of high-laying Stark sub-levels of the ground state multiplets. Also, this explains the significant spectral overlapping of the phonon sidebands of the $^3F_4 \rightarrow {}^3H_6$ transition

and the $^3H_4 \rightarrow {}^3H_5$ transition. This spectral feature is structureless and broad, and appears as a superposition of several vibronic transitions related to the Z_{12} and Z_{13} sub-levels. At LT, one can clearly see sharp peaks corresponded to the $^3H_4 \rightarrow {}^3H_5$ transition appearing above 2300 nm, as shown in Figure IV.67(b).

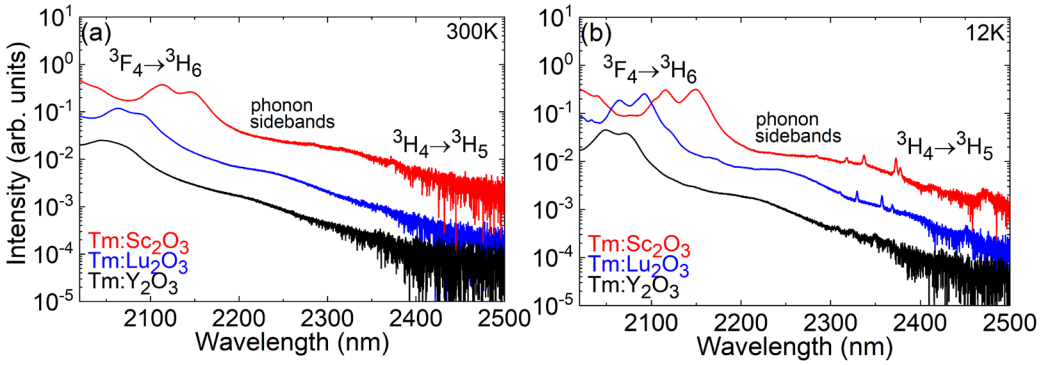

Figure IV.67. Phonon sidebands from the $^3F_4 \rightarrow {}^3H_6$ transition of the Tm^{3+} ions in R_2O_3 crystals: (a) at RT; (b) at 12 K.

Figure IV.68 shows the comparison of the phonon sidebands of the Tm:$(Y,Lu)_2O_3$ ceramic between parent compounds Tm:Y_2O_3 and Tm:Lu_2O_3. The very broad band is centered at 2.23 μm (for Tm:$(Y,Lu)_2O_3$) and takes an intermediate position between those for Tm:Y_2O_3 (2220 nm) and Tm:Lu_2O_3 (2250 nm) which agrees with the difference in the crystal-field strengths.

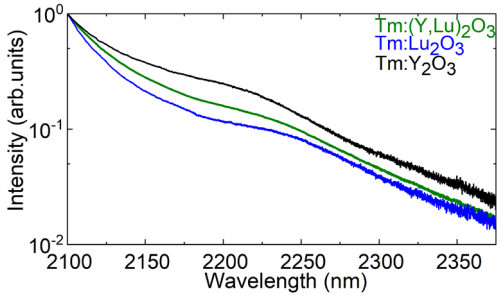

Figure IV.68. RT comparison phonon sidebands of parent Tm:Y_2O_3 and Tm:Lu_2O_3 with solid-solution Tm:$(Y,Lu)_2O_3$ ceramics.

Since the position of the vibronic transitions of Tm^{3+} ions is linked to those of electronic transitions, they can be assigned in absorption and emission spectra. The temperature dependent absorption and emission spectra of the representative Tm:Lu_2O_3 crystal measured in the 300-12 K temperature range are shown in Figure IV.69(a,b). In normalized temperature dependent absorption spectra of the Tm:Lu_2O_3 crystal, one can see the pronounced vibronic positions compared to the luminescence spectra, see Figure IV.69(a). As mentioned in Chapter I.2.I, the strong electron-phonon coupling leads to intense vibronic transitions, therefore high vibronic transition probabilities. Based on this fact, we can assume that Tm^{3+} ions possess a strong electron-phonon interaction in Lu_2O_3 [Mei96]. When temperature decreases the vibronic peaks become more structured.

In Figure IV.69(a), one can see four well resolved peaks corresponding to the transitions $Z_1 \rightarrow Y_i$, where i is ranging from 6 to 9. These transitions from the lowest sub-levels of the

ground state to the high-laying sub-level of the first excited state corresponding to the purely electronic transitions. We assumed that the sharp peaks, which became more clearly at 12 K, they are related to transitions to vibronic energy levels associated with the first excited multiplet. These vibronic energy levels can be constructed by adding the phonon energies to the energies of four high-laying Stark levels of the ground state, i.e., by using the formula $E(Y_6) + h\nu_{ph}$, $E(Y_7) + h\nu_{ph}$, $E(Y_8) + h\nu_{ph}$, and $E(Y_9) + h\nu_{ph}$. The groups of these vibronic energy levels are shown by vertical dashes of different colours. Almost all spectral features of the phonon sidebands can be assigned to one or several transitions to vibronic energy levels. For instance, the positions of most intense peaks are 6358 cm^{-1} (linked with Y_9 sub-level, 143 cm^{-1} the Raman mode), 6414 cm^{-1} (Y_8, 243 cm^{-1}), 6453 cm^{-1} (Y_6 and Y_9, 328 and 243 cm^{-1}, respectively), and 6414 cm^{-1} (Y_6 and Y_7, 452 cm^{-1}). It should be noted that the higher energy vibronic transition could be expected around 6825 cm^{-1}.

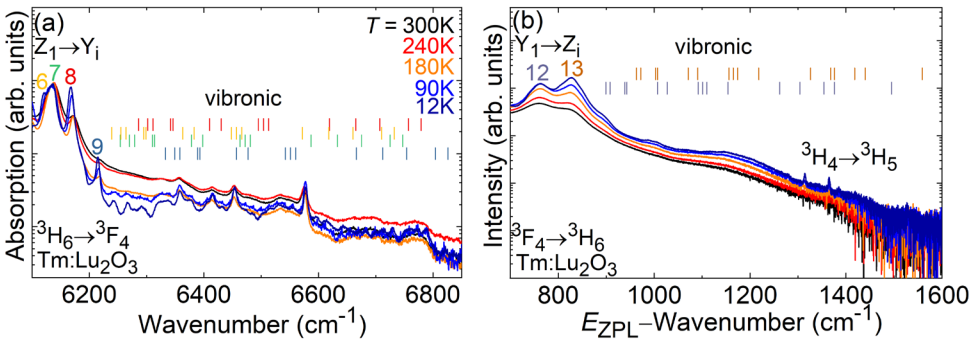

Figure IV.69. Temperature dependent phonon sidebands of the $Tm:Lu_2O_3$ crystal: (a) from the $^3H_6 \rightarrow {}^3F_4$ transition; (b) from the $^3F_4 \rightarrow {}^3H_6$ transition. *Position of each group of vertical dashed lines* indicates the vibronic levels obtained by adding the phonon energy of each Raman mode (see Figure IV.5) to Y_6, Y_7, Y_8 and Y_9 Stark sub-levels in absorption, and to Z_{12} and Z_{13} in emission.

The same assignment of the vibronic transition in the emission spectra of the $Tm:Y_2O_3$, $Tm:Lu_2O_3$ and $Tm:Sc_2O_3$ crystals was done. The vertical dash lines indicate the position of the vibronic energy levels located slightly above the highest electronic sub-levels of the $^3H_6$ multiplet i.e. having an energy $E(Z_{12}) + h\nu_{ph}$ and $E(Z_{13}) + h\nu_{ph}$. The broad vibronic peak around 2250 nm, where the laser operation was achieved, is mainly formed by several vibronic transitions from the Z_{13} sub-level, see Figure IV.69(b). The energy gap between the prominent electronic emission band centered at 2058 nm and the above-described sideband (2250 nm) is ~387 cm^{-1}. This well matches the most intense Raman peak of this material corresponding to vibration with an energy $h\nu_{ph}$ = 385 cm^{-1}.

The similar behaviour was observed for Tm^{3+} ions in different host matrices by [Ell96] and for Pr^{3+} in LaF_3 [Yen64].

As explained in Chapter I.2.I, the electron-phonon coupling parameter $\bar{\alpha}$ derived from fitting the Raman two-phonon process for different transitions provides a good estimation of the electron-phonon coupling strength. To estimate this parameter, we used the line broadening method, see Eq. I.52. To estimate the linewidths, we selected the peaks corresponding to the $Z_1 \rightarrow Y_2$ and $Y_1 \rightarrow Z_{13}$ electronic transitions in absorption and luminescence, respectively. The

linewidth of the absorption peak was determined by FWHM, while linewidth of emission peak was fitted by the Gauss model. Figure IV.70(a,b). shows the temperature dependent linewidths of the $^3H_6 \rightarrow {}^3F_4$ and $^3F_4 \rightarrow {}^3H_6$ transitions for the Tm:Lu_2O_3 crystal. The experimental data well-fitted by Eq. I.52 For the absorption and emission transitions $\bar{\alpha}$ amounts to 185 and 205, respectively. The Debay temperature of 440 K was selected, as it provides a good fit to both sets of experimental data, and a similar value was reported for Yb_2O_3 and Y_2O_3 in [Mak19] and [Lup13], respectively. In fact, the value of $\bar{\alpha}$ varies significantly for different transitions of RE^{3+} ions [Ell95]. This variation is due to differences in electron-phonon coupling strength across different levels.

To better understand the range of $\bar{\alpha}$, it is important to estimate linewidths for a number of lines corresponding to electronic transitions between Stark sub-levels of different transitions. Value obtained for the $^3H_6 \rightarrow {}^3F_4$ and $^3F_4 \rightarrow {}^3H_6$ transitions of Tm^{3+} ions in the Tm:Lu_2O_3 crystal falls between those for the $^1D_2 \rightarrow {}^3F_4$ and $^1G_4 \rightarrow {}^3H_6$ transitions, $\bar{\alpha}$ ranges between 63 – 327 [Ell97a]. [Mei96] reported the influence of the host lattice in the electron-phonon coupling strength measuring line broadening for Pr^{3+}, Nd^{3+} and Gd^{3+} in La_2O_3 and $LiYF_4$ for the same transitions. It was shown that in all cases stronger coupling (higher $\bar{\alpha}$ values) are found for RE^{3+} ions in La_2O_3 due to an increase in covalency in the host lattice. The increase in covalency cause an increase in the spatial extension of the electron wave function of the RE^{3+} ions and the ligands. Therefore, the larger spatial extension of the 4f orbitals and the ligands enhances the electron-phonon coupling strength. To more precisely evaluate $\bar{\alpha}$ for Tm:Lu_2O_3, more data should be obtained.

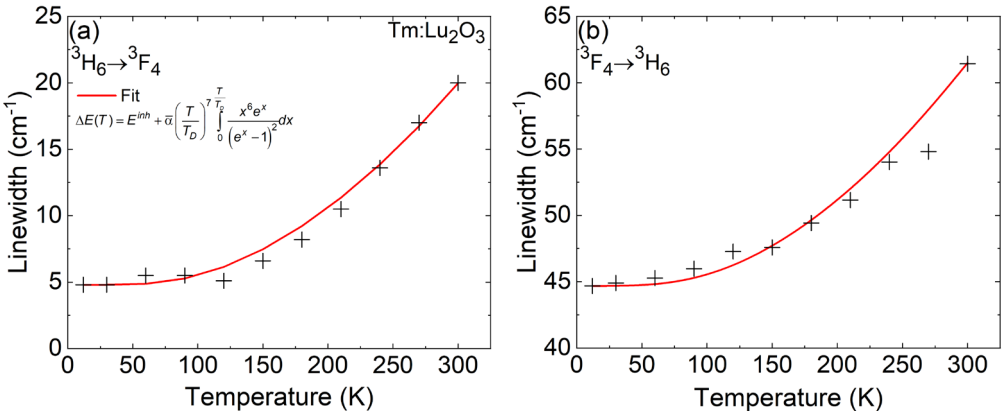

Figure IV.70. Temperature dependent linewidths of two electronic transitions between Stark sub-levels for Tm:Lu_2O_3 crystal: (a) $Z_1 \rightarrow Y_2$ on the $^3H_6 \rightarrow {}^3F_4$ transition; (b) $Y_1 \rightarrow Z_{13}$ on the $^3F_4 \rightarrow {}^3H_6$ transition, *solid line* – their fit by Eq. I.44.

IV.5.D. Energy-transfer upconversion for Tm^{3+} ions in sesquioxides

As mentioned before, the ETU process could assist the 2.3 μm laser operation of Tm-doped materials. The parameters of this process can be derived from ESA cross-section spectra. Consequently, we used the σ_{ESA} spectra of the Tm:Y_2O_3, Tm:Lu_2O_3 and Tm:Sc_2O_3 crystals to estimate the rates (W_{ETU}), the concentration-dependent and independent parameters of ETU. For these calculations, we used the hopping (Burshtein) model describing a migration-assisted energy-transfer. This model considers the transfer of energy between donors as a random

process until the excitation is transferred to an acceptor ion, as shown in Figure IV.71. First, two microparameters C_{DD} and C_{DA} were calculated from the overlap integrals between the SE and absorption (GSA or ESA) cross-section spectra [Pay92a]:

$$C_{D\to D} = \frac{3c}{8\pi^4 n^2}\int \sigma_{SE}(\lambda)\sigma_{GSA}(\lambda)d\lambda, \quad \text{(IV.7)}$$

$$C_{D\to A} = \frac{3c}{8\pi^4 n^2}\int \sigma_{ESA}(\lambda)\sigma_{SE}(\lambda)d\lambda, \quad \text{(IV.8)}$$

where D and A indicate a donor and an acceptor, respectively, C_{DD} represents a donor-donor process (energy migration) and C_{DA} – a donor-acceptor process (direct energy transfer), c the speed of light in vacuum, n is the mean refractive index of the host material, σ_{SE} corresponds to the $^3F_4 \rightarrow {}^3H_6$ transition, σ_{GSA} and σ_{ESA} – to the transitions $^3H_6 \rightarrow {}^3F_4$ (GSA) and $^3F_4 \rightarrow {}^3H_4$ (ESA), respectively, and λ is the light wavelength. In our case, the use of the hopping model is validated because $C_{DD} >> C_{DA}$ (the migration process among Tm^{3+} ions is more likely than the direct energy transfer).

The macroscopic ETU rate in (s^{-1}) was then determined as [Pay94]:

$$W_{ETU} = \pi\left(\frac{2\pi}{3}\right)^{\frac{5}{2}}\sqrt{C_{D\to D}C_{D\to A}}N_{Tm}^2, \quad \text{(IV.9)}$$

$$W_{ETU} = K_{ETU}N_{Tm} = C_{ETU}N_{Tm}^2, \quad \text{(IV.10)}$$

where K_{ETU} and C_{ETU} are the concentration-dependent and concentration-independent ETU parameters expressed in (cm^3s^{-1}) and (cm^6s^{-1}), respectively.

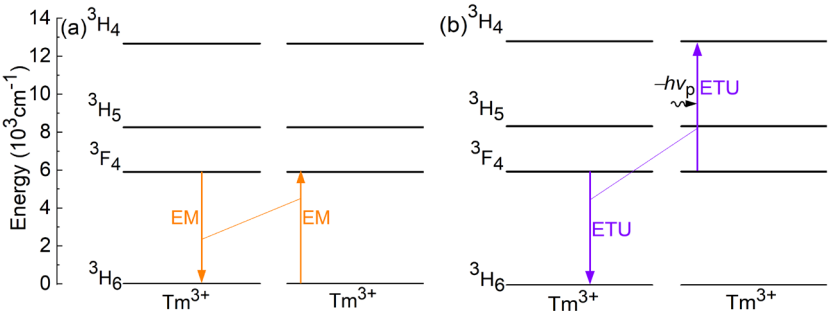

Figure IV.71. Elementary processes corresponding to (a) energy transfer between two donor Tm^{3+} ions (energy migration) and (b) energy transfer between donor and acceptor Tm^{3+} ions (direct energy transfer).

Before performing the calculations, the overlap integrals between the SE, GSA and ESA cross-section spectra should be determined by taking into account the multiphonon sidebands of the emission and absorption spectra since the considered ETU process is non-resonant and phonon assisted. They can be determined by constructing the Stokes and anti-Stokes sidebands for each considered transition. Auzel proposed equations for the dependence of the NR relaxation rates of the Stokes and anti-Stokes phonon-assisted processes on the transition energy [Auz76]. To describe the shape of the absorption and emission phonon sidebands, these equations could be applied [Bra98, Gui20, Loi21]:

$$\sigma_S = \sigma_0 e^{-\alpha_S \Delta E}, \quad \text{(IV.11)}$$

$$\sigma_{AS} = \sigma_0 e^{-\alpha_{AS}\Delta E}, \quad \text{(IV.12)}$$

where S and AS stand for the Stokes and anti-Stokes processes, respectively, ΔE is the energy mismatch between the vibronic (phonon-assisted) and the purely electronic transition, σ_0 is the cross-section at the photon energy of an electronic transition, and the constants α_S and α_{AS} only depend on the host medium. This exponential dependence is characteristic of a weak-coupling ion-lattice interaction which is typical for electronic transitions within the $4f^n$ shell. The α_S and α_{AS} parameters can be further expressed as [Auz76]:

$$\alpha_S = \left(\hbar \nu_{ph}\right)^{-1} \{\ln[< N > / S_0(< n > +1)] - 1\}, \quad \text{(IV.13)}$$

$$\alpha_{AS} = \alpha_S + 1/kT, \quad \text{(IV.14)}$$

where $h\nu_{ph}$ is the maximum phonon energy of the considered host, <*N*> is the average number of phonons involved in the phonon-assisted transition, S_0 is the Pekar-Hung-Rhys constant, <*n*> is the occupation number for the effective phonons with an energy $h\nu_{ph}$.

The Stokes sideband of an absorption band is located at the short wavelength side whereas the anti-Stokes one is located at the long wavelength side. For the emission processes, they are reversed. We applied Eqs. IV.11-12 to construct the absorption ($^3H_6 \rightarrow {}^3F_4$ and $^3F_4 \rightarrow {}^3H_4$) and emission ($^3F_4 \rightarrow {}^3H_6$) phonon sidebands for the studied single-crystals. In Figure IV.72, we show an example of such an approach.

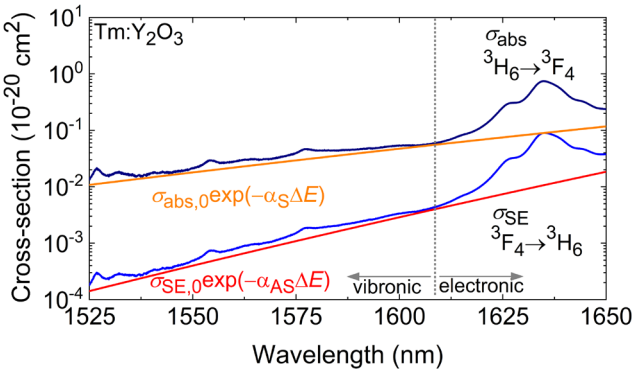

Figure IV.72. An example of constructing the Stokes (α_S) and anti-Stokes (α_{AS}) sidebands for the $^3H_6 \rightarrow {}^3F_4$ and $^3F_4 \rightarrow {}^3H_6$ transitions of Tm^{3+} ions in the Y_2O_3 crystal. The *vertical dashed line* separates the purely electronic and vibronic transitions. *Solid lines* are calculated phonon sidebands using Eq. IV.(11-12). The spectra are plotted in a semi-log scale.

The absorption cross-section spectra were calculated using the RM method from the stimulated-emission cross-section spectra since such weak absorption sideband is not directly accessible with a spectrophotometer. The spectra are plotted in a semi-log scale. In $Tm:Y_2O_3$, the longest wavelength of the electronic transition corresponds to the transition from the lowest Stark sub-level of the emitting state ($^3F_4$, 5612 cm^{-1}) to the highest sub-level of the terminal state ($^3H_6$, 788 cm^{-1}), and equals to 2073 nm. Above this wavelength, the emission is of purely vibronic nature due to the electron-phonon coupling. The transition cross-sections at the longest/shortest wavelengths of purely electronic transitions have the meaning of σ_0 in Eqs. IV.11-12.

The σ_{abs} and σ_{SE} spectra below the shortest-wavelength electronic transition are reasonably well fitted with the exponential law, Eqs. IV.11-12, for all the studied crystals, as shown by orange and red lines for the Stokes and anti-Stokes sidebands in Figure IV.72, respectively. For Tm:Y_2O_3, the α_S and α_{AS} parameters amount to 4.8 ± 0.3 ×10^{-3} and 9.8 ± 0.3 ×10^{-3} cm. For Tm:Lu_2O_3, α_S = 3.1 ± 0.3 ×10^{-3} cm α_{AS} = 8.0 ± 0.3 ×10^{-3} cm, and for Tm:Sc_2O_3, α_S = 2.3 ± 0.3 ×10^{-3} cm and α_{AS} = 7.2 ± 0.3 ×10^{-3} cm. These values decrease with increasing the maximum phonon energy of the sesquioxides from yttria to scandia.

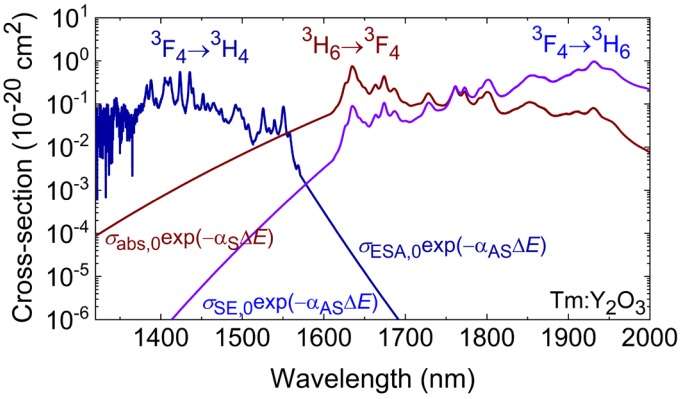

Figure IV.73. ESA ($^3F_4 \rightarrow {}^3H_4$), GSA ($^3H_6 \rightarrow {}^3F_4$) and SE ($^3F_4 \rightarrow {}^3H_6$) cross-section spectra with the phonon sidebands calculated using Eqs. IV.(11-12) to evaluate the ETU parameter for the Tm:Y_2O_3 crystal. The spectra are plotted in a semi-log scale.

Figure IV.73 shows the modified SE, GSA and ESA cross-section spectra in a semi-log scale. Two microparameters $C_{D\rightarrow A}$ and $C_{D\rightarrow D}$ were calculated from the overlap integrals between the cross-section spectra using Eqs. IV.7-8. The values of the microparameters $C_{D\rightarrow A}$ and $C_{D\rightarrow D}$ as well as the ETU parameters are provided in Table.IV.13. For comparison, we provide the ETU parameters for Tm:$LiYF_4$ obtained by the same method.

Table IV.13. The ETU parameters for the studied sesquioxides and Tm:$LiYF_4$ obtained using the hopping model (Burshtein). C_{CR} was experimentally obtained from a study of luminescence dynamics.

	N_{Tm}, 10^{-20} cm^{-3}	$C_{D\rightarrow A}$, 10^{-43} cm^6 s^{-1}	$C_{D\rightarrow D}$, 10^{-39} cm^6 s^{-1}	C_{ETU}, 10^{-40} cm^6 s^{-1}	K_{ETU}, 10^{-20} cm^6 s^{-1}	W_{ETU}, s^{-1}	$^aC_{CR}$, 10^{-37} cm^6 s^{-1}
2.5 at.% Tm:Y_2O_3	6.6	1.74	2.83	4.42	29.16	192	0.50[a]
1.8 at.% Tm:Lu_2O_3	5.1	3.31	1.93	5.04	25.70	131	1.25[a]
2.0 at.% Tm:Sc_2O_3	6.4	10.8	2.90	11.1	71.39	456	0.80[a]
3 at.% Tm:$LiYF_4$[b]	4.1	0.50	3.26	2.56	10.35	43	0.25

a – data obtained from luminescence decay measurements by [Loi18a], *b* – ETU parameters obtained using the same method as the one applied in this work [Gui22].

Let us compare $C_{D\rightarrow A}$ parameters for the three studied sesquioxides. From Table IV.13, one can see that the value of this parameters gradually increasing in the series from yttria to scandia which is due to the increase in spectral overlap of the ESA and SE spectra. This overlap can be understood given the fact that the crystal field strength in this series is progressively increasing, therefore, the total Stark-splitting of the involve multiplets is getting large of Tm^{3+} ions in those sesquioxide matrices. At the same time, the $C_{D\rightarrow D}$ parameter remains almost unchanged. As

compared to the tetragonal $LiYF_4$ crystal, the cubic sesquioxides provide much higher ETU parameters due to the increased crystal field strength, thus the significant contribution ETU to the population of the $^3H_4$ level in Tm-doped sesquioxides is expected. Therefore, the spectral overlapping of ESA spectrum with the SE and GSA spectra becomes stronger.

IV.5.E. Efficient Tm:Lu_2O_3 laser at 2.26 μm

To perform the laser experiment at 2.3 μm, the same laser set-up was used, as shown in Figure II.9 in Chapter II. An uncoated 1.8 at.% Tm:Lu_2O_3 crystal with a thickness of 5 mm and an aperture of 3×3 mm^2 was used. A hemispherical cavity formed by a flat pump mirror (HT at 0.80 μm, HR at 2.18–2.35 μm) and concave (RoC = –100 mm) output couplers with a transmission T_{OC} of 0.65% or 0.8% around 2.3 μm. The pump mirror also provided HT around 2 μm to suppress the competitive $^3F_4 \rightarrow {}^3H_6$ transition. For comparison, we perform laser operation around 2 μm using the flat pump mirror, which was used in the previous laser experiments, and the OCs with T_{OC} of 0.20% and 0.50% around 2 μm. The pump was focused using an achromatic AR-coated lens (f = 75 mm) and the pump absorption (double-pass) was 57%-61%. The pump wavelength was 796 nm. A long-pass filter (1400 nm, Spectrogon) was used to separate laser emission from the residual pump.

The input-output dependences of the CW Tm:Lu_2O_3 laser operating on the $^3F_4 \rightarrow {}^3H_6$ and around 2.3 μm are shown in Figure IV.74.(a,c). For the T_{OC} = 0.5%, the laser generated a maximum output power of 788 mW at 2086-2098 nm with a slope efficiency of 53.7% vs. absorbed pump power and a laser threshold of 61 mW, see Figure IV.74(a,b). After the changing the PM and OCs for 2.3 μm laser operation, the laser generated a maximum output power of 654 mW at 2238-2309 nm with a slope efficiency of 68.9% vs. absorbed pump power and a laser threshold of 700 mW, see Figure IV.74(c,d). It should be noted that for the OC with T_{OC} = 0.80% laser operates at several lines, *e.g.*, at 2260 nm, 2280 nm and 2310 nm. For T_{OC} = 0.60%, laser almost operates at the same lines, but with one additional line at 2326 nm.

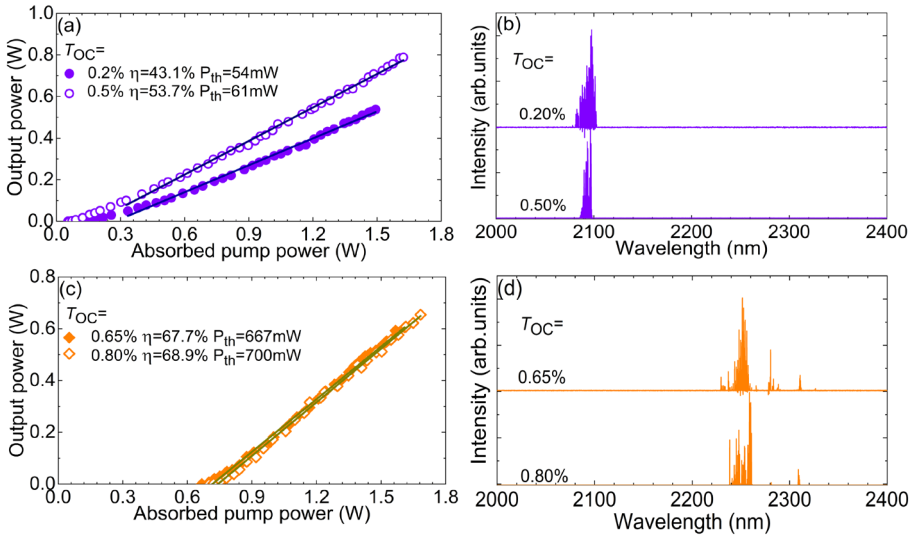

Figure IV.74. 1.8 at.% Tm:Lu_2O_3 laser: (a,c) input-output dependences; (b,d) laser emission spectra.

Let us discus the laser results. In the first case, we achieved a typical laser operation on the longest electronic transition $Y_1 \rightarrow Z_{13}$ (the $^3F_4 \rightarrow {}^3H_6$ transition). As expected, the maximum slope efficiency exceeds the upper limit set by the Stokes efficiency, which amounts to η_S = 796 nm / 2095 nm = 38% due to CR process leading to the "one-for-two" pump process. The low laser threshold behaviour was observed. We plotted the gain cross-section spectra together for the inversion ratios β < 2% for the $^3F_4 \rightarrow {}^3H_6$ transition, including the phonon sideband and laser emission spectra for the OCs with T_{OC} = 0.50% and 0.80% in Figure IV.75. The laser was operating with the inversion ratio around 1.6%.

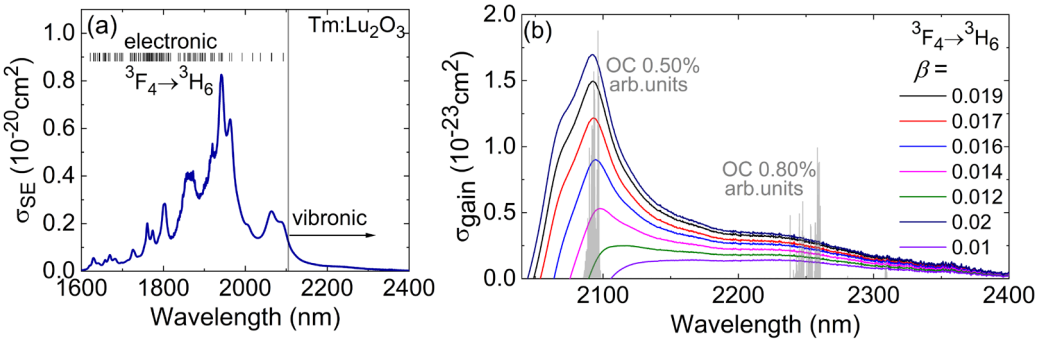

Figure IV.75. Spectroscopy of the Tm: Lu_2O_3 laser crystal: (a) SE cross-section for the $^3F_4 \rightarrow {}^3H_6$ transition. *Vertical dashes* mark all possible wavelengths of electronic transitions. *The solid line* separates the spectra on electronic and vibronic part; (b) calculated gain cross-section spectra for small inversion ratios. The grey lines – laser emission spectra at 2.1 and 2.3 μm.

For the second case, the slope efficiency increased up to 69% that almost reaches the upper limit for the slope efficiency, $\eta < \eta_{St,L}\eta_q\eta_{mode}\eta_{OC} = 69 \pm 3\%$. The laser emission mainly appears at the wavelength corresponding to the phonon sideband, as shown in Figure IV.75. We assume that this laser emission mainly originates from the phonon sideband of the $^3F_4 \rightarrow {}^3H_6$ transition with a contribution of the $^3H_4 \rightarrow {}^3H_5$ transition. Therefore, the laser efficiency exceeded the Stokes limit due to an ETU process.

Figure IV.76 shows the Stark splitting of the $^3H_4$, $^3H_5$, $^3F_4$ and $^3H_6$ manifolds of Tm^{3+} ions in Lu_2O_3. To confirm that the laser operates on the phonon sideband with contribution of the $^3H_4 \rightarrow {}^3H_5$ transition, we assigned the observed laser lines based on crystal-field data and Raman spectroscopy. First, we successfully assigned all the observed laser emission lines to electronic transitions corresponding to the transitions from the A_1 and A_2 sub-levels of the $^3H_4$ manifold, see Figure IV.76(a). To confirm that the observed laser lines correspond to multiphonon-assisted transitions, we added the energy of the Raman modes (from 119 cm^{-1} to 612 cm^{-1}) of the Lu_2O_3 to the Z_{12} and Z_{13} higher-lying sub-levels of the $^3H_6$ ground-state. This is representing an electron-phonon coupling. A set of densely located virtual energy levels extending from 883 cm^{-1} to 1440 cm^{-1} was plotted in Figure IV.76(b). The long-wave laser lines above 2.1 μm is well-explained by transitions from the $^3F_4$ laser level to several vibronic levels. According this analysis, the longest vibronic transition should be around 2.4 μm. It could indicate that the contribution of the phonon sideband of the $^3F_4 \rightarrow {}^3H_6$ transition on the $^3H_4 \rightarrow {}^3H_5$ transition up to 2.4 μm.

Previously, CW laser emission at the wavelength above the longest electronic transition for the $^2F_{5/2} \rightarrow {}^2F_{7/2}$ and $^3F_4 \rightarrow {}^3H_6$ transitions was observed in several Yb^{3+}-doped [Si23, Che23] and Tm^{3+}-doped crystals [Cor04, Loi21], respectively. For instance, [Cor04] used a highly 18 at.% Tm^{3+}-doped BaY_2F_8 crystal enhancing a strong reabsorption at the electronic transitions to achieve laser wavelength above the longest electronic transition. The laser generated 0.24 W at 1990-2027 nm with η = 47%, when the longest electronic transition is at ~1950 nm. By employing a special band-pass OC, [Loi21] reached laser operation of a Tm:$KLu(WO_4)_2$ crystal generating 1.17 W at 2109-2133 nm with η = 39%. The longest electronic transition is at 1948 nm. Moreover, the phonon sideband was the result of additional sidebands in spectra of mode-locked Tm-doped sesquioxide lasers [Suz20, Zha21a].

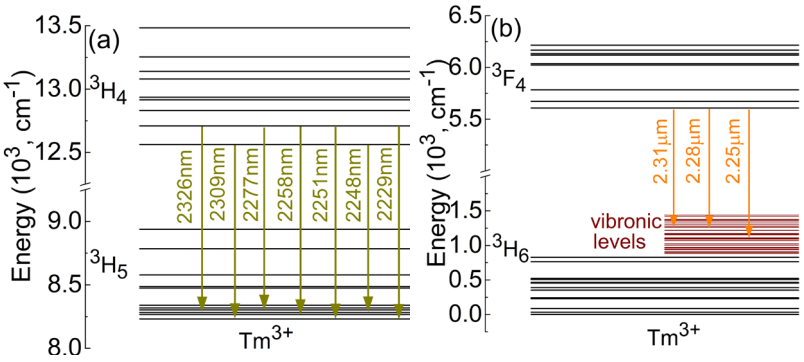

Figure IV.76. Stark splitting of the multiplets of Tm^{3+} ions in Lu_2O_3: (a) the $^3H_4$ and $^3H_5$ multiplets showing the assignment of the observed laser lines relevant to the electronic transitions; (b) the $^3F_4$ and $^3H_6$ multiplets showing the assignment of the observed laser lines relevant to the vibronic transitions. The maroon lines illustrate vibronic energy-levels due to the electron-phonon coupling with the host vibrations participating in laser emission at 2.25 – 2.31 μm.

The first laser operation of 1.8 at.% Tm:Lu_2O_3 crystal around 2.3 μm was achieved. We believe that the laser mainly generated on the vibronic sideband of the $^3F_4 \rightarrow {}^3H_6$ transition with contribution of the $^3H_4 \rightarrow {}^3H_5$ transition providing the two-for-one pump process associated with the ETU refilling the upper laser level.

To conclude this section, R_2O_3 cubic sesquioxides (where R stands for Y, Lu and Sc) doped with moderate Tm^{3+} doping levels of a few at.% exhibit broadband emission bands on the $^3H_4 \rightarrow {}^3H_5$ transition spanning from 2.20 to 2.8 μm with high stimulated-emission cross-sections, and a relatively long luminescence lifetime of the $^3H_4$ upper laser level. It makes them potential candidates for broadband tunable (potentially up to 2.8 μm), highly-efficient and mode-locked lasers at 2.3 μm. High excited-state absorption cross-sections around 1.05 μm indicate the potential for upconversion pumping using commercially available and power-scalable Yb-fiber lasers, which may be more suitable for achieving high-power laser operation around 2.3 μm. The energy-transfer upconversion parameters, which are important for predicting the slope efficiency of laser sources, were calculated.

Due to the spectral overlapping of the $^3F_4 \rightarrow {}^3H_6$ and $^3H_4 \rightarrow {}^3H_5$ transitions vie strong phonon sidebands of cubic sesquioxides, the first laser operation of Tm:Lu_2O_3 crystal around 2.3 μm was achieved.

Conclusions of Chapter IV

In this chapter, based on a detailed spectroscopic study of stoichiometric and binary/ternary solid-solution sesquioxides doped with Tm^{3+} and Ho^{3+} ions, the following conclusions are drawn:

(I) Experimental crystal-field splitting for Tm^{3+} ions in C_2 symmetry sites in parent sesquioxides (Y_2O_3, Lu_2O_3, and Sc_2O_3) is determined for several relevant multiplets for laser applications (from $^3H_6$ to $^3H_4$ Tm^{3+}) and validated using the barycenter plot. They exhibit strong crystal fields for Tm^{3+} in C_2 symmetry sites. These crystal fields mainly determine their optical properties, resulting in remarkably high total Stark splitting of their ground-states ($^3H_6$ Tm^{3+}). The splitting ranges from 788 cm^{-1} to 955 cm^{-1} for Tm^{3+} ions in Y_2O_3 and Sc_2O_3, respectively. Consequently, they produce broadband emission due to the electronic $^3F_4 \rightarrow {}^3H_6$ Tm^{3+} transitions, which extends well beyond 2 μm, effectively avoiding structured water vapor absorption in the atmosphere. For $Tm:Sc_2O_3$, the longest wavelength of a purely electronic transition is 2149 nm. Thus, Tm^{3+}-doped sesquioxides can effectively compete with other Tm^{3+}- and Ho^{3+}-doped materials. Additionally, the first experimental evidence of C_{3i} Tm^{3+} species for sesquioxides is presented. These species are revealed in transitions with a magnetic dipole contribution ($^3H_6 \rightarrow {}^3H_5$ for absorption and $^3H_4 \rightarrow {}^3H_5$ for emission). However, C_{3i} centers do not contribute to the lifetime of the $^3F_4$ upper laser level.

(II) The crystal-field strength for the R_2O_3 isostructural series is highly sensitive to the nature of the host-forming cation R^{3+}. It increases linearly with decreasing ionic radius, leading to corresponding changes in the Stark splitting of Tm^{3+} multiplets. This allows for tuning the emission peaks of Tm^{3+} ions around 2 μm. This trend holds true for both parent and "mixed" compounds.

(III) Based on X-ray diffraction, Raman spectroscopy, and low-temperature absorption/emission spectroscopy, it is confirmed that "mixed" sesquioxide ceramics of the Y_2O_3–Lu_2O_3–Sc_2O_3 ternary system represent substitutional solid solutions with a mixing of the host-forming cations at the atomic level. The strongest broadening is observed for Sc^{3+}-containing materials.

(IV) Moderately Tm^{3+}-doped sesquioxides demonstrated the strong emission at 2.3 μm corresponding to the $^3H_4 \rightarrow {}^3H_5$ Tm^{3+} transition. The significant spectral overlapping the $^3F_4 \rightarrow {}^3H_6$ and $^3H_4 \rightarrow {}^3H_5$ transitions via the phonon sideband from the $^3F_4 \rightarrow {}^3H_6$ was observed. The spectral overlapping of the transitions and the strong ETU process leading to “two-for-one” allowed to achieve first laser operation of the $Tm:Lu_2O_3$ crystal around 2.3 μm with a slope efficiency of ~69%. The measured excided-state absorption spectra of Tm^{3+}-doped cubic sesquioxides indicate their potential for upconversion pumping using commercially available and power-scalable Yb-fiber lasers to achieve laser emission around 2.3 μm. The energy-transfer upconversion parameters, which are important for predicting the slope efficiency of such laser sources, were also calculated from the absorption and emission overlap integrals using the hopping model.

Chapter V.

Thulium Doped Rare-Earth Orthovanadate Crystals with a Strong Electron-Phonon Interaction

The rare-earth orthovanadates (RVO_4) consisting of YVO_4, $GdVO_4$, and $LuVO_4$ constitute a well-established family of laser host crystals. These compounds have been demonstrated to serve as excellent laser gain media when doped with neodymium, ytterbium, erbium, holmium, and thulium ions. The $REVO_4$ crystals feature high thermal conductivity, weak thermal expansion. Their excellent thermo-mechanical properties make rare-earth-doped $REVO_4$ crystals very suitable for efficient and power-scalable to the multi-Watt level output power diode-pumped solid-state lasers. Despite the fact that their structure is ordered, RE^{3+} ions exhibit broad and almost structureless absorption and emission spectra in orthovanadates. The reason for this behavior resides in the strong electron-phonon interaction between the 4f electrons and the host phonon bath.

Tm^{3+}-doped RVO_4 crystals are famous for 2 μm lasers, however, for 2.3 μm lasers, they have not been studied yet. At first glance, 2.3 μm laser emission from the $^3H_4 \rightarrow {}^3H_5$ transition is difficult to achieve in Tm^{3+}-doped orthovanadates due to their high phonon energies leading to a fast nonradiative decay from the $^3H_4$ upper laser level.

In this chapter, the polarized spectroscopy of the $Tm:RVO_4$ crystals in the near- and mid-infrared spectral range are presented. The reasons for the broadband spectral properties are discussed and the first laser operation of these crystals at 2.3 μm is reported.

V.1. Polarized spectroscopy of $Tm:RVO_4$ (R = Gd, Y, Lu) crystals

In this section, the polarized Raman, absorption and emission cross-section, as well as low-temperature absorption and emission spectra of $Tm:RVO_4$, where R stands for Gd, Y, Lu, are reported. The anomalous spectral line broadening and phonon sidebands induced by the strong electron-phonon interaction are confirmed. The laser operation of $Tm:RVO_4$ crystals at 2.3 μm is reported for the first time and the underlying laser scheme is discussed.

V.1.A. Polarized Raman spectroscopy

The series of 1.5 at.% $Tm:GdVO_4$ 2.5 at.% $Tm:YVO_4$, and 1.5 at.% $Tm:LuVO_4$ were synthesized by our colleagues from the Key Laboratory of Laser and Infrared System of Ministry of Education, Shandong University, China. using the Cz method in an argon atmosphere in an iridium crucible. As a seed for the crystal growth, an undoped crystal cut along the c-axis was used. During the crystal growth process, the pulling rate varied from 1.0 to 2.0 mm/h, and the crystal rotation speed was kept at 10 to 20 rpm. After the growth was completed, the crystal was slowly cooled down to room temperature at a stepped rate of 30 to 50 °C/h. A $Tm:LuVO_4$ crystal with dimensions of Φ 30 mm × 25 mm was finally achieved, as shown in Figure V.1. No

scattering centers can be observed illuminating the crystal by a red He-Ne laser which indicates an excellent optical quality.

Figure V.1. As-grown Tm:$LuVO_4$ crystal boule, the growth direction is along the [001] axis.

The RVO_4 crystals belong to the tetragonal class, sp. gr. $I4_1/amd$. Lattice constants are a = 7.123 Å, c = 6.292 Å for $GdVO_4$, a = 7.211 Å, c = 6.350 Å for YVO_4, and a = 7.025 Å, c = 6.235 Å for $LuVO_4$, adopting a zircon-type structure [Rom11]. The fragment of the crystal structure of Tm:YVO_4 is depicted in Figure V.2, revealing the oxide coordination symmetry of rare-earth ions. The Tm^{3+} ions replace the Y^{3+} cations in a single type of site with D_{2d} symmetry and VIII-fold coordination by O^{2-}. The [YO_8] bisdisphenoidal structure encompasses two sets of Y–O bond distances of 2.365 Å and 2.443 Å, and the distance V–O is 1.709 Å in [VO_4] tetrahedron [Cha94].

RVO_4 crystals are optically uniaxial and their optical axis is parallel to the crystallographic ***c***-axis ordination symmetry. The two principal light polarizations are $\boldsymbol{E} \parallel \boldsymbol{c}$ and $\boldsymbol{E} \perp \boldsymbol{c}$ labelled as π and σ, respectively. The corresponding refractive indices are n_o = 1.947 n_e = 2.156 for $GdVO_4$, n_o = 1.944 n_e = 2.148 for YVO_4, and n_o = 1.967 n_e = 2.164 for $LuVO_4$ [Zel10]. It indicates positive uniaxial crystals ($n_o < n_e$). Therefore, the strong natural birefringence of RVO_4 crystals is expected to dominate any thermally induced birefringence thus reducing the depolarization losses under high-power pumping.

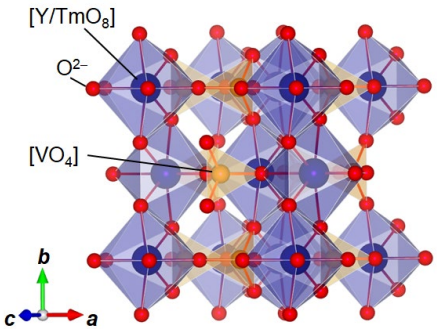

Figure V.2. A fragment of the crystal structure of Tm:YVO_4 in projection to the a-b plane.

The primitive cell of RVO_4 contains two formula units (12 atoms). The 12 atoms of the primitive cell give rise at the center of the Brillouin zone G(k = 0) to 36 phonon branches. The full symmetry group of RVO_4 as follow into the irreducible representations of D_{4h} [Mil68]:

$\Gamma_{36} = (2A_{1g} + 2B_{1u}) + (B_{1g} + A_{1u}) + (A_{2g} + B_{2u}) + (4B_{2g} + 4A_{2u}) + (5E_g + 5E_u)$.

Twelve modes ($2A_{1g}$, $4B_{1g}$, B_{2g}, and $5E_g$) are Raman active and seven modes ($3A_{2u}$ and $4E_u$) are IR active [San12]. It is convenient to divide them into internal and external modes. Among the Raman-active modes, seven modes ($2A_{1g} + 2B_{1g} + 1B_{2g} + 2E_g$) are internal ones, since they

originate from the crystal-field splitting of the vibrational modes of oxygen atoms within the $[VO_4]^{3-}$ tetrahedral groups, see Figure V.2. Four modes ($2B_{1g} + 2E_g$) are referred to as external ones as they are related to translations of the $[VO_4]^{3-}$ groups and R^{3+} ions, and one mode (E_g) relates to vibrations of the whole $[VO_4]^{3-}$ tetrahedra.

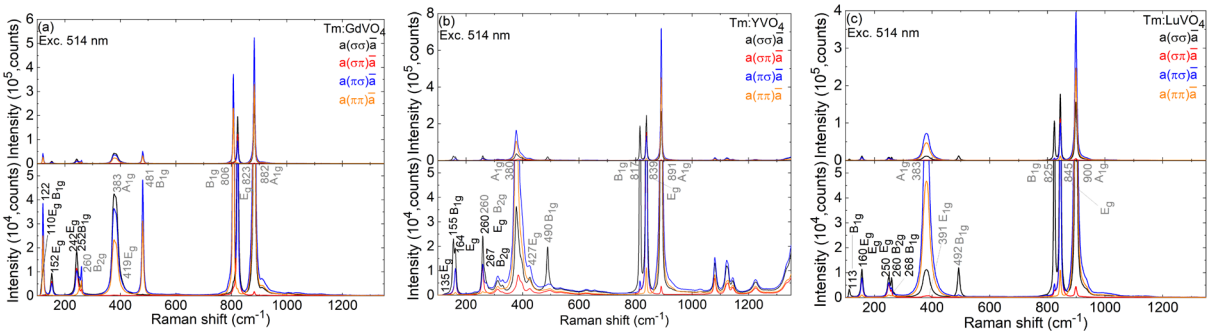

Figure V.3. Polarized Raman spectra of the ***a***-cut Tm:RVO_4 crystals:(a) Tm:$GdVO_4$; (b) Tm:YVO_4; (c) Tm:$LuVO_4$ (b). *Black numbers* indicate the Raman frequencies of the external vibrations, *grey numbers* indicate the internal vibrations of the $[VO_4]^{3-}$ anion. λ_{exc} = 514 nm.

The polarized Raman spectra of ***a***-cut Tm:RVO_4 crystals are shown in Figure V.3. A total of 12 modes are found for Tm:$GdVO_4$ and Tm:YVO_4, while only 11 modes are observed for Tm:$LuVO_4$. The modes were assigned in the spectra [Vor09, San12, Raf20]. The maximum phonon energy corresponding to the most intense Raman mode shifts from 882 to 899 cm^{-1} for $GdVO_4$ to $LuVO_4$, respectively. This mode is associated with the symmetric stretching vibrations of the $[VO_4]^{3-}$ radicals (ν_1 internal mode, A_{1g} symmetry) [Vor09]. As in the case of cubic sesquioxides (Chapter IV), the shift in the Raman modes from shorter to higher frequencies is observed with the decrease in ionic radius of the host forming cations (Gd^{3+}, R_{Gd} = 1.053 Å, Y^{3+},R_Y = 1.019 Å, Lu^{3+}, R_{Lu} = 0.977 Å). With decreasing the ionic radius R_{RE} most of the bond lengths shorten, which results in hardening of Raman frequencies [Ili06].

Additional Raman peaks above 1000 cm^{-1} can be seen in the spectra of the Tm:YVO_4 crystal. They can be caused by the distortion of the $[VO_4]$ tetrahedron due to the change in Y–V stoichiometry around congruent YVO_4. Thus, the change in Y–V stoichiometry enable changes in both external and internal modes of YVO_4 [Jin95, Erd96].

V.1.B. Polarized absorption and stimulated-emission cross-sections

The polarized absorption cross-section spectra from the ground state to the excited states $^3F_4$, $^3H_5$, $^3H_4$, and $^3F_{2,3}$ of Tm^{3+} ions in RVO_4 crystals are shown in Figure V.4.

The absorption spectra of the crystals are broad and possess strong phonon sidebands, *e.g.*, from 1400 to 1600 nm, the $^3H_6 \rightarrow {}^3F_4$. This is the evidence of a strong interaction of the electrons of Tm^{3+} ions with the phonons of the host matrices. Besides the broad spectral properties, they possess high absorption cross-sections, even much higher than in Tm:$YAlO_3$ or Tm:$Y_3Al_5O_{12}$ crystals, see Table V.1. The maximum σ_{abs} is found for the π-polarization for each observed absorption bands. The peak σ_{abs} increases from 3.00×10^{-20} cm^2 to 6.32×10^{-20} cm^2 at ~798 nm for Tm:YVO_4 and Tm:$LuVO_4$, respectively. The corresponding bandwidth (FWHM) decreases from 6.8 nm to 5.3 nm. For the σ-polarization, the absorption bandwidth is broader and

amounts to about 20 nm for Tm:YVO_4 and Tm:$LuVO_4$, and 17 nm in Tm:$GdVO_4$. However, the maximum σ_{abs} is lower and stays between 2.52 × 10^{-20} cm^2 (Tm:YVO_4) and 2.15 × 10^{-20} cm^2 (Tm:$GdVO_4$) at ~797 nm.

The $^3H_6 \rightarrow {}^3H_4$ Tm^{3+} transition is commonly employed for pumping 2.3-μm Tm-lasers directly to the upper laser level ($^3H_4$). It is well addressed by the emission of spatially multimode high-power fiber-coupled AlGaAs laser diodes whose central wavelengths are around 0.79 μm. The broadband absorption properties of Tm^{3+} ions in rare-earth orthovanadates reduce the effect of the temperature drift of the diode wavelength on the pump absorption efficiency.

For the $^3H_6 \rightarrow {}^3F_4$ Tm^{3+} transition, the maximum σ_{abs} is observed for Tm:$LuVO_4$ and amounts to 3.50 × 10^{-20} cm^2 at 1762 nm for π-polarization and 2.36 × 10^{-20} cm^2 at 1737 nm for σ-polarized light. This absorption band can be addressed by high-brightness power-scalable Raman-shifted Er-fiber lasers. The population of the $^3H_4$ upper laser level (for the 2.3 μm laser transition) is expected via an energy-transfer upconversion (ETU) process from the metastable $^3F_4$ state, $^3F_4 + {}^3F_4 \rightarrow {}^3H_4 + {}^3H_6$, although this approach has not been exploited so far in orthovanadates. This same pump transition around 1.7 μm represents the in-band pumping scheme for ~2 μm Tm-lasers.

The phonon sidebands of the $^3H_6 \rightarrow {}^3H_5$ transition around 1090 nm overlaps with the ESA spectra from the $^3F_4 \rightarrow {}^3F_{2,3}$ transitions that makes it possible to use this band to achieve 2.3 μm laser emission by upconversion pumping [Lis08, Gui19].

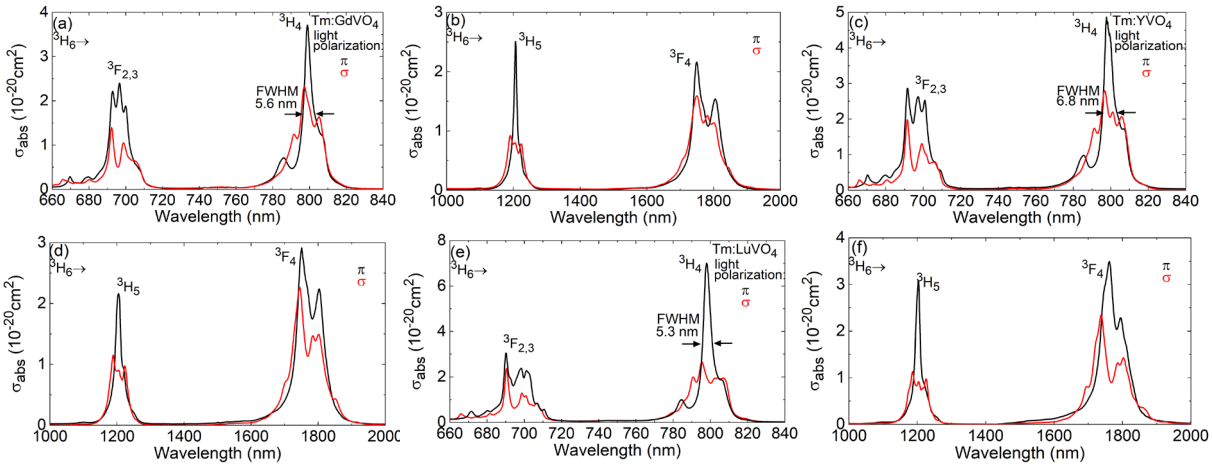

Figure V.4. RT absorption cross-sections for different transitions of Tm^{3+} ions in: (a,b) $GdVO_4$, (c,d) YVO_4, and (e,f) $LuVO_4$ crystals. Light polarization: π and σ.

The polarized SE cross-sections for the $^3H_4 \rightarrow {}^3F_4$ and $^3F_4 \rightarrow {}^3H_6$ transitions in the Tm^{3+}-doped crystals were calculated using F-L formula Eq I.23. For the calculations, we used the radiative and luminescence branching ratios of each transition reported by Lisiecki et al. and obtained by the J-O theory [Lis06].

The results on the SE cross-sections are shown in Figure V.5. The emission spectra of Tm^{3+} ions in RVO_4 are strongly polarized which, together with a strong natural birefringence of this vanadate compound, is a prerequisite for linearly polarized emission in diode-pumped lasers based on ***a***-cut crystals.

For the $^3F_4 \rightarrow {}^3H_6$ Tm^{3+} transition, in the long-wave spectral range where laser operation is

expected due to the reabsorption losses (quasi-three-level laser scheme), for σ-polarization, the maximum σ_{SE} is 0.46, 0.53, and 0.62 × 10^{-20} cm^2 at 1927, 1916 and 1901 nm for Tm:$LuVO_4$, Tm:YVO_4 and Tm:$GdVO_4$, respectively. Other maximum σ_{SE} at high inversion ratios are expected at 1810, 1808, and 1812 nm where the value of SE cross-sections amounts to 3.46, 3.16 and 2.84 × 10^{-20} cm^2 nm for Tm:$LuVO_4$, Tm:YVO_4 and Tm:$GdVO_4$, respectively, for the π-polarization of light.

The current values of absorption and SE cross-sections are in agreement with previously reported data [Lis06, Sul08]

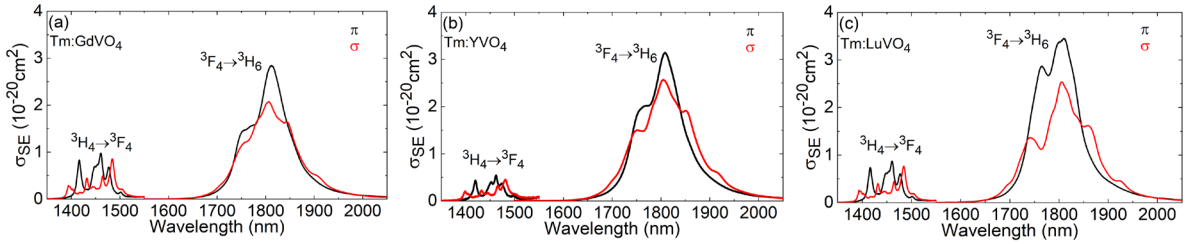

Figure V.5. RT stimulated-emission cross-sections for the $^3H_4 \rightarrow {}^3F_4$ and $^3F_4 \rightarrow {}^3H_6$ different transitions of Tm^{3+} ions in RVO_4 crystals: (a) Tm:$GdVO_4$; (b) Tm:YVO_4; (c) Tm:$LuVO_4$. Light polarization: π and σ.

For the $^3H_4 \rightarrow {}^3F_4$ Tm^{3+} transition giving rise to emission at 1.5 μm, the maximum σ_{SE} is 0.98 × 10^{-20} cm^2 (at 1461 nm) and 0.86 × 10^{-20} cm^2 (at 1484 nm) for π- and σ-polarized light, respectively, for Tm:$GdVO_4$. The lowest SE cross-sections are observed for the Tm:YVO_4 crystal and it amounts to 0.56 × 10^{-20} cm^2 (at 1462 nm) and 0.47 × 10^{-20} cm^2 (at 1480 nm) for π- and σ-polarized light, respectively. The long luminescence lifetime of the $^3F_4$ level represents a limiting factor for the development of 1.5 μm lasers. This can be overcome by utilising Tm-lasers, where the concentration of Tm^{3+} ions is low and the CR processes are reduced. The codoping of Tm-doped materials with Yb^{3+} ions promotes the 1.5 μm intensity through Yb → Tm energy transfer [Bra00]. The operation of a CW laser at 1.5 μm has only been reported for a Yb,Tm:$LiYF_4$ crystal [Die98].

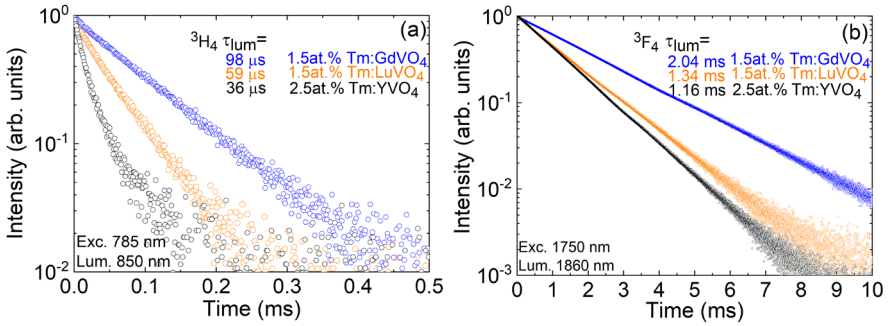

Figure V.6. Luminescence decay curves from (a) the $^3H_4$, λ_{exc} = 785 nm, and λ_{lum} = 850 nm, (b) the $^3F_4$, λ_{exc} = 1750 nm, and λ_{lum} = 1860 nm, of Tm^{3+} ions in RVO_4 crystals.

The luminescence decay curves were measured at 850 nm and 1860 nm representing the decay from the $^3H_4$ and $^3F_4$ Tm^{3+} states, respectively. The decay curves were well fitted with a single-exponential law, see Figure V.6, except the decay curves for 2.5 at.% Tm:YVO_4 since at this doping concentration the CR is strong. The luminescence lifetime τ_{lum} of the intermediate

metastable $^3F_4$ state was determined to be 2.04, 1.34, and 1.16 ms for Tm:$GdVO_4$, Tm:$LuVO_4$, and Tm:YVO_4. For the $^3H_4$ state, τ_{lum} equals to 98, 59, and 36 μs, respectively.

V.1.C. Low-temperature spectroscopy of Tm^{3+} ions

Low-temperature (12 K) absorption and emission spectroscopy was used to determine the crystal-field splitting of the $^3H_4$ (A_i), $^3H_5$ (X_j), $^3F_4$ (Y_m), and $^3H_6$ (Z_n) (*i*, *j*, *m*, and *n* = 1, 2, 3…) multiplets, as shown in Figure V.7 and Table V.1. In RVO_4 crystals the dopant Tm^{3+} ions replace the host-forming Lu^{3+} cations in a single type of site (D_{2d} symmetry, VIII-fold oxygen coordination). In the D_{2d} crystal field, the (2*J* + 1) degeneracy is partially lifted. The $^{2S+1}L_J$ multiplets with *J* = 0, 1, 2, 3, 4, 5, and 6 are split into 1, 2, 4, 5, 7, 8, and 10 irreducible representations, respectively [Lis06]. The lower-lying sub-level of the ground-state $^3H_6$ (A_1) is assigned as Γ_5. Since the electric-dipole transitions observed in absorption at 12 K only originate from this level, they must terminate at Γ_5 sub-levels for the π-polarization and Γ_1, Γ_2, Γ_3, and Γ_4 ones for σ-polarized light. This enables the assignment of electronic transitions in the LT absorption spectra giving access to the splitting of the excited states (from $^3F_4$ to $^3H_4$). In a similar way, the LT emission spectra are analyzed yielding the splitting of the terminal levels ($^3F_4$ and $^3H_6$). Note that some deviations from these selection rules are observed due to the non-negligible magnetic dipole contributions to the transition intensities for certain transitions following the selection rule $\Delta J = 0, \pm 1$.

Table V.1. Experimental crystal-field splitting of Tm^{3+} multiplets in RVO_4.

$^{2S+1}L_J$	No.	Γ_i	*E*, cm^{-1}			$^{2S+1}L_J$	No.	Γ_i	*E*, cm^{-1}		
			$GdVO_4$	YVO_4	$LuVO_4$				$GdVO_4$	YVO_4	$LuVO_4$
$^3H_6$(Z)	1	Γ_5	0	0	0	$^3H_5$(X)	1	Γ_2	8192	8236	8244
	2	Γ_1	18	56	36		2	Γ_1	8229	8272	8278
	3	Γ_4	32	75	57		3	Γ_5	8267	8299	8307
	4	Γ_5	115	112	173		4	Γ_3	8286	8341	8355
	5	Γ_2	129	139	181		5	Γ_5	8330	8377	8373
	6	Γ_3	138	158	210		6	Γ_2	8412	8439	8440
	7	Γ_4	192	192	256		7	Γ_5	8450	8461	8480
	8	Γ_1	220	210	309		8	Γ_4	8467	8490	8524
	9	Γ_5	293	325	359						
	10	Γ_3	311	336	367						
$^3F_4$(Y)	1	Γ_4	5548	5552	5557	$^3H_4$(A)	1	Γ_5	12519	12528	12537
	2	Γ_5	5646	5657	5670		2	Γ_1	12556	12566	12577
	3	Γ_1	5701	5726	5749		3	Γ_2	12631	12641	12645
	4	Γ_2	5745	5754	5781		4	Γ_4	12672	12657	12670
	5	Γ_3	5764	5823	5802		5	Γ_1	12686	12694	12722
	6	Γ_5	5841	5860	5884		6	Γ_5	12705	12714	12740
	7	Γ_1	5860	5880	5904		7	Γ_3	12782	12796	12816

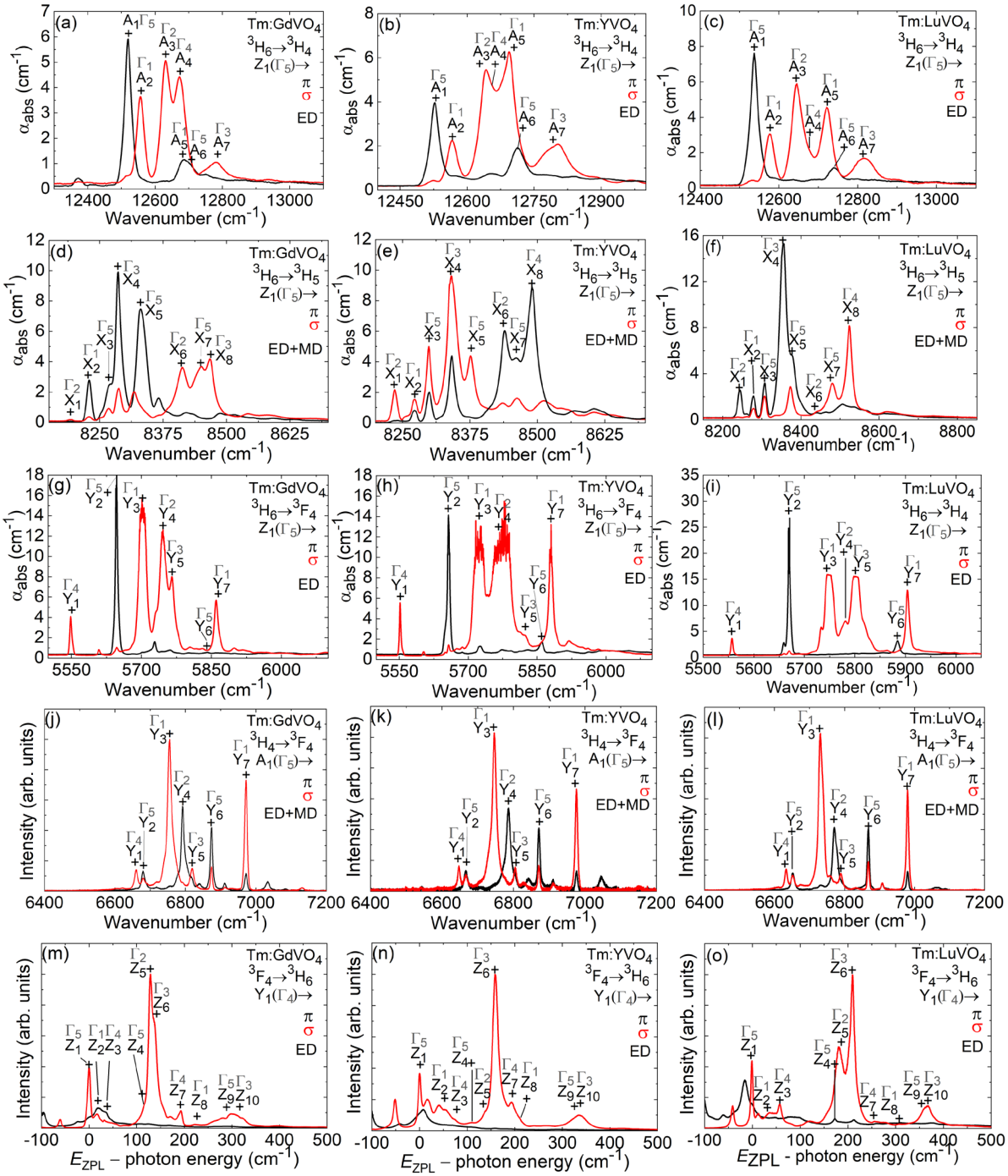

Figure V.7. LT (12 K) spectroscopy of Tm^{3+} ions in (a,d,g,j,m) $GdVO_4$, (b,e,h,k,n) YVO_4, and (c,f,I,l,o) $LuVO_4$ crystals: (a-c) the $^3H_6 \rightarrow {}^3H_4$ transition; (d-f) the $^3H_6 \rightarrow {}^3H_5$ transition; (g-i) the $^3H_6 \rightarrow {}^3F_4$ transition; (j-l) the $^3H_4 \rightarrow {}^3F_4$ transition; (m-o) the $^3F_4 \rightarrow {}^3H_6$ transition, light polarizations: π and σ, "+" indicates electronic transitions, Γ_i - irreducible representations.

V.1.D. Phonon-sidebands for Tm^{3+} ions: evidence of a strong electron-phonon interaction

As mentioned before, Tm^{3+} ions located at the end of the lanthanide series feature particularly strong electron-phonon interaction, which is responsible for the thermal broadening of spectral bands, as well as the appearance of phonon sidebands in the absorption and emission spectra. Tetragonal orthovanadates are known for strong lattice-orbit interaction. As a result,

at room temperature, the spectral profiles of Tm^{3+} ions in RVO_4 become nearly structureless despite the ordered nature of this crystal.

Figure V.8 shows a close look at the phonon sidebands in the absorption ($^3H_6 \rightarrow {}^3F_4$) and emission ($^3F_4 \rightarrow {}^3H_6$) spectra of Tm^{3+} ions in RVO_4 crystals at 12 K. The observed peaks due to vibronic transitions in the absorption spectra are at least spanning from 1600 to 1450 nm. The transitions experience a slight blue shift with decreasing the ionic radius of the host-forming cation, see Figure V.8(a,b,c). This effect can be related to the $Tm:R_2O_3$ crystal family where R stands for Y, Lu, and Sc, crystals in Chapter IV.5.

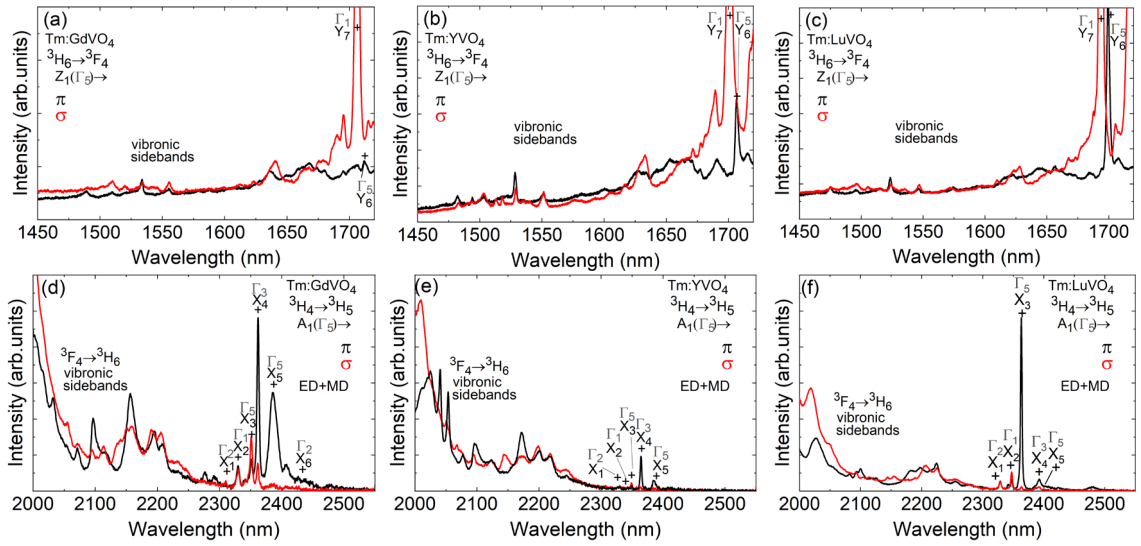

Figure V.8. Close look at the phonon sidebands of $Tm:RVO_4$ crystals in (a,b,c) absorption and (d,e,f) in emission at 12 K for: (a,d) $Tm:GdVO_4$; (b,e) $Tm:YVO_4$; (c,f) $Tm:LuVO_4$.

Low-temperature (12 K) polarized emission spectra of Tm^{3+} in RVO_4 above 2 μm are shown in Figure V.8(d,e,f). Notably for the $^3F_4 \rightarrow {}^3H_6$ electronic transition, the longest wavelength corresponding to a transition between the Y_1 (5557 cm^{-1}, the lowest-energy) and Z_{10} (367 cm^{-1}, the highest-energy) Stark sub-levels amounts to 1928 nm for $Tm:LuVO_4$. The electronic lines from the $^3H_4 \rightarrow {}^3H_5$ electronic transition were assigned, as shown in Figure V.8(d,e,f) using the same approach in Chapter IV.1.D. One can see that the emissions in the considered spectral range may originate either from multiphonon-assisted processes from $^3F_4 \rightarrow {}^3H_6$ transition or the $^3H_4 \rightarrow {}^3H_5$ transition.

The σ_{abs} and σ_{SE} spectra below the shortest- and longest-wavelengths electronic transitions, respectively, are reasonably well fitted with the exponential law using Eqs. IV.11-12. For all studied crystals the α_S and α_{AS} parameters amount to 7 ± 0.3 $\times 10^{-3}$ and 11 ± 0.3 $\times 10^{-3}$ cm. Despite their high phonon energies, these values are close to these for CALGO obtained in this work.

All these results show that the phonon-assisted laser emission of the $^3F_4 \rightarrow {}^3H_6$ transition might be achieved in $Tm:RVO_4$ crystals.

V.1.E. Assessing the suitability of Tm:RVO_4 crystals for laser operation on the $^3H_4 \rightarrow {}^3H_5$ Tm^{3+} transition

The emission spectra at 2.3 μm were measured by employing a similar set-up as in the case of Tm^{3+}-doped cubic sesquioxides, Chapter IV. We used 1.5 at.% Tm^{3+} doped $GdVO_4$ and $LuVO_4$, and 2.5 at.% Tm:YVO_4 crystals.

The measured spectra, shown in Figure V.9(a,b,c), are broadened and extend up to at least 2450 nm. A strong spectral overlap of the phonon sidebands from the $^3F_4 \rightarrow {}^3H_6$ transition with the $^3H_4 \rightarrow {}^3H_5$ transition is observed due to the strong electron-phonon interaction of Tm^{3+} ions in these crystals. A similar behavior was previously observed for Tm^{3+} ions in cubic sesquioxides, see Figure IV.63.

To calculate the stimulated-emission cross-section for the $^3H_4 \rightarrow {}^3H_5$ transition, the same procedure as for Tm:R_2O_3 in Chapter IV.5 was applied for these luminescence spectra. For the calculation, a branching ratio of $B_{JJ'}$ = 4% was used for each crystal. The resulting spectra are shown in Figure V.9(d,e,f). Table V.2 summarizes the maximum SE cross-sections and compares these values with other laser crystals at 2.3 μm.

Among the Tm^{3+} doped vanadates, Tm:$GdVO_4$ exhibit the highest SE cross-section for the π light polarization, which amounts to 2.97 × 10^{-20} cm^2 at 2280 nm corresponding to an emission bandwidth (FWHM) of 42 nm and at longer wavelengths, a weaker (σ_{SE} = 2.26 × 10^{-20} cm^2 at 2364 nm) and broader (FWHM= 79 nm) emission peak appears. Tm:$LuVO_4$ possess a maximum σ_{SE} of 2.48 × 10^{-20} cm^2 at the longest wavelength at 2363 nm for the π-polarization and the bandwidth (FWHM) of the corresponding emission peak is 28 nm. Another intense emission peak is found at a shorter wavelength of 2297 nm with a lower σ_{SE} of 1.89 × 10^{-20} cm^2. For Tm:YVO_4, the broadest emission band reaches 120 nm at 2213 nm with a maximum σ_{SE} of 1.07 × 10^{-20} cm^2 for σ-polarized light. This emission bandwidth is close to that of the structurally disordered Tm:$CaGdAlO_4$ crystal with a strong inhomogeneous spectral line broadening (128 nm for σ-polarization, 226 nm for π-polarization [Dup23]) and is the broadest one among other commonly used Tm^{3+}-doped oxide and fluoride ordered laser crystals. Tm-doped vanadates possess the highest SE cross-section among other laser crystals at 2.3 μm, Table V.2.

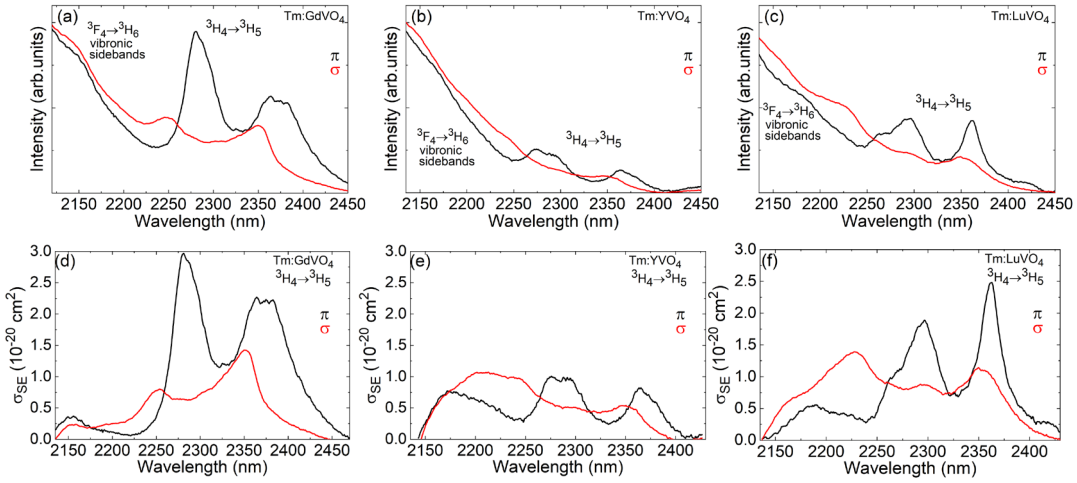

Figure V.9. Luminescence spectra (a,b,c) around 2.3 μm and stimulated emission cross-section for the $^3H_4 \rightarrow {}^3H_5$ transition (d.e.f) of Tm^{3+} ions in RVO_4 crystals.

Table V.2. Absorption and stimulated-emission properties of Tm^{3+} ions in crystals for 2.3-μm lasers.

Gain medium	Absorption ($^3H_6 \rightarrow {}^3H_4$)			Stimulated emission ($^3H_4 \rightarrow {}^3H_5$)				Ref.
	σ_{abs} (10^{-20} cm^2)	Polariz.	FWHM (nm)	σ_{SE} (10^{-20} cm^2)	λ_{em} (nm)	Polariz.	FWHM (nm)	
Oxides (aluminates)								
$Tm:YAlO_3$	1.19	***E*** **||** ***b***	4	0.78	2278	***E*** **||** ***b***	12	[Gui19a]
$Tm:Y_3Al_5O_{12}$	0.65	-	3	0.35	2324	-	37	[Gui20a, Zha22a]
$Tm:CaGdAlO_4$	1.59	π	16	1.14	2324	σ	128	[Dup23]
Oxides (vanadates)								
$Tm:GdVO_4$	3.29	π	7	2.97	2280	π	42	This work
	2.15	σ	17	1.31	2350	σ	87	
$Tm:LuVO_4$	6.32	π	6	2.48	2363	π	28	
	2.49	σ	20	1.39	2228	σ	88	
$Tm:YVO_4$	3.22	π	**12**	1.01	2276	π	**52**	
	2.52	σ	**20**	1.07	2213	σ	**120**	
Fluorides								
$Tm:LiYF_4$	0.64	π	-	0.57	2305	π	25.8	[Loi19a, Raz95]
$Tm:KY_3F_{10}$	0.66	-	3.8	0.34	2345	-	53.8	[Gui20]

The broadband emission properties of Tm^{3+} ions in RVO_4 make this compound promising for broadband wavelength tuning and femtosecond pulse generation in mode-locked lasers. As discussed in Chapter I.1.C, currently, this laser spectral range is dominated by laser sources based on Cr^{2+}-doped ZnS. 2.3-μm Tm-lasers can present a viable alternative to Cr^{2+}-based laser technology as they benefit from the well-developed crystal growth technology (as compared to II-IV chalcogenides) and the availability of commercial pump sources.

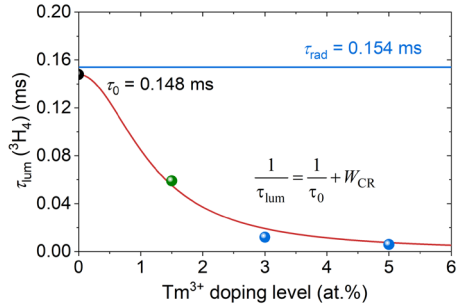

Figure V.10. Luminescence lifetime τ_{lum} of the $^3H_4$ state of Tm^{3+} ions in $LuVO_4$ versus the Tm^{3+} doping level: *green circle* – experiment, this work; *blue circles* – experiment, Ref. [Lis06], *black circle* - fitted intrinsic luminescence lifetime.

However, for both emissions originating from the $^3H_4$ multiplet, namely $^3H_4 \rightarrow {}^3F_4$ (at 1.5 μm) and $^3H_4 \rightarrow {}^3H_5$ (at 2.3 μm), the long luminescence lifetime of the $^3F_4$ level appears as a limiting factor for laser development. For the former transition, it leads to a bottleneck effect, $\tau_{lum}(^3H_4) << \tau_{lum}(^3F_4)$, leading to a self-terminating nature of this transition, and for both laser lines, it is responsible for accumulation of excitations causing unwanted ground-state bleaching. This constraint is released by the ETU process, $^3F_4 + {}^3F_4 \rightarrow {}^3H_4 + {}^3H_6$, draining the metastable level population and refilling the upper laser level. Other strategies include codoping of laser crystals with Tm^{3+} and Tb^{3+} (Eu^{3+}) ions leading to a strong luminescence quenching for the $^3F_4$ Tm^{3+} multiplet [Zha20, Pan22]. However, in this case, the ETU efficiency is also reduced.

In the limit of a very small Tm^{3+} concentration (when the cross-relaxation is nearly vanishing), the intrinsic luminescence lifetime τ_0 is defined as Eqs. I.59-60.

Using the experimental data from this work at 1.5% Tm^{3+} and the $^3H_4$ lifetime reported previously for the doping levels at [Lis06], we plotted the $^3H_4$ lifetime as a function of the Tm doping level (see Figure V.10). The best-fit with Eqs. I.59-60 leads to τ_0 and C_{CR} parameters values of 148 μs and 3×10^{-37} cm^6s^{-1}, respectively.

V.1.F. Efficient and power-scalable $TmRVO_4$ lasers at 2.3 μm and the discussion of the underlying laser scheme

The laser operation was performed by our colleagues the Key Laboratory of Laser and Infrared System of Ministry of Education, Shandong University, China. They employed three RVO_4 crystals, where R stands for Gd, Y, and Lu, doped with 1.5 at.% Tm^{3+} ions which correspond to ion densities of 1.82, 1.87, and 1.94×10^{20} cm^{-3}, respectively. They were oriented for light propagation along the crystallographic ***a***-axis (***a***-cut). This Tm^{3+} doping concentration was selected to balance two effects: (i) to reach sufficiently high pump absorption efficiency which is inaccessible for low doping levels and (ii) to prevent excessive self-quenching of the $^3H_4$ state lifetime by cross-relaxation among adjacent excited Tm^{3+} ions, the process which also favors the unwanted laser emission at 2 μm. Both end faces of the laser crystals (thickness: 10 mm, aperture: 3.0×3.0 mm^2) were anti-reflection coated for both the pump wavelength (792 ± 10 nm, reflectivity $R < 0.5\%$) and the laser wavelength (1850-2360 nm, $R < 1\%$) to avoid Fresnel losses.

In the laser set-up, the laser crystals were wrapped with indium foil, embedded in a 12 °C water-cooled brass heat sink, and pumped by a spatially multimode fiber-coupled AlGaAs laser diode emitting at 794 ± 2 nm. The fiber core diameter and the numerical aperture for the used pump source were 200 μm and 0.22, respectively. A 1:1 optical imaging system with a focal length of 50 mm was used to collimate and focus the pump radiation into the $Tm:RVO_4$ crystals (waist diameter: 200 μm). The compact laser cavity with a geometrical length of ~13 mm was formed by a plane pump mirror coated for high transmission at ~796 nm and high reflection at 1800-2400 nm and a set of plane output couplers with the transmissions T_{OC} in the range of 0.5%-10% at ~2.3 μm. All the OCs additionally provided high transmission above 90% at ~1.9 μm to suppress oscillations on the unwanted high-gain $^3F_4 \rightarrow {}^3H_6$ Tm^{3+} transition. The ~2.3 μm laser emission was separated from the residual pump radiation by employing a long-pass filter (F, FELH900, Thorlabs) with a transmission of ~85% at ~2.3 μm. The laser emission spectra were measured using an optical spectrum analyzer (APE GmbH, Germany).

Laser performance of $Tm:GdVO_4$ crystal. The laser operation in the plano-plano cavity was ensured by the positive thermal lens of $Tm:GdVO_4$. The pump absorption efficiency measured under non-lasing conditions ($\eta_{abs,NL}$) decreased in the range of 74 – 66% (1 – 18 W) due to a combination of the ground-state bleaching and temperature drift of the diode laser wavelength, when increasing the pump level. The pump absorption efficiency under lasing conditions ($\eta_{abs,L}$) was then estimated from the $\eta_{abs,NL}$ value at the threshold pump power, $\eta_{abs,L} = \eta_{abs,NL}(P_{th})$.

The CW diode-pumped Tm:$GdVO_4$ laser generated a maximum output power of 6.09 W at 2275-2291nm at the available maximum absorbed pump power P_{abs} of 32.8 W when using a 5% OC, as shown in Figure V.11(a). The optical efficiency of the laser reached 18.6%. No signs of thermal roll-over nor thermal fracture were observed up to at least the maximum studied pump power. The laser demonstrated excellent power stability when operated at the maximum power level for several hours.

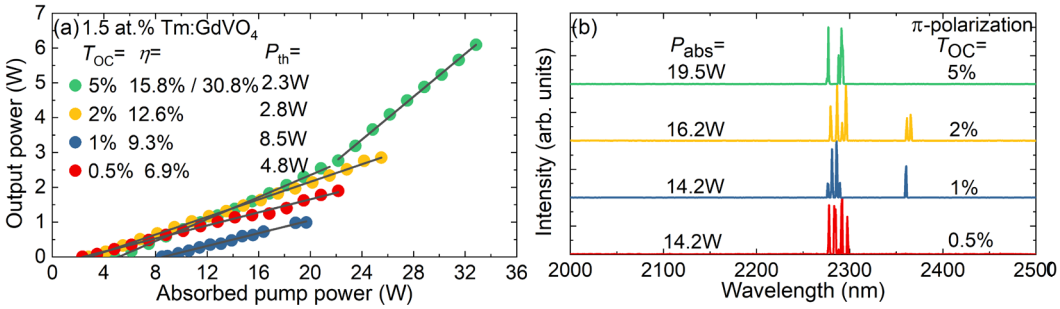

Figure V.11. Diode-pumped 1.5 at.% Tm:$GdVO_4$ laser operating on the $^3H_4 \rightarrow {}^3H_5$ transition: (a) input-output dependences; (b) typical spectra of laser emission measured well above the laser threshold (π-polarized emission).

The power transfer curve of the Tm:$GdVO_4$ laser was nonlinear and the slope efficiency increased from 15.8% (For P_{abs} < 22 W) to 30.8% (for higher pump levels). The latter value was close to the Stokes limit 34.8%. This behavior is assigned to the positive effect of the ETU process among adjacent excited Tm^{3+} ions, refilling the upper laser level ($^3H_4$) at the expense of the intermediate long-living $^3F_4$ level. A similar effect has been observed previously for other 2.3 μm lasers [Loi19]. Such behavior was particularly strong for the 5% OC. We believe that there are two reasons for this. First, for smaller output coupling (0.5% - 2%), the incident pump power was limited to prevent thermal damage of the laser crystal, and the ETU effect is less efficient at low pump levels. Second, the ETU probability increases with higher population of the $^3F_4$ state for high output coupling. The laser threshold gradually increased with T_{OC}, from 1.93 W (0.5% OC) to 4.80 W (5% OC).

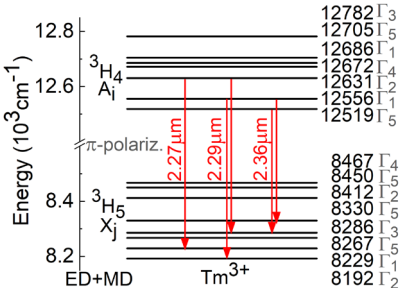

Figure V.12. Stark splitting of the $^3H_4$ and $^3H_5$ Tm^{3+} multiplets in $GdVO_4$, $\Gamma_1 - \Gamma_5$ – irreducible representations, arrows – the observed laser lines.

The laser operated on the fundamental transverse mode, as evidenced by the measured M^2 factors of 1.21 (M_x^2) and 1.26 (M_y^2). The typical spectra of the laser emission measured well above the laser threshold are shown in Figure V.11(b). The laser emission was linearly polarized

(π) in agreement with the anisotropy of the SE cross sections (Figure V.9(b)). The Tm:$GdVO_4$ laser operated in two spectral ranges, 2.29 μm and 2.36 μm, with the power fraction of the former emission being dominant for all OCs and pump power ranges. On increasing the absorbed pump power, a slight power redistribution between the two emission ranges was observed. Multiple laser lines are assigned to the broad gain spectra of Tm^{3+} ions in $GdVO_4$.

The experimental crystal-field splitting of the upper ($^3H_4$) and lower ($^3H_5$) laser manifolds was used to interpret the observed laser lines. The lines at 2.29 μm are assigned to the $A_2 \rightarrow X_1$ and $A_3 \rightarrow X_3$ transitions and those at 2.36 μm to the $A_1 \rightarrow X_4$ and $A_2 \rightarrow X_5$ ones, Figure V.12.

Laser performance of Tm:YVO_4 crystal. The pump absorption efficiency measured under non-lasing conditions for Tm:YVO_4 crystal decreased in the range of 80 – 74% (2 – 22 W).

The Tm:YVO_4 laser generated a maximum output power of 5.52 W at 2275-2298 nm (5% OC). The corresponding slope efficiency increased gradually from 17% to 26% as the pump level increased. For smaller output coupling in the range of 0.5%-5%, there was a similar behavior of the gradual increase in the slope efficiency, as plotted in Figure V.13(a).

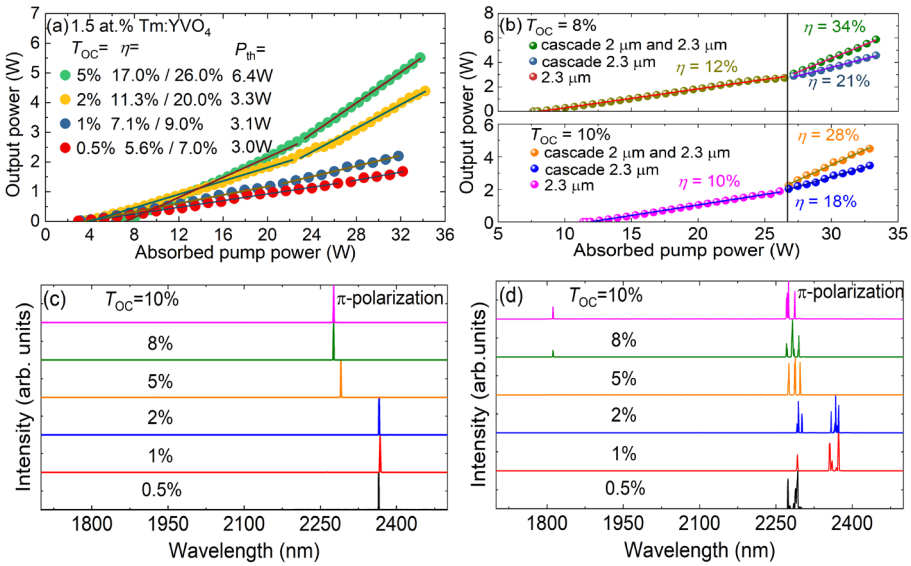

Figure V.13. Diode-pumped 1.5 at.% Tm:YVO_4 laser operating on the $^3H_4 \rightarrow {}^3H_5$ transition: (a,b) input-output dependences for different output couplers: (a) 0.5% - 5% OC and (b) 8% and 10%; (c,d) typical spectra of laser emission measured (c) well above the laser threshold and (d) at the maximum applied pump power (π-polarized emission).

However, the power transfer characteristics for high output coupling of 8%-10% were different from those achieved for 0.5%-5% OCs. Indeed, they did not present a gradual increase in the slope efficiency but instead featured an abrupt and significant increase of this parameter at an incident pump power above 35.7 W, namely from 12% to 34% (8% OC) and from 10% to 28% (10% OC). The resulting maximum CW laser output power reached 5.88 W and 4.49 W, respectively, see Figure V.13(b). The laser emission spectra shown in Figure V.13(d) demonstrate that at P_{inc} > 35.7 W, the Tm:YVO_4 laser simultaneously operated at 2.29 μm and 1.8 μm, which corresponded to the most intense emission peaks of the $^3H_4 \rightarrow {}^3H_5$ and $^3F_4 \rightarrow {}^3H_6$ Tm^{3+} transitions. Although both these OCs were coated for high transmission at ~2 μm to suppress oscillations on the $^3F_4 \rightarrow {}^3H_6$ transition, the Tm:YVO_4 laser still operated on a cascade

scheme at higher pump levels. The cascade lasing of Tm-based lasers was observed previously [Sto91, Hua19]. This is due to a significant accumulation of population in the metastable $^3F_4$ state at high pump levels and high output coupling transmissions enabling sufficient gain on the $^3F_4 \rightarrow {}^3H_6$ transition. The 2.29 μm power contribution was separated from the total output power (at 1.8 μm and 2.29 μm) by the long-pass filter. The input-output dependences of the Tm:YVO_4 cascade laser are shown in Figure V.13(b).

After filtering out the 1.8 μm power contribution, maximum 2.29 μm CW laser output powers of 4.58 W and 3.46 W and slope efficiencies of 21% and 18% were obtained for 8% and 10% OCs, respectively. The ETU process is strongly reduced for the cascade laser due to the reduction of the $^3F_4$ state population down to the level established by the condition "gain is equal to losses". Consequently, we believe that the significant increase in the slope efficiency of the 2.3 μm laser for the cascade laser scheme as compared to operation solely on the $^3H_4 \rightarrow {}^3H_5$ transition, namely from 12% (no cascade laser) to 21% (cascade laser) for the 8% OC and from 10% (no cascade laser) to 18% (cascade laser) for the 10% OC, is due to the addition of the $^3F_4 \rightarrow {}^3H_6$ laser channel. It is mainly explained by the recycling of Tm^{3+} ions stored in the metastable intermediate $^3F_4$ state, which are forced down to the ground-state ($^3H_6$). The bottleneck effect leading to the ground-state bleaching is then efficiently avoided.

The laser emission spectra of the 794-nm laser diode-pumped Tm:YVO_4 laser captured just above the laser threshold and at the maximum applied pump power are shown in Figure V.13(c). Near the laser threshold, for low output coupling of 0.5%-2%, the Tm:YVO_4 laser operated only at 2.37 μm presenting a single laser line. For higher 5%-10% output coupling, the emission wavelength shifted to 2.29 μm presenting a single line in the spectrum. The two observed laser wavelengths of 2.29 μm and 2.37 μm correspond to the two most intense peaks in the stimulated-emission cross-section spectrum for the $^3H_4 \rightarrow {}^3H_5$ Tm^{3+} transition (for π-polarization), see Figure V.9(d). For 1% and 2% OCs, the Tm:YVO_4 lasers operated in two spectral ranges, at 2.37 μm and 2.29 μm, with the power fraction of the former emission being dominant. Note that the 2.3 μm laser emission for all the laser configurations was linearly polarized (pure π-polarization).

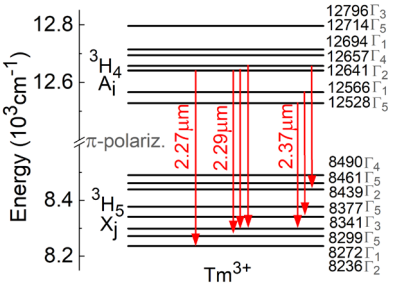

Figure V.14. Stark splitting of the $^3H_4$ and $^3H_5$ Tm^{3+} multiplets in YVO_4, $\Gamma_1 - \Gamma_5$ – irreducible representations, *arrows* – the observed laser lines.

The experimental crystal-field splitting of the upper ($^3H_4$) and lower ($^3H_5$) laser manifolds was used to interpret the observed laser lines. The lines at 2.29 μm are assigned to the $A_3 \rightarrow X_2$, $A_3 \rightarrow X_3$, and $A_4 \rightarrow X_3$, and those at 2.37 μm to the $A_1 \rightarrow X_3$, $A_2 \rightarrow X_4$, and $A_4 \rightarrow X_6$ ones, Figure V.14.

Laser performance of Tm:LuVO$_4$ crystal. The pump absorption efficiency of the Tm:LuVO$_4$ crystal was measured under non-lasing conditions using a pump-transmission experiment and it gradually decreased from 90.8% to 83.7% on increasing the incident pump power from 0.76 W to 19.04 W. The high pump absorption efficiency was reached owing to the large absorption cross-sections of Tm^{3+} ions in the LuVO$_4$ crystal (~3.54×10^{-20} cm^2 at the pump wavelength), and the crystal length (10 mm). The Tm:LuVO$_4$ laser operated on the fundamental transverse mode, as evidenced by the measured beam quality factors M^2 of 1.39 (M_x^2) and 1.43 (M_y^2).

The input-output dependences of the diode-pumped 2.3 μm Tm:LuVO$_4$ laser are shown in Figure V.15(a). For all the studied OCs, the Tm-laser operated solely on the $^3H_4 \rightarrow {}^3H_5$ transition without colasing at 2 μm. The maximum CW output power was achieved using 5% OC, namely 988 mW at ~2290 nm with a laser threshold of 8.51 W and a slope efficiency η of 9.2% (calculated *vs.* absorbed pump power). A slightly higher slope efficiency of 9.4% was obtained with yet higher 8% OC at the expense of the increased laser threshold (11.4 W) and reduced maximum output power (629 mW). On increasing the output coupling from 0.5% to 10%, the laser threshold gradually increased in the range of 3.87 W - 17.6 W. During the operation of the Tm:LuVO$_4$ laser for several hours at high pump levels of at least P_{abs} ~20 W, the measured laser output power was stable, and no thermal fracture of the crystal was observed.

As shown in Figure V.15(a), the laser performance of the Tm:LuVO$_4$ crystal is somewhat inferior as compared to other orthovanadates, Tm:GdVO$_4$, Tm:YVO$_4$ crystals. This is assigned to the stronger thermal effects caused by inferior thermo-mechanical properties of LuVO$_4$, as well as slightly higher maximum phonon energy (899 cm^{-1}). The latter is expected to lead to a stronger NR path and a higher laser threshold. However, we believe the laser performance could be improved by i) optimizing the crystal growth process and the Tm^{3+} doping level, ii) changing the pumping scheme (dual-end pumping, upconversion pumping, tandem pumping) and iii) employing bonded composite crystals to mitigate thermal effects.

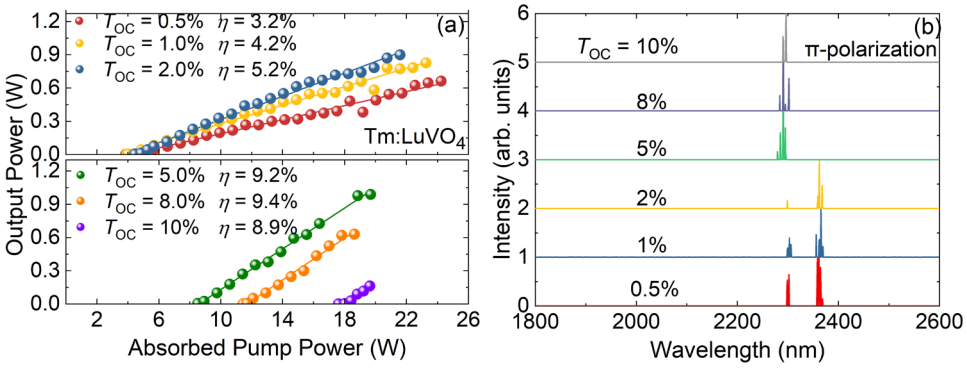

Figure V.15. Diode-pumped 1.5 at.% Tm:LuVO$_4$ laser operating on the $^3H_4 \rightarrow {}^3H_5$ transition: (a) input-output dependences; (b) laser emission spectra measured at the maximum studied pump power.

For the diode-pumped Tm:LuVO$_4$ laser operating on the $^3H_4 \rightarrow {}^3H_5$ transition (quasi-four-level laser scheme), the Findlay-Clay analysis was applied to estimate the round-trip passive resonator loss *L*. This analysis yields *L* of 1.5%.

The polarization of laser emission for all the studied OCs was linear, ***E*** || ***c*** (π-polarization), and it was naturally selected by the gain anisotropy in line with the polarized stimulated-emission cross-section spectra reported in this work. The typical spectra of laser emission are shown in Figure V.15(b). Similar to the Tm:YVO_4 laser, the Tm:$LuVO_4$ laser operated on a single line at 2362-2365 nm for small output couplings of 0.5% to 2%. While for higher output-coupler transmissions of 5% to 10%, the Tm:$LuVO_4$ laser still operated on a single line but at shorter wavelengths of 2291-2293 nm around the threshold pump power. At the studied maximum pump power, multiple laser lines appeared within two spectral ranges around ~2.29 μm and ~2.36 μm for small output coupling, while a laser emission only within one spectral range at ~2.29 μm was observed for T_{OC} in the range of 5% to 10%.

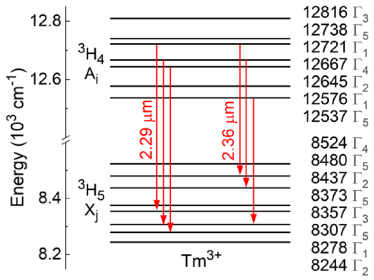

Figure V.16. Stark splitting of the $^3H_4$ and $^3H_5$ Tm^{3+} multiplets in $LuVO_4$, $\Gamma_1 - \Gamma_5$ – irreducible representations, *arrows* – the observed laser lines.

The observed spectral ranges of laser emission correspond to the two most intense emission peaks for the $^3H_4 \rightarrow {}^3H_5$ Tm^{3+} transition (π-polarization), see Figure V.16. The laser lines at ~2.29 μm are assigned to the A_3 (Γ_2) → X_2 (Γ_1), A_4 (Γ_4) → X_3 (Γ_5), and A_5 (Γ_1) → X_4 (Γ_3) electronic transitions and those at ~2.36 μm - to the A_1 (Γ_5) → X_3 (Γ_5), A_4 (Γ_4) → X_6 (Γ_2), and A_5 (Γ_1) → X_7 (Γ_5) ones.

In Table V.3, we compare the output performance of diode-pumped Tm lasers operating on the $^3H_4 \rightarrow {}^3H_5$ transition reported so far [Gui19, Kif20, Zha22, Yu24]. Fluoride (Tm:$LiYF_4$) and oxide (Tm:$Y_3Al_5O_{12}$, Tm:$YAlO_3$, and Tm:YVO_4) crystals have been employed in such lasers. We report on the highest output power from any 2.3 μm thulium laser using a 1.5 at.% Tm:$GdVO_4$ crystal and a compact plano–plano laser cavity.

Table V.3. Output characteristics of diode-pumped thulium lasers operating at 2.3 μm.

Crystal	C_{Tm}, at.%	P_{th}, W	P_{out}, W	η, %	λ_L, μm	Ref.
Tm:$LiYF_4$	3.5	0.72	2.11	26.9	2.30	[Kif20a]
Tm:$Y_3Al_5O_{12}$	3.2	1.67	1.11	9.1	2.19, 2.32	[Kif20a]
	3.5	2.72	1.49	10.1	2.33	[Zha22a]
Tm:$YAlO_3$	1.8	4.53	2.68	33.1	2.27	[Kif20a]
	2	~5	0.74	8.3	2.45	[Gui19a]
	3.5	6.24	2.97	21.4	2.27	[Yu24]
Tm:$GdVO_4$	1.5	4.80	**6.09**	30.8	2.29	
Tm:YVO_4	1.5	7.78	5.52	22.3	2.29	
Tm:$LuVO_4$	1.5	8.51	0.99	9.2	2.29	

Conclusions of Chapter V

Thulium doped orthovanadate crystals, namely Tm:$GdVO_4$, Tm:YVO_4, and Tm:$LuVO_4$, are viable solution for the development of diode-pumped 2.3-μm solid-state lasers power scalable to the multi-Watt level owing to a combination of good thermo-mechanical properties of the host matrices and appealing spectroscopic behavior of Tm^{3+} ions. They exhibit (i) broad absorption spectra and relatively high absorption cross sections supporting pumping by high-power AlGaAs laser diodes at 0.79 μm, as well as high pump absorption efficiencies, (ii) high SE cross sections for the $^3H_4 \rightarrow {}^3H_5$ transition for polarized light (six times higher than those for Tm:$LiYF_4$) leading to linearly polarized laser emission; and (iii) a relatively long upper laser level ($^3H_4$) lifetimes despite the high phonon energies. Owing to a strong electron–phonon interaction, Tm^{3+} ions in RVO_4 also feature broad and smooth gain profiles around 2.3 μm making these materials promising for broadly tunable operation and femtosecond pulse generation.

Based on the spectroscopic study, the high power and the observed increase in the laser efficiency with increasing pump power are explained. Our work sheds light on the roles of energy-transfer upconversion from the intermediate metastable $^3F_4$ Tm^{3+} state, as well as cascade lasing involving a laser transition from this level ($^3F_4 \rightarrow {}^3H_6$) in boosting the 2.3-μm Tm laser performance. Two operation regimes are observed. Without colasing, a gradual increase in the slope efficiency of the 2.3 μm laser is assigned to the positive action of ETU refilling the $^3H_4$ level. When colasing at 2 and 2.3 μm is allowed, the laser slope efficiency at 2.3 μm rapidly changes as the $^3F_4 \rightarrow {}^3H_6$ laser drains the $^3F_4$ metastable state and prevents the bottleneck effect by reducing the ground-state bleaching. This effect has a major influence on the laser performance compared to that caused by ETU.

General Conclusions and Perspectives

General conclusions

Within this PhD thesis, it was demonstrated that thulium and holmium ions in materials with rare-earth ion clustering, structural disorder, and compositional disorder exhibit pronounced inhomogeneous spectral line broadening. This phenomenon manifests as broad and structureless absorption and emission spectra of dopant ions. These materials can exhibit long-wave emission resulting from electron-phonon coupling leading to the laser emission beyond electronic transitions. Additionally, it was observed that materials appearing structurally ordered at first glance display broadband spectral characteristics due to homogeneous mechanisms caused by strong electron-phonon interaction. By combining these features, we can achieve an ideal "glassy-like" spectroscopic behavior and therefore develop new broadly tunable and ultrafast lasers.

• The clustering of thulium and holmium ions in CaF_2 crystals enables "glassy-like" spectroscopic behaviour (smooth and broad spectra) of these dopants and induces nonradiative energy-transfers between them leading to an effective predominantly direct energy-transfer between them due to the formation of at least two types of clusters with only thulium ions and those with thulium and holmium ions. Moreover, the codoping enhances an additional spectral line broadening and pushes emission to a longer wavelength. All these features allowed to achieve the first laser operation of Tm,Ho:CaF_2 crystal in continuous-wave regime and broadly tunable range. The laser generated a high output power of 737 mW with a slope efficiency of 28% around 2.08 μm and a broad tuning range of 129 nm.

• Crystals with a structure disorder, such as tetragonal $CaGdAlO_4$, where the disorder in the structure originates from a random distribution of several host-forming cations of different valence over several non-equivalent lattice sites, enable the inhomogeneous spectral line broadening of dopant ions in these crystals, and the absorption and emission spectra resemble those of glasses. This effect is determined by various compositions of the second coordination sphere around the dopant ions. Based on the first spectroscopic study of holmium-doped $CaGdAlO_4$ crystals, it was confirmed that holmium ions exhibit broad gain bandwidth comparable to that in holmium-doped glasses. Holmium ions experience a strong electron-phonon interaction leading to the temperature broadening of their spectral lines and the appearance of an exponential multi-phonon sideband in the long-wave part of the emission spectrum extending up to at least 2.3 μm. All these features supported the generation of sub-100-fs pulses from a mode-locked Ho:CALGO at wavelengths beyond electronic transitions.

• In solid-solution sesquioxide ceramics of the yttria-lutecia-scandia ternary system doped with thulium ions, we show a strong and nearly linear variation of the crystal-field strength for C_2 symmetry sites with the mean size of the host-forming cation. This allows for the customization of the position and width of the emission band above 2 μm by adjusting the host composition appropriately. It makes the transparent ceramic technology ideal for material engineering of sesquioxides ceramics doped with rare-earth ions for laser applications.

Ceramic compositions based on scandia exhibit the most significant spectral broadening and red-shift due to the small ionic radii of Sc^{3+}. Such materials represent substitutional solid-solutions with a mixing at the atomic level. The inhomogeneous spectral line broadening is a result of variations in the local composition of the second and next coordination sphere around the dopant ions. The combination of strong crystal-fields, leads to a large total Stark splitting of the ground-state of thulium ions, and a strong inhomogeneous broadening, even at ambient temperature, in "mixed" sesquioxide ceramics.

• In this work, we reported on highly efficient ~2-μm laser operation of Tm:Y_2O_3 and Tm:$(Y,Sc)_2O_3$ transparent sesquioxide ceramics. For both the parent and solid-solution ceramics, the achieved laser slope efficiencies (70.2% and 44.7%) represent record-high values for any Tm^{3+}-doped sesquioxide ceramics being comparable with the best results for the corresponding single crystals. It is due to an efficient cross-relaxation under high thulium ions doping level and relatively low-passive losses even for “mixed” compounds owing to an optimized synthesis procedure involving laser-ablated nanoparticles with a mixture of cations at the atomic level. Moreover, we demonstrated the first laser operation of Tm,Ho:$(Y,Sc)_2O_3$ ceramics with a high efficiency of 54% and a widely tunable range of 190 nm conditioned by codoping with both thulium and holmium ions and a significant inhomogeneous spectral line broadening induced by the structure and compositional disorder.

• Electron-phonon interaction is responsible for multiphonon-assisted emission of dopant ions that gives rise to Stokes and anti-Stokes phonon sidebands in emission and absorption spectra. It plays a significant role in achieving optical gain in the long-wave spectral range beyond the electronic fluorescence spectrum. Such phonon sidebands can even bridge the gaps between two different electronic transitions of the same ion as demonstrated for the $^3F_4 \rightarrow {}^3H_6$ and $^3H_4 \rightarrow {}^3H_5$ transitions of thulium ions. It was also demonstrated that holmium ions in $CaGdAlO_4$ exhibit long-wave emission spanning beyond 2.1 μm. It makes possible to develop new vibronic thulium and holmium broadly tunable and mode-locked lasers generating ultrafast pulses in broad spectral ranges. We demonstrated the first phonon-assisted laser operation of a thulium-doped cubic sesquioxide crystal at 2.25 μm thanks to its strong electron-phonon coupling.

Furthermore, our findings indicate that the spectral line broadening of dopant ions in orthorhombic scandates and tetragonal orthovanadates at room temperature is predominantly attributed to homogeneous (thermal) broadening resulting from electron-phonon interaction, rather than an inhomogeneous mechanism. This makes them highly suitable for use in ultrafast lasers.

• Despite the high phonon energies of tetragonal RVO_4, where R stands for Gd, Y, and Lu, thulium ions exhibit a relatively long fluorescence lifetime of the upper laser level ($^3H_4$) leading to intense emission around 2.3 μm due to the $^3H_4 \rightarrow {}^3H_5$ transition. The luminescence spectra at 2.3 μm were detected at the first time for these crystals. In the laser experiment, two operation regimes were observed. Without colasing, the main role in the increase of a slope efficiency of the 2.3 μm laser is played by energy-transfer upconversion refilling the $^3H_4$ level. With colasing at 1.9μm, the laser slope efficiency changes as the $^3F_4 \rightarrow {}^3H_6$ laser drains the $^3F_4$

metastable state and thus prevents the bottleneck effect. This effect has a major influence on the laser performance compared to that caused by ETU.

The use of materials doped with rare-earth ions which combine inhomogeneous spectral line broadening and strong electron-phonon interaction allows to develop ultrabroadband light sources and generate sub-100-femtosecond pulses from mode-locked lasers.

Perspectives

The coverage of the short-wave infrared spectral range of 2 to 3 μm and beyond with rare-earth based lasers, especially those generating ultrashort pulses at high repetition rates, is a great challenge for laser physics. It must be supported by key advances in developing broadly emitting solid-state lasers. Perspectives can be formulated based on the current study and they should be listed as follows.

• *Developing new solid-state laser sources at 2 – 3 μm and beyond*. The next goal of developing new laser sources is to push the limit of lanthanide laser emission in the mid-infrared. To develop new mode-locked thulium lasers emitting around 2.3 μm (the $^3H_4 \rightarrow {}^3H_5$ transition), orthovanadates, aluminates, scandates, and sesquioxides should potentially be used due to their smooth and broad spectra. The occurrence of a bottleneck effect can be overcome by relying on energy-transfer upconversion processes, upconversion pumping schemes or codoping with ytterbium ions. For holmium- and erbium-lasers emitting at 3 μm, low-phonon energy materials can be implemented such as fluoride crystals and certain oxide crystals and ceramics, i.e., sesquioxides, aluminates, scandates. The codoping with praseodymium ions can also be used to avoid the bottleneck effect.

To develop novel laser sources beyond 3 μm, lanthanide ions such as holmium, erbium, dysprosium and praseodymium should be considered since several laser transitions can be found beyond 3 μm. However, to develop this kind of lasers, the use of materials possessing low-phonon energies is crucial, such as chloride and bromide crystals. The 3 – 5 μm spectral range is particularly interesting for applications in mid-infrared communications and for detecting greenhouse gases or air pollutions.

• *Deep understanding the role of electron-phonon interaction*. As shown in this thesis, the interaction of 4f electron of thulium and holmium ions with phonons of a host matrix enables generation of laser lines beyond the long-wavelength electronic transitions. Future work will focus on the deep understanding of the role of long-wave phonon sidebands for reaching laser gain beyond electronic transitions for different lanthanide ions in various potential laser materials. The demonstration of broadly tunable lasers and generation of ultrashort pulses assisted by multiphonon emissions will be performed. For instance, continuous tuning can potentially be achieved with single thulium-doped material across a spectral range of 1.8 – 2.6 μm supported by multiphonon emission spanning between two thulium transitions namely $^3F_4 \rightarrow {}^3H_6$ and $^3H_4 \rightarrow {}^3H_5$. Additionally, Stokes phonon sidebands in absorption from different rare-earth ions in materials should be considered and studied since they can be involved in new pumping schemes (non-resonant ground-state absorption).

Moreover, the quantification of phonon-assisted energy-transfer processes such as energy-transfer upconversion processes in thulium and holmium ions is essential for understanding their role in laser transitions at 2 – 3 μm and for modelling the performance of these lasers.

• *Integrated optics, waveguide structures*. Now laser technologies are marching toward miniaturization and integration for large-scale practical applications. Solid-state materials such as calcium gadolinium aluminate-type, fluoride-type, rare-earth orthovanadate crystals and transparent cubic sesquioxide ceramics doped with thulium and/or holmium ions can be used

as matrices for fabricating waveguide structures in their bulk value for applications in mode-locked and widely tunable lasers operating at 2 μm and beyond. It can significantly reduce the size of the laser set-up. The development of these new laser sources enables their application in integrated optics. The widespread use of the femtosecond direct laser writing technique is particularly attractive as it facilitates the fabrication of various waveguide structures.

• *Applications in optical quantum memory*. Currently, rare-earth ions doped in solids have demonstrated long-lived and efficient optical storage, for instance, in thulium-doped garnets (YAG). It allows their use for long-distance quantum communications. The coherence time T_2 plays an important role in defining the optimal material for quantum memory. While the T_2 time is inversely proportional to the homogenous linewidth, the inhomogeneous broadening could be useful since it enables a storage of a large number of modes on one spatial region. Fluoride-type crystals doped with thulium and holmium ions might be a good candidate for application in quantum memory due to they combine long lifetime and inhomogeneously broadened emission spectra at high doping concentrations. They exhibit narrow linewidth at low doping levels. The control of the dopant concentration in these crystals allows to change their emission bandwidth.

Supplemental Materials

Appendix A. Materials and Methods

A1. Materials

Table A1.1. Materials studied in the framework of this thesis.

Crystal family	Chemical formula	Doping, at.%	Crystal class (space group)	Optical property	Synthesis method	Source
Single crystals						
Fluorides	CaF_2	3-5Tm 0.3-0.5Ho	Cubic ($Fm\bar{3}m$)	Isotropic	BS	CIMAP
Aluminates	$CaGdAlO_4$	1-3.1Ho	Tetragonal ($I4/mmm$)	Uniaxial	Cz	EOT GH
Perovskites	$GdScO_3$	3.7Tm, 0.3Ho	Orthorhombic ($Pnma$)	Biaxial	Cz	SIOFM
Garnets	$Ca_3Nb_{1.5}Ga_{3.5}O_{12}$	10Yb, 0.7-1Ho, 0.07-0.2Eu	Cubic ($Ia3d$)	Isotropic	Cz	SICE SU
Sesquioxides	Y_2O_3, Lu_2O_3, Sc_2O_3	1.8-2.5Tm	Cubic ($Ia\bar{3}$)	Isotropic	NK, HEM	IKZ
Vanadates	RVO_4 (R = Gd, Y, Lu)	1.5-2.5Tm	Tetragonal ($I4_1/amd$)	Uniaxial	Cz	SICE SU
Transparent ceramics						
Sesquioxides	Y_2O_3, Lu_2O_3, Sc_2O_3, $(Y,Lu)_2O_3$, $(Lu,Sc)_2O_3$, $(Y,Lu,Sc)_2O_3$	3Tm	Cubic ($Ia\bar{3}$)	Isotropic	VS	ICHPS RAS
	$(Y,Lu)_2O_3$	3Tm			HIP	SIC
	$(Y,Sc)_2O_3$	3-5Tm, 0.6Ho			VS	IE RAS
Chanel Waveguide						
Fluorides	CaF_2		Cubic ($Fm\bar{3}m$)	Isotropic	Fs-DLW/BS	ALF US /CIMAP

BS – Bridgman-Stockbarger.
Cz – Czochralski.
NK – Nacken-Kyropoulos.
NEM – heat-exchange method.
VS – vacuum sintering.
HIP - high isostatic pressure.
Fs-DLW – femtosecond-direct laser writing.
EOT GH – Electro-Optics Technology Gmbn, Idar-Oberstein, Germany.
SIOFM – Shanghai Institute of Optics and Fine Mechanics, Shanghai, China.
SICE SU – School of Information Science and Engineering, Shandong University, Qingdao, China.
IKZ – Leibniz-Institut für Kristallzüchtung, Berlin, Germany
ICHPS RAS – G.G. Devyatykh Institute of Chemistry of High-Purity Substances of the RAS, Nizhniy Novgorod, Russia.
SIC – Shanghai Institute of Ceramics, Shanghai, China.
ALF US – Aplicaciones del Láser y Fotónica, University of Salamanca, Salamanca, Spain.

A2. Structural and thermal analysis

Different methods were applied including material characterization and optical spectroscopy. They are listed in Table A2.1.

Table A2.1. Summary of characterization methods used to study Tm and Ho-doped materials in this PhD thesis.

Method	Purpose	Partner
Material characterization		
X-ray powder diffraction (XRD)	Phase identification	URV, ICHPS RAS, IE RAS, SIOFM
Rietveld analysis	Structure refinement	IE RAS, URV
Differential thermal analysis (DTA)	Thermal behavior	URV
Laser flash method	Determination of thermal properties	NCFU
Scanning and Transmission electron microscopy (SEM, TEM)	Morphology study	IE RAS, *SIC*
Inductively coupled plasma mass spectrometry (ICP-MS)	Measuring the RE doping level	ICHPS RAS, IE RAS, SIOFM CAS, SICE SU, *SIC*
Spectroscopic study		
Polarized Raman spectroscopy	Vibronic properties	CIMAP*
μ-Raman/μ-luminescence mapping	Study of photonic microstructures	CIMAP*
Polarized absorption spectroscopy	Absorption spectra	CIMAP*
Polarized emission spectroscopy	Luminescence spectra	CIMAP*
Luminescence dynamics study	Luminescence lifetimes	CIMAP*
Low-temperature spectroscopy	Experimental Stark splitting	CIMAP*
Pump-probe method	Excited-state absorption spectra	CIMAP*
Judd-Ofelt analysis	Transition probabilities	VSTU

* – performed by me.

URV – Universitat Rovira i Virgili, Tarragona, Spain.
ICHPS RAS – G.G. Devyatykh Institute of Chemistry of High-Purity Substances of the RAS, Nizhniy Novgorod, Russia.
IE RAS – Institute of Electrophysics, Ural Branch of the RAS, Ekaterinburg, Russia.
SIOFM –Shanghai Institute of Optics and Fine Mechanics, Shanghai, China.
NCFU – North-Caucasus Federal University, Stavropol, Russia.
SIC – Shanghai Institute of Ceramics, Shanghai, China.
SICE SU – School of Information Science and Engineering, Shandong University, Qingdao, China.
VSTU – Vitebsk State Technological University, Vitebsk, Belarus.

A2.1 X-ray diffraction analysis and Rietveld refinement

The analytical technique known as *X-ray powder diffraction* (XRD) is primarily used for crystalline material for its phase identification, and also it can provide information on unit cell dimensions. The material to be analyzed is finely grounded, homogenized, and the average bulk composition is determined. X-ray diffraction is based on constructive interference of monochromatic X-rays and a crystalline sample. The interaction of the incident rays with the sample produces constructive interference (and a diffracted ray) when conditions satisfy Bragg's Law, as shown in Figure A2.1

The law relates the wavelength of electromagnetic radiation, λ, to the diffraction angle, θ, and the lattice spacing in a crystalline sample, *d*. These diffracted X-rays are then detected, processed, and counted. By scanning the sample through a range of 2θ angles, all possible diffraction directions of the lattice should be attained due to the random orientation of the powdered material. Conversion of the diffraction peaks to *d*-spacing allows identification of the crystal structure because each crystals has a set of unique *d*-spacing. Typically, this is achieved by comparison of *d*-spacing with standard reference patterns.

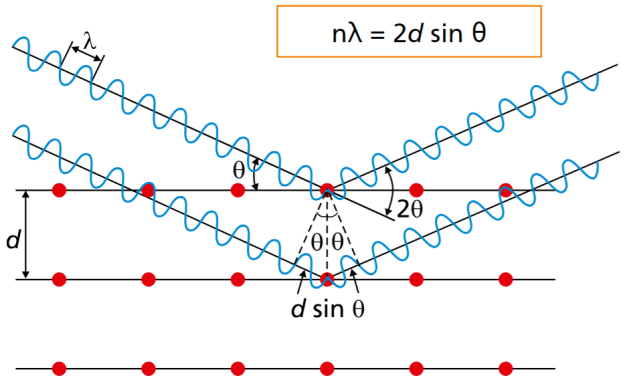

Figure A2.1. Principle of the XRD method. After [Erm13].

Rietveld refinement is conducted by fitting a calculated diffraction pattern to the observed data by adjusting each of the variables that describe the diffraction pattern. Rietveld computations are relatively intensive, and require minimizing the sum of the weighted, squared differences between observed and calculated intensities at every step in a digital powder pattern. The Rietveld method requires knowledge of the approximate crystal structure of all phases present in the specimen. The input data to a refinement include the space group, atomic positions, site occupancies, and lattice parameters.

Case of the Yb,Ho,Eu:CNGG crystal. In Chapter III.3, the XRD measurements for the Rietveld refinement of the crystal structure were carried out using a Bruker-AXS D8-Advance diffractometer equipped with a vertical θ-θ goniometer. The equipment had the incident and diffracted beam Soller slits of 2.5°, a fixed receiving slit of 0.5° and an air-scattering knife on the surface of the sample. The Cu K_α radiation was generated with a copper X-ray tube working at 40 kV and 40 mA. The sample was placed on a Si (510) support with low background. The measurements were performed with an angular step of 0.02° and a step time of 2 s. The X-ray diffraction pattern was recorded in the 2θ angular range of 15–90°. The diffracted X-rays were detected with a LynxEye-XE-T PSD detector, working with an opening angle of 2.94°.

Case of the Tm:R_2O_3 ceramics and their solid-solutions. In Chapter IV.1, the XRD analysis of ceramics was performed on a Shimadzu XRD-7000 diffractometer (Cu K_α radiation, 30 kV/30 mA). The measurements were performed in the Bragg-Brentano geometry in the range of diffraction angles 2θ = 18°–60° with a step of 0.02° and an exposure time of 1 s.

Case of the Tm and Ho doped $(Y,Sc)_2O_3$ ceramics. In Chapter IV.3 and 4, the phase composition of the sintered ceramic sample was studied using a D8 Discover (Bruker AXS,

Germany) diffractometer in the 2θ = 20 – 70° range using Cu K_α radiation. The analysis and the Rietveld refinement of the diffraction data were carried out using the TOPAS 3.0 software.

A2.2 Differential thermal analysis

The objective of calorimetry is the measurement of heat. To measure heat means to exchange heat. The exchanged heat tends to affect a temperature change in a body that can be used as a measure of the heat exchanged, or the process of heat exchange creates a heat flow which leads to local temperature differences along its path which again serve as a measure of the .flowing heat. As chemical reactions and many physical transitions are connected with the generation or consumption of heat, calorimetry is a universal method for investigating such processes. Measuring devices in which an exactly known amount of heat is input into a sample, or abstracted from it, and the temperature change in the sample is measured.

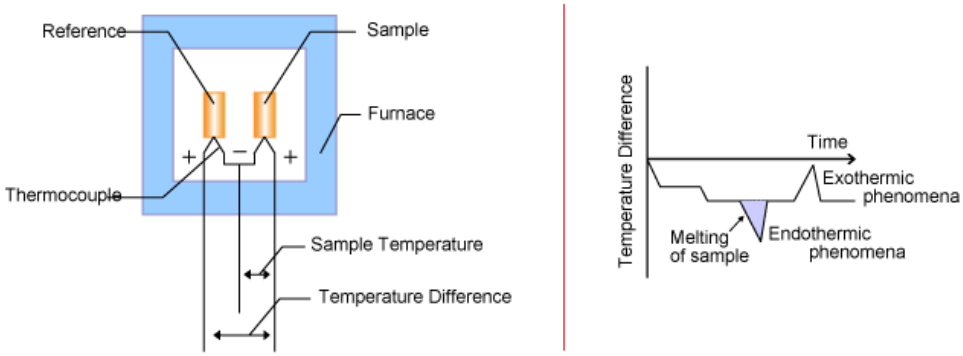

Figure A2.2. Principle of the DTA. After [https://resources.pcb.cadence.com/blog/2020-differential-thermal-analysis-and-pcb-substrate-glass-transitions].

Differential thermal analysis (DTA) is applied to measure the temperature difference between the sample to be investigated and a reference sample as a function of temperature (or time). This temperature difference indicates a heat exchange qualitatively. DTA allows characteristic temperatures to be determined and qualitative statements made on heat due to reaction. The working principle of the DTA is shown in Figure A2.2.

This method was employed for the 3 at.% Tm and 0.3 at.% Ho codoped CaF_2 crystal in Chapter II.1.

A2.3. Laser flash method for measuring the thermal conductivity

The laser flash method in thermal analysis involves exposing the front side of the sample to a brief burst of laser energy, causing the internal temperature to rise and creating a thermal gradient. The heat flow at the rear side of the sample is then measured until the sample reaches thermal stability. At thermal stability, a time-temperature graph is plotted to determine thermal diffusivity. The higher the thermal diffusivity, the faster the temperature rise reaches the rear face. Figure A2.3 shows the working principle of laser flash method.

In Chapter IV.3, the thermophysical characteristics of the ceramics were studied by the laser flash method sing a NETZSCH LFA 467 Hyper-Flash at 25–350°C under Ar atmosphere. The samples were covered with a graphite layer. The thermal conductivity was calculated as:

$$\kappa = \alpha C_p \rho \quad (A.1)$$

where α is the thermal diffusivity, C_p is the specific heat, and ρ is the density evaluated from the XRD analysis.

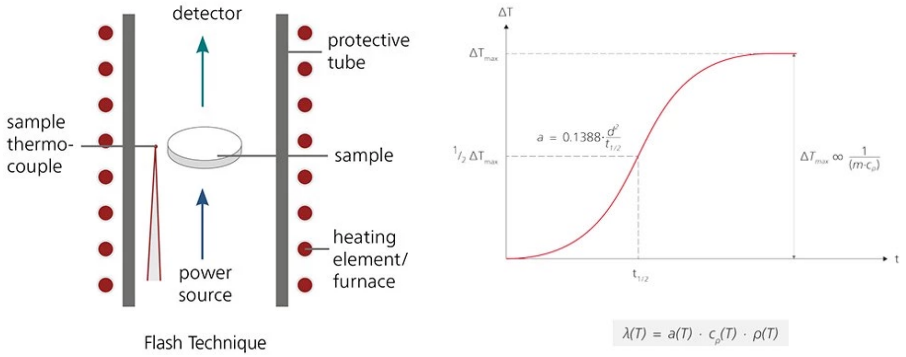

Figure A2.3. Principle of the laser flash method [https://analyzing-testing.netzsch.com/ja/contract-testing/methods/laser-flash-technique-lfa-1].

A2.4. Electron microscopy

Electron microscope, microscope that attains extremely high resolution using an electron beam instead of a beam of light to illuminate the object of study. The conventional electron microscope requires that the electron beam be in a vacuum, because electrons cannot ordinarily travel an appreciable distance in air at atmospheric pressure. The column of the electron microscope is evacuated by pumps, and the specimens and any other necessary apparatus are introduced into the vacuum by means of air locks. The electron microscope has variable-focus lenses, and the distance between specimen and objective lens and the separation of the lenses remain constant. The magnification is determined mainly by the value of the current (for magnetic lenses) through the intermediate and projector lens coils. The image is focused by changing the current through the objective lens coil. In the electron microscope the final image is invariably real and is visualized on a fluorescent screen or recorded for study on a photographic plate in traditional instruments or more usually on a digital imaging system.

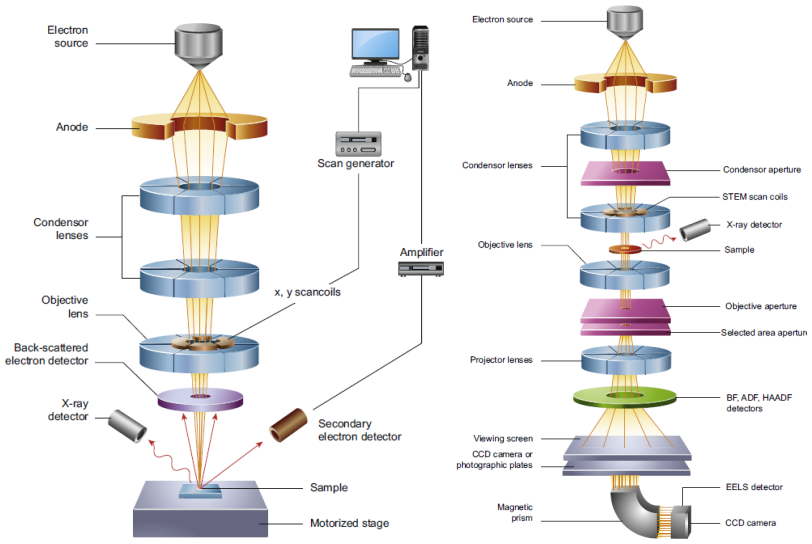

Figure A2.4. Schematic comparing the modes of image formation in the light, transmission, and scanning electron microscopes. After [Ink16].

In this thesis, two types of electron microscopy technique were employed, namely *scanning electron microscopy* (SEM) and *transmission electron microscopy* (TEM). The schematic of the basic SEM and TEM set-ups and its electron path, as well as the schematic of their imaging methodology are shown in Figure A2.4.

In SEM the electron beam is focused to a spot, and is scanned sequentially across the specimen. At each location, signals are emitted from the specimen and collected by detectors. The detector signal is synchronized with known location of the beam on the specimen, and the signal intensity is used to modulate the corresponding image pixel. The signals collected in series are combined to form an image whose dimensions/pixel distribution depends on the scan pattern chosen. Typical electron energies are 1e30 keV. SEM is the technique of choice for analysis of specimen surfaces. It encompasses the electron gun (electron source and accelerating anode), electromagnetic lenses to focus the electrons, a vacuum chamber housing the specimen stage, and a selection of detectors to collect the signals emitted from the specimen, see Figure A2.4.

In TEM the electron beam is incident onto a defined area of the specimen (Fig. 2.2(b)). Electrons transmitted through the specimen are focused by lenses and collected by a parallel detector to form an image. Electron energies in TEM are much higher than SEM, typically 80e300 keV, to enable them to penetrate through material. TEM is the technique of choice for analysis of specimen internal microstructure, evaluation of nanostructures such as particles, fibers, and thin films, and imaging of atoms. The key components of a TEM microscope comprise the electron gun, electrostatic lenses to focus the electrons before and after the specimen, and a transmitted electron detection system, see Figure A2.4.

Case of the Tm doped (Y,Lu)$_2$O$_3$ ceramic. In Chapter IV.2, the thermally etched surfaces of the Tm:LuYO$_3$ ceramics before and after HIPing were characterized using a scanning electron microscope, TM3000, Hitachi, Japan.

Case of the Tm and Ho doped (Y,Sc)$_2$O$_3$ ceramics. In Chapter IV.3 and 4, The structure of the obtained Tm and Ho doped Y$_2$O$_3$ and (Y,Sc)$_2$O$_3$ ceramics were observed on the polished and

chemically etched surface using a scanning electron microscope LEO 982 (LEO Electronenmikroskopie, Germany). In Chapter IV.4, the morphological features of the as-synthesized Tm,Ho:$(Y,Sc)_2O_3$ nanopowder were studied using a JEOL JEM 2100 (JEOL Ltd., Japan) transmission electron microscope.

A2.5. Inductively coupled plasma mass spectrometry

Inductively coupled plasma mass spectrometry (ICP-MS) is a type of atomic spectroscopy used to analyze the elemental composition of a sample. It is typically used to analyze samples that are liquid or can be dissolved. The technique uses argon plasma to convert the sample into ions, which are then measured using a mass spectrometer. Figure A2.5 shows a typical schematic representation of the basic components of ICP-MS. Generally, an ICP-MS instrument consists of (i) a sample introduction system, (ii) an ion source (Inductively Coupled Plasma, ICP), (iii) the electrostatic lenses, (iv) an interface, (v) a mass spectrometer, and (vi) a detector.

Solid samples should preferably be destructed, for example, with nitric acid. Then, the samples are placed into an autosampler, and a peristaltic pump guides them to the nebulizer. Each sample is mixed with argon gas to create an aerosol that enters the spray chamber. The latter extracts the large aerosol droplets because the plasma is inefficient at dissociating them, and then normalizes the flow of the liquid coming from the peristaltic pumps. The aerosol passes through the primary channel of the argon plasma. The high-temperature plasma facilitates the ionization of the sample by vaporizing, decomposing, atomizing, and ultimately ionizing the droplets of the aerosol. The positively charged ions generated are separated from the plasma and directed into the interface region through the orifice at the tip of the sample cone. Subsequently, they pass through the next orifice of the skimmer cone. Between the two cones, the interface pressure remains constant at 150–300 Pa. The skimmer cone serves as the entrance to the high vacuum area ($77 \times 10^{-5} - 1 \times 10^{-3}$ Pa) where the ion lenses and the mass analyzer are located. The electrostatic lenses or ion optics focus and direct the ion beam towards the mass spectrometer (quadrupole or octupole type).

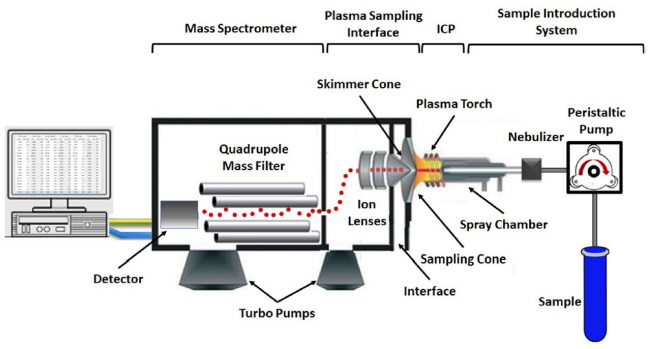

Figure A2.5. Schematic diagram of the main components of an ICP-MS. After [Maz22].

The function of all mass analyzers is based on determining the mass-to-charge ratio (m/z) of ions, which is crucial for separating ions in a sample. At the end of the mass analyzer, the positively charged ions are separated according to their m/z ratio, strike the detector. The resulting culminated signal pulse is referred to as an ion "count" (with units counts per second)

and corresponds to ions with the specific m/z ratio. ICP-MS utilizes a calibration curve to convert the "count" signal to concentration. Calibration curves are constructed for each element that needs to be investigated by measuring solutions of known concentrations.

In this thesis, the actual concentration of dopant ions in crystals was analyzed using an Optima 2100 DV inductively coupled plasma mass spectrometer (ICP MS, Perkin Elmer) and ICP MS, Agilent.

A3. Spectroscopic study

A3.1 Polarized Raman spectroscopy and μ-Raman, μ-luminescence mapping

Raman spectroscopy is based on the inelastic (Raman) scattering of monochromatic radiation by matter and is capable of probing the structure of gases, liquids, and solids, both amorphous and crystalline. Raman scattering is a phenomenon that occurs when incident radiation induces transitions in the atoms or molecules that constitute the scattering medium. [Dev12]

The transition can be rotational, vibrational, electronic, or a combination thereof. In most studies of solids by Raman spectroscopy, the transitions observed are vibrational. Note that Raman scattering in atoms, by definition, cannot induce vibrational transitions; when atomic Raman scattering occurs, it is electronic in nature. With few exceptions, metals are not Raman active, and crystals where all atoms occupy centers of symmetry have no Raman-active vibrations (all vibrations have odd symmetry).

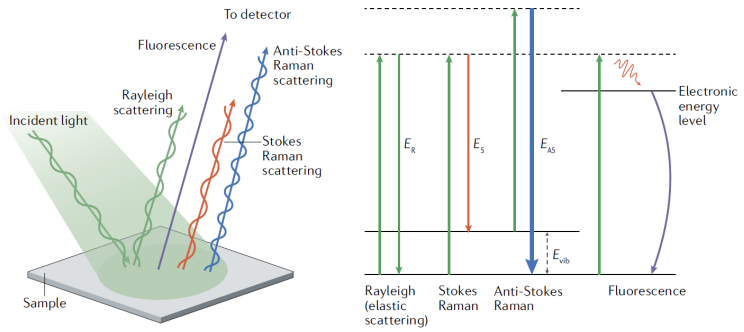

Figure A3.1. Principle of the Raman scattering. After [Mos21]

During a Raman experiment, a sample is irradiated by monochromatic radiation and if the sample is transparent, most of the light is transmitted, a small fraction is elastically (*Rayleigh*) scattered, and a very small fraction is inelastically (*Raman*) scattered, see Figure A3.1. Raman scattering typically results in the excitation of a molecule to a virtual energy level, followed by the emission of a photon at the incident energy minus the energy donated to induce the atom/molecular vibration. This form of Raman scattering known as *Stokes scattering*. A photon incident on a vibrationally excited atom/molecule can also gain energy and be emitted as a photon of a higher energy than the incident photon. This process is known as *anti-Stokes scattering* and at room temperature for higher vibrational modes is a relatively rare event

The collected and dispersed Raman scattered light presents as a Raman spectrum. It plots the intensity of the inelastically scattered light as a function of the shift in wavenumber of the scattered radiation from the wavenumber of the exciting laser. The wavenumber of a photon is the reciprocal of its wavelength and is proportional to its momentum in units of reciprocal centimeters. For vibrational scattering, each peak in the spectrum corresponds to one or more vibrational modes of the solid. The total number of peaks in the Raman spectrum is related to the number of symmetry-allowed, Raman-active modes. Some of the modes may be degenerate (i.e., more than one mode at the same frequency) and some may have Raman frequencies that are too low to be measured on standard Raman equipment, or their intensity may be too low to be detected, despite their symmetry-allowed nature.

Raman spectroscopy provides a range of information, including the strength of interatomic and intermolecular bonds, molecular and/or crystalline symmetry, degree of crystallinity of a solid, orientation, presence of mechanical strain in a solid, composition of multicomponent matter, and the effects of pressure and temperature on phase transformations.

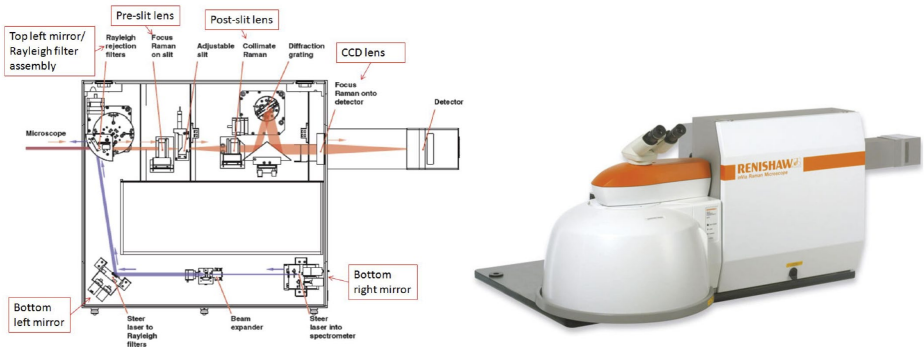

Figure A3.2. InVia Raman spectrometer schematic and instrumental images from the Renishaw manual.

In this PhD thesis, the polarized and unpolarized Raman spectra of the materials were measured using a confocal Raman microscope (inVia, Renishaw) equipped with *a*×50 objective (Leica) and an Ar^+ ion laser with excitation wavelength of 514 nm. To polarize the incident and analyzed signal, a ½ lambda waveplate was used. Schematic and instrumental images of the InVia Raman spectrometer are shown in Figure A3.2. It consists of a light source for providing an excitation radiation; a detector for detecting Raman scattered light; and an optical system for directing the excitation radiation toward the sample, receiving Raman scattered light from the sample and providing the Raman scattered light to the detector.

μ-Raman and μ-luminescence mapping. The confocal Raman microscope is equipped with the function of μ-Raman and μ-luminescence mapping based on the measured Raman and luminescence spectra. μ-Raman mapping of a sample area provides information about the chemical and physical differences across the sample. This technique can confirm the identity and presence of specific components, revealing their location and distribution within the sample with position as 1D profiles, 2D areas or 3D volumes. The Raman microscope is used to collect the spectral information from an array of points on or in the sample. In the case of μ-

luminescence mapping, the information of the distribution of dopant ions within the sample is provided.

μ-Raman mapping can be used for a qualitative and quantitative analysis. This includes particle statistics metrics such as the number of particles, shape, or size. In this way, you can quantify Raman images using objective metrics for direct comparison.

The Raman spectra from each position on the sample are collected by the Raman microscope as shown in Figure A3.3 in two different regimes. The first one is “point focus” (left image in Figure A3.3). The Raman microscope employs a laser to focus onto a specific point on the sample. The sample is placed on a motorized stage, which moves it under the laser. The spectrometer collects spectra from a series of points across the sample. The second method is ”line focus”, where the laser irradiates a vertical line on the sample. It allows to collect spectra from multiple positions on the sample. The higher total laser power can be used without a chance of damaging the sample.

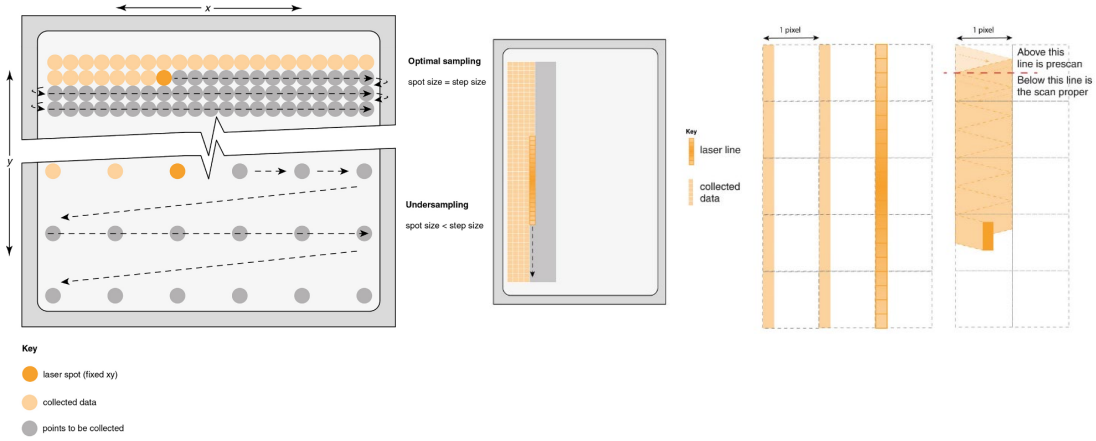

Figure A3.3. Diagrams showing point-by-point imaging, depicting both optimal imaging and undersampling (left) and “line focus” mode [https://www.renishaw.com/en/what-raman-images-can-reveal--25802].

From the mapping experiment, the Raman spectra can be analyzed to obtain 1D profiles, 2D images, or 3D rendered volumes. The Raman map can be analyzed using various methods.

• The intensity at one Raman frequency in the spectrum. However, this method cannot differentiate between intensities arising from a Raman band of interest or those associated with a broad background fluorescence.

• Curve fit parameters, where for each spectrum in the Raman map, allowing for the derivation of Raman band parameters such as Raman shift, band width, or relative intensity. Raman images often show variations in the Raman shift of a band, which can indicate localized stress. They can also show variations in the Raman band width, which can indicate different degrees of crystallinity.

• Multivariate parameters, where many parameters from the entire spectrum are used, not just one Raman parameter.

The μ-Raman and μ-luminescence were employed in Chapter II.2 and Chapter IV.4. In the former case, these techniques were used to characterize the structural modifications induced by the femtosecond pulses and to study the integrity of the inherent crystal structure at the

waveguide core. In Chapter IV.4, we characterized the uniform distribution of host-forming cations and the dopant ions using μ-Raman and μ-luminescence mapping.

A.3.2 Polarized absorption and luminescence spectral measurements

Absorption measurements. The absorption measurement is performed by comparing the intensity of two different monochromatic beams: one passing through the sample and the other serving as a non-absorbed reference. This is done while tuning the wavelength with a monochromator to cover the spectral range of interest. In this study, the measurement is performed using a commercial UV-Vis-NIR Spectrophotometer Cary 5000, with a possible spectral resolution of 0.02 nm. This specific procedure allows for the estimation of crystal absorbance, which can then be used to calculate the absorption cross-section and determine the optimal pump wavelength. It also provides insights into the lattice structure by examining the distribution of Stark sublevels observed within the absorption bands. The shape, width, and to some extent, the spectral position of rare-earth absorption bands arise from the interaction between the energy levels of the rare-earth ions and the local crystal field in which they are embedded. This coupling plays a significant role in shaping the absorption characteristics of the material.

The transparency of the studied materials was measured with the spectral resolution of 0.2 nm in the UV and visible ranges, and 0.5 in the near-IR. To measure the polarized spectra, the Glan-Taylor polarizing prism was used. From the measured transmission spectra, the absorption coefficient α of the materials of thickness l were calculated with the Lambert-Beer law [Bee52, Lam60], which gives the transmitted intensity I as a function of the incident intensity I_0:

$$I(\lambda,l) = I_0(\lambda)\exp\left(-\alpha(\lambda)l\right). \tag{A3.1}$$

From this equation, the absorption coefficient can be determined as follows:

$$\alpha(\lambda) = \frac{1}{l}\ln\frac{I_0(\lambda)}{I(\lambda,l)}. \tag{A3.2}$$

With the ion density N_{dop} of dopant ions, the absorption cross-section can be calculated as follows:

$$\sigma_{abs}(\lambda) = \frac{\alpha(\lambda)}{N_{dop}}. \tag{A3.3}$$

The excitation spectra of Eu^{3+} ions in the Yb,Ho,Eu:CNGG crystals in the visible spectral range was measured using a spectrofluorometer (QuantaMaster)

Luminescence measurements. Luminescence spectroscopy is based on the excitation of a material by light at an absorption wavelength and the collection of the intensity of the spontaneous emission as a function of the wavelength. This allows for the study of the optimal emission wavelength under specific pumping conditions, as well as the width and shape of the emission bands. The luminescence spectrum is crucial for calculating the stimulated emission cross sections using the Füchtbauer–Ladenburg equation, which connects the stimulated emission cross-sections to the spontaneous emission intensity.

To measure, the spontaneous emission of dopant ions in studied materials, we employed the set-up the scheme of which is shown in Figure A3.4. The luminescence of dopant ions was excited using a Ti:Sapphire laser (Spectra Physics, model 3900S) tuned to around 0.79 μm (for Tm^{3+} ions) and 0.89 μm (for Ho^{3+} ions), collected using a CaF_2 lens and a ZrF_4 fiber. The luminescence was detected with an optical spectrum analyzer (OSA). Depending on the spectral range of the luminescence, the different OSA were used. For the 600 – 1300 nm spectral range, the OSA, Ando AQ-6315E, 350 – 1750 nm was used with the resolution of 0.5 nm. For the 1300 – 2400 nm spectral range, the OSA Yokogawa AQ6375B, 1200 – 2400 nm was employed with the resolution of 0.5 nm. For the 2400 – 3250 nm spectral range, the OSA, Yokogawa AQ6376, 1500 – 3400 was used. with a resolution of 2 nm. To reduce the effect of water vapor absorption, the OSAs was purged with N_2 gas. For the non-cubic crystals, the wire grid polarizer, Thorlabs (250 – 4000 nm) was used.

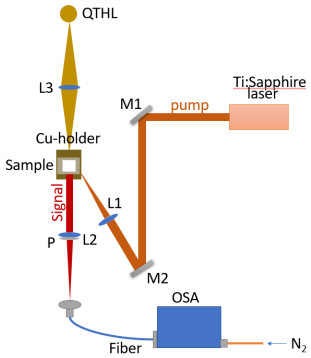

Figure A3.4. Scheme of the set-up for the luminescence measurements. M1 and M2 – high refractive mirrors at pump wavelengths, L1, L2, and L3 – focusing lenses, P – polarizer, fiber – zirconium fluoride, OSA – optical spectrum analyzer, QTHL – quartz tungsten halogen lamp.

Another set-up was built to measure the luminescence of $Tm:R_2O_3$ ceramics (R = Y, Lu, Sc), in Chapter IV.5 and $Tm:RVO_4$ (R = Gd, Y, Lu) in Chapter V.1 around 2.3 μm (the $^3H_4 \rightarrow {}^3H_5$ transition). The set-up consists a 0.6 m monochromator (HRS2, Jobin-Yvon), lock-in amplifier (SR810 DSP, Stanford Research Systems), and InSb detector (J10D series, Judson Infrared) cooled with liquid nitrogen with SBW = 4 nm. A Ti:Sapphire laser (model 3900 S, Spectra Physics) tuned to around 0.79 nm, depending on the absorption peak of the material, was used as the excitation source.

The luminescence of Eu^{3+} ions in the Yb,Ho,Eu:CNGG crystals in the visible spectral range was measured using a spectrofluorometer (QuantaMaster)

A.3.3 Luminescence dynamics study

The luminescence lifetime of any given energy level can be measured exciting the sample at an absorption wavelength with a pulsed monochromatic source and collecting the emission intensity decay. The luminescence dynamics was studied using a ns optical parametric oscillator (Horizon, Continuum) pumped by a Continuum Surelite frequency tripled Nd^{3+} : YAG pulsed laser at 355 nm, a 1/4 m monochomator (Oriel 77200), a photomultiplier (PMT) tube

(for luminescence in visible spectral range), an InGaAs detector (near-infrared luminescence) and an 8 GHz digital oscilloscope (DSA70804B, Tektronix). If possible, powders were prepared from some samples, to avoid the effect of reabsorption (radiation trapping) on the measured Lifetimes.

The measured luminescence decay curves were fitted to obtain the luminescence lifetimes τ_{lum} of the excited levels. In the case, when the intensity of decay $I(t)$ is a single-exponential, it can be fitted with the following equation:

$$I(t) = I_0 \exp\left(-\frac{t}{\tau_{lum}}\right), \quad \text{(A3.4)}$$

with I_0 is the luminescence intensity at $t = 0$.

A.3.4 Low-temperature spectroscopy

Low-temperature spectroscopy is the primary method used to determine the experimental Stark sub-levels of dopant ions in materials. This data is fundamental for crystal-field analysis, through which crystal field parameters and strength can be calculated.

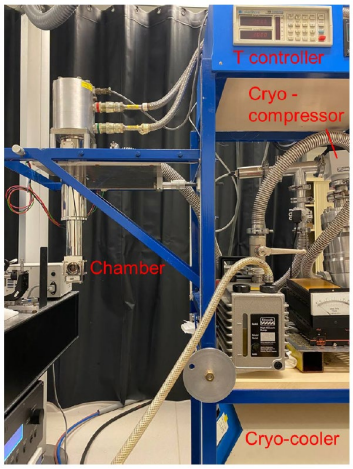

Figure A3.5. Experimental set-up for spectroscopic measurements at cryogenic temperatures (12 K).

For low-temperature (12 K) studies, the sample was mounted on an APD DE-202 closed-cycle cryo-cooler equipped with an APD HC 2 Helium vacuum cryo-compressor and a Laceshore 330 temperature controller, as shown in Figure A3.5. Silver paint was used to maintain the samples. The chamber has two CaF_2 windows transparent from UV to mid-infrared. To measure the luminescence and absorption spectra at LT, the set-up from Figure A3.4 was used. The cryo chamber was placed in the location of the Cu-holder. To measure LT absorption spectra of dopant ions, a quartz tungsten halogen lamp was used. The light of the lamp was focused into the chamber and illuminated the samples. The spectrum of the lamp was measured without the sample passing through the cryo-chamber. It was measured to calibrate the absorption spectra.

A.3.5 Pump-probe method (excited-state absorption measurements)

Excited-state absorption spectra of Tm^{3+} ions in cubic sesquioxides were measured using the classical pump-probe method, as shown in Figure A3.6. In this method, the first intense laser beam (the pump) excites Tm^{3+} ions into the metastable $^3F_4$ state. The second weak beam (the probe) propagates through the pumped area of the sample revealing the additional absorption caused by ESA.

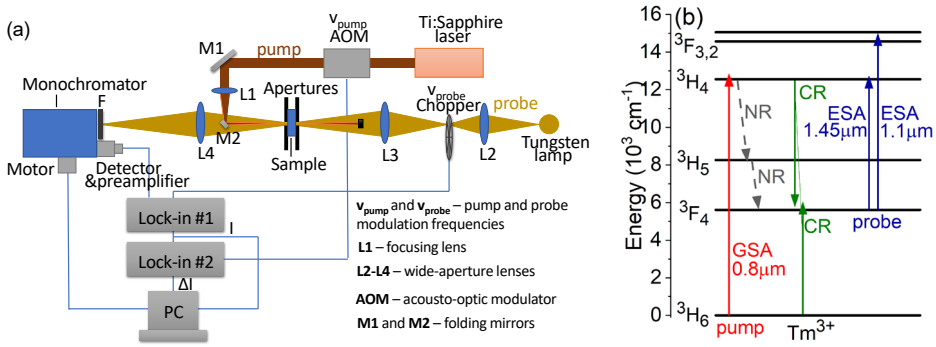

Figure A3.6. (a) Scheme of the pump-probe setup used for the ESA measurements; (b) Energy-level scheme of Tm^{3+} ion illustrating the principle of the pump-probe experiment, CR – cross-relaxation.

The samples were placed between two pinholes with a diameter of 500 μm, ensuring good spatial overlap between the pump and probe beams and helping to limit the probe spot size within the samples.

The pump source was a 1 W Ti:Sapphire laser tuned to 0.79 μm. The pump beam was modulated at a low frequency (ν_{pump} = 10 Hz) to achieve strong rate modulation of the population of the $^3F_4$ level, thanks to its long lifetime of a few milliseconds. Modulation was performed using an acousto-optic modulator (Isomet, model 1205C-2), and the beam was focused into the samples using a lens (L1) with a focal length of 150 mm, resulting in a spot size of approximately 300 μm. The single-pass pump absorption exceeded 50%, leading to a relatively uniform inversion distribution throughout the sample

The probe source was a 100 W halogen-tungsten white-light lamp (Oriel, model 66184) with a broad emission spectrum similar to that of a black body. Its output was modulated at a higher frequency ($\nu_{probe} \approx 1$ kHz) using a mechanical chopper. The probe beam was focused into the sample using a pair of wide-aperture lenses, L2 and L3 (with focal lengths of 50 mm and 100 mm, respectively). After passing through the sample, the beam was reimaged onto the input slit of the monochromator using lens L4 (f = 100 mm).

For measuring the spectra, a 0.64 m monochromator (Jobin-Yvon, HRS2) and an InGaAs detector with two lock-in amplifiers were used. The resolution was approximately 0.2 nm. The double lock-in technique was employed to enhance the sensitivity of the pump-probe method. The first lock-in amplifier (Stanford Research System, model SR510) was locked to ν_{probe} with a low time constant, providing the average transmitted intensity through the samples, I. The second lock-in amplifier (Stanford Research System, model SR830 DSP) was locked to ν_{pump} and

measured the transmission variation, ΔI, induced by the pump. The ratio of ΔI to I ($\Delta I/I$) was the measured signal

The measurement signal connects with the GSA, SE and ESA cross-sections by following equations:

$$\frac{\Delta I}{I}(\lambda) = AN^{*}L\left(\sigma_{GSA}(\lambda) + \sigma_{SE}(\lambda) - \sigma_{ESA}(\lambda)\right), \quad \text{(A3.5)}$$

where A – a calibration factor, L – the optical length of the sample, N^* - population of the $^3F_4$ metastable level, σ_{GSA}, σ_{SE}, and σ_{ESA} are ground-state absorption, stimulated emission, and excited-state absorption cross-sections.

The values of GSA and SE cross-sections are determined independently and the corresponding spectral bands can be used to calibrate the setup. For example, the constant value of AN^*L for each particular sample can be determined. In this way, the spatial and longitudinal distributions of the metastable excited state population do not affect the measured ESA spectra. Eq. A3.5 represents the first order evolution of the transmission of the probe light and is valid in the case of relatively small $\Delta I/I$ variations. This variation was about 10^{-4} … 10^{-3} at the wavelength of the ESA peaks.

List of Publications

Papers in peer-reviewed journals

1. **K. Eremeev**, P. Loiko, A. Braud, P. Camy, J. Zhang, X. Xu, Y. Zhao, P. Liu, S. Balabanov, E. Dunina, A. Kornienko, L. Fomicheva, X. Mateos, U. Griebner, V. Petrov, L. Wang, and W. Chen, "*Spectroscopy of solid-solution transparent sesquioxide laser ceramic Tm:LuYO$_3$,*" Opt. Mater. Express **12**(9), 3749–3762 (2022).
2. **K. Eremeev**, P. Loiko, A. Benayad, G. Brasse, P. Camy, and A. Braud, *"Efficient continuous-wave Tm,Ho:CaF$_2$ laser at 2.1 μm,"* Opt. Lett. **48**(7), 1730–1733 (2023).
3. **K. Eremeev**, P. Loiko, R. Maksimov, V. Shitov, V. Osipov, D. Vakalov, V. Lapin, P. Camy, W. Chen, U. Griebner, V. Petrov, and A. Braud, "*Highly efficient lasing and thermal properties of Tm:Y$_2$O$_3$ and Tm:(Y,Sc)$_2$O$_3$ ceramics,*" Opt. Lett. **48**(15), 3901–3904 (2023).
4. X. Li, **K. Eremeev**, P. Loiko, Y. Zhou, Y. Zhang, J. Liu, Z. Pan, A. Braud, J-L. Doualan, S. Slimi, R. M. Solé, X. Mateos, P. Camy, and H. Xu, "*Spectroscopy of Yb^{3+},Ho^{3+},Eu^{3+}-codoped calcium niobium gallium garnet (CNGG) crystal,*" Opt. Mater. **144**, 114360–1–10 (2023).
5. X. Yu, **K. Eremeev**, Z. Pan, P. Loiko, H. Chu, F. Zha, H. Pan, S. Zhao, A. Braud, P. Camy, and D. Li, "*6 W diode-pumped Tm:GdVO$_4$ laser at 2.29 μm,*" Opt. Lett. **48**(24), 6404-6407 (2023).
6. **K. Eremeev**, P. Loiko, S. Balabanov, T. Evstropov, D. Permin, O. Postnikova, V. Petrov, P. Camy, and A. Braud, *"Spectroscopy of thulium ions in solid-solution sesquioxide laser ceramics: inhomogeneous spectral line broadening, crystal-field engineering and C$_{3i}$ sites,"* Opt. Mater. **148**, 114791–1–16 (2024).
7. **K. Eremeev**, P. Loiko, C. Zhao, Z.-L Lin, X. Mateos, G. Zin Elabedine, P. Camy, A. Braud, U. Griebner, V. Petrov, G. Zhang, S. Li, Y. Hang, and W. Chen, *"Growth, spectroscopy and laser operation of Tm,Ho:GdScO$_3$ perovskite crystal,"* Opt. Express **32**(8), 13527–13542 (2024).
8. X. Yu, **K. Eremeev**, Z. Pan, P. Loiko, H. Chu, H. Pan, A. Braud, P. Camy, and D. Li, "*Polarized spectral properties and 2.3 μm laser performance of the Tm:YVO$_4$ crystal*," Opt. Express **32**(10), 18055–18067 (2024).
9. X. Yu, **K. Eremeev**, Z. Pan, P. Loiko, H. Chu, H. Chu, H. Pan, A. Braud, P. Camy, and D. Li, "*Crystal growth, polarized spectral properties, and 2.3 μm laser performance of Tm:LuVO$_4$ crystal,*" Opt. Express **32**(11), 19611–19625(2024).
10. K. Veselský, P. Loiko, **K. Eremeev**, A. Benayad, A. Braud, J. Šulc, H. Jelínková, and P. Camy, "*Broadly tunable continuous-wave Tm,Ho:SrF$_2$ and Tm,Ho:BaF$_2$ lasers,*" Opt. Lett. **49**(17) (2024).
11. K. Veselský, P. Loiko, **K. Eremeev**, A. Benayad, J. Šulc, H. Jelínková, P. Camy, and A. Braud, "*Broadly tunable Tm:BaF$_2$ and Tm:SrF$_2$ lasers,*" J. Opt. Soc. Am. B **41**(12), E22–E28 (2024).
12. G. Z. Elabedine, K. Subbotin, P. Loiko, Z. Pan, **K. Eremeev**, Y. Zimina, Y. Didenko, S. Pavlov, A. Titov, E. Dunina, L. Fomicheva, A. Kornienko, A. Braud, R. M. Solé, M. Aguiló, F. Díaz, W. Chen, P. Volkov, V. Petrov, and X. Mateos, "*Growth, spectroscopy and 2 μm laser operation of monoclinic Tm^{3+}:ZnWO$_4$ crystal,*" Opt. Mater. **157**, 116039 (2024).

International Conferences

• **Optique Nice,** 4–7 July 2022, Nice, France

1. **K. Eremeev,** P. Loiko, A. Benayad, G. Z. Elabedine, R. M. Solé, X. Mateos, M. Aguiló, F. Díaz, P. Camy, and A. Braud, "*Growth and broadband emission properties of Tm^{3+},Ho^{3+}-codoped calcium fluoride crystals,*" D01 (poster).

• **Advanced Solid State Lasers Conference (ASSL)** 11–15 December 2022, Barcelona, Spain

2. **K. Eremeev,** P. Loiko, S. Balabanov, T. Evstropov, D. Permin, O. Postnikova, P. Camy, and A. Braud, *"Tailoring broadband emission properties of Tm^{3+}-doped solid-solution sesquioxide laser ceramics in the system Y_2O_3-Lu_2O_3-Sc_2O_3,"* Technical Digest Series (Optica Publishing Group, 2022), paper ATh1A.2, (oral).
3. **K. Eremeev**, P. Loiko, A. Benayad, G. Z. Elabedine, R. M. Solé, X. Mateos, M. Aguiló, F. Díaz, P. Camy, and A. Braud, "*Efficient continuous-wave Tm,Ho:CaF_2 laser at ~2.1 μm,*" Technical Digest Series (Optica Publishing Group, 2022), paper AM3A.6, (oral).

• **Lasers and Electro-Optics Europe & European Quantum Electronics Conference (CLEO/Europe-EQEC)** 26–30 June 2023, Munich, Germany

4. **K. Eremeev**, P. Loiko, R. Maksimov, V. Shitov, V. Osipov, P. Camy, and A. Braud, "*Tm,Ho:$(Y,Sc)_2O_3$ ceramic laser at ~2.1 μm,*" Technical Digest Series (Optica Publishing Group, 2023), paper ca_3_3, (oral).
5. **K. Eremeev**, P. Loiko, S. Balabanov, L. Guillemot, P. Camy, C. Kränkel, and A. Braud, "*Efficient Tm:Lu_2O_3 laser at ~2250 nm,*" Technical Digest Series (Optica Publishing Group, 2023), paper ca_11_2, (oral).

• **International Conference on Luminescence (ICL)** 27 August – 1 September 2023, Paris, France

6. **K. Eremeev**, P. Loiko, A. Benayad, P. Camy, and A. Braud, *"Energy transfer and ion clustering in Tm,Ho:CaF_2 crystals,"* Session 7a (oral).

• **Advanced Solid State Lasers Conference (ASSL)** 8–2 October 2023, Seattle, USA

7. **K. Eremeev,** P. Loiko, S. Balabanov, T. Evstropov, D. Kosyanov, S. Filofeev, P. Camy, and A. Braud, "*Novel transparent ceramics based on Tm^{3+}-doped cubic gadolinia and its solid-solutions for 2 μm lasers,*" Technical Digest Series (Optica Publishing Group, 2023), paper SD1.1, (oral).
8. S. Mauree, **K. Eremeev**, G. Durand, P. Loiko, A. Le Coz, M. Poitou, F. Starecki, V. Nazabal, P. Camy, A. Braud, and O. Merdrignac-Conanec, "*Fabrication and emission properties of Cr^{2+}-doped ZnS hot-pressed transparent ceramics,*" Technical Digest Series (Optica Publishing Group, 2023), paper SD1.2, (oral).

• **Conference on Mid-Infrared Coherent Sources (MICS)** 12–14 March 2024, Vienna, Austria

9. **K. Eremeev**, P. Loiko, S. Balabanov, T. Evstropov, D. Kosyanov, S. Filofeev, P. Camy, and A. Braud, "*Prospects of Ho^{3+}-doped sesquioxide laser ceramics for laser emission at 3 μm,*" paper MTu5C.2, (oral).
10. X. Yu, **K. Eremeev**, Z. Pan, P. Loiko, H. Chu, H. Pan, A. Braud, P. Camy, and D. Li, "*5.5 W diode-pumped Tm:YVO_4 laser at 2.29 μm,*" paper JW4A.8, (poster).

• **Optique Normandie,** 1–5 July 2024, Rouen, France

11. **K. Eremeev**, P. Loiko, C. Kränkel, P. Camy, and A. Braud, *"Excited-state absorption of Tm^{3+} ions in cubic sesquioxides,"* 1-C: JNCO-Luminescence (oral).

References

[Abr14] M. V. Abrashev, N. D. Todorov, and J. Geshev, "Raman spectra of R_2O_3 (R–rare earth) sesquioxides with C-type bixbyite crystal structure: a comparative study," J. Appl. Phys. 116, 103508 (2014).

[Akc13] M. S. Akchurin, T. T. Basiev, A. A. Demidenko, M. E. Doroshenko, P. P. Fedorov, E. A. Garibin, P. E. Gusev, S. V. Kuznetsov, M. A. Krutov, I. A. Mironov, and V. V. Osiko, "CaF_2:Yb laser ceramics," Opt. Mater. 35(3), 444-450 (2013).

[Ama83] S. N. Amanyan, P. A. Arsenev, K. S. Bagdasarov, A. M. Kevorkov, D. I. Korolev, A. V. Potemkin, and V. V. Femin, "Synthesis and examination of $GdScO_3$ single crystals activated by Nd^{3+}," J. Appl. Spectrosc. 38(3), 343-348 (1983).

[Ama87] S. N. Amanyan, E. V. Antipov, V. A. Antonov, P. A. Arsenev, Kh. S. M. Bagdasarov, A. M. Kevorkov, L. M. Kovba, and A. V. Rakhmatulin, "Synthesis and structure of $GdScO_3$," Russ. J. Inorg. Chem. 32(9), 1225-1228 (1987)

[Amb00] P. F. Ambrico, A. Amodeo, P. Di Girolamo, and N. Spinelli, "Sensitivity analysis of differential absorption lidar measurements in the mid-infrared region," Appl. Opt. 39(36), 6847-6865 (2000).

[Ami10] S. Amini-Nik, D. Kraemer, M. L. Cowan, K. Gunaratne, P. Nadesan, B. A. Alman, and R. D. Miller, "Ultrafast mid-IR laser scalpel: protein signals of the fundamental limits to minimally invasive surgery," PLoS One 5(9), e13053 (2010).

[Ant00] E. Antic-Fidancev, "Simple way to test the validity of $^{2S+1}L_J$ barycenters of rare earth ions (*e.g.*, $4f^2$, $4f^3$ and $4f^6$ configurations)," J. Alloys Compd. 300, 2-10 (2000).

[Ant02] E. Antic-Fidancev, J. Hölsä, and M. Lastusaari, "Crystal field strength in C-type cubic rare earth oxides," J. Alloys Compd. 341(1-2), 82-86 (2002).

[Ant03] E. Antic-Fidancev, J. Hölsä, and M. Lastusaari, "Crystal field energy levels of Eu^{3+} and Yb^{3+} in the C_2 and S_6 sites of the cubic C-type R2O3," J. Phys. Condens. Matter 15(6), 863-876 (2003).

[Ant90] D. W. Anthon and T. J. Pier, "Laser-pumped 3-μm Ho:YAG and Ho:GGG lasers," in Advanced Solid-State Lasers, p. MML3, Optica Publishing Group, March 1990.

[Ant98] E. Antic-Fidancev, M. Lemaître-Blaise, and P. Porcher, "Optical study of praseodymium 3+ in zircon-type orthovanadate phases," Spectrochim. Acta A: Mol. Biomol. Spectrosc. 54(13), 2151-2156 (1998).

[Ars72] P. A. Arsenev and K. E. Bienert, "Absorption, luminescence, and stimulated emission spectra of Tm^{3+} in $GdAlO_3$ crystals," Phys. Status Solidi A 13(2), K125-K128 (1972).

[Ars72a] P. A. Arsenev and K. E. Bienert, "Spectral properties of Ho^{3+} in $GdScO_3$ crystals," Phys. Status Solidi A 13(2), K129-K132 (1972).

[Aul82] B. Aull and H. Jenssen, "Vibronic interactions in Nd:YAG resulting in nonreciprocity of absorption and stimulated emission cross sections," IEEE J. Quantum Electron. 18(5), 925-930 (1982).

[Auz76] F. Auzel, "Multiphonon-assisted anti-Stokes and Stokes fluorescence of triply ionized rare-earth ions," Phys. Rev. B 13, 2809-2817 (1976).

[Auz83] F. Auzel and O. L. Malta, "A scalar crystal field strength parameter for rare-earth ions: meaning and usefulness," J. Physique 44(2), 201-206 (1983).

[Bai24] Z. Bai, Z. Chen, Y. Xiong, H. Liu, S. Gao, Y. Ren, X. Zhao, F. Liu, Y. Jia, and F. Chen, "Tm, Ho:YLF waveguide lasers at 2.05 μm," Opt. Lett. 49(8), 1977-1980 (2024).

[Bal20] S. Balabanov, K. Demidova, S. Filofeev, M. Ivanov, D. Kuznetsov, J.Li, D. Permin, and E. Rostokina, "Influence of Lanthanum Concentration on Microstructure of $(Ho_{1-x}La_x)_2O_3$ Magneto-Optical Ceramics," Physica status solidi (b), 257(8), 1900500 (2020).

[Bal21] S. Balabanov, D. Permin, T. Evstropov, P. Andreev, L. Basyrova, P. Camy, M. Baranov, X. Mateos, and P. Loiko, "Hot pressing of Yb:Y_2O_3 laser ceramics with LiF sintering aid," Opt. Mater. 119, 111349 (2021).

[Bar03] N. P. Barnes, B. M. Walsh, and E. D. Filer, "Ho:Ho upconversion: applications to Ho lasers," J. Opt. Soc. Am. B 20(6), 1212-1219 (2003).

[Bar18] A. Berrou, O. J. Collett, D. Morris, and M. D. Esser, "Comparative study of high power Tm:YLF and Tm:LLF slab lasers in continuous wave regime," Opt. Express 26(8), 10559-10572 (2018).

[Bar75] A. S. Barker Jr. and A. J. Sievers, "Optical studies of the vibrational properties of disordered solids," Rev. Mod. Phys. 47, S10S179 (1975).

[Bas23] L. Basyrova, "Erbium doped materials for bulk and waveguide laser sources emitting around 2.8 um," Doctoral dissertation, Normandie Université (2023).

[Bee23] W. W. Beers, W. E. Cohen, and A. M. Srivastava, "Temperature dependence of Mn4+ emission intensity and lifetime in TriGain® phosphor (K_2SiF_6:Mn^{4+})," ECS J. Solid State Sci. Technol. 12(11), 116002 (2023).

[Bee52] A. Beer, "Bestimmung der Absorption des rothen Lichts in farbigen Flüssigkeiten," Ann. Phys. 162(5), 78-88 (1852).

[Ben02] E. Ben-Dor, "Quantitative remote sensing of soil properties," in Advances in Agronomy, vol. 75, pp. 173-243, Academic Press, 2002.

[Bin97] K. Binnemans, C. Görller-Walrand, and J.L. Adam, "Spectroscopic properties of Gd3+-doped fluorozirconate glass," Chem. Phys. Lett. 280, 333-338 (1997).

[Bla00] J. Blanusa, M. Mitric, D. Rodic, A. Szytula, and M. Slaski, "An X-ray diffraction and magnetic susceptibility study of $Tm_xY_{2-x}O_3$," J. Magn. Magn. Mater. 213, 75-81 (2000).

[Bla92] G. Blasse, "Vibronic transitions in rare earth spectroscopy," Int. Rev. Phys. Chem. 11(1), 71-100 (1992).

[Bla94] G. Blasse and B. C. Grabmaier, A General Introduction to Luminescent Materials (Springer, 1994).

[Boe11] G. Boehm, A. Bachmann, J. Rosskopf, M. Ortsiefer, J. Chen, A. Hangauer, R. Meyer, R. Strzoda, and M. C. Amann, "Comparison of InP- and GaSb-based VCSELs emitting at 2.3 μm suitable for carbon monoxide detection," J. Cryst. Growth 323(1), 442-445 (2011).

[Boo94] T. Boonyarith, J. P. D. Martin, and N. B. Manson, "Hyperfine resonances in the tetragonal centre of Ho^{3+} in CaF_2," J. Lumin. 59(6), 361-368 (1994).

[Bow90] S. R. Bowman, W. S. Rabinovich, A. P. Bowman, B. J. Feldman, and G. H. Rosenblatt, "3 μm laser performance of Ho:$YAlO_3$ and Nd,Ho:$YAlO_3$," IEEE J. Quantum Electron. 26(3), 403-406 (1990).

[Bra00] A. Braud, S. Girard, J. L. Doualan, M. Thuau, R. Moncorgé, and A. M. Tkachuk, "Energy-transfer processes in Yb:Tm-doped KY_3F_{10}, $LiYF_4$, and BaY_2F_8 single crystals for laser operation at 1.5 and 2.3 μm," Phys. Rev. B 61(8), 5280 (2000).

[Bra98] A. Braud, S. Girard, J. L. Doualan, and R. Moncorgé, "Spectroscopy and fluorescence dynamics of (Tm, Tb) and (Tm, Eu) doped $LiYF_4$ single crystals for 1.5-μm laser operation," IEEE J. Quantum Electron. 34(11), 2246-2255 (1998).

[Bre93] A. Brenier, G. Boulon, C. Madej, C. Pedrini, and L. Lou, "Kinetics of transfer and back transfer in thulium-holmium-doped $Gd_3Ga_5O_{12}$ (Ca, Zr) garnet," J. Lumin. 54(5), 271-277 (1993).

[Bro20] E. E. Brown, Z. Fleischman, J. McKay, and M. Dubinskii, "Optical spectroscopy of low-phonon, holmium-doped barium fluoride (BaF_2) single crystals," ARL-TR-9052 (2020).

[Bud00] P. A. Budni, L. A. Pomeranz, M. L. Lemons, C. A. Miller, J. R. Mosto, and E. P. Chicklis, "Efficient mid-infrared laser using 1.9-μm-pumped Ho:YAG and $ZnGeP_2$ optical parametric oscillators," J. Opt. Soc. Am. B 17(5), 723-728 (2000).

[Bul97] S. R. Bullock, B. R. Reddy, P. Venkateswarlu, and S. K. Nash-Stevenson, "Site-selective energy upconversion in CaF_2: Ho^{3+}," J. Opt. Soc. Am. B 14(3), 553-559 (1997).

[Cai75] J. Caird, L. DeShazer, and J. Nella, "Characteristics of room-temperature 2.3-μm laser emission from Tm^{3+} in YAG and $YAlO_3$," IEEE J. Quantum Electron. 11, 874-881 (1975).

[Cai88] J.A. Caird, S.A. Payne, P.R. Staver, A.J. Ramponi, and L.L. Chase, "Quantum electronic properties of the $Na_3Ga_2Li_3F_{12}$: Cr^{3+} laser," IEEE J. Quantum Electron. 24, 1077-1099 (1988).

[Cai91] J. A. Caird, A. J. Ramponi, and P. R. Staver, "Quantum efficiency and excited-state relaxation dynamics in neodymium-doped phosphate laser glasses," J. Opt. Soc. Am. B 8, 1391-1403 (1991).

[Can17] F. Canbaz, I. Yorulmaz, and A. Sennaroglu, "2.3-μm Tm^{3+}:YLF laser passively Q-switched with a Cr^{2+}:ZnSe saturable absorber," Opt. Lett. 42(9), 1656-1659 (2017).

[Car00] T. J. Carrig, G. J. Wagner, A. Sennaroglu, J. Y. Jeong, and C. R. Pollock, "Mode-locked Cr^{2+}:ZnSe laser," Opt. Lett. 25, 168–170 (2000).

[Car68] W. T. Carnall, P. R. Fields, and K. Rajnak, "Electronic energy levels in the trivalent lanthanide aquo ions. I. Pr^{3+}, Nd^{3+}, Pm^{3+}, Sm^{3+}, Dy^{3+}, Ho^{3+}, Er^{3+}, and Tm^{3+}," J. Chem. Phys. 49(10), 4424-4442 (1968).

[Car71] W.T. Carnall, P.R. Fields, and R. Sarup, "Optical Absorption Spectra of Gd^{3+}:LaF_3 and $GdCl_3 \cdot 6H_2O$," J. Chem. Phys. 54, 1476-1479 (1971).

[Car77] W. T. Carnall, H. Crosswhite, and H. M. Crosswhite, Energy Level Structure and Transition Probabilities of the Trivalent Lanthanides in LaF_3 (Argonne National Laboratory, 1978).

[Car89] W. T. Carnall, G. L. Goodman, K. Rajnak, and R. S. Rana, "A systematic analysis of the spectra of the lanthanides doped into single crystal LaF_3," J. Chem. Phys. 90(7), 3443-3457 (1989).

[Cas16] E. Castellano-Hernandez, M. D. Serrano, R. J. Jimenez Rioboo, C. Cascales, C. Zaldo, A. Jezowski, and P. A. Loiko, "Na modification of lanthanide doped $Ca_3Nb_{1.5}Ga_{3.5}O_{12}$-type laser garnets: Czochralski crystal growth and characterization," Cryst. Growth Des. 16(3), 1480-1491 (2016).

[Cat84] C. R. A. Catlow, A. V. Chadwick, G. N. Greaves, and L. M. Moroney, "Direct observations of the dopant environment in fluorites using EXAFS," Nature 312(5995), 601-604 (1984).

[Cha09] O. Chaix-Pluchery, and J. Kreisel, "Raman scattering of perovskite $DyScO_3$ and $GdScO_3$ single crystals," J. Phys. Condens. 21(17), 175901 (2009).

[Cha11] O. Chaix-Pluchery and J. Kreisel, "Raman scattering of perovskite $SmScO_3$ and $NdScO_3$ single crystals," Phase Transit. 84(5-6), 542-554 (2011).

[Cha94] B. C. Chakoumakos, M. M. Abraham, and L. A. Boatner, "Crystal structure refinements of zircon-type MVO_4 (M = Sc, Y, Ce, Pr, Nd, Tb, Ho, Er, Tm, Yb, Lu)," J. Solid State Chem. 109(1), 197-202 (1994).

[Che11] C. Gheorghe, A. Lupei, V. Lupei, A. Ikesue, and M. Enculescu, "Intensity parameters of Tm^{3+} doped Sc_2O_3 transparent ceramic laser material," Opt. Mater. 33(3), 501-505 (2011).

[Che14] F. Chen and J. R. Vázquez de Aldana, "Optical waveguides in crystalline dielectric materials produced by femtosecond-laser micromachining," Laser Photonics Rev. 8(2), 251-275 (2014).

[Che20] G. Chen, S. Li, L. Zhang, X. Tan, W. Deng, M. He, M. Xu, Y. Yang, S. Zhang, and Y. Hang, "Growth and spectra of Tm^{3+} doped $LuYO_3$ single crystal for 2 μm lasers," Infrared Phys. Technol. 109, 103431 (2020).

[Che22] W. Chen, L. Wang, U. Griebner, G. Zhang, P. Loiko, X. Mateos, J. E. Bae, F. Rotermund, X. Xu, A. Major, and V. Petrov, "Sub-40 fs Kerr-lens mode-locked Tm,Ho:CALGO laser," in EPJ Web Conf. 267, 01025 (EDP Sciences, 2022).

[Che23] Y. Cheng, F. Liang, D. Lu, J. Feng, G. Zhang, H. Yu, H. Zhang, and Y. Wu, "Phonon engineering in Yb:$La_2CaB_{10}O_{19}$ crystal for extended lasing beyond the fluorescence spectrum," Light Sci. Appl. 12(1), 203 (2023).

[Cho10] W. B. Cho, J. H. Yim, S. Y. Choi, S. Lee, A. Schmidt, G. Steinmeyer, U. Griebner, V. Petrov, D. I. Yeom, K. Kim, and F. Rotermund, "Boosting the nonlinear optical response of carbon nanotube saturable absorbers for broadband mode-locking of bulk lasers," Adv. Funct. Mater. 20(12), 1937-1943 (2010).

[Cho11] W. B. Cho, J. W. Kim, H. W. Lee, S. Bae, B. H. Hong, S. Y. Choi, I. H. Baek, K. Kim, D. I. Yeom, and F. Rotermund, "High-quality, large-area monolayer graphene for efficient bulk laser mode-locking near 1.25 μm," Opt. Lett. 36(20), 4089-4091 (2011).

[Cih09] J. Cihelka, I. Matulková, and S. Civiš, "Laser diode photoacoustic and FTIR laser spectroscopy of formaldehyde in the 2.3 μm and 3.5 μm spectral range," J. Mol. Spectrosc. 256, 68-74 (2009).

[Cla78] J. B. Clark, P. W. Richter, and L. Du Toit, "High-pressure synthesis of $YScO_3$, $HoScO_3$, $ErScO_3$, and $TmScO_3$, and a reevaluation of the lattice constants of the rare earth scandates," J. Solid State Chem. 23(1-2), 129-134 (1978).

[Coc87] N. J. Cockroft, D. Thompson, G. D. Jones, and R. W. G. Syme, "Site-selective spectroscopy of hydrogenic sites in CaF_2:Er^{3+} crystals," J. Chem. Phys. 86(2), 521-544 (1987).

[Cor04] F. Cornacchia, D. Parisi, C. Bernardini, A. Toncelli, M. Tonelli, Efficient, diodepumped Tm^{3+}:BaY_2F_8 vibronic laser, Optic Express 12 (2004) 1982-1989.

[Cor82] J. Corish, C. R. A. Catlow, P. W. M. Jacobs, and S. H. Ong, "Defect aggregation in anion-excess fluorites. Dopant monomers and dimers," Phys. Rev. B 25(10), 6425-6438 (1982).

[Dal14] K. Van Dalfsen, S. Aravazhi, C. Grivas, S. M. García-Blanco, and M. Pollnau, "Thulium channel waveguide laser with 1.6 W of output power and ~80% slope efficiency," Opt. Lett. 39(15), 4380-4383 (2014).

[Dam66] T. C. Damen, S. P. S. Porto, and B. Tell, "Raman effect in zinc oxide," Phys. Rev. 142(2), 570 (1966).

[Dan81] J. Danko, D. Pacheco, and B. Di Bartolo, "Thermal behavior of the position and width of the 10488 Å line of Nd^{3+} in $RbMnF_3$," Phys. Status Solidi A 63(1), K31-K34 (1981).

[Dav96] K. M. Davis, K. Miura, N. Sugimoto, and K. Hirao, "Writing waveguides in glass with a femtosecond laser," Opt. Lett. 21(21), 1729-1731 (1996).

[Der12] C. Derks, K. Kuepper, M. Raekers, A. V. Postnikov, R. Uecker, W. L. Yang, and M. Neumann, "Band-gap variation in $RScO_3$ (R= Pr, Nd, Sm, Eu, Gd, Tb, and Dy): X-ray absorption and O K-edge x-ray emission spectroscopies," Phys. Rev. B 86(15), 155124 (2012).

[Dev12] T. M. Devine and F. Adar, "Raman Spectroscopy of Solids," in Characterization of Materials, E. N. Kaufmann, Ed. (2012).

[Dex53] D. L. Dexter, "A theory of sensitized luminescence in solids," J. Chem. Phys. 21(5), 836-850 (1953).

[Di14] J. Di, X. Xu, C. Xia, Q. Sai, D. Zhou, Z. Lv, and J. Xu, "Growth and spectra properties of Tm, Ho doped and Tm,Ho co-doped $CaGdAlO_4$ crystals," J. Lumin. 155, 101-107 (2014).

[Die00] A. Diening and S. Kück, "Spectroscopy and diode-pumped laser oscillation of Yb^{3+},Ho^{3+}-doped yttrium scandium gallium garnet," J. Appl. Phys. 87(9), 4063-4068 (2000).

[Die13] A. Diebold, F. Emaury, C. Schriber, M. Golling, C. J. Saraceno, T. Südmeyer, and U. Keller, "SESAM mode-locked Yb:$CaGdAlO_4$ thin disk laser with 62 fs pulse generation," Opt. Lett. 38(19), 3842-3845 (2013).

[Die63] G. H. Dieke and H. M. Crosswhite, "The spectra of the doubly and triply ionized rare earths," Appl. Opt. 2(7), 675-686 (1963).

[Die98] A. Diening, P. E. A. Mobert, E. Heumann, G. Huber, and B. H. T. Chai, "Diode-pumped cw lasing of Yb,Ho:KYF_4 in the 3 μm spectral range in comparison to Er:KYF_4," Laser Phys. 8(1), 214-217 (1998).

[Die98a] A. Diening, P. A. Möbert, and G. Huber, "Diode-pumped continuous-wave, quasi-continuous-wave, and Q-switched laser operation of Yb^{3+},Tm^{3+}:$YLiF_4$ at 1.5 and 2.3 μm," J. Appl. Phys. 84(11), 5900-5904 (1998).

[Din23] H. Ding, J. Liu, Y. Wang, N. Zhang, Z. Wang, Y. Zhao, X. Xu, Y. Xue, J. Xu, U. Griebner, and V. Petrov, "Mode-locking of a Tm,Ho:CALYGO laser delivering 50 fs pulses at 2.08 μm," Opt. Lett. 48(23), 6267-6270 (2023).

[Don23] X. Dong, B. Zhang, X. Sun, Y. Jia, and F. Chen, "1.8-μm laser operation based on femtosecond-laser direct written Tm:YVO_4 cladding waveguides," Opt. Express 31, 16560-16569 (2023).

[Don92] C. de Mello Donega, A. Meijerink, and G. Blasse, "Vibronic transition probabilities in the excitation spectra of the Pr^{3+} ion," J. Phys.: Condens. Matter 4(45), 8889 (1992).

[Dra08] G. Dražić, S. Kobe, A. C. Cefalas, E. Sarantopoulou, and Z. Kollia, "Observation of nanostructured cluster formation of Tm ions in CaF_2 crystals," Mater. Sci. Eng. B 152(1-3), 119-124 (2008).

[Dup23] H. Dupont, P. Loiko, A. Tyazhev, L. Giordano, Z. Pan, H. Chu, D. Li, B. Viana, A. Hideur, L. Guillemot, and A. Braud, "Tm:CALGO lasers at 2.32 μm: cascade lasing and upconversion pumping," Opt. Express 31(12), 18751-18764 (2023).

[Dup24] H. Dupont, T. Lenfant, L. Guillemot, P. Loiko, X. Delen, P. Loiseau, B. Viana, T. Georges, P. Georges, P. Camy, and F. Druon, "High-power 2.3 μm Tm:YLF laser with intracavity upconversion pumping by a Nd:ASL laser at 1051 nm," Opt. Lett. 49(8), 2093-2096 (2024).

[Ebe80] W. L. Eberhard and R. M. Schotland, "Dual-frequency Doppler-lidar method of wind measurement," Appl. Opt. 19, 2967-2976 (1980).

[Ehr17] G. Ehret, P. Bousquet, C. Pierangelo, M. Alpers, B. Millet, J. B. Abshire, H. Bovensmann, J. P. Burrows, F. Chevallier, P. Ciais, and C. Crevoisier, "MERLIN: A French-German space lidar mission dedicated to atmospheric methane," Remote Sens. 9(10), 1052 (2017).

[Eld10] I. Elder, "Performance requirements for countermeasures lasers," Proc. SPIE 7836, Technologies for Optical Countermeasures VII, 24-37 (2010).

[Eld98] I. Elder and M. Payne, "Lasing in diode-pumped Tm:YAP, Tm,Ho:YAP and Tm,Ho:YLF," Opt. Commun. 145(1-6), 329-332 (1998).

[Eli99] P. G. Eliseev, "Long wavelength (λ > 2 μm) semiconductor lasers," in Semiconductor Lasers II, 71-155 (Academic, 1999).

[Ell95] A. Ellens, H. Andres, M. L. H. Ter Heerdt, R. T. Wegh, A. Meijerink, and G. Blasse, "The variation of the electron-phonon coupling strength through the trivalent lanthanide ion series," J. Lumin. 66, 240-243 (1995).

[Ell96] A. Ellens, S. Schenker, A. Meijerink, and G. Blasse, "Vibronic transitions of Tm^{3+} in various lattices," J. Lumin. 69(1), 1-15 (1996).

[Ell97] A. Ellens, H. Andres, A. Meijerink, and G. Blasse, "Spectral-line-broadening study of the trivalent lanthanide-ion series. I. Line broadening as a probe of the electron-phonon coupling strength," Phys. Rev. B 55(1), 173 (1997).

[Ell97a] A. Ellens, H. Andres, M. L. H. Ter Heerdt, R. T. Wegh, A. Meijerink, and G. Blasse, "Spectral-line-broadening study of the trivalent lanthanide-ion series. II. The variation of the electron-phonon coupling strength through the series," Phys. Rev. B 55(1), 180 (1997).

[Erd96] S. Erdei, B. Jin, F. W. Ainger, A. S. Bhalla, B. Keszei, J. Vandlik, and A. Süveges, "Micro-probe Raman spectroscopy for detection of inhomogeneities in YVO_4 single crystals," J. Appl. Phys. 79(6), 2834-2838 (1996).

[Erm13] M. Ermrich and D. Opper, "XRD for the Analyst: Getting Acquainted with the Principles", 2nd ed. (Panalytical, 2013).

[Eva23] J. W. Evans, S. A. McDaniel, R. W. Stites, P. A. Berry, G. Cook, T. R. Harris, and K. L. Schepler, "Crystal host engineering for transition metal lasers," Opt. Eng. 62(1), 017101-017101 (2023).

[Fan93] T. Y. Fan, "Quasi-three-level lasers," in Solid State Lasers: New Developments and Applications, M. L. Shand and H. P. Jenssen, Eds. (Springer US, 1993), pp. 189-203.

[Far08] S. T. Fard, W. Hofmann, P. T. Fard, G. Bohm, M. Ortsiefer, E. Kwok, M. C. Amann, and L. Chrostowski, "Optical absorption glucose measurements using 2.3 μm vertical-cavity semiconductor lasers," IEEE Photon. Technol. Lett. 20(11), 930-932 (2008).

[Fau80] M. Faucher J. Pannetier, "Refinement of the Y_2O_3 structure at 77 K," Acta Crystallogr. B Struct. Crystallogr. Cryst. Chem. 36, 3209–3211 (1980).

[Fed06] V. V. Fedorov, S. B. Mirov, A. Gallian, D. V. Badikov, M. P. Frolov, Y. V. Korostelin, V. I. Kozlovsky, A. I. Landman, Y. P. Podmar'kov, V. A. Akimov, and A. A. Voronov, "3.77-5.05-μm tunable solid-state lasers based on Fe^{2+}-doped ZnSe crystals operating at low and room temperatures," IEEE Journal of Quantum Electronics, 42(9), 907-917 (2006).

[Fer99] B. Ferrand, B. Chambaz, and M. Couchaud, "Liquid phase epitaxy: A versatile technique for the development of miniature optical components in single crystal dielectric media," Opt. Mater. 11(2-3), 101-114 (1999).

[For48] T. Förster, "Zwischenmolekulare Energiewanderung und Fluoreszenz," Ann. Phys. 437, 55-75 (1948).

[For99] L. Fornasiero, "Nd^{3+} - und Tm^{3+} -dotierte sesquioxide," Ph.D. dissertation, Dept. Phys., Univ. Hamburg, Hamburg, Germany (1999).

[Fre62] A. J. Freeman and R. E. Watson, "Theoretical investigation of some magnetic and spectroscopic properties of rare-earth ions," Phys. Rev. 127(6), 2058 (1962).

[Fuj16] E. Fujita, Y. Mashiko, S. Asaya, M. Musha, and M. Tokurakawa, "High power narrow-linewidth linearly-polarized 1610 nm Er:Yb all-fiber MOPA," Opt. Express 24(23), 26255-26260 (2016).

[Fus11] F. Fusari, R. R. Thomson, G. Jose, F. M. Bain, A. A. Lagatsky, N. D. Psaila, A. K. Kar, A. Jha, W. Sibbett, and C. T. A. Brown, "Lasing action at around 1.9 μm from an ultrafast laser inscribed Tm-doped glass waveguide," Opt. Lett. 36, 1566-1568 (2011).

[Gar96] N. Garnier, R. Moncorgé, H. Manaa, E. Descroix, P. Laporte, and Y. Guyot, "Excited-state absorption of Tm^{3+}-doped single crystals at photon-avalanche wavelengths," J. Appl. Phys. 79(8), 4323–4329 (1996).

[Gau03] R. Gaumé, B. Viana, D. Vivien, J. P. Roger, and D. Fournier, "A simple model for the prediction of thermal conductivity in pure and doped insulating crystals," Appl. Phys. Lett. 83(7), 1355-1357 (2003).

[Gau18] J. C. Gauthier, L. R. Robichaud, V. Fortin, R. Vallée, and M. Bernier, "Mid-infrared supercontinuum generation in fluoride fiber amplifiers: current status and future perspectives," Appl. Phys. B 124, 1-14 (2018).

[Gel57] S. Geller, "Crystallographic studies of perovskite-like compounds. IV. Rare earth scandates, vanadites, galliates, orthochromites," Acta Crystallogr. 10(4), 243-248 (1957).

[Gla72] A. M. Glazer, "The classification of tilted octahedra in perovskites," Acta. Crystallogr. B. 28(11), 3384-3392 (1972).

[Glu15] A. Gluth, Y. Wang, V. Petrov, J. Paajaste, S. Suomalainen, A. Härkönen, M. Guina, G. Steinmeyer, X. Mateos, S. Veronesi, and M. Tonelli, "GaSb-based SESAM mode-locked Tm:YAG ceramic laser at 2 μm," Opt. Express 23(2), 1361-1369 (2015).

[Gol26] V. M. Goldschmidt, "Die gesetze der Krystallochemie," Naturwissenschaften 14(21), 477-485 (1926).

[Gou79] J. Gouteron, J. Zarembowitch, and A. M. Lejus, "Raman-spectra of ytterbium, holmium, yttrium, scandium, cubic sesquioxide single-crystals," C. R. Acad. Sci. Paris 289, 243–246 (1979).

[Gra24] A. Grande, "Femtosecond high power Tm:Ho fiber laser at 2050 nm," Ph.D. dissertation, Université de Bordeaux (2024).

[Gre06] E. Geerlings, M. Rattunde, J. Schmitz, G. Kaufel, H. Zappe, and J. Wagner, "Widely tunable GaSb-based external cavity diode laser emitting around 2.3 μm," IEEE Photon. Technol. Lett. 18, 1913-1915 (2006).

[Gro12] V. Grover, R. Shukla, D. Jain, S. K. Deshpande, A. Arya, C. G. S. Pillai, and A. K. Tyagi, "Complex $GdSc_{1-x}In_xO_3$ oxides: Synthesis and structure driven tunable electrical properties," Chem. Mater. 24(11), 2186-2196 (2012).

[Gru09] J.B. Gruber, G.W. Burdick, U.V. Valiev, K.L. Nash, S.A. Rakhimov, and D.K. Sardar, "Energy levels and symmetry assignments for Stark components of Ho^{3+} ($4f^{10}$) in yttrium gallium garnet ($Y_3Ga_5O_{12}$)," J. Appl. Phys. 106(11), 113523 (2009).

[Gru64] J. B. Gruber, W. F. Krupke, J. M. Poindexter, "Crystal-field splitting of trivalent thulium and erbium J levels in yttrium oxide," J. Chem. Phys. 41(11), 3363-3377 (1964).

[Gru85] J. B. Gruber, R. P. Leavitt, C. A. Morrison, and N. C. Chang, "Optical spectra, energy levels, and crystal-field analysis of tripositive rare-earth ions in Y_2O_3. IV. C_{3i} sites," J. Chem. Phys. 82, 5373-5378 (1985).

[Gui19] L. Guillemot, P. Loiko, R. Soulard, A. Braud, J.L. Doualan, A. Hideur, R. Moncorgé, and P. Camy, "Thulium laser at∼ 2.3 μm based on upconversion pumping," Opt. Lett. 44(16), 4071–4074 (2019).

[Gui19a] L. Guillemot, P. Loiko, A. Braud, J. L. Doualan, A. Hideur, M. Koselja, R. Moncorge, and P. Camy, "Continuous-wave Tm:$YAlO_3$ laser at ∼2.3 μm," Opt. Lett. 44(20), 5077-5080 (2019).

[Gui20] L. Guillemot, P. Loiko, R. Soulard, A. Braud, J. L. Doualan, A. Hideur, and P. Camy, "Close look on cubic Tm:KY_3F_{10} crystal for highly efficient lasing on the $^3H_4 \rightarrow {}^3H_5$ transition," Opt. Express 28(3), 3451-3463 (2020).

[Gui20a] L. Guillemot, P. Loiko, E. Kifle, J. L. Doualan, A. Braud, F. Starecki, T. Georges, J. Rouvillain, A. Hideur, and P. Camy, "Watt-level mid-infrared continuous-wave Tm:YAG laser operating on the $^3H_4 \rightarrow {}^3H_5$ transition," Opt. Mater. 101, 109745 (2020).

[Gui22] L. Guillemot, P. Loiko, J. L. Doualan, A. Braud, and P. Camy, "Excited-state absorption in thulium-doped materials in the near-infrared," Opt. Express 30(18), 31669-31684 (2022).

[Guo23] R. Guo, F. Wang, S. Wang, K. Wu, D. Lu, F. Liang, H Yu, and H. Zhang, "Exploration of the crystal growth and crystal-field effect of Yb^{3+} in orthorhombic $GdScO_3$ and $LaLuO_3$ crystals," Cryst. Growth Des. 23(5), 3761-3768 (2023).

[Gup04] C. K. Gupta and N. Krishnamurthy, "Extractive metallurgy of rare earths," Int. Mater. Rev. 37(1), 197-248 (1992).

[Had97] V. G. Hadjiev, M. Cardona, I. Ivanov, V. Popov, M. Gyulmezov, M. N. Iliev, and M. Berkowski, "Optical phonons probe of the $SrLaAlO_4$ crystal structure," J. Alloys Compd. 251(1-2), 7-10 (1997).

[Han84] F. Hanic, M. Hartmanová, G. G. Knab, A. A. Urusovskaya, and K. S. Bagdasarov, "Real structure of undoped Y_2O_3 single crystals," Acta Crystallogr. Sect. B: Struct. Sci. 40(2), 76-82 (1984).

[Hat64] S. E. Hatch, W. F. Parsons, and R. J. Weagley, "Hot-pressed polycrystalline CaF_2:Dy^{2+} laser," Appl. Phys. Lett. 5(8), 153-154 (1964).

[Hau01] P. H. Haumesser, R. Gaume, B. Viana, E. Antic-Fidancev, and D. Vivien, "Spectroscopic and crystal-field analysis of new Yb-doped laser materials," J. Phys.: Condens. Matter 13(23), 5427 (2001).

[Heh13] M. P. Hehlen, M. G. Brik, and K. W. Krämer, "50th anniversary of the Judd–Ofelt theory: An experimentalist's view of the formalism and its application," J. Lumin. 136, 221-239 (2013).

[Hen89] B. Henderson and G. F. Imbusch, Optical Spectroscopy of Inorganic Solids, Vol. 44 (Oxford University Press, 2006).

[Hob72] L. Hobrock, L. DeShazer, W. Krupke, G. Keig, and D. Witter, "Four-level operation of Tm:Cr:$YAlO_3$ laser at 2.35 μ," IEEE J. Quantum Electron. 8(6), 533-534 (1972).

[Hol00] J. Hölsä, R.J. Lamminmäki, M. Lastusaari, P. Porcher, and R.S. Puche, "Simulation of the spectroscopic and magnetic properties of RE (III) ions in RE oxychlorides based on exact crystal structure from Rietveld refinements," J. Alloys Compd. 300, 45-54 (2000).

[Hon16] J. Hong, L. Zhang, P. Zhang, M. Xu, and Y. Hang, "Ho:LaF_3 single crystal as potential material for 2 μm and 2.9 μm lasers," Infrared Phys. Technol. 76, 636-640 (2016).

[Hon97] E. C. Honea, R. J. Beach, S. B. Sutton, J. A. Speth, S. C. Mitchell, J. A. Skidmore, M. A. Emanuel, and S. A. Payne, "115-W Tm:YAG diode-pumped solid-state laser," IEEE J. Quantum Electron. 33(9), 1592-1600 (1997).

[Hou11] X. Hou, S. Zhou, T. Jia, H. Lin, and H. Teng, "Structural, thermal and mechanical properties of transparent Yb:$(Y_{0.97}Zr_{0.03})_2O_3$ ceramic," J. Eur. Ceram. Soc. 31(5), 733-738 (2011).

[Hua19] H. Huang, S. Wang, H. Chen, O. L. Antipov, S. S. Balabanov, and D. Shen, "High power simultaneous dual-wavelength CW and passively-Q-switched laser operation of LD pumped Tm:YLF at 1.9 and 2.3 μm," Opt. Express 27(26), 38593-38601 (2019).

[Hwa17] J. Hwang, R.R. Rao, L. Giordano, Y. Katayama, Y. Yu, and Y. Shao-Horn, "Perovskites in catalysis and electrocatalysis," Science 358, 751-756 (2017).

[Ike08] A. Ikesue and Y. L. Aung, "Ceramic laser materials," Nat. Photonics 2(12), 721-727 (2008).

[Ike95] A. Ikesue, T. Kinoshita, K. Kamata, and K. Yoshida, "Fabrication and optical properties of high-performance polycrystalline Nd:YAG ceramics for solid-state lasers," J. Am. Ceram. Soc. 78(4), 1033-1040 (1995).

[Ili06] M. N. Iliev, M. V. Abrashev, J. Laverdière, S. Jandl, M. M. Gospodinov, Y. Q. Wang, and Y. Y. Sun, "Distortion-dependent Raman spectra and mode mixing in $RMnO_3$ perovskites (R = La, Pr, Nd, Sm, Eu, Gd, Tb, Dy, Ho, Y)," Phys. Rev. B Condens. Matter Mater. Phys. 73(6), 064302 (2006).

[Ink16] B. J. Inkson, "Scanning electron microscopy (SEM) and transmission electron microscopy (TEM) for materials characterization," in Materials Characterization Using Nondestructive Evaluation (NDE) Methods, pp. 17-43, Woodhead Publishing (2016).

[Jac09] S. D. Jackson, "High-power and highly efficient diode-cladding-pumped holmium-doped fluoride fiber laser operating at 2.94 μm," Opt. Lett. 34(15), 2327-2329 (2009).

[Jaf13] A. Jaffres, S. Ricaud, A. Suganuma, B. Viana, P. Loiseau, P. Georges, and F. Druon, "Yb:CALGO as material for high power ultrafast laser and focus on thermal conductivity variation," Proc. SPIE 8621, 395-401 (2013).

[Jel15] H. Jelínková, M. E. Doroshenko, M. Jelínek, J. Šulc, M. Němec, V. Kubeček, Y. A. Zagoruiko, N. O. Kovalenko, A. S. Gerasimenko, V. M. Puzikov, and V. K. Komar, "Fe:ZnSe and Fe:ZnMgSe lasers pumped by Er:YSGG radiation," Proc. SPIE 9342, Solid State Lasers XXIV: Technology and Devices, 367-372 (February 2015).

[Jin17] W. Jing, P. Loiko, J. Maria Serres, Y. Wang, E. Vilejshikova, M. Aguiló, F. Díaz, U. Griebner, H. Huang, V. Petrov, and X. Mateos, "Synthesis, spectroscopy, and efficient laser operation of "mixed" sesquioxide Tm:$(Lu,Sc)_2O_3$ transparent ceramics," Opt. Mater. Express 7(11), 4192-4202 (2017).

[Jin95] B. M. Jin, S. Erdei, A. S. Bhalla, and F. W. Ainger, "Raman study of oxygen deficient YVO_4 single crystals," Mater. Res. Bull. 30(10), 1293-1300 (1995).

[Joc20] S. D. Jackson and R. K. Jain, "Fiber-based sources of coherent MIR radiation: key advances and future prospects," Opt. Express 28(21), 30964-31019 (2020).

[Jon63] L. F. Johnson, “Optical maser characteristics of rare-earth ions in crystals,” J. Appl. Phys., 34(4), 897–909 (1963).
[Jou94] M. F. Joubert, S. Guy, B. Jacquier, and C. Linares, "The photon-avalanche effect: review, model and application," Opt. Mater. 4(1), 43-49 (1994).
[Jud62] B. R. Judd, "Optical absorption intensities of rare-earth ions," Phys. Rev. 127(3), 750-761 (1962).
[Kam07] A. A. Kaminskii, "Laser crystals and ceramics: recent advances," Laser Photonics Rev. 1(2), 93-177 (2007).
[Kam12] A. A. Kaminskii, X. Xu, O. Lux, H. Rhee, H. J. Eichler, J. Zhang, D. Zhou, A. Shirakawa, K. Ueda, and J. Xu, "High-order stimulated Raman scattering in tetragonal $CaYAlO_4$ crystal-host for Ln^{3+}-lasant ions," Laser Phys. Lett. 9(4), 306 (2012).
[Kam13] A. A. Kaminskii, “Laser crystals: their physics and properties,” 14 (Springer, 2013).
[Kap62] A. A. Kaplyanskii and P. P. Feofilov, "The spectra of divalent rare earth ions in crystals of alkaline earth fluorides. II. Europium and yttrium," Opt. Spectrosc. (USSR) 13, 313-317 (1962).
[Kay23] M. R. Kaysir, J. Song, S. Rassel, A. Aloraynan, and D. Ban, "Progress and perspectives of mid-infrared photoacoustic spectroscopy for non-invasive glucose detection," Biosensors 13(7), 716 (2023).
[Kaz05] S. A. Kazanskii, A. I. Ryskin, A. E. Nikiforov, A. Y. Zaharov, M. Y. Ougrumov, and G. S. Shakurov, "EPR spectra and crystal field of hexamer rare-earth clusters in fluorites," Phys. Rev. B 72(1), 014127 (2005).
[Kel07] U. Keller, "Ultrafast solid-state lasers: 2 Short and ultrashort pulse generation," in Laser Physics and Applications, pp. 33-167 (2007).
[Kif20] E. Kifle, P. Loiko, C. Romero, J. R. V. de Aldana, M. Aguiló, F. Díaz, P. Camy, U. Griebner, V. Petrov, and X. Mateos, "Watt-level ultrafast laser inscribed thulium waveguide lasers," Prog. Quantum Electron. 72, 100266 (2020).
[Kif20a] E. Kifle, P. Loiko, L. Guillemot, J.-L. Doualan, F. Starecki, A. Braud, T. Georges, J. Rouvillain, and P. Camy, "Watt-level diode-pumped thulium lasers around 2.3 μm," Appl. Opt. 59, 7530-7539 (2020).
[Kif21] E. Kifle, P. Loiko, C. Romero, J. R. V. de Aldana, V. Zakharov, Y. Gurova, A. Veniaminov, V. Petrov, U. Griebner, R. Thouroude, and M. Laroche, "Tm^{3+} and Ho^{3+} colasing in in-band pumped waveguides fabricated by femtosecond laser writing," Opt. Lett. 46(1), 122-125 (2021).
[Kim03] M. E. Kim, D. J. Jeoung, and K. S. Kim, "Effects of water flow on dental hard tissue ablation using Er:YAG laser," J. Clin. Laser Med. Surg. 21(3), 139-144 (2003).
[Kim15] W. Kim, G. Villalobos, C. Baker, J. Frantz, B. Shaw, S. Bayya, S. Bowman, B. Sadowski, M. Hunt, B. Rock, and I. Aggarwal, "Overview of transparent optical ceramics for high-energy lasers at NRL," Appl. Opt. 54(31), F210-F221 (2015).
[Kle60] P. G. Klemens, “Thermal resistance due to point defects at high temperatures,” Phys. Rev. 119(2), 507-509 (1960).
[Koe95] J. Koetke and G. Huber, “Infrared excited-state absorption and stimulated-emission cross sections of Er^{3+}-doped crystals,” Appl. Phys. B 61(2), 151–158 (1995).
[Kok13] R.F. Kokaly, B.R. Couvillion, J.M. Holloway, D.A. Roberts, S.L. Ustin, S.H. Peterson, S. Khanna, and S.C. Piazza, "Spectroscopic remote sensing of the distribution and persistence of oil from the Deepwater Horizon spill in Barataria Bay marshes," Remote Sens. Environ. 129, 210-230 (2013).
[Kom95] T. Komukai, T. Yamamoto, T. Sugawa, and Y. Miyajima, "Upconversion pumped thulium-doped fluoride fiber amplifier and laser operating at 1.47 μm," IEEE J. Quantum Electron. 31(11), 1880-1889 (1995).
[Koo11] P. Koopmann, S. Lamrini, K. Scholle, P. Fuhrberg, K. Petermann, and G. Huber, "Efficient diode-pumped laser operation of $Tm:Lu_2O_3$ around 2 μm," Opt. Lett. 36(6), 948-950 (2011).
[Koo11a] P. Koopmann, R. Peters, K. Petermann, and G. Huber, “Crystal growth, spectroscopy, and highly efficient laser operation of thulium-doped Lu_2O_3 around 2 μm,” Appl. Phys. B 102(1), 19-24 (2011).
[Koo12] P. Koopmann, “Thulium- and holmium-doped sesquioxides for 2 μm lasers,” Ph.D. dissertation, Dept. Phys., Univ. Hamburg, Hamburg, Germany (2012).

[Kor04] A. A. Kornienko and E. B. Dunina, "Determination of intensity parameters from the fine details of the Stark structure in the energy spectrum of Tm^{3+} ions in $Y_3Al_5O_{12}$," Opt. Spectrosc. 97, 68-75 (2004).

[Kor05] R. F. Korte, "CXLIX.—Solid solutions," J. Chem. Soc., Trans. 87, 1503-1515 (1905).

[Kor90] A. A. Kornienko, A. A. Kaminskii, and E. B. Dunina, "Dependence of the line strength of f–f transitions on the manifold energy. II. Analysis of Pr^{3+} in $KPrP_4O_{12}$," Phys. Status Solidi B 157(1), 267-273 (1990).

[Kot16] J. Kottmann, J. M. Rey, and M. W. Sigrist, "Mid-Infrared photoacoustic detection of glucose in human skin: towards non-invasive diagnostics," Sensors 16(10), 1663 (2016).

[Kra15] C. Kränkel, "Rare-earth-doped sesquioxides for diode-pumped high-power lasers in the 1-, 2-, and 3-µm spectral range," IEEE J. Sel. Top. Quantum Electron. 21(1), 250-262 (2015).

[Kra22] C. Kränkel, A. Uvarova, C. Guguschev, S. Kalusniak, L. Hülshoff, H. Tanaka, and D. Klimm, "Rare-earth doped mixed sesquioxides for ultrafast lasers," Opt. Mater. Express 12(3), 1074-1091 (2022).

[Kru65] W. F. Krupke and J. B. Gruber, "Optical-absorption intensities of rare-earth ions in crystals: the absorption spectrum of thulium ethyl sulfate," Phys. Rev. 139(6A), A2008 (1965).

[Kur16] S. Kurilchik, N. Gusakova, M. Demesh, A. Yasukevich, V. Kisel, A. Pavlyuk, and N. Kuleshov, "Energy transfer in Tm,Ho:KYW crystal and diode-pumped microchip laser operation," Opt. Express 24(6), 6451-6458 (2016).

[Lac14] B. Lacroix, C. Genevois, J. L. Doualan, G. Brasse, A. Braud, P. Ruterana, P. Camy, E. Talbot, R. Moncorgé, and J. Margerie, "Direct imaging of rare-earth ion clusters in Yb:CaF_2," Phys. Rev. B 90(12), 125124 (2014).

[Lag97] A. A. Lagatskii, N. V. E. Kuleshov, V. G. Shcherbitskii, V. F. Kleptsyn, V. P. Mikhailov, V. G. Ostroumov, and G. Huber, "Lasing characteristics of a diode-pumped Nd^{3+}:$CaGdAlO_4$ crystal," Quantum Electron. 27(1), 15 (1997).

[Lah21] J. Lahyani, J. Le Gouët, F. Gibert, and N. Cézard, "2.05-µm all-fiber laser source designed for CO_2 and wind coherent lidar measurement," Appl. Opt. 60(15), C12-C19 (2021).

[Lam12] S. Lamrini, P. Koopmann, M. Schäfer, K. Scholle, and P. Fuhrberg, "Efficient high-power Ho:YAG laser directly in-band pumped by a GaSb-based laser diode stack at 1.9 µm," Appl. Phys. B 106, 315-319 (2012).

[Lam15] S. Lambert-Girard, M. Allard, M. Piché, and F. Babin, "Differential optical absorption spectroscopy lidar for mid-infrared gaseous measurements," Applied Optics, 54, 1647-1656 (2015).

[Lam60] J. H. Lambert, “Photometria sive de mensura et gradibus luminis, colorum et umbrae”, Sumptibus viduae Eberhardi Klett, typis Christophori Petri Detleffsen (1760).

[Lan12] D.G. Lancaster, S. Gross, A. Fuerbach, H.E. Heidepriem, T.M. Monro, and M.J. Withford, "Versatile large-mode-area femtosecond laser-written Tm:ZBLAN glass chip lasers," Opt. Express 20(25), 27503-27509 (2012).

[Lea82] R. P. Leavitt, J. B. Gruber, N. C. Chang, and C. A. Morrison, “Optical spectra, energy levels, and crystal-field analysis of tripositive rare-earth ions in Y_2O_3. II. Non-Kramers ions in C2 sites,” J. Chem. Phys. 76, 4775-4788 (1982).

[Li11] D. Li, X. Xu, H. Zhu, X. Chen, W. D. Tan, J. Zhang, D. Tang, J. Ma, F. Wu, C. Xia, and J. Xu, "Characterization of laser crystal Yb:$CaYAlO_4$," J. Opt. Soc. Am. B 28(7), 1650-1654 (2011).

[Li13] J. Li, Y. Pan, Y. Zeng, W. Liu, B. Jiang, and J. Guo, "The history, development, and future prospects for laser ceramics: A review," Int. J. Refract. Met. Hard Mater. 39, 44-52 (2013).

[Li21] E. Li, H. Uehara, W. Yao, S. Tokita, F. Potemkin, and R. Yasuhara, "High-efficiency, continuous-wave Fe:ZnSe mid-IR laser end pumped by an Er:YAP laser," Opt. Express 29(26), 44118-44128 (2021).

[Li22] J-H. Li., G-H. Sun, Q-L. Zhang, X-F. Wang, D-M. Zhang, W.-P. Liu J-Y. Gao, L-L. Zheng, S. Han, Z. Chen, and S-T. Yin, “Effect of annealing atmosphere on the structure and spectral properties of $GdScO_3$ and Yb:$GdScO_3$ crystals,” Acta. Phys. Sin. 71(16), 164206 (2022).

[Li23] K. Li, C. Niu, C. Wu, Y. Yu, and Y. Ma, "Development of a 2 µm solid-state laser for lidar in the past decade," Sensors 23(16), 7024 (2023).

[Li93] C. Li, R. Moncorge, J. C. Souriau, and C. Wyon, "Efficient 2.05 μm room temperature Y_2SiO_5:Tm^{3+} cw laser," Opt. Commun. 101(5-6), 356-360 (1993).

[Lia20] V. Llamas, P. Loiko, E. Kifle, C. Romero, J. R. V. de Aldana, J. M. Serres, M. Tonelli, E. Damiano, V. Zakharov, A. Veniaminov, M. Aguiló, F. Díaz, W. Chen, U. Griebner, V. Petrov, and X. Mateos, "Ultrafast laser inscribed waveguide lasers in Tm^{3+}:SrF_2," in Conference on Lasers and Electro-Optics, OSA Technical Digest (Optica Publishing Group, 2020), paper SM3E.7.

[Lib07] A. F. H. Librantz, S. D. Jackson, F. H. Jagosich, L. Gomes, G. Poirier, S. J. L. Ribeiro, and Y. Messaddeq, "Excited state dynamics of the Ho^{3+} ions in holmium singly doped and holmium, praseodymium-codoped fluoride glasses," J. Appl. Phys. 101(12), 123511 (2007).

[Lif04] R. P. Liferovich and R. H. Mitchell, "A structural study of ternary lanthanide orthoscandate perovskites," J. Solid State Chem. 177(6), 2188-2197 (2004).

[Lin23] Z. L. Lin, P. Loiko, H. J. Zeng, W. Z. Xue, G. Zhang, S. Normani, P. Camy, V. Petrov, X. Mateos, H. Lin, and H. Yu, "Kerr-lens mode-locking of an Yb:CLNGG laser," Opt. Express 31(5), 8575-8585 (2023).

[Lis06] R. Lisiecki, P. Solarz, G. Dominiak-Dzik, W. Ryba-Romanowski, M. Sobczyk, P. Černý, J. Šulc, H. Jelínková, Y. Urata, and M. Higuchi, "Comparative optical study of thulium-doped YVO_4, $GdVO_4$, and $LuVO_4$ single crystals," Phys. Rev. B Condens. Matter Mater. Phys. 74(3), 035103 (2006).

[Lis08] R. Lisiecki, W. Ryba-Romanowski, C. Koepke, K. Wiśniewski, and D. Pivatkowski, "Excited state absorption in thulium doped YVO_4 crystals," Appl. Phys. B 91, 65-70 (2008).

[Liu21] Z. Liu, A. Ikesue, and J. Li, "Research progress and prospects of rare-earth doped sesquioxide laser ceramics," J. Eur. Ceram. Soc. 41(7), 3895-3910 (2021).

[Liu23] J. Liu, Y. Wang, Z. Zhang, Z. Zhang, D. Jiang, F. Tang, H. Kou, F. Ma, and L. Su, "Insight into neodymium clusters and spectroscopic properties in CaF_2 single crystals," Opt. Mater. Express 13(8), 2288-2301 (2023).

[Liu24] J. Liu, N. Zhang, Q. Song, H. Ding, Y. Wang, P. Chen, Z. Wang, Y. Xue, J. Xu, Y. Zhao, and X. Xu, "Tunable and mode-locked Tm,Ho:$GdScO_3$ laser," Opt. Lett. 49(8), 2145-2148 (2024).

[Liu24a] S. Liu, P. Wang, K. Li, J. Lv, Y. Jin, X. Xu, Z. Wang, J. Liu, J. Liu, and Y. Zhao, "Sub-60-fs mode-locked Tm, Ho:$CaYLuAlO_4$ laser at 2.05 μm," Opt. Express 32(5), 7513-7519 (2024).

[Lla20] V. Llamas, P. Loiko, E. Kifle, C. Romero, J. R. Vázquez de Aldana, J. M. Serres, M. Tonelli, E. Damiano, V. Zakharov, A. Veniaminov, M. Aguiló, F. Díaz, W. Chen, U. Griebner, V. Petrov, and X. Mateos, "Ultrafast laser inscribed waveguide lasers in Tm^{3+}:SrF_2," in Conference on Lasers and Electro-Optics, OSA Technical Digest (Optica Publishing Group, 2020), paper SM3E.7.

[Lla20a] V. Llamas, P. Loiko, E. Kifle, C. Romero, J.R. Vázquez de Aldana, Z. Pan, J.M. Serres, H. Yuan, X. Dai, H. Cai, Y. Wang, Y. Zhao, V. Zakharov, A. Veniaminov, R. Thouroude, M. Laroche, H. Gilles, M. Aguiló, F. Díaz, U. Griebner, V. Petrov, P. Camy, and X. Mateos, "Ultrafast laser inscribed waveguide lasers in Tm:CALGO with depressed-index cladding," Opt. Express 28, 3528-3540 (2020).

[Loi14] P. Loiko, F. Druon, P. Georges, B. Viana, and K. Yumashev, "Thermo-optic characterization of Yb:$CaGdAlO_4$ laser crystal," Opt. Mater. Express 4(11), 2241-2249 (2014).

[Loi15] P. A. Loiko, K. V. Yumashev, R. Schödel, M. Peltz, C. Liebald, X. Mateos, B. Deppe, and C. Kränkel, "Thermo-optic properties of Yb:Lu_2O_3 single crystals," Appl. Phys. B 120, 601-607 (2015).

[Loi16] P. Loiko and M. Pollnau, "Stochastic model of energy-transfer processes among rare-earth ions. Example of Al_2O_3:Tm^{3+}," J. Phys. Chem. C 120(46), 26480-26489 (2016).

[Loi17] P. Loiko, P. Becker, L. Bohatý, C. Liebald, M. Peltz, S. Vernay, D. Rytz, J.M. Serres, X. Mateos, Y. Wang, and X. Xu, "Sellmeier equations, group velocity dispersion, and thermo-optic dispersion formulas for $CaLnAlO_4$ (Ln= Y, Gd) laser host crystals," Opt. Lett. 42, 2275-2278 (2017).

[Loi18a] P. Loiko, P. Koopmann, X. Mateos, J. M. Serres, V. Jambunathan, A. Lucianetti, T. Mocek, M. Aguilo, F. Diaz, U. Griebner, and V. Petrov, "Highly efficient, compact Tm^{3+}:RE_2O_3 (RE=Y, Lu, Sc) sesquioxide lasers based on thermal guiding," IEEE J. Sel. Top. Quantum Electron. 24(5), 1-13 (2018).

[Loi18b] P. Loiko, A. Volokitina, X. Mateos, E. Dunina, A. Kornienko, E. Vilejshikova, M. Aguilo, and F. Diaz, "Spectroscopy of Tb^{3+} ions in monoclinic $KLu(WO_4)_2$ crystal: application of an intermediate configuration interaction theory," Opt. Mater. 78, 495-501 (2018).

[Loi18c] P. Loiko, Y. Wang, J. M. Serres, X. Mateos, M. Aguilo, F. Diaz, L. Zhang, Z. Lin, H. Lin, G. Zhang, and E. Vilejshikova, "Monoclinic Tm:$MgWO_4$ crystal: Crystal-field analysis, tunable and vibronic laser demonstration," J. Alloys Compd. 763, 581-591 (2018).

[Loi19a] P. Loiko, R. Soulard, L. Guillemot, G. Brasse, J. L. Doualan, A. Braud, A. Tyazhev, A. Hideur, F. Druon, and P. Camy, "Efficient Tm: $LiYF_4$ Lasers at ~2.3 μm: Effect of Energy-Transfer Upconversion," IEEE J. Quantum Electron. 55(6), 1-12 (2019).

[Loi19b] P. Loiko, R. Thouroude, R. Soulard, L. Guillemot, G. Brasse, B. Guichardaz, A. Braud, A. Hideur, M. Laroche, H. Gilles, and P. Camy, "In-band pumping of Tm:$LiYF_4$ channel waveguide: a power scaling strategy for ~2 μm waveguide lasers," Opt. Lett. 44(12), 3010-3013 (2019).

[Loi20] P. Loiko, A. Braud, L. Guillemot, J. L. Doualan, A. Benayad, and P. Camy, "Cross-relaxation and ion clustering in Tm^{3+}:CaF_2 crystals," Proc. SPIE 11357, 120-125 (2020).

[Loi21] P. Loiko, E. Kifle, L. Guillemot, J. L. Doualan, F. Starecki, A. Braud, M. Aguiló, F. Díaz, V. Petrov, X. Mateos, and P. Camy, "Highly efficient 2.3 μm thulium lasers based on a high-phonon-energy crystal: evidence of vibronic-assisted emissions," J. Opt. Soc. Am. B 38(2), 482-495 (2021).

[Loi21a] P. Loiko, L. Basyrova, R. Maksimov, V. Shitov, M. Baranov, F. Starecki, X. Mateos, and P. Camy, "Comparative study of Ho:Y_2O_3 and Ho:$Y_3Al_5O_{12}$ transparent ceramics produced from laser-ablated nanoparticles," J. Lumin. 240, 118460 (2021).

[Loi21b] P. Loiko, G. Brasse, L. Basyrova, A. Benayad, J. L. Doualan, C. Meroni, A. Braud, E. Dunina, A. Kornienko, M. Baranov, and G. Daniil, "Spectroscopy of Tm^{3+}-doped CaF_2 waveguiding thin films grown by Liquid Phase Epitaxy," J. Lumin. 238, 118109 (2021).

[Loi22] P. Loiko, E. Kifle, G. Brasse, R. Thouroude, F. Starecki, A. Benayad, A. Braud, M. Laroche, S. Girard, H. Gilles, and P. Camy, "In-band pumped Tm,Ho:$LiYF_4$ waveguide laser," Opt. Express 30(7), 11840-11847 (2022).

[Lou14] F. Lou, S. Y. Guo, J. L. He, B. T. Zhang, J. Hou, Z. W. Wang, X. T. Zhang, K. J. Yang, R. H. Wang, and X. M. Liu, "Diode-pumped passively mode-locked femtosecond Yb:CTGG laser," Appl. Phys. B 115, 247-250 (2014).

[Luo10] W. Luo, J. Liao, R. Li, and X. Chen, "Determination of Judd–Ofelt intensity parameters from the excitation spectra for rare-earth doped luminescent materials," Phys. Chem. Chem. Phys. 12(13), 3276-3282 (2010).

[Luo20] M. Luo, B. Chen, X. Li, J. Zhang, S. Xu, X. Zhang, Y. Cao, J. Sun, Y. Zhang, X. Wang, and Y. Zhang, "Fluorescence decay route of optical transition calculation for trivalent rare earth ions and its application for Er^{3+}-doped $NaYF_4$ phosphor," Phys. Chem. Chem. Phys. 22(43), 25177-25183 (2020).

[Lup13] A. Lupei, V. Lupei, and C. Gheorghe, "Thermal shifts of Sm^{3+} lines in YAG and cubic sesquioxide ceramics," Opt. Mater. Express 3(10), 1641-1646 (2013).

[Lya15] A. A. Lyapin, P. A. Ryabochkina, A. N. Chabushkin, S. N. Ushakov, and P. P. Fedorov, "Investigation of the mechanisms of upconversion luminescence in Ho^{3+} doped CaF_2 crystals and ceramics upon excitation of $^5I_7$ level," J. Lumin. 167, 120-125 (2015).

[Ma19] J. Ma, Z. Qin, G. Xie, L. Qian, and D. Tang, "Review of mid-infrared mode-locked laser sources in the 2.0 μm–3.5 μm spectral region," Appl. Phys. Rev. 6(2) (2019).

[Mac97] F. J. McAleavey, J. O'Gorman, J. F. Donegan, B. D. MacCraith, J. Hegarty, and G. Maze, "Narrow linewidth, tunable Tm^{3+}-doped fluoride fiber laser for optical-based hydrocarbon gas sensing," IEEE J. Sel. Top. Quantum Electron. 3(4), 1103-1111 (1997).

[Mai60] T. H. Maiman, "Optical and microwave-optical experiments in ruby," Phys. Rev. Lett. 4(11), 564 (1960).

[Mai94] A. Meijerink, C. de Mello Donegá, A. Ellens, J. Sytsma, and G. Blasse, "Vibronic transitions of rare earth ions," J. Lumin. 58(1-6), 26-32 (1994).

[Mak19] T. Makino, T. Asai, T. Takeuchi, K. Kaminaga, D. Oka, and T. Fukumura, "Temperature dependence of dielectric functions in Yb_2O_3 and Lu_2O_3 epitaxial thin films on sapphire (0001)," Jpn. J. Appl. Phys. 59(SC), SCCB13 (2019).

[Mak23] R. Maksimov, V. Shitov, V. Osipov, O. Samatov, D. Vakalov, F. Malyavin, L. Basyrova, P. Loiko, and P. Camy, "Fabrication, microstructure and mid-infrared luminescence of Er:$(Sc_xY_{1-x})_2O_3$ transparent ceramics," Opt. Mater. 137, 113542 (2023).

[Mal63] I. H. Malitson, "A redetermination of some optical properties of calcium fluoride," Appl. Opt. 2, 1103-1107 (1963).

[Mar09] G. D. Marshall, A. Politi, J. C. F. Matthews, P. Dekker, M. Ams, M. J. Withford, and J. L. O'Brien, "Laser written waveguide photonic quantum circuits," Opt. Express 17(15), 12546-12554 (2009).

[Mar69] J. J. Markham, "Configurational Coordinates," in Optical Properties of Solids: Papers from the NATO Advanced Study Institute on Optical Properties of Solids Held August 7–20, 1966, at Freiburg, Germany, pp. 625-626 (Springer US, 1969).

[Mas14] Y. Masubuchi, T. Hata, T. Motohashi, and S. Kikkawa, "Synthesis and crystal structure of K_2NiF_4-type novel $Gd_{1+x}Ca_{1-x}AlO_{4-x}N_x$ oxynitrides," J. Alloys Compd. 582, 823-826 (2014).

[Mas18] O. A. Maslova, X. Iltis, L. Desgranges, M. R. Ammar, C. Genevois, E. De Bilbao, A. Canizarès, S. A. Barannikova, I. N. Leontyev, and P. Simon, "Characterization of an UO_2 ceramic via Raman imaging and electron back-scattering diffraction," Mater. Charact. 147, 280-285 (2019).

[Mat97] M. Mitric, B. Antic, M. Balanda, D. Rodic, and M. L. Napijalo, "An x-ray diffraction and magnetic susceptibility study of $Yb_xY_{2-x}O_3$," J. Condens. Matter Phys. 9, 4103-4111 (1997).

[Maz22] E. C. Mazarakioti, A. Zotos, A. A. Thomatou, A. Kontogeorgos, A. Patakas, and A. Ladavos, "Inductively coupled plasma-mass spectrometry (ICP-MS), a useful tool in authenticity of agricultural products' and foods' origin," Foods 11(22), 3705 (2022).

[Mcd17] S. McDaniel, F. Thorburn, A. Lancaster, R. Stites, G. Cook, and A. Kar, "Operation of Ho:YAG ultrafast laser inscribed waveguide lasers," Appl. Opt. 56(12), 3251-3256 (2017).

[Mei96] A. Meijerink, G. Blasse, J. Sytsma, C. de Mello Donega, and A. Ellens, "Electron-phonon coupling in rare earth compounds," Acta Phys. Pol. A 90(1), 109-119 (1996).

[Mic16] M. Michalska, J. Mikolajczyk, J. Wojtas, and J. Swiderski, "Mid-infrared, super-flat, supercontinuum generation covering the 2–5 μm spectral band using a fluoroindate fibre pumped with picosecond pulses," Sci. Rep. 6, 39138 (2016).

[Mil68] S. A. Miller, H. H. Caspers, and H. E. Rast, "Lattice vibrations of yttrium vanadate," Phys. Rev. 168(3), 964 (1968).

[Mir10] S. Mirov, V. Fedorov, I. Moskalev, D. Martyshkin, and C. Kim, "Progress in Cr^{2+} and Fe^{2+} doped mid-IR laser materials," Laser Photonics Rev. 4(1), 21-41 (2010).

[Mir14] S. B. Mirov, V. V. Fedorov, D. Martyshkin, I. S. Moskalev, M. Mirov, and S. Vasilyev, "Progress in mid-IR lasers based on Cr and Fe-doped II–VI chalcogenides," IEEE J. Sel. Top. Quantum Electron. 21(1), 292-310 (2014).

[Mir18] S. B. Mirov, I. S. Moskalev, S. Vasilyev, V. Smolski, V. V. Fedorov, D. Martyshkin, J. Peppers, M. Mirov, A. Dergachev, and V. Gapontsev, "Frontiers of mid-IR lasers based on transition metal doped chalcogenides," IEEE J. Sel. Top. Quantum Electron. 24(5), 1–29 (2018).

[Miz18] K. Mizutani, S. Ishii, M. Aoki, H. Iwai, R. Otsuka, H. Fukuoka, T. Isikawa, and A. Sato, "2 μm Doppler wind lidar with a Tm:fiber-laser-pumped Ho:YLF laser," Opt. Lett. 43(2), 202-205 (2018).

[Mon22] R. Moncorgé, Y. Guyot, C. Kränkel, K. Lebbou, and A. Yoshikawa, "Mid-infrared emission properties of the Tm^{3+}-doped sesquioxide crystals Y_2O_3, Lu_2O_3, Sc_2O_3 and mixed compounds $(Y,Lu,Sc)_2O_3$ around 1.5-, 2- and 2.3-μm," J. Lum. 241, 118537 (2022).

[Moo70] H. W. Moos, "Spectroscopic relaxation processes of rare earth ions in crystals," J. Lumin. 1, 106-121 (1970).

[Moo70] H. W. Moos, "Spectroscopic relaxation processes of rare earth ions in crystals," J. Lumin. 1, 106-121 (1970).

[Mor17] J. Morris, N.K. Stevenson, H.T. Bookey, A.K. Kar, C.T. Brown, J.M. Hopkins, M.D. Dawson, and A.A. Lagatsky, "1.9 μm waveguide laser fabricated by ultrafast laser inscription in Tm:Lu_2O_3 ceramic," Opt. Express 25(13), 14910-14917 (2017).

[Mor22] Y. Morova, M. Tonelli, and A. Sennaroglu, "Fabrication of femtosecond laser written depressed-cladding waveguides in Tm^{3+}:BaY_2F_8 crystal and laser operation near 2 μm," Opt. Mater. 126, 112121 (2022).

[Mos09] I. S. Moskalev, V. V. Fedorov, and S. B. Mirov, "10-watt, pure continuous-wave, polycrystalline Cr^{2+}: ZnS laser," Opt. Express 17(4), 2048-2056 (2009).

[Mos21] S. Mosca, C. Conti, N. Stone, and P. Matousek, "Spatially offset Raman spectroscopy," Nat. Rev. Methods Primers 1(1), 21 (2021).

[Mou09] P. F. Moulton, G. A. Rines, E. V. Slobodtchikov, K. F. Wall, G. Frith, B. Samson, and A. L. Carter, "Tm-doped fiber lasers: fundamentals and power scaling," IEEE J. Sel. Top. Quantum Electron. 15(1), 85-92 (2009).

[Muj01] M. Mujaji and J. D. Comins, "Aggregation of defects in Ho^{3+}-doped fluorite crystals," Radiat. Eff. Defects Solids 155(1-4), 17-26 (2001).

[Muj92] M. Mujaji, G. D. Jones, and R. W. G. Syme, "Polarization study and crystal-field analysis of the laser-selective excitation spectra of Ho^{3+} ions in CaF_2 and SrF_2 crystals," Phys. Rev. B 46(22), 14398 (1992).

[Mul06] P. Muller, R. Herbst-Irmer, A. Spek, T. Schneider, and M. Sawaya, Crystal Structure Refinement: A Crystallographer's Guide to SHELXL, Vol. 8 (OUP Oxford, 2006).

[Mun11] J. H. Mun, A. Jouini, A. Novoselov, A. Yoshikawa, and T. Fukuda, "Crystal growth and thermal conductivity of an Tm^{3+}-doped Y_2O_3 for IR eye-safe laser," J. Ceram. Process. Res. 12(2), 169-172 (2011).

[Nes88] S. E. Ness, D. J. M. Bevan, and H. J. Rossell, "Cuboctahedral anion clusters in fluorite-related superstructures: the structure of Ca_2YbF_7. Part. 1," Eur. J. Solid State Inorg. Chem. 25(5-6), 509-516 (1988).

[Nie17] H. Nie, P. Zhang, B. Zhang, M. Xu, K. Yang, X. Sun, L. Zhang, Y. Hang, and J. He, "Watt-level continuous-wave and black phosphorus passive Q-switching operation of Ho^{3+},Pr^{3+}:$LiLuF_4$ bulk laser at 2.95 μm," IEEE J. Sel. Top. Quantum Electron. 24(5), 1-5 (2017).

[Nie18] H. Nie, H. Xia, B. Shi, J. Hu, B. Zhang, K. Yang, and J. He, "High-efficiency watt-level continuous-wave 2.9 μm Ho,Pr:YLF laser," Opt. Lett. 43(24), 6109-6112 (2018).

[Nik05] A. E. Nikiforov, A. Y. Zakharov, M. Y. Ugryumov, S. A. Kazanskii, A. I. Ryskin, and G. S. Shakurov, "Crystal fields of hexameric rare-earth clusters in fluorites," Phys. Solid State 47, 1431-1435 (2005).

[Nor17] S. Normani, "Nd Lu CaF_2 for high-energy lasers," Doctoral dissertation, Normandie Université (2017).

[Ofe62] G. S. Ofelt, "Intensities of crystal spectra of rare-earth ions," J. Chem. Phys. 37(3), 511-520 (1962).

[Oka21] K. Okamoto, Fundamentals of Optical Waveguides (Elsevier, 2021).

[Ole05] J. T. Olesberg, M. A. Arnold, C. Mermelstein, J. Schmitz, and J. Wagner, "Tunable laser diode system for noninvasive blood glucose measurements," Appl. Spectrosc. 59(12), 1480-1484 (2005).

[Osi13] V. V. Osipov, V. V. Platonov, V. V. Lisenkov, A. V. Podkin, and E. E. Zakharova, "Production of nanopowders of oxides by means of fiber and pulse-periodical CO_2 lasers," Phys. Status Solidi C 10(6), 926-932 (2013).

[Paa14] J. Paajaste, S. Suomalainen, A. Härkönen, U. Griebner, G. Steinmeyer, and M. Guina, "Absorption recovery dynamics in 2 μm GaSb-based SESAMs," J. Phys. D: Appl. Phys. 47(6), 065102 (2014).

[Paj98] A. Pajaczkowska and A. Gloubokov, "Synthesis, growth and characterization of tetragonal $ABCO_4$ crystals," Prog. Cryst. Growth Charact. Mater. 36(1-2), 123-162 (1998).

[Pal12] A. Pal, R. Sen, K. Bremer, S. Yao, E. Lewis, T. Sun, and K. T. Grattan, ""All-fiber" tunable laser in the 2 μm region, designed for CO_2 detection," Appl. Opt. 51(29), 7011-7015 (2012).

[Pan00] J. C. Panitz, J. C. Mayor, B. Grob, and W. Durisch, "A Raman spectroscopic study of rare earth mixed oxides," J. Alloys Compd. 303, 340-344 (2000).

[Pan18] Z. Pan, Y. Wang, Y. Zhao, M. Kowalczyk, J. Sotor, H. Yuan, Y. Zhang, X. Dai, H. Cai, J. E. Bae, S. Y. Choi, F. Rotermund, P. Loiko, J. M. Serres, X. Mateos, U. Griebner, and V. Petrov, "Sub-80 fs mode-locked Tm,Ho-codoped disordered garnet crystal oscillator operating at 2081 nm," Opt. Lett. 43, 5154-5157 (2018).

[Pan18a] Z. Pan, Y. Wang, Y. Zhao, H. Yuan, X. Dai, H. Cai, J. E. Bae, S. Y. Choi, F. Rotermund, X. Mateos, and J. M. Serres, "Generation of 84-fs pulses from a mode-locked Tm:CNNGG disordered garnet crystal laser," Photon. Res. 6(8), 800-804 (2018).

[Pan18b] Z. Pan, J. M. Serres, E. Kifle, P. Loiko, H. Yuan, X. Dai, H. Cai, M. Aguilo, F. Diaz, Y. Wang, and Y. Zhao, "Comparative study of the spectroscopic and laser properties of Tm^{3+},Na^{+}(Li^{+})-codoped $Ca_3Nb_{1.5}Ga_{3.5}O_{12}$-type disordered garnet crystals for mode-locked lasers," Opt. Mater. Express 8(8), 2287-2299 (2018).

[Pan21] Z. Pan, L. Wang, J. E. Bae, F. Rotermund, Y. Wang, Y. Zhao, P. Loiko, X. Mateos, U. Griebner, V. Petrov, and W. Chen, "SWCNT-SA mode-locked Tm,Ho:LCLNGG laser," Opt. Express 29(24), 40323-40332 (2021).

[Pan21a] Z. Pan, P. Loiko, Y. Wang, Y. Zhao, H. Yuan, K. Tang, X. Dai, H. Cai, J. M. Serres, S. Slimi, and E. B. Salem, "Disordered Tm^{3+},Ho^{3+}-codoped CNGG garnet crystal: Towards efficient laser materials for ultrashort pulse generation at ~2 μm," J. Alloys Compd. 853, 157100 (2021).

[Pan22] Z. Pan, P. Loiko, S. Slimi, H. Yuan, Y. Wang, Y. Zhao, P. Camy, E. Dunina, A. Kornienko, L. Fomicheva, and L. Wang, "Tm,Ho:Ca(Gd,Lu)AlO_4 crystals: Crystal growth, structure refinement and Judd-Ofelt analysis," J. Lumin. 246, 118828 (2022).

[Pan23] Z. Pan, P. Loiko, J. M. Serres, H. Yuan, Y. Wang, L. Wang, Y. Zhao, R. M. Solé, M. Aguiló, F. Díaz, and P. Camy, "Tm,Ho:Ca(Gd,Lu)AlO_4 crystals: polarized spectroscopy and laser operation," J. Lumin. 257, 119638 (2023).

[Par20] S. Parker, M. Cronshaw, E. Anagnostaki, V. Mylona, E. Lynch, and M. Grootveld, "Current concepts of laser–oral tissue interaction," Dent. J. 8(3), 61 (2020).

[Pas08] R. Paschotta, Field Guide to Laser Pulse Generation, Vol. 14 (SPIE Press, 2008).

[Pau30] L. Pauling and M.D. Shappell, "The crystal structure of bixbyite and the C-modification of the sesquioxides," Z. fur Krist. - Cryst. Mater. 75, 128–142 (1930).

[Pay91] S. A. Payne, J. A. Caird, L. L. Chase, L. K. Smith, N. D. Nielsen, and W. F. Krupke, "Spectroscopy and gain measurements of Nd^{3+} in SrF_2 and other fluorite-structure hosts," J. Opt. Soc. Am. B 8(4), 726-740 (1991).

[Pay92] S. A. Payne, L. L. Chase, L. K. Smith, W. L. Kway, and W. F. Krupke, "Infrared cross-section measurements for crystals doped with Er^{3+}, Tm^{3+}, and Ho^{3+}," IEEE J. Quantum Electron. 28(11), 2619–2630 (1992).

[Pay92a] S. A. Payne, L. K. Smith, W. L. Kway, J. B. Tassano, and W. F. Krupke, "The mechanism of Tm to Ho energy transfer in $LiYF_4$," J. Phys. Condens. Matter 4(44), 8525-8534 (1992).

[Pay94] S. A. Payne, G. D. Wilke, L. K. Smith, and W. F. Krupke, "Auger upconversion losses in Nd-doped laser glasses," Opt. Commun. 111(3-4), 263-268 (1994).

[Pet05] J. Petit, P. Goldner, and B. Viana, "Laser emission with low quantum defect in Yb:$CaGdAlO_4$," Opt. Lett. 30(11), 1345-1347 (2005).

[Pet08] P. O. Petit, J. Petit, P. Goldner, and B. Viana, "Inhomogeneous broadening of optical transitions in Yb:$CaYAlO_4$," Opt. Mater. 30(7), 1093-1097 (2008).

[Pet11] R. Peters, C. Kränkel, S. T. Fredrich-Thornton, K. Beil, K. Petermann, G. Huber, O. H. Heckl, C. R. E. Baer, C. J. Saraceno, T. Südmeyer, and U. Keller, "Thermal analysis and efficient high power continuous-wave and mode-locked thin disk laser operation of Yb-doped sesquioxides," Appl. Phys. B 102, 509-514 (2011).

[Pet15] V. Petrov, "Frequency down-conversion of solid-state laser sources to the mid-infrared spectral range using non-oxide nonlinear crystals," Progr. Quantum Electron. 42, 1–106 (2015).

[Pet19] V. Petrov, Y. Wang, W. Chen, Z. Pan, Y. Zhao, L. Wang, M. Mero, S. Y. Choi, F. Rotermund, W. B. Cho, W. Jing, H. Huang, H. Yuan, H. Cai, L. Zhang, Z. Lin, P. Loiko, X. Mateos, X. Xu, J. Xu, H. Yu, H. Zhang, S. Suomalainen, M. Guina, A. Härkönen, and U. Griebner, "Sub-100-fs bulk solid-state lasers near 2-micron," Proc. SPIE 11209, 112094G-1-16 (2019).

[Phe19] R. Phelan, D. Byrne, J. O'Carroll, M. Gleeson, M. Nawrocka, R. Lennox, K. Carney, C. Herbert, J. Somers, and B. Kelly, "Mid-infrared InP-based discrete mode laser diodes," Opt. Fiber Appl., p. 15 (2019).

[Pie20] K. A. Pierpoint, M. E. Doroshenko, O. K. Alimov, A. G. Papashvili, V. A. Konyushkin, A. N. Nakladov, and A. V. Nekhoroshikh, "Spectroscopic properties of Ho^{3+} optical centers in CaF_2 crystals at the two-micron laser transition," J. Lumin. 228, 117584 (2020).

[Pin94] J. F. Pinto, L. Esterowitz, and G. H. Rosenblatt, "Tm^{3+}:YLF laser continuously tunable between 2.20 and 2.46 μm," Opt. Lett. 19, 883-885 (1994).

[Pio22] W. M. Piotrowski, K. Maciejewska, L. Dalipi, B. Fond, and L. Marciniak, "Cr^{3+} ions as an efficient antenna for the sensitization and brightness enhancement of Nd^{3+}, Er^{3+}-based ratiometric thermometer in $GdScO_3$ perovskite lattice," J. Alloys Compd. 923, 166343 (2022)

[Pir21] A. Pirri, B. Patrizi, R. N. Maksimov, V. A. Shitov, V. V. Osipov, M. Vannini, and G. Toci, "Spectroscopic investigation and laser behaviour of Yb-doped laser ceramics based on mixed crystalline structure $(Sc_xY_{1-x})_2O_3$," Ceram. Int. 47(20), 29483-29489 (2021).

[Pir21a] A. Pirri, R. N. Maksimov, V. A. Shitov, V. V. Osipov, E. Sani, B. Patrizi, M. Vannini, and G. Toci, "Continuously tuned $(Tm_{0.05}Sc_{0.252}Y_{0.698})_2O_3$ ceramic laser with emission peak at 2076 nm," J. Alloys Compd. 889, 161585 (2021).

[Pra05] N. S. Prasad, "Optical communications in the mid-wave IR spectral band," J. Opt. Fiber Commun. Res. 6(2), 558-602 (2005).

[Qia23a] Y. Qiao, D. Sun, H. Zhang, J. Luo, C. Quan, L. Hu, Z. Han, K. Dong, Y. Chen, and M. Cheng, "Spectroscopy and 3.01 μm laser performance of Ho:YAP oxide crystal pumped by 1150 nm Raman laser," Opt. Laser Technol. 157, 108728 (2023).

[Qia23b] Y. Qiao, D. Sun, H. Zhang, J. Luo, C. Quan, K. Dong, Y. Chen, Z. Wang, H. Li, and M. Cheng, "Thermal, spectroscopy and optimized ~3 μm CW laser properties for Ho,Pr:YAP crystal," Opt. Express 31(22), 36429-36438 (2023).

[Qua19] L.N. Quan, B.P. Rand, R.H. Friend, S.G. Mhaisalkar, T.W. Lee, and E.H. Sargent, "Perovskites for next-generation optical sources," Chem. Rev. 119(12), 7444-7477 (2019).

[Rab91] W. S. Rabinovich, S. R. Bowman, B. J. Feldman, and M. J. Winings, "Tunable laser pumped 3 μm $Ho:YAlO_3$ laser," IEEE J. Quantum Electron. 27(4), 895-897 (1991).

[Raf20] P. Rafailov, D. Dimitrov, Y. F. Chen, C. S. Lee, and J. Y. Juang, "Symmetry of the optical phonons in $LuVO_4$: A Raman study," Crystals 10(5), 341 (2020).

[Raj67] K. Rajnak and W. F. Krupke, "Energy levels of Ho^{3+} in $LaCl_3$," J. Chem. Phys. 46(9), 3532-3542 (1967).

[Raz95] I. Razumova, A. Tkachuk, A. Nikitichev, and D. Mironov, "Spectral-luminescent properties of Tm:YLF crystal," J. Alloys Compd. 225(1-2), 129-132 (1995).

[Ren12] Y. Ren, G. Brown, A. Ródenas, S. Beecher, F. Chen, and A.K. Kar, "Mid-infrared waveguide lasers in rare-earth-doped YAG," Opt. Lett. 37(16), 3339-3341 (2012).

[Rep95] Y. Repelin, C. Proust, E. Husson, and J. M. Beny, "Vibrational spectroscopy of the C-form of yttrium sesquioxide," J. Solid State Chem. 118, 163-169 (1995).

[Rie92] H. Riesen and E. Krausz, "Persistent spectral hole-burning, luminescence line narrowing and selective excitation spectroscopy of the R lines of Cr (III) tris (2, 2′-bipyridine) in amorphous hosts," J. Chem. Phys. 97(11), 7902-7910 (1992).

[Ris67] L. A. Riseberg, W. B. Gandrud, and H. W. Moos, "Multiphonon relaxation of near-infrared excited states of $LaCl_3:Dy^{3+}$," Phys. Rev. 159(2), 262 (1967).

[Ris68] L. A. Riseberg and H. W. Moos, "Multiphonon orbit-lattice relaxation of excited states of rare-earth ions in crystals," Phys. Rev. 174(2), 429 (1968).

[Ris77] L. A. Riseberg and M. J. Weber, "III relaxation phenomena in rare-earth luminescence," Prog. Opt. 14, 89-159 (1977).

[Riv12] V. A. G. Rivera, F. A. Ferri, and E. Marega Jr, "Localized surface plasmon resonances: noble metal nanoparticle interaction with rare-earth ions," Plasmonics-Principles Appl. 1(11), 283-312 (2012).

[Rob20] L. R. Robichaud, S. Duval, L. P. Pleau, V. Fortin, S. T. Bah, S. Châtigny, R. Vallée, and M. Bernier, "High-power supercontinuum generation in the mid-infrared pumped by a soliton self-frequency shifted source," Opt. Express 28(1), 107-115 (2020).

[Rob67] M. Robinson, and D. P. Devor, "Thermal switching of laser emission of Er^{3+} at 2.69 μ and Tm^{3+} at 1.86 μ in mixed crystals of CaF_2: ErF_3: TmF_3," Appl. Phys. Lett. 10(5), 167–170 (1963).

[Rod95] D. Rodic, B. Antic, and M. Mitric, "The rare earth ion distribution in mixed rare earth-yttrium sesquioxides," J. Magn. Magn. Mater. 140, 1181-1182 (1995).

[Rom11] W. Ryba-Romanowski, R. Lisiecki, H. Jelinková, and J. Šulc, "Thulium-doped vanadate crystals: Growth, spectroscopy and laser performance," Prog. Quantum Electron. 35(5), 109-157 (2011).

[Rou81] D. L. Rousseau, R. P. Bauman, and S. P. S. Porto, "Normal mode determination in crystals," J. Raman Spectrosc. 10, 253-290 (1981).

[Rub14] C. W. Rudy, M. J. Digonnet, and R. L. Byer, "Advances in 2-μm Tm-doped mode-locked fiber lasers," Opt. Fiber Technol. 20(6), 642-649 (2014).

[Rud14] C. W. Rudy, M. J. Digonnet, and R. L. Byer, "Advances in 2-μm Tm-doped mode-locked fiber lasers," Opt. Fiber Technol. 20(6), 642-649 (2014).

[Saf12] A. P. Safronov, O. M. Samatov, A. I. Medvedev, I. V. Beketov, and A. M. Murzakaev, "Synthesis of strontium hexaferrite nanopowder by the laser evaporation method," Nanotechnol. Russ. 7, 486-491 (2012).

[San12] A. Sanson, M. Giarola, B. Rossi, G. Mariotto, E. Cazzanelli, and A. Speghini, "Vibrational dynamics of single-crystal YVO_4 studied by polarized micro-Raman spectroscopy and ab initio calculations," Phys. Rev. B Condens. Matter Mater. Phys. 86(21), 214305 (2012).

[Sau18] P. Saudemont, J. Quanico, Y. M. Robin, A. Baud, J. Balog, B. Fatou, D. Tierny, Q. Pascal, K. Minier, M. Pottier, C. Focsa, M. Ziskind, Z. Takats, M. Salzet, and I. Fournier, "Real-time molecular diagnosis of tumors using water-assisted laser desorption/ionization mass spectrometry technology," Cancer Cell 34(5), 840-851 (2018).

[Sch04] H. Scheife, G. Huber, E. Heumann, S. B¨ar, E. Osiac, Advances in up-conversion lasers based on Er^{3+} and Pr^{3+}, Opt. Mater. 26 (2004) 365–374.

[Sch10] K. Scholle, S. Lamrini, P. Koopmann, and P. Fuhrberg, "2 μm laser sources and their possible applications," in Frontiers in Guided Wave Optics and Optoelectronics, B. Pal, Ed. (Intech, 2010), pp. 471–500.

[Sch10a] A. Schmidt, U. Griebner, H. Zhang, J. Wang, M. Jiang, J. Liu, and V. Petrov, "Passive mode-locking of the Yb:CNGG laser," Opt. Commun. 283(4), 567-569 (2010).

[See79] M. B. Seelbinder and J. C. Wright, "Site-selective spectroscopy of CaF_2:Ho^{3+}," Phys. Rev. B 20(10), 4308 (1979).

[Ser17] M. D. Serrano, J. O. Álvarez-Pérez, C. Zaldo, J. Sanz, I. Sobrados, J. A. Alonso, C. Cascales, M. T. Fernández-Díaz, and A. Jezowski, "Design of Yb^{3+} optical bandwidths by crystallographic modification of disordered calcium niobium gallium laser garnets," J. Mater. Chem. C 5(44), 11481-11495 (2017).

[Sha76] R. D. Shannon, "Revised effective ionic radii and systematic studies of interatomic distances in halides and chalcogenides," Acta Crystallogr. A 32, 751-767 (1976).

[Sha92] R. D. Shannon, R. A. Oswald, J. B. Parise, B. H. T. Chai, P. Byszewski, A. Pajaczkowska, and R. Sobolewski, "Dielectric constants and crystal structures of $CaYAlO_4$, $CaNdAlO_4$, and $SrLaAlO_4$, and deviations from the oxide additivity rule," J. Solid State Chem. 98(1), 90-98 (1992).

[She12] Y. J. Shen, B. Q. Yao, X. M. Duan, G. L. Zhu, W. Wang, Y. L. Ju, and Y. Z. Wang, "103 W in-band dual-end-pumped Ho:YAG laser," Opt. Lett. 37(17), 3558-3560 (2012).

[She23] Y. Shen, Y. Jia, and F. Chen, "Femtosecond laser-induced optical waveguides in crystalline garnets: Fabrication and application," Opt. Laser Technol. 164, 109528 (2023).

[Shi22] R. Shi and A. V. Mudring, "Phonon-mediated nonradiative relaxation in Ln^{3+}-doped luminescent nanocrystals," ACS Mater. Lett. 4(10), 1882-1903 (2022).

[Shi93] K. Shimamura, M. Timoshechkin, T. Sasaki, K. Hoshikawa, and T. Fukuda, "Growth and characterization of calcium niobium gallium garnet (CNGG) single crystals for laser applications," J. Cryst. Growth 128(1-4), 1021-1024 (1993).

[Sht04] L. Shterengas, G. L. Belenky, A. Gourevitch, D. Donetsky, J. G. Kim, R. U. Martinelli, and D. Westerfeld, "High-power 2.3-μm GaSb-based linear laser array," IEEE Photon. Technol. Lett. 16, 2218-2220 (2004).

[Si23] H. Si, F. Liang, D. Lu, H. Yu, H. Zhang, and Y. Wu, "Efficient direct laser generation by three-phonon-assisted transition with Yb:YCOB crystal," Adv. Photon. Res. 4(6), 2300092 (2023).

[Sim20] A. Simonov and A. L. Goodwin, "Designing disorder into crystalline materials," Nat. Rev. Chem. 4(12), 657-673 (2020).

[Sin15] U. N. Singh, B. M. Walsh, J. Yu, M. Petros, M. J. Kavaya, T.F. Refaat, and N.P. Barnes, "Twenty years of Tm:Ho:YLF and LuLiF laser development for global wind and carbon dioxide active remote sensing," Opt. Mater. Express 5(4), 827-837 (2015).

[So06] S. So, J. I. Mackenzie, D. P. Sheperd, W. A. Clarkson, J. G. Betterton, and E. K. Gorton, "A power-scaling strategy for longitudinally diode-pumped Tm:YLF lasers," Appl. Phys. B 84(3), 389-393 (2006).

[Sor02] I. T. Sorokina, E. Sorokin, S. Mirov, V. Fedorov, V. Badikov, V. Panyutin, A. Di Lieto, and M. Tonelli, "Continuous-wave tunable Cr^{2+}:ZnS laser," Appl. Phys. B 74, 607-611 (2002).

[Sor04] I. T. Sorokina, “Cr^{2+}-doped II–VI materials for lasers and nonlinear optics,” Opt. Mater. 26(4), 395–412 (2004).
[Sor14] I. T. Sorokina and E. Sorokin, “Femtosecond Cr^{2+}-based lasers,” IEEE J. Sel. Top. Quantum Electron. 21(1), 273–291 (2014).
[Sto49] D. C. Stockbarger, "Artificial fluorite," J. Opt. Soc. Am. 39(9), 731-740 (1949).
[Sto90] R. C. Stoneman and L. Esterowitz, "Efficient, broadly tunable, laser-pumped Tm:YAG and Tm:YSGG cw lasers," Opt. Lett. 15, 486-488 (1990).
[Sto91] R. C. Stoneman and L. Esterowitz, "Continuous-wave 1.50-μm thulium cascade laser," Opt. Lett. 16(4), 232-234 (1991).
[Str96] N. M. Strickland, "Laser excitation and infrared absorption spectroscopy of rare-earth ion centres in fluorite crystals," Ph.D. dissertation, University of Canterbury (1996).
[Str97] N. M. Strickland and G. D. Jones, "Site-selective spectroscopy of Tm^{3+} centers in CaF_2:Tm^{3+}," Phys. Rev. B 56(17), 10916 (1997).
[Sul08] J. Šulc, P. Koranda, P. Černý, H. Jelínková, Y. Urata, M. Higuchi, W. Ryba-Romanowski, R. Lisiecki, P. Solarz, G. Dominiak-Dzik, and M. Sobczyk, "Tunable lasers based on diode pumped Tm-doped vanadates Tm:YVO_4, Tm:$GdVO_4$, and Tm:$LuVO_4$," in Solid State Lasers XVII: Technology and Devices, Vol. 6871, pp. 521-529, SPIE (2008).
[Sus24] A. Suzuki, Y. Wang, S. Tomilov, Z. Pan, and C. J. Saraceno, "Diode-pumped 88 fs SESAM mode-locked Tm,Ho:CLNGG laser at 2090 nm," Appl. Phys. Express 17(4), 042002 (2024).
[Suz20] A. Suzuki, C. Kränkel, and M. Tokurakawa, "High quality-factor Kerr-lens mode-locked Tm:Sc_2O_3 single crystal laser with anomalous spectral broadening," Appl. Phys. Express 13(5), 052007 (2020).
[Suz21] A. Suzuki, C. Kränkel, and M. Tokurakawa, "Sub-6 optical-cycle combined gain media Kerr-lens mode-locked laser based on Tm:Lu_2O_3 and Tm:Sc_2O_3," Opt. Express 29(13), 19465-19471 (2021).
[Suz22] A. Suzuki, S. Kalusniak, H. Tanaka, M. Brützam, S. Ganschow, M. Tokurakawa, and C. Kränkel, “Spectroscopy and 2.1 μm laser operation of Czochralski-grown Tm^{3+}:$YScO_3$ crystals,” Opt. Express 30(23), 42762-42771 (2022).
[Suz23] A. Suzuki, S. Kalusniak, S. Ganschow, C. Kränkel, and M. Tokurakawa, "Kerr-lens mode-locked 49-fs Tm^{3+}:$YScO_3$ single-crystal laser at 2.1 μm," Opt. Lett. 48(16), 4221-4224 (2023).
[Syt91] J. Sytsma, W. Van Schaik, and G. Blasse, "Vibronic transitions in the emission spectra of Gd^{3+} in several rare-earth compounds," J. Phys. Chem. Solids 52(2), 419-429 (1991).
[Szl09] R. Szlauer, R. Götschl, A. Razmaria, L. Paras, and N. T. Schmeller, "Endoscopic vaporesection of the prostate using the continuous-wave 2-μm thulium laser: outcome and demonstration of the surgical technique," Eur. Urol. 55(2), 368-375 (2009).
[Tac98] T. M. Taczak and D. K. Killinger, "Development of a tunable, narrow-linewidth, cw 2.066-μm Ho:YLF laser for remote sensing of atmospheric CO_2 and H_2O," Appl. Opt. 37(36), 8460-8476 (1998).
[Tai97] T. Taira, W. M. Tulloch, and R. L. Byer, "Modeling of quasi-three-level lasers and operation of cw Yb:YAG lasers," Appl. Opt. 36(9), 1867-1874 (1997).
[Tak05] K. Takaichi, H. Yagi, A. Shirakawa, K. Ueda, S. Hosokawa, T. Yanagitani, and A. A. Kaminskii, "Lu_2O_3:Yb^{3+} ceramics–a novel gain material for high-power solid-state lasers," Phys. Status Solidi A 202, R1-R3 (2005).
[Tal19] E. Talik, J. Kisielewski, P. Zajdel, A. Guzik, E. Wierzbicka, A. Kania, J. Kusz, S. Miga, and M. Szubka, "XPS spectroscopy, structural, magnetic and dielectric investigations of $CaGdAlO_4$ and Yb:$CaGdAlO_4$ single crystals," Opt. Mater. 91, 355-362 (2019).
[The07] D. Theisen-Kunde, V. Ott, R. Brinkmann, and R. Keller, "Potential of a new cw 2 μm laser scalpel for laparoscopic surgery," Med. Laser Appl. 22, 139 (2007).
[Tia11] Y. Tian, B. Chen, R. Hua, J. Sun, L. Cheng, H. Zhong, X. Li, J. Zhang, Y. Zheng, T. Yu, and L. Huang, "Optical transition, electron-phonon coupling and fluorescent quenching of $La_2(MoO_4)_3$:Eu^{3+} phosphor," J. Appl. Phys. 109(5), 053505 (2011).
[Tod13] N. D. Todorov, M. V. Abrashev, V. Marinova, M. Kadiyski, L. Dimowa, and E. Faulques, "Raman spectroscopy and lattice dynamical calculations of Sc_2O_3 single crystals," Phys. Rev. B 87, 104301 (2013).

[Tol14] N. Tolstik, E. Sorokin, and I. T. Sorokina, "Graphene mode-locked Cr:ZnS laser with 41 fs pulse duration," Opt. Express 22, 5564-5571 (2014).

[Tom21] S. Tomilov, M. Hoffmann, Y. Wang, and C. J. Saraceno, "Moving towards high-power thin-disk lasers in the 2 μm wavelength range," J. Phys. Photonics 3(2), 022002 (2021).

[Tom22] S. Tomilov, Y. Wang, M. Hoffmann, J. Heidrich, M. Golling, U. Keller, and C. J. Saraceno, "50-W average power Ho:YAG SESAM-modelocked thin-disk oscillator at 2.1 μm," Opt. Express 30(15), 27662-27673 (2022).

[Tou12] E. Tournie and A. N. Baranov, "Mid-infrared semiconductor lasers: a review," Semiconductors and Semimetals 86, 183–226 (2012).

[Tya23] A. Tyazhev, P. Loiko, L. Guillemot, A. Kouta, R. M. Solé, X. Mateos, M. Aguiló, F. Díaz, H. Dupont, P. Georges, and F. Druon, "Excited-state absorption and upconversion pumping of Tm^{3+}-doped potassium lutetium double tungstate," Opt. Express 31(9), 14808-14820 (2023).

[Tyz23] A. Tyazhev, P. Loiko, L. Guillemot, A. Kouta, R. M. Solé, X. Mateos, M. Aguiló, F. Díaz, H. Dupont, P. Georges, and F. Druon, "Excited-state absorption and upconversion pumping of Tm^{3+}-doped potassium lutetium double tungstate," Opt. Express 31(9), 14808-14820 (2023).

[Tyz24] A. Tyazhev, J. E. Bae, M. Gaulke, P. Loiko, J. Heidrich, M. Golling, S. Idlahcen, L. Guillemot, T. Godin, P. Camy, and U. Keller, "Upconversion-pumped femtosecond thulium laser at 2309 nm mode-locked by a GaSb-based SESAM," Opt. Express 32(9), 15093-15105 (2024).

[Uba08] A. Ubaldini and M. M. Carnasciali, "Raman characterisation of powder of cubic RE_2O_3 (RE= Nd, Gd, Dy, Tm, and Lu), Sc_2O_3 and Y_2O_3," J. Alloys Compd. 454, 374-378 (2008).

[Umy96] A. F. Umyskov, Y. D. Zavartsev, A. I. Zagumennyi, V. V. Osiko, and P. A. Studenikin, "Efficient 3-μm Cr^{3+}:Yb^{3+}:Ho^{3+}:YSGG crystal laser," Quantum Electron. 26(9), 771 (1996).

[Uva23] A. Uvarova, P. Loiko, S. Kalusniak, E. Dunina, L. Fomicheva, A. Kornienko, S. Balabanov, A. Braud, P. Camy, and C. Kränkel, "Stimulated-emission cross-sections of trivalent erbium ions in the cubic sesquioxides Y_2O_3, Lu_2O_3, and Sc_2O_3," Opt. Mater. Express 13, 1385-1400 (2023).

[Vag23] T. Theodoridis, C. Tseleki, and I. Vouros, "Long-term clinical outcomes of Er:YAG or Er,Cr:YSGG lasers utilized as monotherapy or as adjuncts to mechanical therapy in the treatment of chronic periodontitis: A systematic review," Lasers Dent. Sci. 7, 1-15 (2023).

[Veg21] L. Vegard, "Die Konstitution der Mischkristalle und die Raumfüllung der Atome," Z. Phys. 5, 17-26 (1921).

[Vel07] B. Veličkov, K. Volker, B. Rainer, and B. Margitta, "Crystal chemistry of $GdScO_3$, $DyScO_3$, $SmScO_3$ and $NdScO_3$," Z. Kristallogr. 222(9), 466-473 (2007).

[Vic02] A. Vicet, D. A. Yarekha, A. Pérona, Y. Rouillard, S. Gaillard, and A. N. Baranov, "Trace gas detection with antimonide-based quantum-well diode lasers," Spectrochim. Acta A Mol. Biomol. Spectrosc. 58, 2405-2412 (2002).

[Vod00] K. L. Vodopyanov, F. Ganikhanov, J. P. Maffetone, I. Zwieback, and W. Ruderman, "$ZnGeP_2$ optical parametric oscillator with 3.8–12.4-μm tunability," Opt. Lett. 25(11), 841-843 (2000).

[Vod20] K. L. Vodopyanov, "Laser-based mid-infrared sources and applications" (John Wiley & Sons, 2020).

[Vol18] A. Volokitina, P. Loiko, E. Vilejshikova, X. Mateos, E. Dunina, A. Kornienko, N. Kuleshov, and A. Pavlyuk, "Eu^{3+}:$KY(MoO_4)_2$: A novel anisotropic red-emitting material with a layered structure," J. Alloys Compd. 762, 786-796 (2018).

[Vor02] Y. K. Voronko, A. A. Sobol, A. Y. Karasik, N. A. Eskov, P. A. Rabochkina, and S. N. Ushakov, "Calcium niobium gallium and calcium lithium niobium gallium garnets doped with rare earth ions—effective laser media," Opt. Mater. 20(3), 197-209 (2002).

[Vor09] Y. K. Voron'ko, A. A. Sobol', V. E. Shukshin, A. I. Zagumennyĭ, Y. D. Zavartsev, and S. A. Kutovoĭ, "Raman spectroscopic study of structural disordering in YVO_4, $GdVO_4$, and $CaWO_4$ crystals," Phys. Solid State 51, 1886-1893 (2009).

[Vor74] Y. K. Voron'ko, T. G. Mamedov, V. V. Osiko, M. I. Timoshechkin, and I. A. Shcherbakov, "Effect of donor-donor and donor-acceptor interactions on the decay kinetics of the metastable state of Nd^{3+} in crystals," Sov. J. Exp. Theor. Phys. 38, 565 (1974).

[Vor94] Y. K. Voron'ko, N. A. Estkov, S. V. Korolev, A. A. Sobol, and S. N. Ushakov, "Luminescence of activation centers Eu^{3+} in calcium-niobium-gallium garnet crystals," Neorganicheskie Materialy, 30(1), 104-108 (1994).

[Wal00] B. M. Walsh, N. P. Barnes, and B. Di Bartolo, "The temperature dependence of energy transfer between the Tm $^3F_4$ and Ho $^5I_7$ manifolds of Tm-sensitized Ho luminescence in YAG and YLF," J. Lumin. 90(1-2), 39-48 (2000).

[Wal06] B. M. Walsh, "Judd-Ofelt theory: principles and practices," in Advances in Spectroscopy for Lasers and Sensing, B. Di Bartolo and O. Forte, Eds. (Springer, 2006), pp. 403-433.

[Wal08] B. M. Walsh, N. P. Barnes, and R. J. DeYoung, Lanthanide Glass Spectroscopy and Fiber Lasers, Physics and Chemistry of Rare-Earth Ions Doped Glasses (Trans Tech Publications Ltd, 2008).

[Wal09] B. M. Walsh, "Review of Tm and Ho materials; spectroscopy and lasers," Laser Phys. 19, 855-866 (2009).

[Wal96] J. Walker, "Solid Solutions," Sci. Prog. 5(26), 121-132 (1896).

[Wal97] B. M. Walsh, N. P. Barnes, and B. Di Bartolo, "On the distribution of energy between the Tm $^3F_4$ and Ho $^5I_7$ manifolds in Tm-sensitized Ho luminescence," J. Lumin. 75(2), 89-98 (1997).

[Wan00] J. Wang, M. Maiorov, D.S. Baer, D.Z. Garbuzov, J.C. Connolly, and R.K. Hanson, "In situ combustion measurements of CO with diode-laser absorption near 2.3 μm," Appl. Opt. 39, 5579-5589 (2000).

[Wan16] Y. Wang, R. Lan, X. Mateos, J. Li, C. Hu, C. Li, S. Suomalainen, A. Härkönen, M. Guina, V. Petrov, and U. Griebner, "Broadly tunable mode-locked Ho:YAG ceramic laser around 2.1 μm," Opt. Express 24(16), 18003-18012 (2016).

[Wan16a] Y. Wang, G. Xie, X. Xu, J. Di, Z. Qin, S. Suomalainen, M. Guina, A. Härkönen, A. Agnesi, U. Griebner, and X. Mateos, "SESAM mode-locked Tm:CALGO laser at 2 μm," Opt. Mater. Express 6, 131-136 (2016).

[Wan17] Y. Wang, W. Chen, M. Mero, L. Zhang, H. Lin, Z. Lin, G. Zhang, F. Rotermund, Y. J. Cho, P. Loiko, and X. Mateos, "Sub-100 fs Tm:$MgWO_4$ laser at 2017 nm mode locked by a graphene saturable absorber," Opt. Lett. 42(16), 3076-3079 (2017).

[Wan17a] H. Wang, H. Huang, P. Liu, L. Jin, D. Shen, J. Zhang, and D. Tang, "Diode-pumped continuous-wave and Q-switched Tm:Y_2O_3 ceramic laser around 2050 nm," Opt. Mater. Express 7(2), 296-303 (2017).

[Wan18] Y. Wang, Y. Zhao, Z. Pan, J. E. Bae, S. Y. Choi, F. Rotermund, P. Loiko, J. M. Serres, X. Mateos, H. Yu, and H. Zhang, "78 fs SWCNT-SA mode-locked Tm:CLNGG disordered garnet crystal laser at 2017 nm," Opt. Lett. 43(17), 4268-4271 (2018).

[Wan18a] Y. Wang, W. Jing, P. Loiko, Y. Zhao, H. Huang, X. Mateos, S. Suomalainen, A. Härkönen, M. Guina, U. Griebner, and V. Petrov, "Sub-10 optical-cycle passively mode-locked Tm:$(Lu_{2/3}Sc_{1/3})_2O_3$ ceramic laser at 2 μm," Opt. Express 26(8), 10299-10304 (2018).

[Wan20] L. Wang, W. Chen, Y. Zhao, Y. Wang, Z. Pan, H. Lin, G. Zhang, L. Zhang, Z. Lin, J. E. Bae, and T. G. Park, "Single-walled carbon-nanotube saturable absorber assisted Kerr-lens mode-locked Tm:$MgWO_4$ laser," Opt. Lett. 45(22), 6142-6145 (2020).

[Wan20a] Y. Wang, Y. Zhao, Z. Pan, S. Suomalainen, A. Härkönen, M. Guina, U. Griebner, L. Wang, P. Loiko, X. Mateos, and W. Chen, "73-fs SESAM mode-locked Tm,Ho:CNGG laser at 2061 nm," in Solid State Lasers XXIX: Technology and Devices, vol. 11259, pp. 426-431 (SPIE, 2020).

[Wan21] L. Wang, W. Chen, Z. Pan, P. Loiko, J. E. Bae, F. Rotermund, X. Mateos, U. Griebner, and V. Petrov, "Sub-100 fs mode-locked Tm:CLTGG laser," Opt. Express 29(20), 31137-31144 (2021).

[Wan21a] L. Wang, W. Chen, Y. Zhao, P. Loiko, X. Mateos, M. Guina, Z. Pan, M. Mero, U. Griebner, and V. Petrov, "Sub-50 fs pulse generation from a SESAM mode-locked Tm,Ho-codoped calcium aluminate laser," Opt. Lett. 46(11), 2642-2645 (2021).

[Wan22] Y. Wang, P. Loiko, Y. Zhao, Z. Pan, W. Chen, M. Mero, X. Xu, J. Xu, X. Mateos, A. Major, and M. Guina, "Polarized spectroscopy and SESAM mode-locking of Tm,Ho:CALGO," Opt. Express 30(5), 7883-7893 (2022).

[Wan23] Y. Wang, J. Liu, X. Feng, Z. Zhang, Y. Wang, Z. Zhang, F. Ma, J. Liu, and L. Su, "~2.9 μm continuous-wavelength laser operation of fiber-pumped Ho,Pr:CaF_2 single crystals," Opt. Mater. 135, 113329 (2023).

[Web00] M. E. Webber, J. Wang, S. T. Sanders, D. S. Baer, and R. K. Hanson, "In situ combustion measurements of CO, CO_2, H_2O and temperature using diode laser absorption sensors," Proc. Combust. Inst. 28(1), 407-413 (2000).

[Web67] M. J. Weber, Probabilities for radiative and nonradiative decay of Er^{3+} in LaF_3, Phys. Rev. 157 (1967) 262–272.
[Web68] M. J. Weber, "Radiative and multiphonon relaxation of rare-earth ions in Y_2O_3," Phys. Rev. 171(2), 283-291 (1968).
[Wel96] J. P. R. Wells, "Laser spectroscopy of alkaline earth fluoride crystals doped with trivalent samarium and europium ions," Ph.D. dissertation, University of Canterbury (1996).
[Wil51] F. E. Williams and M. H. Hebb, "Theoretical spectra of luminescent solids," Phys. Rev. 84(6), 1181 (1951).
[Wil96] G. D. Wilkins, "Eye-safe free-space laser communications," Proc. IEEE Natl. Aerosp. Electron. Conf. (NAECON), 2, 710-715 (1996).
[Woe97] C. F. Woensdregt, H. W. M. Janssen, A. Gloubokov, and A. Pajaczkowska, "Growth morphology of tetragonal $ABCO_4$ compounds: theory and observations on Czochralski grown crystals," J. Cryst. Growth 171(3-4), 392-400 (1997).
[Woo17] M. Woolman, A. Gribble, E. Bluemke, J. Zou, M. Ventura, N. Bernards, M. Wu, H. J. Ginsberg, S. Das, A. Vitkin, and A. Zarrine-Afsar, "Optimized mass spectrometry analysis workflow with polarimetric guidance for ex vivo and in situ sampling of biological tissues," Sci. Rep. 7, 468 (2017).
[Woo18] R. Woodward, M. Majewski, and S. Jackson, "Mode-locked dysprosium fiber laser: Picosecond pulse generation from 2.97 to 3.30 μm," APL Photonics 3(11), 116106 (2018).
[Xia20] Z. Xiao, S. Yu, Y. Li, S. Ruan, L. B. Kong, Q. Huang, Z. Huang, K. Zhou, H. Su, Z. Yao, and W. Que, "Materials development and potential applications of transparent ceramics: A review," Mater. Sci. Eng. R Rep. 139, 100518 (2020).
[Xie08] G. Q. Xie, D. Y. Tang, H. Luo, H. J. Zhang, H. H. Yu, J. Y. Wang, X. T. Tao, M. H. Jiang, and L. J. Qian, "Dual-wavelength synchronously mode-locked Nd:CNGG laser," Opt. Lett. 33(16), 1872-1874 (2008).
[Xie10] G. Q. Xie, L. J. Qian, P. Yuan, D. Y. Tang, W. D. Tan, H. H. Yu, H. J. Zhang, and J. Y. Wang, "Generation of 534 fs pulses from a passively mode-locked Nd:CLNGG-CNGG disordered crystal hybrid laser," Laser Phys. Lett. 7(7), 483-487 (2010).
[Xio23] Y. Xiong, S. Wang, Z. Chen, X. Sun, H. Liu, Y. Jia, and F. Chen, "Femtosecond laser direct writing of compact Tm:YLF waveguide lasers," Opt. Laser Technol. 167, 109786 (2023).
[Yag07] H. Yagi, T. Yanagitani, K. Takaichi, K. I. Ueda, and A. A. Kaminskii, "Characterizations and laser performances of highly transparent Nd^{3+}:$Y_3Al_5O_{12}$ laser ceramics," Opt. Mater. 29(10), 1258-1262 (2007).
[Yam02] H. Yamamoto, S. Okamoto, and H. Kobayashi, "Luminescence of rare-earth ions in perovskite-type oxides: from basic research to applications," J. Lumin. 100(1-4), 325-332 (2002).
[Yan16] D. Yan, X. Xu, H. Lu, Y. Wang, P. Liu, and J. Zhang, "Fabrication and properties of Y_2O_3 transparent ceramic by sintering aid combinations," Ceram. Int. 42(15), 16640-16643 (2016).
[Yan22] C. Yang, J. Huang, Q. Huang, Z. Deng, Y. Wang, X. Li, Z. Zhou, J. Chen, Z. Liu, and W. Guo, "Optical, thermal, and mechanical properties of $(Y_{1-x}Sc_x)_2O_3$ transparent ceramics," J. Adv. Ceram. 11(6), 901-911 (2022).
[Yao21] S. Yao, S. Lv, and Z. Feng, "Judd-Ofelt analysis of Ho^{3+}-doped $CaYAlO_4$ single crystal," J. Lumin. 238, 118219 (2021).
[Yao22] W. Yao, Y. Wang, S. Tomilov, M. Hoffmann, S. Ahmed, C. Liebald, D. Rytz, M. Peltz, V. Wesemann, and C. J. Saraceno, "8.7-W average power, in-band pumped femtosecond Ho:CALGO laser at 2.1 μm," Opt. Express 30(23), 41075-41083 (2022).
[Yao24] W. Yao, M. Khalili, Y. Wang, M. Hoffmann, M. van Delden, T. Musch, and C. J. Saraceno, "GHz repetition rate, sub-100-fs Ho:CALGO laser at 2.1 μm with watt-level average power," Opt. Lett. 49(6), 1591-1594 (2024).
[Ye22] S. Ye, X. Zhou, S. Huang, H. Nie, J. Bian, T. Li, K. Yang, J. He, and B. Zhang, "Cascade MIR Ho:YLF laser at 2.1 μm and 2.9 μm," Opt. Lett. 47(21), 5642-5645 (2022).
[Yen64] W. M. Yen, W. C. Scott, and A. L. Schawlow, "Phonon-induced relaxation in excited optical states of trivalent praseodymium in LaF_3," Phys. Rev. 136(1A), A271 (1964).
[Yin17] K. Yin, B. Zhang, L. Yang, and J. Hou, "15.2 W spectrally flat all-fiber supercontinuum laser source with >1 W power beyond 3.8 μm," Opt. Lett. 42(12), 2334-2337 (2017).

[Yor18] I. Yorulmaz and A. Sennaroglu, "Low-threshold diode-pumped 2.3-μm Tm^{3+}:YLF lasers," IEEE J. Sel. Top. Quantum Electron. 24, 2791409 (2018).

[Yu22] X. Yu, H. Chu, F. Zha, H. Pan, S. Zhao, Z. Pan, and D. Li, "Watt-level diode-pumped Tm:YVO_4 laser at 2.3 μm," Opt. Lett. 47(21), 5501-5504 (2022).

[Yu24] X. Yu, F. Zha, Z. Pan, H. Chu, H. Pan, and D. Li, "Diode-pumped Tm:YAP laser operating at 2.3 μm with enhanced performance through cascade lasing," Opt. Express 32(3), 3461-3469 (2024).

[Yua21] J. Yuan, W. Wang, Y. Ye, T. Deng, Y. Huang, S. Gu, Y. Chen, and P. Xiao, "2.0 μm ultra broadband emission from Tm^{3+}/Ho^{3+} co-doped gallium tellurite glasses for broadband light sources and tunable fiber lasers," Crystals 11(2), 190 (2021).

[Yum02] K. V. Yumashev, I. A. Denisov, N. N. Posnov, N. V. Kuleshov, and R. Moncorge, "Excited state absorption and passive Q-switch performance of Co^{2+} doped oxide crystals," J. Alloys Compd. 341(1-2), 366–370 (2002).

[Zav93] Y. D. Zavartsev, V. V. Osiko, S. G. Semenkov, P. A. Studenikin, and A. F. Umyskov, "Cascade laser oscillation due to Ho^{3+} ions in a (Cr, Yb, Ho):YSGG yttrium-scandium-gallium garnet crystal," Quantum Electron. 23(4), 312-316 (1993).

[Zel10] D. E. Zelmon, J. M. Northridge, J. J. Lee, K. M. Currin, and D. Perlov, "Optical properties of Nd-doped rare-earth vanadates," Appl. Opt. 49(26), 4973-4978 (2010).

[Zel13] D. E. Zelmon, J. M. Northridge, N. D. Haynes, D. Perlov, and K. Petermann, "Temperature-dependent Sellmeier equations for rare-earth sesquioxides," Appl. Opt. 52, 3824-3828 (2013).

[Zen24] H. J. Zeng, W. Z. Xue, R. T. Murray, C. Cui, L. Wang, Z. Pan, P. Loiko, X. Mateos, F. Yuan, G. Zhang, and U. Griebner, "In-band pumped Kerr-lens mode-locked Tm,Ho-codoped calcium aluminate laser," Opt. Express 32(9), 16083-16089 (2024).

[Zha15] Y. Zhang, V. Petrov, U. Griebner, X. Zhang, H. Yu, H. Zhang, and J. Liu, "Diode-pumped SESAM mode-locked Yb:CLNGG laser," Opt. Laser Technol. 69, 144-147 (2015).

[Zha18] J. Zhang, K. F. Mak, and O. Pronin, "Kerr-lens mode-locked 2-μm thin-disk lasers," IEEE J. Sel. Top. Quantum Electron. 24(5), 1-11 (2018).

[Zha18a] Y. Zhang, B. Chen, S. Xu, X. Li, J. Zhang, J. Sun, X. Zhang, H. Xia, and R. Hua, "A universal approach for calculating the Judd–Ofelt parameters of RE^{3+} in powdered phosphors and its application for the β-$NaYF_4$:Er^{3+}/Yb^{3+} phosphor derived from auto-combustion-assisted fluoridation," Phys. Chem. Chem. Phys. 20(23), 15876-15883 (2018).

[Zha18b] Y. Zhao, Y. Wang, X. Zhang, X. Mateos, Z. Pan, P. Loiko, W. Zhou, X. Xu, J. Xu, D. Shen, and S. Suomalainen, "87 fs mode-locked Tm,Ho:$CaYAlO_4$ laser at ~2043 nm," Opt. Lett. 43(4), 915-918 (2018).

[Zha19] Y. Zhao, Y. Wang, W. Chen, Z. Pan, L. Wang, X. Dai, H. Yuan, Y. Zhang, H. Cai, J. E. Bae, and S. Y. Choi, "67-fs pulse generation from a mode-locked Tm,Ho:CLNGG laser at 2083 nm," Opt. Express 27(3), 1922-1928 (2019).

[Zha20] Y. Zhao, L. Wang, W. Chen, Z. Pan, Y. Wang, P. Liu, X. Xu, Y. Liu, D. Shen, J. Zhang, and M. Guina, "SESAM mode-locked Tm:$LuYO_3$ ceramic laser generating 54-fs pulses at 2048 nm," Appl. Opt. 59(33), 10493-10497 (2020).

[Zha21] Y. Zhang, S. Li, X. Du, J. Guo, Q. Gong, S. Tao, P. Zhang, Q. Fang, S. Pan, C. Zhao, X. Liang, and Y. Hang, "Yb:$GdScO_3$ crystal for efficient ultrashort pulse lasers," Opt. Lett. 46(15), 3641–3644 (2021).

[Zha21a] Y. Zhao, L. Wang, W. Chen, P. Loiko, Y. Wang, Z. Pan, H. Yang, W. Jing, H. Huang, J. Liu, and X. Mateos, "Kerr-lens mode-locked Tm-doped sesquioxide ceramic laser," Opt. Lett. 46, 3428-3431 (2021).

[Zha21b] D. Zhang, W. Lin, Z. Lin, L. Jia, W. Zheng, and F. Huang, "Lu_2O_3: A promising ultrawide bandgap semiconductor for deep UV photodetector," Appl. Phys. Lett. 118(21), 211906 (2021).

[Zha22] N. Zhang, S. Liu, Z. Wang, J. Liu, X. Xu, J. Xu, J. Wang, P. Liu, J. Ma, D. Shen, D. Tang, H. Lin, J. Zhang, W. Chen, Y. Zhao, U. Griebner, and V. Petrov, "SESAM mode-locked Tm:Y_2O_3 ceramic laser," Opt. Express 30(16), 29531-29538 (2022).

[Zha22a] F. Zha, X. Yu, H. Chu, H. Pan, S. Zhao, P. Loiko, Z. Pan, and D. Li, "Compact diode-pumped continuous wave and passively Q-switched Tm:YAG laser at 2.33 μm," Opt. Lett. 47(23), 6265-6268 (2022).

[Zha23] N. Zhang, Q. Song, J. Zhou, J. Liu, S. Liu, H. Zhang, X. Xu, Y. Xue, J. Xu, W. Chen, and Y. Zhao, "44-fs pulse generation at 2.05 μm from a SESAM mode-locked Tm:$GdScO_3$ laser," Opt. Lett. 48(2), 510-513 (2023).

Matériaux à large bande d'émission dopés avec des ions thulium et holmium pour des lasers à l'état solide à 2 µm et au-delà.

Résumé

De nouveaux matériaux inorganiques actifs au laser, dopés avec des ions de thulium et d'holmium, ont été étudiés pour leur potentiel dans les lasers à accord large et ultrarapides fonctionnant dans la gamme spectrale infrarouge à ondes courtes de 2 à 3 µm. Les lasers émettant dans cette gamme spectrale trouvent de nombreuses applications, notamment dans les systèmes de télédétection par laser, la détection de gaz et la médecine. Ils sont utilisés comme systèmes amplificateurs pour la génération d'harmoniques d'ordre élevé, la génération de térahertz, et la conversion ultérieure de fréquence dans la région infrarouge moyen.

La présente thèse de doctorat établit des relations entre les propriétés structurelles des matériaux cristallins d'oxydes et de fluorures, sous forme de monocristaux et de céramiques transparentes, et les propriétés spectroscopiques des ions dopants de thulium et d'holmium, ainsi que leurs caractéristiques laser, qui sont essentielles pour le développement des lasers. De plus, les processus physiques sous-jacents à un comportement laser inattendu sont révélés. Cette étude systématique des matériaux laser permet d'identifier les compositions les plus prometteuses pour le développement de lasers à large accordabilité et à impulsions ultracourtes.

Cette étude se concentre principalement sur des matériaux présentant un élargissement spectral inhomogène significatif, se traduisant par des spectres d'absorption et d'émission larges et sans structure des ions dopants. Afin de promouvoir cet effet, plusieurs stratégies ont été envisagées, notamment l'agrégation d'ions de terres rares, le désordre de la structure locale, le désordre de composition dans les composés à solution solide et les bandes latérales de phonons résultant des interactions électron-phonon.

Mots-clés : ions de thulium et d'holmium ; spectroscopie optique ; luminescence ; transfert d'énergie ; élargissement inhomogène des raies spectrales ; interaction électron-phonon ; matériaux laser ; sesquioxydes ; céramiques transparentes ; solutions solides ; lasers à l'état solide.

Broadband emitting materials doped with thulium and holmium ions for solid-state lasers at 2 µm and beyond

Abstract

Novel laser-active inorganic materials doped with thulium and holmium ions have been investigated for their potential in broadly tunable and ultrafast lasers operating in the short-wave infrared spectral range of 2 to 3 µm. Lasers emitting within this spectral range find numerous applications, including light detection and ranging systems, gas sensing, medicine. They are used as amplifying systems for high harmonic generation and terahertz generation, and further frequency conversion into the mid-infrared region.

The present PhD thesis establishes relationships between the structural properties of oxide and fluoride crystalline materials, in the form of single crystals and transparent ceramics, and the spectroscopic properties of thulium and holmium dopant ions, along with their laser characteristics, which are essential for laser development. Moreover, the physical processes underlying unexpected laser behaviour are revealed. This systematic study of laser materials allows for the identification of the most promising compositions for the development of broadly tunable and ultrashort pulse lasers.

This study mainly focuses on materials that exhibit significant inhomogeneous spectral line broadening, resulting in broad and structureless absorption and emission spectra of the dopant ions. In order to promote this effect, several strategies have been considered, including rare-earth ion clustering, local structure disorder, compositional disorder in solid-solution compounds, and phonon-sidebands arising from electron-phonon interactions.

Keywords: thulium and holmium ions; optical spectroscopy; luminescence; energy transfer; inhomogeneous spectral line broadening; electron-phonon interaction; laser materials; sesquioxides, transparent ceramics; solid-solutions; solid-state lasers.